The CoRoT

The adventure of the ultra high precision photometry from space

Legacy Book

by the CoRot Team. Coordination Annie Baglin

edp sciences

The CoRoT Legacy Book

"This book is dedicated to all the people interested in the CoRoT mission and the beautiful data that were delivered during its six year duration.

Either amateurs, professional, young or senior researchers, they will find treasures not only at the time of this publication but also in the future twenty or thirty years.

It presents the data in their final version, explains how they have been obtained, how to handle them, describes the tools necessary to understand them, and where to find them. It also highlights the most striking first results obtained up to now. CoRoT has opened several unexpected directions of research and certainly new ones still to be discovered."

ISBN 978-2-7598-1876-1

The CoRoT

The adventure of the ultra high precision photometry from space

Legacy Book

by the CoRot Team. Coordination Annie Baglin

edp sciences

Printed in France
ISBN 978-2-7598-1876-1

Cover design and advertising by Patrice Amoyel - www.imago-toulouse.com

The CoRoT Legacy Book

DOI: 10.1051/978-2-7598-1876-1.c001

Foreword

This book, entitled "The CoRoT Legacy Book", is dedicated to all the people interested in the CoRoT mission and the beautiful data that were delivered during its six-year duration. Either amateurs, professional, young or senior researchers find treasures not only at the time of this publication but also in twenty or thirty years ahead.

It presents the data in their final version, explains how they have been obtained, how to handle them, describes the tools necessary to understand them, and where to find them. It also highlights the most striking first results obtained up to now. CoRoT has opened several unexpected directions of research and certainly new ones still to be discovered.

The book consists in 5 Parts, divided into chapters which can be used and also downloaded separately.

Part I recalls the successive steps followed by the scientists and shows that it took a long time to promote this new domain of ultra-high precision and long-duration stellar photometry from space. As it was indeed rapidly understood that this type of research could only be done from space, this domain entered the wild competition of space mission selection. Fortunately, however, this long period of maturation brought about several selections in different countries and opened the way for future more ambitious projects, as described in Part V.

Part II is dedicated to the data themselves. Chapter 1 presents the observing program achieved over the 6 yr of operation, the choice of the regions to be observed, the target selection and the tunings of the instrumental settings, very important indeed to understand the data.

Chapters 2 and 3 describe the successive steps of correction necessary to get rid of the spurious instrumental perturbations, and to obtain the required precision, which has largely overpassed the requirements. Chapter 4 explains how to use the "Ready to use" N2 data, and Chapter 5 where to find them.

Parts III and IV enlighten several major results, in the main directions, addressed by CoRoT:

- the exoplanet-hunting program presented in Part IV with not only the detection of planetary transits, but also the deep characterization of the planets thanks to intensive complementary ground-based observations and their joined analysis;
- star-planet interaction: a new direction of research, initiated by CoRoT but still in its infancy;
- stellar physics: use of the seismology technique to obtain information on the internal structure of the stars under scrutiny but also on their rotation;
- stellar activity and environment: interpretation of the new information from the time-domain photometry;
- ensemble asteroseismology: an entirely new approach of the chemical evolution of our Galaxy.

Part V outlines the major lessons learned on technical as well as managerial domains, and how they have been used to define new projects, thanks to this mission.

The influence of the results of CoRoT on the scientific priorities of the exoplanet and stellar community has been very important, it is emphasized in Chapter 2, and finally Chapter 3 describes the projects of the immediate future.

Enjoy the CoRoT data!

Acknowledgements

The CoRoT adventure has been possible because it was a collective work, done by many different people, engineers, administrators, technicians, scientists.
They all have devoted enormous efforts, their enthusiasm and their skills over the years for the success of this project.

The CoRoT world thanks all its supportive organizations:

The French space agency, CNES, who took the risk of this adventure, and supported it throughout its life. The European Space Agency and the Space agencies of Austria, Belgium, Brazil, Germany, Spain

Ministries of Research, Astronomical societies, academies… of the participating countries

And the many supportive colleagues all around the world.

This book is the last collective publication of the CoRoT Team.

The CoRoT space mission has been developed and operated by CNES, with the contribution of Austria, Belgium, Brazil, ESA, Germany, and Spain.

Contents

Part I. The advent of long duration, ultra-high precision photometry of stars from space

Part II. The CoRoT legacy data

Part III. Major scientific achievements in planetary science

Part IV. Decisive breakthroughs for stellar physics

Part V. CoRoT paved the road to the future

Part I

The advent of long duration, ultra-high precision photometry of stars from space

The CoRoT Legacy Book

DOI: 10.1051/978-2-7598-1876-1.c010

Part I

The advent of long duration, ultra-high precision photometry of stars from space

This Part describes the successive steps of the adventure of Ultra High stellar photometry from space from its first attempts up to CoRoT and *Kepler*, and in the different pioneer countries around the world.

The future missions, many of them paying some heritage to CoRoT, are presented in Part V.

The CoRoT Legacy Book

DOI: 10.1051/978-2-7598-1876-1.c011

I.1

The general framework

A. Baglin

LESIA, Observatoire de Paris, PSL Research University, CNRS, Sorbonne Universités, UPMC Univ. Paris 06, Univ. Paris Diderot, Sorbonne Paris Cité, 5 place Jules Janssen, 92195 Meudon, France

It has been recognized since the early days of Astronomy, that the brightnesses of some cosmic objects, stars in particular, were not constant. The observation interpretation and application of those changes became a permanent preoccupation of astronomers.

The recognition, in the sixties, of the oscillations of the Sun – a seemingly ordinary star – and their application as a "window" into the otherwise hidden interior of the Sun, transformed the subject of stellar photometry.

Solar seismology from space was proposed as early as 1982 and has become a powerful tool to understand our home star.

The first experiment in space, called IPHIR, flew on the Soviet Mars missions PHOBOS 1 and 2 with successful results almost 30 years ago (Froehlich et al. 1991; Toutain et al. 1993). As a consequence, helioseismology became one of three main objectives of ESA's first Horizon 2000 Cornerstone mission SOHO (Solar and Heliospheric Observatory), which was launched in 1995 and that recently received funding for its continued operation until at least the end of 2016 (originally designed for a 2-year lifetime!).

Then, the need to study accurately stellar activity and variability of stars other than the Sun started to be promoted as the new challenge for stellar physics.

In the early eighties, stellar astronomers began to see the incredible potential of extending the techniques of solar seismology to other stars. They also recognized the incredible challenge of detecting Sun-like oscillations in distant stars.

In observing stellar variability, and in particular solar-like oscillations, there are three major requirements: (1) long duration of the time series of data on the same target; (2) the highest possible duty cycle (i.e. continuous or nearly continuous coverage, with very few gaps; and (3) the highest possible photometric precision.

For decades and even centuries, this field had two natural enemies associated with the Earth: the variable transparency of the atmosphere, and the rotation and orbit of our planet (daily sunrises ending nightly data collection, and seasonal changes in what part of the sky are above the horizon at night).

The combination of the demands of stellar seismology and the natural limitations of ground based observations called for a new class of instrumentation and a new vantage point for those instruments.

That vantage was space!

Space astronomy was already underway, but the focus was on accessing wavelengths unobservable from the Earth, namely infra-red and ultra-violet.

The objective of monitoring bright stars from space at visible wavelength and continuously was poorly understood at the beginning. It took a long time to convince the space astronomy community of the importance of such observations. It took even longer to convince the community that such observations were even possible with existing technology.

So many people, in so many countries, dedicated so many years of their lives to demonstrate that ultra-high-precise photometry of stars from space could go from dream to reality.

At the beginning, the scientific objectives were purely stellar, but double: activity and oscillations. Then, the enormous success of helioseismology lead to focus more on oscillations. Finally a major discovery entered the game: the observation of the first extra solar planet, and the immediate conclusion that Ultra High Precision of stars will also be a way to discover small planets through shallow transit signals in photometry from space.

Exoplanetology became a challenging issue. This new perspective added another compelling reason for long duration, continuous, and ultra precise photometry from space and increased significantly the scientific community interested in.

Then after recognizing that such observations were feasible from space, many ideas of space missions have been proposed and discussed in the astronomical community.

The two most ambitious projects were first conceived in the early 1980s: CoRoT in Europe (lead by France,) and Kepler in the United States. In the late 1990s, Canada entered the field with a smaller but effective microsatellite project called MOST.

All these initiatives lead to successful missions.

References

Froehlich, C., Toutain, T., & Schrijver, C. J. 1991, Adv. Space Res., 11, 69

Toutain, T., & Froehlich, C. 1993, ASP Conf. Ser., 40, 713

Acknowledgements: The CoRoT space mission has been developed and operated by CNES, with the contribution of Austria, Belgium, Brazil, ESA, Germany, and Spain.

The CoRoT Legacy Book

DOI: 10.1051/978-2-7598-1876-1.c012

I.2

Seeds take root in Europe

M. Fridlund[1, 2] and I. Roxburgh[2.3]

[1] Department of Earth and Space Sciences, Chalmers University of Technology, Onsala Space Observatory, 439 92 Onsala, Sweden
[2] Leiden Observatory, University of Leiden, PO Box 9513, 2300 RA, Leiden, The Netherlands
[3] Astronomy Unit, School of Physics and Astronomy, Queen Mary University of London, Mile End Road, London E1 4NS, UK

The first ideas were discussed near Ussel (Corrèze, France) in 1981, during an unformal meeting devoted to solar and stellar activity, attended by a small group of scientists interested in stellar magnetism. It is there that the idea of dedicating a small satellite for monitoring stellar activity was born, taking advantage of both the UV access from space, and the possibility to perform long uninterrupted observations. Philippe Lemaire started immediately to draft the design of a simple spectrograph for monitoring simultaneously various lines probing stellar activity at various heights in stellar atmospheres. A month later, in June 1981, another meeting took place in Paris, with the goal of defining in more details the project born in Ussel.

By the late 1970s, helioseismology was a rapidly maturing field and some astronomers saw the advantage of introducing photometry to monitor simultaneously stellar oscillations and stellar activity. This coupling of seismology and activity studies within the same experiment drove most of the proposals that were made in the following years.

In 1982 the French team submitted the first proposal to CNES for a space mission EVRIS (Mangeney et al. 1982) and received funding to develop the concept. The same team submitted the project (renamed PSIVA) in response to a call for ideas from ESA, and as a possible experiment on the Space Station but these were not successful.

Then, an international colloquium organised by Françoise Praderie and André Mangeney at Paris Observatory (Meudon) in 1984 called "Space Research Prospects in Stellar Activity and Variability" gathered a world wide community of 60 participants (Praderie & Mangeney 1984) (Fig. I.2.1). It confirmed the wide and international interest for asteroseismology and stellar activity from space, and can be considered as the cornerstone of this field.

Almost simultaneously, the American community held also a workshop *Improvements in photometry*, held at San Diego in June 18–19 1984 organised by W. Borucki from NASA Ames, confirming the international interest of this new domain.

The first sketches of an instrument were designed by French space laboratories in France (Observatoire de Paris and Laboratoire d'Astrophysique de Marseille). It kicked off a long quest to find a flight opportunity for this instrument, during which many options were pursued.

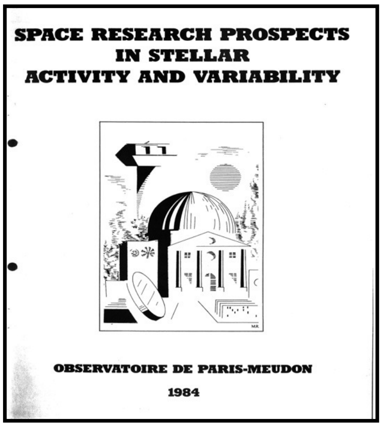
SPACE RESEARCH PROSPECTS
IN STELLAR
ACTIVITY AND VARIABILITY

OBSERVATOIRE DE PARIS-MEUDON
1984

Fig. I.2.1. Cover page of the book of contributions of the colloquium : Space research projets in stellar activity and variability. © Observatoire de Paris

The PRISMA project has been submitted by an international team in response to a call for proposals from ESA (Praderie et al. 1985). It was a dedicated mission combining the two objectives of variability and activity. It was considered for a feasibility study, at ESA, but not selected. It was also proposed to ESA as a possible experiment on the Eureka B platform, but Eureka B was cancelled.

The EVRIS/PSIVA project was studied as a possible experiment to be installed on the interplanetary spacecraft VESTA, a USSR mission to Venus (Praderie et al. 1984) but the mission was cancelled. It was also proposed as an add-on experiment on SOHO (Praderie et al. 1987a) but rapidly rejected as being incompatible with the solar operations.

1. The EVRIS step

EVRIS (Etude de la Variabilité, de la Rotation et des Intérieurs Stellaires) was proposed first by Mangeney et al. (1982), then by Baglin et al. (1988/89) and Praderie et al. (1987b) and was selected to fly on board the USSR mission MARS 92 (which became MARS 96) in the framework of the French-Soviet Space Collaboration.

(a) The EVRIS instrument. © CNES

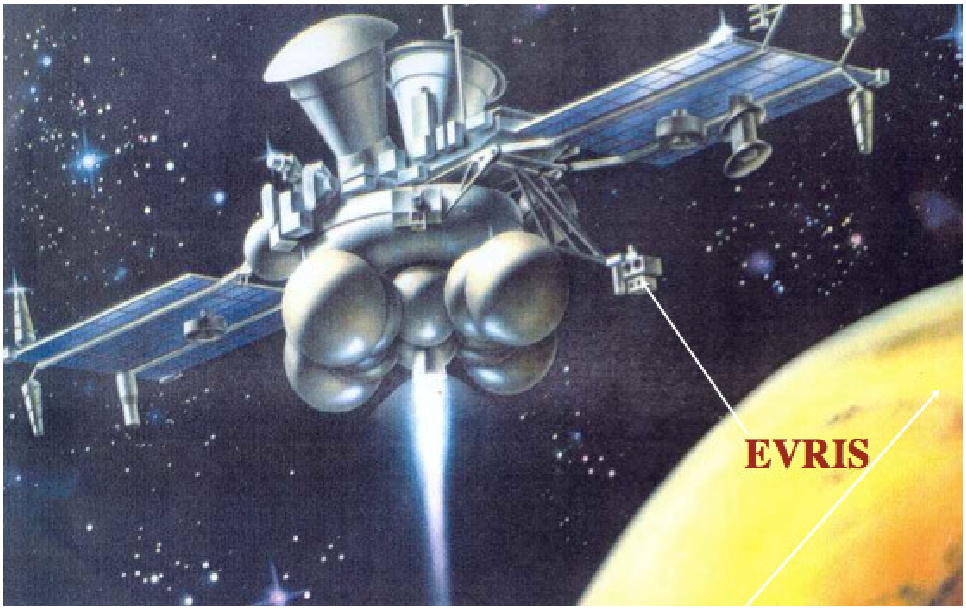

(b) Artistic view of the MARS 96 space craft and the position of EVRIS/PAIS. © pages.erau.edu/~ericksol/courses/sp425/s2003/mars.html

Fig. I.2.2. EVRIS experiment onboard MARS 96.

It was dedicated to stellar seismology and has been designed to observe about 10 of very bright stars (visual magnitude smaller than 6) 20 days each during the 9 months of the cruise to Mars (Michel et al. 1995).

The instrument was a small 9 cm diameter telescope, associated to a stellar sensor for pointing (Vuillemin et al. 1998; Buey et al. 1997; Weiss et al. 1998).

The detector was a photomultiplier built by Hamamatsu (at that time CCDs were not space qualified). The optics was designed to form the image of the entrance pupil on the photocathod of the detector, to gather almost all the stellar photons (Fig. I.2.2a).

It was fixed on a Russian platform PAIS, in charge of the precise pointing, and installed under the solar panels of the spacecraft (Fig. I.2.2b).

Due to political and financial difficulties in Russia, the launch was postponed and the mission became MARS 96.

After a successful launch by a PROTON rocket on October 16th 1996, from the space centre of Baïkonour, it performed three orbital Earth revolutions and due to a failure of the motors in charge of the injection on a Mars trajectory, the whole 6-tons spacecraft and its 46 experiments, including EVRIS, disintegrated in the upper Earth atmosphere above Chile and Bolivia.

2. Attempts in the ESA Horizon 2000 programme

Horizon 2000, the scientific programme of ESA during the years 1985/2000, was the first international space programme in which solar and stellar seismology was seriously considered. This programme consisted of 4 "corner-stones", very large missions and 4 medium size missions.

Several stellar seismology proposals were submitted in response to calls for the medium size mission (M-missions) part of the programme during these years.

The first of these was a second much superior version of PRISMA (Lemaire et al. 1989), which was covering seismology and activity (the latter in the UV). It was first assessed and then selected for a Phase A study (Appourchaux et al. 1993) but in the end, it was not chosen for flight. It lost in competition with the Integral gamma- and X-ray mission launched in 2002.

At the next call for M-mission proposals, in 1993 for a flight opportunity in 2002/2003, the STARS mission (Lemaire et al. 1992; Fridlund et al. 1995) was selected for further study. Initially it had objectives analogous to PRISMA, so that the definition phase started running at full speed.

Then in November 1995 came the stunning announcement that an actual exoplanet, orbiting the solar type star 51 Pegasi had been discovered (Mayor & Queloz 1995) and it was rapidly understood that this stellar mission can be used to simultaneously search for transiting exoplanets. This was an incredible game changer and STARS suddenly began to catch up. Even more, the 51 Pegasi b planet and the next few planets discovered before April 1996 demonstrated that STARS would find a large number of planets and also very easily. It was clear that a category of planets, the "hot Jupiters" that had been discounted by most theoreticians (except Struve 1952), was present in numbers large enough for STARS to find and study many.

It took a minimum of time and effort to implement an additional layer in the study taking the planet finding aspect into account. This led ESA to commission industry to study the exoplanetary requirements of what in principle was a large telescope (STARS the same size as Kepler later became – i.e. a one-meter class telescope) flying in space with an attached spacecraft bus. The two most stringent requirements imposed by adding a planet finding element were to achieve an as large field of view as possible, and a very high pointing stability. The optical design was a triply reflecting 1-m telescope with, a 1.5 deg^2 field designed by M. Badiali (Badiali & Amoretti 1997) (Fig. I.2.3). The jitter requirements have been controllable in a way analogous to the one used onboard CoRoT.

This actually saved STARS that was in competition with what eventually became the PLANCK mission for another few years. The final selection of which mission to fly was to be in April 1996, and STARS was trailing in the opinion polls behind PLANCK.

Nevertheless, STARS lost the game against PLANCK, by only one vote, in April 1996. However, the topics of asteroseismology and exoplanetology were here to stay.

At the next call for mission opportunities, issued by ESA, the EDDINGTON mission was proposed by Ian Roxburgh, Jørgen Christensen-Dalsgaard and Fabio Favata (Fig. I.2.4) (Roxburgh et al. 2000). It was selected as a "reserve mission" in 2000, approved in 2002 and put into development (the CCD detectors began to be manufactured).

EDDINGTON was designed, after MOST and CoRoT, to perform an extensive and far-reaching survey, beginning in 2008. The EDDINGTON payload was a wide-field, high-accuracy optical photometer, and it was characterised by its simplicity and robustness. Thanks to its large field of view, EDDINGTON could acquire data simultaneously on a very large number of targets: high-time-resolution asteroseismic data would have been collected on about 50 000 stars, while planetary transits would have been searched for on about 500 000 stars.

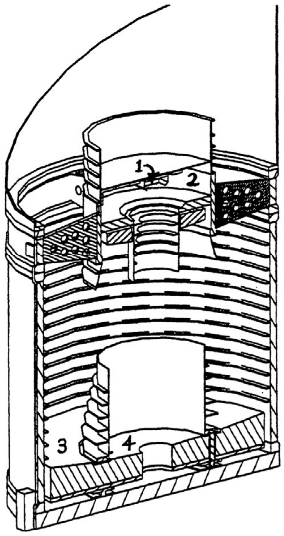

Fig. I.2.3. An exploded view of the payload of STARS. © ESA. The numbers refer to: 1) location of the photometric detector; 2) location of the second instrument: Lyman Alpha Monitor (LAM); 3) Outer section of the main mirror; 4) inner section of the main mirror.

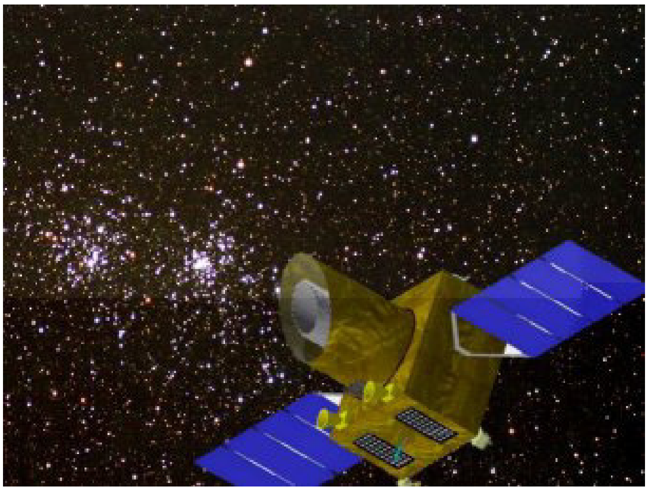

Fig. I.2.4. Artistic view of the Eddington project. © ESA.

The launch vehicle was to be a Soyuz-Fregat rocket launched from the Baïkonour Cosmodrome, and the mission was to be deployed at the L2 Lagrangian point, where it would have stayed for the planned 5-year mission length.

It was cancelled in 2004 for financial reasons (Roxburgh 2006). By that time, CoRoT, although a less ambitious mission, had stepped up to the starting line.

Finally, this long list of rejected proposals to ESA ended with the selection of their ambitious successor PLATO, provisionally scheduled for launch in 2024 (see Part V.3 of this book).

3. MONS in Denmark

MONS was a project proposed by Danish laboratories, to an answer to a call for the Danish Small Satellite Mission,

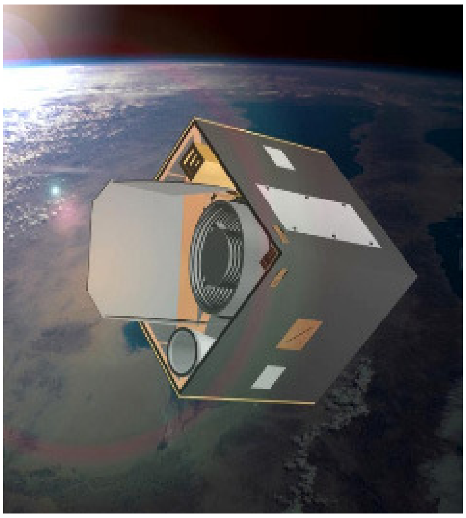

Fig. I.2.5. Artistic view of the MONS satellite. © DSRI, www.space.aau.dk.

as the main instrument on the ROEMER satellite, a small, low cost bus with only one payload and a strong cooperation between industry, universities, and research organisation (Fig. I.2.5)

Its primary objective was to observe the oscillations of 20 solar type stars, during one month (Kjeldsen et al. 2003).

The telescope was a 32-cm reflector, working in optical, and would be launched in an elliptical high apogee orbit. The detailed design phase started in June 2001, for a launch in 2004. But finally the project was not selected.

References

Appourchaux, T., Fridlund, M., Cornelisse, J., & Volonté, S. 1993, ESA J., 17, 239

Badiali, M., & Amoretti, M. 1997, ApOpt, 36, 8877

Baglin A., Mangeney, A., Vuillemin A., & Bisnovatyi- Kogan G., 1988/89, EVRIS: Etude de la Variabilité, de la Rotation et des Intérieurs Stellaires. Proposal for an experiment to use the cruise time on Mars94

Buey, J. T., Auvergne, M., Vuillemin, A., & Epstein, G. 1997, PASP, 109, 140

Fridlund, M., Gough, D., Jones, A., et al. 1995, ASPS Conf. Ser., 76, 41

Kjeldsen, H., Christensen-Dalsgaard, J., & Bedding, T. R. 2003, Adv. Space Res., 31, 363

Lemaire, P., Catala, C., Christensen-Dalsgaard, J., et al. 1989, PRISMA, A Proposal to Study the Microvariability and Activity of Stars from Space. submitted to ESA in response to the call for proposals for the M2 mission

Lemaire, P., Appourchaux, T., Jones, A., et al. 1992, ASP Conf. Ser., 26, 643

Mangeney, A., Baglin, A., Le Contel, J. M., et al. 1982, Projet de mission spatiale pour l'étude de la variabilité et de l'activité des étoiles: EVRIS (Etude de la Variabilité, de la Rotation et des Intérieurs Stellaires) Proposal to CNES

Mayor, M., & Queloz, D. 1995, Nature, 378, 355

Michel, E., Goupil, M. J., Cassisi, S., et al. 1995, ESA SP, 376b, 543

Praderie, F., & Mangeney, A. 1984, Space Research Prospects in Stellar Activity and Variability, Publ. Obs. Paris

Praderie, F., Mangeney, A., & Lemaire, P. 1984, On the PSIVA approach to stellar seismology and activity from space, Adv. Space Res., 4, 163

Praderie, F., Christensen-Dalsgaard Hammer, J. R., Isaak, G., et al. 1985, PRISMA: Probing Rotation and the Interiors of Stars by means of Microvariability and Activity, proposal to ESA

Praderie, F., Mangeney, A., Vuillemin, A., et al. 1987a, EVRIS/ SOHO: Stellar seismology on SOHO. Proposal to ESA

Praderie, F., Combes, M., Cruvellier, P., et al. 1987b, EVRIS, an experiment to use the cruise time on an interplanetary spacecraft, French-Soviet collaboration, CNES and IKI

Praderie, F., Mangeney, A.,Lemaire, P., Puget, P., & Bisnovatyi-Kogan, G. 1988, Prospects for Stellar seismology onboard an interplanetary spacecraft, IAU Symp. 123, 549

Roxburgh, I. W., Favata, F., Christensen-Dalsgaard, J., et al. 2000, Eddington – A Stellar Physics and Planet Finder Explorer. Proposal submitted to ESA in response to the ESA F2/F3 call for proposals

Roxburgh, I. W. 2006, ESA SP, 1306, 521

Struve, O. 1952, The Observatory, 72, 199

Vuillemin, A., Tynok, A., Baglin, A., et al. 1998

Weiss, W.W., Auvergne, M., Repin, S., Bisnovatyi-Kogan, G. 1998, ExAstr 8, 257

Acknowledgements: The CoRoT space mission has been developed and operated by CNES, with the contribution of Austria, Belgium, Brazil, ESA, Germany, and Spain.

The CoRoT Legacy Book

DOI: 10.1051/978-2-7598-1876-1.c013

I.3

The CoRoT story

A. Baglin[1], T. Lam-Trong[2], O. Vandermarcq[2], C. Donny[2], and S. Burgaud[2]

[1] LESIA, Observatoire de Paris, PSL Research University, CNRS, Sorbonne Universités, UPMC Univ. Paris 06, Univ. Paris Diderot, Sorbonne Paris Cité, 5 place Jules Janssen, 92195 Meudon, France
[2] CNES, Centre spatial de Toulouse, 18 avenue Edouard Belin, 31 401 Toulouse Cedex 9, France

As this book is devoted to the global legacy of CoRoT, this chapter called "the CoRoT story", is essentially historical. It recalls how it was a long process full of unexpected events and surprises, during all the phases of the project.

The major events of the prelaunch phase were developed in the "CoRoT book" (Baglin et al. 2006), and are not repeated here.

The technical details of the in-flight operations are described in Part II, Chap. 1.

1. CoRoT 1: a second generation after EVRIS

The CoRoT story started a very long time ago, as, even before the crash of EVRIS, the seismology community already thought about a more ambitious mission, which would be able to do seismology on a variety of stars with very high precision.

A call for ideas issued by CNES in 1993 for scientific missions of small size, called "petites missions", gave to the French scientists the opportunity to propose and launch rapidly, an instrument called CoRoT, more ambitious than EVRIS, devoted to the study of stellar COnvection and internal ROTation. The project was presented at the GONG'94 meeting at Los Angeles on May 16th (Catala et al. 1995).

The scientific objectives of this second generation mission were intermediate between EVRIS and STARS (see. Chap. I.2), the more ambitious mission studied at ESA.

The goal was to provide very high precision measurements of oscillation mode frequencies, for 5 to 7 bright solar-type and F-type stars, to extract new "seismic" indexes: large and small separation of p-modes to obtain constraints for models of internal structure, second order differences to access the physics of convective transport, mode amplitudes and lifetimes to understand the energetics of the excitation mechanism, rotational splitting to start to measure the internal rotation.

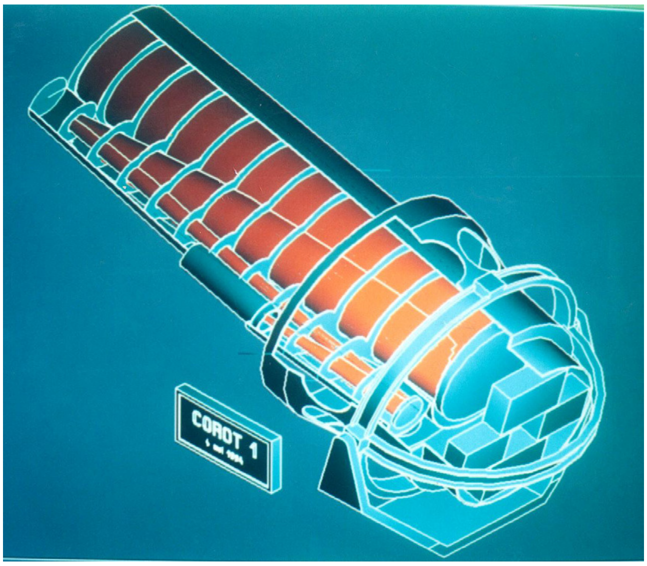

Fig. I.3.1. The design of CoRoT 1, © Laboratoire d'Astronomie Spatiale, Marseille.

These objectives required some technical improvements:

- increase of the photometric accuracy, by increasing the diameter of the telescope (25 cm instead of 9) (Fig. I.3.1);
- increase the duration of the observations leading to more accurate frequency measurements.

Two solutions were proposed for the orbit: either LEO at 800 km, allowing 5 months observations of stars close to the equatorial plane, or a GTO at 36 000 km increasing the number of accessible targets but also the cost!

In addition, the design proposed to test in space conditions, the CCDs detectors, which became available for space uses, in a control camera used essentially as a stellar sensor for the AOCS.

CNES selected the project at the end of 1994 for a launch as early as 1998!

2. The final CoRoT

Two unexpected but major events changed completely the scope of the mission: the failure of EVRIS, CoRoT becoming a first generation mission, and the discovery of the first extrasolar planet in 1995. Indeed, the technical requirements to detect transits of extrasolar planets, even of small sizes, would be quite similar to seismology ones.

This led the project to propose a second version of CoRoT, able to do both seismology and planet search.

Administrative and financial problems have paved the period between the preselection and the final decision from 1995 to 2003.

In 1998, the French Ministry of Research asked for an international blessing and financial contribution. ESA Science Programme as well as Austria, Belgium, Brazil, Germany and Spain decided to contribute to the project, giving to CoRoT an European and even wider impact. This interest of a large scientific community to the project probably helped the final selection, which occurred only in 2000, leading to a 2 years delay.

A second stop of more than one year occurred in 2002, due to a re-evaluation of the different projects in CNES.

This lead to a total of 4 years delay, with a start of the development phase in 2003.

2.1. The development phase

To keep CoRoT its status of a pioneer mission, the launch was foreseen in 2006, which meant that the satellite had to be developed in a very short time (less than 4 years) with a duration of development really out of norms.

Thanks to the efforts of all the engineers, scientists and companies working on the project, a launch at the end of 2006 has been possible.

The total budget was an important matter of concern, as in the framework of the "petite mission" program, it was limited to 70 M€ for the French part. The contribution of the different countries has been helpful in this domain. Difficulties came also from the evolution of the political and technical changes of the launchers landscape (1/3 of the budget in general). The first baseline was to use cheap launchers as the Russian Rockot (Fig. I.3.2.)

A new solution came from the proposal of Arianespace to offer for a non-commercial cost, a maiden flight of the new Soyuz, developed under Starsem leadership, a subsidiary of Arianespace. This version aimed at modernising Soyuz with new third stage engine and digital control, and preparing it for the new Kourou launch pad for the SOYUZ launchers as decided by the European policy (see Lam-Trong 2006).

It was a maiden flight with the additional risk of failure and this risk was an additional factor of pressure for the mission (Fig. I.3.3).

CoRoT has paid its tribute to the promotion of Soyuz in French Guyana!

The results of this very intense development phase are extensively described in *The CoRoT mission, pre-launch status* (Baglin et al. 2006) and will not be repeated here (Fig. I.3.4).

Fig. I.3.2. The Rockot rocket ready to launch the European satellite GOCE on March 4 2004 at the Plesetsk cosmodrome. Credit: EUROCKOT, Khrunichev Space Research & Production Centre.

2.2. The operational phase

The operations started with the launch of the satellite on the 27th of December 2006; CoRoT was injected very accurately by the Soyuz/Fregat launcher on the desired orbit, which saved propulsion capacity for the future. The Launch and Early Orbit Phase (LEOP) lasted 4 days to secure the spacecraft, assess the good health of all the sub-systems and switch to the normal mode. The instrument has been switched on January 2nd, and on January 17th 2007 the cover of the instrument has been opened with the first acquisition of real sky data (Fig. I.3.5)

The CoRoT system, including the satellite and instrument, the CoRoT Control Centre, the CoRoT Mission Centre, the ground station network and the Brazilian and Austrian ground stations of Alcantara and Vienna performed all together successfully.

As we wanted to obtain scientific results as rapidly as possible, it has been decided to use the commissioning phase to both adapt the instrument and point towards stars chosen for their scientific interest. This phase started on February 3rd 2007.

The first in-flight data show that globally the results fulfil the specifications, and even surpass them in many domains (Auvergne et al. 2009; Pinheiro da Silva 2008). This has been confirmed all along the mission.

During the first year, the data (both scientific and housekeeping) were used to obtain a final tuning of the instrument, but also to understand and correct parasitic signals, for instance the role of the crossing of the South Atlantic Anomaly, or the tuning of the faint star field templates.

But most of these perturbations have been corrected as described in Part II, chaps. 2 and 3 of this book.

A number of improvements were introduced at several levels in order to maximize the scientific output of the mission. Let us cite for instance the wish of scientists to visit regions of the sky slightly outside the continuous viewing zone, which lead to a set of orbit manoeuvres to change the

Fig. I.3.3. The launch of CoRoT at the BaÏkonour cosmodrome on december 27th 2006. Credit Arianespace, © Starsem Arianespace.

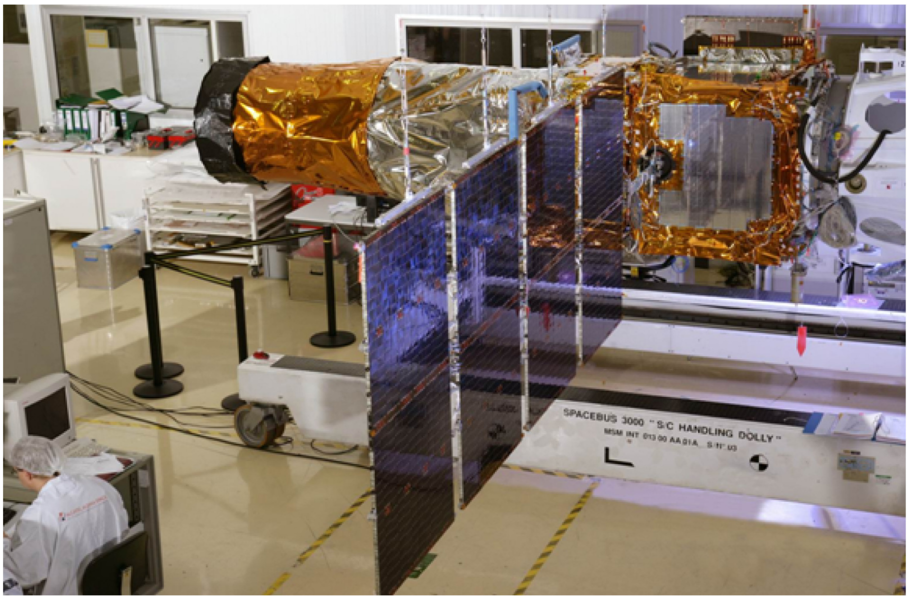

Fig. I.3.4. The CoRoT telescope, during the final tests (opening of the solar panels) at Alcatel (Cannes), © Thales Alenia Space.

inclination of the orbital plane and make it rotate slowly (–3°/year).

To optimise the duration of the scientific observations, the duration of the operations for the positioning of the runs has been constantly decreased, from an average of 11 days per run for the first 4 operations down to 4.1 days in average per run for the last 2 years of operation.

The strategy and monitoring of the downloading of the instrument telemetry has evolved to reduce the telemetry loss that could happen due to ground station anomalies.

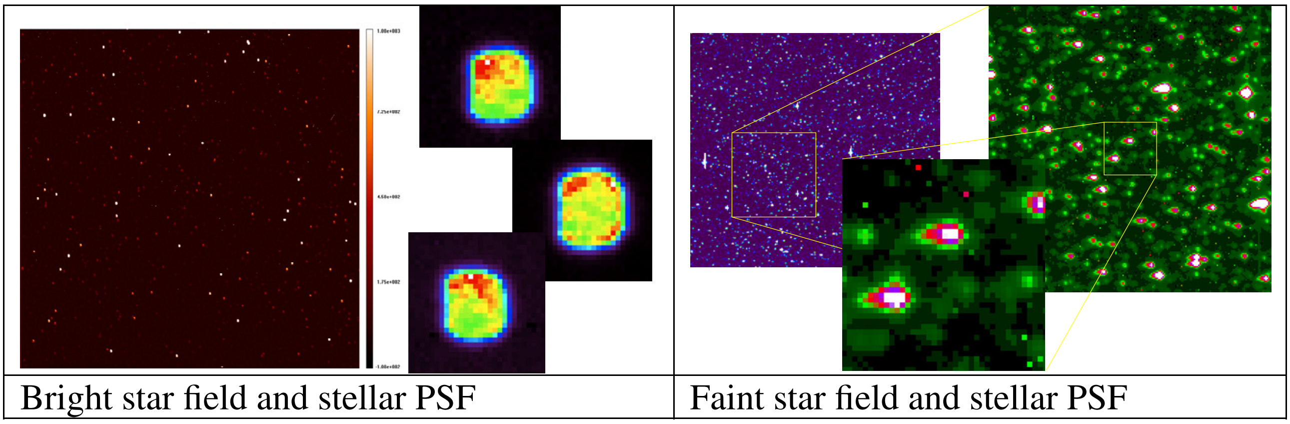

Bright star field and stellar PSF

Faint star field and stellar PSF

Fig. I.3.5. Point spead functions in the two CoRoT fields, with the very broad stellar images in the bright star field (to improve the accuracy of the photometry) and the smaller faint star images in the faint star field, enlarged by the very low resolution prism to extract color information, © CNES.

As for scientific purposes, any discontinuity is a problem the control of the detectors temperature has been optimised to favour the stability for a long period of time.

A total of 26 runs of observation were performed, representing 1981 days of observation with the bright star channel and 1919 days with the faint star channel out of a period of availability of the instrument to perform the scientific mission of 2113 days.

The 6-year flight has been perturbed only by two anomalies:

- on March 8th 2009, the communication between the platform and the photometric chain N° 1 of the instrument has been lost and never restarted. But both the satellite and chain 2 were working perfectly. So the system has been adapted to this new configuration making compromises with the scientific requirements. For instance, the strategy of observation has been modified by rotating the satellite around the direction of the bright star detector between 2 runs (e.g. LRc05, LRc06, see Chap. II.1.4) to allow still long duration (6 months) of the seismology programme, and increase the number of faint stars while exploring with the exoplanet detector two different directions (called later the DR method, after Daniel Rouan idea);
- on November 2nd 2012, the communication with chain N° 2 stopped suddenly, which lead to the end of the mission.

2.3. The end of the space mission

Following the major anomaly that occurred on November 2nd 2012, a tiger team was gathered to analyse and try to understand the reasons why CoRoT stopped abruptly. The study lasted 6 months and the experts went through theoretical analyses, various testings on test benches on the ground but also a series of tests onboard the satellite itself.

A total of 8 tests with different configurations were performed on the satellite trying to switch back on the instrument processor unit but also allowing to gather more information for the investigation team. The last but not the least test was performed in May 2013 and was supposed to give the maximum chances of success in powering ON the instrument through optimal electronic conditions onboard as well as a payload temperature cooled down to the minimum possible, supposedly favourable to the restart.

Fig. I.3.6. Launch of the last telecommand at CNES Control Center on Tuesday 17th June 2013 at 8:27 TU, © CNES.

Unfortunately, all those trials were unfruitful. They gave more information to the experts, but they succeeded neither in bringing the instrument back to life nor in being a hundred percent sure of the anomaly root cause.

The final decision to end the mission was taken in June 2013. CNES went then through the process of selecting technological experiments to be run on the PROTEUS platform. Indeed, the PROTEUS platform, that was created by CNES around 2000 to propose a low cost solution for medium-size scientific instrument, was still fully operational at that time. Seven experiments were chosen such as new guiding and attitude control methods, thermal effects study on solar arrays or other technological feedbacks that would be useful for next generation satellites.

Parallel to those experiments, end of mission operations have been conducted from the satellite control centre in CNES Toulouse. They started end of December 2013 by lowering the satellite orbit, in order to reduce the duration of the atmospheric re-entry to the minimum (Space Operations Law), while ensuring no more liquid propellant was left onboard.

The operation team finally performed the last step of the end of mission by commanding the final discharge of the battery. The very last telecommand was sent from Toulouse on Tuesday 17th June 2013 at 8:27 TU. The final extinction of the satellite was observed a few hours after the telecommand was sent (Fig. I.3.6).

The long trip of CoRoT will end in roughly 30 years from now when it will be low enough to become a shooting star in the sky.

References

Auvergne, M., Bodin, P., Boisnard, L., et al. 2009, A&A, 506, 411

Baglin, A., Fridlund, M., Lochatd, J., & Conroy L. 2006, eds. M. Fridlund, A. Baglin, J. Lochard, & L. Conroy (Noordwijk, The Netherlands: ESA Publications Division), ESTEC, ESA SP, 1306, p. 11

Catala, C., Mangeney, A., Gautier, D., et al. 1995, ASP Conf. Ser., 76, 426

Lam-Trong, T. 2006, ESA SP-1306, p. 255

Pinheiro da Silva, L., Rolland, G., Lapereyre, V., et al. 2008, MNRAS, 384, 1337

Acknowledgements: The CoRoT space mission has been developed and operated by CNES, with the contribution of Austria, Belgium, Brazil, ESA, Germany, and Spain.

The CoRoT Legacy Book

DOI: 10.1051/978-2-7598-1876-1.c014

I.4

Across the Atlantic: Canada's MOST

J. M. Matthews

Department of Physics & Astronomy, University of British Columbia, 6224 Agricultural Road, Vancouver, British Columbia,
V6T 1Z1 Canada

1. Windows of opportunity

In the mid-1990s, it seemed like the only way Canadian astronomers could have direct access to space-based ultra-precise photometry for asteroseismology was to be a minor partner in a European satellite mission. In fact, with this in mind, in 1996 Jaymie Matthews (University of British Columbia) submitted an unsolicited proposal to the Canadian Space Agency for Canada to participate in Eddington at a level of a few Can$M.

Then two unexpected windows opened right after one another.

The first window was built by aerospace engineer Kieran Carroll and opened by astronomer Slavek Rucinski. Rucinski attended a talk by Carroll whose company, Dynacon Inc. had developed a new Attitude Control System (ACS). Carroll explained that this system could stabilize a microsatellite (mass <100 kg; dimensions <1 m) with pointing accuracy of about 1 arcminute. This was about 100 times better than the previous best for such a small platform with such low inertia.

Carroll was looking for potential missions which could demonstrate the new ACS technology on orbit. Rucinski thought there might be an astronomical application and presented a poster at the next CASCA (Canadian Astronomical Society/Societé canadienne d'astronomie) annual meeting, soliciting ideas from the community for a space astronomy mission on a payload of low mass, low volume, low power and modest pointing accuracy. Jaymie Matthews recognized immediately the potential for a stellar photometry satellite and Tony Moffat thought there might applications to Wolf-Rayet stars.

Then the second window opened. The Canadian Space Agency (CSA/ASC) – founded less than a decade earlier – issued an Announcement of Opportunity for space science with a microsatellite. Rucinski, Carroll, Matthews, Moffat and Dimitar Sasselov submitted in 1997 a proposal for a satellite first called STEDY (for STEllar DYnamics, and playing on the steadiness of the proposed pointing system). STEDY was one of 54 proposals, and the *only* one with astronomical goals. It was selected as one of 6 proposals for a six-month Phase A competition.

Matthews took over as Principal Investigator, David Guenther and Gordon Walker joined the team, and the contractors were Dynacon, and CRESTech (Centre for Research in Earth & Space Technology). John Pazder became the optics designer and Peter Ceravolo would fabricate the main optics.

The project was renamed MOST, for Microvariability & Oscillations of STars/Microvariabilité et Oscillations STellaire. Its original scientific objectives were: (1) asteroseismology of solar-type stars; (2) asteroseismology of roAp (rapidly oscillating Ap) stars; (3) characterization of Wolf-Rayet star winds and search for pulsations; and (4) measurement of exoplanet albedo.

MOST won the Phase A competition and was selected to be Canada's first microsatellite and first space telescope.

2. A suitcase in space

MOST was designed to fit inside the secondary payload envelope of a Delta II rocket, to place it into a Sun-synchronous low-Earth (820-km) dusk-dawn orbit. From that vantage point, it would have a Continuous Viewing Zone (CVZ) about 54° wide, allowing uninterrupted monitoring of stars for up to 8 weeks at a time. MOST would stare out above the shadowed portion of the Earth with the solar panels being illuminated continuously by the Sun "behind" the satellite.

The small volume available to "hitchhike" on a Delta II meant MOST had to have the mass and dimensions of a suitcase: 54 kg; $60 \times 60 \times 30$ cm. The aperture of the optical telescope: 15 cm. Maximum power consumption: 30 Watts. No space, mass or power for a separate star tracking system, so the MOST instrument combined science and tracking functions, with twin 47–20 CCDs in the focal plane, custom-packaged by E2V.

Although the Dynacon ACS technology promised pointing which was an order-of-magnitude better than had ever been achieved with a microsat, the accuracy was still only 1 arcminute. Sharp images are not most important for precise photometry, but reliably collecting all the light from a stellar PSF (Point Spread Function) is critical for micromagnitude precision. Walker and Matthews took inspiration from photoelectric astronomical photometry, where the cathode of a phototube is illuminated by the pupil image of the telescope, projected by a Fabry lens to avoid the star image wandering over the inconstant response of the cathode.

For the MOST photometer, the detector would be a CCD, and multiple pupil images would be projected by a 6 × 6 array of Fabry microlenses. One would be illuminated by a target star; others would provide sky background values. The entire array (fabricated by Advanced Microptic Systems in Saarbrücken, Germany) also provides redundancy for damage to any one microlens.

To keep costs low and reliability high, it was decided that the MOST telescope and instrument would have no moving parts. No focusing knob for the telescope? The design is athermal, with components of different CTE (Coefficients of Thermal Expansion) chosen so that the structure keeps the same focus across a wide range of temperature. No mechanical shutter to end exposures? The CCDs have frame transfer buffers for rapid transfer of data charge to end each exposure. The only moving parts on the entire satellite are the spinning reaction wheels of the ACS, and a door which can close if there is risk of the instrument pointing directly at the Sun.

The initial mission design is described by Walker, Matthews et al. (2003).

In the meantime, the Canadian mission acquired two Austrian connections. Rainer Kuschnig was hired to become MOST Instrument Scientist, thanks to his engineering and astrophysical training and his experience with photometry from the Hubble Space Telescope FGS (Fine Guidance Sensor). Werner Weiss, after the disappointment of EVRIS, joined the MOST Science Team in exchange for an additional ground station. Stations in Vancouver, Toronto and now Vienna enhanced data downlink and operational flexibility. The scientific and data processing savvy added by Weiss and his team enhanced the entire mission immeasurably.

3. The little telescope that could

Less than six years after it was first proposed, MOST was carried into orbit aboard three-stage Russian Rockot (a former Soviet nuclear missile, designated an SS-19 Stiletto by the US military), through a contract with the German-Russian consortium Eurocket and the Krunichev Space Research & Production Facility[1] (Fig. I.4.2). The launch date was 30 June 2003, one day before Canada's 136th birthday.

The total cost (from Phase A to Phase E) was 7M US$.

The next six months were dedicated to commissioning the satellite. Two things were evident early on – one good, one not so good. On the positive side of the ledger, the Attitude Control System was working better than the engineers' most optimistic hopes. On the negative side, there were higher levels of stray light (due to scattered earthshine reaching the MOST instrument focal plane) than expected. The stray light is mainly modulated with the orbital period of MOST (101 minutes) and the team quickly adopted data processing and reduction strategies to mitigate the modulated background levels in the photometry (Figs. I.4.1 and I.4.2).

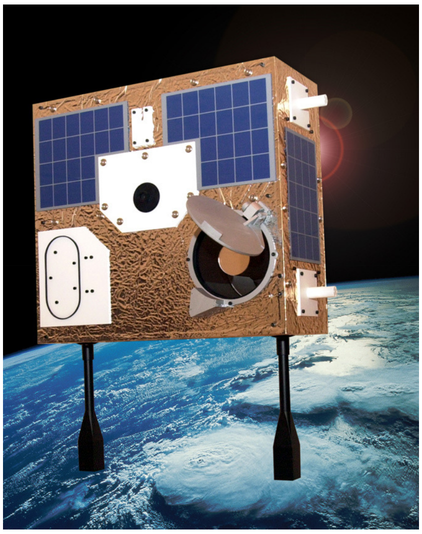

Fig. I.4.1. Model of the MOST microsatellite. Credit: Canadian Space Agency.

Fig. I.4.2. The launch of MOST on 30 June 2003, aboard a Russian Rockot from the Plesetsk Cosmodrome. Credit: EUROCKOT, Khrunichev Space Research & Production Centre.

Science commissioning was carried out during October–December 2003. The first Science Commissioning Targets (young solar-type star kappa 1 Ceti and beta Cephei pulsator delta Ceti) resulted in major scientific findings (Rucinski et al. 2004; Aerts et al. 2006) and kappa 1 Ceti became a regular return target for MOST in the early years of its mission (Walker et al. 2007).

In January 2004, MOST monitored its first Primary Science Target: the bright Sun-like star Procyon. Ground-based radial velocity (RV) measurements had indicated that this star was pulsating in solar-type p-modes, but the MOST light curve did not reveal any oscillations above the detection limit (Matthews et al. 2004). This null result – in which the MOST team described Procyon as a "flat-liner" – defied expectations due to scaling relations and was extremely controversial. Later, MOST took part in a coordinated campaign to observe Procyon, with spectrographs around the globe, to detect and characterize the p-mode eigenspectrum of the star (Huber & Bedding 2011). The Procyon controversy sparked by MOST led to a better understanding of convection and pulsation in stars through co-operation among observers and theorists around the world.

---

[1] The original plan to launch as the secondary payload of the Canadian synthesis aperture radar satellite, Radarsat II, was abandoned when that mission fell far behind schedule. Had it been known that MOST would be the primary payload on a Rocket, there would have been less tight restrictions on dimensions, but the satellite design was locked in by the time the change in launch vehicle took place.

MOST was intended to be a 1-year-long mission to observe 10 bright stars. As of the writing of this article, MOST has been operating for almost 13 years, and has collected about 5000 light curves.

Some MOST science highlights include: direct measurement of differential rotation and the period-latitude relation in a young solar-type star (Rucinski et al. 2004; Walker et al. 2007); measurement of the albedo of exoplanet HD 209458 b (Rowe et al. 2008); determining the power spectrum of accretion in the disk of a T Tauri star (Rucinski et al. 2008; Siwak et al. 2011); asteroseismic fitting of the internal magnetic field of several roAp stars (Gruberbauer et al. 2008); detection of a warm, volatile-rich super-Earth exoplanet (Dragomir et al. 2013); measurement of star-exoplanet interactions due to the tangling of the star's magnetic field with the magnetosphere of the planet (Walker et al. 2008); recognition of a relation between *g*-mode frequencies and internal rotation in SPB and SPBe (Slowly Pulsating B and Be) stars (Saio et al. 2007); detecting nonradial *p*-modes in red giants (at odds with theoretical expectations at the time); opening wider the window on the new field of red giant seismology (Kallinger et al. 2008); and detection of Co-rotating Interaction Regions in the winds of Wolf-Rayet stars (Chené et al. 2011).

CSA/ASC stopped funding of MOST operations in early September 2014. CSA/ASC sold the satellite to the MOST prime contractor (MSCI: Microsatellite Systems Canada Inc., formerly the Space Division of Dynacon, Inc.) and donated the UBC ground station to UBC.

MOST now operates in "pay-per-view" mode, where astronomers pay US$6K per week for photometry of their selected targets. The MOST team anticipates the satellite can operate in its current mode until 2020–22.

References

Aerts, C., Marchenko, S. V., Matthews, J. M., et al. 2006, ApJ, 642, 470

Chené, A.-N., Moffat, A. F. J., Cameron, C., et al. 2011, ApJ, 735, 34

Dragomir, D., Matthews, J. M., Eastman, J. D., et al. 2013, ApJ, 772

Gruberbauer, M., Saio, H., Huber, D., et al. 2008, A&A, 80, 223

Huber, D., Bedding, T. R., Arentoft, T., et al. 2011, ApJ, 731, 94

Kallinger, T., Guenther, D. B., Matthews, J. M., et al. 2008, CoAst, 153, 84

Matthews, J. M., Kuschnig, K., Guenther, D., et al. 2004, Nature, 480, 51

Rowe, J. F., Matthews, J. M., Seager, S., et al. 2008, ApJ, 689, 1345

Rucinski, S., Walker, G. A. H., Matthews, J. M., et al. 2004, PASP, 116, 1093

Rucinski, S. M., Matthews, J. M., Kuschnig, R., et al. 2008, MNRAS, 391, 1913

Saio, H., Cameron, C., Kuschnig, R., et al. 2007, ApJ, 654, 544

Siwak, M., Rucinski, S. M., Matthews, J. M., et al. 2011, MNRAS, 410, 2725

Walker, G., Matthews, J., Kuschnig, R., et al. 2003, PASP, 115, 1023

Walker, G. A. H., Croll, B., , Matthews, J. M., et al. 2007, ApJ, 658, 1328

Walker, G. A H., Croll, B., Matthews, J. M., et al. 2008, A&A, 482, 691

Acknowledgements: The CoRoT space mission has been developed and operated by CNES, with the contribution of Austria, Belgium, Brazil, ESA, Germany, and Spain.

The CoRoT Legacy Book

DOI: 10.1051/978-2-7598-1876-1.c015

I.5

In the United States: the long way to Kepler

W. Borucki

NASA Ames Associate, NASA Ames Research Center, Moffett field, CA 92035, USA

The Kepler Mission is a space observatory (Fig. I.5.1) launched in 2009 by NASA to monitor 170 000 stars for four years to determine the frequency of Earth-size and larger planets in and near the habitable zone (HZ) of solar-like stars, the size and orbital distributions of these planets and the types of stars they orbit (Borucki et al. 2010; Koch et al. 2010).

Kepler is the tenth in the series of NASA Discovery Program missions that are competitively-selected, PI-directed, medium cost missions. The Mission concept and various instrument prototypes were developed at the Ames Research Centre over a period of 18 yr starting with a small amount of funding in 1983. Beginning at the start of the NASA Discovery Program in 1992, the Mission concept was proposed five times to the NASA Discovery program before its acceptance for mission development in 2001. Prior to the launch of the Mission, a ground-based multiband survey of the 4 million stars in the selected field-of-view and an analysis program were conducted to classify the stars in order to select the most promising targets (Brown et al. 2011). An asteroseismology program was also conducted to determine the size and ages of brighter stars found to have transiting planets and for characterizing stellar structure.

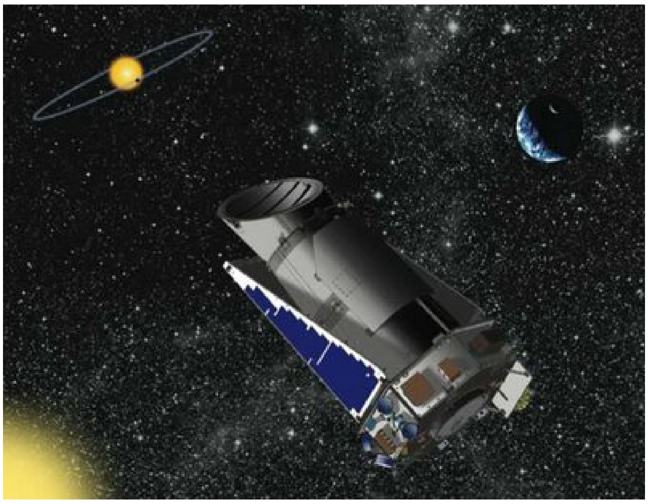

Fig. I.5.1. Artist's conception of the Kepler Mission observing an exoplanet transit. (NASA Image)

1. Mission description

The point-design for the Kepler Mission was based on a total noise value of 20 ppm for a 6.5-hour transit of a 12th magnitude solar-like star by an Earth-size planet in a 1 AU orbit using a 1-m aperture telescope. With shot noise of 14 ppm and a stellar variability of 10 ppm, an instrument precision of 10 ppm for a 6.5-hour transit duration is required to yield root-sum-square noise of 20 ppm. This performance provides a SNR of about 4 per transit (a transit duration of 6.5 hours is chosen because most transits will not be central and because it provides margin for unanticipated noise sources).

Because of the large number of stars surveyed and because the search is over periods between ~1 day and 2 yr, about 10^{11} statistical tests must be executed to search for patterns of transits for 170 000 stars. Consequently, to reduce the number of false-alarms (FA) due to statistical fluctuations to less than 1 FA over the entire mission-duration, the stellar flux time-series data were examined only when the detected transit pattern exceeded 7.1σ significance. Transit patterns that just meet the threshold will be recognized only 50% of the time while those with a transit pattern of 8σ detection will be recognized about 84% of the time. To obtain at least 50 planets in the HZ of Sun-like stars, the Mission was designed to monitor 170 000 stars for a period of four years. Because statistical fluctuations in the data and astrophysical phenomena produce events that can mimic planetary transits, a very elaborate set of procedures was executed to identify and remove false alarms and false positive events.

In order to maximize the number of appropriate target stars in the instrument FOV, a study was conducted prior to the launch to identify the region of the sky with the highest density of bright stars. The ecliptic was excluded because the Sun and solar-system planets would intrude to prevent continuous observations. The chosen location was slightly north of the galactic equator to reduce the prevalence of giant stars; i.e., in the Cygnus region centred on Galactic coordinates N76.53°, +13.29° (Fig. I.5.2). A sunshield designed to allow pointing to within 55° of the Sun and to fit into the launch shroud of the Delta-2 booster was chosen.

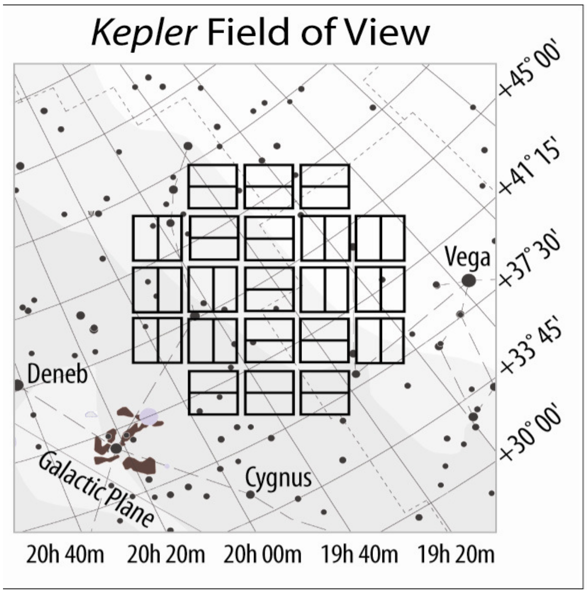

Fig. I.5.2. Kepler stared at the same FOV during the four-year mission to avoid missing transits of planets with long orbital periods. (Star chart from The Sky Software with permission from Bisque.com.)

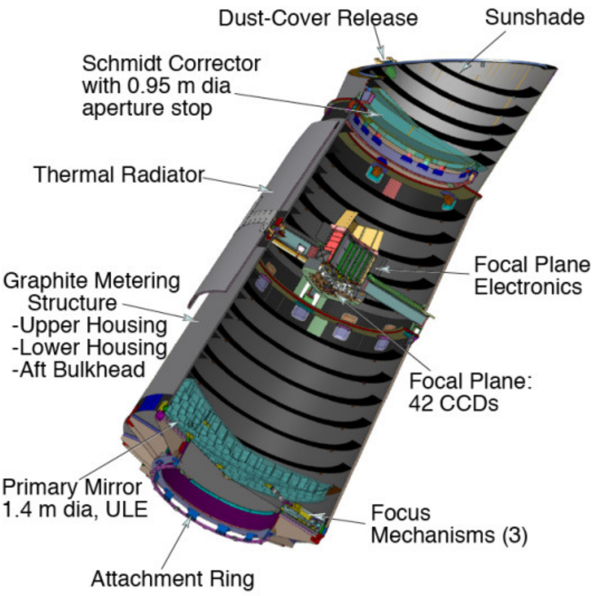

Fig. I.5.3. Cutaway view of the Kepler instrument (Courtesy of Ball Aerospace and Technology Corp.)

The telescope was a Schmidt design with a 0.95 m corrector and a 1.4 m mirror with a focal length of 1.47 m (Fig. I.5.3). To avoid mission failure due to a sticking shutter on the photometer, the instrument was designed to operate without a shutter. Instead the overwrite from the star images that trailed across the detectors during the short readout period was measured at every exposure and removed.

An Earth-trailing 372.5 day heliocentric orbit was chosen to keep the instrument in a thermally stable condition, to allow observations 24 hrs/day almost 365 days per year, and to avoid scattered light from the Earth and Moon.

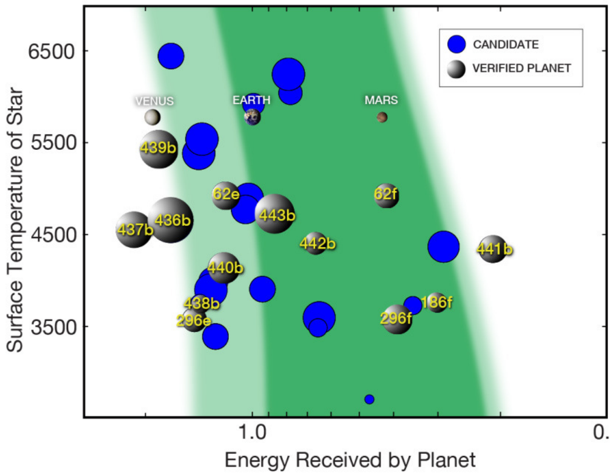

Fig. I.5.4. Small planets and planetary candidates in the habitable zone (HZ) published in Report on Progress to Physics (NASA Image).

Transmission of the data required a high-gain antenna and the loss of a day of data each month when the spacecraft was rotated to point the antenna toward Earth.

The active area of the 42 CCDs covered 105 square degrees. Each 2048 × 2200 format CCD had two outputs that each serviced a 2048 × 1100 section. Pixels were 27 × 27 square microns with a projected area on the sky of $3.8'' \times 3.8''$. Filters restricted the optical passband to a range of 420 to 850 nm. The short-wavelength limit was chosen to reject the stellar variability associated with the Ca II H & K spectral lines.

The cadence was 30 min for 170 000 targets. From these targets, a subset of 512 was also recorded at a 1-min cadence. This option was used to better define the timing of the transits when a planet was discovered and was also used for some of the asteroseismology investigations (Chaplin & Miglio 2013).

2. Highlights

During the four years of operation, Kepler made an unprecedented set of time-series observations of 190 000 stars (including those requested by Guest Observers). Analysis of the data has detected over 4600 planetary candidates, including several hundred Earth-size planetary candidates, over a thousand confirmed planets, Earth-size planets in the habitable zone (Fig. I.5.4), and has provided the information required for estimates of the frequency of planets in our galaxy (Batalha 2014).

The long term observations of the transiting planets allowed gravitational interaction among the planets in a planetary system to shift the times of transit depending on the masses of the planets and their orbital parameters. This variation in transit timing (TTV) was a very productive method of determining planetary masses and complemented those provided from radial velocity (RV) measurements using ground-based telescopes. By combining the Kepler observations with those of RV (Ford et al. 2012; Fabrycky et al. 2012) and TTV to get masses and densities, rocky planets were distinguished from low-density (water, gas, and ice) planets (Lissauer et al. 2014). Ten planets were found orbiting binary stars and several planets were found in orbits that are at large angles to the stellar equator.

The Kepler Mission results show that most stars have planets, many of these planets are similar in size to the Earth, and that planetary systems with several planets are common. With over 100 billion stars in our galaxy, we now know that there are billions of Earth-size planets in the HZ of their stars.

For an extensive discussion of the development of the Kepler Mission, see Borucki (2016).

References

Batalha, N. 2014, Exploring exoplanet populations with NASA's Kepler Mission Proc.Natl. Acad. Sci. USA `http://dx.doi.org/10.1073/pnas.1304196111`

Borucki, W. J., Koch, D., Basri, G., et al. 2010, Kepler planet-detection mission: Introduction and first results. Science 327, 977

Borucki, W. J. 2016, Kepler Mission: Development and Overview, Reports in Progress in Physics, Rep. prog. Phys., 76, 79

Brown, T. M., Latham, D., Everett, M. E., et al. 2011, Astron. J., 142, 112

Chaplin, W., & Miglio, A. 2013, ARA&A, 51, 353

Fabrycky, D., Ford, E. B., Steffen, J. H., et al. 2012, ApJ, 750, 114

Ford, E. B., Fabryckt, D., Steffen, J. H., et al. 2012, ApJ, 750, 185

Koch, D. G., Borucki, W. J., Rowe, J., et al. 2010, Kepler Mission design, realized photometric performance, and early science, ApJ, 713, L79

Lissauer, J. J., Dawson, R. I., & Tremaine, S. 2014, Advances in exoplanet science from Kepler, Nature 513, 336

Acknowledgements: The CoRoT space mission has been developed and operated by CNES, with the contribution of Austria, Belgium, Brazil, ESA, Germany, and Spain.

Part II

The CoRoT legacy data

The CoRoT Legacy Book
© The authors, 2016
DOI: 10.1051/978-2-7598-1876-1.c020

Part II

The CoRoT legacy data

This part is dedicated to the data. It describes how the observations were planned and performed, how the data were processed and finally where data are archived.

The first chapter shows how it has been possible to manage a reasonable mission, taking into account the scientific objectives and the mission constraints. It presents how the scientific specifications have been translated in the observation programme and its successive runs. It describes the observations from all aspects: selection criteria (scientific and operational), tools, implementation, global results and specific results. It shows also how scientists and engineers in charge of the operations at CNES and in the laboratories have adapted the major principles to the results of the first observations and to the instrument in flight.

The second and third chapters deal with the final processing of the data. The second chapter describes the data building, the correction philosophy and the latest algorithms used to generate the legacy CoRoT data delivered to the community. The impacts of several instrumental and environmental effects on the data are described, and the choices made for the correction algorithm developments are detailed. The first steps of the corrections are applied to the effects (either instrumental or environmental) which are understood and can be modelled on both bright stars and faint stars light-curves. An optional step is possible in the faint stars field thanks to the large number of light-curves, and a simple exposure-based algorithm able to remove residual instrumental effects that were not possibly modelled, is described in details in chapter 3.

The fourth chapter describes the format and content of the scientific data. It aims to give the maximal information to handle the data so that they can still be used many years from now!

All data are provided with several levels of corrections; the levels of corrections are available as different extensions in a single FITS file. The data with the highest level of corrections (called N2 data) are on purpose easy to handle and should be used as first choice. Less corrected data (called N1) are available on request but they require a deep understanding of the instrument and the observation conditions to be scientifically helpful. They should be looked at only for specific purposes as instrumental studies, need for 1s sampling data, check of unexpected behaviors in the N2 data…

The fifth chapter indicates where and how the data are archived.

The CoRoT Legacy Book
© The authors, 2016
DOI: 10.1051/978-2-7598-1876-1.c021

II.1

The CoRoT observations

A. Baglin[1], S. Chaintreuil[1], and O. Vandermarcq[2]

[1] LESIA, Observatoire de Paris, PSL Research University, CNRS, Sorbonne Universités, UPMC Univ. Paris 06, Univ. Paris Diderot, Sorbonne Paris Cité, 5 place Jules Janssen, 92195 Meudon, France
[2] CNES, Centre spatial de Toulouse, 18 avenue Edouard Belin, 31 401 Toulouse Cedex 9, France

This chapter explains how it has been possible to propose a reasonable mission, taking into account the scientific objectives and the mission constraints.

It shows how the scientific specifications have been translated in the observation programme and its successive runs.

It describes the observations from all aspects: selection criteria (scientific and operational), tools, implementation, global results and specific results.

A particular focus is made on evolution, showing how scientists and engineers in charge of the operations at CNES and in the laboratories have adapted the major principles to the results of the first observations and to the instrument in flight.

The first section deals with science and presents the process to choose the targets and the result of this scientific choice, i.e. the observed targets, individually for the bright stars and statistically for the faint stars.

The following section gathers many operational aspects: the tools used for the operations as well as for the scientific choices, the work flow followed at the beginning of each run, the resulting overall duty cycle.

The last section concerns the runs one by one. A first table indicates the periods of lack of data. Then specific scientific information is given for each run and, in some cases, complementary remarks useful to interpret the data, such as special processing, anomalies, ...

The concept of the instrument and the definition phase were extensively described in Fridlund et al. (2006), called “The CoRoT book”.

1. The scientific programme

1.1. General overview

The choice of the fields and the targets to be observed has been driven first by the initial objectives of the Core Programme and its evolution (see Michel et al. 2006). Additional Programmes (AP) are accommodated as much as possible, following the proposals of the GIs.

Calls for AP proposals are sent as soon as the field of a run is approximately chosen. They contain either general scientific studies or specific targets.

The necessity to observe at the same time, for long durations, bright targets devoted to the seismology programme, and faint ones for the exoplanet finding objective have lead to difficult compromises on the instrument, the satellite and the mission profile.

A preliminary proposal for a nominal mission of 2.5 yr was built before the mission, but has been adjusted during the flight before each observing period, taking into account the previous results.

And it was also adapted to the instrumental realisation, and “in flight” performances.

Before the end of the nominal phase (3 yr), a new programme has been proposed for a 3-yr extension, which focussed on the CoRoT “niches”, as discovered during the 3 first years.

At the end of this period, as the instrument was still in a good shape, a programme for a second 3-yr extension has been worked out and accepted in October 2012. But unfortunately the instrument stopped sending data a few days later.

1.2. The choice of the fields to be observed

Setting the observational programme consists in defining for each run, successively, a preliminary position of the Field of View (FOV), of the line of sight (LOS), of the roll and a preliminary choice of the targets.

For each run, the process starts by a proposal from the Scientific Committee (SC), based only on the scientific requirements.

The “Core programme” had the highest priority, with an equal weight for seismology and planet hunting.

Additional programmes have been taken into account with a lower priority, essentially in the faint star field.

It starts with a preliminary list of bright targets fulfilling the seismology objectives (as selected in the CoRoTSky database), and the planet hunting requirements on the faint star density, as defined by the Scientific Committee.

Then each proposed pointing is defined by a bright star, the "principal target", with some evaluation of its surrounding in the field of view. The requirement of the exoplanet-hunting programme (a sufficient number of faint dwarf stars) is checked.

Through an iterative process, the best compromise between both programmes optimises the scientific return.

Table II.1.1 summarises the major scientific objectives of each run.

1.3. The scientific selection criteria

* In the Bright Stars Filed (BSF), the order of the priorities was:

  - solar-like stars;
  - A and early F stars to detect/study in more details Delta Scuti and Gamma Doradus variables (already known or suspected);
  - peculiar stars;
  - rare objects

  as extensively described in Michel et al. (2015).

  For each run, the observed targets, classified by the "star type" are listed in Table II.1.2.

  And the total number is given in the last line.

* In the Faint Stars Field (FSF)

  The scientific priority was to detect planets, but the maximum number of windows (5724) is generally larger than the number of good candidates.

* The criteria for planet detection were almost always the same:

  - MV 10-15, Spectral type FGKM, Luminosity class V and IV, contamination <0.2;
  - MV 15-16, Spectral type FGKM, Luminosity class III, contamination <0.2;
  - MV 10-16, Spectral type FGKM, Luminosity class V and IV;
  - MV 10-16, Spectral type OBA, Luminosity class V and IV, contamination <0.2;
  - MV 10-16, contamination <0.3.

  The result of the choice based on these scientific criteria is a collection of thousands stars, with priorities built using CoRoTSky and the EXODAT database. The result of the choice is called the "Exobasket".

* To broaden the scientific objectives, the concept of Additional Programmes (AP) has been created, which can be easily implemented as generally the core programme does not use all the available windows.

After the preliminary choice of the field, a call for proposals was send to the Co-Is and GIs. The requested targets were selected after a review by the Additional Programme Working Group. In a few cases, AP targets are bright stars, but generally they are faint ones; their total number depends of the population of the field, but was limited to 500.

When a specific target is requested by an AP, it can be put in the exobasket with a high priority, to force its selection in EXOWIN.

1.4. Evolution during the mission

During the six years of the mission, the strategy has been adapted to both the evolution of the instrument and the results already acquired. Let us cite the major ones:

- in the BSF, it appeared that most of the A/early F stellar types, are generally "constant", so their priority has decreased;
- using the light curves already obtained, it has been demonstrated that the optimum duration of a run for planet hunting is slightly smaller than previously said: decreasing the length of the run to 80 to 90 days does not decrease significantly the detection rate, and allows to observe more fields. But the optimum duration for seismology remains as long as possible!

After the loss of chain 1, which reduced the observed area by a factor 2, Daniel Rouan proposed a strategy in which a long period is cut in almost equal parts, of 80 days. Then a rotation of the field allows to keep the same seismology targets and to observe a new region in the FSF. This method has been applied for LRc05/LRc06, LRa04/LRa05 and LRc07/LRc08.

2. The operational phase

2.1. Concept of the operations

The programme of observations is based on a yearly cycle of 4 runs which impulses the rhythms of the operations.

During the "summer period" from October to March, the telescope is pointed towards the "anticentre" of the Milky Way and during the "winter period" from April to September, in the opposite direction.

Two observation runs are achieved during each summer and winter period in general.

Using the CoRoTSky tool and the associated stellar databases (see below), the scientific programme is turned into a precise proposal for the pointing with chosen targets and the technical feasibility is assessed.

In parallel, the evolution of the CCD temperature is evaluated over the whole run; the temperature at the beginning of the run is set in order to minimise the total number of changes.

The operations themselves begin then in close collaboration between the team in charge of the operations at CNES and the science and instrument specialists from the laboratories.

As the bright stars are used for the pointing, they are always observed first. The observation of the faint stars generally begins between 2 and 4 days after the observation of the bright stars.

The successive steps of the procedure are detailed below.

2.2. Tuning of the pointing and setting the parameters

* The full image stage: first, the satellite uses its own pointing mode, often called rough pointing, to record images over 3 orbits (excluding the SAA crossing) to built an image of the sky in the position defined by CoRoTSky.

Table II.1.1. The scientific objectives of the successive runs and their characteristics. Abbreviations of the Star types: SL Solar-like, DS: Delta Scuti, EB: Eclipsing binaries, GD: Gamma Dor, RG: Red giants, OBA: spectral type OBA, LPV: long period variable.

The scientific objectives of the successive runs and their characteristics

Run	Start time BSF	SAA crossing	driver	bright stars choice		faint star field choice		Pointing direction in J2000		
		%		Principal Target	Complementary targets	planet search(ps)	Additional programmes	Alpha (°)	Delta (°)	Roll (°)
IRa01	31/01/2007 11:06:34	8.73	HD 49933 + ps	HD 49933	1 DS, 1Ap, 2EBs	classical, some overlap with LRa01	8 ASAS variables 1500 BA, 1458 RG	102.60	–1.70	9.60
SRc01	11/04/2007 15:07:52	8.71	seismology core program	2 DS	2 EB, SL 175726	classical USNO cat, field very inhomogenous	no	284.59	3.08	5.48
LRc01	11/05/2007 13:10:19	8.73	HD 181555, HD 180642 + ps	DS, β cep	SL, Be	classical	RRLyr, DS, OAB, 3988 (1400 osc) RG	290.89	0.43	24.24
LRa01	18/10/2007 08:57:24	8.74	HD 49933, HD 49330 +ps	HD 49933	DS, Be, Ap	best field	Bes, Dolitze 25 (56), 1698 (400 osc) RG WD cand (18), EBs, OBA,	101.66	–0.20	1.92
SRa01	05/03/2008 22:34:26	8.75	NGC 2264		GD, Ap		NGC 2264 in faint star field	101.04	9.02	2.32
LRc02	11/04/2008 20:55:29	8.74	GD + ps	GD	DS, SL	classical	22*	279.66	6.40	16.72
SRc02	09/09/2008 23:03:28	8.84	HD 174532, unique DS with very low sinI	l Bootis, HgMn	classical	14*, 1 EB, Var non ident.	284.10	–2.86	–14.64	
SRa02	08/10/2008 22:44:36	8.76	HD 46375 + ps	HD 46375	6 O stars of NGC 2244	simple	16*	97.55	5.66	–25.36
LRa02	13/11/2008 22:49:46	8.72	HD 52265 + ps	HD 52265	3 early B + DS, low Vsini, Ap, Be	classical	Be, EB, 10 BA, 647 OBA	103.52	–4.38	6.00
					stop of chain 1, March 9th 2009					
LRc03	01/04/2009 20:49:11	8.76	planet search		2 L, 2K	optimised for planet	none	277.47	–7.25	16.24
LRc04	04/07/2009 02:58:56	8.73	HD 169689 + ps	HD 169689	EB, 2 SL,	good	10, 49 OAB	277.72	8.02	6.56
LRa03	01/10/2009 20:57:34	8.73	HD 43587 + exo	HD 43587	d scuti, the coolest Be, F2V candidate d scuti	ok, but quite poor	46 NGC2186 members, 1EB,1DS, 1100 OBA	93.75	5.50	–3.84
SRa03	02/03/2010 21:17:26	8.78	SDB in the faint star field		EB, sol-like	classical 2MASS data	7*, 248 A	98.40	0.99	2.16

Table II.1.1. continued.

start of the extension										
LRc05	06/04/2010 21:13:38	8.74	HD 170580, DS + ps		DS, Ap	classical	2*, 178 A	279.00	3.66	6.77
LRc06	07/07/2010 01:30:32	8.75			DS, Be	classical	IC4756, 2*, 388 OBA	278.95	4.35	16.85
LRa04	28/09/2010 00:14:23	8.16	HD 42618 +exo	HD 42618	Be + DS + Mvar	2MASS data no selection, field very poor		92.57	6.94	5.87
LRa05	17/12/2010 19:26:25	8.00		HD 42618	d scuti +B	2MASS data no selection, field very poor		91.93	7.95	–23.49
LRc07	06/04/2011 15:57:50	8.01	RG	NGC6633 Red giants		classical	194 OBA,	277.60	6.29	23.97
SRc03	01/07/2011 18:30:50		CoRoT 9 new ecclipse	No bright star		CoRoT 9 new ecclipse		279.86	5.57	2.37
LRc08	06/07/2011 14:59:43	8.01	RG	NGC6633 Red giants		classical	211 A	277.14	5.60	–16.03
SRa04	04/10/2011 19:06:57	7.95	HgMn	HD 45975				96.17	–3.84	1.79
SRa05	29/11/2011 18:14:02	8.02	NGC2264, multi satellite			classical + 11 planet cand	YSOVAR 2 +13 EB = 821 OBA	101.12	10.07	–18.60
LRa06	10/01/2012 18:24:40	7.99	reobs CoRoT 7	HD 49933	SL, Be, BS, Ds	CoRoT 7 + CoRoT 12 and CoRoT 21 + classical	1 Dolitze, 18 WD candidates, 4Be, EB, 171 RG, 1370 OBA	101.55	0.22	16.03
LRc09	10/04/2012 20:47:16	7.77	HD 179079 planet host star	HD 179079	RG puls, 2 early F, B	classical	1700 RG, 558 OBA	288.22	–3.18	–1.15
LRc10	06/07/2012 14:22:07	7.98	sec ecclipse HD 169689	HD169689	RG LP, M LPV	classical	800 RG, 2000 0BA	277.74	7.28	–9.63
LRa07	02/10/2012 19:59:38		O stars	HD 46365+4 O (NGC2244)		classical	1000 RG, 470 OBA	96.87	5.19	15.23
stop of chain 2, November 2nd 2012										

Table II.1.2. The bright star targets for each run, as a function of their star types.

The “star types” of the bright targets of the successive runs														
RUN	**Duration in the Bright star field in days h:m:s**	**O**	**B**	**Be**	**β cep δ scuti**	**A/ earlyF**	**δ Scut γ Dor**	**late F/G**	**sol-like F/G/K**	**CP**	**giant *puls**	**K/M**	**Multiple**	**Cluster**
IRa01	60 20:5:41.0			50 846		50 844 50 747 50 405 50 170		292 790	49 933	50 773 51 106	50 890		50 846 50 405 50 170	Dolitze 25
SRc01	27 16:5:29.0		174 884	175 869		175 543 174 987 175 542	174 966 174 936		175 726 175 272		*175 679		174 884	
LRc01	156 17:24:42.0		181 440 182 108	181 231	180 642	181 072 181 555 180 973			181 420 181 906		181 907			
LRa01	137 0:52:11.0		50 064	49 330 50 209	50 230	49 808	49 294 49 434		49 385 49 933	49 862				
SRa01	25 9:9:32.0		48 977 49 677 48 752			263 425 49 607	48 784			49 310	48 976 *49 566 49 161	49 429	48 752	NGC2264
LRc02	148 3:4:30.0		172 046 170 935			171 835 171 536 171 834	172 189 171 218		170 987	171 586	171 427		170 987	
SRc02	26 7:39:31.0		174 648			174 990 174 967	174 532 174 589	175 152		175 640 175 445	174 589	174 796 174 323		
SRa02	34 9:43:52.0	46 966 46 150 46 149 46 223 47 129	46 129 46 179		46 202	46 424			46 375		46 612		47 129 46 149 46 202	
LRa02	117 11:41:52.0		51 756	51 193 51 452		52 130 51 332	51 359 50 870 51 722		52 265	51 844			51 756 51 844	

Table II.1.2. continued.

stop of chain 1, march 9th 2009														
LRc03	91 7:4:47.0					169 868		169 556	169 392		*169 751 *169 370			NGC 2186
LRc04	87 7:5:0.0		169 689			170 133 170 511		169 822			*169 689 *170 008		169 822 169 689	
LRa03	150 11:39:50.0		43 317	43 913		43 823	44 195		43 587				43 587	
SRa03	26 10:52:29.0		46 769			47 485 46 799		47 530					47 361	
LRc05	89 8:30:50.0				170 580 170 783					170 973	171 264		170 580	
LRc06	79 6:38:21.0			171 219	170 580 170 783		170 699				171 264		170 580	IC 4756
LRa04	79 4:54:49.0			43 285		43 338	TYC144-3031-1		42 618			42 787		
LRa05	94 12:20:44.0		42 597			42 299	41 641	42 089	42 618					
LRc07	83 3:24:10.0		170 200								*170 053 *170 031 *170 231 *170 174		170 200	NGC 6633
SRc03	3 11:02:58 (Faint star field)													
LRc08	85 15:25:12.0		170 200								*170 053 *170 031 *170 231 *170 174		170 200	NGC 6633
SRa04	54 12:16:15.0		45 418		45 546	45 517				45 975		45 398		NGC2232
SRa05	40 17:41:52.0		48 752 48 977				48 784				49 566	49 429	48 752	NGC2264
LRa06	78 16:29:15.0			49 585	50 230		49 608		49 933 49 385					Dolitze 25
LRc09	85 8:8:17.0		179 192			178 169 178 243			179 079		*178 484			
LRc10	86 17:3:43.0		169 689			170 133		169 822			170 270 *169 689	V 585 Oph	169 689	
LRa07	31 0:19:11.0	46 149 46 223 46 150			46 202				46 375			46 241 (perte pointage)	46 202 46 149	
stop of chain 2 november 2nd 2012														
Total		**5**	**23**	**11**	**7**	**33**	**18**	**7**	**14**	**10**	**21 *11**	**8**	**20**	**3+**

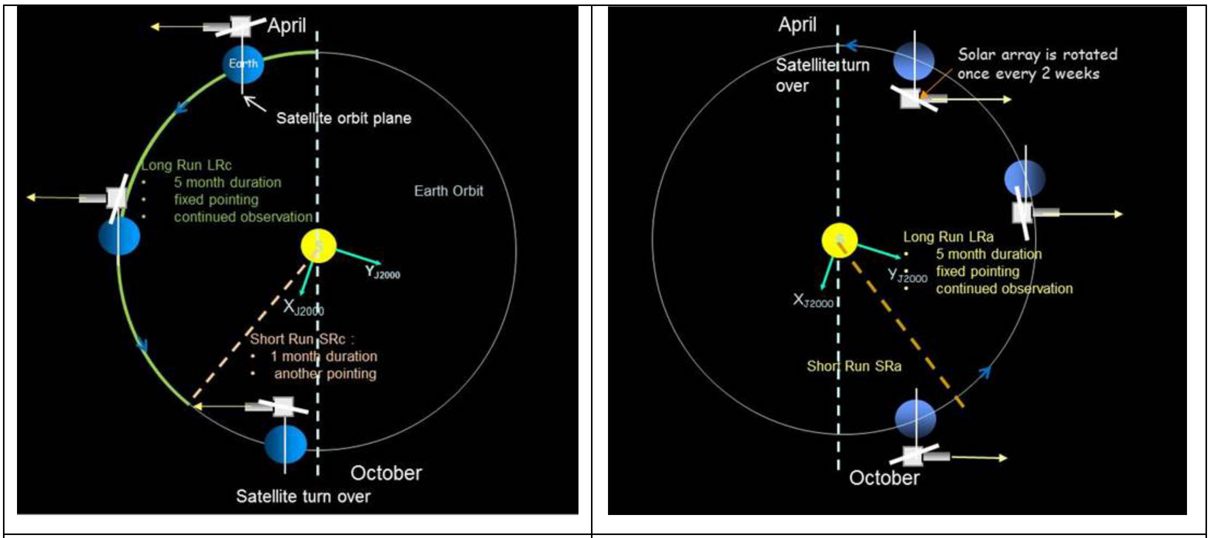

Summer observation in the Centre direction

Winter observations in the anticentre direction

Fig. II.1.1. "The yearly rythm of the pointings: In the outer and inner regions of the Galaxy, and long and short alternate observations", © CNES.

* The field recognition: one of the images recorded previously is used to recognise the field.
To do so, this image is compared to a synthetic image obtained using the Tycho catalogue.

* The choice of the bright targets: the procedure checks that targets chosen for observation by the scientific proposal have been well identified, the five targets with higher priority and good feasibility are selected, as well as the two stars used for fine pointing.

* The setting of the photometric mask for the bright targets.
On the full image, a first mask is designed for each target. The mask is a collection of contiguous pixels for which the photons are collected for a given target; it is adapted to each target by computing recursively the contribution of each pixel to the total flux.
Then, when the fine pointing is settled, small images called imagettes are recorded and are used to adjust the mask by adding pixels until the S/N ratio decreases. This more precise mask is used during the rest of the run. The discontinuity in the flux implied by the changing of the mask is then corrected in the pipeline (see Part III, Chap. 1 in this book).

* The choice of the faint targets.
Then, full images of the field in the E1 and E2 CCDs are observed and recorded.
The targets of the "exobasket" are recognised using the EXOWIN tool (Karioty et al. 2006) software and given a template chosen by EXOWIN in a set of predefined templates, optimising the S/N ratio, as defined in Llebaria & Guterman (2006).
This set of templates and the position of the associated window on the CCD are uploaded on board at the beginning of the observations, with an associated sampling rate (see Ollivier in this book).

* The choice of the targets observed as imagettes in the faint star field.
In the faint star field, 40 imagettes can be produced aboard and downloaded. They were first supposed to be used for calibrations. As it appeared rapidly that it was not necessary, a new scientific objective has been given to this possibility: observing the bright targets (magnitude around 9 to 10), which may be saturated, but for which the planet detection could have a better sensitivity.
So for runs later than LRa02, the 40 imagettes have been put on very bright and saturated stars. The imagettes were used to build light-curves delivered with all other light-curves. They can be found as imagettes in L1 deliveries (see Part II, chap. 4, in this book).

2.3. Continuity of the data

The total duration of the scientific observations is 1981 days (in the bright star field), whereas the total duration of the mission is 2137 days.

In order to devote as much time as possible to the scientific programme, the operations have always minimised the interruptions.

For instance, data acquisition was not stopped, contrary to what had been planned before launch. This minimised the loss of data due to the SAA crossing that depends slightly of the direction of the observation and of the period in the year (Pinheiro da Silva et al. 2008). As shown in Table II.1.1 Col. 3, it is always lower than 8.9% and decreases at the end of the mission.

An unavoidable stop was due to the rotation of the solar panels to optimise the energy supply: it happens every two weeks, lasted 10 to 15 min, usually on Wednesdays between 11:50am and 12:05pm, leading to periodical interruptions corresponding to a loss of approximately 0.07%.

In rare cases, the pointing was lost and it was necessary to start again from the beginning the pointing procedure.

In addition, a few losses of telemetry occurred, but were very seldom, thanks to the efficient network of communication.

The global duty cycle is always higher than 90%.

Missing data are filled by the Inpainting process (Ollivier et al., this book; Pires et al. 2015) and identified with a specific STATUS value. The quality of the filling by Inpainting depends on the duration on which the filling is requested; for SAA crossings, rotation of the solar panels and short interruptions, a limit of 2 hours appears as optimal.

2.4. Tools and databases

Several tools and databases are necessary for the choices at scientific and operational levels.

2.4.1. The CoRoTSky tool

It proposes to place the CCDs on the sky, where targets are presented, using the information (Magnitude, position, spectral type. . .) contained in the databases.

It also takes into account several technical constraints.

It has been developed by CNES based on specifications from the Scientific Committee.

It builds the proposal files, which contain for both fields the list of the requested targets, with priorities.

2.4.2. The CoRoTSky database

It is described in Charpinet et al. (2006).

It has two parts, the bright star base and the faint star base.

* The bright star CoRoTSky base.
It relies on the extensive programme of ground-based observations, described in Catala et al. (2006).
All the data (photometric and spectroscopic) are available in the GAUDI archive[1].

* The faint star CoRoTSky base.
It is composed of extractions of the EXODAT database around the proposed field of view of the faint star field. The EXODAT database was first described in Deleuil et al. (2006) and in Meunier et al. (2009) and in Damiani (Chap. III.5 in this book).

2.4.3. The EXOWIN tool

Developed in the laboratories, it compares the “exobasket” to the true image, identifies stars and transforms the proposal into a list of observable targets, with their associated mask (see Karioty 2006).

During this process, several targets (no more than 10%) are unobservable, either because they have not been found in the field with a correct magnitude and position, or because the shape of their PSF does not allow to fix a template of the set.

This list is send to the instrument through a sequence of commands describing the programming of the 6000 stars; the upload sequence lasts from 12 to 15 min.

As it had been foreseen before launch, the set of templates of the Faint Stars Filed (FSF) has been updated using flight images after the three first runs (IRa01, SRc01 and LRc01). This has no impact on the fluxes because the shape and size of the templates are taken into account in the processing.

3. Specificities of the runs

This chapter presents useful information concerning the data.

First, it addresses the continuity of the data, giving the date of the main holes or longer than 2 hours.

Then it gives, run by run, every aspect of the observations, from the specific scientific criteria for the selection to operational constraints and anomalies in the resulting data.

And finally, we report the detection of one unknown object: the crossing of the field of view in several runs.

*** *IRa01***

The constraints of the launcher (a maiden flight of Soyuz 2-I-b) have postponed the launch to the end of 2006. This first run (called Initial Run) has been used for both commissioning and scientific observations.

Due to the special interest of this field in the anticentre direction, it has been decided to point it even though the observation could not last more than 2 months.

In the BSF, one star had the highest priority: HD 49933 a “solar analogue” though a little more massive, with a good faint star environment. Following the successful detection of solar-like oscillations during this run, it has been reobserved twice in LRa01 and LRa06.

Rem:

- On this first run, observations do not begin on the same day on channel 1 and channel 2;
- Time-frequency analysis shows that CID 123 (HD 50844) and 214 (HD 51106) have a jitter residue;
- In the four first runs, in FSF, the duration of the gaps, including these due to the rotation of the solar panels, are not correctly synchronised on 16*32s tops; as a consequence, all gaps are not filled, regardless of their duration.

*** *SRc01***

This run was dedicated to the seismology core programme, and in particular to Delta Scuti stars, considered as interesting even in a short run, as they have large amplitudes.

The FSF remains very poor, and extremely inhomogeneous, and as they were no specific observations, the USNO catalogue has been used.

Rem:

- In the four first runs, in FSF, the duration of the gaps, including these due to the rotation of the solar panels, are not correctly synchronised on 16*32s tops; as a consequence, all gaps are not filled, regardless of their duration;
- In the four first runs, in FSF, the duration of the gaps, including these due to the rotation of the solar panels, are not correctly synchronised on 16*32s tops; as a consequence, all gaps are not filled, regardless of their duration.

*** *LRc01***

The position of the BSF is strongly constrained by both the need to catch a delta Scuti star and a solar-like target in addition to the principal target, and also instrumental constraint. So strong gradients and inhomogeneities in the FSF were unavoidable.

---

[1] `http://svo.cab.inta-csic.es/main/index.php`

Table II.1.3. Interruptions longer than 2 hours.

Run	Start of missing data	End of missing data	Duration	
LRc01	20/05/07 05:12	20/05/07 07:44	2:32	
LRa01	19/10/07 20:19	19/10/07 23:37	3:18	
	29/10/07 20:22	30/10/07 00:07	3:45	
	01/11/07 17:33	02/11/07 07:27	13:54	
	19/01/08 22:42	22/01/08 08:02	2 days 9:20	Channel 1 only
LRc02	21/05/08 15:13	21/05/08 17:15	2:02	
	04/06/08 14:13	04/06/08 17:57	3:44	
	19/08/08 17:43	20/08/08 00:45	7:02	
SRc02	28/09/08 09:43	28/09/08 13:16	3:33	
	28/09/08 19:53	29/09/08 00:51	4:58	
	29/09/08 02:47	29/09/08 08:03	5:16	
SRa02	31/10/08 03:11	31/10/08 06:09	2:58	
LRa02	28/01/09 17:05	28/01/09 20:34	3:29	
	20/01/09 09:53	20/01/09 12:07	2:14	
LRc03	16/04/09 14:05	17/04/09 00:36	10:31	
	22/04/09 07:23	22/04/09 10:40	3:17	
	25/04/09 07:31	25/04/09 10:49	3:18	
	25/04/09 18:01	25/04/09 21:35	3:34	
LRc04	27/08/09 23:44	28/08/09 03:11	3:27	
LRa03	27/10/09 17:30	28/10/09 01:01	7:31	
	02/11/09 15:28	03/11/09 02:17	10:49	
	27/01/10 19:09	28/01/10 03:52	8:43	
	02/02/10 23:48	03/02/10 02:17	2:29	
SRa03	19/03/10 21:34	20/03/10 01:08	3:34	
LRc05	05/05/10 16:18	05/05/10 20:21	4:03	
	31/05/10 16:25	31/05/10 19:59	3:34	
LRc06	20/08/10 11:02	20/08/10 13:19	2:17	
LRa04	03/10/10 19:18	03/10/10 23:40	4:22	
	09/10/10 17:04	09/10/10 19:28	2:24	
	20/10/10 01:49	20/10/10 07:56	6:07	
	15/11/10 01:18	15/11/10 08:57	7:39	
	05/12/10 03:27	05/12/10 06:20	2:53	
LRa05	19/01/11 19:48	19/01/11 23:09	3:21	
	05/03/11 17:41	05/03/11 23:37	5:56	
LRc07	08/06/11 03:03	08/06/11 06:06	3:03	
	21/06/11 06:56	21/06/11 09:29	2:33	
LRc08	21/08/11 14:59	21/08/11 18:02	3:03	
Sra04	08/10/11 00:59	08/10/11 02:56	1:57	
Sra05	21/12/11 22:58	22/12/11 17:37	18:39	
LRc09	19/06/12 21:58	20/06/12 00:22	2:24	
LRc10	21/09/12 15:29	21/09/12 20:32	5:03	
LRa07	22/10/12 00:34	25/10/12 17:34	3 days 17:00	

Rem:

- In the FSF, a set of new templates computed from the images of the commissioning was uploaded and tested on board on channel 2 in the last 10 days of the run: these data were used for testing reasons, not for scientific use. Therefore, the scientific observations in channel 2 (end October 5th 2008) are 9 days shorter than in channel 1 (end October 15th 2008);
- In the four first runs, in FSF, the duration of the gaps, including these due to the rotation of the solar panels, are not correctly synchronised on 16*32s tops; as a consequence, all gaps are not filled, regardless of their duration.

* *LRa01*

As we now know that we are able to detect solar-like oscillations in stars, in a sufficiently long run, it has been decided to have LRa01 before the short run of the same season SRa01. But the total time available (less that 160 days) lead to stop LRa01 after 134 days and leave 26 days for SRa01.

The field of LRa01 is considered as the best field for exoplanet hunting. It contains also an open cluster, Dolitze 25, and many red giants.

More precise ground based observations are available in the EXODAT database.

Re-observation of HD 49933 is considered as a very high priority. It implies some overlap of the fields with IRa01.

Rem:

- Due to a breakdown of channel 1 between 19/01/2008 22:50 and 22/01 08:02 no data were received from this channel. Bright stars and faint stars are concerned. Gap is not filled in the FSF;
- Time-frequency analysis shows that the CID 100 (HD 49434) has a jitter residue,
- In the four first runs, in FSF, the duration of the gaps, including these due to the rotation of the solar panels, are not correctly synchronised on 16*32s tops; as a consequence, all gaps are not filled, regardless of their duration;
- Six changes of the temperature of the CCDs: not easy to handle!
  For the later runs, the thermal analysis of the whole run was performed at the beginning of the run in order to minimise the numbers of changes of the set point inside the run.

*** *SRa01***

The Scientific Committee decided to devote some short runs to additional programmes; and SRa01 was the first one.

Three proposals were selected after a phase A. And the observation of the open cluster NGC2264 in the FSF won! A very long preparation, with ground based observations, has been necessary to select the targets, as contamination was quite strong.

The run has been very successful, and triggered a new observation of this cluster in a multi-satellite campaign (SRa05).

Rem:

- CID 2503 (HD 49161): because of very high flux, the precision on the wings of the PSF is lower than usual, leading to a rougher correction from satellite jitter and to a significant jitter residue;
- in the BSF, poor correction of the jumps due to the change of the photometric mask.

*** *LRc02***

The position was difficult to accommodate, as the proposed roll to observe some major targets was not compliant with the constraints on the thermal equilibrium of the satellite, but finally accepted!

*** *SRc01***

It was devoted to the seismology exploratory core programme, and was driven by the observation of HD 174532, a unique Delta Scuti star with a very low rotation.

Rem:

- Ad-hoc elimination of the aliasing applied to CID 7519, positioned on the first rows of the CCD;
- The CID 7524 (HD 174967) and 7663 (HD 174589) have a jitter residue.

*** *SRa02***

It was devoted to the second priority of the phase A study for Aps.

The main target was HD 46375, a solar-like star with a non-transiting planet, with the hope to detect both oscillations and reflected light on the planet.

Fortunately, six O stars belonging to the cluster NGC2244 have been observed as secondary targets.

*** *LRa02***

Due to the run was devoted to the core programme, but the choice of the field has been extremely difficult, as there were conflicts with scientific priorities and instrumental constraints.

Rem:

- The CID 579 (HD 51756) has a jitter residue;
- In the FSF, the CIDs 30000315, 110741824 and 300003271 are observed as imagettes and contain the star and one or two contaminant (this can be seen in the corresponding EN2_WINDESCRIPTOR files);
- Addition of one second on December 31st 2008: 3 points are withdrawn: (2 points at 23:59:58 and the point at 23:59:59).

*** *LRc03***

It was decided to devote it to the exoplanet programme, which has chosen the field independently of any bright star constraint. Unfortunately the loss of chain 1 reduced the field.

The position has been fixed in maximising the density of bright stars. The BSF field is quite poor.

*** *LRc04***

The choice of the field was partly driven by the interest of an eclipsing binary HD 169689 in which pulsations in the red giant as well as binary modelling have been successful, but the field is tuned to optimise the dwarfs density and is quite good.

Rem:

- The CID 9861 (HD 170008) has a jitter residue.

*** *LRa03***

Dedicated to HD 43587. The FSF is poor, but there is an open cluster NGC 2186.

Rem:

- CID 3093(HD 43823) is positioned on a dead column, which produces a jitter residue;
- CID 3412 (HD 43317) and 3474 (HD 43587) also have some jitter residue.

*** *SRa03***

The run is dedicated to the observation of an SdB in the faint star field, as the third priority of the AP phase A Study.

A very wide spectrum of oscillations has been found.

But the field has not been observed from the ground and relies only on 2MASS data.

In the BSF there are some interesting targets.

Rem:

- CID 374 (HD 47361) is positioned on a dead column as can be seen in the AN2_WINDESCRIPTOR; it produces a jitter residue.

* *LRc05/LRc06*

The DR method has been used, which couples LRc05 and LRc06.

Rem:

- In LRc06, CID 8167 (HD 171264), CID 8303 (HD 170783) and 8385 (HD 171219) have a jitter residue.

* *LRa04/LRa05*

These runs use also the DR method.

Rem:

- In LRa04, CID 4243 (HD 43338) and 4910 (HD 42618) have a jitter residue.
- CID 4910 (HD 42618) is observed in both LRa04 & LRa05. Strangely, the flux is not stable at the beginning of each run, it increases during 5 to 6 days before stabilisation; no valid explanation was found for this phenomenon. Ad-hoc elimination of the aliasing has been applied to this target in both runs.

* *LRc07/LRc08*

These runs use also the DR method.

Rem:

- In LRc07, CID 8943 (HD 170174) has a jitter residue;
- In LRc08, all 5 stars in the BSF have a jitter residue: CID 8831 (HD 170200), 8852 (HD 170031), 8943 (HD 170174), 9044 (HD 170231), and 9109 (HD 170053);
- Ad-hoc elimination of the aliasing has been applied to CID 9109.

* *SRc03*

Observation of CoRoT 9 for 5 days, in order to follow the predicted transit.

Rem:

- No specific choice of the targets as the duration is too short;
- Bright stars have not been processed;
- No worry about the dates of the full image associated with this run: the image is correct even if the dates are in April.

* *SRa04*

This run of intermediate length (53 days) is dedicated to the observation of a chemically peculiar star. The chosen target is a member of the young cluster NGC 2232 and 4 other members are also observed.

Rem:

- The star HD 45965 (CID1824) is quite near contaminating star, as it can be seen in the corresponding AN2_WINDESCROPTOR. It is recommended to look at the imagette (AN1_IMAGETTE, available in N1 archives) if some new evaluation of the photometry is needed;
- In Sra04, all 5 stars in the BSF have a jitter residue: CID 1824 (HD 45965), 2031 (HD 45418), 2069 (HD 45398), 2070 (HD 45546), and 2153 (HD 45517);
- Ad-hoc elimination of the aliasing was applied to CID 1824.

* *SRa05*

This run was dedicated to the multi-satellite campaign on NGC 2264, which gave strong constraints on the date and the duration of the observation.

Rem:

- During the shutdown of the instrument between December 21st to 22nd 2011, the synchronisation of the aboard clock was lost, which prevents from a strict resynchronisation of the data after the recovery of the observations;
- CID 2983 (HD 49429) and 3573 (HD 48752) have a jitter residue;
- Ad-hoc elimination of the aliasing was applied to CID 2983;
- One outlier (value about 2E9) is quite visible on December 1st 2011 at 15:56:56 on all five targets (CIDs 2820, 2983, 3437, 3573 and 3619); no explanation could be found for this phenomenon. The following value at 15:15:57 is correct;
- Due to the renumbering inside EXODAT, the CID 400007811 might be incorrectly identified as well as CID 616780499.

* *LRa06*

Dedicated to the re-observation of CoRoT 7; it has been decided to use an imagette to increase the photometric accuracy. The field allows also the reobservation of CoRoT 12.

In the BSF, HD 49933 has been reobserved for the third time, with a coordinated ground based campaign to try to detect its magnetic field.

Rem:

- The standard pointing correction limits the excursion of the jitter at 1.5 pixel, which has been sufficient for the whole mission except for a few days in this run:
  - from January 20th to 23rd 2012, the maximal excursion (MAX_JIT) was limited to 1.7 pixel;
  - from March 26th to March 29th 2012, MAX_JIT = 1.8 is needed.

* *LRc09*

LRc09 is dedicated to the exoplanet programme in the BSF: the observation for 85 days of HD 179070, a star hosting planet, to try to detect inner transiting planets, if they exist.

Rem:

- Addition of a supplementary second on July 1st 2012 at 1h 59min 60s; the doubled second is withdrawn in the CoRoT data;
- The CID 8111 (HD 179079) has a jitter residue;
- Ad-hoc elimination of the aliasing was applied to CorotID 7981 (HD 178169) because the standard correction leaves a too important residue.

* *LRc10*

LRc10 was driven by the re-observation of the Eclipsing binary HD 169689 for which the primary eclipse was observed incompletely in LRc04.

Rem:

- Ad-hoc elimination of the aliasing had to be applied to CorotID 9540 (HD 169689) and CorotID 9775 (HD 169822).
- CID 9368 (HD 170270) and 9540 (HD 169689) have a jitter residue.
- In September 26th 2012, the changing of the temperature set point took place at the time of the rotation of the solar panels (from 11h56:23 to 12h03:20); therefore, for some light-curves, the correction is not as good as usual.

* *LRc09*

This run was devoted to O stars, which were observed only in SRa02, with great success. Once more the region of NGC 2232 has been chosen.

Rem: It has encountered several perturbations:

- After 20 days the pointing was lost (on October 22nd 2012) and restarted 3 days later;
- After 7 more days later, on November 2nd 2012, chain 2 stopped definitively.

* *Unknown object?*

One object crossing the field of view has been detected in several runs: the object is seen generally 4–5 min in one orbit, and in 6 to 10 contiguous orbits (one orbit lasts about 1h40min).

It has been identified in:

LRa01: 2007/11/20
LRa06: 2012/01/22; 2012/02/15; 2012/03/07
LRc09: 2012/06/17

but it might be present elsewhere.

Some residue of the object is detectable in the stars light-curves.

References

Baglin, A., & Fridlung, M. 2006, ESA SP 1306, in eds. M. Fridlund, A. Baglin, J. Lochard, & L. Conroy, Noorwijk, The Netherlands: ESA Publication Division, ESTEC, ISBN 92-9092-465-9, referred as “The CoRoT book”
Catala, C., Poretti, E., Garrido R., et al. 2006, ESA SP, 1306, 329
Charpinet, S., Cuvilo, J., Platzer, J., et al. 2006, ESA SP, 1306, 353
Deleuil, M., Moutou, C., Deeg, H. J., et al. 2006, ESA SP, 1306, 341
Fridlund, M., Baglin, A., Lochard, J., & Conroy, L. 2006, Noorwijk, The Netherlands: ESA Publication Division, ESTEC, ISBN 92-9092-465-9, referred as “The CoRoT book”
Karioty, F., Auvergne, M., Llebaria, A., et al. 2006, ESA SP, 1306, 305
Llebaria, A., Guterman, P. 2006, ESA SP, 1306, 293
Meunier, J. C., Granet, Y., Agneray, F., et al. 2009, EXODAT The Exoplanets Database from the COROT Project: Evolution and Updates, ASPC, 411, 454
Michel, E., Deleuil, M., & Baglin, A. 2006, ESA SP, 1306, 473
Michel, E., & Baglin, A. 2015, CoRoT3-KASC7 meeting, EPJ web conf., 101, 06002
Pinheiro da Silva, L., Rolland, G., Lapeyrere, V., & Auvergne, M. 2008, MNRAS, 384, 1337
Pires, S, Mathur, S, García, R., et al. 2015, A&A, 574, A18

For more information

Auvergne, M., Boisnard, L., Lam-Trong, T., et al. 2009, A&A, 506, 411
Boisnard, L., Baglin, A., Auvergne, M., et al. 2006, ESA SP1306, p. 465
Epstein, G. 2006, ESA SP, 1306, 165

Acknowledgements: The CoRoT space mission has been developed and operated by CNES, with the contribution of Austria, Belgium, Brazil, ESA, Germany, and Spain.

The CoRoT Legacy Book
© The authors, 2016
DOI: 10.1051/978-2-7598-1876-1.c022

II.2

Description of processes and corrections from observation to delivery

M. Ollivier[1,2], A. Deru[2], S. Chaintreuil[2], A. Ferrigno[2], A. Baglin[2], J.-M. Almenara[3], M. Auvergne[2], S. Barros[4], F. Baudin[1], P. Boumier[1], P.-Y. Chabaud[3], H. Deeg[5], P. Guterman[3,6], L. Jorda[3], R. Samadi[2], and T. Tuna[2,7]

[1] Institut d'Astrophysique Spatiale, UMR 8617, CNRS/Univ. Paris-Sud, Université Paris-Saclay, Bât 121, Université Paris-Sud, 91405 Orsay cedex, France
[2] LESIA, Observatoire de Paris, PSL Research University, CNRS, Sorbonne Universités, UPMC Univ. Paris 06, Univ. Paris Diderot, Sorbonne Paris Cité, 5 place Jules Janssen, 92195 Meudon, France
[3] Laboratoire d'Astrophysique de Marseille, UMR 7326, 13388, Marseille, France
[4] Centro de Astrofisica da Universidade do Porto, Rua das Estrelas, 4150-762 Porto, Portugal
[5] Instituto de Astrofisica de Canarias, Dept. de Investigacion, C/ Via Lactea s/n, 38200 La Laguna, Tenerife, Spain
[6] Division Technique INSU, BP 330, 83507, La Seyne cedex, France
[7] now at the Centre Européen de Recherche et d'Enseignement des Géosciences de l'Environnement, Aix en Provence, France

1. Introduction

The CoRoT observatory, launched the 27th of December 2006 stopped its observations the 2nd of November 2012 after the failure of the second readout detection chain. After 6 months of investigations, the scientific mission was officially ended the 20th of June 2013. The desorbitation procedure of the satellite has been initiated in March 2013, bringing the satellite from its initial orbit at 896 km to a polar orbit at an altitude of 650 km. CoRoT was completely passivated the 17th of June 2013 and should finally fall down on the Earth in about 35 yr.

During its observation phase, CoRoT recorded the photometric light curve of about 150 distinct bright stars (with a visible magnitude between 5.8 and 8) using the bright stars channel (also known as the seismology channel) and more than 160 000 faint stars (with a visible magnitude between 10.5 and 16) using the faint stars channel (also known as the exoplanet channel). Even if the instrument principle and design has been extensively detailed in the literature (Boisnard & Auvergne 2006), the aboard processing, the final data processing pipeline and the successive correction routines have never been extensively described. That is the aim of this paper. We thus present the global data generation, the correction philosophy and the associated algorithms. The detail of corrections applied to the different extends at each version of the data is described in Chaintreuil et al. (2015) in this book.

2. The CoRoT data generation and correction philosophy

The CoRoT camera is made of 4 E2V CCDs:

- two CCDs dedicated to the observation of a few bright stars, with a main scientific goal of asteroseismology (this channel was usually defined as the Asteroseismology channel). The image on the detector is slightly defocused to avoid the pixels saturation. The integration sampling rate is 1 readout per second for 5 bright stars per CCD. The acquisition is driven by the instrument clock.
- two CCDs dedicated to the observation of faint stars, with a main scientific goal of planets hunting (Exoplanet channel). About 6000 stars are simultaneously observed per CCD and their image is slightly dispersed on the detector using a double prism in the optical path. This leads to "chromatic" products where pixels are added in order to obtain 3 "colored" fluxes. Contrary to the bright stars channel, the acquisition sampling rate is 1 readout per 32 s. The acquisition at 32 s is driven by the platform clock. Data at 512-s sampling rate are obtained by stacking aboard 16 measurements at the 32-s sampling rate (see next section). Observation always begins at 512-s sampling rate; it is then updated during the observation run thanks to an algorithm that analyses

directly the data when they are acquired and detects transit candidates, the sampling rate is adjusted (alarm mode: Quentin et al. 2006; Surace et al. 2008; Chabaud et al. 2011; Bonomo et al. 2012). The sampling rate of each target can thus be changed during the observation run. That is why several targets (e.g. CoRoT-2b, Alonso et al. 2008) exhibits various sampling rates on a same light curve.

The CCDs are driven by 2 separate chains of electronics for redondancy. Each chain processes 1 CCD of each program. The CCDs are read half by half, and the gain and offset are adapted to each readout process.

The number of oversampled stars in the faint stars channel is limited by the global telemetry budget. At the beginning of the mission, where telemetry had to deal with the four CCDs, the number of oversampled stars was limited to 500 stars per CCD (over about 6000 observed stars). After the failure of one of the two detection chains in March 2009, the telemetry budget could strongly be relaxed and the number of oversampled targets was increased to reach 2000 stars on the remaining CCD.

In the same time, “imagettes” (small parts of the CCD) were acquired on both channels. For the bright stars channel, the star windows are 35×35 pixels large and correspond to the observed stars (5 per CCD). For the faint stars channel, 20 windows of 15 × 10 pixels per CCD sampled at 32 s could be acquired and downloaded. At the beginning of the project, they were considered to monitor in real time the evolution of the instrument and the quality of the image (engineering use), in order to anticipate a mismatch between the stellar images and the available photometric masks. After the failure of the first detection chain, the number of imagettes on the remaining faint stars CCD (E2) was increased to 40 and the imagettes were used for science. For instance, imagettes were put on slightly saturated stars (V magnitude slightly higher than 10), in order to optimize the photometry measurement and get good S/N ratio light curves.

The CoRoT final data are the result of a complex process that happens at different levels:

- on board: some corrections are directly performed during the observation phase, and before the data transfer to the Earth;
- on the ground: thanks to two successive pipelines.

During the observation phase, the CoRoT photometric data are packed and transmitted to the ground from the satellite through telemetry packets. They are collected at CNES after reception at Kiruna, Wien, Aussagel, and Natal facilities. The telemetry packets are then gathered to generate the first level (0-level) of data named N0. The N0 data can thus be considered as the “raw data” and should be processed before distribution to the scientists.

The global correction philosophy, adopted by the project from the beginning, is to consider and correct only effects that can be identified, quantified and modeled because they can be associated to a well defined effect (e.g.: background, cross talk, temperature jumps...). It means that no systematics removal algorithm is used in the process (at least not before the end of the complete process), and no correction is applied if the origin, nature or amplitude of the effect to be corrected is not identified.

The raw data then enter two successive pipelines of corrections:

- the level 0 to level 1 pipeline (also named pipeline N0->N1): in this pipeline, corrections are made on the fly when data are available and do not require parameters that should be computed using the whole data set. It means that N1 data are ready more or less at the end of the observation run, and do not include any correction made with a further knowledge of the instrument behavior or ageing;
- the level 1 to level 2 pipeline (also named pipeline N1->N2): corrections are applied at the end of the run, and use quantities or parameters evaluated with the data of the complete run. In some cases, corrections were applied only at the end of the mission, thanks to a better understanding of the instrument, its response, its ageing...

In this paper, we will first describe the corrections made aboard, and then on the ground without distinguishing systematically whether they are performed on level 0 or level 1 data. The data contained in the legacy archive are level 2 data. They are available at CDS[1] at IAS[2], and associated mirror site at NASA and in Spain. Level 1 data however are available upon request either on the IAS archive or at CNES but require a deep understanding of the instrument and the observation conditions to be scientifically usable.

3. Onboard processes and corrections

During observation phases, several processes are run aboard. They gather a bunch of routines driving key-actions:

- acquisition of the astrophysical signal and other quantities (background, offsets...);
- performing basic signal processing elements: subtraction of biases, stacking of observations, sum of pixels contents, evaluation of observation quality...

Each channel (bright stars and faint stars) has its own set of corrections. In this section, we describe these processes. A more detailed description of each process including the complete algorithms can be found in the software User Requirements Documents written by Plasson (2009).

3.1. Bright stars channel

In the bright stars channel, fluxes are computed every second.

The Astero Scientific Processing Service (ASPS) is the service run on the bright stars channel during the observation runs. It is successively made of:

The Astero Offset window Processing (AOP)
Each offset window is used to determine the electronic mean level of the associated half-CCD updated at each exposure. The software computes for each offset window:

- the median value of each offset window;
- the number of bright and impacted pixels using a threshold applied to the deviation to the median offset value;

---

[1] `http://vizier.u-strasbg.fr/viz-bin/VizieR-2`
[2] `http://idoc-corot.ias.u-psud.fr/`

- the arithmetic mean of non impacted and non-bright pixels;
- the variance on non-impacted and non-bright pixels;
- the electronic offset value on each half CCD.

The Astero Background Local Processing (ABLP)
This processing is made to determine the mean and variance values of the local sky background. This value is computed for each window and updated at each exposure. The computation is based on a moving average and variance of the non-impacted pixels of the window, of the last 30 exposures. The software :

- subtracts the electronic offset to all the pixels;
- computes the median pixel intensity;
- computes the number of impacted and brilliant pixels;
- computes the arithmetic mean of non-impacted and non-bright pixels;
- computes the variance of non-impacted and non-bright pixels;
- computes the value of the sky background per pixel.

The Astero Star window Main Processing (ASMP)
This processing was made to perform noise corrections and a temporal photometry of each observed star using a mask method. In the case of a SAA crossing, the processing could be modified to detect and correct additional noises due to the proton impacts. As proton impacts did not disrupt the processing aboard, the parameters were set so that this mechanism was not functional. For each stellar window, the software:

- subtracts the electronic offsets to all the pixels;
- subtracts the sky background value to all the pixels;
- computes the barycenter (photocenter) of the windows;
- computes the total intensity (photometric process);
- writes the computed parameters in the corresponding product.

The Astero Star window Accumulation Processing (ASAP)
This processing was designed to record small parts of images called “imagettes” accumulated aboard. This processing was performed only on several selected astero windows and only if the previous ASMP processing did not detect errors during noise correction.

In conclusion, one should bear in mind that, in the case of bright stars, offsets windows as well as background windows are computed on-board and subtracted on-board to the flux of the stars.

3.2. Faint stars channel

Observations last 32 s; the ordinary behaviour is to accumulate 16 observations, leading to a 512-s sampling. Some chosen stars are observed at 32 s, in a so-called oversampling rate.

The Exo Scientific Processing Service (ESPS) is the service run on the faint stars channel during the observation runs. It is made of:

Exo Monochromatic window Processing (EMP)
This process computes the raw flux of all the exoplanet monochromatic windows. The software :

- sums the intensity of each image in the case of 32-s sampling rate. The result is the final intensity;
- performs data accumulation (16 times the previous process) in the case of data sampled at 512 s;
- computes the mean and standard deviation of each of the 16 images, in the case of data sampled at 512 s;
- computes the number of bright pixels.

Exo Chromatic window Processing (ECP)
This process computes the raw flux in each chromatic zone of all the chromatic windows. The software :

- computes the exo spectrum by adding the flux in each column of the mask;
- computes the blue, green and red fluxes by summing the flux of spectral elements in the specific chromatic zones defined by the chromatic mask limits, as defined during the observation setup phase, at a 32-s sampling rate;
- performs data accumulation (16 times the previous process) to get data sampled at 512 s;
- computes the mean and standard deviation of each chromatic flux of the 16 integrations, in the case of data sampled at 512 s.

Chromatic processing applies to the brightest stars (magnitude from 10 to 14) whereas monochromatic processing applies to fainter stars. Monochromatic processing also applies to offset and background windows; all types of windows are undifferentiated on-board. They are processed differently only on ground where offsets and backgrounds are subtracted from the light-curves of the stars.

Exo Imagette window Processing (EIP)
This processing is performed on each imagette window to transmit all the pixels of each exposure. Let us remind than an imagette is a 10×15 pixels window, acquired at a sampling rate of 1 exposure per 32 s.

4. Ground-based processes and corrections

In this section, we only describe the final version of the pipelines and associated algorithms and data. For a detailed list of the process versions, see Chaintreuil et al. (2015) in this book.

In this paper, we decided to detail only the effects and algorithms that have not been described extensively previously. This paper should thus be associated to other ones: Auvergne et al. (2009) that was published after 2 yr in orbit and Lapeyrere (2006) for the specific question of the detectors.

4.1. Chronology of ground based corrections

4.1.1. Bright stars channel data

After several corrections made aboard (cf. previous section), several corrections are applied to the bright stars channel data, thanks to the two ground-based pipelines generating level 1 and 2 data.

The successive global or specific processes leading to level 1 and 2 data and their various extends from level 0 data are described on Fig. II.2.1.

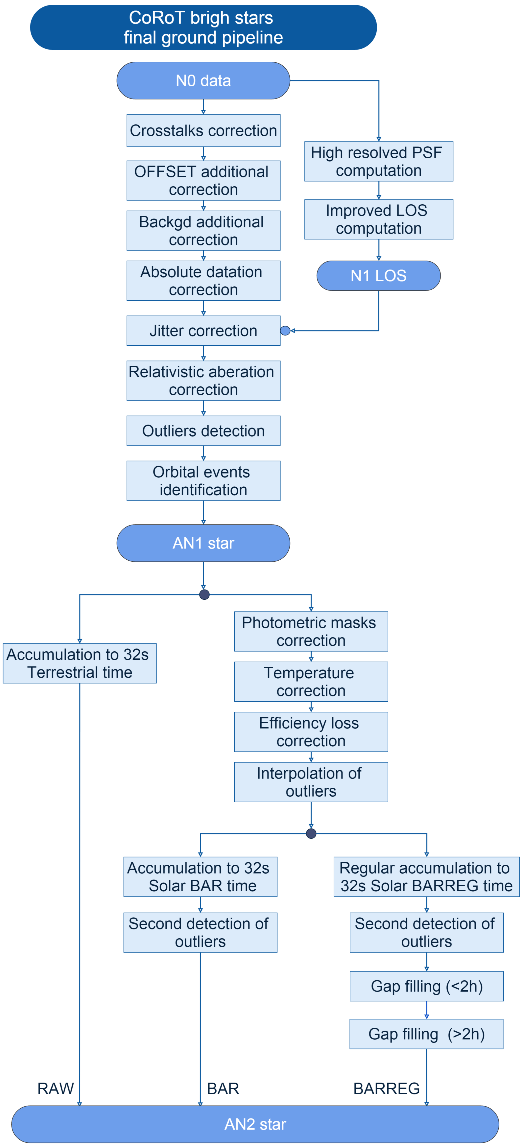

Fig. II.2.1. Synoptic view of the Level 1 and 2 data generation from N0 data, on the bright stars channel. AN1 star data are intermediary products corrected only using on-the-fly algorithms and do not include corrections that are made globally considering the whole run data.

4.1.2. Faint stars channel data

Contrary to the bright stars, no correction are performed aboard for the faint stars. The data corrections are made only from the ground and are detailed on Fig. II.2.2.

In the next subsections, we detail the main correction algorithms.

4.1.3. Faint stars channel imagettes

The faint stars channel imagettes are acquired and transmitted as they are to the ground where they are processed to get the light curves. The detail of the imagette pipeline is given on Fig. II.2.3. Note that the colored light curves once created are processed by the same pipeline as described in previous section (except for what concerns the creation of white photometry and the correction of jumps).

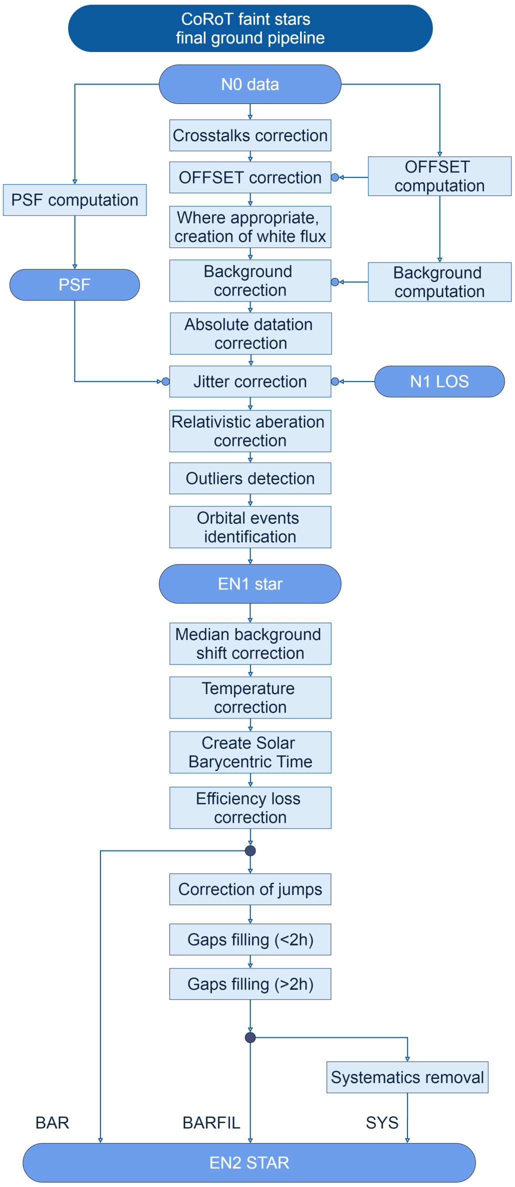

Fig. II.2.2. Synoptic view of the Level 1 and 2 data generation from N0 data, on the faint stars channel. EN1 star data are intermediary products corrected only using on-the-fly algorithms and do not include corrections that are made globally considering the whole run data.

Important fact: in the case of faint stars channel data, whatever they are extracted from (classical photometry or imagettes), several extends are created:

- BAR: data processed and time given in barycentric time;
- BARFILL: same as before but the "jumps" are corrected using a two step correction algorithm (see Sect. 4.2.14) and the gaps due to data loss (SAA crossing or telemetry loss) are filled using an Inpainting algorithm (see Sect. 4.2.15). These data are particularly useful when a continuous time serie is required for analysis;
- SYS: it is BARFILL data plus a systematics removal algorithm (see Sect. 4.2.16). These data are particularly suited for research programs that require very clean and continuous data.

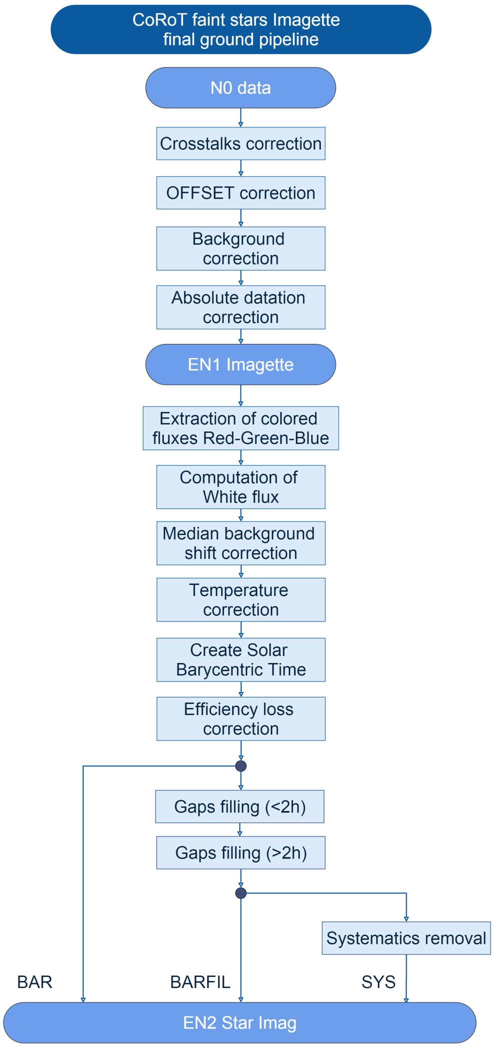

Fig. II.2.3. Synoptic veiw of the imagette pipeline.

An exemple of the same light curve but in its different extends BAR, BARFILL and SYS is given on Fig. II.2.4

4.2. Correction algorithms

4.2.1. Elimination of the aliasing (crosstalk)

This process concerns both channels data. Crosstalk results from the fact that bright stars and faint stars CCDs are not read and operated the same way aboard:

- bright stars CCDs are windowed around the observed targets (5 stars per CCD) and the 5 stellar and background windows are read once every second. The process is driven by the instrument clock;
- faint stars CCDs are read once every 32 s. The process is driven by the clock of the service module.

Fortunaltely, both processes are synchronized by the service module clock, so that the perturbation patterns on both types of CCD are stable in time, each perturbation corresponding to a specific command (one of the 15 low level commands such as pixel digitisation, line transfer to the register...). Because of the stability of the process, the amplitude of the pattern associated to one specific low-level command can be calibrated and a final global crosstalk pattern can be computed for each CCD. A complete description of crosstalk components and images of associated patterns can be found in Auvergne et al. (2009).

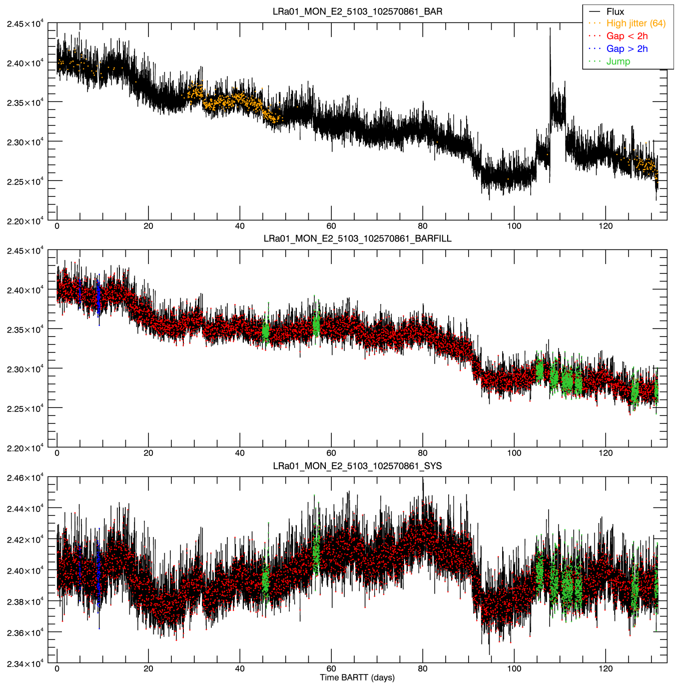

Fig. II.2.4. Example of data of the faint stars channel in its 3 extends BAR, BARFILL and SYS.

The elimination of the aliasing is thus a simple process where the crosstalk pattern effet is computed for each photometric mask and its global effect is subtracted from the corresponding light curve.

In very few cases, when the star is positioned in the lower rows of the CDD, read at first, the calibrated correction introduces a periodical artefact at a period of 32 s. This is quite penalizing, thus, in this case, an ad-hoc correction is applied.

4.2.2. Elimination of offset and background contribution

This process concerns only the faint stars channel data. For the bright stars channel data, the process is performed aboard (see previous section).

The background estimation all over the CCD is given by 196 windows (10 × 10 pixels), defined during the observation setup phase and distributed all over the CCDs in dark starless zones; 147 windows are sampled at 512 s and 49 others at 32s, per CCD as shown in Fig. II.2.6. The background correction is done in 3 steps:

- removal of the background median value, the method is extensively described in Drummond (2007), and Drummond et al. (2008);
- correction of the Y-dependency, due to the ageing of the detectors and the increase of the dark current with time;
- correction of the differences between the 32-s and 512-s median background estimations, due to a bias in the positioning of the background windows at different sampling rates.

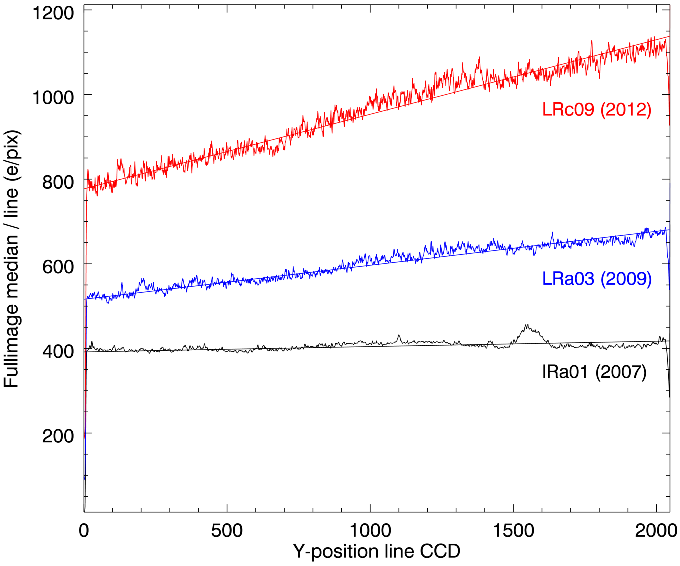

Fig. II.2.5. Evolution of the background due to the dark current as a function of time.

With the ageing of the telescope, phenomena that were minimized at the beginning of the mission are now very influential, like the value of the dark-current. The median method used in a first time (step 1 of the process described above), is not adapted any longer to properly evaluate the level of the background. Assuming that the faint stars CCD readout process duration is 23 s, the increase of the dark current causes a dependency between the background level and the position on the CCD, especially with the Y axis, along the readout direction. This dependency is modelled at the beginning of each run by a first order model, and used to adjust the background correction as following.

$$\mathrm{Flux}_{\mathrm{corrected}}\ (t, y_{\mathrm{CCD}})) = Flux(t) - BG_{\mathrm{median}} - (a * y_{\mathrm{CCD}} + b) \quad (1)$$

where y_{CCD} is the y position of the star on the CCD, and $\{a, b\}$ the parameters of the dark current model. The parameters $\{a, b\}$ are a function of the run, and are evaluated thanks to the field image acquired at the beginning of each run. Figure II.2.5 shows clearly that the dark current increases with time.

The last part of the background correction is done in the N1 to N2 pipeline. The mapping of the 196 background windows on the CDD is biased: the distribution between the 512-s windows and the 32-s ones is not namely homogenous along the Y axis (i.e.: the barycentre of the windows distribution is not the same, see Fig. II.2.6). Since the Y position has an impact on the background level, the median level estimated thanks to the windows at the different sampling rate is not the same, leading to a bias between 32-s and 512-s sampled data. This bias leads to a jump in the photometry when the sampling rate is changed during the observation sequence. By resampling the 32-s windows at 512 s, a global median value is computed on the 196 windows, and then used to compute the mean shift to apply to each part.

$$Shift_{32} = < BGMed_{32}(t) - BGMed_{\mathrm{global}}(t) > \quad (2)$$
$$Shift_{512} = < BGMed_{512}(t) - BGMed_{\mathrm{global}}(t) > \quad (3)$$

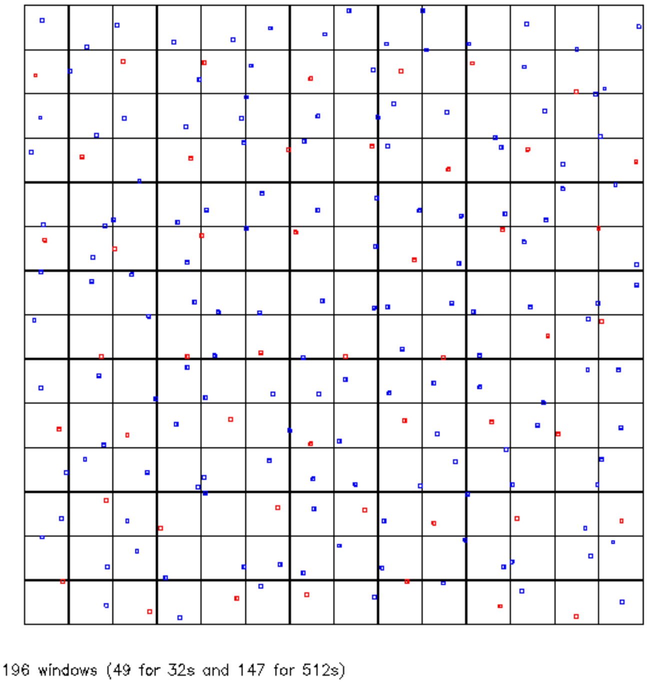

Fig. II.2.6. Position of the background windows at 512-s sampling rate (blue) and 32-s sampling rate (red).

The corrected flux reaches the mean level it would have had if the 196 background windows were used to compute the median background level.

4.2.3. Correction of the exposure time

This process concerns both bright stars and faint stars channels data.

As already mentioned above, the CoRoT satellite includes several aboard clocks: among them, one:

- at the service module level (platform clock), giving a top every 32 seconds and used to drive the faint stars channel and synchronize the bright stars channel processes;
- at the instrument level (instrument clock), giving a top at each second, driving the bright stars channel acquisition processes.

Both clocks are driven by oscillating quartzs, but do not have the same accuracy. The platform clock has a stability of about 2 microseconds per second. This stability is a function of the satellite temperature while the instrument clock is much more accurate. Because the 32-s integration cycle for both channels is driven by the platform clock, the faint stars channel exposure times exhibit fluctuations with time and temperature. In addition, because the 1-second integration process in the bright stars channel is driven by the instrument clock and the overall 32-seconds cycle driven by the platform clock, elementary integration time (and thus flux) corrections have to be done. These corrections have been described extensively by Samadi et al. (2007).

On the bright stars channel, the 32 s are in fact 31 s given by the instrument clock plus a duration corresponding to the time between the 31st second top given by the instrument clock and the platform top that synchronizes the two channels every 32 s, at the accuracy of the platform clock. The correction is done using the aboard GPS time considered as the primary reference. The value of each counter and corresponding GPS time is recorded at each platform top so that it is possible to know the exact duration of the last "second" of bright star channel integration process. The correction applied is thus a simple proportional correction to know the exact duraction of the last second of integration.

On the faint star channel, the GPS time is used to determine the exact duration of the integration and the exact date of the exposure.

At the end of the process of correction at L1/N1 level, the flux is given:

- per second (TT) for the bright stars channel data;
- per 32 seconds (TT) for the faint stars channel data.

4.2.4. Absolute datation

This process concerns both bright stars and faint stars channels data.

The way data are absolutely dated changed from what it was at the beginning of the mission. Now (final version of the data), absolute datation is done as following:

- on the bright stars channel: the absolute date is the barycentre of the integration phases;
- in the faint stars channel: the absolute date is the middle of the integration process.

Datation is now done in terrestrial time (TT) which is much more accurate than Universal Time (UT). The conversion from UT to TT has been done using the relation:

$$\mathrm{TT} = \mathrm{DATEJD} + \frac{32,184\mathrm{s} + \mathrm{offset}}{86400} \qquad (4)$$

with offset = 35, 34 or 33.

4.2.5. Data resampling

This process concerns only the bright stars channel data.

The data of the bright stars channel are a stack of 32 elementary integrations acquired at a 1-second sampling rate. During the resampling, only the valid acquisitions are taken into account if they are sufficiently numerous. If there are too many invalid exposures, all the 32 acquisitions are combined and the status of the resulting point is set accordingly. The minimum number of valid exposures taken into account varies between the different extends of the data. For the RAW extend, only 7 valid exposures upon 32, are necessary to consider the point as valid. For the 2 other extends, BAR and BARREG, at least 16 valid exposures upon 32 are required to consider the point as valid. If less than 16 (or 7 for the RAW) exposures are valid, then the 32 exposures are cumulated and the points are flagged as invalid.

4.2.6. Correction of mask switch jumps

This process concerns only the bright stars channel data.

In observation mode on the bright stars channel, two successive photometric masks are applied to each star. The first one is a rough mask used for the calibration at the beginning of the run. The second one is the specific mask computed and adapted to accurate stellar photometry. However the modification of the masks leads to a discontinuity in the light curve, which needs to be corrected.

By superposing the photometric masks with a time serie of imagettes recorded at the beginning of the run, the mean flux produced by each mask can be measured. The ratio of the 2 fluxes gives the amplitude of the discontinuity, and can be used as a multiplicative factor to correct the light curve of the first sequence. With this method, a table is created, containing a multiplicative factor for each star of the bright stars channel.

In few cases (it happened 2 or 3 times), this method does not give the expected results. In these cases, an empiric method is used to correct the mask discontinuity. The amplitude of the discontinuity is directly measured on the light curve and the first sequence is adjusted to the level of the second sequence. To know which correction was used in the data, a keyword in the primary header of the file has been created: "MASK_COR". If it is equal to 1, the first method using the mask is used, and if it is equal to 2, then the empirical one is used.

4.2.7. Correction of jitter effects

The jitter effects are a slight variation of the line of sight of the instrument linked to the intrinsic performance of the plateform pointing system (AOCS). In the case of CoRoT, the AOCS was driven by the instrument itself, in order to increase the stability performance. Nevertheless, pointing residuals reaching 0.3 arcsec (about 1/10th of pixel) at 1σ per axis could be observed in the raw data. The pointing residuals were frequencially located at even harmonics of the orbital period, and in a large spectral band around 5×10^4 μHz (Auvergne et al. 2009).

Specific methods of correction based on PSF fitting have been developed for the bright stars (Drummond 2007; Drummond et al. 2008) and the faint stars (Fialho et al. 2007) channels. These methods require 5 steps:

- building of reference PSFs on both channels, with a spatial resolution higher than the resolution of the CoRoT images;
- estimation of the global fluctuations of the line of sight, using the housekeeping and the information given by the AOCS and the instrument;
- estimation of the position fluctuations of each star on the field assuming the line of sight variations, using the observation geometrical model;
- evaluation of photometric consequences of the jitter on a well spatially sampled grid, thanks to the reference PSFs, and construction of a jitter surface;
- interpolation of the grid at any position fluctuation given by the AOCS for any star in the field.

The difference between bright and faint stars channel is only in the spatial resolution of the PSF used for the jitter surface construction. The consequences of correction on the Fourier spectra of photometric light curves is shown in Auvergne et al. (2009). Because of spatial variations of the PSFs over the field of view, the process should be optimized for a specific region of each CCD.

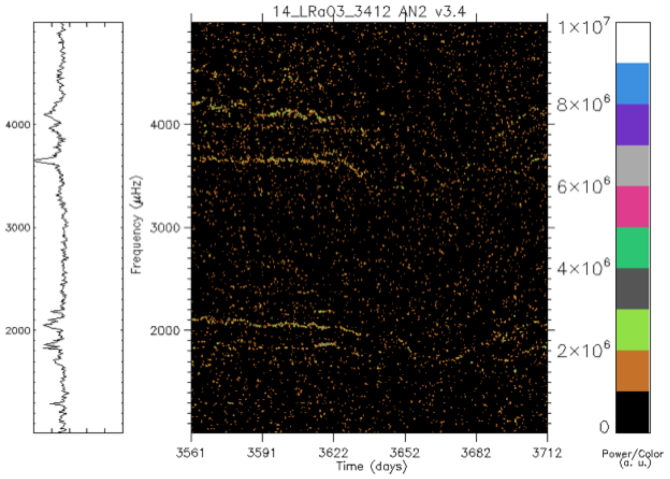

Fig. II.2.7. Evolution of the spectrum of HD 43317 with time for which jitter residuals are well visible and identified (power between 2000 and 4000 μHz; see the text for complete description) in LRa03.

The process has been implemented on both channels and runs routinely. The only case where the process is not efficient appears on the bright stars channel, when the photometric mask is too tight compared to the size of the stellar image. In that case, photometric information is lost due to mask side effects.

4.2.8. Pointing anomalies and effects on light curves

The effects of the residual jitter of the satellite is corrected on the light curves thanks to an accurate and permanent determination of the line of sight (see previous section). However, a careful examination of some bright stars channel light curves shows clearly some uncorrected flux fluctuations strongly correlated to the fluctuations of the photocentre of the stars that are used for the line of sight determination and the satellite orbital attitude control system. Practically, we observe (cf. Fig. II.2.7):

- the presence of frequency bands around 2 and 4 mHz (2 mHz = 500 s) in the Fourier transform of the stellar flux;
- artifacts are identical on several stars of a same run;
- but all the stars of a same run are not affected;
- the frequency of the artifacts is not constant and the firts band in the spectrum is between 1.5 and 2.5 mHz;
- there is power in the harmonics but it decreases quickly.

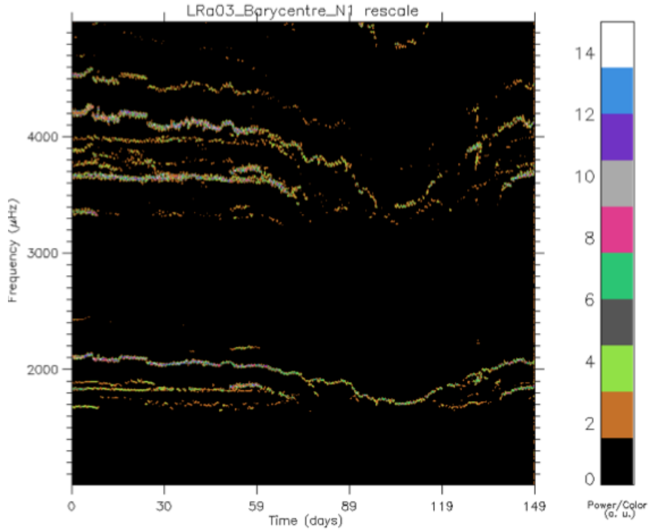

Fig. II.2.8. Spectrum of the photocentre of HD 43317.

After investigations, we came to the conclusion that it was jitter residuals because it was correlated with the barycentre signal (Fig. II.2.8) and that the jitter algorithm itself was not involved in this effect because a large majority of the other observation runs does not exhibit such an effect. After deeper investigations we also came to the conclusion that, in some cases, the size of the window used to estimate the photocentre of the guiding stars (35 × 35 pixels windows) was too small compared to the extend of the PSF in some part of the bright stars CCDs. As a consequence, the barycentre and the variations of the line of sight determined using the guiding stars are slightly biased and noised. Unfortunately, part of the line of sight information is lost and cannot be extrapolated. We decided to keep the light curves associated with these runs uncorrected and to deliver the position of the photocentre in a special file (AN2_POINTING).

4.2.9. Correction of relativistic aberration

This process concerns both bright stars and faint stars channels data.

The relativistic aberration is an apparent change in the direction of an object observed by a moving observatory, and in our case, by CoRoT on its orbit around the Earth, which orbits around the sun. Theoretically speaking let θ_s be the angle between the direction of the target and the moving direction of CoRoT . Then the apparent deflection angle θ_0 is given by the relation:

$$\cos(\theta_0) = \frac{\cos(\theta_s) - \frac{v}{c}}{1 - \frac{v}{c}\cos\theta_s} \qquad (5)$$

where v is the speed of CoRoT with respect to the observed source and c is the speed of light in vacuum. On the image, the global effect of the relativistic aberration is a field distorsion. The orbital motion of CoRoT around the Earth at about 7.4 $\mathrm{km\,s^{-1}}$ is negligible compared to the motion of the Earth around the Sun at about 30.8 $\mathrm{km\,s^{-1}}$. In the formula above, the speed vector of the observatory is thus the speed vector of the Earth around the Sun. The relativistic aberration is thus maximum more or less in the middle of long runs, when the Earth motion is perpendicular to the line of sight of the instrument. In that case, $\theta_s = \frac{\pi}{2}$ and $\theta_0 = \frac{v}{c} \sim 10^{-4}$ rad $\sim$ 20 arcsec. This corresponds to about 8 pixels. Fortunately, the first order of the effect is a global translation of the field and is corrected by the attitude control system of the satellite, thanks to the CoRoT instrument that works as a fringe tracker. Only the differential residuals from one side of the field to the other one have to be corrected. It gives a dilatation (resp contraction) of the field of view, equivalent to a focal length slow variation, i.e.: a radial shift of the stars position with respect to the line of sight. Assuming a field of view of 1.7 square degrees, this leads to a differential shift (top-left to bottom-right corners) of less than 10^{-5} rad, i.e. 2 arcsec, which is less than a pixel (pixel size: 2.3 arcsec).

The correction of the relativistic aberration was not considered in the first versions of the pipeline. At present, the correction of the effect is included in the jitter correction algorithm (see previous subsection), and particularly in the estimation of the line of sight variations. The focus of the telescope, slightly variable with time, is considered in the computation of the observation geometrical model. Thus, the stellar image shift due to the relativistic aberration, which is a function of the position of the stellar image on the field can be estimated, and is added to the global field jitter due to AOCS fluctuations. Relativistic aberration effects are slow compared to jitters variations. The associated variation of the size of the images, both in the faint and in the bright stars channels, and due to the slight defocus, are negligible and neglegted.

4.2.10. Correction of the detection chain loss of efficiency

This process concerns both bright stars and faint stars channels data.

During the mission duration, several effects led to a degradation of the detection chain efficiency:

- loss of transmission due to optical ageing;
- increase of the dark current;
- electronic noise increase;
- loss of electron transfer efficiency within the CCD;
- ...

As a consequence, the efficiency of the photons collection decreased and caused a long linear trend, especially visible over a complete long run. The average efficiency loss has been estimated by Auvergne et al. (2009) to about 10%. The value of the slope of the linear trend is different for each star, It is directly linked to the intensity of the star. At the end of the mission, all the available data were used to build a model which links the intensity of a star to the slope of the linear decrease of the efficiency.

$$\mathrm{Loss}_{\mathrm{slope}}(\bar{f}) = \alpha_2 x \bar{f}^2 + \alpha_1 * \bar{f} \tag{6}$$

Where $\bar{f}$ is the mean flux of the star, and (α_2,α_1) are the two parameters of the model.

In the pipeline, the efficiency loss correction works in two phases:

- the mean flux of the star is used with the model to compute the estimated linear slope of the efficiency loss;
- the light curve is corrected by adding the estimated loss along the time.

$$\mathrm{Flux}_{\mathrm{corr}}(t, \bar{f}) = \mathrm{flux}(t) - \mathrm{Loss}_{\mathrm{slope}}(\bar{f}) * t \tag{7}$$

The slope used to correct the curve is given in the primary header of the file, in the field "COR_SLOP".

Figure II.2.9 shows an example of transmission loss correction on a bright star from LRa04.

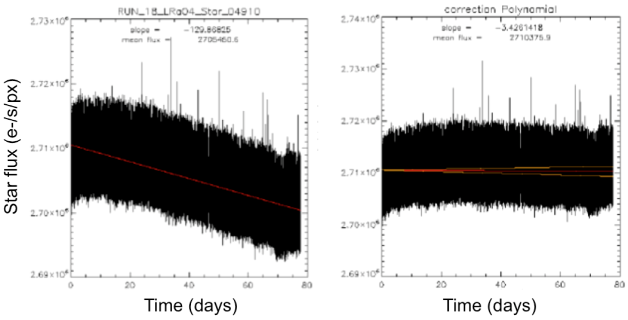

Fig. II.2.9. A light curve before (*left*) and after (*right*) correction of the efficiency loss.

4.2.11. Identification of orbital events and detection of outliers

CoRoT was placed on a near circular polar orbit, with an apogee at 911 km, a perigee at 888 km, and a period of 6184 seconds. Because it is an inertial orbit, the spacecraft crosses regularly specific zones over the Earth:

- the South Atlantic Anomaly (SAA): it is a wide region of South America and South Atlantic Ocean where the magnetic field is a bit stronger, leading to a decrease of the altitude of the inner part of the Van Halen belts. As a consequence, at a given altitude, the proton impact rate is higher in this region compared to the other ones. In the case of CoRoT, the SAA crossing leads to a dramatic amount of proton impacts on the detector so that the stellar photometric information is partially lost or at least strongly affected. In order to better identify these events, a flag has been created to mark the data acquired during the SAA crossing. CoRoT also helped to draw a more accurate map of this region (see Auvergne et al. 2009);
- the Earth shadow: corresponding more or less to the fly over night regions. The first effect on the photometric light curves is a strong modification of the scattered light, but also, short-term thermal effects at ingress and regress in the shadow of the Earth, modificating for a few seconds the stability of the line of sight. Once again, ingress and regress are flagged because line of sight sudden variations create a strong jitter effect on the photometric light curves (see Pinheiro da Silva et al. 2008).

4.2.12. Creation of the white photometry

This process concerns only the chromatic light curves of the faint stars channel. The white photometry is the result of a simple co-addition of the blue, green and red photometry previously computed aboard. This white light curve has at least two advantages:

- for detection: the signal to noise ratios of the white light curves are much higher than those of colored light curves;
- the jitter effects, and particularly due to colors borders are strongly reduced.

4.2.13. Correction of thermal jumps

This process concerns both bright stars and faint stars channels data.

The temperature of the CoRoT instrument was not actively servo-controlled. The focal plane of the instrument was connected to a radiator, decreasing its temperature to a value between -50 and -40 Celsius. This temperature depends on the orientation of the radiator with respect to the Sun. As a consequence, the radiator temperature varies along the Earth orbit, and particularly during a long run. In order to avoid the focal plane temperature varying during an observation run, a stable reference temperature is set by heating the plate where the detectors are mounted and controlling the final temperature. The temperature of the radiator along the orbit and the corresponding temperature of the focal plane are estimated thanks to an abacus assuming the field of view to be observed, and the corresponding orientation of the satellite with respect to the Sun, all along the duration of the run. The reference temperature, applied to the temperature controller is chosen to be slightly higher than the highest temperature given by the abacus, so that the order of the servo control is not changed during the observation and the final temperature of the detector is stable during the run.

The temperature of the CCDs of the satellite was effectively controlled, therefore the time variations of the measured temperature are small enough to avoid requesting a correction along the run. However during the mission, it happened that the order of the temperature control system had to be changed during a run because the controller could not work properly, causing steps in the temperature curves of the detectors. As an example, the temperature order had been changed six times during the LRa01 observation run. Those orders need to be corrected. The purpose of this correction is to match the jumps seen on the temperature curve (HK) and the effects seen on the light curve. Since the exact function, converting a temperature jump into the corresponding jump in the electronic signal, has too many parameters to be correctly computed, the correction uses the optimisation of a numerical model of the jump. The following equations are established on a short window around the temperature jump.

$$\text{Light curve model }(t) = a(t-b) - c * T2(t) + d \tag{8}$$

with t in a window of n points, and where $T2$ is a temperature curve, normalised as a function of the mean level before the jump:

$$T2(t) = \frac{HK(T)}{\frac{1}{k}\sum_{i=1}^{k} HK(t_i)} - 1 \tag{9}$$

with k the index of the jump, in the considered window ($k < n$).

Then the four parameters of the light curve model a, b, c, d are optimised to fit the light curve, on a window around the date of the temperature order. During the optimisation process, several lengths of windows are tested, from 8 hours to 2 days, in order to avoid fitting the stellar activity of the star. Once the fit is complete, the best model is chosen to generate a correction factor. Actually, only the parameter c of the model is used; it represents the amplitude of the jump. The correction factor is applied from the first point after the change of temperature to the next order, or to the end of the data set, if no other temperature jump is encountered.

$$\text{Corr}_{\text{factor}}(t) = 1 + \left(\frac{HK(t)}{\frac{1}{k}\sum_{i=1}^{k} HK(t_i)} - 1\right) * c \tag{10}$$

In the header of the N2 data, specific fields give information about the temperature correction results:

- NB_CONSI: gives the number of temperature orders in the run;
- DATE_TPE: gives the date at which the temperature order changes. This field is duplicated 6 times, because it is the maximum number of temperature jumps recorded in the data, but most of the time there is only one;
- COR_TPE: also duplicated 6 times, it gives the status of the temperature correction for the considered jump. This flag can take 3 values:
  - 0: means the correction worked without issues;
  - 1: means the correction worked but with a warning. It may be either a failure during the optimisation process on one of the windows, even though at least one of the other windows worked, or a mismatch between the date of the temperature change and the data, especially if the temperature change happened before the beginning of the faint star sequence;
  - -1: means the correction did not work.

4.2.14. Correction of non-thermal jumps

This process concerns only the faint stars channel data. It is necessary for aboard computed light curves, not for the light curves obtained on the ground from aboard imagettes; therefore, it is not applied on the later.

The purpose of the jumps correction is to detect and correct the jumps not compensated by the previous algorithm. The CoRoT data, and especially the faint star light curves, show two kinds of jumps:

- the result of impacts of protons on the CCD; they are leading to a sudden increase of the flux in the light curve, followed by a rather exponential decrease. The decrease time is usually unknown and can strongly vary from one jump to another one;
- an abnormal behaviour of the aboard software , leading to an alternation between two states, and between two different reference levels.

  In a first time, the algorithm detects the jumps by comparing the mean values before and after each point of the curve. The size of the moving windows used to compute the mean value depends on the sampling rate of the curve (see Table II.2.1). If the difference with the mean values is greater than 7σ then a jump is detected.

For each detected jump, a negative exponential model, is fitted on a short window after the jump. The model is used to adjust the light curve as a function of the median level before the jump. The lengths of the windows used to compute the median level or to fit the model are detailed in Table II.2.1.

$$\text{Jump model}(t) = \mathrm{e}^{a(t-c)} + b \quad (\text{with } a \leq 0) \tag{11}$$

$$\text{Flux}_{\text{corr}}(t) = \frac{\text{Flux}(t)}{\text{Jump model}(t)} * \text{Median}_{\text{before jump}} \tag{12}$$

An example of proton impact induced jump correction is given on Fig. II.2.10.

In some cases, the jump detection can identify structures which are not discontinuities, like eclipses of binary stars or the transits of exoplanets. To avoid those events being corrected by the jump detection algorithm, a special

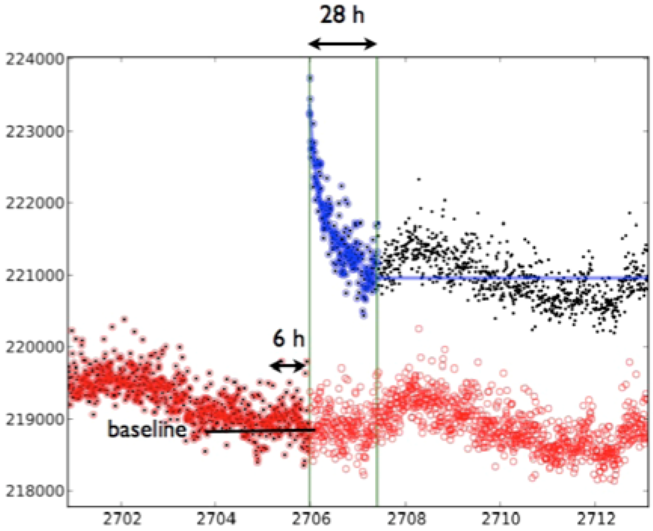

Fig. II.2.10. Example of a proton impact-induced.

Table II.2.1. Lengths of the windows used to compute the median level or to fit the model as a function of the sampling rate.

	32 s	512 s
Nb of points used to compute the mean before and after a jump	150 points 1.3 hour	20 points 2.8 hours
Nb of points used to fit the model	200 points 1.77 hour	200 points 28.4 hours
Nb of points used to compute the median level before the jump	40 points 21.3 min	40 points 5.7 hours

treatment is applied to all the binaries and the transit candidates detected by the exoplanet team. Their parameters, ephemerides, period and transit duration, and their associated errors (Deleuil et al., 2015) are used as an input of the function; if a jump is detected in a region of a transit-like event, the jump is not corrected. The safety region around the transit events is determined taking into account the transit duration and its associated uncertainty. In practice, the safety region duration is about a few hours, which corresponds to the longest time window used in the correction algorithm. In some specific cases, the algorithm failed and detected non existing (real) jumps. The correction process introduced extra perturbations. This phenomenum has been identified in about one third of the objects of a specific sample of RR lyrae. This point is considered in Appendix A at the end of the paper.

4.2.15. Filling the gaps

This process concerns both bright stars and faint stars channels data.

The Inpainting method developed by Pires et al. (2015) is used on the CoRoT data to fill the gaps in the light curves. The gaps can either result from some missing values during the inflight acquisition, or from the removal of invalid data during the ground-based processes. All the gaps are filled, even those of several days. But to ensure the proper behaviour of the algorithm, process is performed in two steps:

- the short timescale gaps (less than two hours) are first corrected;
- the remaining gaps are filled without limit of duration.

The distinction between the two steps is possible thanks to the status of the new points, each step having a specific status. On the bright stars channel, the BARREG extend is perfectly filled and ready to use in spectral analysis, with a proper 32-s sampling. On the faint star channel, the BARFIL extend is also filled, but it is possible to find some specific gaps in the data. Indeed for the light curves with an oversampling, the gaps between the two parts at different sampling rates, 32s and 512s, cannot be filled. In addition, some gaps do not last an exact number of 32 exposures, and thus cannot be corrected. Those gaps can especially be found at the beginning of the mission. An example of gap filled light curve is given on Fig. II.2.11.

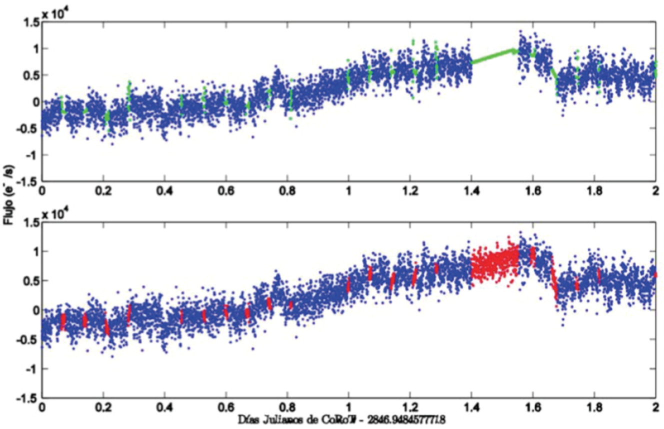

Fig. II.2.11. Example of gap filling, using the Inpainting method (Pires et al. 2015).

4.2.16. Correction of systematics

This process concerns only the faint stars channel data.

Even if the global phylosophy for the data processing consists of correcting only effects that can be clearly identified, modeled or physically quantified, one must admit, that, at the end of the global data processing, some light curve alterations are still visible, and remain uncorrected. Even if one cannot always exactly identify the origin of these residuals – some of them are due to cross correlations between several effects that are corrected individually – we can notice that they are:

- present on each light curve (systematics);
- with an amplitude that cannot always be quantified using a simple parametric description.

At the beginning of the project, it was proposed to apply a “last chance algorithm”, a systematic removal algorithm such as the SYSREM algorithm (Tamuz et al. 2005). The method has been optimized and led to a process described by Guterman et al. (2015). The algorithm works on gap filled and jump corrected data, and has been implemented on the last version of the pipeline. A new extend named SYS has been created in that purpose (see Fig. II.2.2).

4.2.17. Second detection of outliers

This process concerns only bright stars channel data.

A second detection of outliers is performed for the stars of the bright channel during the N1 to N2 pipeline. The parameters of the search, as the size of the moving window or the threshold of the sigma value, are manually tuned for each star. The detected outliers are flagged in the BAR extend and they are replaced by "inpainting" points in the BARREG extend (see the gap filling section).

4.2.18. Creation of final flags and file header

This process concerns both bright stars and faint stars channels data.

At the end of the process, each element of the photometric data is flagged using an unsigned long integer (32 bits) named STATUS and giving information of the data, including the orbital events. The final values of STATUS are given in Chaintreuil et al. in this book.

All the information describing the data set and several corrections made within the pipeline are gathered in the file header.

5. Other facts about the CoRoT instrument ageing and end of life

5.1. Ageing of the instrument and efficiency loss

The space environment leads to ageing of the instrument and at the end of the detection chain, a global efficiency loss. The efficiency loss is difficult to estimate, because:

- no absolute photometry is performed by CoRoT . This means that the instrument has not been absolutely calibrated using photometric standards and is not calibrated in flight;
- a very few number of long-term stable stars have been re-observed and can be used to estimate the long-term efficiency loss;
- when stars have been re-observed, the orientation of the line of sight and the image position on the CCDs were not identical. Because of the variation of the PSF over the focal plane, and the specificity of the masks used for the photometry, it is difficult to compare the absolute photometry from one observation to the other.

However, a first order estimation of the detection chain efficiency loss made on a limited number of stars with comparable observation conditions led to an effeciency loss of the detection chain of about 10% during the whole mission duration (Auvergne et al. 2009). At this level, it is also difficult to assign exactly what is due to:

- a loss of optical transmission;
- a decrease of the quantum efficiency;
- a loss of charge transfer efficency.

5.2. Degradation of the images optical quality

The CoRoT telescope structure is made of carbon fibers. One of the key questions raised by the use of this material was its behaviour in space and particularly, the evolution of the telescope bars length with time. Carbon fibers are wrapped with an epoxy resin which contains water. In space, and particularly just after the launch, a desorption of the carbon fiber bars was expected, leading to a variation of the telescope effective focusing. The initial variation was anticipated and the telescope was focused on the ground assuming an expected focus variation during the first three months of the mission. After three months in space, the telescope was effectively perfectly focused as expected. The question was to investigate a potential defocus after the three first months of mission. The variation of the position of the stars in the field cannot be used as an indicator of defocus (breathing of the field), because it is corrected simultaneously with the jitter and the relativistic aberration (see Sect. 4.2.9). We proposed thus to monitor the variations of the size of the bright star channel images. These images are slightly defocused to avoid the CCDs saturation. In that way, the size of these images can be an indicator of the focus variations. Because of the optical formula of CoRoT (wide field telescope and dioptric objective), the size and the shape of the PSFs are not constant over the field. Thus, we split the A2 CCD in 9 square regions where we estimated the size of the PSF along the mission lifetime (6 yr). Results are given on Fig. II.2.12. Even if the dispersion is large because the number of images is small, the average size of the PSF (black curve) does not exhibit a significant increase or decrease, tending to show that the focus remained globally unchanged after the initial phase of bars desorption. In the same time, no significant changes have been observed in the images of stars on the faint stars channel, and an update of the photometric mask has not been necessary.

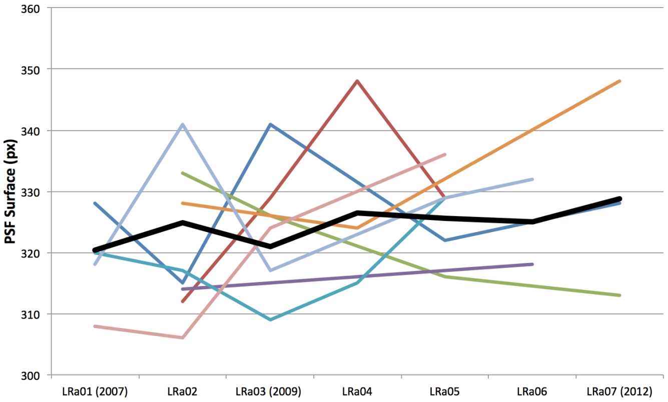

Fig. II.2.12. Evolution of the bright star PSF size with time showing no significant change during the mission lifetime (see the text for discussion).

5.3. Detector ageing

The detector and front-end electronics ageing leads to a global degradation of the performance of the detection chain:

- loss of charge transfer efficiency, as demonstrated on the HST (Goudfrooij et al. 2006);
- decrease of the quantum efficiency;
- increase of the dark current.

The two first effects cannot be investigated using only the data that are available. The last effect has been clearly observed and led to a change in the way the background in the bright and faint stars channels is corrected (see corresponding section in this paper).

5.4. Origins of the instrument failure

The instrument failure happened in two steps:

- the 8th of March 2009: loss of the communication with one of the two detection chains leading to the loss of the A1 (bright stars) and E1 (faint stars) CCDs;
- the 2nd of November 2012: loss of the communication with the second detection chain, leading to the end of the scientific mission after further investigation in June 2013.

Even now and after several months of dedicated investigations and tests on the instrument, including a complete switch-off and reboot of all the sub-systems, the instrument remained silent, and the origins of these two failures are not clearly understood. They are certainly due to the ageing of several electronic devices in charge of the power control of the detection chain, preventing from normal reboot of the DPU. Let us remind that the mission was designed for a mission duration of 3 yr, and the final lifetime of the second detection chain reached almost 6 yr.

6. Conclusions

The CoRoT legacy data are now delivered to the community. The corrections applied to the raw data correspond to the state-of-the-art knowledge of the instrument behaviour and evolution. Several extends, with different sets of corrections or post-processing are available to maximize their scientific uses. Anyway, our final knowledge is certainly not complete and other effects may be identified in the data in the future, and further investigation may be needed, particularly in the context of CHEOPS and PLATO, for which the same type of detectors will be used. A priori, no new version of the data including new corrections will be created.

Acknowledgements. The CoRoT space mission, launched on December 27, 2006, has been developed and operated by the CNES with the contribution of Austria, Belgium, Brasil, ESA, Germany, and Spain.

References

Alonso, R., Auvergne, M., Baglin, A., et al. 2008, A&A, 482, L21
Auvergne, M., Bodin, P., Boisnard, L., et al. 2009, A&A, 506, 411
Boisnard, L., & Auvergne, M. 2006, ESA-SP-1306, 19
Bonomo, A. S., Chabaud, P.-Y., Deleuil, M., et al. 2012, A&A, 547, A110
Chabaud, P.-Y., Agneray, F., Meunier, J.-C., et al. 2011, ASP Conf. Proc., 442, 339
Chaintreuil, S., Deru, F., Baudin, F., et al. 2015, this book
Deleuil, M., Moutou, C., Cabrera, J., et al. 2015, this book
Drummond, R., Lapeyrere, V., Auvergne, M., et al. 2008, A&A, 487, 1209
Drummond, R. 2007, Calibration of the CoRoT Space Mission: correction of the photometry for pointing jitter and background changes, Katholieke Universiteit Leuven
Fialho De Oliveira, F., Lapeyrere, V., Auvergne, M., et al. 2007, PASP, 119, 337
Goudfrooij, P., Bohlin, R. C., & Maíz-Appellaníz, J. 2006, PASP, 118, 1455
Guterman, P., Mazeh, T., & Faigler, S. 2015, this book
Lapeyrere, V. 2006, Etalonnage des détecteurs de CoRoT: adaptation aux besoin spécifiques de la mission, PhD Thesis, Université Pierre et Marie Curie (in French)
Pinheiro da Silva, L., Rolland, G., Lapereyre, V., et al. 2008, MNRAS, 384, 1337
Pires, S., Mathur, S., Garcia, R., et al. 2015, A&A, 574, id.A18
Plasson, P. 2009, CoRoT SW user requirement, COROT/DESPA.00.019
Quentin, C. G., Barge, P., Cautain, R., et al. 2006, ESA-SP-1306, 409
Samadi, R., Fialho, F., Costa, J. E. S., et al. 2007, eprint [arXiv:astro-ph/0703354]
Surace, C., Alonso, R., Barge, P., et al. 2008, Proc SPIE, 7019, id. 70193B
Tamuz, O., Mazeh, T., & Zucker, S. 2005, MNRAS, 356, 1466

Appendix A: Jump detection failure

The jump detection algorithm overcomes the star variability in the light curve by computing a differential vector normalised by the local standard deviation. Thus the impact of the local variability of the star is minimised. For each point of the light curve, the differential vector is computed as following:

$$\Delta(i) = \frac{\overline{\mathrm{flux}}_{\mathrm{after}\,i} - \overline{\mathrm{flux}}_{\mathrm{before}\,i}}{\sqrt{\sigma^2_{\mathrm{before}\,i} + \sigma^2_{after\,i}}}$$

Then to detect a jump, each point is compared to the global standard deviation of the full length of the differential vector σ_0.. A jump is detected at the “i” index if:

$$\Delta(i) > 7.2\,\sigma_0$$

Where:

$$\sigma_0 = stddev(\Delta)$$

This method allows considering the global disturbance level of the star. For a strongly perturbed star the σ_0 value will be higher and the detection of a jump will be more rigorous.

However the method presents two limitations. It works in term of elements and does not consider the time vector. It works only on the filtered data and does not take into account the points recorded during the SAA crossing.

These limitations can lead to false detections especially with highly variable stars as the RR Lyrae stars, because of an unfortunate synchronisation of the star patterns and SAA crossing.

Figure A.1 shows a jump detection failure, the SAA crossing is synchronized with the intensity increase of the star, causing an abnormal increase of the differential value. A SAA crossing longer than usual is sufficient to make the differential vector exceed the detection value (red line).

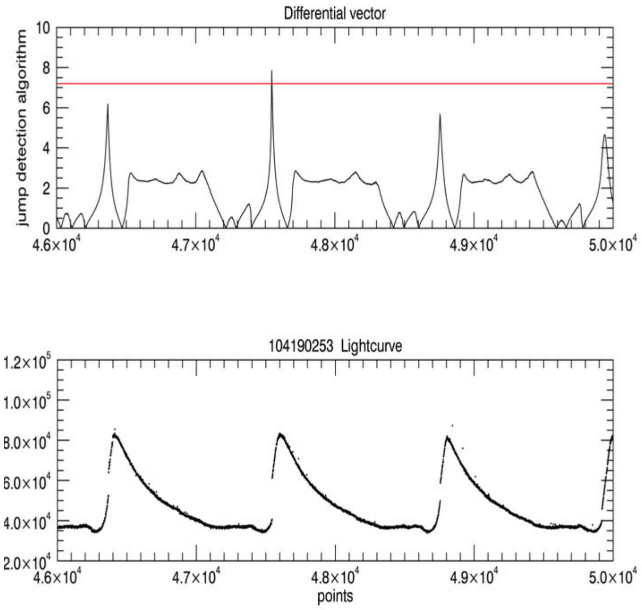

Fig. A.1. Jump detection failure. *Top*: differential vector. *Bottom*: light curve in points. The peaks of the differential vector are synchronized with the gaps caused by filtering the SAA crossing. The red line is the detection limit. In abscissa, points, not time.

The false detection is then corrected by the jump correction causing severe discontinuities in the light curve, see Fig. A.2. It shows also that a reduction of the amplitude can happen.

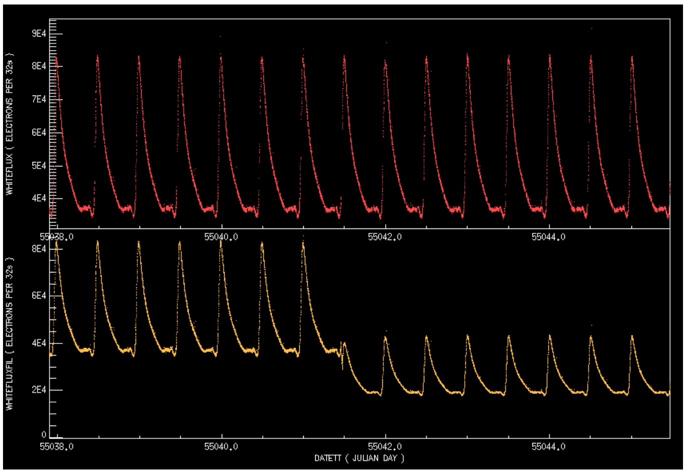

Fig. A.2. Jump correction failure showing the variation of the mean level and of the amplitude. *Top*: light curve before correction. *Bottom*: light curve after correction. In abscissa, the time in Julian date.

These correction errors are not frequent but they exist!

When such an anomally is detected (through a visual inspection), only the BAR extension, available in the N2 final data, has to be used, as this extension does not include the jump correction.

Acknowledgements: The CoRoT space mission has been developed and operated by CNES, with the contribution of Austria, Belgium, Brazil, ESA, Germany, and Spain.

The CoRoT Legacy Book

DOI: 10.1051/978-2-7598-1876-1.c023

II.3

Exposure-based algorithm for removing systematics out of the CoRoT light curves

P. Guterman[1, 2], T. Mazeh[3], and S. Faigler[3]

[1] Division Technique INSU, BP 330, 83507 La Seyne cedex, France
[2] LAM (Laboratoire d'Astrophysique de Marseille), UMR 7326, 13388 Marseille, France
[3] School of Physics and Astronomy, Tel Aviv University, Tel Aviv 69978, Israel

1. Introduction

The CoRoT space mission (Baglin et al. 2006) was operating for almost 6 yr, producing thousands of continuous photometric light curves. The readout of each CCD exposure transfers simultaneously the flux of 6000 stars. The temporal series of exposures are processed by the production pipeline, correcting the data for known instrumental effects, such as gain, background, jitter, EMI, SAA discarding, time corrections (Samadi et al. 2006; Auvergne et al. 2009). But even after these model-based corrections, some collective trends are still visible in the light curves (Fig. II.3.1). The flux gradually decreases with unknown shape and a different slope for each star. Previous work to correct these effects has been suggested, including MagZeP (Mazeh et al. 2009), that uses a zero-point magnitude correction, associated with the SysRem systematics algorithm (Tamuz et al. 2005).

Algorithms for removing systematics consist of two parts: 1) identify the effects among a set of stars by combining all light curves like SysRem (Tamuz et al. 2005), see also (Ofir et al. 2010), finding combination of a few representative stars (Kovács et al. 2005) or fitting a model for each exposure based on observational (Kruszewski & Semeniuk 2003) or instrumental quantities (Mazeh et al. 2009); then 2) remove them by properly adapting them to each light curve. An effect is a pattern that appears among a large set of independent stars. Effects can be additive, multiplicative or follow any law that needs to be determined. In the common techniques, the effects are derived from a training set of stars using correlation methods like the iterative SysRem (Tamuz et al. 2005). The training set can be a properly selected subset of stars or even the whole set itself.

After their global determination, the effects need to be scaled and subtracted from each of the light curves. Classical fitting techniques like least square are not satisfactory because the resulting coefficient is partly pulled by the light curve's natural shape and disturbs the scientific signal. For example, the gradual loss of sensitivity visible in Fig. II.3.1 correlates with any long-period stellar variability, resulting in removing some real signal. To avoid this critical drawback, we propose here a technique similar to MagZeP (Mazeh et al. 2009) that fits the instrumental effects to each exposure independently. The effect of each exposure is a function of only two instrumental stellar parameters, position on the CCD and photometric aperture. The advantage is that the effect is not a function of the stellar flux, and therefore much more robust.

A previous version of this paper was published as a proceeding paper in SF2A meeting (Guterman et al. 2015). It is structured as follows: Sect. 2 describes the systematics removal method and its application to CoRoT, Sect. 3 reviews the derived effects and the performances of the method and Sect. 4 summarizes and concludes this work.

2. Method

We compute the residual per pixel of each star by removing its zero point

$$r(t) = \frac{f(t) - \bar{f}}{m}, \tag{1}$$

where f is the star's flux and m is the mask surface in pixels. The fluxes are divided by the photometric aperture size m because systematics are at the pixel scale. The average flux $\bar{f}$ is integrated over the first 4 days of the run, before any drift could occur. Thus, all residuals are distributed around zero at the beginning of the run. Fig. II.3.2 (left), which depicts the histogram of the stellar flux during the 4 last days of the run, shows that by the end of the run, the residuals are significantly below zero. The fluxes loose about 30 e^-/pix on average after 140 days. This offset does not seem proportional to the flux itself, but rather linked to the position of the star on the CCD (Fig. II.3.2 right). Moreover, the dependence is close to linear, hence suggesting a model

$$S_{ij} = C_i + A_i x_j + B_i y_j, \tag{2}$$

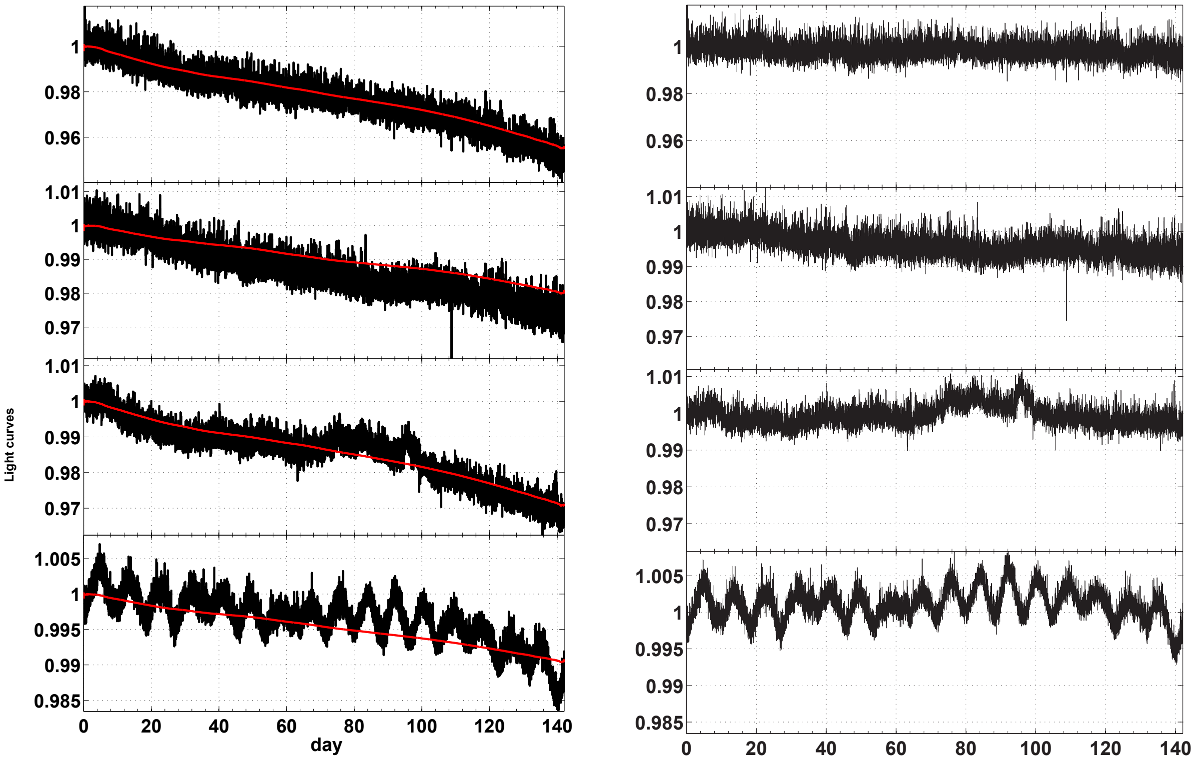

Fig. II.3.1. Corrected stellar trends. *Left*: light curves without correction. The considered light curves are from run LRc01, CCD 2. The black line is the normalized flux, the red line is the predicted systematic (see below). *Right*: same curves after correction.

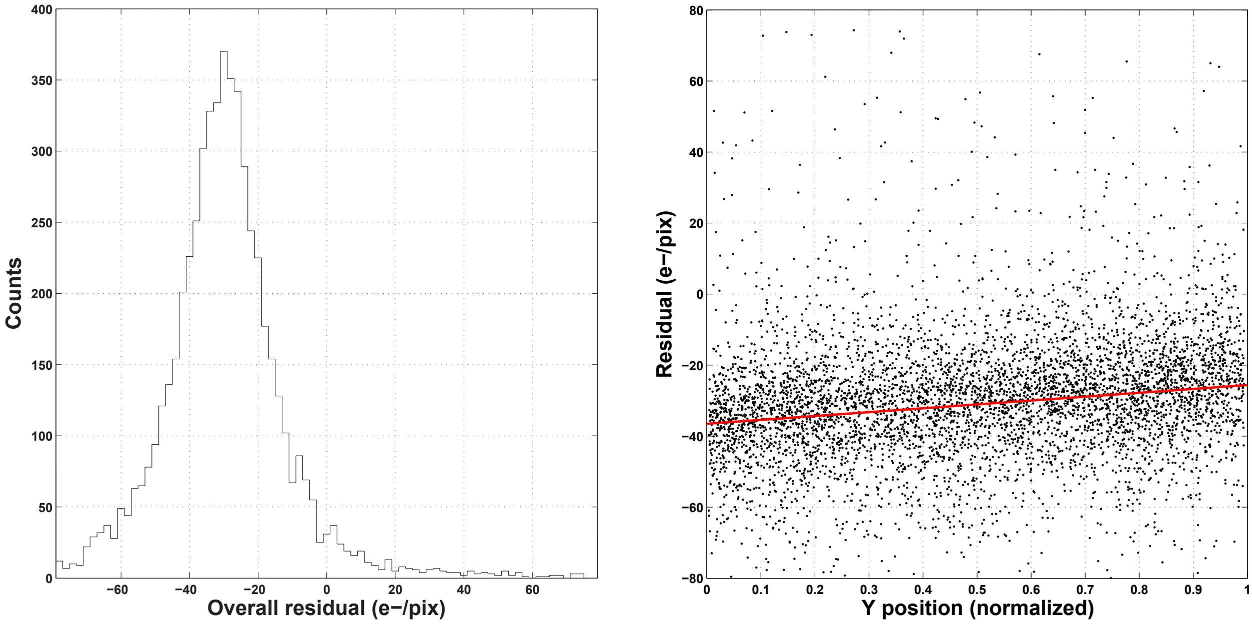

Fig. II.3.2. Systematic offset. *Left*: an histogram of all light curves residuals for an single exposure at the end of LRc01. *Right*: same residuals as a function of x positions. The red line is the linear approximation of the dependence.

with S_{ij} being the systematic offset of the ith exposure of the jth star located at position x_j, y_j on the CCD. The coefficients A_i and B_i form the position dependence and C_i is the common offset at exposure i. For each exposure we fit the three parameters A_i, B_i and C_i using a robust estimator. Next, we smooth the derived A, B and C temporal curves (Fig. II.3.3), and then subtract the resulting S_{ij} model from each exposure of each star.

2.1. Processing

Several steps are necessary to process the CoRoT data.

1. Resynchronising the run data
   The CoRoT data is a collection of files, each containing the run light curve of a single star. We pack all the files of a run into a single matrix of star × exposure that contains the whole data of that run. The difficulty is that

although simultaneously acquired, the time label of an exposure differs across files, depending on star position and roundoff errors among others. Consequently we had to gather all measurements within a common 4-s interval across the whole file set as belonging to the same exposure.

2. Binning to 512-s
   Some of the stars are sampled at a 32-s cadence while the rest are at 512-s cadence. A 512-s measurement is the onboard concatenation of 16 successive 32-s exposures. The timestamp is the center of the exposure interval in both cases. The present step consists on binning the data matrix to a common 512-s time frame in the same way that CoRoT would have done onboard.
3. Deriving the effects coefficients
   We compute the residual of each star (Eq. (1)) and produce the residual matrix of the run. Then, for each exposure i of that matrix, we estimate the coefficients A_i, B_i and C_i (Eq. (2)) using robust multi-linear regression (Holland & Welsch 1977). This way, the procedure is insensitive to outliers due to spurious cosmic rays or stellar variability. Another benefit of such an estimator is that there is no need to select a training set.
   The resulting A, B and C temporal coefficients are then strongly smoothed using a 30-days sliding average to remove high-frequency noise caused by the fitting process and modeling imperfections. Fig. II.3.3 shows the temporal evolution of the A, B, C coefficients for the run LRc01.
4. Removing the systematic effects model
   We derive the S_{ij} matrix (Eq. (2)) and subtract it from the residual matrix. The resulting residuals are then reverted back to light curves through the inverse of Eq. (1). This part is performed by the production pipeline that stores the result into a specific extend of the legacy fits files. This process takes place after the gap filling and the jumps corrections stages.

3. Results

3.1. Effects

Figure II.3.3 shows the evolution of the model coefficients during the 142 days of run LRc01. In blue, the common offset coefficient C shows that all light curves gradually loose up to 37 e$^-$/pix during the 142 days of the run. This long-term trend may reflect the loss of efficiency of the CCD, attributed to ageing effects. In red (green), the x (y) coefficients A (B) show patterns of lower amplitude, probably caused by the star shift inside its mask, probably due to small rotational depointing or aberration. The larger value of the B coefficient (red) relative to the A coefficient (green) could come from stretching of the CoRoT PSF along the x direction (Llebaria et al. 2004). Thus, a small displacement in the y direction influences the signal proportionally more than the same displacement along the x axis.

A change of the CCD temperature is visible as a discontinuity at $t \sim 50$ days, particularly in the red curve. Smaller details are visible down to the order of 1 e$^-$/pix in the 1.5-day magnified section. The faster oscillations are the residual of the CoRoT satellite orbital period, namely 13.97 day^{-1}. A daily pattern variation is also clearly visible. Although interesting for analysis purposes, such details are removed from the operational coefficients by the smoothing process, because the model is not accurate enough for these patterns.

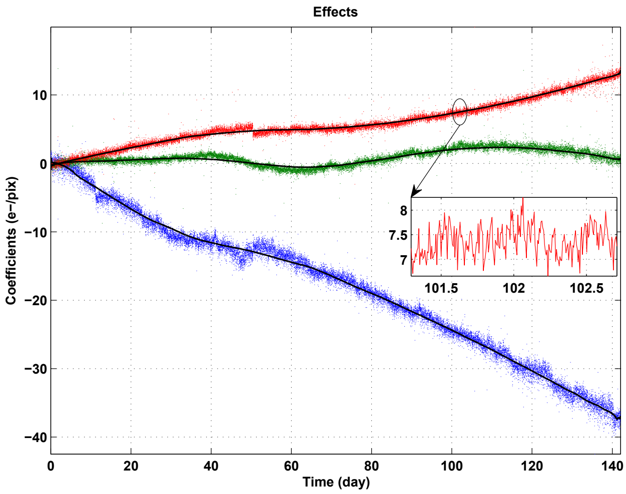

Fig. II.3.3. Effects as a function of time for the long run LRc01. Blue-offset C; green-A (x dependence); red-B (y dependence). The magnified section illustrates finer details on a shorter time scale which we ignore. The time is the number of days since the beginning of the run.

3.2. Absolute offset

Fig. II.3.4 represents the raw variation of the common offset C across the whole CoRoT mission. Separately, the effect of each run starts from zero by definition of the residuals (Eq. (1)). The Fig. II.3.4 concatenates all individual relative effects into the absolute variation of C during the mission. There are little gaps between two runs. In this figure, each run starts from the level reached by the end of the previous run, layered down during the gap with a -0.15 e$^-$/pix/day step. This slope corresponds to the best linear fit of the 2096 days. The slope is derived by iteratively leveling the individual effects, computing the residuals of a linear fit and so on. The result is the dashed line on Fig. II.3.4.

The steepest decrease occurs at the beginning of the mission for LRc01 and LRa01 (Fig. II.3.4). The profile of the C effect turns gradually more patterned and noisy as time passes. An anomaly is seen for LRa04 whose offset shows strong variations.

3.3. Performance

Figure II.3.5 shows the flux loss histograms in LRc01 before and after the correction, and illustrates that our method efficiently corrects the flux decrease. Before correction (solid line), the overall difference $\Delta = f_{\text{end}} - f_{\text{begin}}$ spreads around 2% loss in 142 days. This 2% loss is equivalent to ~1000 e$^-$/pix, assuming an average mask area. After correction (dashed line), in addition to removal of the bias, the histogram is sharper. This reduction of differences between stars illustrates the effectiveness of the position-based approach.

While this method is efficient on average, visual inspection of many stars reveals its limitations. For many

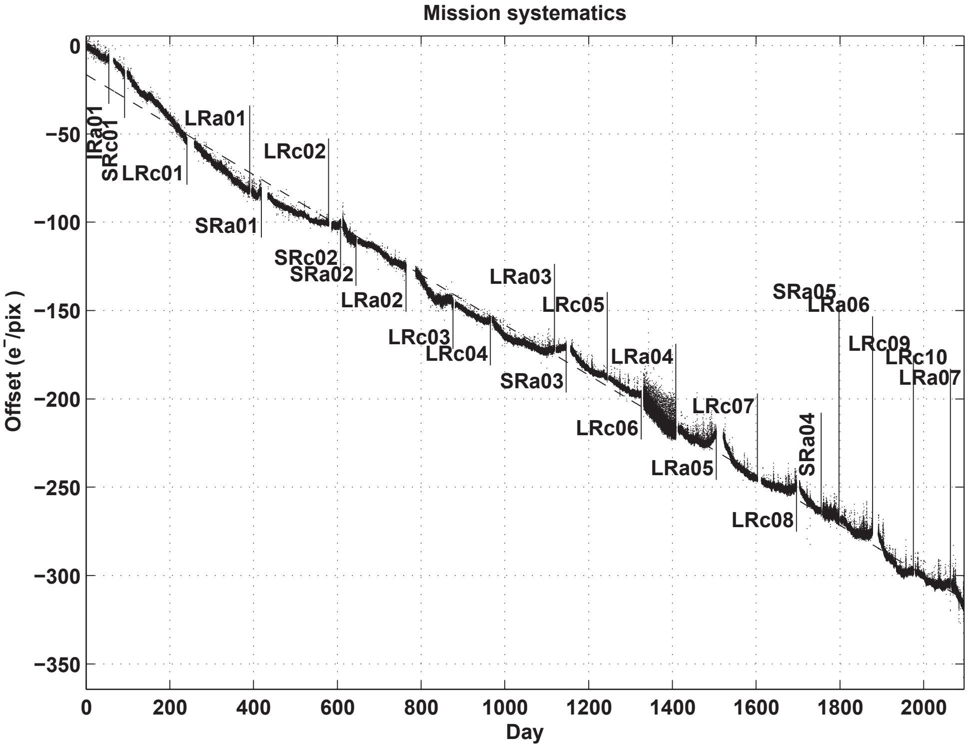

Fig. II.3.4. Absolute offset. Dots: the offset C of successive runs concatenated. Dashed: linear fitting.

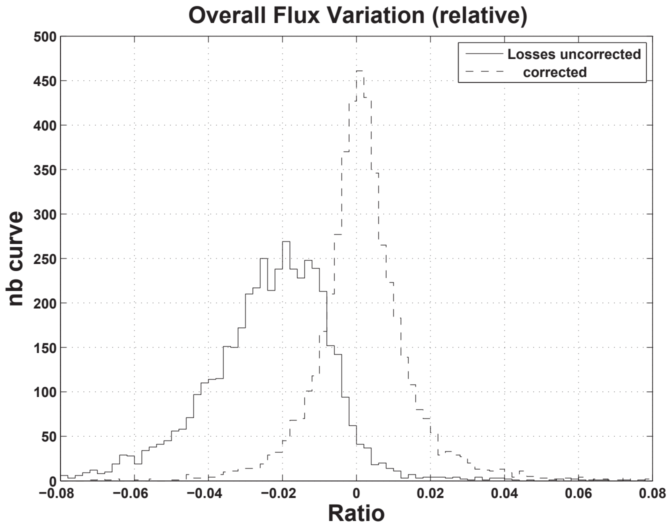

Fig. II.3.5. Results. Black line: histogram of flux losses at the end of run LRc01. The loss is intended relatively to the initial flux. Dashed: same after correction.

stars, the systematics model nicely fits the light curve. However, for other stars over/under corrections can be seen. We tested several possibilities for explaining this. We checked the influence of the photometric masks geometry with collective depointing. For this, we used the full pixel images recorded before the run. We also checked the smearing due to readout pattern across columns. We even performed a blind search for correlations with combinations of available parameters like spectral type, magnitude, mask surface and others but we were not able to identify any additional factor that could explain the suspected over/under correction.

4. Summary and conclusions

We present a simple method to remove systematics from the light curves of the CoRoT satellite without altering the scientific information. We apply a 3 parameter linear model per exposure to identify and correct most long-term systematics. The robust estimation algorithm allows to use the full information of the CoRoT sample of a run without selecting a training subset. The derived systematics only depend on the stellar position and mask area and not on the corresponding light curve. Consequently, no fitting based on the light curve itself can modify the real stellar variation, even when it resembles the systematics profile.

As an example, we show that the ∼2% long-term variation of the early LRc01 is nicely detrended on average, and the spread of stars variations is reduced. This systematics removal process is part of the CoRoT legacy data pipeline.

Acknowledgements. This research has received funding from the European Community's Seventh Framework Programme (FP7/2007-2013) under grant-agreement numbers 291352 (ERC).

References

Auvergne, M., Bodin, P., Boisnard, L., et al. 2009, A&A, 506, 411
Baglin, A., Auvergne, M., Barge, P., et al. 2006, ESA Special Publication, 1306, 33
Holland, P. W., & Welsch R. E. 1977, Communications in Statistics: Theory and Methods, A6, 813
Guterman, P., Mazeh, T., & Faigler, S. 2015 [arXiv:1509.03403]
Kovács, G., Bakos, G., & Noyes, R. W. 2005, MNRAS, 356, 557

Kruszewski, A., & Semeniuk, I. 2003, Acta Astron., 53, 241
Llebaria, A., Auvergne, M., & Perruchot, S. 2004, Proc. SPIE, 5249, 175
Mazeh, T., Guterman, P., Aigrain, S., et al. 2009, A&A, 506, 431
Ofir, A., Alonso, R., Bonomo, A. S., et al. 2010, MNRAS, 404, L99
Samadi, R., Fialho, F., Costa, J. E. S., et al. 2006, ESA Special Publication, 1306, 317
Tamuz, O., Mazeh, T., & Zucker, S. 2005, MNRAS, 356, 1466
Baker, N. 1966, in Stellar Evolution, eds. R. F. Stein, & A. G. W. Cameron (Plenum, New York) 333
Balluch, M. 1988, A&A, 200, 58
Cox, J. P. 1980, Theory of Stellar Pulsation (Princeton University Press, Princeton) 165
Cox, A. N., & Stewart, J. N. 1969, Academia Nauk, Scientific Information 15, 1
Mizuno, H. 1980, Prog. Theor. Phys., 64, 544
Tscharnuter, W. M. 1987, A&A, 188, 55
Terlevich, R. 1992, in Relationships between Active Galactic Nuclei and Starburst Galaxies, ed. A. V. Filippenko, ASP Conf. Ser., 31, 13
Yorke, H. W. 1980a, A&A, 86, 286
Zheng, W., Davidsen, A. F., Tytler, D. & Kriss, G. A. 1997, preprint

Acknowledgements: The CoRoT space mission has been developed and operated by CNES, with the contribution of Austria, Belgium, Brazil, ESA, Germany, and Spain.

The CoRoT Legacy Book
© The authors, 2016
DOI: 10.1051/978-2-7598-1876-1.c024

II.4

The “ready to use” CoRoT data

S. Chaintreuil[1], A. Deru[1], F. Baudin[2], A. Ferrigno[1], E. Grolleau[1], and and R. Romagnan[1]

[1] LESIA, Observatoire de Paris, PSL Research University, CNRS, Sorbonne Universités, UPMC Univ. Paris 06, Univ. Paris Diderot, Sorbonne Paris Cité, 5 place Jules Janssen, 92195 Meudon, France
[2] Institut d’Astrophysique Spatiale, UMR8617, CNRS, Université Paris XI, Bâtiment 121, 91405, Orsay Cedex, France

1. Introduction

1.1. Overview of the document

This document presents the “Ready to use” data of the CoRoT Mission, which can be used by a scientist without a priori knowledge of the instrument.

It describes:

- the LEGACY data (version 4), the last one to be delivered at the end of the project;
- the previous versions (version 1 to 3) which have been delivered along the mission to the scientific community; they were the only data available during the mission and just after but should not be used any more.

The differences of the data processing according to the data versions are displayed in Sect. 4.

Only the legacy data (V4) should be used from now on.

Important changes have been introduced in the final version: they concern the time stamping of the exposures, the introduction of complementary and more refined corrections, and different levels of corrections given in the different EXTENDS.

These data are public, available in 2016 at the mission archive[1] and at CDS in the Vizier environment[2].

1.2. Overview of the data

From the point of view of the processing, these data are N2 data. They derive from N1 data that are available on request at CNES and at IAS.

As described in Baglin & Fridlund (2006), the CoRoT mission was built to record light curves, which are relative variations of the brightness of a target as a function of time.

The instrument had two different observing channels (see Baglin & Fridlund 2006), so, there are two different types of Light Curves (LC):

- **AN2_STAR files** created from the bright star channel (previously called asteroseismology channel) where stars with magnitude between 6 and 9 are observed;
- **EN2_STAR files** coming from the faint star channel (previously called exo channel) observing stars from the magnitude between 10 and 16. Three types of files exist for faint stars:
  - **EN2_STAR_CHR** corresponding to targets observed on board with “pseudo-colours” leading to three light curves on board added on ground to obtain a fourth light curve,
  - **EN2_STAR_MON** corresponding to targets where all the pixels of the target are added, leading to a single light curve,
  - **EN2_STAR_IMAG** containing a single light curve where all the pixels of on board imagettes are processed and added on ground.

Though CoRoT N2 data are in principle ”Ready to Use”, some auxiliary information might be of interest: observation timing, sky background, environmental parameters, applied corrections, astrophysical characteristics of the target, etc.

This information is included either:

- in the header of the LC files:
  - a few parameters describing the observation and indexes of characterisation of the signal;
  - astrophysical characteristics of the target (coordinates, spectral type, etc.) from the CoRoTSKY and EXODAT databases;
  - information on data treatment (version number);
- in additional files:
  - **AN2_POINTING files** provide, every second, the precise position of the line of sight of the telescope;
  - **AN2_WINDESCRIPTOR** and **EN2_WINDESCRIPTOR files** provide information on the surrounding of the target and on CCD windows and masks;

---

[1] http://idoc-corot.ias.u-psud.fr/

[2] http://vizier.u-strasbg.fr/viz-bin/VizieR?-source=B/corot

Table II.4.1. Summary of the corrections according to the extends for both bright and faint stars.

Bright stars		**Faint stars**	
RAW	Correction from aliasing, offsets, backgrounds and of the jitter of the satellite Time scale is Terrestrial Time scale	BAR	Correction from aliasing, offsets, backgrounds and of the jitter of the satellite Correction of the change of the temperature set point and of the loss of long-term efficiency
BAR	RAW + correction of the differences in the flux due to the change of the mask, the change of the temperature set point and the loss of long term efficiency. Spurious points are replaced by interpolation	BARFILL	BAR + correction of the jumps + replacement of the invalid and missing data using the Inpainting method
BARREG	BAR + replacement of the invalid and missing data using the Inpainting method (Pires et al. 2015)	SYSTEMATIC	BARFILL + correction of residual systematics skews in the whole set of light curves of the run (see Chap. II.3)

  - **AN1_FULLIMAGE** and **EN1_FULLIMAGE** give the global field of view seen by each CCD. It is observed at the beginning of each run;
- – or included in the binary data of star files (sky background).

All files are FITS files, with one or several extensions.

For STAR files, the extensions are used to provide three different levels of correction: the first extend provides less corrected data whereas the last extend includes all the corrections.

Table II.4.1 shows the corrections according to the extension.

In all extends, the values of the flux come together with STATUS codes indicating spurious points in the time series and give information on the processing applied to these points. Depending on the version and the level of processing, the points can be used or not. The meaning of the STATUS codes is fully described in the next sections, where the primary header is also called main header.

Together with the data, some routines are provided to open and handle these files easily; the routines are available in the same location than the archives.

1.3. Complementary information

1.3.1. Time scales and time stamps

During the mission, the time scale used was Universal Time (UT) delivered by the GPS constellation; it remains used in TM, N0, N1 and old N2, versions 1 to 3.

The dating changed completely between N2 version 4 and N2 versions 1 to 3.

In version 4:

- the time stamp of the measurements is the weighted average of the integration time;
- time scale is the Barycentric Dynamical Time scale (except for bright stars RAW data that are in Terrestrial Time);
- Dates are expressed in usual Julian day numbers after the first leading digits are removed (JD − 2 400 000) as commonly done in the astronomical literature; therefore, dates are expressed either in Julian Day$_{\text{(Terrestrial Time)}}$ for bright stars RAW data or in Julian Day$_{\text{(Barycentric Dynamical Time)}}$ for other star extensions.

In versions 1 to 3:

- time was stamped at the end of the exposure;
- time scale is Heliocentric time scale and UT time for RAW Bright star data;
- Dates are expressed in ‘CoRoT’ Julian day numbers beginning January 1st 2000 at noon (20000101T120000).

Warning:

- one leap second has been added to UTC twice during the mission: December 31st 2008 and June 30th 2012.

1.3.2. Naming of the runs

Each run is described by a name with the format <type>R<d><nn>

- <type>is a char and refers to the type of run (“S”: short, “L”: long, “I”: initial);
- “R” refers to “RUN”;
- <d>refers to the direction of the observation with respect to the centre of the Galaxy (“a”: anticentre direction, “c”: centre direction);
- <nn>are two digits corresponding to the run number.

Examples: “IRa01”, “SRc01”, “LRa01”, “LRc02”, etc. The list of all runs with their characteristics is available in Chap. II.1.

1.3.3. Naming of the files

The names of the files are normalized; they contain the type of the file, the number of the target in the CoRoT databases and the date of the beginning and of the end of the observation:

AN2_STAR_<*COROTID*>_<*START_DATE*>_<*END_DATE*>.fits

A means that it was observed in the bright stars field (E means observed in the faint stars filed), N2 means data level 2.

The COROTID is a number always coded on 10 digits.

The format of the dates is: YYYYMMDDTHHMMSS, compliant with ISO-8601.

For instance: AN2_STAR_0000012345_20070411T150824_20070508T213552.fits

When needed, the code of the run or the name of the CCD is inserted in the name of the file.

1.3.4. Standard data types

The standard data types used throughout this entire document are the following:

Type	**Format**	**Size**
Float	Floating point, simple precision	32 bits
Double	Floating point, double precision	64 bits
Int	(Short) signed Integer	16 bits
Long	Long signed integer	32 bits
Long64	Long 64bits signed integer	64 bits
Byte	Byte	8 bits
String	String	Up to 80 characters of the restricted ASCII set, used in the headers of the FITS files

1.3.5. Acronyms

BS: Bright Star channel
FS: Faint Star channel
AN2: files containing data from the bright star channel (previously called asteroseismology channel)
EN2: files containing data from the faint star channel (previously called exo-planet channel)
LR: Long Run longer than 60 days
SR: Short Run shorter than 60 days
IR: Initial Run
CCD: Charge-Coupled Device
CDC: CoRoT Data Centre
EMI: Electro-Magnetic Interferences or diaphony
LC: Light Curve
LOS: Line Of Sight
SAA: South Atlantic Anomaly

2. N2 Legacy files (version 4)

The description of the complete processing for the Legacy can be found in Chapter II.2.

2.1. AN2 Products from the bright star channel

The main products are the AN2_STAR that give the evolution over the run of the flux of the observed targets. Each AN2_STAR comes with:

- its AN2_WINDESCRIPTOR companion that provides the mask applied to the target and its environment;
- one auxiliary file named AN2_POINTING giving precise information on the pointing of the satellite; it is presented in this section because this information is acquired from the “bright star” channel; this information is provided to help users to identify spurious frequencies due to the pointing (see Chap. II.2).

In addition, the sky observed in each CCD at the beginning of each run is provided in the AN2_FULLIMAGE files.

2.1.1. The AN2_WINDESCRIPTOR product

This product gathers the information on the observation setup, for a given target. It is produced once per observed star. It is stored in the file:

AN2_WINDESCRIPTOR_<*CoRoT_ID*>_<*START_DATE*>_<*END_DATE* >.fits

2.1.1.1. The AN2_WINDESCRIPTOR main header

See Table II.4.2 next page.

2.1.1.2. The AN2_WINDESCRIPTOR binary table extension (BINTABLE)

The header of the BINTABLE of the AN2_WINDESCRIPTOR product is displayed in Appendix 1 (5.1.1).

The description of the binary table BINTABLE of the AN2_WINDESCRIPTOR product is displayed Table II.4.3 next page.

2.1.2. The AN2_STAR product

It is stored in the file:

AN2_STAR_<*COROTID*>_<*START_DATE*>_<*END_DATE* >.fits

It contains a main header and three extensions, RAW, BAR and BARREG:

- the RAW extension contains slightly corrected data; they are N1 data accumulated over 32 seconds. At N1 level, data are corrected for aliasing, from residual offsets, from residuals of the background and from the jitter of the satellite.
  The outliers are detected and marked and orbital events such as SAA, inbound and outbound crossing of the Earth shadow are marked.
  At N2 level, data are accumulated on a 32-s scale. The time stamp of each exposure is the mean time of the 32 exposures of the accumulation; it is expressed in Terrestrial Time.
  In this extend, are also given the values of the background used to corrected the flux: they have been measured on board in a “black” window positioned on the CCD as near as possible to the star window.

Table II.4.2. Main header of the AN2_WINDESCRIPTOR.

Name	Description	Type	Unit/ex...
SIMPLE	Mandatory: means that the file is fully compliant to FITS format	Boolean	True
BITPIX	Mandatory: Nb of bits by pixel (for images)	int	8
NAXIS	Mandatory:: 0 means binary extensions	int	0
EXTEND	Means that the creation of extend is possible	Boolean	T (= True)
TELESCOP	Telescope name	string	COROT
ORIGIN	Processing site	string	CDC
CREA_DAT	Date of the creation of the file (UT)	string	yyyy-mm-dd Thh:mm:ss
FILENAME	Name of the file	string	
PIPE_VER	Version of the process that created the file	string	
N2_VER	Version of the N2 data	string	
COROTID	CoRoT identifier of the target	int	
RUN_CODE	Run during which the target has been observed	string	
HLFCCDID	Half CCD on which the target was observed	string	
START_DATE	Date of the first measurement of the run In UT	string (23 char)	yyyy-mm-dd Thh:mm:ss
END_DATE	Date of the last measurement of the run in UT	string (23 char)	yyyy-mm-dd Thh:mm:ss

Table II.4.3. Binary table extension of the AN2_WINDESCRIPTOR.

Name	Description	Type	Unit/ex...
T_START_WIN	Time of the beginning of the observation of the target	string	Calendar (UT)
T_END_WIN	Time of the end of the observation of the target	string	Calendar (UT)
WIN_ID	ID of the on-board window used to observe the star	long	0–>436 for bright stars
SIZEX	Window size in the X direction	int	pixel
SIZEY	Window size in the Y direction	int	pixel
ORIGINX	X origin of the target window on the CCD	int	pixels
ORIGINY	Y origin of the target window on the CCD	int	pixel
MASK_ID	ID of the photometric mask applied to the target.	int	0 to 255
MASK_SIZE	Total number of pixels within the photometric mask	int	pixel
CCD_WINREF	Sub-image of size (NXIMGREF, NYIMGREF) extracted from AN2_FULLIMAGE (see Sect. 2.1.4)	int	e^-/pix/s
NXIMGREF	Size of the subimage CCD_WINREF in X	int	pixel
NYIMGREF	Size of the subimage CCD_WINREF in Y	int	pixel
POSXIMGREF	X position of the bottom left corner of the sub-image CCD_WINREF in the FULLIMAGE	int	pixel
POSYIMGREF	Y position of the bottom left corner of the sub-image CCD_WINREF in the FULLIMAGE	int	pixel
MASK	Mask applied to the target on-board in the window of size (SIZEX, SIZEY). 1 indicates that the flux on the pixel is added, 0 indicates that the pixel is outside the photometric mask.	Int	

- the BAR extension contains data also accumulates every 32 s. They also derive from N1 data, so they have received the same corrections as RAW data. But, before the accumulation, the following corrections are applied:
  - the difference of the flux is normalized taking into account the optimisation of the photometric mask after a few days of observation;
  - the changes of the temperature set point are corrected;
  - the curves are detrended from the loss of long term efficiency;
  - and finally, the data are accumulated over 32 exposures. Only valid exposures are taken into account and the time stamp of the exposure is the barycentre of the timestamps of the valid exposures (unless more than 16 exposures are invalid, in which case all data are accumulated and status is invalid). It is then converted to the Barycentric Dynamical Time scale.

  These data are the best-corrected data from the known, measured or modelled, instrumental and environmental effects.
- Data in the BARREG extension are first corrected as previously and invalid and/or missing data are interpolated as described in Pires et al. (2015). Also the charges are distributed to a strictly regular Barycentric Dynamical Time scale. These data are provided to allow easy use of the FFT algorithm.

All dates are given in “reduced” Julian date, i.e. JD −2 400 000.

2.1.2.1. Status code for RAWSTATUS, STATUSBAR, STATUSBARREG

STATUS is a bit mask. This means that all the values can be combined.

For instance STATUS = 5 is the combination of (1) and (4), which means that the measurement is considered as out of range and that it has been acquired during an SAA crossing.

The meaning of the values depends on the extension.

Values with STATUS = 0 are always fully valid data.

The routines provided in the archives to open and handle the N2 files give the choice of the data to be returned according to their STATUS. All combinations can be chosen but a choice has been made for the default return. The values considered “included” or “excluded” by default are indicated in the following tables.

RAWSTATUS

See Table II.4.4 next page.

STATUSBAR

See Table II.4.5 next page.

STATUSBARREG

See Table II.4.6 next page.

2.1.2.2. The AN2_STAR main Header

See Table II.4.7 next page.

2.1.2.3. RAW extension of the file AN2_STAR

The header of the RAW extension of AN2_STAR is displayed in Appendix 1 (5.1.2).

The description of the RAW extension of AN2_STAR is displayed in Table II.4.8 next page.

2.1.2.4. BAR extension of the file AN2_STAR

The header of the BAR extension of AN2_STAR is displayed in Appendix 1 (5.1.3).

The description of the BAR extension of AN2 STAR is displayed in Table II.4.9 next page.

2.1.2.5. BARREG extension of the file AN2_STAR

The header of the BARREG extension of the AN2_STAR is displayed in Appendix 1 (5.1.4).

The description of the BARREG extension of the AN2 STAR is displayed in Table II.4.10 next page.

2.1.3. The AN2_POINTING product

An auxiliary file giving precise information about the pointing of the satellite.

It is stored in the file:
AN2_POINTING_<RUN_ID>_<NUM_CCD>

_<START_DATE >_<END_DATE>.fits
Sampling rate is 1 second.

2.1.3.1. The AN2_POINTING main Header

See Table II.4.11 next page.

2.1.3.2. The AN2_POINTING binary table extension

See Table II.4.12 next page.

Index 0 to 4 refers to the index of the CID in the main header. Ex: BARY_X2, BARY_Y2 are the coordinates of the barycentre of the COROT_ID given in CID_2.

CAUTION: to synchronise the data with the LOS information, some NaN were added in the barycentre coordinates: it is especially true at the beginning of the runs, when only the two stars used for pointing are recorded. The NaN must be looked for and removed before using the data.

2.1.4. The AN2_FULLIMAGE product

The aim of this product is to give the environment of the stars. The file contains two extensions, one for the AN2 Fullimage and one for the background image, both in e^-/pixel/sec, both of the same size (2048, 2048) pixels. It is stored in the file:

AN2_FULLIMAGE_<NUM_CCD>_<START_DATE>_
<END_DATE>.fits

2.1.4.1. The AN2_FULLIMAGE primary extension

See Table II.4.13 next page for the header of the primary extension.

Table II.4.4. RAWSTATUS.

code	Meaning	Default behaviour
0	Flux measurement is valid	valid
1	Data considered as outlier (e.g. energetic particles or glitch)	excluded
2	Data marked invalid from on-board (spare value or EXPORANK value)	excluded
4	SAA crossing	excluded
8		
16		
32	Discontinuity due to change in mask (sequence change)	excluded
64		
128		
256	Satellite entering the earth penumbra*	included
512	Satellite leaving the penumbra*	included
1024	Jitter excursion out of range: flux is replaced by a calculated value	included

Notes. (*) Information derived from the orbital information. Asymmetric information can be encountered (entering the penumbra without leaving or vice versa); this comes from the accumulation from 1 to 32 s and is not worrying.

Table II.4.5. STATUSBAR.

Value	Meaning	Default behaviour
0	Flux measurement is valid	valid
1	Outliers are detected and the flux is interpolated	included
2	Data marked invalid from on-board (spare value or EXPORANK value)	excluded
4	SAA crossing	excluded
8		
16		
32	Discontinuity due to change in mask	excluded
64		
128	Outlier detected (2nd detection); flux is interpolated**	included
256	Satellite entering the Earth penumbra*	included
512	Satellite leaving the penumbra*	included
1024	Jitter excursion out of range: flux is replaced by a calculated value	included

Notes. (*) This information is derived from the orbital information. Asymmetric information can be encountered (entering the penumbra without leaving or vice versa); this comes from the accumulation from 1 to 32 s and is not worrying. (**) In the BAR extension of the AN2_STAR, this value of the status should be used with caution because it might happen that it marks stellar activity as well as outliers. Data should thus be verified before excluding the value.

Table II.4.6. STATUSBARREG.

code	information	Default behaviour
0	Flux measurement is valid	valid
1	Outlier detected (1st detection); flux is interpolated	included
2		
4		
8	Gap filling using Inpainting method (<2 hours)	included
16	Gap filling using Inpainting method (>2 hours)	included
32		
64		
128		
256	Satellite entering the Earth penumbra*	included
512	Satellite leaving the penumbra*	included
1024	Jitter excursion out of range: flux is replaced by a calculated value	included

Notes. All the data with STATUS 2, 4, 32, 128 (and any combination of these) in the previous extensions are replaced using the Inpainting method: those data get a STATUS 8 in the BARREG extension. (*) See BAR extension.

Table II.4.7. Main header of the AN2_STAR product.

Name	Description	Type	Unit/ex...
SIMPLE	Mandatory: means that the file is fully compliant to FITS format	Boolean	True
BITPIX	Mandatory: Nb of bits by pixel (for images)	int	8
NAXIS	Mandatory: 0 means binary extensions	int	0
EXTEND	Means that several extends exist	Boolean	True
TELESCOP	Telescope name	string	COROT
ORIGIN	Processing site	string	CDC
CREA_DAT	Creation date of the file in UT	string	yyyy-mm-ddThh:mm:ss
FILENAME	Name of the file	string	
PIPE_VER	Version of the N1_N2 pipeline (not useful for the N2 users)	string	
N2_VER	Version of the N2 data	string	
STARTDAT	Date of the first measurement **In UT**	string	yyyy-mm-ddThh:mm:ss
END_DATE	Date of the last measurement **In UT**	string	yyyy-mm-ddThh:mm:ss
COROTID	Identification of the target	long	
RUN_CODE	Run during which the target has been observed	string	See Sect. 1.3.2
HLFCCDID	Half CCD from which the product originates	string	See Appendix 2 Sect. 6
ALPHA	Right ascension of the target (equinox 2000)	double	Degrees (decimal)
DELTA	Declination of the target (equinox 2000)	double	Degrees (decimal)
STARNAME	Usual name of the target*	string	Ex: HD 49933
MAGNIT_V	Visual magnitude of the target*	float	
ABSM_V	Absolute visual magnitude*	float	
COL_B_V	Colour index*	float	
SPECTYPE	Spectral type*	string (5)	O, B...
SUBCLASS	Subclass of the spectral type*	string (5)	1, 2
LUMCLASS	Luminosity class*	string (5)	I, IV
TEFF	Effective temperature*	float	d°Kelvin
GRAVITY	$\log_{10}$ of the surface gravity* in m/s^2	float	m/s^2
METAL	Star metallicity*	float	$\log_{10}(Fe/H)/$ $\log_{10}(Fe/H)_{Sun}$
LC_MEAN	Mean value of the flux in the BARREG extend; meaningful as all data are valid in extend BARREG	float	e^-/sec
LC_RMS	RMS of the flux in the BARREG extend	float	e^-/sec
NBPHOTPIX	Number of hot pixels detected	int	
COR_SLOP	Estimated slope of the efficiency loss	double	e^-/sec^2
COR_DELT	Range delta of the estimated COR_SLOP	double	e^-/sec^2
NB_CONSI	Number of temperature jumps of the run	int	Between 0 and 6
DATE_TPE1..6	Date of the 1st...6th temperature jump **in UT**	float	CoRoT Julian Day (***)
COR_TPE1...6	Flag of the temperature correction 0 = OK, −1 not executed, +1 done with warning**	int	0, −1, +1
MASK_COR	Code of the correction of known discontinuities, mainly mask discontinuity in BS channel 0 = no correction, +1 = standard correction, +2=empirical correction (see Chap. II.2)	int	0, +1, +2

Notes. (*) From the COROTSKY database. (**) For the meaning of the warning, see Chap. II.2. (***) Add 51545 to get the date of the jump in standart Julian Day; for the precise date of the jumps in Terrestrial Time, refer to any target in the FS field of the same run.

Table II.4.8. Binary table of the RAW extension of AN2_STAR.

Name	Description	Type	Unit/ex...
DATETT	Date of measurement	double	Terrestrial Time
RAWFLUX	N1 flux light curve*	double	e^-/sec
RAWFLUXDEV	Standard deviation of the 1-s measurement in the 32-s interval	double	e^-/sec
RAWSTATUS	Flag for the status	ulong (unsigned)	
BG	Background flux already subtracted	float	e^-/pix/sec

Notes. (*) Sampled at 32 s, as a sum of 1-s measurements, divided by valid exposures.

Table II.4.9. Binary table of the BAR extension of AN2_STAR.

Name	Description	Type	Unit/ex...
DATEBARTT	Date of measurement in the solar barycentric reference frame	double	Solar barycentric Terrestrial Time**
FLUXBAR	Flux light curve*	double	e^-/sec
FLUXDEVBAR	Standard deviation of the 1-s measurement	double	e^-/sec
STATUSBAR	Flag for the status	long	See 2.1.2.1

Notes. (*) Irregular sampling, 32 s in average. (**) Time stamp at the barycentre of the valid exposures.

Table II.4.10. Binary table of the BARREG extension of AN2_STAR.

Name	Description	Type	Unit/ex...
DATEBARREGTT	Date of the measurements in the solar barycentric reference frame, with a strict regular sampling	double	Solar barycentric Terrestrial time**
FLUXBARREG	Flux light curve*	double	e^-/sec
FLUXDEVBARREG	Standard deviation of the 1-s measurement	double	e^-/sec
STATUSBARREG	Flag for the status	long	See 2.1.2.1

Notes. (*) Regular sampling, 32 s. (**) Time stamp at the middle of the 32 exposures.

Table II.4.11. Main header of the AN2_POINTING product.

Name	Description	Type	Unit/ex...
SIMPLE	Mandatory: means that the file is fully compliant to FITS format	Boolean	True
BITPIX	Mandatory: Nb of bits by pixel (for images)	int	16
NAXIS	Mandatory: 0 means binary extensions	int	0
EXTEND	Means that several extends exist	Boolean	True
TELESCOP	Telescope name	string	COROT
ORIGIN	Processing site	string	CDC
CREA_DAT	Date of the final processing	string	yyyy-mm-ddThh:mm:ss
FILENAME	Name of the file	string	
N2_VER	Version of the N2 data	string	
PIPE_VER	Version of the process (not useful for N2 users)	string	
START_DAT	Date of the first measurement In UT	string	yyyy-mm-ddThh:mm:ss
END_DATE	Date of the last measurement In UT	string	yyyy-mm-ddThh:mm:ss
NB_STARS	Number of targets observed in the run*	integer	10 or 5
RUN_CODE	Name of the run	string	
NUMCCD	ID of CCD	string	
CID_0/.../4	COROTIDs of the targets observed in the run, for the given NUMCCD	String	

Notes. (*) 10 for the first runs (to LRa02 included) and 5 for the later ones.

Table II.4.12. Binary table of the AN2_POINTING product.

Name	Description	Type	Unit/ex...
DATE	Time stamp in UT in calendar format	String (23 char)	yyyy-mm-ddThh:mm:ss.sss
DATETT	Time stamp in TT (sampling at 1 s)	double	Standard Julian day
DELTA_PHI	Yaw variation of the LOS (bore sight frame)	double	arcsec
DELTA_THETA	Pitch variation of the LOS (bore sight frame)	double	arcsec
DELTA_PSI	Roll variation of the LOS (bore sight frame)	double	arcsec
F_EST	Estimated focal length	double	meter
BARY_X0/.../BARY_X4	X coordinate of the star barycentre*	float	pixels
BARY_Y0/.../BARY_Y4	Y coordinate of the star barycentre*	float	pixels

Notes. Index 0 to 4 refers to the index of the CID in the main header. Ex: BARY X2, BARY Y2 are the coordinates of the barycentre of the COROT ID given in CID 2. (*) X,Y coordinates in the 50 × 50 pixels window.

Table II.4.13. Main header of the AN2_FULLIMAGE file.

Name	Description	Type	Unit/ex...
TELESCOP	Telescope name	string	COROT
ORIGIN	Processing site	string	CDC
DATE	Date of the first measurement of the image	string	yyyy-mm-ddThh:mm:ss
EXTNAME	Name of the extend	string	
FILENAME	Name of the file	string	
N2_VER	Version of the N2 data	string	
CREA_DAT	Creation date of the file in UT	string	yyyy-mm-ddThh:mm:ss
CSMEAR	Flag of the smearing correction	int	1 if smearing corrected
CBCK	Flag of background correction	int	1 if background subtracted
CGAIN	Flag of the gain correction	int	1 if gain corrected
COFST	Flag of the offset correction	int	1 if offset subtracted
EMI_CORR	Flag of the EMI correction	int	1 if EMI corrected
CHAINID	ID of the photometric channel used	int	1 or 2
NUMCCD	ID of the CCD	string	
OFFSET_R	The value of the offset used to correct the right half of the CCD	float	ADU
OFFSET_L	The value of the offset used to correct the left half of the CCD	float	ADU
RON_R	Readout noise of the right half of the CCD	float	e^-/PIX
RON_L	Readout noise of the left half of the CCD	float	e^-/PIX
GAIN_L	Gain applied to correct the left half CCD	float	e^-/ADU
GAIN_R	Gain applied to correct the right half CCD	float	e^-/ADU
RUN_CODE	Run during which the target has been observed	string	See Sect. 1.3.2

2.1.4.2. The AN2_FULLIMAGE backgroung extension

The header of this extension contains the average backgound in electron/pixel/second (AVG_BCK).

The background image (2048, 2048) comes from the process of detection and identification of the stars in the operational phase.

2.2. EN2 Products from the faint star channel

There are five different products:

- the windescriptor which describes the windows and the masks defined to observe the targets;
- 3 STAR products: the EN2_STAR_CHR product, which correspond to the windows treated in the chromatic mode, the EN2_STAR_MON product for the monochromatic windows, and the EN2_STAR_IMAG product associated to the targets observed as imagettes;
- the image of the full CDD recorded at the beginning of the run during 3 orbits with no SAA crossing.

The star products contain data sampled at 32 s, 512 s or both samplings. The sampling rate can be found in the side file EN2_WINDESCRIPTOR (EXPTIME, see 2.2.2).

The files contain a main Header and 3 extensions: BAR, BARFIL and SYSTEMATIC:

In the BAR extension, the corrections applied to the data are:

- elimination of the aliasing;
- subtraction of the offsets recorded on board;
- subtraction of the background acquired on board; the method used for this processing has evolved along the mission according to the ageing of the instrument;
- correction of the jitter of the satellite;
- detection of the outliers: the points are marked but not corrected;
- orbital events such as SAA, inbound and outbound crossing of the Earth shadow are marked;
- the changes of the temperature set point are corrected;
- the curves are detrended from the loss of long term efficiency.

These data are corrected from known instrumental and environmental effects, using from measurements or modelled data.

In the BARFIL extension, the “jumps” are corrected (on on-board LC, not on LC from imagettes, see Chap. II.2) and the gaps are filled. The sampling is unchanged, 512 s, 32 s or a mixture of these.

In the SYSTEMATIC extension, all data are resampled to 512 s and then, an overall trend is modelled and suppressed (see Chap. II.3).

2.2.1. STATUS CODE for the “faint stars” products

See Table II.4.14 next page.

See Table II.4.15 next page.

2.2.2. The EN2_WINDESCRIPTOR product

This product gathers the information on the observation setup, for a given target. It is produced just once per observed star. It is stocked in the file:

EN2_WINDESCRIPTOR_<*CoRoT_ID*>_<*START_DATE*>_<*END_DATE* >.fits

2.2.2.1. The EN2_WINDESCRIPTOR main Header

See Table II.4.16 next page.

2.2.2.2. The EN2_WINDESCRIPTOR binary table extension

The header of the BINTABLE of EN2_WINDESCRIPTOR is displayed in Appendix 1 (5.1.5).

The description of the bianary table of EN2_ WINDESCRIPTOR is displayed in Table II.4.17 next page.

2.2.3. The EN2_STAR_CHR product

Contains the information about the chromatic stars of a run. It is stocked in the file:

EN2_STAR_CHR_<*COROTID*>_<*START_DATE*>_<*END_DATE* >.fits

For all extends, the time stamp of the measurements is at the mean time of the exposure.

2.2.3.1. The EN2_STAR_CHR main Header

See Table II.4.18 next page.

2.2.3.2. BAR extension of the files EN2_STAR_CHR

The header of the BAR extension of the EN2_STAR_CHR is displayed in Appendix 1 (5.1.6).

The description of the BAR extension of the EN2_STAR_CHR is displayed in Table II.4.19 next page.

2.2.3.3. BARFILL extension of the files EN2_STAR_CHR

The header of the BARFILL extension of the EN2_STAR_CHR is displayed in Appendix 1 (5.1.7).

The description of the BARFILL extension of the EN2_STAR_CHR is displayed in Table II.4.20 next page.

Table II.4.14. STATUS (BAR extension).

Value	**Information**	Default behaviour
0	Flux measurement valid	valid
1	Cosmic event detected by the N0-N1 pipeline	excluded
2	Spare value detected by the N0-N1 pipeline	excluded
4	SAA crossing (N0-N1)	excluded
8	Flux perturbed by an Earth eclipse (inbound)	included
16	Flux perturbed by an Earth eclipse (outbound)	included
32	SAA crossing (N1-N2)	excluded
64	Interpolated data due to a high jitter	included
128	Local high jitter value (EN2_STAR_IMAG only)	included

Table II.4.15. STATUSFIL and STATUSSYS.

Value	**Information**	**Default behaviour**
0	Flux measurement valid	included
1	(*)	
2	(*)	
4	(*)	
8	Flux perturbed by an Earth eclipse (inbound)	included
16	Flux perturbed by an Earth eclipse (outbound)	included
32	(*)	
64	Interpolated data due to a high jitter	included
128	Local high jitter value (EN2_STAR_IMAG only)	included
256	Gap filling using Inpainting method (<2 hours)	included
512	Gap filling using Inpainting method (>2 hours)	included
1024	Jump correction (see Chap. II.2)	included

Notes. (*) All excluded data in the BAR extension are not taken into account, which creates “holes” filled using the Inpainting method. So data with previous values 1, 2, 4 or 32 (or any combination) have a STATUSFIL or STATUSSYS = 256.

Table II.4.16. Main header of EN2_WINDESCRIPTOR.

Name	**Description**	**Type**	**Unit/ex...**
SIMPLE	Mandatory: means that the file is fully compliant to FITS format	Boolean	True
BITPIX	Mandatory: Nb of bits by pixel (for images)	int	16
NAXIS	Mandatory: 0 means binary extensions	int	0
EXTEND	Means that the creation of extend is possible	Boolean	True
TELESCOP	Telescope name	string	COROT
ORIGIN	Processing site	string	CDC
CREA_DAT	Creation date of the file in UT	string	yyyy-mm-ddThh:mm:ss
FILENAME	Name of the file	string	
PIPE_VER	Version of the process	string	
N2_VER	Version of the N2 data	string	
COMMENT	Commentary (2 lines)	string	
COROTID	CoRoT identifier of the target	int	
RUN_CODE	Run during which the target has been observed	string	See Sect. 1.3.2
HLFCCDID	Half CCD from which the product originates	string	
START_DATE	Date of the first measurement of the run in UT	string	yyyy-mm-ddThh:mm:ss
END_DATE	Date of the last measurement of the run in UT	string	yyyy-mm-ddThh:mm:ss

Table II.4.17. Binary table BINTABLE of product EN2_WINDESCRIPTOR.

Name	Description	Type	Unit/ex...
T_START_WIN	List of start time for the use of a given window for the target	float	Calendar (UT)
T_END_WIN	List of end time for the use of a given window for the target	float	Calendar (UT)
WIN_ID	ID of the target window	long	0 to 8191
SIZEX	Window size in the X direction	int	pixel
SIZEY	Window size in the Y direction	int	pixel
ORIGINX	X origin of the target window on the CCD	int	pixels
ORIGINY	Y origin of the targeted window on the CCD	int	pixel
TPL_ID	ID of the template associated to the target	int	0 to 255
TPL_SIZE	Number of pixels in the template applied on board	int	pixel
NRPIX	Number of "red" pixels	int	pixel
NGPIX	Number of "green" pixels	int	pixel
NBPIX	Number of "blue" pixels	int	pixel
NB	Position of the right edge of the blue part for CHR windows (−1 for MON files)**	int	pixel
NR	Position of the left edge of the red part of the CHR windows (−1 for MON files)**	int	pixel
NBFRAC	Position of the right edge of the blue part extracted form imagettes, −1 otherwise**	float	pixel
NRFRAC	Position of the left edge of the red part extracted form imagettes, −1 otherwise**	float	pixel
CCD_WINREF	Preprocessed sub-image showing the neighbourhood of the target	float	e^-/pix/s
TEMPLATE	Image of the template used to sum pixels on-board	byte	***
NXIMGREF	Size of the subimage CCD_WINREF in X	int	pixel
NYIMGREF	Size of the subimage CCD_WINREF in Y	int	pixel
POSXIMGREF	X position on the CCD of the bottom left corner of CCD_WINREF	int	pixel
POSYIMGREF	Y position on the CCD of the bottom left corner of CCD_WINREF	int	pixel
EXPTIME	Exposure time*	int	second

Notes. (*) Indicates of the measures are oversampled (32 s) or not (512 s). If a change occurs during a run (from 512 to 32 or the reverse) EXPTIME = −1. (**) Blue part from 1 to NB, green part from NB+1 to NR-1, the red part from NR to 15. (***) Pixels with value 1 are inside the mask.

Table II.4.18. Main header of the EN2_STAR_CHR product.

Name	Description	Type	Unit/ex...
SIMPLE	Mandatory: means that the file is fully compliant to FITS format	Boolean	True
BITPIX	Mandatory: Nb of bits by pixel (for images)	int	16
NAXIS	Mandatory: 0 means binary extensions	int	0
EXTEND	Mandatory for the creation of several extend	Boolean	True
TELESCOP	Telescope name	string	COROT
ORIGIN	Processing site	string	CDC
CREA_DAT	Creation date of the file in UT	string	yyyy-mm-ddThh:mm:ss
FILENAME	Name of the file	string	
N2_VER	Version of the N2 data	string	
PIPE_VER	Version of the process used to produce the data	string	
STARTDAT	Date of the first measurement in UT	string	yyyy-mm-ddThh:mm:ss
END_DATE	Date of the last measurement in UT	string	yyyy-mm-ddThh:mm:ss
COROTID	CoRoT identifier of the target	Long	
RUN_CODE	Run during which the target has been observed	string	See Sect. 1.3.2
HLFCCDID	Half CCD from which the product originates	string	
WIN_ID	ID of the window associated to the target	int	
MAGNITUD	Visual R magnitude of the target*	float	
ALPHA	Right ascension of the target* (equinox 2000)	double	Degrees (decimal)
DELTA	Declination of the target* (equinox 2000)	double	Degrees (decimal)
CONTFACT	Contamination factor*	float	[0,1]
EXPTIME	Exposure time	int	32/512/—1
MAGNIT_B/V/R/I	Star magnitude B/V/R/I*	float	
COLTEMP	Star colour temperature*	float	
SPECTYPE	Spectral type* (If none available “K5III” or “unknown”)	string	O, B. . . ..
LUMCLASS	Luminosity class*	string	I, IV
NBPHOTPIX	Number of hot pixels detected in the template	int	
LC_MEANR/G/B/W	Mean of the flux in R/G/B/W channels***	float	e^- per 32 s
LC_RMS_R/G/B/W	Standard deviation of the flux in R/G/B/W channels***	float	e^- per 32 s
COR_SLOP	Estimated slope of the efficiency loss	double	e^-/sec^2
COR_DELT	Range delta of the estimated COR_SLOP	double	e^-/sec^2
NB_CONSI	Number of temperature jumps in the run.	int	
DAT_TPE1. . . 6	Julian date of the 1st/../6th temperature jump in Terrestrial Time	float	Standart Julain Day Julian date
COR_TPE1...6	Flag of the 1st. . . 6th temperature jump correction: 0 = OK, −1 not executed, +1 done with warning**	int	0, −1, +1

Notes. (*) From the EXODAT database. (**) For the meaning of the warning, see Chap. II.2. (***) Calculated in the BAR extension on values with STATUS = 0.

Table II.4.19. Binary table of the BAR extension of EN2_STAR_CHR.

Name	Description	Type	Unit/ex...
DATE	Calendar date	string	yyyy-mm-ddThh:mm:ss
DATETT	Date of the measurement in Terrestrial Time	double	Terrestrial Time, Julian day
DATEBARTT	Date of the measurement in the solar barycentric reference frame	double	Solar barycentric Terrestrial Time, Julian day
STATUS	Flag of the status	int	see Sect. 3.2
REDFLUX	Integrated red flux*	float	e^- per 32 s
REDFLUXDEV	Standard deviation of the 16 exposures of 32 s in the red channel added for the 512 sampling	float	e^- per 32 s
GREENFLUX	Integrated green flux*	float	e^- per 32 s
GREENFLUXDEV	Standard deviation of the 16 exposures of 32 s in the green channel added for the 512 sampling	float	e^- per 32 s
BLUEFLUX	Integrated blue flux*	float	e^- per 32 s
BLUEFLUXDEV	Standard deviation of the 16 exposures of 32 s in the red channel added for the 512 sampling	float	e^- per 32 s
WHITEFLUX	White flux calculated from Red, Green, Blue*	float	e^- per 32 s
BG	Background flux already subtracted	float	e^- per pix per 32 s

Notes. (*) 32-s or 512-s sampling.

Table II.4.20. Binary table of the BARFILL extension of EN2_STAR_CHR.

Name	Description	Type	Unit/ex...
DATETT	Date of the measurement in Terrestrial Time	double	Terrestrial Time, Julian day
DATEBARTT	Date of the measurement in the solar barycentric reference frame	double	Solar barycentric Terrestrial Time, Julian day
WHITEFLUXFIL	White flux, after the gap filling correction	float	e^- per 32 s
STATUSFIL	Flag of the status	int	see Sect. 3.2
T_EXP	Exposure time	int	32 s or 512 s

2.2.3.4. SYSTEMATIC extension of the files EN2_STAR_CHR

The header of the SYSTEMATIC extension of the EN2_STAR_CHR is displayed in Appendix 1 (5.1.8).

The description of the SYSTEMATIC extension of theEN2_STAR_CHR is displayed in Table II.4.21 next page.

2.2.4. The EN2_STAR_MON product

Contains the information about the monochromatic stars of a run. It is stocked in the file:

EN2_STAR_MON_<*COROTID*>_<*START_DATE* >_<*END_DATE*>.fits

For all extends, the time stamp of the measurements is at the mean time of the exposure.

2.2.4.1. The EN2_STAR_MON main Header

See Table II.4.22 next page.

2.2.4.2. BAR extension of the files EN2_STAR_MON

The header of the BAR extension of EN2_STAR_MON is displayed in Appendix 1 (5.1.9).

The description of the BAR extension of EN2_STAR_MON is displayed in Table II.4.23 next page.

2.2.4.3. BARFILL extension of the EN2_STAR_MON table

The header of the BARFILL extension of EN2_STAR_MON is displayed in Appendix 1 (5.1.10).

The description of the BARFILL extension of EN2_STAR_MON is displayed in Table II.4.24 next page.

2.2.4.4. SYSTEMATIC extension of the files EN2_STAR_MON

The header of the SYSTEMATIC extension of EN2_STAR_MON is displayed in Appendix 1 (5.1.11).

The description of the SYSTEMATIC extension of EN2_STAR_MON is displayed in Table II.4.25 next page.

2.2.5. The EN2_STAR_IMAG product

Contains the fluxes of the stars observed as imagettes. The light curve sums the pixels of the imagettes over the PSF. Four light curves are generated, three “colours” and the white flux that contains all the pixels of the mask.

It is stocked in the file:

EN2_STAR_IMAG_<*COROTID*>_<*START_DATE* >_<*END_DATE*>.fits

For all extends, the time stamp of the measurements is at the mean time of the exposure.

The time sampling of EN2_STAR_IMAG is 32 s.

2.2.5.1. The EN2_STAR_IMAG main Header

See Table II.4.26 next page.

2.2.5.2. BAR extension of the files EN2_STAR_IMAG

The header of the BAR extension of EN2_STAR_IMAG is displayed in Appendix 1 (5.1.12).

The description of the BAR extension of EN2_STAR_IMAG is displayed in Table II.4.27 next page.

2.2.5.3. BARFILL extension of the files EN2_STAR_IMAG

The header of the BARFILL extension of EN2_STAR_IMAG is displayed in Appendix 1 (5.1.13).

The description of the BARFILL extension of EN2_STAR_IMAG is displayed in Table II.4.28 next page.

2.2.5.4. SYSTEMATIC extension of the EN2_STAR_IMAG table

The header of the SYSTEMATIC extension of EN2_STAR_IMAG is displayed in Appendix 1 (5.1.14).

See Table II.4.29 next page.

2.2.6. Full images of the faint stars channel: EN2_FULLIMAGE

The files contain one extension composed of one header, one image and the table containing the flux in (electrons/pixel) of each pixel of the image. It is stored in the file:

EN2_FULLIMAGE_<NUM_CCD>_<START_DATE >_

<END_DATE>.fits

The time stamp of the image is at the end of the first exposure of the accumulation, i.e., the beginning of accumulation plus 32 s.

2.2.6.1. Header of EN2_FULLIMAGE primary extension

See Table II.4.30 next page.

2.2.6.2. Image of EN2_FULLIMAGE

The primary image corresponds to the square corrected image; a SizeX × SizeY array, used to describe the environment of the stars on the CCD.

Type: double

Unit: electrons/pixel

Table II.4.21. Binary table of the SYSTEMATIC extension of the EN2_STAR_CHR.

Name	Description	Type	Unit/ex...
DATEBARTT	Date of the measurement in the solar barycentric reference frame	double	Solar barycentric Terrestrial Time, Julian day
WHITEFLUXSYS	White flux, after the correction of the systematics	float	e^- per 32 s
STATUSSYS	Flag of the status	int	see Sect. 3.2

Table II.4.22. Main header of the EN2_STAR_MON product.

Name	Description	Type	Unit/ex...
SIMPLE	Mandatory: means that the file is fully compliant to FITS format	Boolean	True
BITPIX	Mandatory: Nb of bits by pixel (for images)	int	16
NAXIS	Mandatory: 0 means binary extensions	int	0
EXTEND	Mandatory for the creation of several extend	Boolean	True
TELESCOP	Telescope name	string	COROT
ORIGIN	Processing site	string	CDC
CREA_DAT	Creation date of the file in UT	string	yyyy-mm-ddThh:mm:ss
FILENAME	Name of the file	string	
N2_VER	Version of the N2 data	string	
PIPE_VER	Version of the process used to produce the data	string	
STARTDAT	Date of the first measurement in UT	string	yyyy-mm-ddThh:mm:ss
END_DATE	Date of the last measurement in UT	string	yyyy-mm-ddThh:mm:ss
COROTID	CoRoT identifier of the target	Long	
RUN_CODE	Run during which the target has been observed	string	See Sect. 1.3.2
HLFCCDID	Half CCD from which the product originates	string	
WIN_ID	ID of the window associated to the target	int	
MAGNITUD	Visual R magnitude of the target*	float	
ALPHA	Right ascension of the target* (equinox 2000)	double	Degrees (decimal)
DELTA	Declination of the target* (equinox 2000)	double	Degrees (decimal)
CONTFACT	Contamination factor*	float	[0,1]
EXPTIME	Exposure time (32s, 512s or −1 when mixed sampling)	int	32/512/−1
MAGNIT_B/V/R/I	Star magnitude B/V/R/I*	float	
COLTEMP	Star colour temperature*	float	
SPECTYPE	Spectral type* (If none available "K5III" or "unknown")	string	O, B...
LUMCLASS	Luminosity class*	string	I, IV
NBPHOTPIX	Number of hot pixels detected in the template	int	
LC_MEAN	Mean of the flux***	float	e^- per 32 s
LC_RMS	Standard deviation of the flux***	float	e^- per 32 s
COR_SLOP	Estimated slope of the efficiency loss	double	e^-/sec^2
COR_DELT	Range delta of the estimated COR_SLOP	double	e^-/sec^2
NB_CONSI	Number of temperature jumps in the run.	int	
DAT_TPE1...6	Julian date of the 1st/../6th temperature jump in Terrestrial Time	float	Standart Julian Day
COR_TPE1...6	Flag of the 1st...6th temperature jump correction: 0 = OK, −1 not executed, +1 done with warning**	int	0, −1, +1

Notes. (*) From the EXODAT database. (**) For the meaning of the warning, see Chap. II.2. (***) Calculated in the BAR extension on values with STATUS = 0.

Table II.4.23. Binary table of the BAR extension of EN2_STAR_MON.

Name	**Description**	**Type**	**Unit/ex. . .**
DATE	Calendar date	string	yyyy-mm-ddThh:mm:ss
DATETT	Date of the measurement in Terrestrial Time	double	Terrestrial Time, Julian day
DATEBARTT	Date of the measurement in the solar barycentric reference frame	double	Solar barycentric Terrestrial Time, Julian day
STATUS	Flag of the status	int	see Sect. 3.2
WHITEFLUX	White flux of the star	float	e^- per 32 s
WHITEFLUXDEV	Standard deviation of the 16 exposures of 32 s, added for the 512 sampling	float	e^- per 32 s
BG	Background flux already subtracted	float	e^- per pix per 32 s

Table II.4.24. Binary table of the BARFILL extension of EN2_STAR_MON.

Name	**Description**	**Type**	**Unit/ex. . .**
DATETT	Date of the measurement in Terrestrial Time	double	Terrestrial Time, Julian day
DATEBARTT	Date of the measurement in the solar barycentric reference frame	double	Solar barycentric Terrestrial Time, Julian day
WHITEFLUXFIL	White flux, after the gap filling correction	float	e^- per 32 s
STATUSFIL	Flag of the status	int	see Sect. 3.2
T_EXP	exposure time	int	32 s or 512 s

Table II.4.25. Binary table of the SYSTEMATIC extension of EN2_STAR_MON.

Name	**Description**	**Type**	**Unit/ex. . .**
DATEBARTT	Date of the measurement in the solar barycentric reference frame	double	Solar barycentric Terrestrial Time, Julian day
WHITEFLUXSYS	White flux, after the correction of the systematics	float	e^- per 32 s
STATUSSYS	Flag of the status	int	see Sect. 3.2

Table II.4.26. Main header of the EN2_STAR_IMAG product.

Name	Description	Type	Unit/ex...
SIMPLE	Mandatory: means that the file is fully compliant to FITS format	Boolean	True
BITPIX	Mandatory: Nb of bits by pixel (for images)	int	16
NAXIS	Mandatory: 0 means binary extensions	int	0
EXTEND	Mandatory for the creation of several extend	Boolean	True
TELESCOP	Telescope name	string	COROT
ORIGIN	Processing site	string	CDC
CREA_DAT	Creation date of the file in UT	string	yyyy-mm-ddThh:mm:ss
FILENAME	Name of the file	string	
N2_VER	Version of the N2 data	string	
PIPE_VER	Version of the process used to produce the data	string	
STARTDAT	Date of the first measurement In UT	string	yyyy-mm-ddThh:mm:ss
END_DATE	Date of the last measurement In UT	string	yyyy-mm-ddThh:mm:ss
COROTID	CoRoT identifier of the target	Long	
RUN_CODE	Run during which the target has been observed	string	See Sect. 1.3.2
HLFCCDID	Half CCD from which the product originates	string	
WIN_ID	ID of the window associated to the target	int	
MAGNITUD	Visual R magnitude of the target*	float	
ALPHA	Right ascension of the target* (equinox 2000)	double	Degrees (decimal)
DELTA	Declination of the target* (equinox 2000)	double	Degrees (decimal)
CONTFACT	Contamination factor*	float	[0,1]
EXPTIME	Exposure time (32s, 512s, −1 or when mixed sampling)	int	32/512/-1
MAGNIT_B/V/R/I	Star magnitude B/V/R/I*	float	
COLTEMP	Star colour temperature*	float	
SPECTYPE	Spectral type* (If none available "K5III" or "unknown")	string	O, B...
LUMCLASS	Luminosity class*	string	I, IV
NBPHOTPIX	Number of hot pixels detected in the template	int	
LC_MEANR/G/B/W	Mean of the flux in R/G/B/W channels***	float	e^- per 32 s
LC_RMS_R/G/B/W	Standard deviation of the flux in R/G/B/W channels***	float	e^- per 32 s
COR_SLOP	Estimated slope of the efficiency loss	double	e^-/sec^2
COR_DELT	Range delta of the estimated COR_SLOP	double	e^-/sec^2
NB_CONSI	Number of temperature jumps in the run.	int	
DAT_TPE1...6	Julian date of the 1st/../6th temperature jump in TT	float	Standart Julian Day
COR_TPE1...6	Flag of the 1st....6th temperature jump correction: 0 = OK, -1 not executed, +1 done with warning**	int	0, −1, +1

Notes. (*) From the EXODAT database. (**) For the meaning of the warning, see Chap. II.2. (***) Calculated in the BAR extension on values with STATUS = 0.

Table II.4.27. Binary Table of the BAR extension of EN2_STAR_IMAG.

Name	Description	Type	Unit/ex...
DATE	Calendar date	string	yyyy-mm-ddThh:mm:ss
DATETT	Date of the measurement in Terrestrial Time	double	Terrestrial Time, Julian day
DATEBARTT	Date of the measurement in the solar barycentric reference frame	double	Solar barycentric Terrestrial Time, Julian day
STATUS	Flag of the status	int	see Sect. 2.2
REDFLUX	Integrated red flux extracted from the imagettes (32-s sampling)	double	e^- per 32 s
GREENFLUX	Integrated green flux extracted from the imagettes (32-s sampling)	double	e^- per 32 s
BLUEFLUX	Integrated blue flux extracted from the imagettes (32-s sampling)	double	e^- per 32 s
WHITEFLUX	White flux calculated from Red, Green, Blue	double	e^- per 32 s
BG	Background flux already subtracted	float	e^- per pix per 32 s
CENX	X position of the star centroid	float	pixels
CENY	Y position of the star centroid	float	pixels

Table II.4.28. Binary table of the BARFILL extension of EN2_STAR_IMAG.

Name	Description	Type	Unit/ex...
DATETT	Date of the measurement in Terrestrial Time	double	Terrestrial Time, Julian day
DATEBARTT	Date of the measurement in the solar Barycentric reference frame	double	Solar barycentric Terrestrial Time, Julian Day
WHITEFLUXFIL	White flux, after the gap filling correction	double	e^- per 32 s
STATUSFIL	Flag of the status	int	see Sect. 2.2

Table II.4.29. Binary table of the SYSTEMATIC extension of EN2_STAR_IMAG.

Name	Description	Type	Unit/ex...
DATEBARTT	Date of the measurement in the solar barycentric reference frame	double	Solar barycentric Terrestrial Time, Julian day
WHITEFLUXSYS	White flux, after the gap filling correction	double	e^- per 32 s
STATUSSYS	Flag of the status	int	see Sect. 2.2

Table II.4.30. Header of the EN2_FULLIMAGE primary extension.

Name	Description	Type	Unit/ex...
SIMPLE	Mandatory: means that the file is fully compliant to FITS format	Boolean	True
BITPIX	Mandatory: Nb of bits by pixel (for images)	int	16
NAXIS	Mandatory: 0 means binary extensions	int	0
EXTEND	Means that the creation of extend is possible	Boolean	True
TELESCOP	Telescope name	string	COROT
ORIGIN	Processing site	string	CDC
CREA_DAT	Creation date of the file in UT	string	yyyy-mm-ddThh:mm:ss
EXTNAME	Name of the extend	string	
FILENAME	Name of the file	string	
N2_VER	Version of the N2 data	string	
DATE	Date of the first measurement of the image	string	yyyy-mm-ddThh:mm:ss
CHAINID	ID of the photometric channel used	int	1 or 2
GAIN_R	Gain applied to correct the right half CCD	float	e^-/ADU
GAIN_L	Gain applied to correct the left half CCD	float	e^-/ADU
SIZEX	Size of the image upon X axis	int	=2048
SIZEY	Size of the image upon Y axis	int	=2048
EMI_CORR	Flag of the EMI correction	int	1 if EMI corrected
OFFSET_R	The value of the offset used to correct the right half of the CCD	float	ADU
OFFSET_L	The value of the offset used to correct the left half of the CCD	float	ADU
BRIGHTPI	Bright pixels processed	int	
THRESHOL	Threshold parameter for bright pixel	int	
NBPIX	nbpix parameter for bright pixel	int	
RUN_CODE	Run during which the target has been observed	string	See Sect. 1.3.2

3. Previous versions of N2 files

As written before, these versions are older versions: they should not be used anymore.

3.1. AN2 Products from the “bright star” channel

There is one single format for the light curves from the bright star channel. Files contain 3 extensions.

3.1.1. Status code for RAWSTATUS, STATUSHEL, STATUSHELREG

STATUS is a bit mask. This means that all the values can be combined.

For instance STATUS = 13 is the combination of (1), (4) and (8) which means that the measurement is considered as out of range, the data have been acquired during an SAA crossing and that the data have been calculated by interpolation.

See Table II.4.31 on previous page.

3.1.2. The AN2_STAR product

It is stocked in the file:

AN2_STAR_<*COROTID*>_<*START_DATE*>_<*END_DATE* >.fits

It contains a main Header and 3 extensions: RAW, HEL and HELREG:

- as from its name, the RAW extension contains raw data; it means that these data are as N1 data, simply accumulated over 32 seconds. This extension contains the values of the background measured in a background window positioned on the CCD as near as possible to the star window;
- the HEL extension contains data also accumulates on 32 s. Before accumulation, the data at 1-s sampling have been corrected:
  - the difference of the flux is normalized before and after the change of the mask (from version 3.4 only);
  - the changes of the temperature set point are corrected;
  - the curves are detrended from the loss of long term efficiency;
  - the points acquired when the satellite crosses the South Atlantic Anomaly are interpolated;
  - finally, the date of the exposure is converted to heliocentric scale; this leads to a slightly non regular time scale;
- data in the HELREG extension are corrected exactly as previously at the 1-s level but, the fluxes are distributed so that the sampling in heliocentric scale is strictly regular at 32 s.

The time stamp of the data of the RAW and HEL extension is positioned at the end of the 32 of the exposures.

DATEJD

Description: dates of the end of the measurements <u>in the satellite reference frame</u>, in CoRoT Julian day.
Type: double float.
Unit: CoRoT Julian day (origin 1 January 2000 12:00.00).

DATEJDHEL

Description: dates of the end of the measurements <u>in the heliocentric reference frame</u> (giving an <u>irregular sampling</u>), in CoRoT Julian day.
Type: double float.
Unit: CoRoT Julian day (origin 1 January 2000 12:00.00)

DATEJDHELREG

Description: dates of the measurements <u>in the heliocentric reference frame</u>, in CoRoT Julian day, with a strict <u>regular</u> 32-s sampling.
Type: double.
Unit: CoRoT Julian day (origin 1 January 2000 12:00.00).

3.1.2.1. The AN2_STAR main Header

See Table II.4.32 next page.

3.1.2.2. RAW extension of the files AN2_STAR

The header of the RAW extension of the AN2_STAR table is given in Appendix 1 (5.2.1).

The description of the RAW extension of the AN2_STAR table is given in Table II.4.33 next page.

3.1.2.3. HEL extension of the files AN2_STAR

The header of the HEL extension of the AN2_STAR table is given in Appendix 1 (5.2.2).

The description of the HEL extension of the AN2_STAR table is given in Table II.4.34 next page.

3.1.2.4. HELREG extension of the AN2_STAR table

The header of the HELREG extension of the AN2_STAR table is given in Appendix 1 (5.2.3).

The description of the HELREG extension of the AN2_STAR table is given in Table II.4.35 next page.

3.2. EN2 Products from the "faint star" channel

There are four different products, the windescriptor which describes the selected windows, the EN2_STAR_CHR product, which correspond to the windows treated in the chromatic mode, the EN2_STAR_MON product for the monochromatic windows, and the EN2_STAR_IMAG product associated to the targets observed as imagettes.

It is stored in files:

EN2_STAR_<TYPE>_<*COROTID*>_<*START_DATE*>_<*END_DATE* >.fits

where TYPE = CHR, MON or IMAG according to the type of the aboard acquisition.

Table II.4.31. STATUS code for RAWSTATUS, STATUSHEL and STATUSHELREG (V1 ≥ 3).

Bit number	**Type**	**Code**	**Information**
bit 0	false	(0)	Flux measurement valid
bit 0	true	(1)	Data considered as out of range (e.g. energetic particles or glitch)*
bit 1	true	(2)	Data invalid (original value is a default value, or no data accumulated (EXPORANK = 0)**
bit 2	true	(4)	SAA crossing
bit 3	true	(8)	Interpolated data
bit 4	true	(16)	Discontinuity detected in the LC
bit 5	true	(32)	Discontinuity due to the change of mask (once at the beginning of each run)
bit 6	true	(64)	Flux extracted from imagette
bit 7	true	(128)	New hot pixel detected
bit 8	true	(256)	Satellite entering the earth penumbra***
bit 9	true	(512)	Satellite leaving the penumbra****
bit 10	true	(1024)	Jitter excursion out of range. Original value replaced by a calculated value*****

Notes. (*) Corresponds to OVER = 1 in N1 products. (**) Corresponds to OVER = 2 in N1 products. (***) Orbital event 3, OVER = 8 in N1 products. (****) Orbital event 6, OVER = 16 in N1 products. (*****) OVER = 32 in N1 products.

Table II.4.32. Main header of the AN2_STAR product (V1 ≥ 3).

Name	Description	Type	Unit/ex...
SIMPLE	Mandatory: means that the file is fully compliant to FITS format	Boolean	True
BITPIX	Mandatory: Nb of bits by pixel (for images)	int	8
NAXIS	Mandatory: 0 means binary extensions	int	0
EXTEND	Means that several extend exist	Boolean	True
TELESCOP	Telescope name	string	COROT
ORIGIN	Processing site	string	CDC
CREA_DAT	Creation date of the file in UT	string	yyyy-mm-ddThh:mm:ss
FILENAME	Name of the file	string	
PIPE_VER	Version of the N1_N2 pipeline/Version of the N2 data	string	ex.: 2.8/3.4 pipeline version 2.8 data version 3.4
START_DAT	Date of the first measurement **In UT**	string	yyyy-mm-ddThh:mm:ss
END_DATE	Date of the last measurement **In UT**	string	yyyy-mm-ddThh:mm:ss
COROTID	Identification of the target	long	
RUN_CODE	Run during which the target has been observed	string	See Sect. 1.3.2
HLFCCDID	Half CCD from which the product originates	string	See Appendix 2 Sect. 6
ALPHA	Right ascension of the target (equinox 2000)	double	Degrees (decimal)
DELTA	Declination of the target (equinox 2000)	double	Degrees (decimal)
STARNAME	Usual name of the target*	string	Ex: HD 49933
MAGNIT_V	Visual magnitude of the target*	float	
ABSM_V	Absolute visual magnitude*	float	
COL_B_V	Colour index*	float	
SPECTYPE	Spectral type*	string (5)	O, B...
SUBCLASS	Subclass of the spectral type*	string (5)	1,2
LUMCLASS	Luminosity class*	string (5)	I, IV
TEFF	Effective temperature*	float	d°Kelvin
GRAVITY	$\log_{10}$ of the surface gravity* in m/s^2	float	m/s^2
METAL	Star metallicity*	float	$\log_{10}(Fe/H)/\log_{10}(Fe/H)_{Sun}$
LC_MEAN	Mean value of the HELREG flux	float	e^-/sec
LC_RMS	RMS of the HELREG flux	float	e^-/sec
NBPHOTPIX	Number of hot pixels detected (not implemented)	int	Value is always – 1
COR_SLOP	Estimated slope of the efficiency loss	double	e^-/sec^2
COR_DELT	Range delta of the estimated COR_SLOP	double	e^-/sec^2
NB_CONSI	Number of temperature jumps of the run (implemented from V3.1)	int	
DATE_TPE1..6	Date of the 1st...6th temperature jump in Terrestrial Time	float	Standart Julian Day
COR_TPE1...6	Flag of the temperature correction (implemented from V3.1); 0 = OK, -1 not executed, +1 done with warning**	int	0, –1, +1
MASK_COR	Code of the mask discontinuity correction 0 = no corr, +1 = measured corr, +2 = empirical corr	int	0, +1, +2

Notes. (*) From the COROTSKY database. (**) For the meaning of the warning, see Chap. II.2.

Table II.4.33. Binary table of the RAW extension of AN2_STAR (V1 $\geq$ 3).

Name	Description	Type	Unit/ex...
DATEJD	Date of measurement	double	CoRoT Julian Day**
RAWFLUX	N1 flux light curve*	double	e^-/sec
RAWFLUXDEV	Standard deviation of the 1-s measurement in the 32-s interval	double	e^-/sec
RAWSTATUS	Flag for the status	long	See Sect.? 32bits
BG	Background flux already subtracted	float	e^-/pix/sec

Notes. (*) Sampled at 32 s, as a sum of 1-s measurements, divided by the number of valid exposures. (**) Origin: 1 Jan 2000, 12:00:00 TU.

Table II.4.34. Binary table of HEL extension of the AN2_STAR (V1 $\geq$ 3).

Name	Description	Type	Unit/ex...
DATEJDHEL	Date of measurement in the heliocentric reference frame	double	CoRoT Julian Day**
FLUXHEL	Flux light curve*	double	e^-/sec
FLUXDEVHEL	Standard deviation of the 1-s measurement	double	e^-/sec
STATUSHEL	Flag for the status	long	32 bits

Notes. (*) Irregular sampling, 32 s in average. (**) Origin: 1 Jan 2000, 12:00:00 TU.

Table II.4.35. Binary table of the HELREG extension of the AN2_STAR table (V1 $\geq$ 3).

Name	Description	Type	Unit/ex...
DATEJDHELREG	Date of the measurements in the heliocentric reference frame, with a strict regular sampling	double	CoRoT Julian Day**
FLUXHELREG	Flux light curve*	double	e^-/sec
FLUXDEVHELREG	Standard deviation of the 1-s measurement	double	e^-/sec
STATUSHELREG	Flag for the status	long	See Sect. 32bits

Notes. (*) Regular sampling, 32 s. (**) Origin: 1 Jan 2000, 12:00:00 TU.

Table II.4.36. Main header of EN2_WINDESCRIPTOR (V1 $\geq$ 3).

Name	Description	Type	Unit/ex...
SIMPLE	Mandatory: means that the file is fully compliant to FITS format	Boolean	True
BITPIX	Mandatory: Nb of bits by pixel (for images)	int	16
NAXIS	Mandatory: 0 means binary extensions	int	0
EXTEND	Means that the creation of extend is possible	Boolean	True
TELESCOP	Telescope name	string	COROT
ORIGIN	Processing site	string	CDC
CREA_DAT	Creation date of the file in UT	string	yyyy-mm-ddThh:mm:ss
FILENAME	Name of the file	string	
PIPE_VER	Version of the process	float	
N2_VER	Version of the N2 data	string	
COMMENT	Commentary (2 lines)	string	
COROTID	CoRoT identifier of the target	int	
RUN_CODE	Run during which the target has been observed	string	See Sect. 1.3.2
HLFCCDID	Half CCD from which the product originates	string	
START_DATE	Date of the first measurement of the run in UT	string	yyyy-mm-ddThh:mm:ss
END_DATE	Date of the last measurement of the run in UT	string	yyyy-mm-ddThh:mm:ss

The file can contain data sampled at 32 s, 512 s or both samplings. The sampling rate can be found in the side file EN2_WINDESCRIPTOR (EXPTIME).

The file contains a main header and one extension called BINTABLE.

The corrections applied to the data are presented in Chap. II.2:

- elimination of the aliasing;
- subtraction of the offsets recorded on board;
- subtraction of the background acquired on board; the method used for this processing has evolved along the mission according to the ageing of the instrument;
- correction of the jitter of the satellite;
- detection of the outliers: the points are marked but not corrected;
- orbital events such as SAA, inbound and outbound crossing of the Earth shadow are marked;
- the changes of the temperature set point are corrected;
- the curves are detrended from the loss of long term efficiency.

The corrections applied to the data can differ from one version to another (see Table II.4.46 for a complete description of the corrections according to the version of the data).

The time stamp of the exposure is:

- the time of the end of the exposure for 32 s data;
- the time of the end of the first exposure for 512-s data.

It is expressed in Universal Time in the satellite reference frame and in Heliocentric Time, in “CoRoT” Julian time (reference January 1st 2000 at 12:00:00).

3.2.1. The EN2_WINDESCRIPTOR product

This product gathers the information on the observation setup, for a given target. It is produced once per target and per run. It is stocked in the file:

EN2_WINDESCRIPTOR_<*CoRoT_ID*>_<*START_DATE*>_<*END_DATE* >.fits

3.2.1.1. The EN2_WINDESCRIPTOR main Header

See Table II.4.36 on previous page.

3.2.1.2. The EN2_WINDESCRIPTOR binary table extension (BINTABLE)

The header of the BINTABLE extension of EN2_ WINDESCRIPTOR is given in Appendix 1 (5.2.4).

The description of the BINTABLE extension of EN2_WINDESCRIPTOR is given in Table II.4.37 next page.

3.2.2. STATUS CODE for the EN2_STAR_CHR, EN2_STAR_MON, EN2_STAR_IMAG tables

See Table II.4.38 next page.

3.2.3. The EN2_STAR_CHR product

Contains the light-curve of the chromatic targets. It is stocked in the file:

EN2_STAR_CHR_<*COROTID*>_<*START_DATE*>_<*END_DATE*>.fits

3.2.3.1. The EN2_STAR_CHR main Header

See Table II.4.39 next page.

3.2.3.2. The BINTABLE extension of the files EN2_STAR_CHR

The header of the BINTABLE extension of EN2_STAR_CHR is given in Appendix 1 (5.2.5).

The description of the BINTABLE extension of EN2_STAR_CHR is given in Table II.4.40 next page.

3.2.4. The EN2_STAR_MON product

Contains the information about the monochromatic star of a run. It is stocked in the file:

EN2_STAR_MON_<*COROTID*>_<*START_DATE*>_<*END_DATE*>.fits

3.2.4.1. The EN2_STAR_MON main Header

See Table II.4.41 next page.

3.2.4.2. The BINTABLE extension of the files EN2_STAR_MON

The header of the BINTABLE extension of EN2_STAR_MON is given in Appendix 1 (5.2.6).

The description of the BINTABLE extension of EN2_STAR_MON is given in Table II.4.42 next page.

3.2.5. The EN2_STAR_IMAG product

Contains the light-curves built from the imagettes of the stars; this method is in principle of better quality than the classical method which sums on board the flux over the PSF. As it is very TM consuming, it is performed only on very few selected targets. It is stocked in the file:

EN2_STAR_IMAG_<*COROTID*>_<*START_DATE*>_<*END_DATE*>.fits

3.2.5.1. The EN2_STAR_IMAG main Header

See Table II.4.43 next page.

3.2.5.2. The BINTABLE extension of the EN2_STAR_IMAG table

The header of the BINTABLE extension of EN2_STAR_IMAG is given in Appendix 1 (5.2.7).

The description of the BINTABLE extension of EN2_STAR_IMAG is given in Table II.4.44 next page.

Table II.4.37. Binary table BINTABLE of the EN2_WINDESCRIPTOR product.

Name	Description	Type	Unit/ex...
T_START_WIN	List of start time for the use of a given window for the target	float	CoRoT Julian Day
T_END_WIN	List of end time for the use of a given window for the target	float	CoRoT Julian Day
WIN_ID	ID of the target window	long	0 to 8191
SIZEX	Window size in the X direction	int	pixel
SIZEY	Window size in the Y direction	int	pixel
ORIGINX	X origin of the target window on the CCD	int	pixels
ORIGINY	Y origin of the targeted window on the CCD	int	pixel
TPL_ID	ID of the template associated to the target	int	0 to 255
TPL_SIZE	Number of pixels in the template	int	pixel
NRPIX	Number of red pixels ***	int	pixel
NGPIX	Number of green pixels ***	int	pixel
NBPIX	Number of blue pixels ***	int	pixel
NB	Position of the right edge of the blue part ***, ****	int	pixel
NR	Position of the left edge of the red part ***, ****	int	pixel
NBFRAC	Position of the right edge of the blue part extracted form imagettes, −1 otherwise ****	float	pixel
NRFRAC	Position of the left edge of the red part extracted form imagettes, −1 otherwise ****	float	pixel
CCD_WINREF	Preprocessed sub-image of the neighbourhood of the target	float	e^-/pix/s
TEMPLATE	Image of the template used **	byte	
NXIMGREF	Size of the sub-image CCD_WINREF in X	int	pixel
NYIMGREF	Size of the sub-image CCD_WINREF in Y	int	pixel
POSXIMGREF	X position on the CCD of the bottom left corner of CCD_WINREF	int	pixel
POSYIMGREF	Y position on the CCD of the bottom left corner of CCD_WINREF	int	pixel
EXPTIME	Exposure time*	int	second

Notes. (*) Indicates of the measures are oversampled or not. If during a run a change occurs in the sampling (from 512 to 32 or the reverse) EXPTIME = -1. (**) Pixels with value 1 are inside the mask. (***) −1 for Monochromatic windows, or if the flux is extracted from imagettes data. (****) Blue part from 1 to NB, green part from NB+1 to NR-1, the red part from NR to 15.

Table II.4.38. STATUS code for EN2_STAR_CHR, EN2_STAR_MON, EN2_STAR_IMAG (V1 $\geq$ 3).

Bit number	Type	Code	Information
bit 0	false	(0)	Flux measurement valid
bit 0	true	(1)	Cosmic event detected by the N0-N1 pipeline
bit 1	true	(2)	Spare value detected by the N0-N1 pipeline
bit 2	true	(4)	SAA crossing (added in N0->N1 pipe-line)
bit 3	true	(8)	Flux perturbed by an Earth eclipse (inbound)
bit 4	true	(16)	Flux perturbed by an Earth eclipse (outbound)
bit 5	true	(32)	SAA crossing (added in N1->N2 pipe-line)
bit 6	true	(64)	Interpolated data due to a large jitter
bit 7	true	(128)	New hot pixel detected
bit 8			*not used*
bit 9			*not used*
bit 10	true	(1024)	Flux flagged as "incorrect" by the flight s/w (VALIDFLUX = 1
bit 11	true	(2048)	Flux flagged as "incorrect" by the flight s/w (VALIDFLUX = 2)

Table II.4.39. Main header of the EN2_STAR_CHR product (V1 $\geq$ 3).

Name	Description	Type	Unit/ex...
SIMPLE	Mandatory: means that the file is fully compliant to FITS format	Boolean	True
BITPIX	Mandatory: Nb of bits by pixel (for images)	int	16
NAXIS	Mandatory: 0 means binary extensions	int	0
EXTEND	Mandatory for the creation of several extend	Boolean	True
TELESCOP	Telescope name	string	COROT
ORIGIN	Processing site	string	CDC
CREA_DAT	Creation date of the file in UT	string	yyyy-mm-ddThh:mm:ss
FILENAME	Name of the file	string	
PIPE_VER	Version of the process	float	
N2_VER	Version of the N2 data	string	
STARTDAT	Date of the first measurement In UT	string	yyyy-mm-ddThh:mm:ss
END_DATE	Date of the last measurement In UT	string	yyyy-mm-ddThh:mm:ss
COROTID	CoRoT identifier of the target	Long	
RUN_CODE	Run during which the target has been observed	string	See Sect. 1.3.2
HLFCCDID	Half CCD from which the product originates	string	
WIN_ID	ID of the window associated to the target when unique (–1 otherwise)	int	
MAGNITUD	Visual R magnitude of the target*	float	
ALPHA	Right ascension of the target* (equinox 2000)	double	Degrees (decimal)
DELTA	Declination of the target* (equinox 2000)	double	Degrees (decimal)
CONTFACT	Contamination factor*	float	[0,1]
EXPTIME	Exposure time	int	32/512/-1
CHRDEG	D°of chromaticity (not completed)	float	0.0
ACTILEV	Level of activity (not completed)	float	0.0
VARCLASS 1/2/3	Class of variability**	string	
PRBCLASS 1/2/3	Probability associated to the class of variability**	float	
MAGNIT_B/V/R/I	Star magnitude B/V/R/I*	float	
COLTEMP	Star colour temperature*	float	
SPECTYPE	Spectral type*	string	O, B...
LUMCLASS	Luminosity class*	string	I, IV
NBPHOTPIX	Number of hot pixels detected in the template	int	
LC_MEANR/G/B/W	Mean of the flux in R/G/B/W channels****	float	e^-/sec
LC_RMS_R/G/B/W	Standard deviation of the flux in R/G/B/W channels****	float	e^-/sec
COR_SLOP	Estimated slope of the efficiency loss	double	e^-/sec^2
COR_DELT	Range delta of the estimated COR_SLOP	double	e^-/sec^2
NB_CONSI	Number of temperature jumps in the run; valid only for version 3.1 and later	int	
DAT_TPE1...6	Julian date of the 1st/../6th temperature jump in TU; valid only for version 3.1 and later	float	CoRoT Julian date
COR_TPE1...6	Flag of the temperature correction; valid only for version 3.1 and later 0 = OK, −1 not executed, +1 done with warning***	int	0, −1, +1

Notes. (*) From the EXODAT database. (**) Defined in Debosscher et al. 2009, A&A, 506, 519. (***) For the meaning of the warning, see Chap. II.2.

Table II.4.40. BINTABLE extension of EN2_STAR_CHR.

Name	Description	Type	Unit/ex...
DATE	Calendar date	string	yyyy-mm-ddThh:mm:ss
DATEJD	Date of the measurement in UT	double	CoRoT Julian Day*
DATEHEL	Date of the measurement in the heliocentric reference frame	double	CoRoT Julian Day*
STATUS	Flag of the status	int	see Sect. 3.2
REDFLUX	Integrated red flux**	double	e^-/sec
REDFLUXDEV	Standard deviation of the 16 exposures of 32 s in the red channel added for the 512 sampling	double	e^-/sec
GREENFLUX	Integrated green flux**	double	e^-/sec
GREENFLUXDEV	Standard deviation of the 16 exposures of 32 s in the green channel added for the 512 sampling	double	e^-/sec
BLUEFLUX	Integrated blue flux**	double	e^-/sec
BLUEFLUXDEV	Standard deviation of the 16 exposures of 32 s in the red channel added for the 512 sampling	double	e^-/sec
WHITEFLUX	White flux calculated from Red, Green, Blue	double	e^-/sec
JCFW	Jitter correction for the white flux	float	e^-/sec
BG	Background flux already subtracted	float	e^-/sec
CORREC_RED	Difference with N1 of the red flux	float	e^-/sec
CORREC_GREEN	Difference with N1 of the green flux	float	e^-/sec
CORREC_BLUE	Difference with N1 of the blue flux	float	e^-/sec

Notes. (*) Origin: 1 Jan 2000, 12:00:00 TU.

Table II.4.42. BINTABLE extension of the EN2_STAR_MON table.

Name	Description	Type	Unit/ex...
DATE	Calendar date	string	yyyy-mm-ddThh:mm:ss
DATEJD	Date of the measurement in UT	double	CoRoT Julian Day*
DATEHEL	Date of the measurement in the heliocentric reference frame	double	CoRoT Julian Day*
STATUS	Flag of the status	int	see Sect. 3.2
WHITEFLUX	White flux of the star	float	e^-/sec
WHITEFLUX_DEV	Standard deviation of the 16 exposures of 32 s, added for the 512 sampling	float	e^-/sec
BG	Background flux already subtracted	float	e^-/sec
CORREC	Difference with N1 of the flux	float	e^-/sec

Table II.4.41. Main header of the EN2_STAR_MON product (V1 ≥ 3).

Name	Description	Type	Unit/ex...
SIMPLE	Mandatory: means that the file is fully compliant to FITS format	Boolean	True
BITPIX	Mandatory: Nb of bits by pixel (for images)	int	16
NAXIS	Mandatory: 0 means binary extensions	int	0
EXTEND	Mandatory for the creation of several extend	Boolean	True
TELESCOP	Telescope name	string	COROT
ORIGIN	Processing site	string	CDC
CREA_DAT	Creation date of the file in UT	string	yyyy-mm-ddThh:mm:ss
FILENAME	Name of the file	string	
PIPE_VER	Version of the process	float	
N2_VER	Version of the N2 data	string	
STARTDAT	Date of the first measurement in UT	string	yyyy-mm-ddThh:mm:ss
END_DATE	Date of the last measurement in UT	string	yyyy-mm-ddThh:mm:ss
COROTID	CoRoT identifier of the target	Long	
RUN_CODE	Run during which the target has been observed	string	See Sect. 1.3.2
HLFCCDID	Half CCD from which the product originates	string	
WIN_ID	ID of the window associated to the target when unique (–1 otherwise)	int	
MAGNITUD	Visual R magnitude of the target*	float	
ALPHA	Right ascension of the target* (equinox 2000)	double	Degrees (decimal)
DELTA	Declination of the target* (equinox 2000)	double	Degrees (decimal)
CONTFACT	Contamination factor*	float	[0,1]
EXPTIME	Exposure time	int	32/512/–1
CHRDEG	D°of chromaticity (not available)	float	0.0
ACTILEV	Level of activity (not available)	float	0.0
VARCLASS 1/2/3	Class of variability	string	
PRBCLASS 1/2/3	Probability associated to the class of variability**	float	
MAGNIT_B/V/R/I	Star magnitude B/V/R/I*	float	
COLTEMP	Star colour temperature*	float	
SPECTYPE	Spectral type*	string	O, B...
LUMCLASS	Luminosity class*	string	I, IV
NBPHOTPIX	Number of hot pixels detected in the template	int	
LC_MEAN	Mean of the flux****	float	e^-/sec
LC_RMS	Standard deviation of the flux****	float	e^-/sec
COR_SLOP	Estimated slope of the efficiency loss	double	e^-/sec^2
COR_DELT	Range delta of the estimated COR_SLOP	double	e^-/sec^2
NB_CONSI	Number of temperature jumps in the run; valid only for version 3.1 and later	int	
DAT_TPE1...6	Julian date of the 1st/../6th temperature jump in TU; valid only for version 3.1 and later	float	CoRoT Julian date
COR_TPE1...6	Flag of the temperature correction; valid only for version 3.1 and later 0 = OK, −1 not executed, +1 done with warning***	int	0, -1, +1

Notes. (*) From the EXODAT database. (**) Defined in Debosscher et al. 2009, A&A, 506, 519. (***) For the meaning of the warning, see Chap. II.2. (****) Computed on valid values, i.e. with STATUS = 0.

Table II.4.43. Main header of the EN2_STAR_IMAG product (V1 $\geq$ 3).

Name	Description	Type	Unit/ex...
SIMPLE	Mandatory: means that the file is fully compliant to FITS format	Boolean	True
BITPIX	Mandatory: Nb of bits by pixel (for images)	int	16
NAXIS	Mandatory: 0 means binary extensions	int	0
EXTEND	Mandatory for the creation of several extend	Boolean	True
TELESCOP	Telescope name	string	COROT
ORIGIN	Processing site	string	CDC
CREA_DAT	Creation date of the file in UT	string	yyyy-mm-ddThh:mm:ss
FILENAME	Name of the file	string	
PIPE_VER	Version of the process	string	
N2_VER	Version of the N2 data	string	
STARTDAT	Date of the first measurement In UT	string	yyyy-mm-ddThh:mm:ss
END_DATE	Date of the last measurement In UT	string	yyyy-mm-ddThh:mm:ss
COROTID	CoRoT identifier of the target	Long	
RUN_CODE	Run during which the target has been observed	string	See Sect. 1.3.2
HLFCCDID	Half CCD from which the product originates	string	
WIN_ID	ID of the window associated to the target when unique (-1 otherwise)	int	
MAGNITUD	Visual R magnitude of the target*	float	
ALPHA	Right ascension of the target* (equinox 2000)	double	Degrees (decimal)
DELTA	Declination of the target* (equinox 2000)	double	Degrees (decimal)
CONTFACT	Contamination factor*	float	[0,1]
EXPTIME	Exposure time	int	32/512/–1
CHRDEG	D° of chromaticity (not available)	float	0.0
ACTILEV	Level of activity (not available)	float	0.0
VARCLASS 1/2/3	Class of variability**	string	
PRBCLASS 1/2/3	Probability associated to the class of variability**	float	
MAGNIT_B/V/R/I	Star magnitude B/V/R/I*	float	
COLTEMP	Star colour temperature*	float	
SPECTYPE	Spectral type*	string	O, B...
LUMCLASS	Luminosity class*	string	I, IV
NBPHOTPIX	Number of hot pixels detected in the template	int	
LC_MEANR/G/B/W	Mean of the flux in R/G/B/W channels	float	e^-/sec
LC_RMS_R/G/B/W	Standard deviation of the flux in R/G/B/W channels	float	e^-/sec
COR_SLOP	Estimated slope of the efficiency loss	double	e^-/sec^2
COR_DELT	Range delta of the estimated COR_SLOP	double	e^-/sec^2
NB_CONSI	Number of temperature jumps in the run. Valid only for version 3.1 and later	int	
DAT_TPE1...6	Julian date of the 1st/../6th temperature jump in TU	float	CoRoT Julian date
COR_TPE1...6	Flag of the temperature correction; valid only for version 3.1 and later 0 = OK, -1 not executed, +1 done with warning***	int	0, -1, $+1$

Notes. (*) From the EXODAT database. (**) Defined in Debosscher et al. 2009, A&A, 506, 519. (***) For the meaning of the warning, see Chap. II.2.

4. Description of the processing according to the version of the data

The purpose of this section is to present roughly the processing applied to the CoRoT data according to the version of the data.

The version of the data is given by the keyword N2_VER in the primary header of the fits files[3].

The final version of the data (V4) have a different structure and above all, a different time stamping: TU and heliocentric from version 1 to 3, TT and barycentric for version 4.

In this section, we give a short description of the general processing and then, we present the different versions of each type of data.

The whole processing can be found in Auvergne (2009) and Ollivier (in this book, Chap. II.2).

In the faint stars channel, each STAR file comes with a EN2_WINDESCRIPTOR file; the version of the windescriptor file is the same as the version of the light curve.

4.1. Short description of the successive steps of the processing

4.1.1. Version 4

The description of the complete processing for the Legacy can be found in Chapter II.2.

As already mentioned, the corrections fall into 2 categories: the instrumental and environmental corrections, well understood or modeled, and second step corrections that facilitate the use of the data but might not be always legitimate.

For faint stars, the suppression of the non-thermal jumps belongs to this second category. It appears that false jump detection can happen for rapidly variable stars such as RR-Lyrae. In this case, it is essential to use the data without this correction, i-e to use BAR data.

4.1.2. Versions 1 to 3

- **N0 ->N1 processing:**
  - The corrections are applied in the following order:
    - **Elimination of the aliasing** appearing on a CCD when reading another CDD: this is done by using patterns measured in the calibration phase;
    - on the **BS** field, elimination of the residuals of **offset and background;**
    - on the **FS** field, subtraction of the **offset** and of the **background** obtained as the **median** of the observed **backgrounds** in order to eliminate the hot pixels in the background light curves;
    - on the FS chromatic light curves, **computation of the white light;**
    - correction of the duration of the exposure and absolute dating;
    - **jitter corrections** using high resolution PSF on the seismo field and medium resolution PSF on the exo field;
    - Correction of relativistic aberration via the modification of the focal equivalent to the dilatation (resp contraction) of the field of the of view;
    - Detection of energetic particle impacts: a point is considered as an impact when the difference between the signal and the median calculated on a sliding window is higher then 5σ. Data are not modified at that step, a warning is included in the data (see STATUS word in Sect. 3.1.1 and 3.2.2);
    - Orbital events are indicated taking into account the absolute date of the data: SAA, inbound and outbound Earth eclipses (see STATUS word below).
- **N1 ->N2 processing:**
  - For both BS and Fs data:
    - Translation from UTC to heliocentric time basis;
    - the diminution of the quantum efficiency is compensated;
    - the effect of the changing of the CCD temperature is corrected.
    - Creation of a “windescriptor” file containing an extraction of the on-board full image, the size of the on-board mask and some useful information about the observed target.
  - For BS data:
    - resampling from a 1-s basis to a 32-s;
    - Resampling to regular heliocentric time basis;
    - Elimination of the discontinuity due the changing of the on-board mask.
  - For FS data:
    - Merging of 512-s and 32-s files;
    - Hot pixels are detected and flagged;

4.1.2.1. Bright star channel

See Table II.4.45 next page.

4.1.2.2. Faint stars channel

Faint stars are observed using different methods:

- a few stars, up to 40, are acquired as a small portion (10*15 pixels) of the image called imagette observed during 32 seconds;
- the other stars, up to 11,400, are observed as light curves. The light curves are either “chromatic” or monochromatic; some of them, up to 2000, are acquired at 32-s rate while most of them are accumulated over 16 exposures leading to a 512-s sampling.

The exact number of each set of stars depends upon the run (Baglin, in this book).

Data from onboard light curves

See Table II.4.46 next page.

---

[3] The keyword PIPE_VER indicates the version of the pipe-line used to produce the data, not the version of the data. It has been used for processing purpose and is of no use for the final user.

Table II.4.44. BINTABLE extension of the EN2_STAR_IMAG table.

Name	Description	Type	Unit/ex...
DATE	Calendar date	string	yyyy-mm-ddThh:mm:ss
DATEJD	Date of the measurement in UT	double	CoRoT Julian Day*
DATEHEL	Date of the measurement in the heliocentric reference frame	double	CoRoT Julian Day*
STATUS	Flag of the status	int	see Sect. 3.2
REDFLUX_IMAG	Integrated red flux extracted from the imagettes (32-s sampling)	double	e^-/sec
GREENFLUX_IMAG	Integrated green flux extracted from the imagettes (32-s sampling)	double	e^-/sec
BLUEFLUX_IMAG	Integrated blue flux extracted from the imagettes (32-s sampling)	double	e^-/sec
WHITEFLUX_IMAG	White flux calculated from Red, Green, Blue	double	e^-/sec
BG_IMAG	Background flux already subtracted	float	e^-/sec
CENX	X position of the star centroid	float	Pixels in the window frame
CENY	Y position of the star centroid	float	pixels in the window frame

Notes. (*) Origin: 1 Jan 2000, 12:00:00 TU.

Table II.4.45. Processing of the light curves in the BRIGHT STARS CHANNEL according to the versions (V1 $\geq$ 3)

Version	Corrections
1.0	• Cross-talk corrections using ground-measured patterns • Correction of the offsets and of the backgrounds are improved from on-board measurements • First and rough jitter correction where the line of sight is continuous only by segments
1.1; 1.2	• Optimisation of the computation of the PSF
1.3; 1.4	• Correction of a bug in the reading of the gain: the correct value for each half-CCD is now used • Better jitter correction: the excursion is computed relatively to the same mean value along the whole run
1.8	• Correction of the discontinuity caused by the breakdown of DPU1 • Warning on the data where the jitter excursion can't be corrected; in this case, the value is interpolated • Correction of minor bugs on the STATUS word (valid/invalid data)
1.9; 2.1	• Incorporation of the flag for ingress and egress of the earth eclipses
3.0	• Better dating of the SAA and earth eclipses: the flags are coherent between N1 and N2 pipe-lines • Only positive impacts are marked (instead of positive and negative) • **The effect of the decrease of the quantum efficiency is corrected**
3.1; 3.2 3.3	• **New jitter correction: the relativistic aberration is taken into account through the variation of the focal of the telescope** • **The changes of the temperatures of the CCDs are corrected**
3.4	• New version of the correction of the loss of efficiency according to the flux: the coefficients of the correction have be recomputed using the data of all the runs • The fluxes of the two sequences are normalized using small images (imagettes); new words added in the primary header (COR_SLOP, COR_DELT, MSK_COR) characterise the correction.

Light curves from onboard small images ("imagettes")

See Table II.4.47 next page.

References

Auvergne, M., Bodin, P., Boisnard, L., et al. 2009, A&A, 506, 411

Baglin, A. Chaintreuil, S., & Vandermarcq, O., in this book, part II

Baglin, A., & Fridlung, M. 2006, ESA SP 1306, in eds M. Fridlund, A. Baglin, J. Lochard, & L. Conroy, Noorwijk, The Netherlands: ESA Publication Division, ESTEC, ISBN 92-9092-465-9, referred as ”The CoRoT book”

Ollivier, M., Deru A., Chaintreuil S., et al., in this book, Chap. II.2

Pires, S., Mathur, S., García, R., et al. 2015, A&A, 574, A18

Table II.4.46. Processing of the light curves in the FAINT STARS CHANNEL according to the versions (V1 $\geq$ 3).

Version	**Corrections**
1.1	• Cross-talk corrections, offset subtraction, backgrounds subtraction. • Very rough jitter correction on chromatic light curves • No jitter corrections on mono-chromatic light curves
1.2; 1.3	• Correction of a bug in the reading of the gain: the correct value for each half-CCD is now used • Addition of lacking information in the headers of the files
1.4	• Incorporation of the flag for ingress and egress of the earth eclipses • Correction of the discontinuity caused by the breakdown of DPU1
2.0	• **Computation of a “white flux” on chromatic light curves by addition of the 3 “colours”** • New calculation of the line of sight based on the computation of the PSF
2.1 2.1b	• Better dating of the SAA and earth eclipses: the flags are coherent between N1 and N2 pipe-lines • Change in the indication of impacts: only positive outliers are marked (instead of positive and negative)
2.2	• Better PSF determination due to hot pixel elimination before calculation • Adjustment of the filtering of the outliers on the duration of the orbit
3.0	• **New jitter correction: the relativistic aberration is taken into account through the variation of the focal of the telescope** • **Correction of the loss of efficiency** • **Correction of the changes of the temperature of the CCDs** • Pipe-line version 2.3: the star information in the EN2_WINDESCRIPTOR is updated from EXODAT via a web service
3.1*	• Change in the order of the correction: the effect of the jumps of the CCD temperature are applied after the correction of the loss of global efficiency (this is not correct and is fixed in version 3.4)
3.2*	• the increase of the dark current with the position of the star on the CCD is taken into account (with a small bug fixed in version 3.4)
3.3	• New version of the correction of the loss of efficiency according to the flux: the coefficients of the correction have be recomputed using the data of all the runs
3.4, 3.5	• Correction of the previous bugs
3.6	• Improvement in the correction of background: both 32 s and 512 s median values are upgraded to the overall median value.

Notes. (*) Versions 3.1 and 3.2 include bugs.

Table II.4.47. Processing of the building of the light curves from aboard small images (imagettes) according to the versions (V1 ≥ 3).

Co-Is version	**Corrections**
1.0 1.0b 1.1	• Calculation of light curves from on board imagettes • Correction of the cross-talk, subtraction of the offset and of the background • The algorithm is based on the determination of a significant mask • The reconstruction is performed using the LOS
1.2	• Improvements of the STATUS word and of the position of the orbital events • Information in WINDESCRIPTORs are read directly from Exodat via a web service
2.0	• **Major change: the centroid of the spread image is calculated and its coordinates are given in two new columns** • Improved corrections of the jitter • Correction of the jumps of the CCD temperature: their date and the "quality" of the correction are given in the primary header • Correction of the global loss of efficiency • The number of pixels of the reconstructed colours are integers (previous bug fixed)
2.1	• Improvement in the correction of background including better correction of the dark current
2.2	• Subtraction of the loss of efficiency according to the mean flux of the light curve
2.3	• New improvement in the correction of background: both 32 s and 512 s median value are upgraded to the overall median value

5. Appendix 1: Headers of the extensions

5.1. Headers of the extensions in version 4 data

5.1.1. Header of the BINTABLE of the N2_WINDESCRIPTOR product

Name	Description	Type	Value
XTENSION	Mandatory (indicates the type of the extend)	string	BINTABLE
BITPIX	Mandatory (for images)	int	8
NAXIS	Mandatory word;	int	2: BINTABLE extension
NAXIS1	Number of bytes per row	int	
NAXIS2	Number of rows	int	
PCOUNT	Mandatory but not used		
GCOUNT	Mandatory but not used		
TFIELDS	Number of columns	int	15
EXTNAME	Name of the extension	string	BINTABLE’
TFORM1	Format of column 1	string	23A
TTYPE1	Label of column 1	string	T_START_WIN
TUNIT1	Unit of column 1	string	Calendar date (UT)
TFORM2	Format of column 2	string	19A
TTYPE2	Label of column 2	string	T_END_WIN
TUNIT2	Unit of column 2	string	Calendar date (UT)
TFORM3	Format of column 3	string	J (long integer)
TTYPE3	Label of column 3	string	WIN_ID
TUNIT3	Unit of column 3	string	
TFORM4	Format of column 4	string	I (integer)
TTYPE4	Label of column 4	string	SIZEX
TUNIT4	Unit of column 4	string	
TFORM5	Format of column 5	string	I (integer)
TTYPE5	Label of column 5	string	SIZEY
TUNIT5	Unit of column 5	string	
TFORM6	Format of column 6	string	I (integer)
TTYPE6	Label of column 6	string	ORIGINX
TUNIT6	Unit of column 6	string	
TFORM7	Format of column 7	string	I (integer)
TTYPE7	Label of column 7	string	ORIGINY
TUNIT7	Unit of column 7	string	
TFORM8	Format of column 8	string	I (integer)
TTYPE8	Label of column 8	string	MASK_ID
TUNIT8	Unit of column 8	string	
TFORM9	Format of column 9	string	I (integer)
TTYPE9	Label of column 9	string	MASK_SIZE
TUNIT9	Unit of column 9	string	pixel
TFORM10	Format of column 10	string	2500D
TTYPE10	Label of column 10	string	CCD_WINREF
TDIM10	Array dimensions for column 10	string	(50,50)
TUNIT10	Unit of column 10	string	Electron/px/s
TFORM11	Format of column 11	string	I (int)
TTYPE11	Label of column 11	string	NXIMGREF
TUNIT11	Unit of column 11	string	
TFORM12	Format of column 12	string	I
TTYPE12	Label of column 12	string	NYIMGREF
TUNIT12	Unit of column 12	string	
TFORM13	Format of column 13	string	I
TTYPE13	Label of column 13	string	POSXIMGREF
TUNIT13	Unit of column 13	string	
TFORM14	Format of column 14	string	I
TTYPE14	Label of column 14	string	POSYIMGREF
TUNIT14	Unit of column 14	string	
TFORM15	Format of column 15	string	2500D
TTYPE15	Label of column 15	string	MASK
TDIM15	Array dimensions for column 15	string	(50,50)
TUNIT15	Unit of column 15	string	
COMMENT **. . .** **COMMENT**	Lines of comments, describing the contents of the BINTABLE specially the small images.	string	80 characters max.

5.1.2. Header of the RAW extension of the AN2_STAR table

Name	Description	Type	Value
BITPIX	Mandatory: (for images)	int	8
NAXIS	Mandatory word;	int	2: BINTABLE extension
NAXIS1	Number of bytes per row	int	
NAXIS2	Number of rows	int	
PCOUNT	Not used		
GCOUNT	Not used		
TFIELDS	Number of columns	int	5
EXTNAME	Name of the extension	string	RAW
TFORM1	Format of column 1	string	D (double)
TTYPE1	Label of column 1	string	DATETT
TUNIT1	Unit of column 1	string	Terrestrial Time
TFORM2	Format of column 2	string	D (double)
TTYPE2	Label of column 2	string	RAWFLUX
TUNIT2	Unit of column 2	string	electron/s
TFORM3	Format of column 3	string	D (double)
TTYPE3	Label of column 3	string	RAWFLUXDEV
TUNIT3	Unit of column 3	string	electron/s
TFORM4	Format of column 4	string	J (long)
TTYPE4	Label of column 4	string	RAWSTATUS
TUNIT4	Unit of column 4		
TFORM5	Format of column 5	string	E (float)
TTYPE5	Label of column 5	string	BG
TUNIT5	Unit of column 5	string	electron/px/s
COMMENTS		string	

5.1.3. Header of the BAR extension of the AN2_STAR table

Name	Description	Type	Value
BITPIX	Mandatory: (for images)	int	8
NAXIS	Mandatory word;	int	2: BINTABLE extension
NAXIS1	Number of bytes per row	int	
NAXIS2	Number of rows	int	
PCOUNT	Not used		
GCOUNT	Not used		
TFIELDS	Number of columns	int	4
EXTNAME	Name of the extension	string	BAR
TFORM1	Format of column 1	string	D (double)
TTYPE1	Label of column 1	string	DATEBARTT
TUNIT1	Unit of column 1	string	Barycentric time (irreg)
TFORM2	Format of column 2	string	D (double)
TTYPE2	Label of column 2	string	FLUXBAR
TUNIT2	Unit of column 2	string	electron/s
TFORM3	Format of column 3	string	D (double)
TTYPE3	Label of column 3	string	FLUXDEVBAR
TUNIT3	Unit of column 3	string	electron/s
TFORM4	Format of column 4	string	J (long)
TTYPE4	Label of column 4	string	STATUSBAR
TUNIT4	Unit of column 4		
COMMENTS		string	

5.1.4. Header of the BARREG extension of the AN2_STAR table

Name	Description	Type	Value
BITPIX	Mandatory: (for images)	Int	8
NAXIS	Mandatory word;	Int	2: BINTABLE extension
NAXIS1	Number of bytes per row	Int	
NAXIS2	Number of rows	Int	
PCOUNT	Not used		
GCOUNT	Not used		
TFIELDS	Number of columns	int	4
EXTNAME	Name of the extension	string	BARREG
TFORM1	Format of column 1	string	D (double)
TTYPE1	Label for column 1	string	DATEBARREGTT
TUNIT1	Unit of column 1	string	Barycentric time (reg)
TFORM2	Format of column 2	string	D (double)
TTYPE2	Label for column 2	string	FLUXBARREG
TUNIT2	μ Unit of column 2	string	electron/s
TFORM3	Format of column 3	string	D (double)
TTYPE3	Label for column 3	string	FLUXDEVBARREG
TUNIT3	Unit of column 3	string	electron/s
TFORM4	Format of column 4	string	J (long)
TTYPE4	Label of column 4	string	STATUSBARREG
TUNIT4	Unit of column 4	string	
COMMENTS		string	

5.1.5. Header of the BINTABLE of the product EN2_WINDESCRIPTOR

Name	Description	Type	Value
BITPIX	Mandatory (for images)	int	8
NAXIS	Mandatory word;	int	2: BINTABLE extension
NAXIS1	Number of bytes per row	int	
NAXIS2	Number of rows	int	
PCOUNT	Mandatory but not used		
GCOUNT	Mandatory but not used		
TFIELDS	Number of columns	int	23
TTYPE1	Label of column 1	string	T_START_WIN
TFORM1	Format of column 1	string	23A
TUNIT1	Unit of column 1	string	Calendar (UT)
TTYPE2	Label of column 2	string	T_END_WIN
TFORM2	Format of column 2	string	19A
TUNIT2	Unit of column 2	string	Calendar (UT)
TTYPE3	Label of column 3	string	WIN_ID
TFORM3	Format of column 3	string	J (long)
TUNIT3	Unit of column 3	string	
TTYPE4	Label of column 4	string	SIZEX
TFORM4	Format of column 4	string	I (int)
TUNIT4	Unit of column 4	string	pixels
TTYPE5	Label of column 5	string	SIZEY
TFORM5	Format of column 5	string	I (int)
TUNIT5	Unit of column 5	string	pixels
TTYPE6	Label of column 6	string	ORIGINX
TFORM6	Format of column 6	string	I (int)
TUNIT6	Unit of column 6	string	pixels
TTYPE7	Label of column 7	string	ORIGINY
TFORM7	Format of column 7	string	I (int)
TUNIT7	Unit of column 7	string	pixels
TTYPE8	Label of column 8	string	TPL_ID
TFORM8	Format of column 8	string	I (int)
TUNIT8	Unit of column 8	string	
TTYPE9	Label of column 9	string	TPL_SIZE
TFORM9	Format of column 9	string	I (int)
TUNIT9	Unit of column 9	string	pixels
TTYPE10	Label of column 10	string	NRPIX
TFORM10	Format of column 10	string	I (int)

Name	Description	Type	Value
TUNIT10	Unit of column 10	string	pixels
TTYPE11	Label of column 11	string	NGPIX
TFORM11	Format of column 11	string	I (int)
TUNIT11	Unit of column 11	string	pixels
TTYPE12	Label of column 12	string	NBPIX
TFORM12	Format of column 12	string	I (int)
TUNIT12	Unit of column 12	string	pixels
TTYPE13	Label of column 13	string	NB
TFORM13	Format of column 13	string	I (int)
TUNIT13	Unit of column 13	string	
TTYPE14	Label of column 14	string	NR
TFORM14	Format of column 14	string	I (int)
TUNIT14	Unit of column 14	string	
TTYPE15	Label of column 15	string	NB_FRAC
TFORM15	Format of column 15	string	E (float)
TUNIT15	Unit of column 15	string	
TTYPE16	Label of column 16	string	NR_FRAC
TFORM16	Format of column 16	string	E (float)
TUNIT16	Unit of column 16	string	
TTYPE17	Label of column 17	string	CCD_WINREF
TFORM17	Format of column 17	string	E (float)
TUNIT17	Unit of column 17	string	e^-/pix/s
TTYPE18	Label of column 18	string	TEMPLATE
TFORM18	Format of column 18	string	B (byte)
TUNIT18	Unit of column 18	string	
TTYPE19	Label of column 19	string	NXIMGREF
TFORM19	Format of column 1	string	I (int)
TUNIT19	Unit of column 19	string	
TTYPE20	Label of column 20	string	NYIMGREF
TFORM20	Format of column 20	string	I (int)
TUNIT20	Unit of column 20	string	
TTYPE21	Label of column 21	string	POSXIMGREF
TFORM21	Format of column 21	string	I (int)
TUNIT21	Unit of column 21	string	
TTYPE22	Label of column 22	string	POSYIMGREF
TFORM22	Format of column 22	string	I (int)
TUNIT22	Unit of column 22	string	
TTYPE23	Label of column 23	string	EXPTIME
TFORM23	Format of column 23	string	I (int)
TUNIT23	Unit of column 23	string	SECOND
TDIM17		string	(40,26)
TDIM18		string	(40,26)
EXTNAME	name of the extension	string	BINTABLE

5.1.6. Header of the BAR extension of the EN2_STAR_CHR

Name	Description	Type	Value
BITPIX	Mandatory (for images)	int	8
NAXIS	Mandatory word;	int	2: BINTABLE extension
NAXIS1	Number of bytes per row	int	
NAXIS2	Number of rows	int	
PCOUNT	Mandatory but not used		
GCOUNT	Mandatory but not used		
TFIELDS	Number of columns	int	16
TTYPE1	Label of column 1	string	DATE
TFORM1	Format of column 1	string	23A
TUNIT1	Unit of column 1	string	yyyy-mm-ddThh:mm:ss
TTYPE2	Label of column 2	string	DATETT
TFORM2	Format of column 2	string	D (double)
TUNIT2	Unit of column 2	string	JULIAN DAY
TTYPE3	Label of column 3	string	DATEBARTT
TFORM3	Format of column 3	string	D (double)
TUNIT3	Unit of column 3	string	JULIAN DAY
TTYPE4	Label of column 4	string	STATUS

Name	Description	Type	Value
TFORM4	Format of column 4	string	J (long)
TUNIT4	Unit of column 4	string	
TTYPE5	Label of column 5	string	REDFLUX
TFORM5	Format of column 5	string	E (float)
TUNIT5	Unit of column 5	string	ELECTRONS PER 32 s
TTYPE6	Label of column 6	string	REDFLUXDEV
TFORM6	Format of column 6	string	E (float)
TUNIT6	Unit of column 6	string	ELECTRONS PER 32 s
TTYPE7	Label of column 7	string	GREENFLUX
TFORM7	Format of column 7	string	E (float)
TUNIT7	Unit of column 7	string	ELECTRONS PER 32 s
TTYPE8	Label of column 8	string	GREENFLUXDEV
TFORM8	Format of column 8	string	E (float)
TUNIT8	Unit of column 8	string	ELECTRONS PER 32 s
TTYPE9	Label of column 9	string	BLUEFLUX
TFORM9	Format of column 9	string	E (float)
TUNIT9	Unit of column 9	string	ELECTRONS PER 32 s
TTYPE10	Label of column 10	string	BLUEFLUXDEV
TFORM10	Format of column 10	string	E (float)
TUNIT10	Unit of column 10	string	ELECTRONS PER 32 s
TTYPE11	Label of column 11	string	WHITEFLUX
TFORM11	Format of column 11	string	E (float)
TUNIT11	Unit of column 11	string	ELECTRONS PER 32 s
TTYPE12	Label of column 12	string	BG
TFORM12	Format of column 12	string	E (float)
TUNIT12	Unit of column 12	string	ELECTRONS PER PIXEL PER 32 s
EXTNAME	Name of the extension	string	BAR

5.1.7. Header of the BARFILL extension of the EN2_STAR_CHR

Name	Description	Type	Value
BITPIX	Mandatory (for images)	int	8
NAXIS	Mandatory word;	int	2: BINTABLE extension
NAXIS1	Number of bytes per row	int	
NAXIS2	Number of rows	int	
PCOUNT	Mandatory but not used		
GCOUNT	Mandatory but not used		
TFIELDS	Number of columns	int	4
TTYPE1	Label of column 1	string	DATEBARTT
TFORM1	Format of column 1	string	D (double)
TUNIT1	Unit of column 1	string	JULIAN DAY
TTYPE2	Label of column 2	string	WHITEFLUXFIL
TFORM2	Format of column 2	string	E (float)
TUNIT2	Unit of column 2	string	ELECTRONS PER 32 s
TTYPE3	Label of column 3	string	STATUSFIL
TFORM3	Format of column 3	string	J (long)
TUNIT3	Unit of column 3	string	
TTYPE4	Label of column 4	string	T_EXP
TFORM4	Format of column 4	string	I (int)
TUNIT4	Unit of column 4	string	
EXTNAME	name of the extension	string	BARFILL

5.1.8. Header of the SYSTEMATIC extension of the EN2_STAR_CHR

Name	Description	Type	Value
BITPIX	Mandatory (for images)	int	8
NAXIS	Mandatory word;	int	2: BINTABLE extension
NAXIS1	Number of bytes per row	int	
NAXIS2	Number of rows	int	
PCOUNT	Mandatory but not used		
GCOUNT	Mandatory but not used		
TFIELDS	Number of columns	int	3
EXTNAME	name of the extension	string	SYSTEMATIC
TTYPE1	Label of column 1	string	DATEBARTT
TFORM1	Format of column 1	string	D (double)
TUNIT1	Unit of column 1	string	JULIAN DAY
TTYPE2	Label of column 2	string	WHITEFLUXSYS
TFORM2	Format of column 2	string	E (float)
TUNIT2	Unit of column 2	string	ELECTRONS PER 32 s
TTYPE3	Label of column 3	string	STATUSSYS
TFORM3	Format of column 3	string	J (long)
TUNIT3	Unit of column 3	string	

5.1.9. Header of the BAR extension of the EN2_STAR_MON

Name	Description	Type	Value
BITPIX	Mandatory (for images)	int	8
NAXIS	Mandatory word;	int	2: BINTABLE extension
NAXIS1	Number of bytes per row	int	
NAXIS2	Number of rows	int	
PCOUNT	Mandatory but not used		
GCOUNT	Mandatory but not used		
TFIELDS	Number of columns	int	16
TTYPE1	Label of column 1	string	DATE
TFORM1	Format of column 1	string	23A
TUNIT1	Unit of column 1	string	yyyy-mm-ddThh:mm:ss
TTYPE2	Label of column 2	string	DATETT
TFORM2	Format of column 2	string	D (double)
TUNIT2	Unit of column 2	string	JULIAN DAY
TTYPE3	Label of column 3	string	DATEBARTT
TFORM3	Format of column 3	string	D (double)
TUNIT3	Unit of column 3	string	JULIAN DAY
TTYPE4	Label of column 4	string	STATUS
TFORM4	Format of column 4	string	J (long)
TUNIT4	Unit of column 4	string	
TTYPE5	Label of column 5	string	WHITEFLUX
TFORM5	Format of column 5	string	E (float)
TUNIT5	Unit of column 5	string	ELECTRONS PER 32 s
TTYPE6	Label of column 6	string	WHITEFLUXDEV
TFORM6	Format of column 6	string	E (float)
TUNIT6	Unit of column 6	string	ELECTRONS PER 32 s
TTYPE7	Label of column 7	string	BG
TFORM7	Format of column 7	string	E (float)
TUNIT7	Unit of column 7	string	ELECTRONS PER PIXEL PER 32 s
EXTNAME	name of the extension	string	BAR

5.1.10. Header of the BARFILL extension of the EN2_STAR_MON

Name	Description	Type	Value
BITPIX	Mandatory (for images)	int	8
NAXIS	Mandatory word;	int	2: BINTABLE extension
NAXIS1	Number of bytes per row	int	
NAXIS2	Number of rows	int	
PCOUNT	Mandatory but not used		
GCOUNT	Mandatory but not used		
TFIELDS	Number of columns	int	4
TTYPE1	Label of column 1	string	DATEBARTT
TFORM1	Format of column 1	string	D (double)
TUNIT1	Unit of column 1	string	JULIAN DAY
TTYPE2	Label of column 2	string	WHITEFLUXFIL
TFORM2	Format of column 2	string	E (float)
TUNIT2	Unit of column 2	string	ELECTRONS PER 32 s
TTYPE3	Label of column 3	string	STATUSFIL
TFORM3	Format of column 3	string	J (long)
TUNIT3	Unit of column 3	string	
TTYPE4	Label of column 4	string	T_EXP
TFORM4	Format of column 4	string	I (int)
TUNIT4	Unit of column 4	string	
EXTNAME	name of the extension	string	BARFILL

5.1.11. Header of the SYSTEMATIC extension of the EN2_STAR_MON

Name	Description	Type	Value
BITPIX	Mandatory (for images)	int	8
NAXIS	Mandatory word;	int	2: BINTABLE extension
NAXIS1	Number of bytes per row	int	
NAXIS2	Number of rows	int	
PCOUNT	Mandatory but not used		
GCOUNT	Mandatory but not used		
TFIELDS	Number of columns	int	3
EXTNAME	name of the extension	string	SYSTEMATIC
TTYPE1	Label of column 1	string	DATEBARTT
TFORM1	Format of column 1	string	D (double)
TUNIT1	Unit of column 1	string	JULIAN DAY
TTYPE2	Label of column 2	string	WHITEFLUXSYS
TFORM2	Format of column 2	string	E (float)
TUNIT2	Unit of column 2	string	ELECTRON PER 32 s
TTYPE3	Label of column 3	string	STATUSSYS
TFORM3	Format of column 3	string	J (long)
TUNIT3	Unit of column 3	string	

5.1.12. Header of the BAR extension of the EN2_STAR_IMAG

Name	Description	Type	Value
BITPIX	Mandatory (for images)	int	8
NAXIS	Mandatory word;	int	2: BINTABLE extension
NAXIS1	Number of bytes per row	int	
NAXIS2	Number of rows	int	
PCOUNT	Mandatory but not used		
GCOUNT	Mandatory but not used		
TFIELDS	Number of columns	int	11
TTYPE1	Label of column 1	string	DATE
TFORM1	Format of column 1	string	23A
TUNIT1	Unit of column 1	string	yyyy-mm-ddThh:mm:ss
TTYPE2	Label of column 2	string	DATETT
TFORM2	Format of column 2	string	D (double)
TUNIT2	Unit of column 2	string	JULIAN DAY
TTYPE3	Label of column 3	string	DATEBARTT
TFORM3	Format of column 3	string	D (double)
TUNIT3	Unit of column 3	string	JULIAN DAY
TTYPE4	Label of column 4	string	STATUS
TFORM4	Format of column 4	string	J (long)
TUNIT4	Unit of column 4	string	
TTYPE5	Label of column 5	string	REDFLUX
TFORM5	Format of column 5	string	D (double)
TUNIT5	Unit of column 5	string	ELECTRONS PER 32 s
TTYPE6	Label of column 6	string	GREENFLUX
TFORM6	Format of column 6	string	D (double)
TUNIT6	Unit of column 6	string	ELECTRONS PER 32 s
TTYPE7	Label of column 7	string	BLUEFLUX
TFORM7	Format of column 7	string	D (double)
TUNIT7	Unit of column 7	string	ELECTRONS PER 32 s
TTYPE8	Label of column 8	string	WHITEFLUX
TFORM8	Format of column 8	string	D (double)
TUNIT8	Unit of column 8	string	ELECTRONS PER 32 s
TTYPE9	Label of column 9	string	BG
TFORM9	Format of column 9	string	E (float)
TUNIT9	Unit of column 9	string	ELECTRONS PER PIXEL PER 32 s
TTYPE10	Label of column 10	string	CENX
TFORM10	Format of column 10	string	E (float)
TUNIT10	Unit of column 10	string	
TTYPE11	Label of column 11	string	CENY
TFORM11	Format of column 11	string	E (float)
TUNIT11	Unit of column 11	string	
EXTNAME	name of the extension	string	BAR

5.1.13. Header of the BARFILL extension of the EN2_STAR_IMAG

Name	Description	Type	Value
BITPIX	Mandatory (for images)	int	8
NAXIS	Mandatory word;	int	2: BINTABLE extension
NAXIS1	Number of bytes per row	int	
NAXIS2	Number of rows	int	
PCOUNT	Mandatory but not used		
GCOUNT	Mandatory but not used		
TFIELDS	Number of columns	int	3
TTYPE1	Label of column 1	string	DATEBARTT
TFORM1	Format of column 1	string	D (double)
TUNIT1	Unit of column 1	string	JULIAN DAY
TTYPE2	Label of column 2	string	WHITEFLUXFIL
TFORM2	Format of column 2	string	E (float)
TUNIT2	Unit of column 2	string	ELECTRONS PER 32 s
TTYPE3	Label of column 3	string	STATUSFIL
TFORM3	Format of column 3	string	J (long)
TUNIT3	Unit of column 3	string	
EXTNAME	name of the extension	string	BARFILL

5.1.14. Header of the SYSTEMATIC extension of the EN2_STAR_IMAG

Name	Description	Type	Value
BITPIX	Mandatory (for images)	int	8
NAXIS	Mandatory word;	int	2: BINTABLE extension
NAXIS1	Number of bytes per row	int	
NAXIS2	Number of rows	int	
PCOUNT	Mandatory but not used		
GCOUNT	Mandatory but not used		
TFIELDS	Number of columns	int	3
TTYPE1	Label of column 1	string	DATEBARTT
TFORM1	Format of column 1	string	D (double)
TUNIT1	Unit of column 1	string	JULIAN DAY
TTYPE2	Label of column 2	string	WHITEFLUXSYS
TFORM2	Format of column 2	string	E (float)
TUNIT2	Unit of column 2	string	ELECTRONS PER 32 s
TTYPE3	Label of column 3	string	STATUSSYS
TFORM3	Format of column 3	string	J (long)
TUNIT3	Unit of column 3	string	
EXTNAME	name of the extension	string	SYSTEMATIC

5.2. Headers of the extension of the files in versions 1 to 3

5.2.1. Header of the RAW extension of the AN2_STAR table (V1 $\geq$ 3)

Name	Description	Type	Value
BITPIX	Mandatory: (for images)	int	8
NAXIS	Mandatory word;	int	2: BINTABLE extension
NAXIS1	Number of bytes per row	int	
NAXIS2	Number of rows	int	
PCOUNT	Not used		
GCOUNT	Not used		
TFIELDS	Number of columns	int	5
EXTNAME	Name of the extension	string	RAW
TFORM1	Format of column 1	string	D (double)
TTYPE1	Label of column 1	string	DATEJD
TUNIT1	Unit of column 1	string	CoRoT Julian Day
TFORM2	Format of column 2	string	D (double)
TTYPE2	Label of column 2	string	RAWFLUX
TUNIT2	Unit of column 2	string	electron/s
TFORM3	Format of column 3	string	D (double)
TTYPE3	Label of column 3	string	RAWFLUXDEV
TUNIT3	Unit of column 3	string	electron/s
TFORM4	Format of column 4	string	J (long)
TTYPE4	Label of column 4	string	RAWSTATUS
TUNIT4	Unit of column 4		
TFORM5	Format of column 5	string	E (float)
TTYPE5	Label of column 5	string	BG
TUNIT5	Unit of column 5	string	electron/px/s
COMMENTS		string	

5.2.2. Header of the HEL extension of the AN2_STAR table (V1 $\geq$ 3)

Name	Description	Type	Value
BITPIX	Mandatory: (for images)	int	8
NAXIS	Mandatory word;	int	2: BINTABLE extension
NAXIS1	Number of bytes per row	int	
NAXIS2	Number of rows	int	
PCOUNT	Not used		
GCOUNT	Not used		
TFIELDS	Number of columns	int	4
EXTNAME	Name of the extension	string	HEL
TFORM1	Format of column 1	string	D (double)
TTYPE1	Label of column 1	string	DATEJDHEL
TUNIT1	Unit of column 1	string	CoRoT Julian Day
TFORM2	Format of column 2	string	D (double)
TTYPE2	Label of column 2	string	FLUXHEL
TUNIT2	Unit of column 2	string	electron/s
TFORM3	Format of column 3	string	D (double)
TTYPE3	Label of column 3	string	FLUXDEVHEL
TUNIT3	Unit of column 3	string	electron/s
TFORM4	Format of column 4	string	J (long)
TTYPE4	Label of column 4	string	STATUSHEL
TUNIT4	Unit of column 4		
COMMENTS		string	

5.2.3. Header of the HELREG extension of the AN2_STAR table (V1 $\geq$ 3)

Name	Description	Type	Value
BITPIX	Mandatory: (for images)	int	8
NAXIS	Mandatory word;	int	2: BINTABLE extension
NAXIS1	Number of bytes per row	int	
NAXIS2	Number of rows	int	
PCOUNT	Not used		
GCOUNT	Not used		
TFIELDS	Number of columns	int	4
EXTNAME	Name of the extension	string	HELREG
TFORM1	Format of column 1	string	D (double)
TTYPE1	Label for column 1	string	DATEJDHELREG
TUNIT1	Unit of column 1	string	CoRoT Julian Day
TFORM2	Format of column 2	string	D (double)
TTYPE2	Label for column 2	string	FLUXHELREG
TUNIT2	μ Unit of column 2	string	electron/s
TFORM3	Format of column 3	string	D (double)
TTYPE3	Label for column 3	string	FLUXDEVHELREG
TUNIT3	Unit of column 3	string	electron/s
TFORM4	Format of column 4	string	J (long)
TTYPE4	Label of column 4	string	STATUSHELREG
TUNIT4	Unit of column 4	string	
COMMENTS		string	

5.2.4. Header of the BINTABLE of the EN2_WINDESCRIPTOR product (V1 $\geq$ 3)

Name	Description	Type	Value
BITPIX	Mandatory (for images)	int	8
NAXIS	Mandatory word;	int	2: BINTABLE extension
NAXIS1	Number of bytes per row	int	
NAXIS2	Number of rows	int	
PCOUNT	Mandatory but not used		
GCOUNT	Mandatory but not used		
TFIELDS	Number of columns	int	23
TTYPE1	Label of column 1	string	T_START_WIN
TFORM1	Format of column 1	string	23A
TUNIT1	Unit of column 1	string	CoRoT Julian day
TTYPE2	Label of column 2	string	T_END_WIN
TFORM2	Format of column 2	string	19A

Name	Description	Type	Value
TUNIT2	Unit of column 2	string	CoRoT Julian day
TTYPE3	Label of column 3	string	WIN_ID
TFORM3	Format of column 3	string	J (long)
TUNIT3	Unit of column 3	string	
TTYPE4	Label of column 4	string	SIZEX
TFORM4	Format of column 4	string	I (int)
TUNIT4	Unit of column 4	string	pixels
TTYPE5	Label of column 5	string	SIZEY
TFORM5	Format of column 5	string	I (int)
TUNIT5	Unit of column 5	string	pixels
TTYPE6	Label of column 6	string	ORIGINX
TFORM6	Format of column 6	string	I (int)
TUNIT6	Unit of column 6	string	pixels
TTYPE7	Label of column 7	string	ORIGINY
TFORM7	Format of column 7	string	I (int)
TUNIT7	Unit of column 7	string	pixels
TTYPE8	Label of column 8	string	TPL_ID
TFORM8	Format of column 8	string	I (int)
TUNIT8	Unit of column 8	string	
TTYPE9	Label of column 9	string	TPL_SIZE
TFORM9	Format of column 9	string	I (int)
TUNIT9	Unit of column 9	string	pixels
TTYPE10	Label of column 10	string	NRPIX
TFORM10	Format of column 10	string	I (int)
TUNIT10	Unit of column 10	string	pixels
TTYPE11	Label of column 11	string	NGPIX
TFORM11	Format of column 11	string	I (int)
TUNIT11	Unit of column 11	string	pixels
TTYPE12	Label of column 12	string	NBPIX
TFORM12	Format of column 12	string	I (int)
TUNIT12	Unit of column 12	string	pixels
TTYPE13	Label of column 13	string	NB
TFORM13	Format of column 13	string	I (int)
TUNIT13	Unit of column 13	string	
TTYPE14	Label of column 14	string	NR
TFORM14	Format of column 14	string	I (int)
TUNIT14	Unit of column 14	string	
TTYPE15	Label of column 15	string	NB_FRAC
TFORM15	Format of column 15	string	E (float)
TUNIT15	Unit of column 15	string	
TTYPE16	Label of column 16	string	NR_FRAC
TFORM16	Format of column 16	string	E (float)
TUNIT16	Unit of column 16	string	
TTYPE17	Label of column 17	string	CCD_WINREF
TFORM17	Format of column 17	string	E (float)
TUNIT17	Unit of column 17	string	
TTYPE18	Label of column 18	string	TEMPLATE
TFORM18	Format of column 18	string	B (byte)
TUNIT18	Unit of column 18	string	
TTYPE19	Label of column 19	string	NXIMGREF
TFORM19	Format of column 1	string	I (int)
TUNIT19	Unit of column 19	string	
TTYPE20	Label of column 20	string	NYIMGREF
TFORM20	Format of column 20	string	I (int)
TUNIT20	Unit of column 20	string	
TTYPE21	Label of column 21	string	POSXIMGREF
TFORM21	Format of column 21	string	I (int)
TUNIT21	Unit of column 21	string	
TTYPE22	Label of column 22	string	POSYIMGREF
TFORM22	Format of column 22	string	I (int)
TUNIT22	Unit of column 22	string	
TTYPE23	Label of column 23	string	EXPTIME
TFORM23	Format of column 23	string	I (int)
TUNIT23	Unit of column 23	string	SECOND
TDIM17	Dimension of the image CCD_WINREF	string	(40,26)
TDIM18	Dimension of the image TEMPLATE	string	(40,26)
EXTNAME	name of the extension	string	BINTABLE

5.2.5. Header of the BINTABLE extension of the EN2_STAR_CHR table (V1 $\geq$ 3)

Name	Description	Type	Value
BITPIX	Mandatory (for images)	int	8
NAXIS	Mandatory word;	int	2: BINTABLE extension
NAXIS1	Number of bytes per row	int	
NAXIS2	Number of rows	int	
PCOUNT	Mandatory but not used		
GCOUNT	Mandatory but not used		
TFIELDS	Number of columns	int	16
TTYPE1	Label of column 1	string	DATE
TFORM1	Format of column 1	string	23A
TUNIT1	Unit of column 1	string	yyyy-mm-ddThh:mm:ss
TTYPE2	Label of column 2	string	DATEJD
TFORM2	Format of column 2	string	D (double)
TUNIT2	Unit of column 2	string	CoRoT Julian Day
TTYPE3	Label of column 3	string	DATEHEL
TFORM3	Format of column 3	string	D (double)
TUNIT3	Unit of column 3	string	CoRoT Julian Day
TTYPE4	Label of column 4	string	STATUS
TFORM4	Format of column 4	string	J (long)
TUNIT4	Unit of column 4	string	
TTYPE5	Label of column 5	string	REDFLUX
TFORM5	Format of column 5	string	E (float)
TUNIT5	Unit of column 5	string	electrons/s
TTYPE6	Label of column 6	string	REDFLUXDEV
TFORM6	Format of column 6	string	E (float)
TUNIT6	Unit of column 6	string	electrons/s
TTYPE7	Label of column 7	string	GREENFLUX
TFORM7	Format of column 7	string	E (float)
TUNIT7	Unit of column 7	string	electrons/s
TTYPE8	Label of column 8	string	GREENFLUXDEV
TFORM8	Format of column 8	string	E (float)
TUNIT8	Unit of column 8	string	electrons/s
TTYPE9	Label of column 9	string	BLUEFLUX
TFORM9	Format of column 9	string	E (float)
TUNIT9	Unit of column 9	string	electrons/s
TTYPE10	Label of column 10	string	GREENFLUXDEV
TFORM10	Format of column 10	string	E (float)
TUNIT10	Unit of column 10	string	electrons/s
TTYPE11	Label of column 11	string	WHITEFLUX
TFORM11	Format of column 11	string	E (float)
TUNIT11	Unit of column 11	string	electrons/s
TTYPE12	Label of column 12	string	JCWF
TFORM12	Format of column 12	string	E (float)
TUNIT12	Unit of column 12	string	electrons/s
TTYPE13	Label of column 13	string	BG
TFORM13	Format of column 13	string	E (float)
TUNIT13	Unit of column 13	string	electrons/s
TTYPE14	Label of column 14	string	CORREC_RED
TFORM14	Format of column 14	string	E (float)
TUNIT14	Unit of column 14	string	electrons/s
EXTNAME	name of the extension	string	BINTABLE
TFORM15	Format of column 15	string	E (float)
TFORM16	Format of column 16	string	E (float)
TTYPE15	Label of column 15	string	CORREC_GREEN
TTYPE16	Label of column 16	string	CORREC_BLUE

5.2.6. Header of the BINTABLE extension of EN2_STAR_MON (V1 $\geq$ 3)

Name	Description	Type	Value
BITPIX	Mandatory (for images)	int	8
NAXIS	Mandatory word;	int	2: BINTABLE extension
NAXIS1	Number of bytes per row	int	
NAXIS2	Number of rows	int	
PCOUNT	Mandatory but not used		
GCOUNT	Mandatory but not used		
TFIELDS	Number of columns	int	16
TTYPE1	Label of column 1	string	DATE
TFORM1	Format of column 1	string	23A
TUNIT1	Unit of column 1	string	yyyy-mm-ddThh:mm:ss
TTYPE2	Label of column 2	string	DATEJD
TFORM2	Format of column 2	string	D (double)
TUNIT2	Unit of column 2	string	CoRoT Julian Day
TTYPE3	Label of column 3	string	DATEHEL
TFORM3	Format of column 3	string	D (double)
TUNIT3	Unit of column 3	string	CoRoT Julian Day
TTYPE4	Label of column 4	string	STATUS
TFORM4	Format of column 4	string	J (long)
TUNIT4	Unit of column 4	string	
TTYPE5	Label of column 5	string	WHITEFLUX
TFORM5	Format of column 5	string	E (float)
TUNIT5	Unit of column 5	string	electrons/s
TTYPE6	Label of column 6	string	WHITEFLUXDEV
TFORM6	Format of column 6	string	E (float)
TUNIT6	Unit of column 6	string	electrons/s
TTYPE7	Label of column 7	string	BG
TFORM7	Format of column 7	string	E (float)
TUNIT7	Unit of column 7	string	electrons/s
TTYPE8	Label of column 8	string	CORREC
TFORM8	Format of column 8	string	E (float)
TUNIT8	Unit of column 8	string	electrons/s
EXTNAME	name of the extension	string	BINTABLE

5.2.7. Header of the BINTABLE extension of EN2_STAR_IMAG (V1 $\geq$ 3)

Name	Description	Type	Value
BITPIX	Mandatory (for images)	int	8
NAXIS	Mandatory word;	int	2: BINTABLE extension
NAXIS1	Number of bytes per row	int	
NAXIS2	Number of rows	int	
PCOUNT	Mandatory but not used		
GCOUNT	Mandatory but not used		
TFIELDS	Number of columns	int	16
TTYPE1	Label of column 1	string	DATE
TFORM1	Format of column 1	string	23A
TUNIT1	Unit of column 1	string	yyyy-mm-ddThh:mm:ss
TTYPE2	Label of column 2	string	DATEJD
TFORM2	Format of column 2	string	D (double)
TUNIT2	Unit of column 2	string	CoRoT Julian Day
TTYPE3	Label of column 3	string	DATEHEL
TFORM3	Format of column 3	string	D (double)
TUNIT3	Unit of column 3	string	CoRoT Julian Day
TTYPE4	Label of column 4	string	STATUS
TFORM4	Format of column 4	string	J (long)
TUNIT4	Unit of column 4	string	
TTYPE5	Label of column 5	string	REDFLUX_IMAG
TFORM5	Format of column 5	string	D (double)
TUNIT5	Unit of column 5	string	electrons/s
TTYPE6	Label of column 6	string	GREENFLUX_IMAG
TFORM6	Format of column 6	string	D (double)
TUNIT6	Unit of column 6	string	electrons/s

Name	Description	Type	Value
TTYPE7	Label of column 7	string	BLUEFLUX_IMAG
TFORM7	Format of column 7	string	D (double)
TUNIT7	Unit of column 7	string	electrons/s
TTYPE8	Label of column 8	string	WHITEFLUX_IMAG
TFORM8	Format of column 8	string	D (double)
TUNIT8	Unit of column 8	string	electrons/s
TTYPE9	Label of column 9	string	BG_IMAG
TFORM9	Format of column 9	string	E (float)
TUNIT9	Unit of column 9	string	electrons/pixel/s
EXTNAME	name of the extension	string	BINTABLE
TFORM10	Format of column 10	string	E (float)
TFORM11	Format of column 11	string	E (float)
TTYPE10	Label of column 10	string	CENX
TTYPE11	Label of column 11	string	CENY

6. Appendix 2: Coordinates in the CCD frame

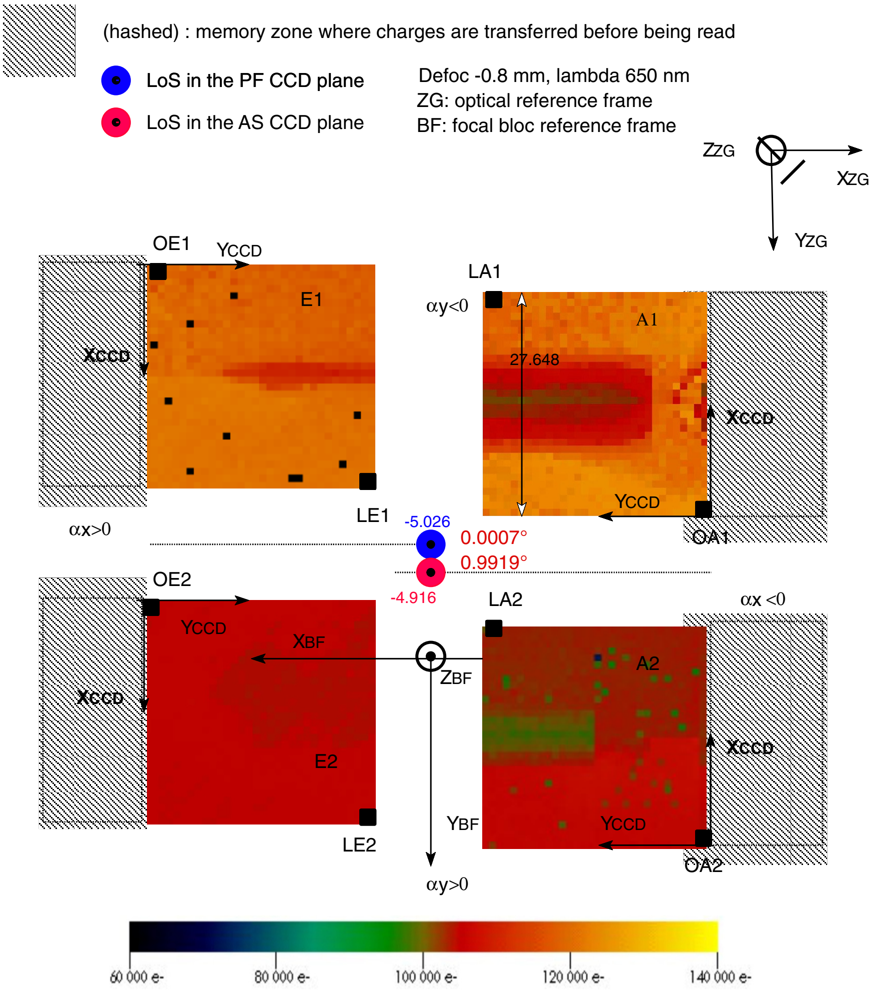

For each CCD, $\mathrm{O_{CCD}}$ is the origin of the CCD; $\mathrm{L_{CCD}}$ is located opposite to the origin.

A given pixel is identified by its coordinates (x, y) where x is the subscript for the raw number and y is the line number.

The numbering of lines follows the direction of the frame: the first line is the first to be transferred into the buffer, and the first to be next transferred into the reader storage.

For each CCD, pixels are numbered aboard from 1 to 2048: $1 \leqslant x \leqslant 2048$; $1 \leqslant y \leqslant 2048$.

CAUTION: when reading the FITS files, pixels in the images might be numbered from 0 to 2047.

Acknowledgements: The CoRoT space mission has been developed and operated by CNES, with the contribution of Austria, Belgium, Brazil, ESA, Germany, and Spain.

The CoRoT Legacy Book
© The authors, 2016
DOI: 10.1051/978-2-7598-1876-1.c025

II.5

Where to find the CoRoT data?

S. Chaintreuil[1], A. Bellucci[2], F. Baudin[3], P. Ocvirk[4], H. Ballans[3], G. Landais[4], F. Ochsenbein[4], and J.-L. Orcesi[3]

[1] LESIA, Observatoire de Paris, PSL Research University, CNRS, Sorbonne Universités, UPMC Univ. Paris 06, Univ. Paris Diderot, Sorbonne Paris Cité, 5 place Jules Janssen, 92195 Meudon, France
[2] CNES, Centre spatial de Toulouse, 18 avenue Edouard Belin, 31401 Toulouse Cedex 9, France
[3] Institut d'Astrophysique Spatiale, UMR8617, CNRS, Université Paris XI, Bâtiment 121, 91405 Orsay Cedex, France
[4] Centre de Données de Strasbourg, Observatoire astronomique de Strasbourg, Université de Strasbourg, Strasbourg, France

1. The different levels of the CoRoT products

The CoRoT data to be used for science are N2 (level 2) data. They derive from the raw telemetry received by the ground station by several successive layers of processing:

- N0 (or L0): the raw telemetry from the satellite reformatted to understandable information;
- N1 (or L1): stars' light curves with usual standard corrections (e.g. background, offset, timestamps, cosmic rays, jitter, PSF...);
- N2 (or L2): stars' light curves with additional specific corrections or flags (hot pixels, jumps, gain drifts..), and associated metadata.

N2 products are "science-ready" products.

- ⋆ CNES is responsible for archiving level 0 and level 1 data:
  The N0 products are available under request at CNES/SERAD;
  N1 products are available at CNES and at IAS/IDOC, also under request.
- ⋆ IAS and CDS are responsible for archiving level 2 data:
  The N2 products are publicly available at CDS and at IAS/IDOC.
- ⋆ N2 data are also available at the mirrors of the IAS archive at LAEX in Spain and NASA Exoplanet Archive.

The present addresses of these archives are given in Table II.5.1.

2. The CNES archive

CNES is responsible for the archiving of CoRoT Level 0 and Level 1 data, as well as of the relevant documentation and software. This task is done within the SERAD project (Service de Référencement et d'ARchivage des Données).

N1 products have a low level of correction for instrumental effects, whereas N0 products have no correction, only conversion from TM to reconstructed meaningful data. They may however be of interest for researchers who need to work with raw data, for instance for training algorithms in the frame of the preparation of new projects. Their proper use therefore implies a reasonable level of technical and/or scientific skills. A non-professional use of these data could be misleading, and could lead to wrong interpretations. Therefore, the access to the N0 and N1 data is possible for the scientific community through authentication.

As for other CNES missions, CoRoT data are archived in STAF, the long-term facility for data archiving on disks and tapes. This CNES service guarantees long term preservation of data files. SIPAD-NG, a generic tool developed by CNES, is used for the diffusion of archived data to final users through a web interface. This web-server also gives access to a selection of documents related to the CoRoT mission.

For the CoRoT mission, following Table II.5.2 presents the list and volumes of archived data.

Level 0 data produced by CMC in CNES are FITS files grouped in tar.gz packages to reduce the number of files to manage. For each observation run, for each data type, there is one tar.gz package for each identifier. For instance, there are four tar.gz packages for the data type AN0_FULLIMAGE in each run, one for each value of the half-CCD identifier.

Level 1 data, produced by LESIA after final reprocessing, are FITS files. In one run, for one data type, there are one or two FITS files for each identifier. When there are two FITS files for the same identifier, start and stop dates (always included in file names) are used to differentiate them.

CoRoTSky databases have been extracted as text files to be archived.

Table II.5.1. List of the different archives.

Archive		URL	Location
CNES	N0, N1	https://sipad-corot.cnes.fr/	Toulouse, France
IAS	N2, N1	idoc-corot.ias.u-psud.fr/	Orsay, France
CDS[1]	N2	http://vizier.u-strasbg.fr/viz-bin/VizieR?-source=B/corot	Strasbourg, France
CAB	N2	sdc.cab.inta-csic.es/corotfa/jsp/searchform.jsp	Madrid, Spain
NASA	N2	exoplanetarchive.ipac.caltech.edu/applications/ETSS/CoRoT_exo_index.html and exoplanetarchive.ipac.caltech.edu/applications/ETSS/CoRoT_astero_index.html	Pasadena, USA

Notes. (1) Long-term archive.

Table II.5.2. Volume of the data archived at CNES.

Level 0 data	24 data types	244 266 files	350 Go
L1 data	20 data types	630 735 files	2.5 To
L1 Housekeeping parameters	101 data types	214 932 files	54.8 Go
L0 Auxiliary data	4 data types	223 files	200 Mo
L0 Housekeeping parameters	20 data types	548 files	14 Go
L1 Auxiliary data	8 data types	208 files	8.2 Go
CoRoTSky data	2 data types	78 files	21 Mo

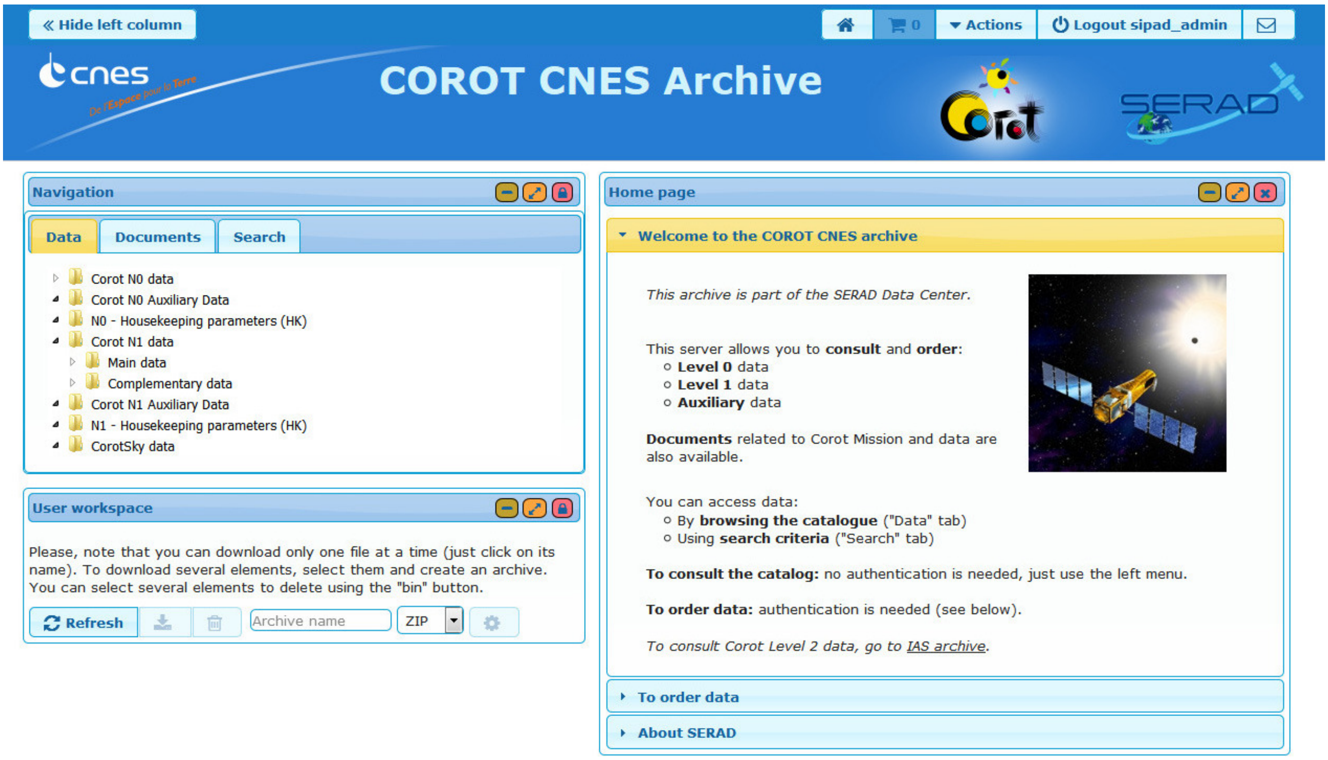

Please, note that you can download only one file at a time (just click on its name). To download several elements, select them and create an archive. You can select several elements to delete using the "bin" button.

This archive is part of the SERAD Data Center.

This server allows you to **consult** and **order**:
- **Level 0** data
- **Level 1** data
- **Auxiliary** data

Documents related to Corot Mission and data are also available.

You can access data:
- By **browsing the catalogue** ("Data" tab)
- Using **search criteria** ("Search" tab)

To consult the catalog: no authentication is needed, just use the left menu.

To order data: authentication is needed (see below).

To consult Corot Level 2 data, go to IAS archive.

Fig. II.5.3. CNES interface for CoRoT data. © CNES

All the archived data and the selection of documents are available[1]. This web server offers a web interface to search, select and order CoRoT data (Fig. II.5.3). Data of the same type are grouped in datasets and datasets are grouped in directories. A short description of data (content and formats) is available for each dataset. Users can browse the list of data using a treeview or using selection criteria. Visualization of the list of existing data is available for any public user. Registration is required to order data. Access to level 0 data is limited to expert users to prevent incorrect use of those data. Access to level 1 data is open more widely.

---

[1] https://sipad-corot.cnes.fr/

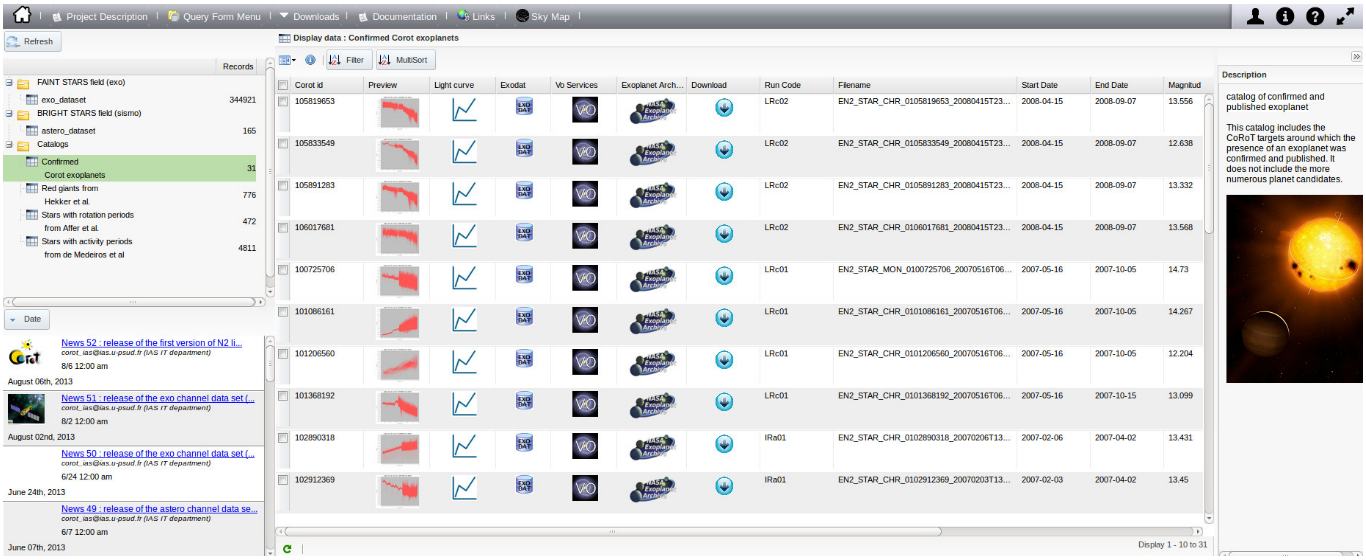

	Records
FAINT STARS field (exo)	
exo_dataset	344921
BRIGHT STARS field (sismo)	
astero_dataset	165
Catalogs	
Confirmed Corot exoplanets	31
Red giants from Hekker et al.	776
Stars with rotation periods from Affer et al.	472
Stars with activity periods from de Medeiros et al	4811

News 52 : release of the first version of N2 li...
corot_ias@ias.u-psud.fr (IAS IT department)
8/6 12:00 am
August 06th, 2013

News 51 : release of the exo channel data set (...
corot_ias@ias.u-psud.fr (IAS IT department)
8/2 12:00 am
August 02nd, 2013

News 50 : release of the exo channel data set (...
corot_ias@ias.u-psud.fr (IAS IT department)
6/24 12:00 am
June 24th, 2013

News 49 : release of the astero channel data se...
corot_ias@ias.u-psud.fr (IAS IT department)
6/7 12:00 am
June 07th, 2013

Display data : Confirmed Corot exoplanets

☐	Corot id	Run Code	Filename	Start Date	End Date	Magnitud
☐	105819653	LRc02	EN2_STAR_CHR_0105819653_20080415T23...	2008-04-15	2008-09-07	13.556
☐	105833549	LRc02	EN2_STAR_CHR_0105833549_20080415T23...	2008-04-15	2008-09-07	12.638
☐	105891283	LRc02	EN2_STAR_CHR_0105891283_20080415T23...	2008-04-15	2008-09-07	13.332
☐	106017681	LRc02	EN2_STAR_CHR_0106017681_20080415T23...	2008-04-15	2008-09-07	13.568
☐	100725706	LRc01	EN2_STAR_MON_0100725706_20070516T06...	2007-05-16	2007-10-05	14.73
☐	101086161	LRc01	EN2_STAR_CHR_0101086161_20070516T06...	2007-05-16	2007-10-05	14.267
☐	101206560	LRc01	EN2_STAR_CHR_0101206560_20070516T06...	2007-05-16	2007-10-05	12.204
☐	101368192	LRc01	EN2_STAR_CHR_0101368192_20070516T06...	2007-05-16	2007-10-15	13.099
☐	102890318	IRa01	EN2_STAR_CHR_0102890318_20070206T13...	2007-02-06	2007-04-02	13.431
☐	102912369	IRa01	EN2_STAR_CHR_0102912369_20070203T13...	2007-02-03	2007-04-02	13.45

Display 1 - 10 to 31

catalog of confirmed and published exoplanet

This catalog includes the CoRoT targets around which the presence of an exoplanet was confirmed and published. It does not include the more numerous planet candidates.

Fig. II.5.4. IAS interface for CoRoT data. © IAS

3. The IAS archive

The original CoRoT archive (the "mission archive") is located at the Institut d'Astrophysique Spatiale (IAS) in France. In order to ensure a wide access to the community at large, two other public archives are synchronized with the IAS archive: the NASA Exoplanet Archive in the USA, the other at the Centro de Astrobiologìa (CAB, Spain). In addition to these archives, the Centre de Données de Strasbourg will ensure the permanence on the very long-term of CoRoT data access through their VizieR tool. The data available at these different archives are identical, each archive providing different interfaces to access them.

At IAS, two interfaces allow the search through all "bright" stars ($6 < mV < 9$, commonly used for asteroseismology, but not only), and "faint" stars ($10 < mV < 16$, initially observed for exoplanet search and used for many more purposes). This represents a total of 165 light curves for bright stars and 176 492 for faint stars. They can be searched and selected using various criteria, such as their magnitude, their position in the sky, their spectral type, etc. In the case of faint stars, star selection can also be performed using the CoRoT Variable Classification (see Debosscher et al. 2009), which provides the probability for a star to belong to a given class of variable stars (such as β Cephei, δ Scuti, T Tauri, etc.). Another way to search for data is the use of published catalogues for some kinds of targets: for example red giant stars, or list of stars with a known period of rotation (Fig. II.5.4).

In addition to these interfaces, it is also possible to retrieve a whole run (including several thousands of targets) through the IAS archive.

For a given target, data are available in the form of FITS files, as well as VOTables.

For some targets, the light curves are computed on the ground from downloaded small images ("imagettes") recorded aboard. Both light curves (N2) and imagettes (N1) are available, allowing a view of the target and its surrounding pixels on the detector. For each target, a file called WINDESCRIPTOR summarizing the context of the observed target is also available. Further information is provided for a target through a link to the Exodat database such as spectral type, magnitudes in various bands, names of the target in different catalogues (USNO, 2MASS...). Some interactive tools allow the user to get more information about the targets selected. For example, a preview of the light curve is available, leaving to the user the possibility of a global view or a more detailed one by zooming interactively at his convenience. Another tool is provided through a link to the NASA Exoplanet Archive: a periodogram of the selected data is computed at request.

In addition to the N2 data, ready for the scientific use, N1 data are available under request for specific purposes.

4. Distribution of CoRoT data through the VizieR database at CDS

VizieR is the reference database for tabular data from astronomical catalogues and tables published in scientific papers. Tables are stored, along with homogeneous "metadata". This metadata consists of a range of information describing the data, such as the magnitude system used, the coordinate system and its epoch, the units of the columns, the type of data (magnitudes, sizes, positions. . .), stored as Unified Content Descriptors. This set of metadata can be queried, allowing users to discover catalogues relevant for their research. Another strength of this approach is that VizieR allows for instance to perform cone queries in all of the >14 000 catalogues stored in one simple click. Vizier is fully VO-compatible and communicates with a number of important astronomical resources and software such as the CDS SIMBAD database, Aladin and TOPCAT.

These features have made VizieR a very popular resource among astronomers, and as a result, there have been 300 000 queries/day during the last year. Thousands of astronomers have decided that VizieR is the right place to make their data available to the community, and institutional data providers such as ESO and ESA have also trusted the service to distribute their surveys. The VizieR team has worked in close collaboration with the CoRoT project to distribute their data. The VizieR interface allows users to quickly discover and access the mission data, and ulterior catalogues using this data.

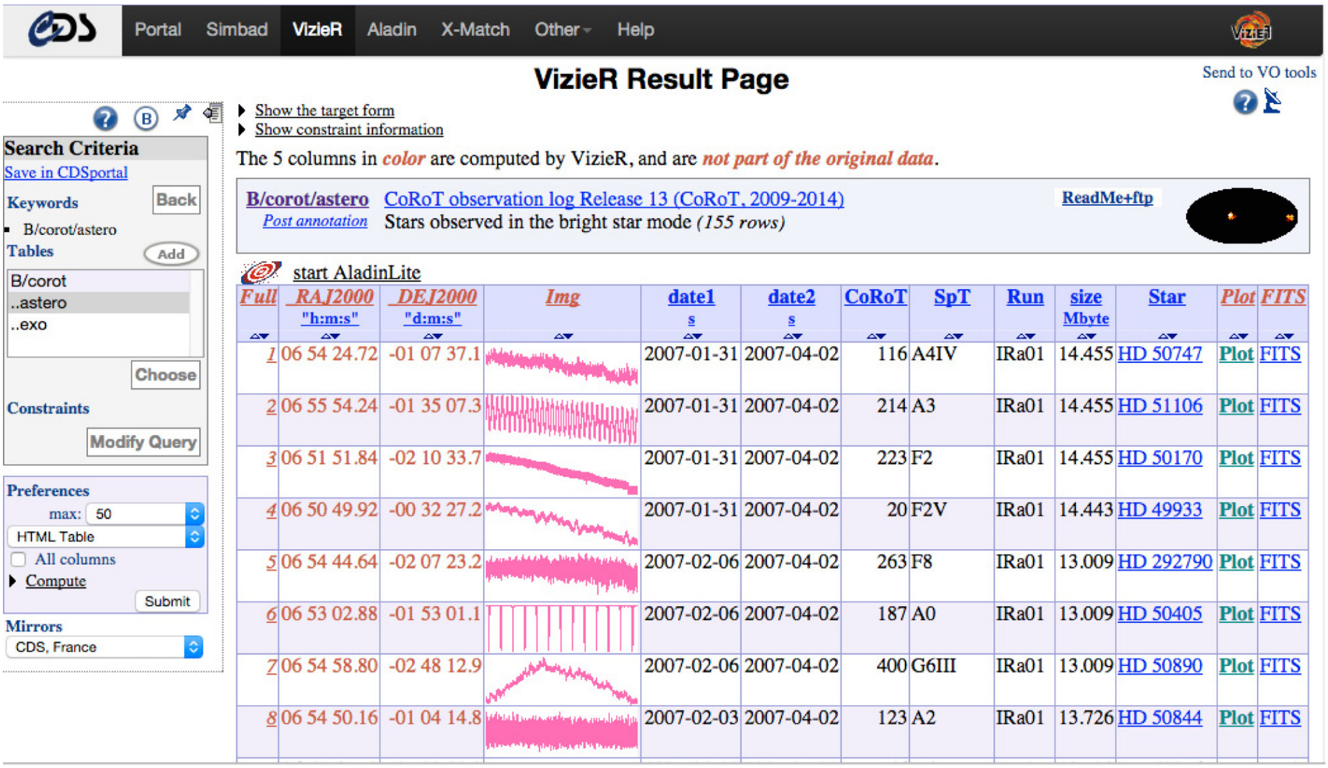

VizieR Result Page

The 5 columns in *color* are computed by VizieR, and are *not part of the original data*.

B/corot/astero CoRoT observation log Release 13 (CoRoT, 2009-2014)

Stars observed in the bright star mode *(155 rows)*

Full	*RAJ2000* "h:m:s"	*DEJ2000* "d:m:s"	*Img*	date1 s	date2 s	CoRoT	SpT	Run	size Mbyte	Star	*Plot*	*FITS*
1	06 54 24.72	-01 07 37.1		2007-01-31	2007-04-02	116	A4IV	IRa01	14.455	HD 50747	Plot	FITS
2	06 55 54.24	-01 35 07.3		2007-01-31	2007-04-02	214	A3	IRa01	14.455	HD 51106	Plot	FITS
3	06 51 51.84	-02 10 33.7		2007-01-31	2007-04-02	223	F2	IRa01	14.455	HD 50170	Plot	FITS
4	06 50 49.92	-00 32 27.2		2007-01-31	2007-04-02	20	F2V	IRa01	14.443	HD 49933	Plot	FITS
5	06 54 44.64	-02 07 23.2		2007-02-06	2007-04-02	263	F8	IRa01	13.009	HD 292790	Plot	FITS
6	06 53 02.88	-01 53 01.1		2007-02-06	2007-04-02	187	A0	IRa01	13.009	HD 50405	Plot	FITS
7	06 54 58.80	-02 48 12.9		2007-02-06	2007-04-02	400	G6III	IRa01	13.009	HD 50890	Plot	FITS
8	06 54 50.16	-01 04 14.8		2007-02-03	2007-04-02	123	A2	IRa01	13.726	HD 50844	Plot	FITS

Fig. II.5.5. VizieR interface for CoRoT data. © CDS

The query web page allows to search CoRoT data by constraints on the observations or objects' parameters. The results web page was specifically designed to allow rapid browsing through the light curves, as shown on Fig. II.5.5.

The CoRoT catalogue acts in VizieR as any other catalogue, which means that users do not need to know about CoRoT observations to get CoRoT data when it exists: a simple cone search intersecting the CoRoT field or a query for photometric time-series through VizieR will retrieve and display CoRoT data, among other relevant catalogues[2].

References

Debosscher, J., Sarro, L. M., Lopez., M., et al. 2009, A&A, 506, 519

Acknowledgements: The CoRoT space mission has been developed and operated by CNES, with the contribution of Austria, Belgium, Brazil, ESA, Germany, and Spain.

---

[2] The service can be accessed at `http://vizier.u-strasbg.fr/viz-bin/VizieR?-source=B/corot` and at `http://cdsarc.u-strasbg.fr/assocdata/?obs_collection=B/corotforVOaccess`

Part III

Major scientific achievements in planetary science

The CoRoT Legacy Book
© The authors, 2016
DOI: 10.1051/978-2-7598-1876-1.c030

Part III

Major scientific achievements in planetary science

The interest of a high precision photometric instrument like CoRoT for the search of transiting planets has been very early identified, just after the discovery of the first exoplanets. As soon as the first exoplanet transit was observed in 1999, it became a priority. While asteroseismology and planet search did not share exactly the same observing requirements, the mission managed to balance the needs of the two. Since then, we have also learnt how complementary the two techniques could be, as the uncertainties on our knowledge of the host star set fundamental limitations when trying to characterize exoplanets (Chap. IV.4). Measuring both the radius and the mass of exoplanets reveals their nature, and accurate measurements give first constraints to their internal structure and formation mechanisms. In this field, CoRoT has been a precursor for several other space-based missions in search for transiting planets, while being complemented by ground-based transit surveys, mostly sensitive to short-period companions.

During the year which preceded the launch of the instrument, scientists interested in the exoplanets quest decided not to work in parallel but instead to organize themselves as a single international team. Indeed, the project commitment stopped to the delivery to the community of light curves properly reduced and corrected for the main instrumental defaults and ready for scientific analyses. The detection of planetary transits was thus left to the discretion of the various teams at the exception of the real-time detection carried out in the “Alarm mode”. The later consisted in a weekly analysis of raw light curves carried out in order to detect the most obvious transits and subsequently tune the time sampling to the cadence of 32-s. This real-time detection aimed at having the possibility to observe the possible forthcoming transit events with the highest temporal cadence, so that to accurately derive their shape. It had however another interesting consequence: for the most promising candidates, it gave the possibility to start follow-up observations very early after the beginning of a run, without a six-month delay.

As the launch date approached, it became clear that a wild competition between the teams was likely to be a brake and to undermine the scientific returns. European scientists thus decided to work as a single team and to set up an organization structure able to allow the fair share of the workload and results. This organization also included the complementary observations, whose need was identified early in the mission preparation phase. Such observations were required first to prepare the exoplanet field selection and optimise the target selection process in a given field according to their spectral type and luminosity class (Chap. IV.5). In a second step, they were also mandatory to identify false positives and gather all information that might help the complete characterization of the planets. There were thus see as a key aspect of the mission and early on, a working group was dedicated to the coordination of complementary observations.

Members of this international collaboration on the Exoplanet program of CoRoT took the name of CoRoT Exoplanet Science Team. They identified the necessary analysis steps to get from the light curves to fully secured and characterized planets: 1) the transit detection; 2) the planet parameters factory; 3) the stellar fundamental parameters; 4) the follow-up observations. All that was toped by a coordination team whose role was to ensure that the work was properly done in a timely manner. Members of the collaboration then choose the tasks they were willing to contribute to, thanks to their expertise or their interest in, with, for each of the task, a team leader in charge of providing the final information to the coordination team. In addition to regular yearly meetings, protected Wiki pages were set up to ensure the free share of the information and of relevant documents. They were also used to organize the work on transit detection in the CoRoT light curves and for the follow-up observations of the planet candidates. The advantages of the wiki format was indeed to allow the dynamical editing of the pages by well-identified users and thus regular updates following the rhythms of results. For example, the transit lists issued by the various members of the detection team were posted on these pages and automatically merged. The final ranking of those that were seen as planet candidates was done by the team members during teleconferences where they together assessed a likely origin of the signal, stellar or planetary, for all the candidates identified in a given run. This analysis resulted in a list of ranked planetary candidates worthy of further complementary observations. In addition to the candidates parameters, including ephemerides to be used for the calculation of forthcoming transit epochs, the list provided also some feedbacks to people that carried out follow-up observations.

The team in charge of the follow-up observations has been operating about more than a dozen of telescopes in Europe, Hawaii, Israel and Chile, with size varying from 1 m to 8 m. They have involved various techniques: photometric observations, high contrast imaging (Guenther et al. 2013), and spectroscopy including radial velocity measurements. This important effort has allowed to filter out more than four hundred of candidates and to characterize a few tens of planets. The various steps of this collaborative work and the results achieved that way on both light curves analyses and follow-up observations are presented in Chap. IV.1.

CoRoT was well adapted to explore the close-in planet population. It has opened the domain of the Super-Earth planets, a population that was not predicted by planet formation models but was later demonstrated by Kepler to be numerous. CoRoT has also shown the existence of close-in brown dwarfs that account for about 10% of the substellar objects it detected. This has also resurfaced the question of what distinguishes massive planets from light brown dwarfs (Chap IV.6). For the later, CoRoT has allowed to measure their radii, bringing the first observational constraints to models (Chap IV.8).

For giant planets, the contribution of CoRoT has been very valuable. Massive planets have been found around host stars that are at odds with the regular solar-type stars on which radial velocity surveys concentrate: fast rotators, active stars and even a case of a planetary system whose host star exhibits pulsations (Chap IV.7). The long duration, high photometric precision of the light curves of their host stars, combined with high precision radial velocity measurements has enabled detailed analyses on the planetary system properties, shedding new light on this population.

Beyond the mere detection, the determination of planets parameters with a much better precision than what could be achieved from the ground has allowed detailed analyses on the planets' composition. Accurate masses and radii have allowed the estimate of the amount of heavy elements in a very large diversity of gaseous planet structures, from 0 to 60% of the planet mass (Chap. IV.3). Obtaining, in addition, the complete set of planet orbital parameters, including the eccentricity, has been valuable to explore the orbital evolution of some systems and to set constraints on the planet migration and theories of tidal interactions (Chap. IV.9.2). Finally, the out-of-transit variations induced by star spots at the surface of active stars give us the opportunity to determine the properties of the stellar spots, to determine the rotation of the host star and to better understand the stellar activity (Chap. IV 9.1). Activity features, however, leave their imprints on both radial velocity diagnostics and on the light curve, distorting the transit profiles in the same time. As a consequence, as illustrated by the CoRoT-7b case which orbits an active star, inferring planet's parameters in presence of stellar activity can be very challenging (Chap. IV.2). This has triggered subsequent studies including on the most appropriate observational approach, showing that CoRoT raised new scientific questions, and opened new fields of research.

More interestingly, CoRoT has been a benchmark for the European exoplanet community. It has triggered a new generation of young scientists that became familiar with ultra-high precision photometry and have acquired expertise in it. In a sense the CoRoT light curves have served also as a starting point to prepare future and more ambitious exoplanet missions such as PLATO. In the rising and competitive domain of exoplanets, CoRoT has also demonstrated the value and efficiency of collaborative work, that benefits from different approaches and complementary expertises.

M. Deleuil
Université Aix-Marseille , CNRS, Laboratoire
d'Astrophysique de Marseille,
UMR 7326, 13388 Marseille, France

The CoRoT Legacy Book

DOI: 10.1051/978-2-7598-1876-1.c031

III.1

Transit features detected by the CoRoT/Exoplanet Science Team

M. Deleuil[1], C. Moutou[1], J. Cabrera[2], S. Aigrain[3], F. Bouchy[1], H. Deeg[4], P. Bordé[5],
and the CoRoT Exoplanet team

[1] Aix Marseille Université, CNRS, LAM (Laboratoire d'Astrophysique de Marseille) UMR 7326, 13388, Marseille, France
[2] Institute of Planetary Research, German Aerospace Center, Rutherfordstrasse 2, 12489 Berlin, Germany
[3] Department of Physics, Denys Wilkinson Building Keble Road, Oxford, OX1 3RH
[4] Instituto de Astrofisica de Canarias, 38205 La Laguna, Tenerife, Spain and Universidad de La Laguna, Dept. de Astrofísica, 38206 La Laguna, Tenerife, Spain
[5] Institut d'astrophysique spatiale, Université Paris-Sud 11 & CNRS (UMR 8617), Bât. 121, 91405 Orsay, France

1. Introduction

CoRoT has observed 26 stellar fields located in two opposite directions for transiting planet hunting. The fields observed near $6h\ 50m$ in right ascension are referred as (galactic) "anti-center fields", and those near $18h\ 50m$ as "center fields". The observing strategy consisted in staring a given star field for durations that ranged from 21 to 152 days. The mission profile indeed allowed some flexibility and thus the exact observation duration and the number of pointings per year have been revised along the course of the mission in function of the scientific needs. As illustrated in Fig. III.1.1 which shows the location of the 26 fields, it allowed the re-observation of the same field a few years apart, as well exemplified by the SRc03 field. This pointing was indeed dedicated to the re-observation of a single transit of CoRoT-9b (Deeg et al. 2010) and thus lasted for five days only. The various fields can thus present an overlap. As a consequence some targets were observed twice or even three times. Most of the time the re-observations was carried out with a slightly different instrumental configuration. In particular, the photometric mask used to perform the on-board photometric measurements could be different from one observation to the other which impacts mostly on the contamination rate inside the photometric mask. Typical targets in the exoplanet channel have magnitude in the range 11 to 16 but some could be brighter and thus exhibit some level of saturation.

In total the instrument has provided us 176 802 light curves with a time sampling of 32 s or 8 min. Taking into account the fact that some stars have been observed more than a single time, this corresponds to a total of 163 665 stars. According to the revised exoplanet input catalog, 66 710 of these targets have been attributed a luminosity class V. This number nearly double and increases to 109 940 if one classifies as dwarf stars those with luminosity classes IV and V. The dwarf – giant identification was based on a simple color-mag separation (Deleuil et al. 2009). While this is reliable on a statistical point of view, individual targets could be misclassified (Damiani et al. *this book*) and these numbers are mostly indicative of the overall stellar population properties. They show however that, in a given field, classes V and IV represent the majority of the targets. Figure III.1.2 displays how these stars classified as class IV and V distribute over spectral types F, G, K, and M. G-type are the most numerous, followed by F-type. This results from a careful selection of the target stars in the fields, in order to maximize the planet detections. There are however noticeable differences from one field to another due to variations in the stellar populations, given their position in the Galaxy, and from different reddening between the fields.

2. CoRoT planets

Compared to the overview given by Moutou et al. (2013), 12 new planets have been published or announced in conferences and some robust planet candidates are still in the final stage of the validation process. Today CoRoT accounts for 34 transiting planets detected in the CoRoT light curves, secured and fully characterized thanks to an intense and efficient accompanying ground-based follow-up program.

Among these 34 objects labelled as planets, there are in fact 2 brown dwarfs, CoRoT-15b (Bouchy et al. 2011) and CoRoT-33b (Csizmadia et al. 2015) and one object, CoRoT-3b (Deleuil et al. 2008) whose exact nature, light brown dwarf or massive planet, remains an open question.

All the other new planets (Almenara et al. 2013; Cabrera et al. 2015) belong to the close-in giant population except CoRoT-22b (Moutou et al. 2014), whose radius is $4.88 \pm 0.17\ R_\oplus$. This planet, which has an orbital period of 9.7566 ± 0.0012 days, is the second smallest in size after CoRoT-7b but, in this case, the faintness of its host star prevented us from a precise estimate of its

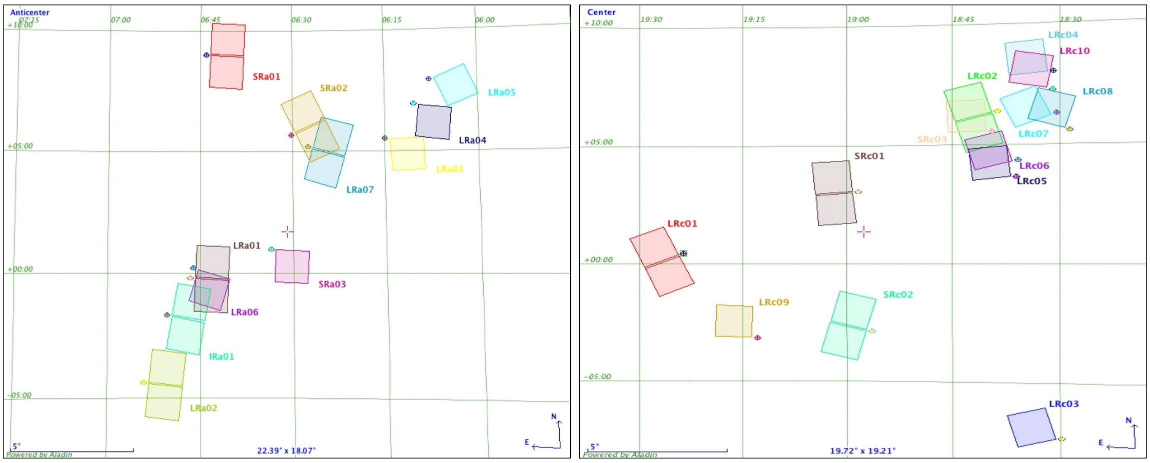

Fig. III.1.1. Position of all the faint stars fields observed by CoRoT in the anti-centre (*left*) and the centre (*right*) directions.

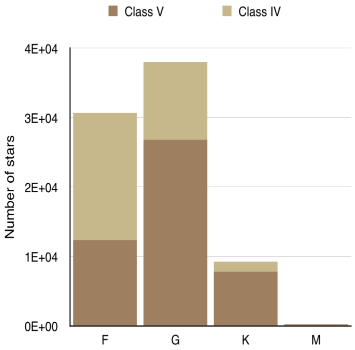

Fig. III.1.2. Distribution of class IV and V over F, G, K, and M types of all targets observed in the exoplanet fields.

mass. We could estimate only an upper limit of its mass of $49 M_{\oplus}$ through radial velocity measurements. The dearth of small-size planets in the CoRoT field reported by Bonomo et al. (2012) is thus still holding. These authors estimated that, compared to the frequency of Kepler candidates, the CoRoT planet yield in this small-size planet domain is too low by more than a factor two. Among the various reasons, this discrepancy could have its origin in differences in the stellar population the two missions have observed. In addition, a fraction of these small-size planets might be missed due to discontinuities in the CoRoT light curves caused by hot pixels. Now that the final version of the CoRoT pipeline corrects for these discontinuities, it would be interesting to check if it results in an increase of the number of detections, especially in the small-size domain.

While multi-planet systems account for about 40% of the Kepler Objects of Interest (KOI), only one multi-planet transiting system, CoRoT-24 (Alonso et al. 2014) has been reported by CoRoT. This system hosts 2 Neptune-sized planets. The second multi-planet system is CoRoT-7 (Queloz et al. 2009). Its second planet was however not detected in the CoRoT light curve but its existence has been definitely established from the intensive radial velocity campaigns carried out to measure CoRoT-7b' mass (Haywood et al. 2014). The observed lack of multi-planet detections is consistent with Kepler's results, which show that these systems are indeed numerous but in the low mass regime of Neptune and Earth size planets, and in the long orbital period range, a domain which is beyond the limit of CoRoT sensitivity.

3. Detection and classification of transit-like features

3.1. Detection and vetting

Before arriving at a well-identified planet, there is long path that starts at the detection level and requires complex investigations. There was no official transit detection pipeline at mission level. Instead, the detection has been carried out in parallel with various algorithms from different partner institutions, and the results were gathered, compared, and merged by the CoRoT detection team. Once detected, the transit-like features were divided in obvious eclipsing binaries and planet candidates. For each run, these lists of candidates were ranked manually, and then compared by the team members. Each candidate was individually discussed with its light curve manually inspected, to better assess a likely origin of the signal, stellar or planetary, and to identify obvious false alarms. With more than ten times fewer light curves to inspect than the total number per run (12 000 at once, when the two CCDs were still in operation), this manual and interactive approach was still feasible. It had the advantage to enable the use of different methods, some that were more appropriate than others for the detection of certain types of transits. It also allowed to train the detection team on light curve analyses especially during the first years after the launch, when the instrumental effects were not completely understood and corrected for. Each of the detection algorithms run in parallel indeed, and had its own set of light-curve pre-conditioning filters. The downside is, that it makes it difficult to provide an overall assessment of the mission's sensitivity to transits of different depths and periods. With time, the number of algorithms used in the transit search has decreased and the procedures have converged, the differences being mostly in the light curve filtering and detrending methods that were used. A description of the approches used for the analysis of CoRoT light curves is given in Carpano et al. (2009); Cabrera et al. (2009); Erikson et al. (2012); Carone et al. (2012); Cavarroc et al. (2012).

Two phenomena are the main sources of false detections at instrumental level:

1. hot pixels that cause discontinuities in the light curves. They can be at the origin of false detections but also might prevent the detection as shown by Bonomo et al. (2012). It also made more difficult a full automation of the detection.
2. a nearby bright eclipsing binary whose light leaks over one or more columns of pixels and leaves its photometric imprint in the light curve of neighbor targets. The much shallower depth in the contaminated target can leave one to believe to a small-size planet candidate and a systematic verification is thus of prime importance. Such false positives can be however identified by phase folding the light curve of the target and those of its closest neighbors at the period of the detected transit signal.

This process ended up with a single list of planet-candidates per field, ranked on a simple priority scale that was then provided to the follow-up team. Those with the highest priority have been further observed with various ground-based facilities so that a planet could be securely identified and characterized.

In total, over the mission lifetime, transit-like signals have been detected in a little bit more than 4000 light curves for all the exo-fields, excepting SRc03, which was left aside of the detection process. Once false detections, variables, and ghost signals were filtered out, we ended up with 3045 remaining transit events. 80% of these events were classified as binaries in a first round, based on the depth of their eclipses, on the detection of a secondary eclipse or from off-eclipse light curve modulations. 594 were flagged as candidates worth for follow-up observations. Among them were 18 candidates that were detected in two fields. This total number also includes 27 single transit events whose parameters, depth and duration, are compatible with a planetary scenario with a planet orbit longer than the duration of the run.

3.2. Assessing the nature of the candidates

The final CoRoT catalog of all the transit events identified in the CoRoT light curves by the exoplanet teams was finally established through a late but homogeneous analysis of all of them. To that purpose, starting from the first set of parameters for all transits events, namely, the epoch, the period, the transit depth and duration, we used an automated software developed and implemented at Cambridge. Based on the Mandel & Agol (2002) formalism, the transits were fitted with five free parameters: the period P, the transit epoch T_0, the planet-to-star radius ratio $R_\mathrm{p}/R_\mathrm{s}$, the system scale a/R_s, and the impact parameter b. The quadratic limb-darkening coefficients u_a and u_b are kept fixed at 0.44 and 0.23 respectively, the values given by Sing (2010) for a Sun-like star in the CoRoT bandpass. Using the equations of Seager & Mallén-Ornelas (2003), which do not take limb-darkening into account, and are thus approximate only, additional parameters that were derived were the orbital inclination, the stellar density, the transit depth, and the transit durations T_{14} and T_{23} between outer and inner contacts, respectively.

Detection is a first important step, but the most touchy part is to assess which candidates have the highest chance being a planet. The ranking of the candidates indeed directly impacts the follow-up strategy and the amount of telescope time that becomes devoted to the confirmation of the candidates' nature and the characterization of proven planets. The approach that was finally chosen in the last years of the mission, was to have each candidate robustness evaluated over a series of criteria. The outcomes of this evaluation are recorded in the form of six binary flags, which are also included in the final CoRoT/exoplanet catalog. The flags are:

- F_det: low detection significance, set if the transit depth in the white light curve is less than 5 times corresponding uncertainty;
- F_sec: secondary eclipse detected, set if the secondary eclipse depth (at phase 0.5) is more than 3 times corresponding uncertainty;
- $F_\mathrm{odd/even}$: odd/even depth differences, set if if the odd/even depth ratio is more than 1.1 at 3σ confidence level;
- F_col: strong colour dependence, set if the ratio of the deepest to the shallowest of the transits in the 3 colour channels is more than 1.5 at 3σ confidence level;
- F_V: V-shaped transit, set if the best-fit transit model is grazing;
- F_long: transit too long, set if the best-fit stellar radius is $>2\,R_\odot$ at 3σ confidence level.

While the first four flags are directly related to the transit fit, the lasts two are associated to stellar physical parameters. Because the spectral classification was judged poorly reliable, we did not use it for candidate evaluation. Instead, stellar radii were derived from stellar densities based on the transit-parameters and assuming a Mass-Radius relation: $R_\star = M_\star^{0.8}$. Note however that these flags were intended for a first order, quick-look sorting of the candidates: they are by no means unequivocal, in the sense that a real planetary candidate could have one or more flag set (see Sect. 5), and many candidates, which were later found to be astrophysical false alarms, had none. All the candidates, including the planets and some binaries that were rejected from the candidates list in a second level analysis, have thus been automatically re-analyzed with this tool.

The period distribution of the candidates peaks around 2.2 days but extends up to 40 days with some candidates at greater orbital period. 75% of the detected events have an orbital period below 10 days, as expected for the population of massive planets which dominates the CoRoT planets. The depth distribution of candidates shows a maximum at 0.125%, with 60% of the candidates having a depth of less than 0.5%; more details will be given in Deleuil et al., in prep.).

3.3. Eclipsing binaries classification

Because binaries come as a natural by-product, the CoRoT catalog also provides information related to those that were identified in the CoRoT light curves. Prior to the final transit fitting process, binaries were visually classified in 4 sub-classes:

1. eclipsing binaries with a detected secondary eclipse at phase 0.5;

Table III.1.1. Summary of the transit events detected in the CoRoT light curves.

Binaries			
(1)	(2)	(3)	(4)
1322	282	167	664

Candidates status after follow up			
(5)	(6)	(7)	planets
134	188	253	34

Notes. (1) eclipsing binaries with a detected secondary eclipse at phase 0.5; (2) eccentric eclipsing binaries with a detected secondary eclipse not at phase 0.5; (3) eclipsing binaries with no secondary eclipse detected; (4) contact binaries; (5) contaminating eclipsing binaries; (6) eclipsing binaries; (7) candidates whose nature is still unresolved;

2. eccentric eclipsing binaries with a detected secondary eclipse not at phase 0.5;
3. eclipsing binaries without detected secondary;
4. contact binaries that present no clear eclipse but a noticeable modulation of their light curve.

While for the first three sub-classes the complete fitting process was performed with the same tool as the one used for the planetary transit parameters, for the last class the catalog provides the epoch and period of the binary signal only. The final count of the various classes of binaries found in the observed fields is given in Table III.1.1.

4. Follow-up observations of the candidates

The CoRoT exoplanet program has been supported by a large accompanying ground-based observation program (Deleuil et al. 2006; Bouchy et al. 2009; Deeg et al. 2009; Guenther et al. 2013). This approach has the advantage to allow to identify false positives, to fully secure planets and to determine their parameters and properties. On the other hand, the complete screening process has sometimes required more than one year for some of the candidates (e.g. Moutou et al. 2009; Cabrera et al. 2009).

In total, 435 candidates among the 595 (73%) have been subject to ground-based complementary observations. They represent 82.2% in the anti-center and 68.3% in the center fields. As Fig. III.1.3 shows, follow-up observations have been carried out over the whole range of candidate magnitudes but there is a marked dependency on the targets magnitude in follow up completeness. Nearly all the candidates in the range 12 to 14 have been observed, but this decreases to 50% completeness for very faint stars with r-mag > 15.5. There are also differences from one field to another in terms of completeness. The percentage of targets that were observed from ground is only 38% for the LRc06 field while 100% of the candidates have been observed in the LRa02. This is explained by both the distribution of candidates in magnitude from one field to another in addition to the fact that earlier fields were targeted during more than 3 observation seasons.

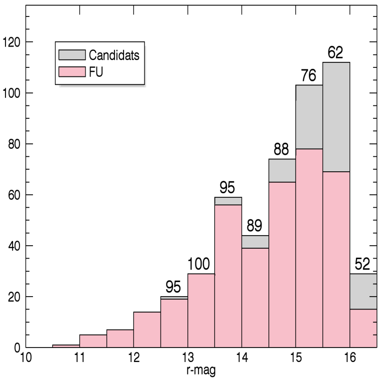

Fig. III.1.3. r-mag distribution of candidates that received follow-up observa- tions (pink) compared to the overall candidate distribution. The number at the top of the bins give the % of candidates observed by ground-based facilities in this bin.

Based on results achieved through follow-up observations but also from the second level of their light curve analysis which allowed to identify false detections and binaries, planet candidates can be divided in 4 classes:

1. *Contaminating eclipsing binaries (CEB)* which correspond to configurations in which the source of the transit has been identified as an eclipsing binary independent of the target, but whose light contributes to the one measured in CoRoT's photometric aperture.
2. *Eclipsing binaries (EB)*, where the source of the transiting signal coincides with the target. Their nature has been assigned through a much deeper analysis of the light curve or through radial velocity measurements. The later allow to identify spectroscopic binaries (SB1 or SB3) in a very few measurements.
3. *Planets* whose nature has been secured thanks to complementary observations.
4. *Unresolved candidates.* They could be due either to the fact that a candidate was not followed up or because the follow up observations remained un-conclusive. In this category we found (i) faint stars that challenge radial velocity measurements and that are responsible for a large part of this class; (ii) host-stars whose nature is either a hot star or a fast rotator, two characteristics that prevent assessing the nature of the detected companion with the usual current techniques; (iii) bright targets for which ground-base time series observations did not point out any contaminating star as the source of the signal but for which no clear radial velocity signal could be detected either.

Figure III.1.4 displays this distribution of the filtered candidates. Unresolved cases account for 41.5% of the candidates. Eclipsing binaries are the main source of false positives with 30.9%, then contaminating eclipsing binaries represent 22.0%. Planets account for 5.1% and brown dwarfs for 0.5%, assuming that CoRoT-3b belongs to this class. There is no marked difference in the occurrences of the various classes as a function of the observing direction (galactic enter or antic enter). This should be investigated in more details, but the absence of clear difference is also consistent with similar counts in the F, G, K and M-type targets of class V in the two directions (25 055 in the anti-centre fields and 22 157 in the centre fields).

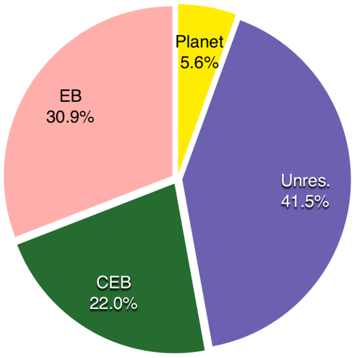

Fig. III.1.4. Nature of the candidates according to follow-up observations and a second level analysis of their light curve.

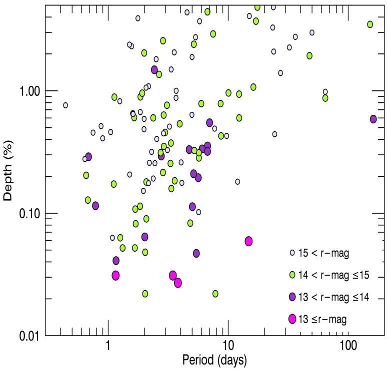

Fig. III.1.5. Distribution in the Depth-Period diagram of the unresolved can- didates whose host-star has an estimated luminosity class V. The size and the color of the symbols vary according to the r-mag range.

Among the total number of resolved configurations, eclipsing binaries account for 52.7%, CEBs for 37.5% and planets/brown dwarfs are 9.8%. Considering among them those which were identified through follow-up observations only, it gives a false positive rate of 86% for both directions and an effectiveness of ground-based observations to address the nature of the transiting bodies of 64%. Despite the small number of brown dwarfs, if we separate these from the planets, and if one assumes that unresolved candidates would distribute with the same proportions between eclipsing binaries, CEBs, planets and brown dwarfs, it gives 22 planets and 2 brown dwarfs that may still be hidden in this sample. The difficulty in confirming these planets is mostly coming from the limited performance of follow-up observations for these typically faint targets.

As shown on Fig. III.1.5, among the 67% of the unresolved candidates that have been classified as dwarf (luminosity class IV or V) most of them (85%) have a r-mag $\geq$ 14. For Jupiter-size planets radial velocity measurements remain difficult at the faint end of the CoRoT magnitude range (typically for r-mag $>$ 14.5). For those whose host-star is brighter, the domain of Neptune-size planets and smaller is still challenging the current spectrograph performances. The later is well exemplified by CoRoT-22b (Moutou et al. 2014) whose nature could not be fully secured by radial velocity measurements and ground-based imaging and required a complex process of planet validation carried out with the PASTIS software (Diaz et al. 2014).

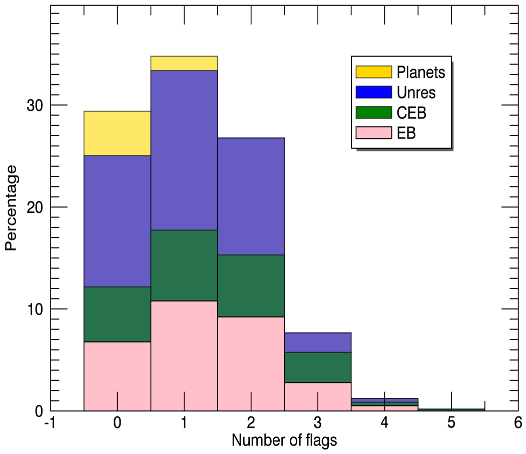

Fig. III.1.6. Stacked histogram of the percentage of candidates in a given class as a function of the number of flags received.

5. Assessing the classification of the candidates

The large follow-up effort carried out on the candidates allows to check the robustness of the flagging process. To that purpose, we compared the flags attributed to each candidats to the outcomes of follow up observations. For each class of candidates as defined in Sect. 4, we checked their distribution over the number of flags. Figure III.1.6 shows how the various classes of candidates, including planets, distribute as a function of the number of flags. While for the 3 classes, eclipsing binaries, contaminating eclipsing binaries and unresolved, their distribution remains nearly constant over the three first bins (2 flags or less), then significantly decreases, the CoRoT planets included in this analysis were allocated no flag or just one. A verification of the planets with triggered flags shows that the flags they received are well related to a real characteristics of the systems (Table III.1.2). A reliable spectral typing of the targets in the stellar fields observed in the faint stars channel may have allowed to remove the transit duration flag for some of the planets, but those related to the presence of a shallow secondary or a grazing transit would have remained unchanged. According to Fig. III.1.6, follow-up observations that would have concentrated on the candidates that received at the most one flag, that is 64% of the candidates, would not have missed any planet around a solar-like star.

6. Conclusions

A full catalog of all the transiting features identified in the CoRoT light curves during the mission lifetime is to be released (Deleuil et al., in prep.). It includes homogeneously derived parameters, validation diagnostics and a summary of the outcome of follow-up observations when they were carried out on planet candidates. The tool used for the validation process over basic tests, based on a simple binary flag system, has been also benchmarked against candidates for which follow-up observations were performed. With more than 400 candidates that were the targets of complementary observations, CoRoT data provides a good opportunity to set up tools to be used for an automated and reliable ranking of candidates of future space missions.

Table III.1.2. CoRoT planets with one flag triggered.

Planet	Flag	Host-star spectral type	$R\star$ $[R_\odot]$
CoRoT-1	secondary	G0V	1.11 ± 0.05
CoRoT-10	V-shape	K1V	0.79 ± 0.05
CoRoT-17	duration	G5V	$1.19^{+0.14}_{-0.13}$
CoRoT-22	color-depth	G0V	$1.136^{+0.038}_{-0.09}$
CoRoT-24	secondary	K1V	0.86 ± 0.09
CoRoT-25	V-shape	F9V	$1.19^{+0.14}_{-0.03}$
CoRoT-26	duration	G5IV	$1.79^{+0.18}_{-0.09}$
CoRoT-28	duration	G8/9IV	1.78 ± 0.11

References. (1) Barge et al. (2008); (2) Bonomo et al. (2010); (3) Csizmadia et al. (2011); (4) Moutou et al. (2014); (5) Alonso et al. (2014); (6) Almenara et al. (2013); (7) Cabrera et al. (2015)

In addition to the last planets pending to be published soon, among the candidates whose status is not resolved, there are still potentially some 20 planets and a few brown dwarfs to be identified as such. Some would require a radial velocity precision that is beyond those of actual spectrographs. A new generation of high precision spectrographs may help to secure the nature of some of these candidates, some being potentially small mass planets.

Acknowledgements. The French exo-team thanks the CNES for its continuous support before, during and after CoRoT operations, especially for the grants provided for post docs who worked on tasks related to the mission. The authors wish to thank the staff at ESO La Silla Observatory for their support and for their contribution to the success of the HARPS project and operation. H.D. acknowledges support by grant AYA2012-39346-C02-02 of the Spanish Secretary of State for R&D&i (MINECO).

References

Almenara, J. M., Bouchy, F., Gaulme, P., et al. 2013, A&A, 555, A118
Alonso, R., Moutou, C., Endl, M., et al. 2014, A&A, 567, A112
Barge, P., Baglin, A., Auvergne, et al. 2008, A&A, 482, 17
Bonomo, A. S., Santerne, A., Alonso, R., et al. 2010, A&A, 520, 65
Bonomo, A. S., Chabaud, P. Y., Deleuil, M., et al. 2012, A&A, 547, A110
Bouchy, F., Moutou, C., Queloz, D., et al. 2009, IAU Symp., 253, 129
Bouchy, F., Deleuil, M., Guillot, T., et al. 2011, A&A, 525, A68
Cabrera, J., Fridlund, M., Ollivier, M., et al. 2009, A&A, 506, 501
Cabrera, J., Csizmadia, S., Montagnier, G., et al. 2015, A&A, 579, A36
Carone, L., Gandolfi, D., Cabrera, J., et al. 2012, A&A, 538, A112
Carpano, S., Cabrera, J., Alonso, R., et al. 2009, A&A, 506, 491
Cavarroc, C., Moutou, C., Gandolfi, D., et al. 2012, Ap&SS, 337, 511
Csizmadia, S., Moutou, C., Deleuil, M., et al. 2011, A&A, 531, A41
Csizmadia, S., Hatzes, A., Gandolfi, D., et al. 2015, A&A, 584, A13
Deeg, H. J., Gillon, M., Shporer, A., et al. 2009, A&A, 506, 343
Deeg, H. J., Moutou, C., Erikson, A., et al. 2010, Nature, 464, 384
Deleuil, M., Moutou, C., Deeg, H. J., et al. 2006, ESA SP, 1306, 341
Deleuil, M., Deeg, H. J., Alonso, R., et al. 2008, A&A, 491, 889
Deleuil, M., Meunier, J. C., Moutou, et al. 2009, AJ, 138, 649
Díaz, R. F., Almenara, J. M., Santerne, A., et al. 2014, MNRAS, 441, 983
Erikson, A., Santerne, A., Renner, S., et al. 2012, A&A, 539, A14
Guenther, E. W., Fridlund, M., Alonso, R., et al. 2013, A&A, 556, A75
Haywood, R. D., Collier Cameron, A., Queloz, D., et al. 2014, MNRAS, 443, 2517
Mandel, K., & Agol, E. 2002, ApJ, 580, L171
Moutou, C., Pont, F., Bouchy, F., et al. 2009, A&A, 506, 321
Moutou, C., Deleuil, M., Guillot, T., et al. 2013, Icarus, 226, 1625
Moutou, C., Almenara, J. M., Díaz, R. F., et al. 2014, MNRAS, 444, 2783
Queloz, D., Bouchy, F., Moutou, C., et al. 2009, A&A, 506, 303
Seager, S., Mallén-Ornelas, G. 2003, ApJ, 585, 1038
Sing, D. K. 2010, A&A, 510, A21

Acknowledgements: The CoRoT space mission has been developed and operated by CNES, with the contribution of Austria, Belgium, Brazil, ESA, Germany, and Spain.

The CoRoT Legacy Book
© The authors, 2016
DOI: 10.1051/978-2-7598-1876-1.c032

III.2

Activity modelling and impact on planet's parameters

The case of CoRoT-7

S. C. C. Barros[1,2], R. D. Haywood[3,4], and M. Deleuil[2]

[1] Centro de Astrofísica, Universidade do Porto, Rua das Estrelas, 4150-762 Porto, Portugal
e-mail: susana.barros@astro.up.pt
[2] Aix Marseille Université, CNRS, LAM (Laboratoire d'Astrophysique de Marseille) UMR 7326, 13388, Marseille, France
[3] SUPA, School of Physics and Astronomy, University of St Andrews, St Andrews KY16 9SS, UK
[4] Harvard-Smithsonian Center for Astrophysics, 60 Garden Street, Cambridge, MA 02138, USA

1. Introduction

CoRoT-7b was the first transiting super-Earth discovered (Léger et al. 2009) and is one of the most exciting planets detected by CoRoT. This planet with an orbital period of ∼0.85 days was detected in the LRa01 run of CoRoT that started on 2007, October 24 and ended on 2008, March 3. The host star was found to be a young (1.2−2.3 Gyr) G9V type star with $\log g = 4.47 \pm 0.05$, $[\mathrm{Fe/H}] = 0.12 \pm 0.06$, $T_{\mathrm{eff}} = 5250 \pm 60$ K (Bruntt et al. 2010). The star is very active, showing a 2% amplitude variability in the LRa01 light curve. The stellar activity affected the observed transits and transit derived parameters and severely affected the radial velocity (RV) follow-up observations needed to confirm the planet (Queloz et al. 2009).

The normalised transit depth is 0.01784 ± 0.00047 (Barros et al. 2014), which is approximately one third of the rms of the light curve, therefore the effect of activity in the transit is not obvious. However, it was suspected that the stellar activity also affected the derived transit parameters of CoRoT-7b (Léger et al. 2009) because the stellar density derived from transit fitting was found to be much lower ($\rho_* = 0.12\rho_\odot$) than the derived spectroscopic value ($\rho_* = 1.4\rho_\odot$). This was supported by the fact that when subsets of 4−5 transits were fitted separately, the resulting stellar density was in agreement with the expected value for a G9V type star. To avoid the underestimation of the stellar density, the spectroscopic derived radius was used as a prior in their transit fitting (Léger et al. 2009).

The effect of stellar activity in the RVs was even more problematic. During the RV observations, the semi-amplitude of activity-induced RV variability was 20 m/s which is much larger than the expected planet RV amplitude of ∼1.6−5.7 m/s. Several methods were developed to correct the activity-induced RV variability. Queloz et al. (2009) applied a pre-whitening procedure followed by a harmonic decomposition. This way they obtained a planetary mass $m_{\mathrm{b}} = 4.8 \pm 0.8\ M_\oplus$ and found a second planet in the system with a period of 3.69 days and a mass $m_{\mathrm{c}} = 8.4 \pm 0.9\ M_\oplus$. Lanza et al. (2010) modelled the light curve with a maximum entropy spot model and synthesised RVs. Since the modelled activity-induced RV variations did not contain periodic signals coincident with the orbital period of either CoRoT-7b nor c, their planetary nature was confirmed. Hatzes et al. (2010) showed that the full width at half-maximum (FWHM), bisector span and Ca II H&K line emission also did not contain periodicities at the planet orbital period which supported the existence of the planets. The authors suggested the existence of a third planet in the system, CoRoT-7d, with a period of 9.02 days and a mass of $m_{\mathrm{d}} = 16.7 \pm 0.42\ M_\oplus$. In another paper, Hatzes et al. (2011) used the fact that CoRoT-7b's orbital period is much shorter than the stellar rotation period ($P_{\mathrm{rot}} = 23.81 \pm 0.03$; Haywood et al. 2014). They assumed that on any given night, the variations in RV are solely due to the planet's orbital reflex motion and that the activity-induced variations can be treated as a constant offset on each night. This allowed to determine a mass $m_{\mathrm{b}} = 7.42 \pm 1.21\ M_\oplus$. Pont et al. (2011) presented another study with a maximum entropy spot model but including a correlated noise term. They obtained a mass $m_{\mathrm{b}} = 2.3 \pm 1.8\ M_\oplus$ which lead them to question the significance of CoRoT-7b. The SOAP tool was used by Boisse et al. (2011) to simulate the spot induced variations in the RVs. These were used to correct for the activity and derive planetary masses $m_{\mathrm{b}} = 5.7 \pm 2.5\ M_\oplus$ and $m_{\mathrm{c}} = 13.2 \pm 4.1\ M_\oplus$. Another version of the high-frequency filter was applied by Ferraz-Mello et al. (2011), who obtained slightly higher planetary masses $m_{\mathrm{b}} = 8.0 \pm 1.2\ M_\oplus$ and $m_{\mathrm{c}} = 13.6 \pm 1.4\ M_\oplus$. A table summarising the mass determinations for CoRoT-7b can be found in Hatzes et al. (2011). Although most of these analyses gave consistent results, it is clear that the determination of the masses of both CoRoT-7b and c strongly depends on how the activity-induced RV variations are modelled.

To better understand and characterise this iconic system, CoRoT-7 was re-observed with the CoRoT satellite for an additional 80 days, from 2012, January 10 to 2012, March 29. This allowed us to improve our estimates of the transit parameters of CoRoT-7b, despite its shallow transits and the high levels of activity (Barros et al. 2014). Furthermore, a second HARPS campaign was carried out for 26 consecutive clear nights from 2012, January 12 to February 6 in conjunction with the CoRoT photometry. The simultaneous photometry provided unique additional information on the surface activity of the star, enabling us to model the activity-induced RV variations more faithfully and thus determining more precise and accurate masses for CoRoT-7b (as well as CoRoT-7c).

2. Stellar activity effect in the transit parameters

Even for high signal-to-noise transit light curves of large planets, the effects of stellar activity are difficult to recognise and to correct as has been shown by Barros et al. (2013). For smaller-sized planets, the effects can be larger but are even more difficult to distinguish because the individual transits are not resolved due to their lower signal-to-noise.

Stellar activity can affect the transit light curves in two different ways (Czesla et al. 2009). Dark spots or bright faculae outside the transit chord (projected path of the planet in the stellar surface) alter the out-of-transit stellar flux and can introduce trends in the normalisation and an unknown offset since the real stellar flux is not accessible. Spots or faculae inside the transit chord (planet-spot occultations) will affect the transit shape. Both effects will influence the parameter estimation.

The out-of-transit stellar variability of CoRoT-7b during the LRa01 CoRoT observations was modelled by Lanza et al. (2010) who found that the photometric variability is dominated by cool spots with reduced facular contribution in comparison to the Sun. This was also confirmed by ground-based colour-photometry acquired from Decembre 2008 to February 2009 (Queloz et al. 2009).

During the new observation of CoRoT-7b, the star was in a lower activity level. The light curves for both observations are shown in Fig. III.2.1. During the new observation, the flux variability was 1% and the spectroscopic activity index ($\log R'_{\mathrm{HK}}$) measured in both RV data sets also decreased from -4.60 ± 0.03 to -4.73 ± 0.03. Futhermore, the spot mean latitudes have also changed (Lanza et al. 2010; Lanza et al. in prep). This resulted in the light curve of CoRoT-7 taken during LRa06 being less affected by activity.

The transits observed by CoRoT in the runs LRa01 and LRa06 were modelled by Barros et al. (2014) with the PASTIS MCMC code (Díaz et al. 2014). To analyse the transit shape, the authors compared the posteriors of a geometric fit (no stellar prior information) of each individual observation. The parameter posterior distributions of a/R_*, i, and Rp/R_* for LRa01 and LRa06 are shown in Fig. III.2.2. It is obvious that the distributions are very different for the two runs. The transit-derived stellar density for LRa01 is $0.27^{+0.17}_{-0.10}\ \rho_\odot$, significantly different from that obtained for LRa06 which is $3.79^{+0.12}_{-3.2}\ \rho_\odot$. The latter is higher than the stellar density derived from spectroscopic analysis of the host star but consistent within the errors.

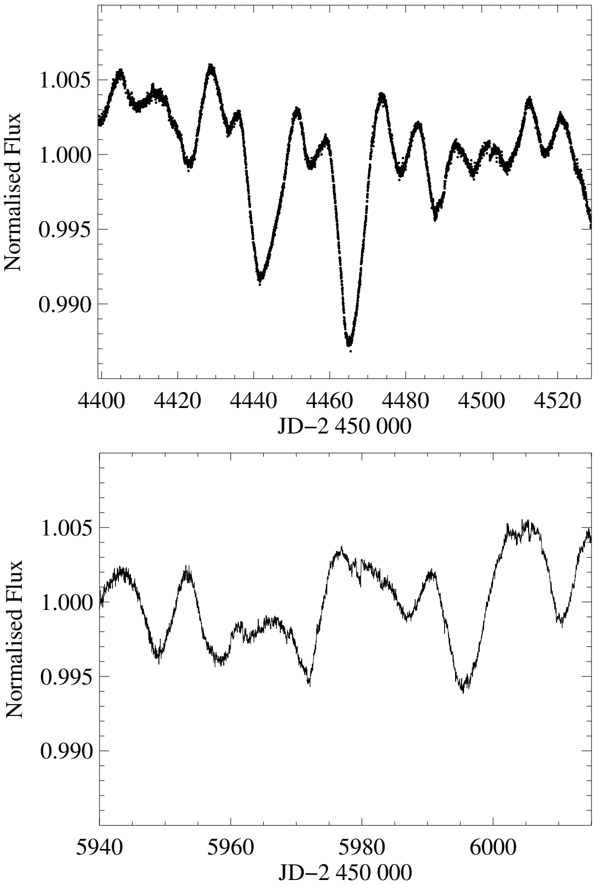

Fig. III.2.1. Light curve of CoRoT-7 binned to 30 min for clarity during the first CoRoT run LRa01 (*top*) and last CoRoT run LRa06 (*bottom*). It is clear that the variability level during LRa01 is twice that in the LRa06 CoRoT light curve. Adapted from Barros et al. (2014) © A&A.

Barros et al. (2014) performed simulations assuming white noise and showed that overestimation of the stellar density in LRa06 is due to low signal-to-noise of the transits. In this case ingress/egress times cannot be well constrained leading to a degeneracy in the transit solution. Therefore, stellar parameter priors need to be included in the transit analysis in order to derive the transit parameters.

However, in the case of LRa01, Barros et al. (2014) showed that the transit shapes were deformed. They were able to discard the low signal-to-noise of the individual transit and out-of-transit variability due to either activity or instrumental noise as causes of the transit shape deformation. The authors argued that the transit shape deformation was due to planet-spot occultation events. This was supported by the fact that the transit times showed a periodicity equal to half of the rotation period of the star. Moreover, they found that transits with out-of-transit flux higher than the median level are less distorted. In Fig. III.2.3, we show a comparison of the posterior distributions of a/R_* and i for the high and low flux levels of each run. Barros et al. (2014) found that the posterior distributions are all similar except for the selection of the low flux level of LRa01. They concluded that the low flux level transits of LRa01 appear to have more extra noise than the other samples. To avoid

Table III.2.1. CoRoT-7 transit parameters from Barros et al. (2014).

Planet orbital period, P [days]	$0.85359159 \pm 5.7e{-7}$
Mid-transit time, T [BJD]	$2\,454\,398.07756^{+4.5e-4}_{-7.4e-4}$
Orbit inclination, i [deg]	$80.78^{+0.51}_{-0.23}$
Orbital semi-major axis, a [AU]	$0.017016^{+1.7e-4}_{-3.6e-5}$
semi-major axis/radius of the star, $a/R_\star$	4.484 ± 0.070
Radius ratio, $k = R_p/R_\star$	0.01784 ± 0.00047
Transit duration, T_{14} [h]	1.059 ± 0.026
Impact parameter, b	$0.713^{+0.017}_{-0.026}$
Planet radius, $R_\mathrm{b}[R_\oplus]$	1.585 ± 0.064

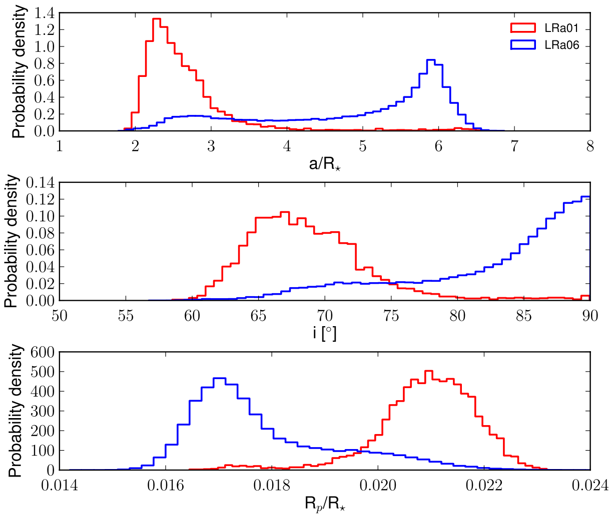

Fig. III.2.2. Posterior distribution of the geometric parameters for the separate fits of the LRa01 (red) and the LRa06 (blue) runs. Adapted from Barros et al. (2014) © A&A.

biasing the derivation of the transit parameters, only transits occurring when the star had higher flux were used in their final analysis. The final transit parameters obtained by Barros et al. (2014) are given in Table III.2.1.

3. Stellar activity effect in the RVs

During the 2012 RV HARPS campaign, the activity-induced RV variations were also smaller than in 2009. More importantly, the simultaneous CoRoT observations allow to use the photometry to correct the RVs. Haywood et al. (2014) used the out-of-transit flux to estimate the RV variations using the FF' method (Aigrain et al. 2012). The FF' method assumes that the suppression of convective blueshift in active regions and the flux blocked by spots are the dominant RV activity signal. In this case, the RV variations can be approximated with a model that depends on the photometric flux F and its first time derivative F'. However, Haywood et al. (2014) found that this model was not sufficient to account for all the quasi-periodic (thus activity-induced) signals present in the RVs. This indicates that other activity-related phenomena such as limb-brightened facular emission, photospheric inflows towards active regions, or faculae that are not spatially associated with spot groups which are not accounted for in the FF' method might have a significant effect on the observed RVs.

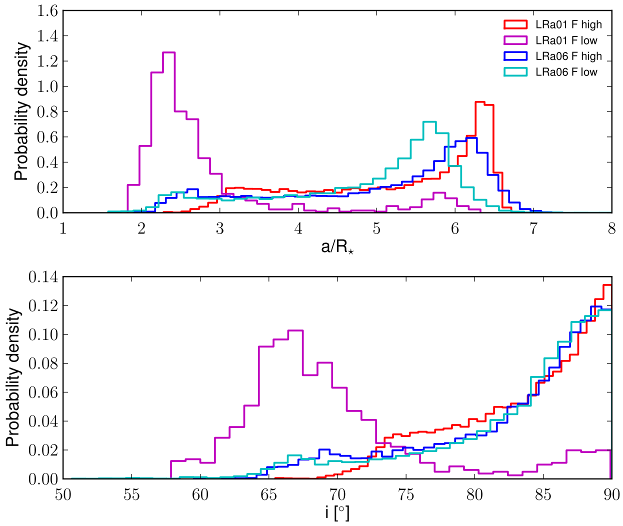

Fig. III.2.3. Posterior distribution of a/R_* (*top*) and i (*bottom*) for pure geometric fits of the transit selections based on the out-of-transit flux. The transits at high flux levels are shown in red for LRa01 and blue for LRa06 while the one at the low flux levels are shown in magenta for LRa01 and cyan for LRa06. Adapted from Barros et al. (2014) © A&A.

To model such an additional activity-induced RV signal, Haywood et al. (2014) used a Gaussian process (GP) with a quasi-periodic covariance function that refleted the frequency structure of the light curve. The chosen GP kernel (Rasmussen & Williams 2006) has 4 hyperparameters: the amplitude of the GP, the timescale for growth and decay of active regions, a smoothing parameter, and the recurrence timescale which was chosen to be the rotation period of the star. The first three parameters were determined by training the GP on the simultaneous light curve. Only the amplitude of the GP was allowed to vary. The planet orbital signals were modelled as Keplerians. The best fit parameters of this model were determined via an MCMC procedure (see Haywood et al. (2014) for further details).

In Fig. III.2.4 we show the decomposition of the observed RVs into the different activity components: the two FF' basis functions, the additional term modelled as the a GP and the two Keplerian orbits for CoRoT-7b and CoRoT-7c. Using Bayesian model comparison, the authors found that the two planets model is more likely. Indeed, the signal at 8−9 days is better modelled by a GP with a quasi-periodic covariance function than by a Keplerian signal, implying that this signal is not fully periodic or coherent. They found planetary masses $m_\mathrm{b} = 4.73 \pm 0.95\ M_\oplus$ and $m_\mathrm{c} = 13.56 \pm 1.08\ M_\oplus$.

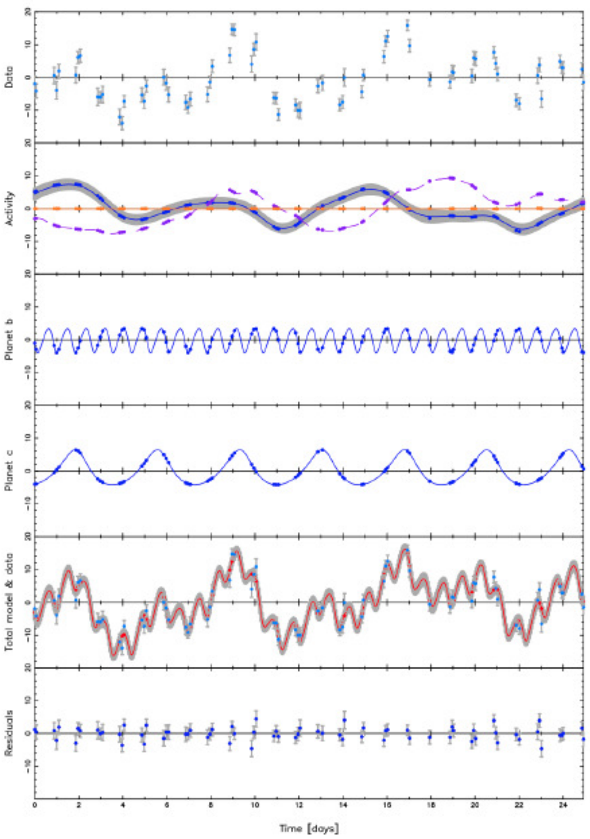

Fig. III.2.4. *Top panel*: observed radial velocities of CoRoT-7. *Second panel*: the 3 fitted components of the activity signal the RV due to rotation in orange full line, the RV due to convective blueshift in purple dashed line), and the additional RV signal models with the GPs in blue full line with grey error band. *Third panel*: RV signal due to planet b. *Fourth panel*: RV signal due to planet c. *Fifth panel*: observed RV with the total RV final model overploted. Sixth panel: RV residuals of the model. All RVs are given in m/s. Adapted from Haywood et al. (2014) © A&A.

4. Conclusions

As the precision of planet observations increases, intrinsic stellar variability is becoming the dominant limitation in the study and characterisation of exoplanets. Moreover, detecting smaller planets is easier for smaller late-type main sequence stars, which are generally more active. This will in turn undermine our ability to determine the radius and the mass of the planet via RV follow-up observations; in some cases, activity-induced RV variations may prevent us from confirming a planet candidate at all. It is therefore crucial to understand the effects of stellar activity in the derived exoplanet parameters.

The re-observation of CoRoT-7 with the CoRoT satellite and a simultaneous observation with HARPS offers a good opportunity to explore in more details the impact of stellar activity and a better understanding on how stellar activity affects the derivation of system parameters. In addition, it also allowed to much better constraints on the system parameters of CoRoT-7.

- In low signal-to-noise transits with only white noise, the ingress/egress times are not well defined leading to an overestimation of the inclination angle. In this case, to avoid biasing the transit parameters a prior on the stellar parameters derived from spectroscopy should be used (Barros et al. 2014).
- Although invisible, planet-spot crossing events in low signal-to-noise transit can deform the transit shape, leading to an underestimation of the inclination angle. When the planet-spot crossing events are not directly detectable in the transits, tests need to be made to ensure that the transit shape is not deformed. To quantify this effect, we suggest to compare the parameters of transits that occur when the star is at a higher flux level with the ones of transits that occur when the star has a lower flux level. The later happens when planet-spot occultation has a higher probability of occurring. If differences are detected, then the transits occurring during lower flux level should be discarded to derive unbiased transit parameters.
- In very active stars like CoRoT-7, the FF' method (Aigrain et al. 2012) that uses the out-of-transit photometric variability to derive the activity-induced RV variability is not enough to fully reproduce the observations.
- Haywood et al. (2014) found that the FF' method combined with a Gaussian process with the same frequency properties as the light curve overcomes the limitations of applying the FF' method only. Indeed, they found that it reproduces the activity-induced RV variations very well. For the specific case of CoRoT-7, it allowed them to determine reliable planetary masses. In practice, it is difficult to obtain high precision (space-based) photometric observations simultaneously with RV observations. The covariance properties of the star's magnetic activity should, however, be present in observables other than the photometry, such as the spectroscopic indices (eg. the FWHM, bisector span and $R'_{\rm HK}$). Rajpaul et al. (2015) have recently developed a method whereby the activity-induced RV variations are modelled with a GP, whose covariance kernel is a combination of that of the FWHM, bisector span and $R'_{\rm HK}$ variations. As they mention, GPs are naturally well-suited to model activity-induced signals that are of stochastic nature, and are often quasi-periodic and coherent only on short timescale. The GP framework also allows a rigorous propagation of uncertainties which results in a more honest uncertainty in the mass, that reflects the effects of stellar activity.

CoRoT-7 system is a good test case to prepare the analysis of planetary systems (with small-size planets) around active stars that TESS and PLATO will provide us.

Acknowledgements. SCCB acknowledges support by grants 98761 by CNES and the Fundação para a Ciência e a Tecnologia (FCT) through the Investigador FCT Contract No. IF/01312/2014. We acknowledge the support from Fundação para a Ciência e a Tecnologia (FCT, Portugal) in the form of grant reference PTDC/FIS-AST/1526/2014." RDH acknowledges support from STFC studentship grant ST/J500744/1. RDH gratefully acknowledges a grant from the John Templeton Foundation. The opinions expressed in this publication are those of the authors and do not necessarily reflect the views of the John Templeton Foundation.

References

Aigrain, S., Pont, F., & Zucker, S. 2012, MNRAS, 419, 3147
Barros, S. C. C., Boué, G., Gibson, N. P., et al. 2013, MNRAS, 430, 3032

Barros, S. C. C., Almenara, J. M., Deleuil, M., et al. 2014, A&A, 569, A74

Boisse, I., Bouchy, F., Hébrard, G., et al. 2011, A&A, 528, A4

Bruntt, H., Deleuil, M., Fridlund, M., et al. 2010, A&A, 519, A51

Czesla, S., Huber, K. F., Wolter, U., Schröter, S., & Schmitt, J. H. M. M. 2009, A&A, 505, 1277

Díaz, R. F., Almenara, J. M., Santerne, A., et al. 2014, MNRAS, 441, 983

Rasmussen, E. C. & Williams C. K. I 2006, in Gaussian processes for machine learning (MIT Press)

Ferraz-Mello, S., Tadeu Dos Santos, M., Beaugé, C., Michtchenko, T. A., & Rodríguez, A. 2011, A&A, 531, A161

Hatzes, A. P., Dvorak, R., Wuchterl, G., et al. 2010, A&A, 520, A93

Hatzes, A. P., Fridlund, M., Nachmani, G., et al. 2011, ApJ, 743, 75

Haywood, R. D., Collier Cameron, A., Queloz, D., et al. 2014, MNRAS, submitted

Lanza, A. F., Bonomo, A. S., Moutou, C., et al. 2010, A&A, 520, A53

Léger, A., Rouan, D., Schneider, J., et al. 2009, A&A, 506, 287

Pont, F., Aigrain, S., & Zucker, S. 2011, MNRAS, 411, 1953

Queloz, D., Bouchy, F., Moutou, C., et al. 2009, A&A, 506, 303

Rajpaul, V., Aigrain, S., Osborne, M. A., Reece, S., & Roberts, S. 2015, MNRAS, 452, 2269

Acknowledgements: The CoRoT space mission has been developed and operated by CNES, with the contribution of Austria, Belgium, Brazil, ESA, Germany, and Spain.

The CoRoT Legacy Book

DOI: 10.1051/978-2-7598-1876-1.c033

III.3

CoRoT's planets: A family portrait

T. Guillot[1] and M. Havel[2]

[1] Université de Nice-Sophia Antipolis, Observatoire de la Côte d'Azur, CNRS UMR 7293, 06304 Nice Cedex 4, France
e-mail: tristan.guillot@oca.eu
[2] University of Columbia, New York, USA

1. Introduction

While the tens of exoplanets discovered by CoRoT now seem like a drop in the ocean of thousands of exoplanets known, each discovery has helped to push our understanding at a time when much fewer objects were known. Still now, owing both to the quality of the photometry from the spacecraft and the great amount of follow-up work, the ensemble of CoRoT planets remain among the ones which are best characterized, i.e., for which we have precise determination of planetary radius and mass. They also form a homogeneous ensemble which is relatively complete, at least for the planets orbiting stars up to magnitude ~14.

We take this look back at the ensemble of the CoRoT confirmed planets in terms of their properties, internal structure and evolution. This chapter is based in part on the review by Moutou et al. (2013), which we update when necessary. We also show the result of a homogeneous analysis limited to the giant planets of the family.

2. The gallery of CoRoT giant planets

Figure III.3.1 shows an ensemble of 23 giant planets detected by CoRoT. In order to have a homogeneous approach, we have omitted from this gallery the super-Earth CoRoT-7b, brown dwarfs, as well as planets for which no radial-velocity signal was detected. A few planets are still to be announced – these have not been included.

In spite of this selection, the variety of conditions is still large: masses range from 0.2 to 11 M_{Jup}, densities between 0.2 g cm^{-3} (CoRoT-5 b, Rauer et al. (2009)) and 12.6 g cm^{-3} (CoRoT-10 b, Bonomo et al. (2010)), equilibrium temperature (inversely related to orbital distance) between 410 K (CoRoT-9 b, Deeg et al. (2010)) and 1950 K (CoRoT-14 b, Tingley et al. (2011)), and radii from 0.59 (CoRoT-8 b, Bordé et al. (2010)) to 1.49 (CoRoT-1 b, Barge et al. (2008)) Jupiter radius.

The planetary radius and age in Fig. III.3.1 were obtained using the ensemble of published parameters for the planets and are compared to planetary evolution models calculated with the CEPAM code using a homogeneous approach (e.g., Guillot & Havel 2011; Havel et al. 2011).

The planets in this ensemble can be put into three categories: (i) Planets which are smaller than "standard" theoretical evolution models for pure solar-composition gaseous planets and thus require added heavy elements to match their size; (ii) Planets which are larger than these "standard" evolution models but which can be explained by advocating that a small fraction (~1%) of the incoming stellar energy is dissipated in the planet's interior; (iii) planets that are even larger and would require even higher energy dissipation rates to explain their size.

We show in the next section that the first two sets of planets can be explained with the same hypotheses, i.e. the downward transport of kinetic energy in these planets and a variable mass of heavy elements. How to explain the third ensemble is still unclear but we provide a tentative explanation in Sect. 4.

3. The inflation problem & the compositions of giant planets

As seen in Fig. III.3.1, a fraction of the giant planets of the CoRoT sample are significantly larger than would be expected from the evolution of a hydrogen-helium planet. This is a classical problem (e.g., Bodenheimer et al. 2001; Guillot & Showman 2002) which is quantified by calculating the *radius anomaly*, defined as the difference between the measured radius and that calculated for a solar-composition planet with no core of the same mass, age and equilibrium temperature (Guillot et al. 2006). 8/23 planets (CoRoT-1b, 2b, 5b, 6b, 11b, 12b, 18b, 19b) have positive radius anomalies, indicating that the inflation mechanism is widespread, in line with what found for the ensemble of giant exoplanets (e.g., Guillot 2008; Laughlin et al. 2011). Generally, the problem can be solved for all of these planets by invoking that a non-radiative process leads to the conversion of a small fraction of the stellar absorbed irradiation (of order 1%) to kinetic energy and its dissipation at later depths (e.g., Guillot & Showman 2002; Batygin & Stevenson 2010, plus many other more recent works).

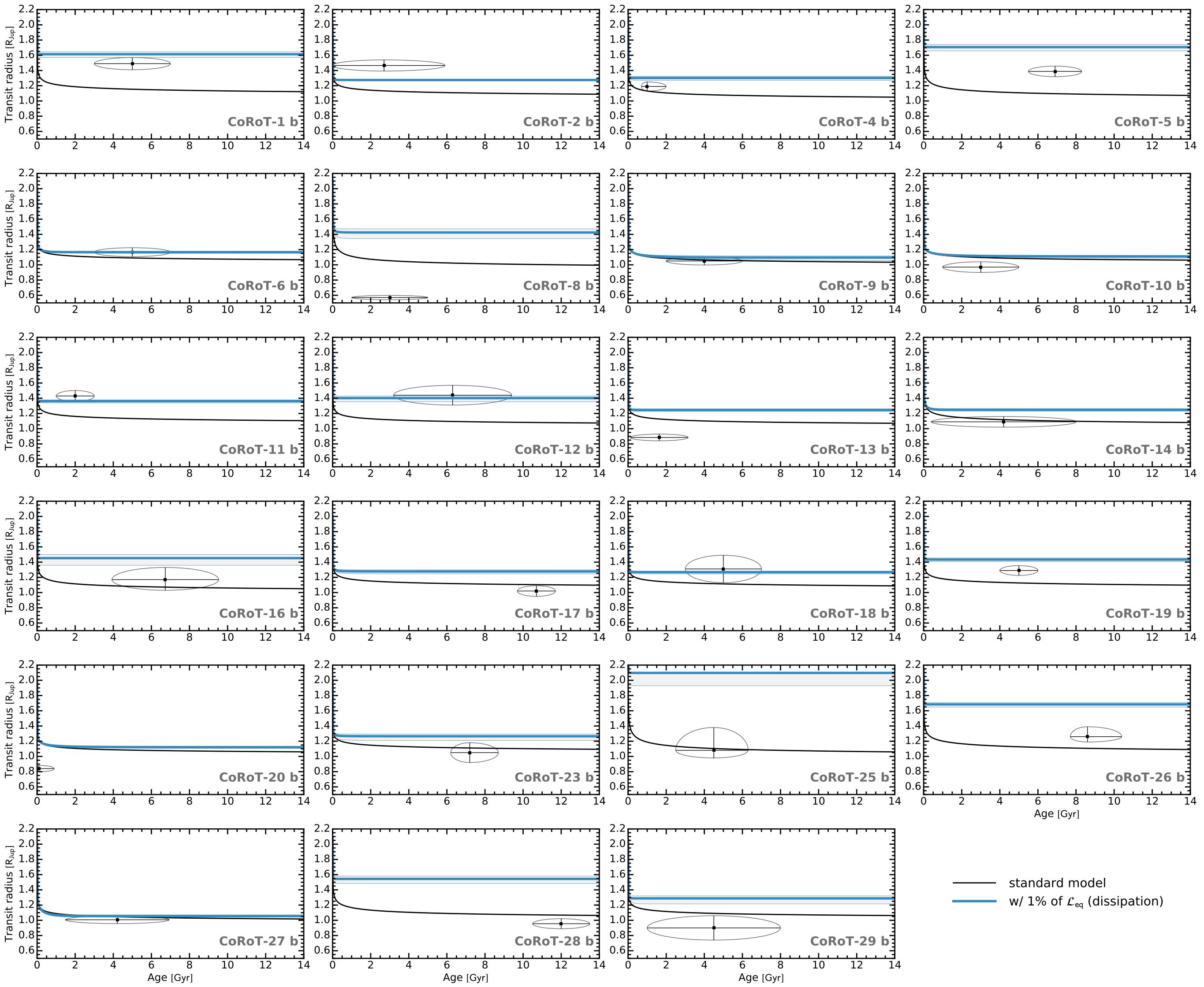

Fig. III.3.1. Gallery of the CoRoT giant planets, showing in each case planetary radius as a function of age. The ellipses indicate solutions obtained from the photometric, radial velocimetry and spectroscopic constraints (see text). The curves show theoretical evolution models for solar composition planets. The black lines correspond to standard models (including irradiation but no extra energy source), the blue lines assume that 1% of the incoming energy is dissipated deep into the planets.

However, one of the CoRoT planets is found to resist standard explanations so-far: CoRoT-2b has a radius that is not amongst the largest so far, but it is massive, and explaining its size thus requires a considerable amount of additional energy (Alonso et al. 2009; Gillon et al. 2010), of about 25% of the absorbed solar luminosity if this is a long-term feature (Guillot & Havel 2011). Interestingly, CoRoT-2 shows all the signs of being young, and the possibility of a recent (10 to 30 Ma) giant impact or circularization from a large eccentricity has been invoked to explain the large planetary radius (Guillot & Havel 2011). We will come back to this case in the next section.

Once a prescription for the missing physics is assumed, the mass of heavy-elements in the giant planets may be calculated (see Guillot et al. 2006): the presence of additional heavy elements either as a central core or inside the envelope generally leads to a shrinking of the planet compared to solar-composition models and naturally explains the negative δ_{anomaly} values. For simplicity, this is done by assuming that a fraction of the incoming energy is dissipated at the planet's center, and that all the heavy elements are embedded as a central core.

When plotted against stellar metallicity, the giant planets in the CoRoT sample appear to have amounts of heavy elements that are correlated with that of their parent star, confirming the trend observed for many planets (Guillot et al. 2006; Burrows et al. 2007; Guillot 2008; Laughlin et al. 2011; Moutou et al. 2013). The correlation coefficient between $10^{[\text{Fe/H}]}$ and $M_Z^{\text{b}}/M_{\text{p}}$ for the CoRoT planets is $r = 0.52$ and a Spearman's test indicate that its statistical significance is 2.3σ. When including other planets, the value of r remains the same, but the significance increases to 3.5σ (Moutou et al. 2013).

However, some of the CoRoT planets have small radii for large masses and require masses of heavy elements in excess of what is usually envisioned by formation models.

This is the case of CoRoT-10b, 13b, 14b, 17b, 20b and 23b which all require core masses in excess of 70 $M_\oplus$ to explain their small size. The large amounts of heavy elements found for these planets was unexpected from planet synthesis models. The relatively high frequency of these superdense planets among the CoRoT sample is also surprising. It appears to be larger than in the general sample, which may be attributed to the fact that these planets are generally smaller and more difficult to detect from the ground. On the theoretical standpoint, for large M_Z values, the assumption that all the heavy elements are in the core and the very high central pressures both probably imply that M_Z is significantly overestimated (see Deleuil et al. 2012; Baraffe et al. 2008). In any case, further work both on the internal structure of these planets and their formation is required.

4. Young planets?

Three CoRoT stars with planets, CoRoT-2, 18 and 20 appear to be younger than 1 Ga. When accounting for the main-sequence lifetime of stars and the age of the Galaxy, this is consistent with a uniform age distribution. Over this effective temperature range, none of the other known transiting planets are that young. This can be explained by two factors: first most of the usual transit surveys are biased towards non-active stars both because of the photometric stability requirement for the transit detection and because of the easier radial-velocity follow-up. Second, the CoRoT systems have been studied more thoroughly than the average exoplanet, with in particular measurements of chromospheric activity, lithium abundance and stellar spin. These measurements are important to detect signs of youth which are generally not accessible from the study of the evolution tracks themselves.

Two CoRoT systems are particularly interesting because of their complex lightcurves revealing that the stars are heavily spotted, the fast stellar spin and presence of a close-in, relatively massive giant planet. This is the case of CoRoT-2 and 18. Interestingly, these two systems are almost twins of each other. The two stars, CoRoT-2 (Alonso et al. 2008) and CoRoT-18 (Hébrard et al. 2011) have comparable effective temperatures (5450 vs. 5440 K), metallicities (0.0 vs. −0.1), spin periods (4.5 vs. 5.4 days) and $v \sin i$ (12 vs. 8.0 km s^{-1}), and they are both active, with peak to peak photometric variabilities of $\sim$4% and $\sim$2%, respectively. In addition CoRoT-2 and CoRoT-18 are the fastest-spinning stars with a known planet and an effective temperature below 6000 K.

The two systems show signs of youth: an analysis of the X-ray activity of CoRoT-2 and its fast spin indicate an age of 100 to 300 Ma (Schröter et al. 2011), whereas the spin of CoRoT-18 and its lithium abundance seem to indicate an age between 400 to 600 Ma (Hébrard et al. 2011). The latter is problematic however, as the age obtained from evolution tracks would indicate an age in excess of 1 Ga (or a star on the pre-main sequence, which is very unlikely).

A third young system is CoRoT-20: the star's spin is not as important ($v \sin i = 4.5 \pm 1.0$ km s^{-1}), but it exhibits a clear lithium line, indicative of an age younger of 100^{+800}_{-40} Ma (Deleuil et al. 2012). In this case, stellar evolution tracks only provide upper limits on the star's age (below 5 Ga, within 1σ). Without the lithium measurement, this star would probably have been attributed an older mean age compatible with a star on the main sequence. This examples illustrates how detailed follow-up studies are important in order to fully characterize these exoplanetary systems. Interestingly, this case also share similarities with the two others: the planet is massive (4.24 ± 0.23 $M_{\rm Jup}$), it has a larger orbital period ($P = 9.24285$ days) but a high eccentricity implies that it makes close approaches with the star and last but not least, its inferred size is also problematic. This time, it is too small, as shown by the very low radius anomaly and extremely high M_Z value that is inferred to fit its radius ($M_Z = 1.75$ M_{Jup}!).

The fact that these three systems pose particular problems (the large size of CoRoT-2b, the inconsistent age determinations for CoRoT-18 and the small size of CoRoT-20b) seems to indicate that our knowledge of young, rapidly spinning, spotted stars is incomplete.

Indeed, a survey of stars with companions have shed new light on this problem. Poppenhaeger & Wolk (2014) have shown that the main star of the CoRoT-2 system has a K-dwarf companion, CoRoT-2B, and that, unlike CoRoT-2A, it is a very weak X-ray emitter. This implies that CoRoT-2B is at least 5 Ga. Given that companions of multiple systems should have the same age, it appears that CoRoT-2A should in fact be old. What happened? In fact, this is evidence that CoRoT-2A has been spun up by its close-in massive planetary companion. This means that gyrochronology, the set of empirical relation that relate stellar spin to age cannot be used. The same is true for indicators linked to chromospheric activity as it is also directly linked to the star's magnetic field intensity and hence to its spin rate.

As can be seen from the fully set of solutions obtained by Guillot & Havel (2011), when using old instead of young ages, the inferred planetary radius of CoRoT-2b decreases. This allows finding solutions with lower values of the dissipation rate. However, a qualitative estimate using the Guillot & Havel (2011) results indicates that a still high value of the dissipation rate ($\gtrsim 5\%$) may be needed. One possibility to be investigated is whether the spin up of the star by the planetary companion may lead to differential rotation inside the star and alter its internal structure and evolution.

The analysis of the CoRoT data combined with further follow-up observations should shed light on this important issue which bears directly on the problem of the formation of planetary systems.

5. CoRoT-7b: the first transiting super-Earth

Of course, this family portrait would be incomplete without mentioning CoRoT-7b, the first transiting super-Earth known (Léger et al. 2009; Queloz et al. 2009) which heralded many to come discovered by the Kepler mission (e.g., Howard et al. 2012). With a size of 1.585 ± 0.064 $R_\oplus$ (Barros et al. 2014) and a mass of 4.73 ± 0.95 (Haywood et al. 2014), CoRoT-7b has the density expected for a planet of the same composition as our Earth (Valencia et al. 2010; Barros et al. 2014). However, we stress that this solution assumes a relatively young age of 1.32 ± 0.75 Ga for the star, based on gyrochronology. If, based on the experience of CoRoT-2 we choose to leave out the gyrochonology constraint, the preferred age solution then becomes $8.4^{+5.0}_{-3.3}$ Ga yielding a much larger inferred planetary radius, $1.94 \pm 0.1\ R_\oplus$ (Barros et al. 2014). It is not clear at the moment why the star would be rotating so fast if it is old: contrary to the massive CoRoT-2b, little CoRoT-7b is incapable of spinning its star up, its angular momentum being too small (e.g., Damiani & Lanza 2015). This would thus require the recent ingestion of a more massive planet, a scenario which is less likely than a relatively young age for the system.

Another important issue with CoRoT-7b and the ensemble of very close-in super-Earths is their origin. Mass-loss is an important part of their evolution, and it is energetically possible that such close-in super-Earths are stripped-off cores of giant planets (Valencia et al. 2010). On the other hand, super-Earths appear to be much more common than giant planets (e.g., Howard et al. 2012), making that possibility less likely.

6. Conclusion

The family of planets detected by CoRoT sheds light on planetary formation and evolution and on the interactions between stars and planets. A large fraction of close-in giant planets are oversized, implying the existence of a yet unidentified mechanism to slow their evolution (or possibly, increase their size). Some giant planets are smaller than expected for solar-composition objects, implying that they must contain significant amounts of heavy elements in their interior (in their core, or throughout their envelope). We see a correlation between the metallicity of the star and that inferred for the planets, requiring the existence of a process leading to an efficient collection of heavy elements by the forming planets. Finally, the study of binary systems shows evidence for massive planets spinning up their parent star – the most striking example being that of the complex CoRoT-2 system.

The success of CoRoT in that respect lied in the combination of great quality photometry and intense, dedicated follow-up for each object. This made possible to efficiently discover even rare systems, characterize them accurately (determination of planetary mass, stellar spin rate, eccentricity when possible, etc.) and model them in detail. It is most important for future space exoplanet missions to fully integrate the analysis of space data to intense follow-up mostly with ground-based telescopes.

References

Alonso, R., Auvergne, M., Baglin, A., et al. 2008, A&A, 482, L21

Alonso, R., Guillot, T., Mazeh, T., et al. 2009, A&A, 501, L23

Baraffe, I., Chabrier, G., & Barman, T. 2008, A&A, 482, 315

Barge, P., Baglin, A., Auvergne, M., et al. 2008, A&A, 482, L17

Barros, S. C. C., Almenara, J. M., Deleuil, M., et al. 2014, A&A, 569, A74

Batygin, K. & Stevenson, D. J. 2010, ApJ, 714, L238

Bodenheimer, P., Lin, D. N. C., & Mardling, R. A. 2001, ApJ, 548, 466

Bonomo, A. S., Santerne, A., Alonso, R., et al. 2010, A&A, 520, A65

Bordé, P., Bouchy, F., Deleuil, M., et al. 2010, A&A, 520, A66

Burrows, A., Hubeny, I., Budaj, J., & Hubbard, W. B. 2007, ApJ, 661, 502

Damiani, C. & Lanza, A. F. 2015, A&A, 574, A39

Deeg, H. J., Moutou, C., Erikson, A., et al. 2010, Nature, 464, 384

Deleuil, M., Bonomo, A. S., Ferraz-Mello, S., et al. 2012, A&A, 538, A145

Gillon, M., Lanotte, A. A., Barman, T., et al. 2010, A&A, 511, A3

Guillot, T. 2008, Physica Scripta Volume T, 130, 014023

Guillot, T. & Havel, M. 2011, A&A, 527, A20

Guillot, T., Santos, N. C., Pont, F., et al. 2006, A&A, 453, L21

Guillot, T. & Showman, A. P. 2002, A&A, 385, 156

Havel, M., Guillot, T., Valencia, D., & Crida, A. 2011, A&A, 531, A3

Haywood, R. D., Collier Cameron, A., Queloz, D., et al. 2014, MNRAS, 443, 2517

Hébrard, G., Evans, T. M., Alonso, R., et al. 2011, A&A, 533, A130

Howard, A. W., Marcy, G. W., Bryson, S. T., et al. 2012, ApJS, 201, 15

Laughlin, G., Crismani, M., & Adams, F. C. 2011, ApJ, 729, L7

Léger, A., Rouan, D., Schneider, J., et al. 2009, A&A, 506, 287

Moutou, C., Deleuil, M., Guillot, T., et al. 2013, Icarus, 226, 1625

Poppenhaeger, K. & Wolk, S. J. 2014, A&A, 565, L1

Queloz, D., Bouchy, F., Moutou, C., et al. 2009, A&A, 506, 303

Rauer, H., Queloz, D., Csizmadia, S., et al. 2009, A&A, 506, 281

Schröter, S., Czesla, S., Wolter, U., et al. 2011, A&A, 532, A3

Tingley, B., Endl, M., Gazzano, J.-C., et al. 2011, A&A, 528, A97

Valencia, D., Ikoma, M., Guillot, T., & Nettelmann, N. 2010, A&A, 516, A20

Acknowledgements: The CoRoT space mission has been developed and operated by CNES, with the contribution of Austria, Belgium, Brazil, ESA, Germany, and Spain.

The CoRoT Legacy Book

DOI: 10.1051/978-2-7598-1876-1.c034

III.4

CoRoT planet host stars

M. Fridlund[1, 2, 3], G. Bruno[4], M. Deleuil[4], D. Gandolfi[5], and the CoRoT CEST team

[1] Leiden Observatory, Leiden University, Postbus 9513, 2300 RA, Leiden, The Netherlands)
e-mail: fridlund@strw.leidenuniv.nl
[2] Department of Earth and Space Sciences, Chalmers University of Technology, Onsala Space Observatory, SE-439 92, Onsala, Sweden
[3] Max Planck Institute for Astronomy Königstuhl 17, 69117, Heidelberg, Germany
e-mail: fridlund@mpia-hd.mpg.de
[4] Aix Marseille Université, CNRS, LAM (Laboratoire d'Astrophysique de Marseille) UMR 7326, 13388, Marseille, France
[5] Zentrum für Astronomie, Fakultät für Physik und Astronomie, Mönchhofstr. 12-14, 69120, Heidelberg, Germany

1. Introduction

One topic that has taken on more and more importance in the field of exoplanetology during the period of the flight of the CoRoT and Kepler space missions, is the role of the host star. The fundamental parameters – those that can be measured directly – for an exoplanet are its radius and mass. For the host star, the fundamental parameters are its mass, radius, metallicity and age, and it is generally assumed that the two latter parameters are also applicable to associated planets. Obtaining these parameters allow the characterisation of the planet, the star and the system as such to take place. The two sets of parameters, planetary and stellar are intimately connected, since the planetary parameters depend on the measurement of the stellar values. The transit method measuring the radius of the planet and the radial velocity method obtaining the planetary (minimum) mass will only provide these parameters in terms of the stellar ones. As the launch of photometers into space has provided the opportunity for a photometric accuracy at the part-per-million (ppm) level and given that the almost simultaneous development of stabilised and well-calibrated ground based radial velocity measurements are reaching a level of accuracy better than 1 m s^{-1}, it has become possible to begin to carry out high precision physics on our elusive exoplanetary targets. But the increasing precision in measurements of the planets parameters is not coupled to a similar increase in the measurements of the stellar parameters. For a direct measurement of the stellar masses and radii, we require that the star is either going to be very close (allowing interferometry to measure the diameter directly) and/or in an eclipsing binary system (Double-lined Eclipsing Spectroscopic Binary systems, usually designated SB2). The number of such objects is very low and those with (transiting) known exoplanets are even more rare. It was realised very early during the CoRoT project (when literally thousands of excellent light curves were being obtained), that good spectra of the large numbers of potential host stars were going to be required. As a consequence, large amounts of time were successfully applied for the ESO VLT/UVES combination, as well as later through a separate agreement with NASA on the Keck/HIRES instrument. This meant that modelling of the host stars spectra in order to determine the stellar parameters could begin. The process for how this was done is described in the individual papers relating to the discovery and confirmation of each CoRoT planet, as well as in Bruno (2015) and in Fridlund et al. (in prep.). Here we will briefly describe the methods and some of the conclusions reached. Later on during the flight of CoRoT, less and less VLT and Keck time were allocated to dedicated stellar spectra. But as time was passing the number of radial velocity spectra, obtained in order to determine the planetary masses, was building up and consequently so was the signal to noise (S/N) in the accumulated spectrum for each star. Therefore these radial velocity spectra (those obtained with the HARPS spectrograph have almost twice the resolution compared to the UVES/HIRES spectra) could be used for stellar modelling.

At the moment, the only way to determine stellar masses, radii and ages, is to obtain very high S/N spectra of the star in question with an as high as possible spectral resolution (R). Then one models the spectrum, fits the model to the data and, after (usually) having iterated the process a number of times, arrives at an effective temperature, a value for the local gravity at the surface, the abundances and the rotational velocity as well as the turbulent velocities. From these values and the light curve, one can estimate the stellar mass and then model where the star should be on its evolutionary track, and read of its radius and age. Although, this process appears pretty straightforward, there are a number of problems to be addressed. The first concerns the quality of the spectrum itself. A "high S/N" means larger than $S/N = 100$ and is ideally better than $S/N = 200$. For a spectrum with a resolution of $R = 60\,000$ this means that typically one night is required on an 8 m class telescope for a star in the brighter half of the CoRoT magnitude range of 12−16 in order to obtain a $S/N > 100$. For the Kepler stars that are typically 3 magn brighter, you can obtain spectra of two such stars per night with a 10 m class telescope, but on the other hand you have many more bright targets because of the larger field of the Kepler telescope. In order to follow-up a planet candidate, one needs ultimately to obtain the radial velocity signature of the planet, and there is a direct relation between the apparent brightness of the star and the precision with which one can measure the radial velocity amplitude. It means that the smaller the planet is the brighter the star has to be, in order to confirm the nature and then derive the planets mass. A consequence of this was that a large number of potential planet candidates observed with CoRoT that had host stars fainter than about magnitude 15 could not be followed up at the time, and had to be postponed to an uncertain future (e.g. observations with the CARMENES and ESPRESSO spectrographs). To accurately measuring the fundamental stellar parameters (and properly understand stars in general), the way forward is going to be dependent on another major result from space. First obtained with CoRoT and then confirmed and enhanced with NASA's Kepler mission, it was demonstrated that the accuracy commensurate with the precision of the stellar fundamental parameter measurements could be achieved using asteroseismology. Since space observations are required for bulk measurements, this is now, since the selection in March 2014 of PLATO (Rauer et al. 2014) as ESA's M3 mission on the horizon. Unfortunately, the launch of PLATO will still be about one decade into the future, and we have literally thousands of light curves from CoRoT and Kepler, as well as thousands of high precision radial velocity curves and associated data awaiting further interpretation. It is therefore needed to determine the fundamental physical parameters of exoplanetary host stars as well as it is currently possible with the available methods.

2. Required stellar parameters

In order to correctly analyze the exoplanet parameters, the most important stellar parameters that are required are the mass and radii. Acquiring those makes it possible to estimate the average density, with the errors in the planetary parameters depending only on the errors in the actual measurements, and, the errors in the estimation of the stellar parameters. And here lie the crux. It can be shown (e.g. Rauer et al. 2014), that in order to be able to classify planets and draw reasonable conclusions from the bulk densities, one needs to determine the planetary radii to a precision of 2% and the masses to definitely better than 10% and preferably better than 5%. It is sometimes assumed that we know the mass-luminosity relation, both from measurements of Double-lined Eclipsing Spectroscopic Binary systems (SB2), and from theoretical modeling, well enough. The problem is that most stars searched for planets, either with radial velocities or with transits, are low-mass, low-luminosity objects. And the scatter on the empirical mass-luminosity relation is greatest for stars of masses less than one solar mass. Which is of course the great majority. This scatter is probably, in part, due to age effects in the star, as it gets brighter already on the main sequence. The Sun has brightened by an estimated 30% so far during its main sequence life and will brighten by more during the rest of its main sequence phase of almost 10^{10} years, while it only loses a negligible amount of mass through the solar wind during the same time. The solution that has been put forward is to use the new method of asteroseismology (developed to a large extent due to the observations of CoRoT). By observing the power spectrum of acoustically induced variations in the light output of the star, it is possible to determine the current mass and radii of the star with the required precision. This has been amply demonstrated with the CoRoT and Kepler space missions, but unfortunately the technology for making observations of the power spectrum of exoplanetary host stars in bulk is still, about 10 years away with the launch of the PLATO spacecraft. Instead we are required to analyze the optical spectrum of the host star with the highest possible precision. But it is not enough to determine the mass and radii. The rotational velocity of the star, as well as the macro- and micro-turbulent velocities, is important − particularly in the context of the activity and age of the star. And the age of the star is of course required when we want to say something about the evolutionary state of the planetary system in question. As an example, one can point out that the distribution of planets in most systems requires the age of the system in order to account for migration or the stability of the orbits. In order to study the star with available tools, there are essentially only two: photometry and spectroscopy. Using a photometric method is in practice the same as obtaining a very low-resolution spectrum. Photometry depends on introducing carefully designed and measured filters into the ray path which would allow only specific parts of the stellar spectrum to impinge on the detector. The flux through different filters can be subtracted from each other to create color indexes, which can be shown to depend on certain of the fundamental stellar parameters such as $T_{\rm eff}$, log g, the interstellar extinction and the metallicity. It is a very coarse method, with large individual errors and best useful for evaluating large statistical materials or for creating e.g. input catalogues. Spectroscopy provides very high resolution and detail. There are literally millions of atomic and molecular lines superposed on the continuum, as well as the shape of the continuum, that can be used to determine the fundamental parameters, including the stellar velocities. The drawback is that one achieves the best results when one is observing individual objects, with large telescopes, for a long time. Fiber-fed spectrographs can be made multi-tasking (i.e. a large number of fibres can be feeding the same spectrograph simultaneously), but then the resolution will be limited due to the finite size of the detector.

3. Analysing the spectrum

There are several ways and means of analyzing the optical spectrum of an exoplanetary host star, but they all have in common that one has to start with a high quality (S/N and spectral resolution) spectrum. From this we can discern the stellar velocities, both the projected rotational and turbulent velocities, the effective temperature, log g, the [Fe/H], and other abundances. From the transiting light curve, we also get an independent estimate of the stellar density and log g. From these parameters we can derive the masses and radii and put the star onto model evolutionary tracks and estimate the age, albeit with very large error bars. We also get an estimate of the stellar activity (which can also be used under certain circumstances as an age index). The presence of e.g. Lithium in the spectrum can either indicate youth, or in hotter solar type stars be a way to determine the exact spectral class. As mentioned above, the idea is to take the observed spectrum, normalize it and then compare it to our models and eventually find the model that is most likely to represent reality. There is a large amount of parameters to fit, which on the one hand make the process complex, but on the other hand make it more robust in order to find a unique solution. One method is to use the equivalent width of metal lines. Three parameters are usually used as input to the process: the equivalent width (EW), the excitation potential, and the abundance of the metal in question. The EW is found from the spectrum, the excitation potential from atomic data and the abundance is derived through curve of growth analysis. Different atmospheric parameters produce different curves of growth and, by analyzing a large amount of different metal lines and excitation parameters, one can fit the abundance. This is the procedure used by the Versatile Wavelength Analysis (VWA) package (Bruntt et al. 2010), and which has automated the process and has been used for a number of CoRoT stars. One needs to start with the normalized spectrum and select several hundred (ideally) weak, unblended metal lines. Using a first guess of $T_{\rm eff}$, log g, [Fe/H] and the velocities $V_{\rm micro}$, $V_{\rm macro}$ and $v \sin i$, a synthetic spectrum is calculated, the equivalent width of the selected metal lines are calculated and fitted to the observed spectrum. After visual inspection and the discarding of complicated lines, a series of models is iteratively calculated and the results are minimized with respect to the observed spectrum. The other main approach is by fitting the whole spectrum, thus the actual shape of the calculated spectra to the observed and normalized spectrum. This is the method used by Spectroscopy Made Easy (SME; Valenti & Piskunov, 1996). SME calculates the spectral model using a grid of models (Kurucz 2005 or MARCS, Gustafsson et al. 2008). The SME utilizes automatic parameter optimization using a Levenberg-Marquardt minimization algorithm. Synthetic spectra are calculated on the fly by a built in spectrum synthesis code, for a set of global model parameters and specified spectral line data. Starting from the user-provided initial values, synthetic spectra are computed for small offsets in different directions for a subset of parameters defined to be “free”. The model atmospheres required for this are calculated through interpolating the grid of models mentioned above. SME allows one to choose which parameters to fit or to fix, or to solve for all the atmospheric parameters at the same time. Normally, one begins by separately fitting the wings of the profiles of one or more of the Balmer lines, and solving for $T_{\rm eff}$. The next step is to get an idea about the abundances, particularly [Fe/H] and the metal lines used for the determination of log g. Keeping the $T_{\rm eff}$ estimate and the abundances as fixed parameters, we then fit the spectrum of log g sensitive lines, especially the pressure-sensitive strong metal lines such as CaI at 6122 Å, 6162 Åand 6438 Å, the Mg Ib triplet at 5160−5185 ÅÅ, and/or the NaI D lines. After several fits with varying starting values, the standard deviation of the results gives the internal uncertainties on the derived parameters. Fixing some parameters, moreover, is helpful when the spectrum has a low S/N ratio. It has also been possible to determine the fundamental parameters of stars with large $v \sin i$ with SME such as e.g. CoRoT-11 (Gandolfi et al. 2010) that has a $v \sin i$ of 40 km s^{-1}. Further, we refer to Bruno (2015), Fridlund et al. (in prep.) and the individual CoRoT-papers for detail of the process of determining the stellar parameters. Here we, finally, only stress the two main problems with the spectral analysis.

4. The two problems

There are two major problems with both of these methods (VWA and SME). Both require spectra with high S/N to work well. This is especially true for the determination of log g where VWA requires the identification of a very large number of weak metal lines at high S/N, while SME has the problem of there being very few pressure sensitive metal lines found in the available parts of the spectrum. Furthermore, several of those lines, such as the Mg I triplet, are in regions where the continuum is depressed by large number of metal lines, making any determination of the log g based on them uncertain. The calculated value of log g is very sensitive both to $T_{\rm eff}$ and to the abundance of the particular metal. It is possible, in the individual case to determine log g to ±0.1 dex but a more realistic 1σ error is ±0.2 dex. The $T_{\rm eff}$ is easily determined for solar type star with temperatures between 4500 K and 7000 K, especially by fitting the wings of the Hα Balmer line (Hβ has depressed wings due to a large amount of metal lines and Hγ is usually not present in the Echelle spectra obtained with the spectrographs in question). The Hα line is usually found at or close to the edge of the Echelle order in the spectrographs used such as UVES, SOPHIE and HARPS. This is of course because Hα is uninteresting when determining radial velocities. Having Hα with its extremely broad (for $T_{\rm eff} > 5000$ K) wings make it difficult to determine the continuum exactly − particularly if the spectrum have poor S/N. Such errors can manifest themselves as errors in Teff of ±200 K or even larger. This has a strong impact on the determination of particularly the value of log g (e.g. Fuhrmann et al. 2011). There are exceptions. The FIES spectrograph at the Nordic Optical Telescope in La Palma have the Hα line well centered in the order where it is found, and tests have shown that in a well/exposed spectrum of a G0V star one can determine $T_{\rm eff}$ with a measurement error of ±70 K. In Table III.4.1 we present the $T_{\rm eff}$ as determined with several methods from very good (high S/N). It is clear that with such good material different methods give a good result. The original observations that are somewhat different were obtained using only one model instead of a complete grid of different models on which to iterate to a minimum fitting. One must always remember that the errors in this modelling does not include the errors due to the imperfections and assumptions present within the models themselves.

If one has a material obtained with a spectrograph that provides less accurate $T_{\rm eff}$, it may be profitable to initiate a separate program for the determination of the effective temperature alone using a suitable spectrograph (preferable a long slit spectrograph with representative resolution) that allows a good determination of this crucial parameter.

Table III.4.1. Effective temperature derivation for the first 9 CoRoT host stars. T_{eff} is derived using SME 4.43 with ATLAS12 models, SME 4.43 with MARCS models, the *VWA* method with MARCS models, and the T_{eff} from the original discovery paper.

Target	T_{eff} (K) ATLAS12	T_{eff} (K) MARCS	T_{eff} (K) VWA ion eq.	T_{eff} (orig.)	Orig. Source
CoRoT-1	6145 ± 75	6075 ± 75	6090 ± 80	5950 ± 150	Barge et al. (2008)
CoRoT-2	5330 ± 75	5300 ± 75	5580 ± 80	5450 ± 120	Alonso et al. (2008)
CoRoT-3	6575 ± 100	6575 ± 100	6600 ± 40	6740 ± 140	Deleuil et al. (2008)
CoRoT-4	5975 ± 100	5975 ± 100	6090 ± 50	6190 ± 60	Moutou et al. (2008)
CoRoT-5	6065 ± 100	5980 ± 100	6030 ± 50	6100 ± 65	Rauer et al. (2009)
CoRoT-6	6025 ± 100	6025 ± 100	6060 ± 50	6090 ± 70	Fridlund et al. (2010)
CoRoT-7	5290 ± 44	–	5297 ± 13	5275 ± 75	Léger et al. (2009)
CoRoT-8	4950 ± 100	5095 ± 100	5050 ± 50	5080 ± 80	Bordé et al. (2010)
CoRoT-9	5575 ± 100	5575 ± 100	5580 ± 70	5625 ± 80	Deeg et al. (2010)

5. A future evolution beyond CoRoT

As stated in the previous section, their are several problems with determining the fundamental stellar parameters from the spectrum of the host star, resulting in the physical parameters of the planet (s) having uncertainties large enough to obstruct comparisons with theoretical models. Some relief is expected from the Gaia catalogue to emerge in a few years since its improved distances for essentially all CoRoT and Kepler stars will provide a better value for T_{eff}. Nevertheless, the mass and radius of any host star not located in a suitable binary system will rely on evolutionary models. The age of the system will remain uncertain to a very high degree.

The solution to this and the methods that will allow exoplanetology turning into a true comparative science – allowing comparisons between different (types of) exosystems and even with our own Solar System – is to implement asteroseismology systematically. As has been proven unambiguously – first by CoRoT and then by Kepler asteroseismology can provide information about the host star that will allow ultimately the determination of the stellar host parameters to the required precision of a few percent (in the case of age maybe 10 or a few tens of percent), allowing exoplanet geology and atmospheric research to make the transition into detailed and individual science. All that is needed is the long and uninterrupted high precision photometric light curve of the host star in question. This is the basis for the PLATO M3 mission of ESA to be launched towards the middle of the next decade. For brighter stars (magnitude brighter than 11.5) reversing the asterseismological parameters will then give very high precision of, among other things, the stellar mass, radius and age.

When PLATO eventually flies, and very likely changes not only exoplanetology but also stellar physics and everything relating to these two topics, it should be recalled that this work started with the CoRoT mission. The little spacecraft that could do its job.

Acknowledgements. MF is grateful to MPIA in Heidelberg and to T. Henning who provided a research grant allowing him to stay in Heidelberg during 2015.

References

Alonso, R., Auvergne, M., Baglin, A., et al. 2008, A&A, 482, L21

Barge, P., Baglin, A., Auvergne, M., et al. 2008, A&A, 482, L17

Bonomo, A. S., Santerne, A., Alonso, R., et al. 2010, A&A, 520, A65

Bordé, P., Bouchy, F., Deleuil, M., et al. 2010, A&A, 520, A66

Bouchy, F., Deleuil, M., Guillot, T., et al. 2011, A&A, 525, A68

Bruno, G. 2015, Ph.D. Theses, LAM

Bruntt, H., Bedding, T. R., Quirion, P.-O., et al. 2010, MNRAS, 405, 1907

Cabrera, J., Bruntt, H., Ollivier, M., et al. 2010, A&A, 522, A110

Deeg, H. J., Moutou, C., Erikson, A., et al. 2010, Nature, 464, 384

Deleuil, M., Deeg, H.,J., Alonso, R., et al. 2008, A&A, 491, 889

Fridlund, M., Hebrard, G., Alonso, R., et al. 2010, A&A, 512, A14

Fuhrmann, K., Chini, R., Hoffmeister, V. H., et al. 2011, MNRAS, 411, 2311

Gandolfi, D., Hebrard, G., Alonso, R., et al. 2010, A&A, 524, A55

Gillon, M., Hatzes, A., Csizmadia, Sz., et al. 2010, A&A, 520, A97

Gustafsson, B., Edvardsson, B., Eriksson, K., et al. 2008, A&A, 486, 951

Kurucz, R. L., 2005, MSAIS, 8, 14

Léger, A., Rouan, D., Schneider, J., et al. 2009, A&A, 506, 287

Moutou, C., Bruntt, H., Guillot, T., et al. 2008, A&A, 488, L47

Rauer, H., Queloz, D., Csizmadia, Sz., et al. 2009, A&A, 506, 281

Rauer, H., Catala, C., Aerts, C., et al. 2014, ExA, 38, 249

Tingley, B., Endl, M., Gazzano, J.-C., et al. 2011, A&A, 528, 97

Valenti, J. A., Piskunov, N., et al. 1996, A&AS, 118, 595

The CoRoT Legacy Book
© The authors, 2016
DOI: 10.1051/978-2-7598-1876-1.c035

III.5

Stellar classification in CoRoT faint stars fields

C. Damiani[1, 2], J.-C. Meunier[1], C. Moutou[1], M. Deleuil[1], and F. Baudin[2]

[1] Aix-Marseille Université, CNRS, Laboratoire d'Astrophysique de Marseille, UMR 7326, 13388, Marseille, France
e-mail: cilia.damiani@ias.u-psud.fr
[2] Université Paris-Sud, CNRS, Institut d'Astrophysique Spatiale, UMR8617, 91405 Orsay Cedex, France

1. Introduction

The extremely precise photometric time-series provided by the faint stars channel of the CoRoT mission serve a very large number of scientific objectives. In addition to major contributions in the faint stars field, let us recall also that the CoRoT faint stars chanel has allowed to produce important results in stellar physics (see the numerous contributions in this book). For either the core or additional programs, both the selection of the targets and the exploitation of the light curve require at least a basic knowledge of the targets, such as their colours or spectral type and luminosity class.

This is one of the reasons why the Exodat (Deleuil et al. 2009) database was built. Its prime objective was to provide position, colours and stellar classification for the stars in the observable zones of CoRoT, the so-called "CoRoT eyes". Exodat is an information system and a database that gathers an extended body of data of various origin, and delivers it to the community through a user friendly web interface[1](Agneray et al. 2014). It contains data for more than 51 million stars providing information for both the potential targets of the exoplanet program (with $11 \leq r \leq 16$), and also the fainter background sources. The later are needed in order to estimate the targets' level of light contamination. To help the selection of the targets and the preparation of the observations, a first order stellar classification (FOSC) was conducted using broad-band multi-colour photometry available through Exodat. Any detailed analysis of targets of particular interest would require complementary observations for a better characterisation. Indeed it has been done on a target to target basis, especially for planet hosting stars, but also on more consequent samples (see Sect. 4). Overall, no more than 15% of the targets observed over the mission lifetime were the object of complementary observations. Notwithstanding, stellar parameters are essential to the scientific exploitation of the CoRoT light curves. For the vast majority of targets, to this day, and at least until the third data release of the GAIA mission, scheduled in late 2017/2018[2], the only source of information concerning the spectral classification of all stars observed in the exoplanet channel is Exodat.

A final refined treatment of the light curves has been recently applied to the complete CoRoT data set and a new and ultimate version of N2 products has been released. The spectral classification has also been revised for this last version, taking into account the particularities of each CoRoT runs. While an overview of the FOSC method is given in Deleuil et al. (2009), they do not provide an estimation of the reliability of the final results. In this paper, we give a thorough description of the method in Sect. 2. In Sect. 3 we give the statistical error expected from the FOSC as estimated using a synthetic survey of the Milky Way. In Sect. 4 we compare our results to the classification obtained by spectroscopic campaigns. We give our conclusions in Sect. 5.

2. Classification method

The FOSC method is adapted from the automatic classification technique developed by Hatziminaoglou et al. (2002) for celestial objects classification and quasar identification. It consists of fitting the apparent broad-band photometry magnitudes of the target to the spectral energy distribution (SED) of template stars of different spectral types. The templates are taken from the Pickles stellar spectral flux library UVKLIB (Pickles 1998). This library encompasses spectral types from O to M and luminosity classes from supergiants to dwarfs with good completeness and uniformity. To avoid introducing too many degeneracies, only solar abundance templates are used in the FOSC. Hence, the classification is done over 106 different spectral types including dwarfs, subgiants, giants, bright giants and supergiants with effective temperatures ($T_{\rm eff}$) comprised between $3.398 \leq \log T_{\rm eff} \leq 4.600$. There are 36 templates for dwarf stars, which roughly correspond to a sampling of about one template every two subclasses in the main-sequence. Templates of extragalactic sources, white dwarfs and brown dwarfs are not used in the FOSC because it is expected that the number of such objects in the considered range of magnitudes and galactic regions is small enough to be safely neglected. Templates of binary stars are not used neither despite the fact that the proportion of binary stars in the sample is expected to be significant. Again, this limitation is conceded to avoid too many degeneracies, because broad-band photometry does not allow to clearly distinguish the binary nature of the target. If the spectral

---

[1] `http://cesam.lam.fr/exodat/`
[2] see `http://www.cosmos.esa.int/web/gaia/release`

type of the two components are similar, the resulting spectral classification would give the same result when using the template of a single star, since it is insensitive to the absolute magnitude of the target. On the other hand, if the spectral type of the two components are very different, the colours of the binary would largely be undistinguishable from the colours of the brightest component, due to the extremely different luminosities of the two components in the considered wavelength range. In those cases, the spectral type of a binary determined with the FOSC method will thus correspond to the one of the primary star. In intermediate cases, we expect that the spectral type determination will be degraded when the target is a binary. However to ensure the reliability of the result, the binary nature of the target should be known before attempting the classification. This was not the case prior to the mission, but the results of the planetary transit search in CoRoTlight curves has identified a number of eclipsing binaries. In this case a second order classification, suited for binary targets, would produce better results. This is out of the scope of this paper, and will be tackled in a dedicated study of CoRoT binaries.

To take into account the effect of interstellar absorption, the SEDs of the UVKLIB library are used to produce a library of reddened templates. They were created for a range of colour excess from $E_{B-V} = 0$ to $E_{B-V} = 4$ in steps of 0.05. The extinction law is taken from Fitzpatrick (1999) using the average value of the ratio of total to selective extinction $R_V = \frac{A_V}{E_{B-V}} = 3.1$. The actual value of R_V does not matter here given that in the wavelength range considered in this study (350 nm $\leq \lambda \leq 2.2\,\mu$m), the extinction curve is insensitive to R_V variations. For a given value of the colour excess E_{B-V}, the reddened flux distribution is then multiplied with the appropriate relative spectral response curves of the different bands.

The bands used are Harris B and V and Sloan-Gunn r' and i' for about two thirds of the targets, RGO U for only 3% of them, and 2MASS J, H, and K_s bands for almost all of them (98%). We will refer to this set of magnitude as the "Obscat" catalogue. When the B, r' or i' bands are not available, the PPMXL catalogue (Roeser et al. 2010) was used instead. It combines the USNO-B1.0 blue, red and infrared magnitudes with the 2MASS magnitudes and provides accurate position and mean motion in the ICRS. The photometric calibration of the USNO-B1.0 catalogue is of marginal quality. As detailed in Monet et al. (2003), the root of the problem is the lack of suitable faint photometric standards. Moreover, the original catalogue does not provide an error for each individual measurement, but it is estimated to have an accuracy of about 0.3 mag. Acknowledging that the magnitudes from USNO-B1.0 should be used with care, we used a relative error of 3% for all filters. Consequently, the quality of the fit when using USNO-B1.0 photometry is expected to be degraded. This concerns about a third of all the CoRoT targets.

Integrating the transmitted flux over the filter's wavelength range provides the reddened template fluxes in the different bands. It was chosen to use magnitudes in the Vega system, and observed magnitudes are converted to this system if required. The spectral energy distribution of α Lyrae (Vega) was treated in the same way to obtain the reference flux in every band.

For each target, the apparent magnitudes are converted to fluxes which are normalised to the flux in the band where the photometric error is the smallest. The photometric error ϵ_i is also converted to an error in flux σ_i, taking into account the error on the zero point ϵ_{0i} for the corresponding filter i, using the relationship[3]

$$\sigma_i = \frac{2.3}{2.5}\sqrt{\epsilon_i^2 + \epsilon_{0i}^2}\,. \tag{1}$$

The observed flux is then confronted with the computed fluxes for all the reddened templates by computing

$$\chi_j^2(E_{B-V}) = \sum_{i=1}^{n} \frac{\left(F^i_{\text{obs}} - F^i_{\text{mod}_\text{j}}(E_{B-V})\right)^2}{\sigma_i^2} \tag{2}$$

where F^i_{obs} is the observed flux in the i band, $F^i_{\text{mod}_\text{j}}(E_{B-V})$ is the flux in the same band for the template j reddened with a colour excess E_{B-V}, σ_i is the estimated error of the observed flux in this band and n is the number of bands that are used.

Finding the minimum χ^2 then leads to the attribution of a spectral type and a colour excess that best reproduce the observed magnitudes. The reduced χ^2 is used as quality index QI

$$\text{QI} = \chi^2/(\text{n} - 3). \tag{3}$$

As already pointed out by Hatziminaoglou et al. (2002), a classification scheme based on the χ^2 technique may lead to degeneracies, which are class-dependent. Multiple minima may occur in the parameter space and such degeneracies can only be solved by including additional information in the classification procedure. In the following we describe the strategy used to avoid the main degeneracies.

2.1. Dwarfs and giants degeneracy

The effect of luminosity on stellar energy distributions is often seen in some metallic lines that are usually shallow and/or narrow. It is thus very difficult to distinguish dwarf and giant stars when adjusting SEDs to broad-band photometry only. To avoid strong degeneracies with the FOSC method, we first use a preselection tool of the luminosity class based on a colour-magnitude diagram (CMD) before the identification of the best-fitting stellar template. For each observed field, the J vs. $J - K$ CMD plane is divided in two regions defined by a linear function that is adapted to the mean extinction of the field. Stars are hitherto identified as dwarfs or giants, and their subsequent classification is done separately. The method is particularly reliable close to the Galactic plane where the typical extinction is enhancing the gap between the bluer dwarfs and redder giants. Specifically, the bluer part of the diagram should not contain any giants, while the redder may well contain cool dwarfs, especially at faint magnitudes (see also Sect. 3). Following this separation, the targets are then distributed to two separate pipelines: one only uses "dwarfs" templates, which includes luminosity classes IV and V, while the other only uses "giants" templates, which includes luminosity

---

[3] The numerical factor in the the right-hand-side of Eq. (1) comes from the Taylor expansion of the decimal logarithm used in the computations of magnitudes

classes I, II, and III. If the 2MASS magnitudes are not available, the classification is done using both dwarf and giant templates. In some rare instances, a particular target may have been observed by CoRoT in 2 different runs (or more) and it might result in different pre-classifications, because in regions of steep extinction gradients, the mean extinction may be different even for overlapping runs. In this case, the classification that has the minimum χ^2 is selected and the corresponding spectral type and luminosity class are adopted for all the runs.

2.2. Interstellar reddening

The main problem one faces when dealing with stellar classification is the role of interstellar extinction, which modifies the observed colours of stars. This problem is particularly important in our study, since the CoRoT fields are located within a few degrees from the Galactic Plane. A distant, strongly reddened early-type star could be identified as a closer cooler (intrinsically redder) star. One way to handle this would be to use an independent measurement of the extinction along the line of sight and set it as fixed parameter in the fitting procedure. However, this would require to know the distance to the target, which is not the case here. Consequently, we let the reddening be a free parameter in the classification scheme, but limit it within a reasonable range. Dust emission is one of the major foregrounds hampering the study of the cosmic microwave background (CMB). Thus one of the products associated with the 2013 release of data from the Planck mission[4] was a new parametrisation of dust emission that covers the whole sky, based on data from the High Frequency Instrument (HFI) (Planck Collaboration et al. 2014). We use the τ_{353} maps to constrain the range of E_{B-V} in our stellar classification. For every run, the region of the CoRoT CCD was extracted from the τ_{353} maps, and converted to E_{B-V} using the scaling factor $E_{B-V}/\tau_{353} = 1.49 \times 10^4$ (Planck Collaboration et al. 2014). We must stress that adopting the scaling factor estimated using the correlations with quasars in diffuse directions could systematically overestimate E_{B-V} in denser regions. Thus we took the value of the 90% percentile of the distribution of E_{B-V} for a given run to set the value of the corresponding upper bound of the range of E_{B-V} values allowed in the fitting procedure. For two runs in the centre direction located near dense clouds (SRc01 and LRc03), this value was too high to produce a significant constraint for the fitting procedure, and we set the upper bound to the more reasonable value of $E_{B-V} \leq 4$.

3. Comparison with synthetic galactic populations

Given that the method is based on χ^2 minimisation, it is expected that the greater source of uncertainty will come from the intrinsic degeneracy between spectral type and reddening. However, even if we set the reddening to its actual values, the intrinsic limitations of the method (such as the sampling in effective temperature, in luminosity classes, or overlooking metallicity) must introduce systematic errors. In order to evaluate the systematics of the method over the entire space of parameter covered by the classification we used the Padova isochrones (Marigo et al. 2008). We computed a synthetic catalogue containing stars with any combination of spectral type and colour excess, and that is not limited by the selection of targets introduced by the instrument. This shows that in favourable conditions, the FOSC can return a spectral type that is correct to about a few subclasses. However, if the magnitudes are affected by severe reddening, or if some bands are missing, the accuracy of the result can be severely limited, especially for early-type stars lacking a measurement of U.

Stars observed by CoRoT are limited in apparent magnitudes by the instrumental capacities. In this case, it is reasonable to expect that reddening and spectral type will be correlated to some extent. Moreover, the magnitudes used for the FOSC come from several catalogues, with heterogeneous properties. Thus to estimate the average error made on the spectral type of CoRoT targets, it is necessary to include those effects into the synthetic sample. The spatial distribution of CoRoT targets spans over a wide area and different points have very different galactic longitudes, latitudes and interstellar extinction. We used the Galaxia code (Sharma et al. 2011) to generate synthetic galactic populations in each of the directions observed during the 26 runs of CoRoT. Galaxia is a publicly available code based on the Besanon model of the Galaxy (Robin et al. 2003) that is particularly suited to generate synthetic surveys over wide areas. We made no modification to the source code and use it as it is described in Sharma et al. (2011). The synthetic model of galaxy produces a population of stars that has the same statistical properties as stars of the Milky way in terms of distance to the sun, age, mass and heavy elements distribution, as a function of the pointing direction. The only major unknown is interstellar absorption. This may induce systematic differences in stellar properties because the observed sample is magnitude limited. For each run, we use the CCD footprints of CoRoT to select in the model the portion of the sky that exactly corresponds to the observed area and we adjust the synthetic magnitudes to the observed ones. This is done by introducing a correction factor that scales the synthetic E_{B-V} produced by Galaxia. This factor is obtained by minimising the difference between the synthetic distribution of $J - K$ and the ones of the input catalogue for the observed field. Next, the errors on synthetic magnitudes are generated to reproduce the systematics and random behaviour of the errors in the input catalogue. The magnitudes and errors of the synthetic catalogue is then confronted to the input catalogue by performing a Kolmogorov-Smirnov test. In all instances, the null hypothesis of the two catalogues being drawn form the same population cannot be rejected at the 0.5% level.

3.1. Luminosity class

Here, we will not attempt to assess the validity of the FOSC results in terms of individual luminosity classes, but we will examine the basic distinction between dwarfs and giants. As previously described, this is not in itself a result of the χ^2 minimisation of the FOSC, but it is based on the position of the target in a colour-magnitude diagram. The result of this classification is binary, with stars being either dwarfs or

---

[4] `http://www.esa.int/Planck`

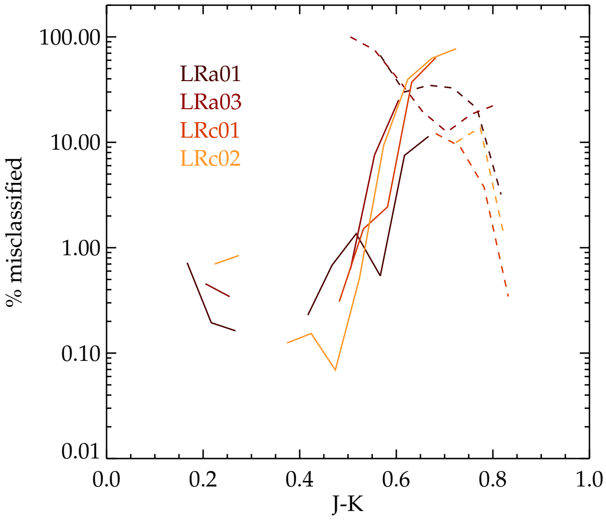

Fig. III.5.1. Percentage of misclassified targets as a function of $J-K$ for different runs. The percentage of dwarfs (stars with $\log g \geq 3.5$) wrongly classified as giants (luminosity class I, II or III) is given in solid lines, and the percentage of giants (stars with $\log g > 3.5$) misclassified as dwarfs (luminosity class IV or V) is given in dotted lines. The colours of the lines correspond to the different runs, as indicated on the plot.

giants. The significance of this classification can be assessed using the synthetic catalogue by producing a ($J-K$, J) CMD and apply the selection criterion used for the targets. We can then compare the classification as dwarf of giants to the $\log g$ of the synthetic stars. Results are displayed in Fig. III.5.1 for a few representative runs.

We see that overall, the classification is more often wrong for giants than for dwarfs, as expected. For $J-K < 0.5$ and $J-K > 0.8$, there are less than 1% of the stars in a class that are misclassified, because there is no overlap of the two populations in this part of the diagram. In this case, the luminosity classification can be considered correct to a very high level of significance. The greater uncertainty evidently lies within the stars that have a $J-K$ close to the criterion used for the selection, some of which being almost certainly misclassified. However, due to the gap between dwarfs and giants in a ($J-K$, J) CMD, this actually represents a very small percentage of the total sample. Integrating over the values of $J-K$ yields between 1 and 10% of the misclassified stars in the dwarf sample. Respectively, between 3 and 15% of stars classified as giants are actually dwarfs. Overall, the percentage of wrongly classified stars in the entire sample is less than 7%. Note finally that when the J or K magnitude, or both, are missing, the preselection between dwarfs and giants can not be performed. In this case, the FOSC is run using both dwarfs and giants templates, and the luminosity class is thus decided by the χ^2 minimisation. This results in severely degraded performances, with 10 to 50% of the stars classified as dwarfs that are actually giants, and from 30 to 65% of stars misclassified stars in giants, depending on mean extinction. Moreover, the spectral classification is also affected, with typical errors multiplied a few times. Extreme caution should be taken when dealing with those few stars for which infrared magnitudes are unavailable. Let us stress again that this concerns only a very small proportion of the whole sample of CoRoT/Exoplanet targets.

3.2. Effective temperature of CoRoT targets

The majority of targets have Obscat magnitudes, which produce a smaller uncertainty on the spectral type compared to what is obtained when using the lower qualitity USNO-B1.0 magnitudes. We have created a population representative of the whole sample by merging the catalogues obtained for the different runs, and performing the FOSC taking magnitudes from the two catalogues in proportion of what they are in the population of targets. The stars are randomly attributed to one or the other catalogue, and the process is repeated 100 times. Each time, the median of the relative error is computed. As a measure of the spread of the distribution of the relative error, we compute the difference between the values of the 15th percentile and the 85th, which we note 2σ. Then we take the average of those values found over the 100 trials. Overall, we find an average median absolute temperature difference $|\Delta T_{\rm eff}| = 533 \pm 6$ K for the whole sample of stars classified as dwarfs and $|\Delta T_{\rm eff}| = 280 \pm 3$ K for the whole sample of giant stars. The corresponding standard deviation is of about 925 ± 5 K for dwarfs and 304 ± 4 K for giants. This is the performance expected from classification methods using broad-band photometry. For example Farmer et al. (2013) give a median difference of 500 K for the dwarfs of the Kepler input catalogue, but they perform better for giants with a reported median $\Delta T_{\rm eff}$ of 50 K. This is probably due their use of different filters, and especially their custom D51 filter, which is sensitive to surface gravity (2011). Nevertheless, we can safely conclude that the spectral classification obtained by the FOSC method is generally good up to half a spectral class for the majority of CoRoT targets.

4. Comparison with spectroscopic data

To complement the statistical study presented in the previous section, we compare the result of the FOSC to the spectral type obtained by independent measurement such as mid or high-resolution spectroscopy. We have chosen, in the available literature, catalogues of spectral types containing a large number of targets and obtained with homogenous methods. As a result, we compare the FOSC with two different spectral catalogues. The first one contains the fundamental stellar parameters for 1127 stars in the LRa01, LRc01 and SRc01 CoRoT fields (Gazzano et al. 2010, hereafter Gaz10). The second one gives an estimation of the spectral type obtained for 11466 stars in the IRa01, LRa01, LRa02 and LRa06 fields (Sebastian et al. 2012; Guenther et al. 2012, hereafter jointly cited as SG12).

In terms of luminosity class, the agreement between the FOSC and spectral methods is very good for main-sequence stars. We find that more than 97% of stars classified as dwarfs are also attributed a $\log g \geq 3.5$ by Ga10, and 85% of dwarfs are also classified as such by SG12. On the other hand, there are only 75% of stars classified as giants by the FOSC that also have $\log g < 3.5$ from the Ga10 analysis and 70% that agree with the classification of SG12. This is a bit lower than what was estimated from the synthetic sample, for which the proportion of correctly classified giants was between 85 and 97 %, but still consistent within the uncertainty given by Ga10 and SG12.

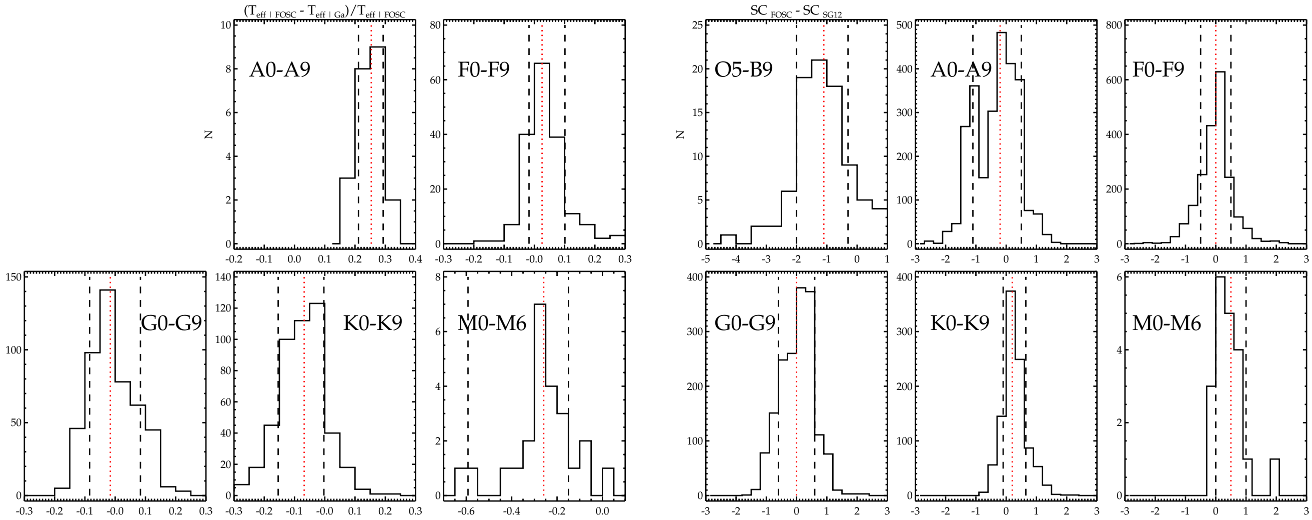

Fig. III.5.2. *Left*: distribution of relative temperature difference found by Ga10 and the FOSC. *Right*: distribution of difference in spectral class found by SG12 and the FOSC. The spectral class alphabetical scale has been converted to a numerical scale, attributing numbers from 0 to 8 to the classes O through M. Furthermore, the sub-class is converted as a decimal value. Each plot corresponds to a subsample selected by spectral class as determined by the FOSC and labeled on the plot. The vertical red dotted line shows the median value and the black dashed lines give the value of the 15th and 85th percentiles.

Regarding the spectral type, as can be seen in Fig. III.5.2, there are consistent systematics when comparing the FOSC to Ga10 and SG12. In both cases, early-types found by the FOSC tend to overestimate the effective temperature and later-types tend to underestimate it [5]. This trend was clearly found with the synthetic catalogue for hot stars. Except for M-type stars, the precision and accuracy of the FOSC are similar when estimated with the synthetic galactic population and with results from spectroscopy. Typically for late-type stars, the median error is less than about ±5% and the interval between the 15th and 85th percentiles has a spread of 10 to 20% in effective temperature, or about 1 spectral class. Those values are doubled for earlier type-stars. The comparison with Ga10 indicates that the uncertainty for the effective temperature of M-type stars is of the same order, but it is difficult to see if it is also the case when comparing with SG12 due to a very small sample size. It is possible that the greater error in the classification of M stars is related to their metallicity. We recommend exercising caution when using the sample of stars classified as M-type with the FOSC.

5. Conclusions

In this paper, we have described the procedure used to estimate the spectral type of CoRoT targets. This information is delivered together with the CoRoT data, and is available online through the Exodat database. Due to the faintness and the number of the targets, we use a method based on broad-band photometry. The photometry obtained during a mission-dedicated observational campaign are used whenever possible, but it was necessary to resort to poorer quality photometry for about a third of the targets. Using a synthetic catalogue, we were able to quantify how the performance of the classification are affected by the quality of the photometry. We also provide a statistical estimate of the precision and accuracy of the classification. We find consistent results by confronting the result of the FOSC to other independent estimates of the spectral type. We find that the luminosity class is estimated with great significance, and that the typical uncertainty on the spectral type given by the FOSC is of half a spectral class.

Our method cannot provide a precise error bar for individual CoRoT targets but is valid in a statistical way. Let us note that in particular there are two CoRoT runs pointed in directions of particularly high interstellar absorption (SRc01 and LRc03) where the validity of these results may be limited. However, the strong reddening in this case dims the magnitude of distant targets to a point where they exit the fainter magnitude limits of CoRoT targets. This effectively removes almost all giants of the target sample, and filters out the dwarfs that would be too severely reddened to ensure good performances of the FOSC. It can be expected thus that the performances of the FOSC on the remaining targets, not strongly reddened, would be equivalent to what is shown here. Finally, this study has made clear that interstellar absorption is the main source of uncertainty on the spectral type. The performances of the FOSC are significantly improved by limiting the range of possible values for the reddening. This was only performed in the latest version of the FOSC, and previous versions are expected to produce significantly more uncertain results.

Acknowledgements. CD acknowledges support by CNES grant 426808 and ANR (Agence Nationale de la Recherche, France) program IDEE (ANR-12-BS05-0008) "Interaction Des Étoiles et des Exoplanètes". This publication makes use of data products from the Two Micron All Sky Survey, which is a joint project of the University of Massachusetts and the Infrared Processing and Analysis Center/California Institute of Technology, funded by the National Aeronautics and Space Administration and the National Science Foundation. This work is based in part on services provided by the GAVO data center. This research has made use of the VizieR catalogue access tool, CDS, Strasbourg, France. This research uses observations obtained with Planck, an ESA

---

[5] This results in negative and positive spectral class difference respectively because they are sorted by order of decreasing effective temperature

science mission with instruments and contributions directly funded by ESA Member States, NASA, and Canada. The authors thank M.-A. Miville-Deschnes and N. Ysard for providing them with the *Planck* data. CD is grateful to P.-Y. Chabaud and F. Agneray for their work on the Exodat database and information system. She wishes to thank J.M. Almenara, S.C.C. Baros and R.F. Diaz and the CoRoT Exoplanet Science Team for helpful discussions.

References

Agneray, F., Moreau, C., Chabaud, P., Damiani, C., & Deleuil, M. 2014, in Astronomical Society of the Pacific Conference Series, Vol. 485, Astronomical Data Analysis Software and Systems XXIII, eds. N. Manset, & P. Forshay, 203

Bertelli, G., Bressan, A., Chiosi, C., Fagotto, F., & Nasi, E. 1994, A&AS, 106, 275

Deleuil, M., Meunier, J. C., Moutou, C., et al. 2009, AJ, 138, 649

Farmer, R., Kolb, U., & Norton, A. J. 2013, MNRAS, 433, 1133

Fitzpatrick, E. L. 1999, PASP, 111, 63

Gazzano, J.-C., de Laverny, P., Deleuil, M., et al. 2010, A&A, 523, A91

Girardi, L., Bressan, A., Bertelli, G., & Chiosi, C. 2000, A&AS, 141, 371

Guenther, E. W., Gandolfi, D., Sebastian, D., et al. 2012, A&A, 543, A125

Hatziminaoglou, E., Groenewegen, M. A. T., da Costa, L., et al. 2002, A&A, 384, 81

Marigo, P., & Girardi, L. 2007, A&A, 469, 239

Marigo, P., Girardi, L., Bressan, A., et al. 2008, A&A, 482, 883

Monet, D. G., Levine, S. E., Canzian, B., et al. 2003, AJ, 125, 984

Pickles, A. J. 1998, PASP, 110, 863

Planck Collaboration, Abergel, A., Ade, P. A. R., et al. 2014, A&A, 571, A11

Robin, A. C., Reylé, C., Derrière, S., & Picaud, S. 2003, A&A, 409, 523

Roeser, S., Demleitner, M., & Schilbach, E. 2010, AJ, 139, 2440

Sebastian, D., Guenther, E. W., Schaffenroth, V., et al. 2012, A&A, 541, A34

Sharma, S., Bland-Hawthorn, J., Johnston, K. V., & Binney, J. 2011, ApJ, 730, 3

Acknowledgements: The CoRoT space mission has been developed and operated by CNES, with the contribution of Austria, Belgium, Brazil, ESA, Germany, and Spain.

The CoRoT Legacy Book
© The authors, 2016
DOI: 10.1051/978-2-7598-1876-1.c036

III.6

Exploration of the brown dwarf regime around solar-like stars by CoRoT

Sz. Csizmadia[1]

DLR, Institut für Planetenforschung, 12489 Berlin, Rutherfordstr 2, Germany,
e-mail: szilard.csizmadia@dlr.de

1. Introduction

How shall we classify brown dwarfs? Are they gaseous giant planets as Hatzes & Rauer (2015) suggest, or are they stars as we can find in Trentham et al. (2001), or do they form a separate class of celestial objects in their own right?

Beyond the classification problem, their role is not well understood in planet formation, in evolution of planetary systems, in the chemical and dynamical evolution of the Galaxy; their impact on habitability is not well known both as host objects as well as additional objects in a planetary system; they can have moons whose habitability is not clear; and they are not studied well enough as planet hosts, although they can harbour planets up to about 5 Earth-masses (Payne & Lodato 2007).

When the minimum mass-limit to hold nuclear fusion was investigated some decades ago, it was found that a hydrogen gas sphere over 80 $M_{\rm jup}$ has enough mass to hold nuclear fusion – fusion of hydrogen, helium or heavier elements – for millions to billions of years, so they are called stars; below 13 $M_{\rm jup}$ we find the regime of planetary objects who exhibit no natural fusion at all. Between these limits sit brown dwarfs who fuse deuterium (D) or lithium (Li) to helium-3 and helium-4, respectively, but only for typically $\sim$0.1 Myrs which sounds a very episodic event in their life-cycle because after this phase they simply cool down and contract (Baraffe et al. 2003). Their evolution after this event is quite similar to the contraction of Jupiter-like gas planets. This is not surprising because they consist of mostly hydrogen-forming degenarate electron gas core inside and this structure, of course, resembles the structure of gas giant planets. The modern lower and upper limits for brown dwarfs are 11–16 $M_{\rm jup}$ depending in exact internal chemical composition (Spiegel et al. 2011) and 75–80 $M_{\rm jup}$ (Baraffe et al. 2002), respectively.

The number of known brown dwarfs is over 2200 and more than 400 are in binary systems, the rest are single (Johnston 2015). Only 66 brown dwarfs orbit their host stars on closer orbit than 2 au (65 are listed in Ma & Ge 2014 and we extended their list with CoRoT-33b, see Csizmadia et al. 2015). Only 12 or 13 transiting bona fide brown dwarfs are known (Table III.6.1), depending on how we count the status of KOI-189b whose mass is 78 ± 5 Jupiter-masses, so it is at the brown dwarf – star boundary. There are at least two eclipsing binary systems known in which two brown dwarfs orbit each other (see Table III.6.1). At least one eclipsing binary system is known where a brown dwarf orbits an M-dwarf (NLTT 41135Ab, Irwin et al. 2010). The remaining eclipsing brown dwarfs orbit solar-like stars (defined as main sequence or just slightly evolved FGK stars). For the study of their evolution, internal structure and impacts in the aforementioned issues we need very precise and model-independent mass, radius, luminosity and chemical composition values. Transiting systems can provide mass and radius with good precision and therefore they are important cases.

Here we summarize the contribution of CoRoT to the development of our knowledge of brown dwarfs, especially of those which are in binary systems around solar-like stars.

2. Brown dwarfs found by CoRoT

CoRoT has reported three brown dwarf discoveries. This is comparable to the four brown dwarfs detected by Kepler (see Table III.6.1) since both mission observed about the same number of stars (ca. 150,000) but for different time-intervals (30–150 days vs four years). Notice that the detection bias for Jupiter-sized objects are the same at short periods and in this size-range. Therefore it is not surprising that the derived brown dwarf occurence rates were found similar by both space missions (Csizmadia et al. 2015; Santerne et al. 2015). Hereafter we discuss the individual cases one by one and in the next section we concentrate on the occurence rates.

2.1. CoRoT-3b: the first habitant of the brown dwarf desert

Brown dwarfs, as companion objects in binary systems, exhibit a much smaller occurence rate than stars and planets

Table III.6.1. Basic data of known transiting brown dwarfs. ρ is the mean density of the brown dwarf component. Below the line one can find the questionable systems. Periods are truncated after the third decimal place. This table is an extended and updated version of the one published in Csizmadia et al. (2015) © A&A.

Name	Mag	$M_{\rm star}/M_\odot$	$R_{\rm star}/R_\odot$	$T_{\rm star}$ [K]	[Fe/H]	P (days)	e	$M_{\rm BD}/M_{\rm Jup}$	$R_{\rm BD}/R_{\rm Jup}$	ρ [g/cm^3]	Ref.
2M0535-05a[a]	19.21R					9.779	0.3225 ± 0.0060	56.7 ± 4.8	6.5 ± 0.33	0.26 ± 0.06	1
2M0535-05b[a]						9.779	0.3225 ± 0.0060	35.6 ± 2.8	5.0 ± 0.25	0.35 ± 0.08	1
CoRoT-3b	13.29V	1.37 ± 0.09	1.56 ± 0.09	6740 ± 140	-0.02 ± 0.06^b	4.256	0.0	21.66 ± 1.0	1.01 ± 0.07	26.4 ± 5.6	2
CoRoT-15b	15.4R	1.32 ± 0.12	$1.46^{+0.31}_{-0.14}$	6350 ± 200	$+0.1 \pm 0.2$	3.060	0	63.3 ± 4.1	$1.12^{+0.30}_{-0.15}$	59 ± 29	3
CoRoT-33b	14.25R	0.86 ± 0.04	$0.94^{0.14}_{-0.08}$	5225 ± 80	$+0.44 \pm 0.10$	5.819	0.0700 ± 0.0016	$59.0^{+1.8}_{-1.7}$	1.10 ± 0.53	55 ± 27	4
KELT-1b	10.63V	1.335 ± 0.063	$1.471^{+0.045}_{-0.035}$	6516 ± 49	$+0.052 \pm 0.079$	1.217	$0.01^{+0.01}_{-0.007}$	27.38 ± 0.93	$1.116^{+0.038}_{-0.029}$	$24.5^{1.5}_{-2.1}$	5
Kepler-39b[c]	14.43R	$1.10^{+0.07}_{-0.06}$	$1.39^{+0.11}_{-0.10}$	6260 ± 140	-0.29 ± 0.10	21.087	$0.121^{+0.022}_{-0.023}$	$18.00^{+0.93}_{-0.91}$	$1.22^{+0.12}_{-0.10}$	$12.40^{+3.2}_{-2.6}$	6
Kepler-39b[c]		$1.29^{+0.06}_{-0.07}$	1.40 ± 0.10	6350 ± 100	$+0.10 \pm 0.14$	21.087	0.112 ± 0.057	$20.1^{+1.3}_{-1.2}$	$1.24^{+0.09}_{-0.10}$	$13.0^{+3.0}_{-2.2}$	7
KOI-189b[d]	12.29K	0.764 ± 0.051	0.733 ± 0.017	4952 ± 40	-0.07 ± 0.12	30.360	0.2746 ± 0.0037	78.0 ± 3.4	0.998 ± 0.023	97.3 ± 4.1	8
KOI-205b	14.47i	0.925 ± 0.033	0.841 ± 0.020	5237 ± 60	$+0.14 \pm 0.12$	11.720	<0.031	39.9 ± 1.0	0.807 ± 0.022	75.6 ± 5.2	9
KOI-205b		$0.96^{+0.03}_{-0.04}$	0.87 ± 0.020	5400 ± 75	$+0.18 \pm 0.12$	11.720	<0.015	$40.8^{=1.1}_{-1.5}$	0.82 ± 0.02	$90.9^{+7.2}_{6.8}$	7
KOI-415b	12.66K	0.94 ± 0.06	$1.15^{+0.15}_{-0.10}$	5810 ± 80	-0.24 ± 0.11	166.788	0.698 ± 0.002	62.14 ± 2.69	$0.79^{+0.12}_{-0.07}$	$157.4^{+51.4}_{-52.3}$	10
LHS 6343C[e]	13.88V	0.370 ± 0.009	0.378 ± 0.008	3130 ± 20	$+0.04 \pm 0.08$	12.713	0.056 ± 0.032	62.7 ± 2.4	0.833 ± 0.021	109 ± 8	11
LHS 6343C[e]		0.381 ± 0.019	0.380 ± 0.007	3431 ± 21	$+0.03 \pm 0.26$	12.713	0.030 ± 0.002	64.6 ± 2.1	0.798 ± 0.014	170 ± 5	17
WASP-30b	11.91V	1.166 ± 0.026	1.295 ± 0.019	6201 ± 97	-0.08 ± 0.10	4.156	0	60.96 ± 0.89	0.889 ± 0.021	107.6 ± 1.1	12
NLTT 41135b	8.44V	$0.188^{0.026}_{0.022}$	0.21 ± 0.015	3230 ± 130	0.0	2.889	n/a	33.7 ± 2.8	$1.13^{+0.27}_{-0.17}$	29^{+23}_{-15}	14
EPIC 2038a[i]						4.451	0.3227 ± 0.0042	23.22 ± 0.47	2.75 ± 0.05	1.38 ± 0.08	18
EPIC 2038b[i]						4.451	0.3227 ± 0.0042	25.79 ± 0.58	2.485 ± 0.004	2.09 ± 0.07	18
1SWASP J1407b[f]	12.4V	0.9	0.99 ± 0.11	4400^{+100}_{-200}	n/a	3725 ± 900	n/a	20 ± 6	n/a	n/a	13
Kepler-27c[g]	n/a	0.65 ± 0.16	0.59 ± 0.15	5400 ± 60	0.41 ± 0.04	31.330	n/a	$<13.8^h$	0.44	n/a	15
Kepler-53b[g]	16.0V	0.89	0.98	5858	n/a	18.648	n/a	$<18.41^h$	0.26	n/a	16
Kepler-53c[g]	16.0V	0.89	0.98	5858	n/a	38.558	n/a	$<15.74^h$	0.28	n/a	16
Kepler-57b[g]	15.5V	0.83	0.73	5145	n/a	5.729	n/a	$<18.86^h$	0.195	n/a	16

Notes. (a) 2M0535-05 is an extreme young eclipsing system in which two brown dwarfs orbit each other. Identical to V2384 Orionis. (b) [M/H] value is reported in the reference. Notice that $[M/H] \approxeq [Fe/H]$; we did not convert the inhomogeneous [Fe/H] to the same scale. (c) Aka KOI-423b. (d) Díaz et al. (2014) concluded that KOI-189b can be either a high-mass brown dwarf or a very low mass star, too, therefore its status is uncertain. (e) the brown dwarf orbits companion A of a binary system, and data of the component A is given here. Star B has $M = 0.30 \pm 0.01 M_\odot$, $T_{\rm eff} = 3030 \pm 30$ K (Johnson et al. 2011). (f) The host star is young (16 Myr) and surrounded by a multiring-structured (protoplanetary?) disc, see Mamajek et al. (2012). (g) Masses are TTV masses, not RV. (h) Upper limit. (i) Full name is EPIC 203 868 608. Similar system to 2M0535-05: two brown dwarfs orbit each other.

References. 1: Stassun, Mathieu & Valenti (2006); 2M0535-05 2: Deleuil et al. (2008), 3: Bouchy et al. (2011a), 4: Csizmadia et al. (2015) 5: Siverd et al. (2012), 6: Bouchy et al. (2011b), 7: Bonomo et al. (2015), 8: Díaz et al. (2014), 9: Díaz et al. (2013), 10: Moutou et al. (2013), 11: Johnson et al. (2011), 12: Anderson et al. (2011) 13: Kenworthy et al. (2014) 14: Irwin et al. (2010) 15: Steffen et al. (2012) 16: Steffen et al. (2013) 17: Montet et al. (2015) 18: David et al. (2015)

and this is called the “brown dwarf desert”. It was found and confirmed by the radial velocity method (Marcy & Butler 2000; Lafrenière et al. 2007; Patel et al. 2007; Wittenmyer et al. 2009; Sahlmann et al. 2011), as well as by adaptive optics direct imaging (Metchev & Hillenbrand 2009).

The discovery of CoRoT-3b definitely means a breakthrough and a significant milestone in brown dwarf research (Deleuil et al. 2008). It was the first object in the brown dwarf desert whose mass and radius were measured from its transiting nature. It was also a surprise because nobody expected the existence of a brown dwarf so close – only 7.8 stellar-radii – to a solar-like star ($P_{orb} = 4.26$ days) because radial velocity surveys did not detect any similar object before the discovery of CoRoT-3b (only two suspected objects between a minimum mass of 10 and 20 Jupiter-masses were known at that time, see Deleuil et al. 2008). Therefore it was not clear then, that CoRoT-3b is a brown dwarf or a “super-planet”. A super-planet could be formed via core-accretion whose mass can be up to 25 $M_{\rm jup}$ without deuterium-burning or such a high-mass object can be formed via collision of several smaller planetesimals or planets (Deleuil et al. 2008 and references therein). The origin of CoRoT-3b is still under debate. Notice that model calculations of Mordasini et al. (2009) predict that high mass planets and brown dwarfs can form up to 40 $M_{\rm jup}$ via core-accretion but none of these objects get closer than 1 au to their host star (cf. Fig. 9 of Mordasini et al. 2009). Although Armitage & Bonnell (2002) proposed a very effective migration process for brown dwarfs, it is questionable that it is really so effective that the majority of them are engulfed by their host stars and this is the cause of the rarity of close-in brown dwarfs. Therefore, if CoRoT-3b ($\sim$22 $M_{\rm jup}$) and NLTT 41135b ($\sim$34 $M_{\rm jup}$) formed via core-accretion, then it is an intriguing question how they moved so close to their host stars.

At the time of the detection of CoRoT-3b, the authors thought that this object confirms the suspicion that “transiting giant planets ($M > 4\ M_{\rm jup}$) can be found preferentially around more massive stars than the Sun” (Deleuil et al. 2008). The discovery of NLTT 41135b, a $\sim 34 M_{\rm jup}$ gaseous giant planet (or a brown dwarf) around an M-dwarf is a remarkable counter-example (Irwin et al. 2010).

2.2. CoRoT-15b, an oversized brown dwarf

CoRoT-15b was the second detected transiting brown dwarf (Bouchy et al. 2011a). Its most exciting feature is its high radius relative to its mass ($1.12^{+0.30}_{-0.15}\ R_{\rm jup}$, a mass of $63.3 \pm 4.1\ M_{\rm jup}$). Notice that brown dwarfs contract slowly until the equilibrium size in most of their lifetime: but at the beginning they can have as large radius as 4–5 Jupiter radii, but at the age of the Universe and at the mass of CoRoT-15b the radius should be around 0.8 Jupiter-radii. The radius-variation is very fast in the first 5 Gyrs (Baraffe et al. 2003). The estimated age of the host star is between 1.14–3.35 Gyr using STAREVOL and 1.9±1.7 Gyr obtained by CESAM. These do not contradict each other but the age is not well constrained – this is a point where PLATO with its well-measured (better than 10%) ages will play a role in the study of brown dwarfs and of planets (Rauer et al. 2014). Therefore Bouchy et al. (2011a) left the question open as to why this brown dwarf has large radius: either the system is young, or cold spots on the brown dwarf surface help to inflate the radius or atmospheric processes blow up it with disequilibrium chemistry. The irradiation effects were found to be negligible in the inflation-process of brown dwarfs.

Interestingly, CoRoT-15b may be a double-synchronous system: the orbital period of the brown dwarf and the rotational period of the star can be equal to each other, but the precision of the rotational period measurement is not enough to make this statement conclusive (Bouchy et al. 2011a). If subsequent investigation can confirm this suspicion, then it seems that tidal interaction between stars and close-in brown dwarfs are strong enough to synchronize their stars or trap it in some resonance. We further discuss this in the light of CoRoT-33b.

2.3. CoRoT-33b, a key object for tidal evolution

This system was reported in Csizmadia et al. (2015). CoRoT-33A could be the presently-known most metal-rich brown dwarf host star because its metallicity is a $[Fe/H] = +0.44 \pm 0.1$ (the other candidate for this title is HAT-P-13A with $[Fe/H] = +0.43 \pm 0.1$, see Bakos et al. 2009).

The host stars of the brown dwarfs in binary systems seem to be metal-poor (Ma & Ge 2014), therefore this system helps to extend the sample to the tails of the distribution.

The host star seems to be older than 4.6 Gyrs and likely it is even older (maybe as old as 11–12 Gyr). The rotation period is too small for a G9V star when we compare it to the braking-mechanisms of the single-star scenarios of Bouvier et al. (1997). The measured $v \sin i$, stellar radius, as well as the observable spot modulation on the light curve show that $P_{rot} = 8.95$ days. Another interesting feature of CoRoT-33b, whose mass is 59 $M_{\rm jup}$, is its eccentric orbit ($e = 0.07$). Since the orbital period is just 5.82 d, the circularization time-scale for such a system is much shorter than the age of the system. Even more interestingly, the orbital period of the brown dwarf is within 3% of a 3:2 commensurability with the rotational period of the star.

Béky et al. (2014) listed six hot Jupiters where strange commensurabilities can be observed between the stellar rotational rate and orbital periods of the planetary companions. They also suspected that these are just random coincidences between the stellar rotational period and the planetary companions’ orbital periods (maybe a stellar spot at a certain latitude may mimic such a coincidence due to the differential rotation of the star). However, several host stars of brown dwarfs rotate faster – even if we take into account the normal rate for stellar differential rotation – than we expect from their ages, so such random coincidences cannot explain the observed phenomena in star-brown dwarf systems in general. More likely, we see a long-term interaction between the star and the close-in, high mass brown dwarf system. This interaction consists of tidal interaction as well as magnetic braking effects. Such a combination of star – planet/brown dwarf interaction can explain the observed properties – even the eccentric orbit – of CoRoT-33 and other systems. Details of this physical mechanism and the results can be found in Ferraz-Mello et al. (2015).

3. Distance-occurance rate relationship?

The CoRoT data allowed us to determine the relative frequency ratio of brown dwarfs to hot Jupiters in the $P < 10$ days orbital period range. Using the true frequency of hot Jupiters as given in Wright et al. (2012), an $0.20 \pm 0.15\%$ true occurence rate of brown dwarfs was found around solar-like stars for $P < 10$ days (Csizmadia et al. 2015). It is also suspected that this occurence rate follows a power-law up to at least 1000 au orbital separations:

$$f = \alpha \left(\frac{a}{1\mathrm{au}} \right)^{\beta} \tag{1}$$

where f is the occurence rate of brown dwarfs around solar like stars below 1000 au orbital separation and first estimates give, $\alpha = 0.55^{+0.8}_{-0.55}\%$, $\beta = 0.23 \pm 0.06$ (Csizmadia et al. 2015). The occurence rate-separation relationship considers radial velocity, microlensing and direct imaging results, too (see the discussion and references in Csizmadia et al. 2015). Although ground-based transit surveys like HAT, WASP etc. did not report this frequency rate so far, the analysis of Kepler data is fully compatible with the CoRoT-results and also supports the aformentioned relationship (Santerne et al. 2015). The meaning of this possible relationship and its connection to formation theories of planetary systems is not studied yet. However, it is worth mentioning that models by Mordasini et al. (2009) predicted the formation of brown dwarfs via core accretion up to 40 M_{jup} but none of these objects get closer than 1 au according to their Fig. 9. Observational results of CoRoT, Kepler and ground based surveys (Table III.6.1) shows that somehow these brown dwarfs moved inward significantly.

4. Summary and future prospects for transiting brown dwarf hunting

CoRoT detected three transiting brown dwarfs, including the first known such object. All three are very close to their host stars ($P_{\mathrm{orb}} < 10$ days). Two of them (CoRoT-15b and -33b) show interesting commensurabilities between the orbital period of the transiting object and the rotational period of the host star (maybe 1:1 in the case of 15b and a strict 3:2 in the case of 33b). Well-measured masses and first estimates of the radii were reported. CoRoT-33b also has an eccentric orbit and all three objects can be subject of future tidal evolution studies. The occurence rate of brown dwarfs was estimated for the ten days orbital period range and it was found to be $0.2\% \pm 0.15\%$ and this was confirmed by an analysis of the Kepler-data later (Santerne et al. 2015). The presence of such close-in brown dwarfs is a challange for presently known formation theories.

Transiting brown dwarfs are gold-mines for their studies. The mass and radius (hence their mean density) can be measured in a model-independent way for them, and the random and systematic uncertainties of their parameters in such binary systems are dominated mostly by the stellar parameters (in double-lined systems this kind of uncertainty does not appear). This will be improved by the next generation of instruments which will be more sensitive for secondary eclipses and phase curves, like PLATO. Since the age can be measured by isochrone fitting or by asteroseismology in the future (Rauer et al. 2014), the predicted contraction rate of brown dwarfs and thus the theoretical models of them (Baraffe et al. 2003) can be checked.

Although almost a dozen transiting brown dwarfs are known, this is still too small a sample for such studies. Since the size of brown dwarfs is in the Jupiter-sized range or it can be bigger (up to several Jupiter-radii) for young ones, they can easily be detected from ground, too. However, interestingly, several brown dwarfs are grazing transiters (like NLTT 41135b or CoRoT-33b) and that decreases the observed transit depth making the discovery hard from ground. For some yet unkown reason, space observatories detected higher brown dwarf/hot Jupiter ratio than what we can suspect from ground based surveys if we simply divide the number of the observed brown dwarfs by the number of hot Jupiters. It is quite unlikely that space observatories missed hot Jupiters, more probably this may be a selection effect of the ground based surveys.

We foresee several ongoing or planned space missions which are able to detect transiting brown dwarfs, like Gaia (launched 2013), CHEOPS and TESS (to be launched 2017), PLATO (to be launched in 2024). Also, EUCLID (to be launched in 2022) may detect a limited number of microlensing brown dwarfs as a by-product. Gaia is also able to detect brown dwarfs via its primary technique, namely via astrometry.

CHEOPS targets known planets and candidates detected by radial velocity technique (RV). CHEOPS may search for the possible transits of these RV-detected objects which would allow to determine the inclination and hence their true masses instead of a lower mass limit; also, their radius becomes known. One can propose that CHEOPS may extend its program by checking the possible transits of RV-detected brown dwarf candidates.

There also are several ongoing ground-based surveys which are able to find transiting (NGTS, WASP, HAT, for instance) or microlensing brown dwarfs. However, the low efficiency or observational biases of ground based survey are hard to understand and requires further study and a careful check of the existing data for undetected brown dwarfs. The same is to apply to space-based observatories' data.

References

Anderson, D. R., Collier Cameron, A., et al. 2011, ApJ, 726, L19

Armitage, P. J., & Bonnell, I. A. 2002, MNRAS, 330, 11

Bakos, G. Á. Howard, A. W., Noyes, R. W., et al. 2009, ApJ, 707, 446

Baraffe, I., Chabrier, G., Allard, F., & Hauschildt, P. H. 2002, A&A, 382, 563

Baraffe, I., Chabrier, G., Barman, T. S., et al. 2003, A&A, 402, 701

Béky B., Holman, M. J., Kipping, D. M., & Noyes, R. W. 2014, ApJ, 788, 1

Bonomo, A. S., Sozzetti, A., Santerne, A., et al. 2015, A&A, 575, A85

Bouchy, F., Deleuil, M., Guillot, T., et al. 2011a, A&A, 525, A68

Bouchy, F., Bonomo, A. S., Santerne, A., et al. 2011b, A&A, 533, A83

Bouvier, J., Forestini, M., & Allain, S. 1997, A&A, 326, 1023

Csizmadia Sz., Hatzes, A., Gandolfi, D., et al. 2015, A&A, 584, A13

David, T. J., Hillenbrand, L. A., Cody, A. M., Carpenter, J. M., Howard, A. W. 2015, ApJ, submitted (arXiv:org:1510.08087)

Deleuil, M., Deeg, H. J., Alonso, R., et al. 2008, A&A, 491, 889

Díaz, R. F., Damiani, C., Deleuil, M., et al. 2013, A&A, 551, L9

Díaz, R. F., Montagnier, J. L., Bonomo, A. A., et al. 2014, A&A, 572, A109

Ferraz-Mello, S., Tadeu dos Santos, M., Folonier, H., et al. 2015, ApJ, 807, 78

Hatzes, A., & Rauer, H. 2015, ApJ, 810, L25

Irwin, J., Buchhave, L., Berta, Z., et al. 2010, ApJ, 718, 1553

Johnson, J. A., Apps, K., Gazak, J. Z., et al. 2011, ApJ, 730, 79

Johnston, W. R. 2015, http://www.johnstonsarchive.net/astro/browndwarflist.html, checked on 14 June 2015

Kenworthy, M., Lacour, S., Kraus, A., et al. 2014, MNRAS, 446, 411

Lafrenière, D., Doyon, R., Marois, Ch., et al. 2007, ApJ, 670, 1367

Ma, G., & Ge, J. 2014, MNRAS, 439, 2781

Marcy, G. W., & Butler, R. P. 2000, PASP, 112, 137

Metchev, S. A., & Hillenbrand, L. A. 2009, ApJS, 181, 62

Montet, B. J., Johnson, J. A., Muirhead, Ph. S., et al. 2015, ApJ, 800, 134

Mordasini, C., Alibert, Y., & Benz, W. 2009, A&A, 501, 1139

Moutou, C., Bonomo, A. S., Bruno, G., et al. 2013, A&A, 558, L6

Payne, M. J., & Lodato, G. 2007, MNRAS, 381, 1597

Patel, S. G., Vogt, S. S., Marcy, G. W., et al. 2007, ApJ, 665, 744

Rauer, H., Catala, C., Aerts, C., et al. 2014, ExA, 38, 249

Sahlmann, J., Ségransan, D., Queloz, D., et al. 2011, A&A, 525, A95

Santerne, A., Moutou, C., Tsantaki, M. G., et al. 2015, A&A, accepted, arXiv:151100643

Siverd, R. J., Beatty, T. G., Pepper, J., et al. 2012, ApJ, 761, 123

Spiegel, D. S., Burrows, A., & Milsom, J. A. 2011, ApJ, 727, 57

Stassun, K. G., Mathieu, R. D., & Valenti, J. A. 2006, Nature, 440, 311

Steffen, J. H., Fabrycky, D. C., et al. 2012, MNRAS, 421, 2342

Steffen, J. H., Fabrycky, D. C., Agol, E., et al. 2013, MNRAS, 428, 1077

Trentham, N., Möller, O., Ramirez-Ruiz, E. 2001, MNRAS, 322, 658

Wittenmyer, R. A., Endl, M., Cochran, 2009, AJ, 137, 3529

Wright, J. T., Marcy, G. W., Howard, A. W., et al. 2012, ApJ, 753, 160

Acknowledgements: The CoRoT space mission has been developed and operated by CNES, with the contribution of Austria, Belgium, Brazil, ESA, Germany, and Spain.

The CoRoT Legacy Book
© The authors, 2016
DOI: 10.1051/978-2-7598-1876-1.c037

III.7

Planets orbiting stars more massive than the Sun

E. W. Guenther[1], D. Sebastian[1], D. Gandolfi[2], P. Montañés-Rodríguez[3, 4], St. Geier[5, 6], Sz. Csizmadia[7], F. Cusano[8], H. J. Deeg[3, 4], M. Fridlund[9], S. Grziwas[10], U. Heber[6], C. Heuser[6], F. Rodler[11, 12, 13], and L. Tal-Or[14], and the CoRoT-team[⋆]

[1] Thüringer Landessternwarte Tautenburg, 07778 Tautenburg, Germany
e-mail: guenther@tls-tautenburg.de
[2] Zentrum für Astronomie Heidelberg,, Landessternwarte Heidelberg-Königstuhl 12, D-69117 Heidelberg, Germany
[3] Instituto de Astrofísica de Canarias, 38205 La Laguna, Tenerife, Spain
[4] Dpto. de Astrofísica, Universidad de La Laguna, 38206 La Laguna, Tenerife, Spain
[5] ESO, Karl-Schwarzschild-Str. 2 85748 Garching bei München, Germany
[6] Astronomisches Institut, der Universität Erlangen-Nürnberg, Dr. Remeis-Sternwarte, Sternwartstr. 7, 96049 Bamberg, Germany
[7] Institute of Planetary Research, German Aerospace Center, Rutherfordstraße 2, 12489 Berlin, Germany
[8] INAF-Osservatorio Astronomico di Bologna, Via Ranzani 1, I-40127 Bologna, Italy
[9] Max-Planck-Institut für Astronomie, Königstuhl 17, D-69117 Heidelberg, Germany
[10] Rheinisches Institut für Umweltforschung an der Universiät zu Köln, Aachener Straße 209, 50931 Köln, Germany
[11] Harvard-Smithsonian Center for Astrophysics, Cambridge, MA 02138, USA
[12] Institut de Cienci'e s de l'Espai (CSIC-IEEC), Campus UAB, Fac. Ciencies, C5 p2, E-08193 Barcelona, Spain
[13] Max-Planck-Institut für Astronomie, Königstuhl 17, D-69117 Heidelberg, Germany
[14] Institut fur Astrophysik (IAG), Friedrich-Hund-Platz 1, 37077 Göttingen, Germany

1. Introduction

Although thousands of transiting extrasolar planets have been discovered, less than 4% orbit stars in the mass-range $\mathrm{M_{star}} = 1.3 - 2.1\ \mathrm{M}_\odot$. This means that we know only very little about planets of these intermediate mass stars (IMSs). This is unfortunate, because studies with the SPITZER telescope demonstrate that the life-time of planet-forming disks is on average about half as long as that for solar-like stars ($\tau_{\rm disk} = 1.2$ Myrs for $M_* \geq 1.3\ M_\odot$ compared to $\tau_{\rm disk} = 2.5$ Myrs for $M_* \sim 1\ M_\odot$; Mamajek 2009). Thus, although the disks of IMSs are on average more massive than those of solar-like stars, there is, on average, less time to form planets. However most theories still predict a higher frequency of massive planets of IMSs than for solar-like stars (Laughlin et al. 2004; Ida & Lin 2005; Kennedy & Kenyon 2008; Alibert et al. 2011; Hasegawa & Pudritz 2013), but not all agree (Kornet et al. 2004; Boss 2004).

Studies of giant stars and direct imaging surveys confirm that the frequency of massive planets is higher for IMSs than for solar-like stars (Vigan et al. 2012; Johnson et al. 2010a, 2010b). This means that massive planets can form within about 1.2 Myrs. However, these types of surveys are limited to planets at orbital distances larger than 0.5 AU.

We thus do not know the frequency of close-in planets of IMSs, as only very few discoveries have been made (e.g. Collier Cameron et al. 2010). The question is whether they can not only form but also migrate inwards while the disk is still there. Gas-giant planets can migrate via the so-called Type II migration in by planet-disk interaction (e.g., Lin et al. 1996). If Type II migration were the dominant process, the frequency of close-in planets would strongly depend on the migration-rate (Williams & Cieza 2011). By measuring the frequency of close-in, massive planets, we thus constrain speed of Type II migration. Based on data obtained for subgiants stars, Bowler et al. (2010) argue that there is a significant lack of close-in planets of IMSs.

[⋆] Based on observations obtained with CoRoT. The CoRoT space mission, launched on December 27, 2006, has been developed and is operated by the CNES, with the contribution of Austria, Belgium, Brazil, ESA (RSSD and Science Program), Germany and Spain. The ground-based observations were obtained at the European Southern Observatory, with the the Large Binocular Telescope, with the 2.2-m and 3.5-m telescopes at CAHA, with the NOT, with the 2.1-m telescope at McDonald observatory, with the Alfred-Jensch telescope, and with the IAC-80-cm telescope.

In their sample of 31 stars, they can rule out planets of more than 1.0 $\mathrm{M_{Jup}}$ within 1 AU. They furthermore argue that this lack of planets is not due to an observational bias but must be real.

Planets of stars with $\mathrm{M_{star}} \geq 1.2\ \mathrm{M_\odot}$ (corresponding to $T_\mathrm{eff} \geq 6250$ K) are, in contrast to planets of lower-mass stars, quite often misaligned (Winn et al. 2010). This result is surprising, since Beaugé et al. (2012) has shown that the interaction between the planet and the disk leads to a damping of the orbital inclination of the planets. Planets that migrate inwards via Type II migration should thus be co-planar. The discovery that planets of IMSs are often misaligned thus led to intensive discussions (Albrecht et al. 2012; Albrecht et al. 2013; Chaplin et al. 2013; Hirano et al. 2012; Lai et al. 2011; Sanchis-Ojeda et al. 2012; Van Eylen 2014; Huber et al.2013; Xue et al. 2014).

Another interesting aspect is engulfment of close-in planets in IMSs during the post-main sequence phase. Which kind of planets are engulfed, and whether planets can survive the engulfment to reappear at later stages is still an open question. As shown in Villaver & Livio (2009) tidal interactions lead to the engulfment of close-in planets when the star becomes a giant. The minimum distance at which a planet can survive depends on its mass (Kunitomo 2011). A planet with the mass of Jupiter orbiting a star with 1.5 $\mathrm{M_{Sun}}$ has to be at a distance of more than 1.5 AU to survive the red giant phase. The short-period planets that we discuss in this article are thus unlikely to survive the red giant phase.

The effects of the engulfment of brown dwarfs (BDs) and massive planets can have quite dramatic consequences for the star. The accretion of BDs and planets can induce the ejection of shells around giant stars, changes the abundance pattern, and lead to significant spin-up (Bear & Soker 2012; Beuermann et al. 2012; Charpinet et al. 2011; Livio & Soker 2002; Massarotti 2008; Pasquini et al. 2007; Politano et al. 2008; Siess & Livio 1999a; Siess & Livio 1999b; Silvotti et al. 2007).

The discovery of a post-red-giant host stars with giant planets orbiting as close as 0.116 AU, and two nearly Earth-sized bodies orbiting the hot B Subdwarf star (sdB) at distances of 0.0060 and 0.0076 AU shows that at least these planets must have survived the engulfment (Charpinet et al. 2011). According to Charpinet et al. (2011), the sdB-planets are the dense cores of evaporated giant planets that were transported closer to the star during the engulfment and triggered the mass loss necessary for the formation of the sdB. Furthermore, it has been suggested that close-in planets are also important for the shaping of planetary nebulae (Soker 1997; De Marco & Soker 2011). However, this model requires that 20% of the planetary nebulae are affected by close-in planets. Thus, also in the context of stellar evolution it is important to find out, what the frequency of close-in, massive planets is.

In summary, the determination of the frequency of close-in planets of IMSs sets important constraints for the theories of planet formation and evolution, and it is also important for our understanding of post-main sequence stellar evolution. We have therefore started a search for close-in transiting planets around IMSs using the CoRoT data. The main focus of our survey are planets of B-, and A-stars, because most planets of F-stars are expected to have been found already in the regular planet-survey of CoRoT.

2. The survey

Because of the lack of absorption lines, and the rapid rotation of B-, A-, and early F-stars, radial-velocity (RV) surveys for planets of these types of stars are not efficient (Desort 2009a; Desort 2009b; Guenther et al. 2009; Galland et al. 2006; Galland et al. 2010; Borgniet et al. 2014). Transit surveys are more suitable, because they do not suffer from these difficulties. The only challenges of transit surveys is that the planetary transit are shallower than for solar-like stars, and that many IMSs oscillate. Ground-based transit surveys have already discovered planets of IMSs, for example HD15082b (Collier Cameron et al. 2010). However, detecting planets of A-stars with ground-based telescopes is also not easy. Nevertheless, HD15082b is up to now the only known transiting planet of an A-star were the mass has been determined (Lehmann et al. 2014). The noise-level of CoRoT is 80 ppm, 110 ppm, 200 ppm and 280 ppm for a a single 3 h transit for stars of 11.5, 12.5, 13.5, and 14.5 mag, respectively (Auvergne et al. 2009). Since we are only interested in short-period planets with the size of Jupiter, the noise-levels are about 16, 22, 40, 56 ppm, if we limit our survey to the long runs (LRa-, LRc-, and the IRa-field[1]) and to planets with orbital periods $P \leq 6\ d$, and if we co-add and phase-folded transits. A transit with a depth of 3400 ppm, as it is expected for a Jupiter-sized planet orbiting a A5V star ($R_* = 1.7\ \mathrm{R_\odot}$) is thus easily detected by CoRoT. This means that CoRoT must have detected all transiting giant planets with short orbital periods in these fields. To determine the frequency of close-in planets and BDs, all we have to do is to find out whether the transits are false-positives (FPs), eclipsing binaries, or not. After excluding binaries, and all types of FPs, all remaining objects have to be planets or BDs. The main focus of our survey are B- and A-stars, because we expect that almost all planets of F-stars were already found in the main survey of CoRoT. CoRoT has in fact already discovered a number of planets and BDs orbiting stars more massive than the Sun (Table III.7.1).

According to EXODAT (Deleuil et al. 2009), CoRoT has observed 1126 B-stars, 18450 A-stars, 23826 F-stars, 40959 G-stars, 38601 K-stars, and 2220 M-stars in the LR-fields. Counting only stars classified as luminosity-class IV and V, there are 1044 B-stars, 18394 A-stars, 22578 F-stars, 29753 G-stars 6714 K-stars, and 79 M-stars in these fields. Since CoRoT discovered 11 planets with $R_\mathrm{p} \geq 0.5\ \mathrm{R_{Jup}}$ with $P \leq 6\ d$ of G, K, and M-stars in the LR-fields, we expect to find about 6 substellar-objects of A-, and B-stars, if the frequency of planets were the same. If there are as many close-in planets of IMSs as there are planets at larger distance, we should find about 8 of them.

3. The candidates

Given that, in the CoRoT survey, planet candidates are selected without any bias against certain spectral types of the host stars, we expect that many have alredy been identified in the main planet survey. However, since the discovery of planets transiting B- and A-type stars is not easy, it is very well possible that some planets of A- and

---

[1] LRa stands for “Long-Run-galactic-Anti-centre field”, LRc for “Long-Run-galactic-centre field”, and IRa for “initial field”. The IRa-field was also located in the “antic-centre” direction.

Table III.7.1. Planets of stars more massive than 1.1 $M_\odot$ discovered by CoRoT.

Name	$M_{\rm star}$ [$M_\odot$]	Spec-type	Period [d]	$R_{\rm planet}$ [$R_{\rm Jup}$]	$M_{\rm planet}$ [$M_{\rm Jup}$]	Density [g cm^{-3}]	Ref.
CoRoT-3b	1.37 ± 0.09	F3V	4.3	1.01 ± 0.07	21.7 ± 1.0	26.4 ± 5.6	Deleuil et al. 2008
CoRoT-15b	1.32 ± 0.12	F7V	3.0	1.12 ± 0.23	63.3 ± 4.1	59 ± 35	Bouchy et al. 2011
CoRoT-21b	1.29 ± 0.09	F8IV	2.7	1.30 ± 0.14	2.53 ± 0.37	1.53 ± 0.53	Pätzold et al. 2012
CoRoT-11b	1.27 ± 0.05	F6V	3.0	1.43 ± 0.03	2.33 ± 0.34	0.99 ± 0.15	Gandolfi et al. 2010
CoRoT-19b	1.20 ± 0.05	F9V	3.9	1.29 ± 0.03	1.14 ± 0.05	0.51 ± 0.05	Guenther et al. 2009
CoRoT-4b	1.16 ± 0.02	F8V	9.2^1	1.17 ± 0.05	0.75 ± 0.01	0.58 ± 0.15	Moutou et al. 2008
CoRoT-22b	1.15 ± 0.08	G0IV	9.7^1	0.52 ± 0.12	<0.15	<1.3	Moutou et al. 2014
CoRoT-20b	1.14 ± 0.08	G2V	9.2^1	0.84 ± 0.04	4.24 ± 0.23	9.87 ± 1.10	Deleuil et al. 2012
CoRoT-23b	1.14 ± 0.08	G0V	3.6	1.05 ± 0.13	2.8 ± 0.3	3.3 ± 1.0	Rouan et al. 2012
CoRoT-14b	1.13 ± 0.09	F9V	1.5	1.09 ± 0.07	7.6 ± 0.6	7.3 ± 1.5	Tingley et al. 2011
CoRoT-34b	~1.4	F5V	5.6	~1.9	<1.4	–	^{2}

Notes. $^{(1)}$ $P \geq 6$ d, thus object should not be counted. $^{(2)}$ Planet candidate that is being studied, the CoRoT number is preliminary.

Table III.7.2. New candidates for substellar objects.

Win-ID	Spec. type	V [mag]	$M_{\rm star}$ [$M_\odot$]	Period [d]	Depth [%]	Remarks
LRa02_E1_1475^1	A4V	14.2	2.3	2.12	0.3	BD or low-mass stellar companion
LRc07_E2_0307^2	F3V	13.1	1.5	5.15	0.2	planet
LRc09_E2_3322^1	A5IV	15.7	2.1	3.2	1.04	planet candidate
IRa01_E2_2721^2	A6V	13.0	2.0	0.61	0.8	UVES: $M_{\rm p} \leq 10$ $M_{\rm Jup}$
LRa01_E2_0963^2	F0V	13.8	1.7	4.65	0.3	FIES+CAFÉ: $M_{\rm p} \leq 30$ $M_{\rm Jup}$
LRa02_E2_4150^1	B5V	11.0	6.0	8.17^3	0.7	FIES: $M_{\rm p} \leq 90$ $M_{\rm Jup}$
LRc03_E2_2657^1	A7V	13.1^4	1.9	5.15	0.2	UVES: $M_{\rm p} \leq 15$ $M_{\rm Jup}$
LRc08_E2_4203^1	A5V	15.6	2.1	3.28	0.35	UVES: $M_{\rm p} \leq 15$ $M_{\rm Jup}$
LRc10_E2_3265^1	A5V	14.5	2.1	4.83	0.08	TWIN: $M_{\rm p} \leq 30$ $M_{\rm Jup}$
IRa01_E1_4591^1	A7V	13.9	1.9	4.29	0.3	SB1, or SB2
LRa01_E2_0203	F5IV	11.6	1.3	1.86	<1.0	UVES: SB2
LRa01_E2_1578	F5IV	13.4	1.3	16.06^3	0.6	SB1
LRa02_E1_0725	A5IV	13.1	2.1	9.09^3	1.4	SB1
LRa02_E2_1023^1	F4V	13.4	1.4	0.78	0.2	LC-analysis: binary
LRc02_E1_0132	F6II	11.9	1.3	3.69		SB2
LRc07_E2_0108	A9IV	11.2	1.8	14.45^3	1.8	SB1
LRc07_E2_0146	F8V	12.5	1.2	0.49		LC-analysis: binary
LRc07_E2_0187	F8V	12.8	1.2	3.88	0.09	LC-analysis: binary
LRc07_E2_0482	F7V	12.9	1.2	1.82		SB2

Notes. $^{(1)}$ Object found in regular CoRoT survey. $^{(2)}$ Object found in this survey. $^{(3)}$ Period $P \geq 6$, thus not strictly part of the survey.

B-stars might have been overlooked. We thus used the information given in EXODAT (Deleuil et al. 2009) to select all A-, and B-stars, as well as early F-stars observed in the IRa, LRa and LRc fields and analysed their light-curves in detail. Altough we limit our survey to $P \leq 6$ d, we hesitated to throw away candidates with longer periods. From this list of stars we selected all potentially interesting candidates that had transits less than 1.5% deep. We also collected all so called "No-CCF-stars". These are targets with planet-like transit signals that have been already observed at least once by the spectroscopic follow-up program of CoRoT. Cross-correlation function (CCF) with a G-type template/mask show no significant correlation peak, implying that these stars are either rapid rotators, or early-type objects, or both. We reanalyzed the acquired spectra and found that most of these objects are indeed rapidly rotating early-type stars. Table III.7.2 gives an overview of candidates identified.

The detailed reanalysis of the light-curves of LRa02_E2_1023, LRc07_E2_0146, LRc07_E2_0187 showed that these stars are binaries with very shallow secondary eclipses. For the remaining candidates, we obtained

RV-measurements with the Echelle spectrographs SANDIFORD (McDonald 2.1-m telescope), CAFÉ (Calar Alto 2.2-m telescope), and FIES (NOT 2.6-m telescope) and the medium resolution spectrograph TWIN (Calar Alto 3.5-m telescope). These observations showed that another seven candidates are spectroscopic binaries. However, the fact that we are able to detect binaries with such shallow eclipses shows that CoRoT has the potential to detect giant planets around B- and A-stars. Although our primary goal was to find planets of B- and A-stars, we also included early F-stars in order not to miss any planet of an A-star just because of a slight mistyping of the spectral type.

As a next step, we obtained observing time with UVES on the VLT for the best candidates. Although the UVES spectra are of superb quality, we could only obtain upper limits for the companion masses of IRa01_E2_2721, LRc03_E2_2657, and LRc08_E2_4203. It is thus still possible that these are planets but it will not be easy to show that. Other good candidates are LRa02_E1_1475, LRc09_E2_3322, LRa02_E2_4150, and LRc07_E2_0307. It is interesting to note that the most promising candidates were already found in the regular planet survey of CoRoT. This shows that the regular planet survey is essentially complete for giant, close-in planets. In this article, we will mostly discuss LRc07_E2_0307 and LRa02_E2_4150, because LRa02_E1_1475 and LRc09_E2_3322 will be described in forthcoming articles.

4. The candidate LRc07_E2_0307

LRc07_E2_0307 was continuously observed with the CoRoT satellite from 2011 April 8 (HJD: 2455660.094879911) to June 28 (HJD: 2455741.311633067) over a period of 81.2 days in the chromatic mode. The coordinates, proper motion, and brightnesses of the stars are given in Table III.7.3. In total 218,441 data-points were obtained in three colours with a 32-second time sampling. Fifteen transits can already be seen in the raw-data. A low-resolution spectrum obtained with the NASMYTH spectrograph of the Alfred-Jensch telescope in Tautenburg shows that it is an F3V or F5IV star, which is in agreement with the temperature and log(g)-values derived from the high-resolution spectra (Table III.7.3).

In order to prove that this star has a substellar companion, we have shown that it is not an FP, and that the companion is not a low-mass star. As shown by Almenara et al. (2009) most of the binaries and FPs can already be identified with a very detailed analysis of the light-curve. After this had been done, we obtained seeing-limited images in- and out-of transit to exclude that it is an FP (see Deeg et al. 2009 for details on this method). We obtained two sets of data, one with the IAC-80-cm telescope, the other with the WISE-1-m-telescope. Both the observations show that none of the stars within CoRoT photometric mask with a distance larger than 2″ is the source of the transit signal. The transit is even cleraly seen in the data obtained with the WISE-1-m-telescope, which also helps to improve the ephemeris.

However, seeing limited observation can only confirm that the transiting object is within 2″ from the target, not that the transiting object is exactly this star. The next step thus had to be AO-observations, which we obtained with PISCES at the Large Binocular Telescope (LBT). The aim of these observations was to find out whether there are any stars within a few arcsec from the target that are bright enought to be FPs (see Guenther et al. 2013 for details on this method). We detected two previously unknown stars. Star No. 1 is $1\farcs94 \pm 0\farcs02$ W, $0\farcs30 \pm 0\farcs03$ S, and has $J = 15.7 \pm 0.1$, $K = 16.2 \pm 0.1$, and star No. 2 is $3\farcs42 \pm 0\farcs02$ E, $0\farcs53 \pm 0\farcs02$ N, and has $J = 17.1 \pm 0.1$, $K = 16.8 \pm 0.1$ (Fig. III.7.1). Both stars are not visible in the images taken obtained with the WISE and IAC-80-cm telescopes. The colours of the two stars are not consistent with physical companions, and both are far too faint to be potential FPs. Using RV-measurements obtained with FIES@ NOT, we derived an upper limit for the mass of the companion of $M_p \leq 2.9\ M_{Jup}$.

Table III.7.3. Parameters of the planet and the star LRc07_E2_0307.

Coordinates	
RA (2000)	$18^h31^m00\fs241$[1]
Dec (2000)	$+07°11'00\farcs6$[1]
Brigthness	
B	13.724 ± 0.045[2]
V	13.055 ± 0.066[2]
R	12.742 ± 0.063[2]
I	12.436 ± 0.02[2]
J	11.859 ± 0.026[3]
H	11.641 ± 0.022[3]
K	11.592 ± 0.021[3]
Ephemeris	
Orbital period P [days]	5.616531 ± 0.000023
Epoch T_0 [BJD]	2456864.459 ± 0.005[4]
Transit parameters	
Transit duration d_{tr} [h]	4.853 ± 0.022
transit depth [%]	0.934 ± 0.024
Spectroscopic parameters of the star	
Effective temperature $T_{\rm eff}$ [K]	6430 ± 70
Surface gravity log g [cgs]	~ 4.0
Spectral type	F3V-F5IV
Physical parameters	
semi-mayor axis [AU]	0.0697
M_v	2.8 ± 0.1[3]
interstellar extinction A_V [mag]	0.84 ± 0.14
Distance of the star d [pc]	723 ± 30
Star mass [$M_\odot$]	1.43 ± 0.04[5]
Star radius [$R_\odot$]	1.93 ± 0.01[5]
Age of the star [Gyr]	2.3 ± 0.2[5]
Planet mass M_p [M_{Jup}]	<1.4
Planet radius R_p [R_{Jup}]	1.87 ± 0.03
λ [deg] [6]	90

Notes. (1) PPMXL Catalog (Roeser et al. 2010). (2) EXODAT (Deleuil et al. 2009). (3) 2MASS (Skrutskie et al. 2006). (4) Heliocentric Julian date. (5) Derived by using the evolutionary tracks published by Girardi et al. (2000). The values are in agreement with STAREVOL tracks. (6) Sky-projected angle between the planetary orbital axis and the stellar rotation axis.

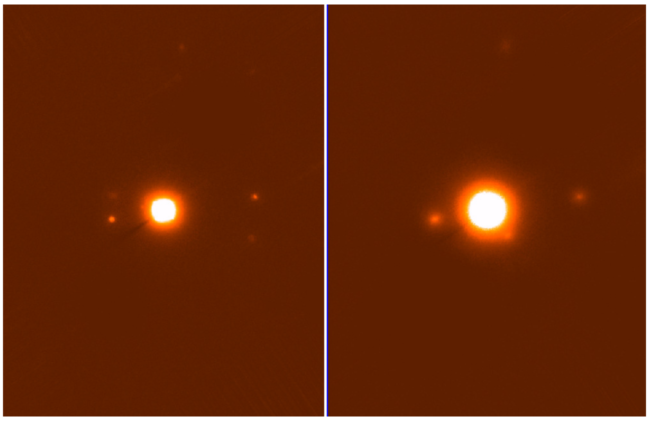

Fig. III.7.1. Images taken with the AO-system PISCES at the LBT in the K (*left*) and in the J-band (*right*). The size of the image is only about $6 \times 8''$, north is up and east is left. Two previously unknown stars are detected at distances of $1''.96 \pm 0''.04$ and $3''.46 \pm 0''.04$.

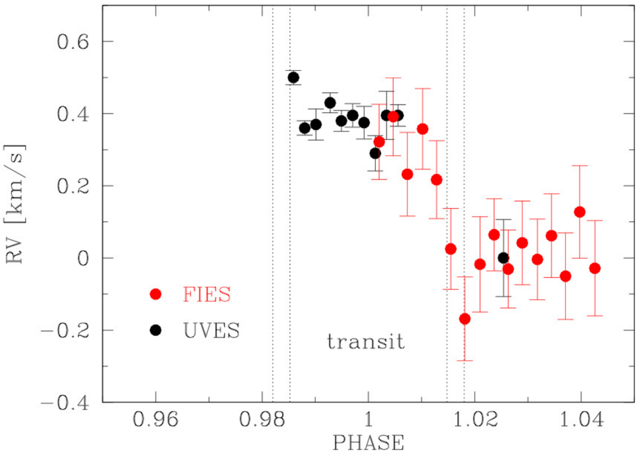

Fig. III.7.2. RV-values taken during and after the transit with UVES and FIES (instrumental offset removed). Both datasets are consistent with a planet in a polar orbit.

5. Time resolved spectroscopy of LRc07_E2_0307

Time resolved spectroscopy is a new method that allows to cofirm a planet without the need to determine its mass by means of RV-measurements. This method was pioneered by Collier Cameron et al. (2010). This method has some similarity with the classical Rossiter-McLaughlin (RM) method but has the advantage that it works also for rapidly rotating stars.

We obtained two independent data-sets. One with UVES on ESO VLT UT-2 (KUEYEN). The transit was observed on 6 August 2013. Each in-transit spectrum was exposed for 970 s, the out of transit spectrum was exposed for 1450 s. The in-transit observations were obtained for 2^h55^m, and the out-of-transit spectrum was taken 2^h9^m after the end of the in-transit observations in the same night. We obtained the second data-set with the fibre-fed Echelle spectrograph FIES in the night 25−26 July 2013.

We analyzed the UVES-data in two different ways. Once by using time resolved spectroscopy as explained in Collier Cameron et al. (2010), and also by measuring the classical RM-effect. The shadow of the transiting planet is clearly seen in the time-resolved spectroscopy and the RM-analysis shows a constant shift of the RV during transit. This implies that the planet is in a polar orbit. In case of the FIES data, we only applied the classical RM-method, because of the lower S/N. This data-set confirms the UVES results (Fig. III.7.2). After having excluded all other possibilities, we therefore regard LRc07_E2_0307 as a planet. The properties of the planet are summarized in Table III.7.3.

6. LRa02_E2_4150

LRa02_E2_4150 (HD 295605) is a very interesting object, because it is the only candidate that is a B-star. The stellar parameters are $T_{\rm eff} = 15\,800$ K, $\log(g) = 4.40$, which gives $M_* \sim 6$ $M_\odot$, $R_* = 3.8$ $R_\odot$, which is consistent with a B5V-star. The difficulty with this object is that it oscillates. On top of these oscillations there are transit-like events which have a depth of about 0.7%. This would imply that the transiting object would have a size of $R_{\rm p} = 0.3$ $R_\odot$, or $R_{\rm p} = 3$ $R_{\rm Jup}$, if there is a transiting object. Although this makes it unlikely to be a planet, or BD, we still obtained RV-measurements with CAFÉ, HARPS, the SANDIFORD, and FIES. The seeing-limited acquisition images taken with STANCAM during the RV follow-up performed with FIES, showed a sightly elongated source, suggesting that the target might be a visual binary with an angular separation of $\sim 2''$. We obtained images with the V, R, I, and Hα at the IAC-80-cm telescope to search for a hypothetical stellar companion or HII-region associated to the target but none was found. We thus regard the elongation of the STANCAM acquisition image as an artifact.

Unfortunately, the transit-like events have a period period of 8.17 days which is longer than the individual observing runs. We thus have to merge the RV-measurements obtained at different campaigns. Combining all the data, we derived an upper limit of about 90 $M_{\rm Jup}$ for the mass of the companion. The hypothetical eclipsing object thus cannot be a stellar companion. Whether this star hosts a transiting planet, or a BD, or whether it is a FP caused by the oscillations can not be deduced from data.

7. Discussion and conclusions

As discussed in Sect. 2, we expected to find about 6–8 substellar-objects of A-, and B-stars. Our RV-measurements clearly demonstrate that it is possible to detect the RV-signal of a BD with an orbital period $\leq$6 days of an A-star, despite the rapid rotation and the oscillations of these stars. Our experience with HD15082b shows that hundreds of spectra are needed to determine the mass of planet orbiting an A-star (Lehmann et al. 2014). However, the number of candidates that we found corresponds exactly to our expectation, if we assume that the frequency of massive close-in planets of A-stars is the same as that of G-stars. All our candidates are bright enough to be observed with TESS and PLATO which, combined with multi-colour phtometry of the transit, will eventually show whether these objects are planets, or not. The future of searching for planets of IMSs is thus bright.

Acknowledgements. We acknowledge support by the Deutsche Forschungsgemeinschaft (DFG) through grant GU 464/15-1,GU 464/16-1, GU 464/17-1, and GU 464/18-1. The ground-based observations were obtained with the VLT at the European Southern Observatory at Paranal, Chile (291.C-5028(A), 092.C-0222(A), and 093.C-0027(A), with the 2.2-m and 3.5-m telescope at German-Spanish Astronomical Center at Calar Alto (H12-2.2-037, H14-2.2-043), with the Nordic Optical Telescope at La Palma (NOT runs P45-109, P45-206, P46-113, P46-215, P47-105, P47-211, P48-217, P49-205; funding from the European Union Seventh Framework Programme FP7/2013-2016 under grant agreement No. 312430, OPTICON), the 2.1-m at McDonald observatory, Texas, the 80-cm telescope of the Instituto de Astrofísica de Canarias at the observatorio del Teide, the Alfred-Jensch telescope in Tautenburg, and the Large Binocular Telescope. The NOT is operated on the island of La Palma jointly by Denmark, Finland, Iceland, Norway, and Sweden, in the Spanish Observatorio del Roque de los Muchachos of the Instituto de Astrofísica de Canarias. The 2.2-m and 3.5-m telescopes of the Centro Astronómico Hispano Alemán (CAHA) is located in the Sierra de Los Filabres (Andalucía, Southern Spain) north of Almeria. It is operated jointly by the Max-Planck-Institut for Astronomie (MPIA) in Heidelberg, Germany, and the Instituto de Astrofísica de Andalucía (CSIC) in Granada/Spain. The LBT is an international collaboration. LBT Corporation partners are: The University of Arizona on behalf of the Arizona university system; Istituto Nazionale di Astrofisica, Italy; LBT Beteiligungsgesellschaft, Germany, representing the Max-Planck Society, the Astrophysical Institute Potsdam, and Heidelberg University; The Ohio State University, and The Research Corporation, on behalf of The University of Notre Dame, University of Minnesota and University of Virginia. This publication makes use of data products from the Two Micron All Sky Survey, which is a joint project of the University of Massachusetts and the Infrared Processing and Analysis Center/California Institute of Technology, funded by the National Aeronautics and Space Administration and the National Science Foundation.

References

Albrecht, S., Winn, J. N., Johnson, J. A., et al. 2012, ApJ, 757, 18

Albrecht, S., Winn, J. N., Marcy, G. W., et al. 2013, ApJ, 771, 11

Alibert, Y., Mordasini, C., & Benz, W. 2011, A&A, 526, A63

Almenara, J. M., Deeg, H. J., Aigrain, S., et al. 2009, A&A, 506, 337

Auvergne, M., Bodin, P., Boisnard, L., et al. 2009, A&A, 506, 411

Bear, E., & Soker, N. 2012, ApJ, 749, L14

Beaugé, C., & Nesvorný, D. 2012, ApJ, 751, 119

Beuermann, K., Dreizler, S., Hessman, F. V., & Deller, J. 2012, A&A, 543, 138

Borgniet, S., Boisse, I., Lagrange, A.-M., et al. 2014, A&A, 561, A65

Boss, A. P. 2006, ApJ, 644, L79

Bouchy, F., Deleuil, M., Guillot, T., et al. 2011, A&A, 525, A68

Bowler, B. P., Johnson, J. A., Marcy, G. W., et al. 2010, ApJ, 709, 396

Chaplin, W. J., Sanchis-Ojeda, R., Campante, T. L., et al. 2013, ApJ, 766, 101

Charpinet, S., Fontaine, G., Brassard, P., et al. 2011, Nature, 480, 496

Collier Cameron, A., Guenther, E., Smalley, B., et al. 2010, MNRAS, 407, 507

Deeg, H. J., Gillon, M., Shporer, A., et al. 2009, A&A, 506, 343

Deleuil, M., Deeg, H. J., Alonso, R., et al. 2008, A&A, 491, 889

Deleuil, M., Meunier, J. C., Moutou, C., et al. 2009, AJ, 138, 649

Deleuil, M., Bonomo, A. S., Ferraz-Mello, S., et al. 2012, A&A, 538, A145

De Marco, O., & Soker, N. 2011, PASP, 123, 402

Galland, F., Lagrange, A.-M., Udry, S., et al. 2005, A&A, 444, L21

Galland, F., Lagrange, A.-M., Udry, S., et al. 2006, A&A, 447, 355

Gandolfi, D., Hébrard, G., Alonso, R., et al. 2010, A&A, 524, A55

Girardi, L., Bressan, A., Bertelli, G., & Chiosi, C. 2000, A&AS, 141, 371

Desort, M., Lagrange, A.-M., Galland, F., et al. 2009, A&A, 506, 1469

Desort, M., Lagrange, A.-M., Galland, F., et al. 2009b, A&A, 499, 623

Guenther, E. W., Hartmann, M., Esposito, M., et al. 2009, A&A, 507, 1659

Guenther, E. W., Díaz, R. F., Gazzano, J.-C., et al. 2012, A&A, 537, A136

Guenther, E. W., Fridlund, M., Alonso, R., et al. 2013, A&A, 556, A75

Hasegawa, Y., & Pudritz, R. E. 2013, ApJ, 778, 78

Hirano, T., Sanchis-Ojeda, R., Takeda, Y., et al. 2012, ApJ, 756, 66

Huber, D., Carter, J. A., Barbieri, M., et al. 2013, Science, 342, 331

Ida, S., & Lin, D. N. C. 2005, ApJ, 626, 1045

Johnson, J. A., Howard, A. W., Bowler, B. P., et al. 2010a, PASP, 122, 701

Johnson, J. A., Bowler, B. P., Howard, A. W., et al. 2010b, ApJ, 721, L153

Jones, M. I., Jenkins, J. S., Bluhm, P., Rojo, P., & Melo, C. H. F. 2014, A&A, 566, A113

Kennedy, G. M., & Kenyon, S. J. 2008, ApJ, 673, 502

Kornet, K., Różyczka, M., & Stepinski, T. F. 2004, A&A, 417, 151

Kunitomo, M., Ikoma, M., Sato, B., Katsuta, Y., & Ida, S. 2011, ApJ, 737, 66

Lai, D., Foucart, F., & Lin, D. N. C. 2011, MNRAS, 412, 2790

Laughlin, G., Bodenheimer, P., & Adams, F. C. 2004, ApJ, 612, L73

Léger, A., Rouan, D., Schneider, J., et al. 2009, A&A, 506, 287

Lehmann, H., Guenther, E., Sebastian, D., et al. 2015, A&A, 578, L4

Lin, D. N. C., Bodenheimer, P., & Richardson, D. C. 1996, Nature, 380, 606

Livio, M., & Soker, N. 2002, ApJ, 571, L161

Mamajek, E. E. 2009, AIP Conf. Ser., 1158, 3

Massarotti, A. 2008, AJ, 135, 2287

Moutou, C., Bruntt, H., Guillot, T., et al. 2008, A&A, 488, L47

Moutou, C., Almenara, J. M., Díaz, R. F., et al. 2014, MNRAS, 444, 2783

Pasquini, L., Döllinger M. P., Weiss, A., et al. 2007, A&A, 473, 979
Pätzold, M., Endl, M., Csizmadia, S., et al. 2012, A&A, 545, A6
Politano, M., Taam, R. E., van der Sluys, M., & Willems, B. 2008, ApJ, 687, L99
Queloz, D., Bouchy, F., Moutou, et al. 2009, A&A, 506, 303
Roeser, S., Demleitner, M., & Schilbach, E. 2010, AJ, 139, 2440
Rouan, D., Parviainen, H., Moutou, C., et al. 2012, A&A, 537, A54
Sanchis-Ojeda, R., Fabrycky, D. C., Winn, J. N., et al. 2012, Nature, 487, 449
Schlaufman, K. C., & Winn, J. N. 2013, ApJ, 772, 143
Sebastian, D., Guenther, E. W., Schaffenroth, V., et al. 2012, A&A, 541, A34
Siess, L., & Livio, M. 1999a, MNRAS, 308, 1133
Siess, L., & Livio, M. 1999b, MNRAS, 304, 925 A&A, 545, A76
Silvotti, R., Schuh, S., Janulis, R., et al. 2007, Nature, 449, 189
Skrutskie, M. F., Cutri, R. M., Stiening, R., et al. 2006, AJ, 131, 1163
Soker, N.1997, ApJS, 112, 487
Tingley, B., Endl, M., Gazzano, J.-C., et al. 2011, A&A, 528, A97
Van Eylen, V., Lund, M. N., Silva Aguirre, V., et al. 2014, ApJ, 782, 14
Vigan, A., Patience, J., Marois, C., et al. 2012, A&A, 544, 9
Villaver, E., & Livio, M. 2009, ApJ, 705, L81
Williams, J. P., & Cieza, L. A. 2011, ARA&A, 49, 67
Winn, J. N., Fabrycky, D., Albrecht, S., & Johnson, J. A. 2010, ApJ, 718, L145
Xue, Y., Suto, Y., Taruya, A., et al. 2014, ApJ, 784, 66

Acknowledgements: The CoRoT space mission has been developed and operated by CNES, with the contribution of Austria, Belgium, Brazil, ESA, Germany, and Spain.

The CoRoT Legacy Book

DOI: 10.1051/978-2-7598-1876-1.c038

III.8

Exoplanets versus brown dwarfs: The CoRoT view and the future

J. Schneider

LUTh – Observatoire de Paris, France

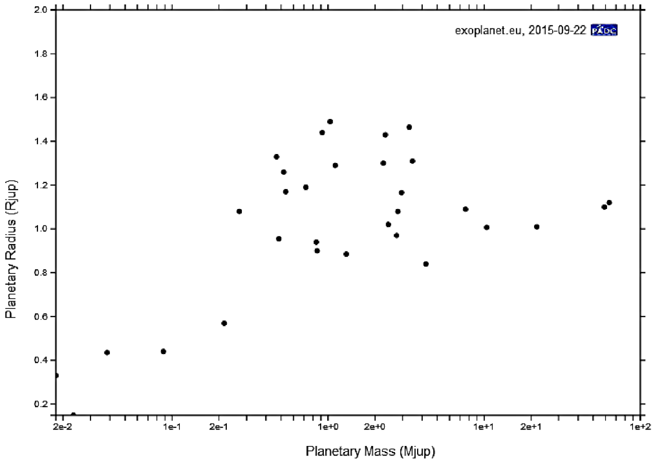

Fig. III.8.1. Mass-radius relation for CoRoT objects (15 Oct. 2015), from `exoplanet.eu`.

CoRoT has detected by transit several tens of objects (Moutou & Deleuil 2015) whose radii run from 1.67 Earth radius (CoRoT 7b, Leger et al. 2009) to 1.5 Jupiter radius (CoRoT−1 b, Barge et al. 2007)[1]. Their mass run from less than 5.7 Earth mass (CoRoT-24 b, Alonso et al. 2014) to 63 Jupiter mass (CoRoT-15 b, Bouchy et al. 2011). Their mass-radius diagram is represented on Fig. III.8.1. One could be tempted to think that the more massive the object is, the larger it is in size and that there is some limit in mass and/or radius beyond which objects are not planets but very low mass stars below the 80 Jupiter mass limit to trigger nuclear fusion (namely "brown dwarfs"). CoRoT findings contribute to the planet versus brown dwarf debate, since Fig. III.8.1 shows that there is no clear mass-radius relation.

One is thus facing two problems: terminology (what is a planet? what is a brown dwarf?) and classification (how to decide if a given object is a planet or a brown dwarf according to a given definition?). Let us discuss these two aspects and the CoRoT contribution.

What is a planet?

The debate, open by several authors (see for example Baraffe et al. 2010; Schneider et al. 2011; Hatzes & Rauer 2015), is still ongoing and will not be closed by the present contribution. Names are arbitrary conventions, but the naturel trend is to make them designate sufficiently elaborated concepts. Derived from the solar system analogy, exoplanets (in short planets) designate small bodies orbiting around stars and formed by condensation in a circumstellar dust disk. A first question is of course how small has the body to be for being a planet. The problem here is that there are small bodies orbiting stars which are probably not formed like planets, namely brown dwarfs forming, like stars, by collapse of a (possibly dusty) gas cloud.

From the heaven of concepts to the hell of observations

So we have a clear conceptual discrimination between planets and brown dwarfs (keeping in mind that it is a convention). But it is based on a criterion involving an inobservable concept, namely its formation scenario, because we do not have the formation movie at hand. We can only rely on actual observables. Standard basic bulk observables are the object mass, radius, temperature. An ideal situation would be that, at least for one of these observables, there are two domains $\mathrm{D}_{\mathrm{planet}}$ and $\mathrm{D}_{\mathrm{brown\,dwarf}}$ of values which do not intersect. It is unfortunately not the case since there are planets smaller or larger, heavier or lighter, cooler or hotter than objects we believe to be brown dwarfs, Even worse, there are a few pulsar companions with masses lower than 30 Jupiter mass. They are probably the relict of stellar companions eroded by the pulsar strong wind (Ray & Loeb 2015). One can argue that as such they are not planets nor brown dwarfs, their formation process being very different. But one cannot exclude that such erosion mechanism happend also for low mass compenions of main sequence stars with strong winds (see *e.g.* Sanz-Forceda et al. 2010). The choice made by the Extrasolar Encyclopaedia at

---

[1] Data as of October 15, 2015.

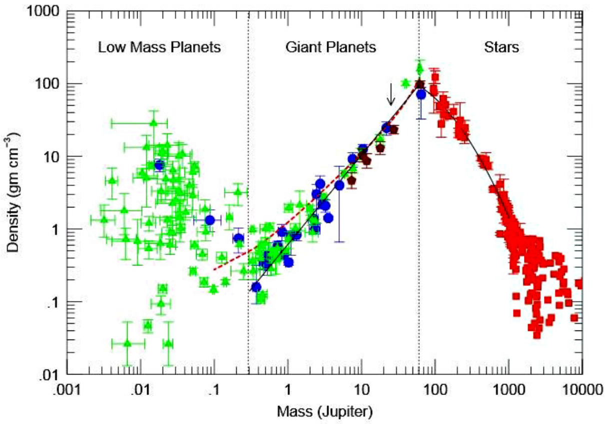

Fig. III.8.2. Empirical mass-density relation (Hatzes & Rauer 2015) © ApJ.

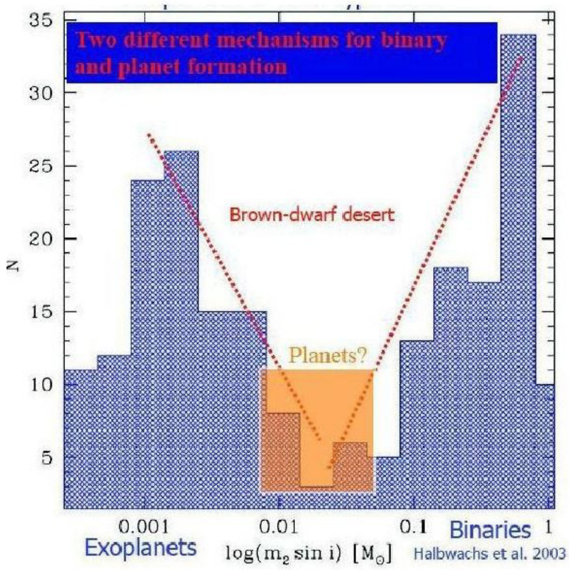

Fig. III.8.3. Mass histogramme of objects (Udry et al. 2010).

exoplanet.eu, based on Hatzes & Rauer (2015), is to take all objects below 60 Jupiter mass.

The Hatzes & Rauer argument is that the mass-radius and the mass-density relations presents no particular feature in the giant planet regime (i.e. more massive than Saturn) and that there is a change in the slope of distribution at 60 Jupiter mass (Fig. III.8.2). But unfortunately their statistics in the 30−60 Jupiter mass region is poor (the so-called desert) since they rely only on transiting planets and the authors do no consider the mass histogramme in this region. Earlier data suggested a dip around 40 Jupiter mass (Sahlman et al. 2011; Udry et al. 2010 − Figs. III.8.3 and III.8.4) in the mass histogramme. More statistics will come in the near future, including radial velocity data from the ground and astrometric data from Gaia, to see if a feature around 40 Jupiter mass in the mass-radius diagram exists or not.

A future improvement to separate the planet and brown dwarf populations will come from advanced observables, like the spectral type and species composition. They will help to constrain the formation mechanism of the object (accretion in a dust disk or collapse of a gas cloud).

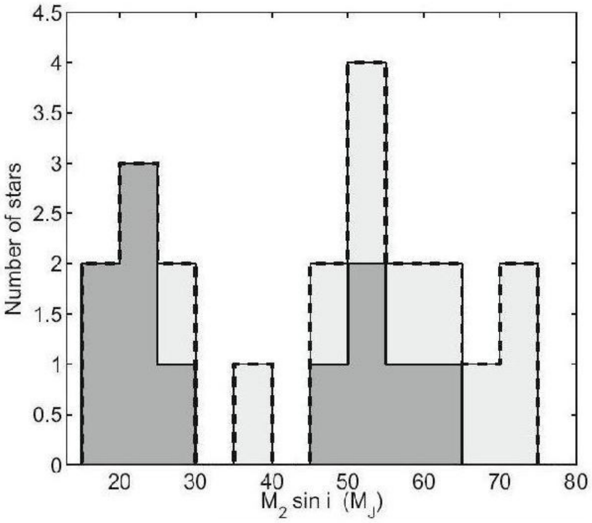

Fig. III.8.4. Low-mass objects histogramme in the 20−75 Jupiter mass region (Sahlman et al. 2011) © A&A.

At least one conclusion is clear, the former mass limit of exoplanets at 13 Jupiter mass, corresponding to the triggering of nuclear burning of Deuterium, is not relevant since an object can be formed by dust accretion and acquire a final mass greater than 13 Jupiter.

There is a second, more factual, problem: the value of observables can be very uncertain. This is especially the case for objects detected by imaging where the mass cannot be infered from radial velocity measurements but only from spectra and models. A typical example is the object 2M1207 (Chauvin et al. 2005) with a Jupiter mass of 4 ± 1 Jupiter mass that can be derived from its spectra. Indeed, in these cases the star-planet separation is so wide that the semi-amplitude $K = \sqrt{(GM_{\text{star}}/a_{\text{planet}})}$ of the stellar radial velocity variation induced by the planet motion is too low to be measurable. Even more: when the mass determination is as precise as a percent (in case of radial velocity or astrometric measurements), one faces the absurd situation of a sharp mass limit. For example, what to do with objects like CoRoT-15 b with $M = 63.3 \pm 4\ M_{\text{Jup}}$?

A last problem, which we do not address here because the concerned population is generally supposed to be small, is the "intersteller wanderers", i.e. planets ejected by dynamical interaction from a well-formed planetary system.

Conclusion

Assuming that the definition of a planet and a brown dwarf is adopted according to their formation mechanism, to separate the two populations is not an easy task. Any catalogue contains necessarily a mixture of both populations. Since catalogues are useful not only to list characteristics of objects but also to make statistics on these characteristics, I recommend to take low constraints (for our case, a mass limit as high as 60 Jupiter mass) on the properties used to define a sample, in order not to miss interesting objects. Modern software used to read electronic catalogues allow to easily eliminate objects from a catalogue which do not fullfil the criteria of definition of each user, who is free to impose his own criteria.

References

Alonso, R., Moutou, C., Endl, M., et al. 2014, A&A, 567, 112

Baraffe, I., Chabrier, G., & Barman, T. 2010, Rep. Progr. Phys., 73, 016901

Barge, P., Baglin, A., Auvergne, M., et al. 2008, A&A, 482, L17

Bouchy, F., Deleuil, M., Guillot, T., et al. 2011, A&A, 525, A85

Chauvin, G., Lagrange, A.-M., Dumas, C., et al. 2004, A&A, 425, L29

Csizmadia, Sz. 2016 Exploration of the brown dwarf regime around solar-like stars by CoRoT in “The CoroT legacy book”, eds. Annie Baglin et al., Publisher: EDP Sciences [arXiv:1603.07597]

Hatzes, A., & Rauer, H. 2015, ApJ, 810, L25

Leger, A., Rouan, D., Schneider, J., et al. 2009, A&A, 506, 287

Moutou, C., & Deleuil, M. 2015, C.R. Acad. Sci. Paris, 347, 153

Ray, A., & Loeb, A. 2015 ApJ, submitted [arXiv:1510.06418]

Sahlman, J., Ségransan, D., Queloz, D., et al. 2011, A&A, 525, A95

Sanz-Forcada, J., Ribas, I., Micela, G., et al. 2010, A&A, 511, L8

Schneider, J., Dedieu, C., Le Sidaner, P., et al. 2011, A&A, 532, A79

Udry, S. 2010, *Detection and characterization of exoplanets: from gaseous giants to super-Earths*, in Proceedings of Proceedings of the conference In the Spirit of Lyot 2010: Direct Detection of Exoplanets and Circumstellar Disks. October 25−29, 2010. University of Paris Diderot, Paris, France. Edited by Anthony Boccaletti.

Acknowledgements: The CoRoT space mission has been developed and operated by CNES, with the contribution of Austria, Belgium, Brazil, ESA, Germany, and Spain.

The CoRoT Legacy Book
DOI: 10.1051/978-2-7598-1876-1.c039

III.9

Star-planet Interactions

A. F. Lanza[1] and S. Ferraz-Mello[2]

[1] INAF-Osservatorio Astrofisico di Catania, Via S. Sofia, 78 - 95123 Catania, Italy
e-mail: nuccio.lanza@oact.inaf.it

[2] Instituto de Astronomia, Geofísica e Ciências Atmosféricas (IAG), Universidade de São Paulo, Brasil
e-mail: sylvio@iag.usp.br

Among the numerous lessons learnt thanks to the CoRoT mission, it is now clear that stellar systems should be considered as a whole, i.e. including both the planets and their host star.

While the communities interested in exo-planetary sciences and stellar physics were bound together by the same instrument, CoRoT, it soon appeared that they share a large number of common interests and that they address similar physical problems among which the star-planet interaction is the most striking.

The first is related to the determination of stellar and planetary parameters, and is discussed partly in Chapters IV.4 and IV.5. Indeed, understanding the planet-star systems requires the determination of the age, mass, and radius of the planet(s), key parameters that are inferred relatively to those of their host star.

And, determining accurate stellar parameters for planetary systems is a mandatory step to constrain the scenarios of planet formation and to determine under which initial conditions and at what stage of their evolution planets can provide a propitious environment for life. Since the formation of planets is intricately related to the formation and evolution of their host star, the ages of planets are directly inferred from those of their parent stars.

Beyond the need for a global approach to characterise the star-planet systems, our ability to understand and model those complex physical systems depends on our capacity to consider properly the interactions between planets and their host star.

They are certainly multiple. Indeed, radiation, magnetic, and gravitational fields are important ingredients to account for.

Understanding this relation is a challenging task since all those physical processes are intimately intricate with each others.

With the CoRoT data, some steps forward have been done. Two of them are presented in this chapter.

Acknowledgements: The CoRoT space mission has been developed and operated by CNES, with the contribution of Austria, Belgium, Brazil, ESA, Germany, and Spain.

The CoRoT Legacy Book

DOI: 10.1051/978-2-7598-1876-1.c139

III.9-1

Investigating star-planet interactions with CoRoT

A. F. Lanza

INAF-Osservatorio Astrofisico di Catania, Via S. Sofia, 78 - 95123 Catania, Italy
e-mail: nuccio.lanza@oact.inaf.it

1. Introduction

The method of transits allows to detect a planet by the periodic light dips it induces on its host star when it passes in front of it once per orbital period. Since the probability of having a suitably oriented orbital plane is R/a, where R is the radius of the star and a the orbital semimajor axis in the case of a circular orbit, this technique strongly favours the discovery of close-in planets. CoRoT (Auvergne et al. 2009) opened a new era in extrasolar planetary studies by allowing for the first time a systematic space-borne search yielding planets with sizes approximately between that of the Earth and Jupiter (Léger et al. 2009; Moutou et al. 2013).

The proximity of those planets to their hosts makes the study of the mutual interactions particularly important. Stars interact with planets through their radiation, magnetic, and gravitation fields. Here, I focus on magnetic interactions considering also the role of tides because they can affect rotation and magnetic activity of the host stars. CoRoT light curves contain a wealth of information to pursue these studies and allow us to address important questions about the way massive close-in planets affect the rotation and hydromagnetic dynamos of their hosts. This is relevant for the measurement of the stellar age through gyrochronology (Barnes 2007; Meibom et al. 2015) and the determination of the planet mass because magnetic activity induces a jitter that limits the accuracy of the radial velocity measurements for planets orbiting active stars.

2. Tidal interaction

Stars are fluid bodies and the gravitational field of a nearby planet induces a deformation of their isopotential equilibrium surfaces that adds to the effect of stellar rotation producing deviations of their shape from spherical symmetry. In addition to this equilibrium tide, the time-varying gravitational potential of the orbiting planet can excite different kinds of oscillations inside the star (dynamic tide). The tidal bulge of the equilibrium tide is carried by stellar rotation away from the line joining the barycentres of the two orbiting bodies. This produces a dissipation of the kinetic energy of the tidal flow, particularly in stars with outer convective envelopes. Similarly, the kinetic energy of the waves excited by the dynamic tide is dissipated in stellar convection zones and radiative interiors. Eventually, the dissipation ceases when the stellar spin becomes aligned with the orbital angular momentum, the orbit is circularized, and the rotation periods of the two bodies become equal to the orbital period (e.g., Zahn 2008; Souchay et al. 2013).

Our current understanding of tides is hampered by a lack of knowledge about the processes that dissipate their kinetic energy leading to the establishment of the above equilibrium state (or the fall of the planet onto its host, in the case its orbital angular momentum is not large enough to reach the equilibrium state). Estimates of the time scale to attain the equilibrium state often span $2-3$ orders of magnitudes. The discovery of close-in planets allows to investigate tidal dissipation in an hitherto unexplored regime characterized by orbital periods from a few to tens of days and a mass ratio of the two bodies $\leq 10^{-3}$. Statistical studies of the distribution of the orbital periods of hot Jupiters provided some constraints on tidal dissipation (e.g., Jackson et al. 2008; Hansen 2010, 2012), but there is still considerable uncertainty because of our ignorance of the initial state and the ages of the considered systems.

Tides affect magnetic activity by modifying the evolution of stellar rotation that plays a fundamental role in controlling the stellar hydromagnetic dynamo (cf. Fig. III.9-1.1). Equilibrium tides might perturb the shape and affect the stability of magnetic flux tubes at the bottom of the convection zone, thus producing preferential longitudes for magnetic activity (Holzwarth & Schüssler 2003a,b), while waves excited by the dynamic tides may affect stellar turbulence, modifying dynamo parameters, notably the magnetic diffusivity. In extreme cases, the dynamo might be quenched by tidal effects (Pillitteri et al. 2014b). On the other hand, the continuum loss of angular momentum produced by a magnetized stellar wind affects tidal evolution on timescales of hundreds of Myrs or Gyrs, possibly preventing the reaching of a final equilibrium state, i.e., leading to the infall of the planet into the star during its main-sequence lifetime (e.g., Damiani & Lanza 2015).

The modification of stellar rotational evolution produced by tides affects the possibility of estimating stellar age by means of gyrochronology with a strong impact on our understanding of planetary systems.

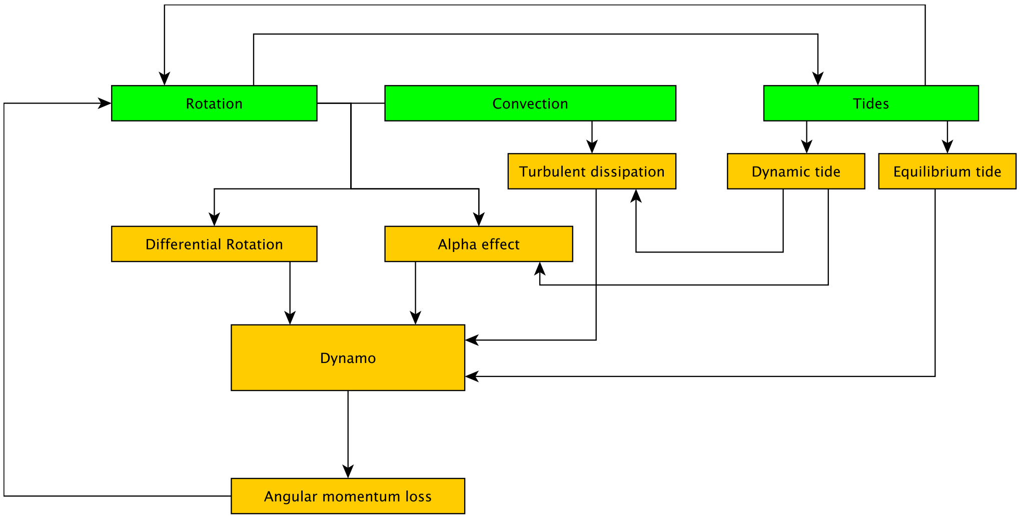

Fig. III.9-1.1. Main connections between stellar rotation, convection, and tides. Rotation and tides directly interact with each other. On the other hand, the interaction of rotation and convection produces differential rotation and the α effect – associated with the helicity of the turbulent flows – that, together with turbulent dissipation, are the basic ingredients of solar-like hydromagnetic dynamos operating in late-type stars. The dynamo affects rotation by producing a steady loss of angular momentum in a magnetized stellar wind. In turn, this modifies the tidal evolution of a planetary system. Equilibrium tides interact with the dynamo by perturbing the shape of large-scale magnetic flux tubes at the base of the stellar convection zone, thus affecting their stability (see the text), while the dynamic tide (by exciting various types of waves) can affect the turbulent dissipation and possibly the α effect.

2.1. Some CoRoT results

CoRoT provided precise measurements of rotation periods in late-type stars with transiting hot Jupiters thanks to the detection of the flux modulation produced by starspots. It measured stars with an activity level too low to reach the same precision from the ground, such as in the case of CoRoT-4 (Aigrain et al. 2008). Since most of the main-sequence lifetime of planetary hosts of F, G, or K-type is characterized by rather low levels of activity, CoRoT allowed to study their rotation without the limitation of spectroscopy that is rather inaccurate for slowly rotating stars. Moreover, CoRoT allowed us to measure a lower limit for the amplitude of surface differential rotation by tracing the longitude migration of starspots vs. time (cf. Lanza et al. 2009a,b, 2011a). Differential rotation affects the age determination by gyrochronology because the rotation period of starspots depends on their latitude. Its measurement is important also for a better understanding of tidal interaction in planetary systems (Guenel et al. 2014).

CoRoT allowed a precise timing of planetary transits with typical errors ranging from a few to tens of seconds on bright stars. This opens the possibility of directly measuring tidal dissipation in some transiting systems. Assuming a tidal dissipation comparable to that observed in close binary stars, precisely a modified stellar tidal quality factor $Q'_{\rm s} = 10^6$, we expect a variation of the epoch of mid transit of 5−10 s in one or two decades in the most strongly interacting systems with respect to a constant-period ephemeris. This is within our reach by combining CoRoT measurements with future measurements by CHEOPS or PLATO 2.0. Systems with a star rotating slower than the orbit should display a shortening of the orbital period, while systems with a star rotating more rapidly, such as CoRoT-11, show an increase of the period (Lanza et al. 2011b). These observations have the potential to put strong constrains on the intensity of tidal interaction allowing to discriminate among different models of tidal dissipation (e.g., Ogilvie & Lin 2007; Ogilvie 2014).

The duration of transits is another parameter that is worth of being measured because it can be changed by the precession of the orbital plane when the stellar spin is oblique to the orbital angular momentum. Rapidly rotating stars, such as CoRoT-11 or WASP-33, have a remarkable quadrupole moment inducing a relatively fast nodal precession (e.g., Damiani & Lanza 2011; Johnson et al. 2015). For both the determination of the orbital evolution and the nodal precession, a sample consisting of several systems is recommended in order to avoid spurious detections due to the perturbations produced by third bodies in the systems. CoRoT-11 is particularly suitable for this kind of measurements because the light curve shows no signs of magnetic activity that could distort the transit profile and affect their timing (cf. Lanza et al. 2011b).

Another important contribution of CoRoT is the measurement of the projected obliquity in the CoRoT-2 system by means of spot occultations during transits (Nutzman et al. 2011). The obliquity between the stellar spin and the orbital angular momentum depends on the mechanism that produced the inward migration of the hot Jupiter after its formation: a loss of angular momentum by planet-disc interaction would produce small obliquity, while planet-planet scattering or Kozai-type mechanisms would induce higher obliquity (for a recent review see Winn & Fabrycky 2015, also discussing other mechanisms). The Rossiter-McLaughlin effect can be used to measure the projected obliquity, but it requires high-precision radial velocity measurements and a sufficiently rapidly rotating star (say, at least $v \sin i \sim 3$ km s^{-1}). On the other hand, the method introduced by Nutzman et al. exploits only high-precision photometry to constrain the projected obliquity. In a nearly aligned system, the same spots are repeatedly occulted during successive transits when the stellar rotation bring them again along the transit chord. Combining out-of-transit precise rotation measurements with the observations of spot features during transits, this method has been extensively applied to Kepler systems (e.g., Sanchis-Ojeda & Winn 2011; Sanchis-Ojeda et al. 2012, just to cite two interesting cases). In the case of oblique systems, it allows to find the latitude of spot formation in a solar-like star and its migration along the activity cycle (Sanchis-Ojeda & Winn 2011; Llama et al. 2012). The correction for nodal precession in the case of rapidly rotating hosts can be derived from the variation of the duration of the transits or estimated from theory.

From a wider perspective, CoRoT provided some of the best characterized transiting planetary systems. Here we focus on the importance of a precise measurement of stellar rotation and the estimate of the amplitude of differential rotation using the light modulation produced by starspots. For a comparison of gyrochronological ages to those derived by isochrone fitting, Maxted et al. (2015) selected a sample of 28 stars with transiting exoplanets whose rotation periods are accurately known, including five CoRoT systems with estimates of the amplitude of the differential rotation that is relevant to controlling one fundamental source of error in the gyro age determination. The discovery of CoRoT-4, with a host star that appears to rotate synchronously in spite of the weak tidal interaction predicted by the theory (Aigrain et al. 2008; Lanza 2010), and of CoRoT-6 and CoRoT-11, whose hosts are rotating more rapidly than the orbital period (Fridlund et al. 2010; Gandolfi et al. 2010) are other valuable results that will certainly allow long-term studies of the tidal effects in systems with close-by planets. CoRoT-6 is also particularly relevant for the study of magnetic star-planet interactions because CoRoT clearly detected its spot activity (Lanza et al. 2011a).

3. Magnetic interactions

Chromospheric hot spots rotating in phase with the orbit of their close-in massive planets have been reported in υ And and HD 179949 by Shkolnik et al. (2005), although the phenomenon is certainly not a steady one (Shkolnik et al. 2008). Pillitteri et al. (2011, 2014a, 2015) found evidence of flaring activity occurring after the occultation egress of the hot Jupiter in HD 189733 in a restricted range of orbital phases ($\phi \simeq 0.52-0.65$) and suggested that, as an alternative to magnetic interaction, the energy could be released by the infall of material evaporated or stripped from the planet onto the star (see the numerical models of Matsakos et al. 2015). In HD 17156, hosting a massive planet on an eccentric orbit with a period of 21 days, there is some preliminary indication of flaring activity preferentially occurring close to periastron (Maggio et al. 2015). In the case of photospheric activity, Béky et al. (2014) reported the case of starspots that rotate in close commensurability with the orbital period in HAT-P-11 and possibly Kepler-17, while Hernán-Obispo et al. (2015) suggested the presence of a close-in planet with a related light curve modulation at the synodic period in BD+20°1790. Details on the theoretical models proposed to account for such observations can be found in, e.g., Lanza (2008, 2012, 2013), while general reviews are presented in Lanza (2011, 2015).

Statistical studies revealed apparent correlations between chromospheric or coronal emissions and close-in massive planets that were successively attributed to biases in the sample selection or to the rather limited number of stars considered (see Poppenhaeger et al. 2010; Poppenhaeger & Schmitt 2011; Canto Martins et al. 2011; Miller et al. 2015, and references therein). The only correlation that gained support by extending the sample and refining the selection criteria was that between the chromospheric log $R'_{\rm HK}$ index and the surface gravity of transiting planets (Hartman 2010; Figueira et al. 2014; Fossati et al. 2015).

3.1. The role of CoRoT

CoRoT played a fundamental role in the study of stellar magnetic activity and of star-planet magnetic interactions by demonstrating the possibility of mapping the surface of active stars using suitable spot modelling techniques applied to high-precision light curves. CoRoT-2 became a benchmark in the field because it has been mapped with different approaches, including spot occultations during transits, thus providing a reliable account of the potentials and the limitations of spot modelling (cf. Lanza et al. 2009a; Huber et al. 2010; Silva-Valio & Lanza 2011, see Fig. III.9-1.2). Spot occultations allowed to derive the distributions of size, contrast and longitude of the spots along the transit chord (Silva-Valio et al. 2010; Silva-Valio & Lanza 2011). Previous comparisons between spot models and maps obtained with Doppler Imaging techniques provided much less definite conclusions on the potentiality of spot modelling (cf. Lanza et al. 2006).

CoRoT-2 is an extremely interesting system in itself. The planet is strongly inflated (Guillot & Havel 2011) and it is possible that stellar activity plays a role in this phenomenon. A crucial parameter to understand this system is its age. From the activity level of the host star and its short rotation period, CoRoT-2 appears younger than ∼0.5 Gyr. However, Poppenhaeger & Wolk (2014), on the basis of the lack of any detectable X-ray emission from its K-type visual companion, proposed an age of at least ∼5 Gyr for the system (cf. Schröter et al. 2011). A similar discrepancy, although not so extreme, was found in HD 189733 that hosts another massive close-in planet. Recently, Maxted et al. (2015) found other planet hosts with ages derived by isochrone fitting significantly older than gyrochronological ages. A tidal spin-up of those stars or a decrease of the magnetic wind braking due to the close-in planet could be possible explanations (see Lanza 2010). To make the case even more intriguing, the Lithium abundance favors a young age in the case of CoRoT-2 (Schröter et al. 2011). The impact of starspots on these measurements is usually regarded as minimal (Pallavicini et al. 1993), but a recent work by Somers & Pinsonneault (2015) suggests that possible effects of activity on Lithium abundance should be investigated.

CoRoT-2 displayed a short-term spot cycle whose period is close to ten times the synodic period of the planet (Lanza et al. 2009a). A similar phenomenon was found in Kepler-17, although no commensurability with the planet orbit was apparent there (Bonomo & Lanza 2012). These short-term cycles have been observed in the Sun close to the maxima of some eleven-year cycles (Rieger et al. 1984; Oliver et al. 1998) and have been suggested in the active close binary system UX Ari (Massi et al. 2005), but their discovery in CoRoT-2 is the first case in another solar-like star. As in the case of the Sun, they are expected to be transient phenomena.

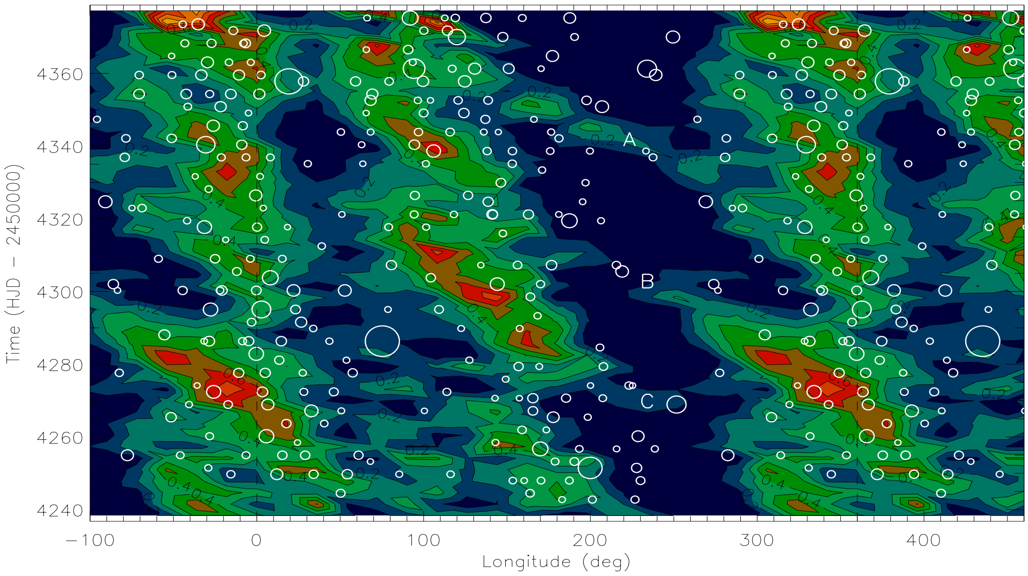

Fig. III.9-1.2. A comparison of the maximum entropy map of the starspot filling factor in CoRoT-2 vs. longitude and time, and the position of the spots occulted during transits (white open circles, the symbol size is proportional to the effective area of the spot). The maximum filling factor corresponds to orange-yellow and red areas, while the minimum is dark blue. Three bridges of spots connecting the two main active longitudes are labelled A, B, and C. Spots detected through their occultation during transits are preferentially located at the active longitudes found in the maximum entropy map of the out-of-transit light curve. This gives strong support to the possibility of mapping spot longitudes using CoRoT out-of-transit light curves (see Silva-Valio & Lanza 2011, for details) (Credit: Silva-Valio & Lanza (2011), reproduced with permission, © ESO).

Another interesting system is CoRoT-1 (Barge et al. 2008) whose chromospheric emission level was found to be remarkably lower than in similar systems (cf. Fig. 2 in Fossati et al. 2013). A possible interpretation is a torus of circumstellar plasma filled by the evaporation of the planet and absorbing in the cores of the Ca II H&K resonance lines. The relatively low surface gravity of the planet may enhance the evaporation thus making this star more absorbed (Lanza 2014).

Finally, CoRoT played a fundamental role in the investigation of the radial velocity jitter associated with stellar magnetic activity, thanks to the discovery of CoRoT-7, the first transiting super-Earth that prompted two campaigns of simultaneous high-precision radial velocity measurements with HARPS. They allowed to discover a second and possibly a third planet in the system. CoRoT-7 fostered the development of several techniques to reduce the impact of the activity-induced jitter on the measurement of the mass of its planets (e.g., Queloz et al. 2009; Hatzes et al. 2011; Ferraz-Mello et al. 2011; Aigrain et al. 2012; Haywood et al. 2014) as well as the treatment of the activity-induced distortions of its transits (Barros et al. 2014). The activity and rotation of this host could be studied in detail thanks to the high-precision CoRoT light curve (Lanza et al. 2010).

4. Conclusions and future prospect

CoRoT achieved very important results in the field of star-planet interactions because it provided very accurate rotation periods and differential rotation amplitudes for several stars with close-in transiting planets, allowing to study their magnetic activity at the photospheric level. Activity features directly associated with the orbiting planet have possibly been found in the case of CoRoT-6 (Lanza et al. 2011a) and CoRoT-4 (Lanza et al. 2009b), but the latter host is rotating synchronously, so any evidence is much less sound. Chromospheric or photospheric features associated with a close-in planet, if real, are characterized by a remarkable time variability with long time intervals without any detectable effect (cf. Santos et al. 2003; Shkolnik et al. 2008). Therefore, a long-term investigation of selected systems is required to confirm and study this kind of interaction; alternatively, a large statistical sample could be monitored for shorter time intervals. This will become possible first with TESS (Ricker et al. 2015) and then with PLATO 2.0 (Rauer et al. 2014) that will target bright stars ($V \leq 12{-}13$), the only ones for which such subtle effects can be detected. Moreover, those telescopes will allow the detection of short-term Rieger-like spot cycles in other late-type stars and a confirmation of those reported in CoRoT-2 and Kepler-17.

The high precision rotation periods determined by CoRoT (and Kepler) are unrivalled in the case of G and K hosts with period longer than 15−20 days because the amplitude of their rotational modulation is at the limit of ground-based photometry. This has contributed to show that in a substantial fraction of host stars with massive close-in planets the age derived from the rotation period through gyrochronology is at variance with the age estimated by isochrone fitting (Maxted et al. 2015). In the case of CoRoT-2, the discrepancy is confirmed by the X-ray observations of its visual companion (Poppenhaeger & Wolk 2014). Again, bright hosts are the best for this kind of investigation because they allow a much better characterization of the parameters of the systems which is difficult in the case of the rather faint targets of Kepler. TESS and PLATO 2.0 will certainly provide very interesting data for a better understanding of the discrepancy, thanks to the observations of planets in wide binaries and in clusters, for which alternative age estimates will be possible. Furthermore, age estimates by asteroseismology

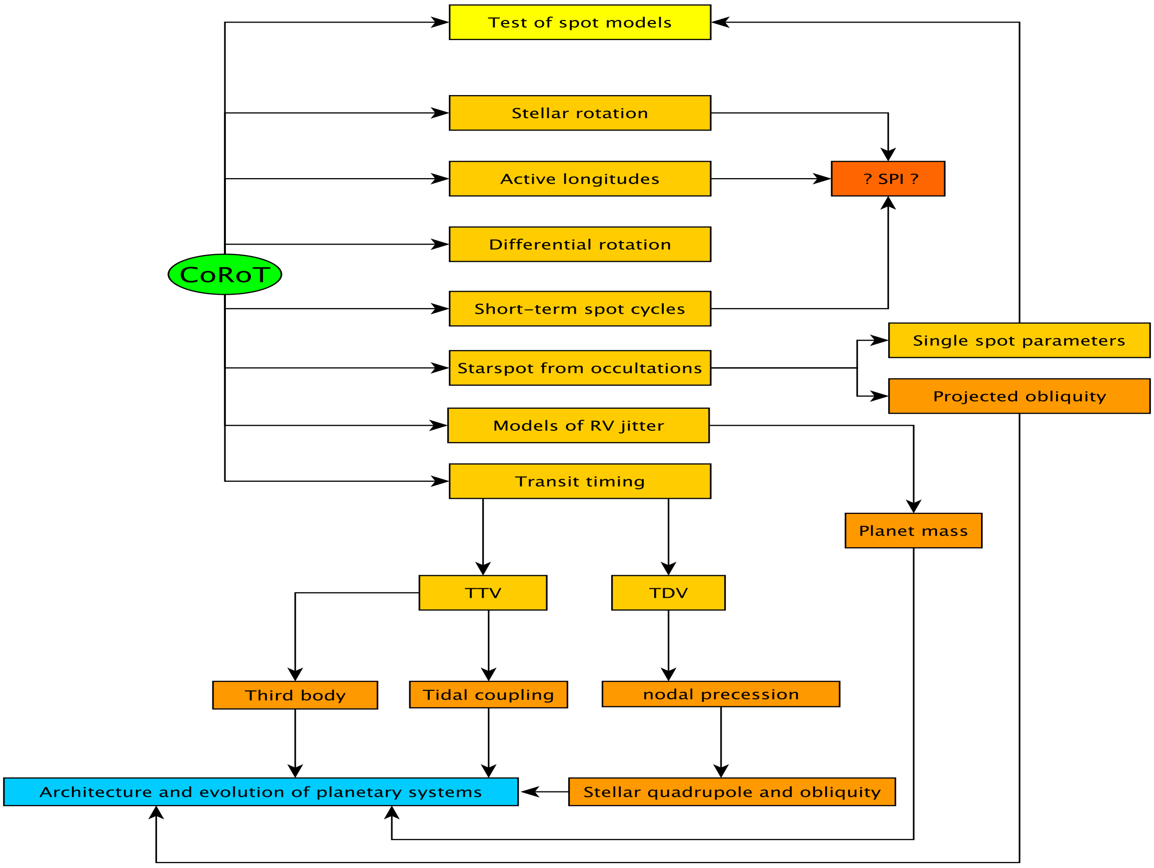

Fig. III.9-1.3. CoRoT main results that are relevant for the study of star-planet interactions. Stellar rotation, active longitudes, and short-term spot cycles might be affected by some direct effect of a close-in massive planet on the stellar dynamo, indicated with SPI. Spot occultations during transits allow us to derive accurate parameters for individual spots to test out-of-transit spot modelling, while providing information on the projected stellar obliquity. Simultaneous high-precision photometry can be used to model and reduce the radial velocity jitter due to stellar activity, thus improving the measurement of a planet's mass. The accurate long-term transit timing possible by combining CoRoT data with those coming from forthcoming space-borne telescopes will allow us to measure transit mid-time variations (TTV) and transit duration variations (TDV) that can be related to the presence of a third body or to angular momentum transfer by tides, and to orbital nodal precession, respectively.

will be provided by PLATO 2.0 with an accuracy of ∼10 percent.

Finally, the re-observation of the bright CoRoT systems with hot Jupiters will provide an estimate of the stellar tidal quality factor $Q'_{\rm s}$, i.e., a measurement of tidal dissipation in solar-like stars. A direct measure of a $Q'_{\rm s} \sim 10^6$ is possible with a time baseline of 15−20 yr in the best cases. Even a non-detection of the expected timing effect will put a lower limit on $Q'_{\rm s}$ ruling out models that predict a strong interaction (cf. Ogilvie & Lin 2007).

A summary of the main results obtained by CoRoT that are relevant for the study of star-planet interactions is provided on Fig. III.9-1.3.

Acknowledgements. The author is grateful to Dr. Annie Baglin and Prof. Magali Deleuil for their kind invitation to review star-planet interactions in the light of CoRoT results. AFL acknowledges support from the National Institute for Astrophysics (INAF) through the *Progetti premiali* funding scheme of the Italian Ministry of Education, University and Research.

References

Aigrain, S., Collier Cameron, A., Ollivier, M., et al. 2008, A&A, 488, L43
Aigrain, S., Pont, F., & Zucker, S. 2012, MNRAS, 419, 3147
Auvergne, M., Bodin, P., Boisnard, L., et al. 2009, A&A, 506, 411
Barge, P., Baglin, A., Auvergne, M., et al. 2008, A&A, 482, L17
Barnes, S. A. 2007, ApJ, 669, 1167
Barros, S. C. C., Almenara, J. M., Deleuil, M., et al. 2014, A&A, 569, A74
Béky, B., Holman, M. J., Kipping, D. M., & Noyes, R. W. 2014, ApJ, 788, 1
Bonomo, A. S., & Lanza, A. F. 2012, A&A, 547, A37
Canto Martins, B. L., Das Chagas, M. L., Alves, S., et al. 2011, A&A, 530, A73
Damiani, C., & Lanza, A. F. 2011, A&A, 535, A116
Damiani, C., & Lanza, A. F. 2015, A&A, 574, A39
Ferraz-Mello, S., Tadeu Dos Santos, M., Beaugé, C., Michtchenko, T. A., & Rodríguez, A. 2011, A&A, 531, A161
Figueira, P., Oshagh, M., Adibekyan, V. Z., & Santos, N. C. 2014, A&A, 572, A51
Fortier, A., Beck, T., Benz, W., et al. 2014, Proc. SPIE, 9143, 91432J introduction
Fossati, L., Ayres, T. R., Haswell, C. A., et al. 2013, ApJ, 766, L20

Fossati, L., Ingrassia, S., Lanza, A. F. 2015, ApJ, 812, L35
Fridlund, M., Hébrard, G., Alonso, R., et al. 2010, A&A, 512, A14
Gandolfi, D., Hébrard, G., Alonso, R., et al. 2010, A&A, 524, A55
Gandolfi, D., Collier Cameron, A., Endl, M., et al. 2012, A&A, 543, L5
Guenel, M., Baruteau, C., Mathis, S., & Rieutord, M. 2014, SF2A-2014: Procs. of the Annual meeting of the French Society of Astronomy and Astrophysics, 233
Guillot, T., & Havel, M. 2011, A&A, 527, A20
Hansen, B. M. S. 2010, ApJ, 723, 285
Hansen, B. M. S. 2012, ApJ, 757, 6
Hartman, J. D. 2010, ApJ, 717, L138
Hatzes, A. P., Fridlund, M., Nachmani, G., et al. 2011, ApJ, 743, 75
Haywood, R. D., Collier Cameron, A., Queloz, D., et al. 2014, MNRAS, 443, 2517
Hernán-Obispo, M., Tuomi, M., Gálvez-Ortiz, M. C., et al. 2015, A&A, 576, A66
Holzwarth, V., & Schüssler, M. 2003a, A&A, 405, 291
Holzwarth, V., & Schüssler, M. 2003b, A&A, 405, 303
Huber, K. F., Czesla, S., Wolter, U., & Schmitt, J. H. M. M. 2010, A&A, 514, A39
Jackson, B., Greenberg, R., & Barnes, R. 2008, ApJ, 678, 1396
Johnson, M. C., Cochran, W. D., Collier Cameron, A., & Bayliss, D. 2015, ApJ, 810, L23
Lanza, A. F. 2008, A&A, 487, 1163
Lanza, A. F. 2010, A&A, 512, A77
Lanza, A. F. 2011, Ap&SS, 336, 303
Lanza, A. F. 2012, A&A, 544, A23
Lanza, A. F. 2013, A&A, 557, A31
Lanza, A. F. 2014, A&A, 572, L6
Lanza, A. F. 2015, 18th Cambridge Workshop on Cool Stars, Stellar Systems, and the Sun, eds. G. van Belle, & H. C. Harris, Proceedings of the Lowell Observatory, Flagstaff AZ USA, 811
Lanza, A. F., Piluso, N., Rodonò, M., Messina, S., & Cutispoto, G. 2006, A&A, 455, 595
Lanza, A. F., Pagano, I., Leto, G., et al. 2009a, A&A, 493, 193
Lanza, A. F., Aigrain, S., Messina, S., et al. 2009b, A&A, 506, 255
Lanza, A. F., Bonomo, A. S., Moutou, C., et al. 2010, A&A, 520, A53
Lanza, A. F., Bonomo, A. S., Pagano, I., et al. 2011a, A&A, 525, A14
Lanza, A. F., Damiani, C., & Gandolfi, D. 2011b, A&A, 529, A50
Léger, A., Rouan, D., Schneider, J., et al. 2009, A&A, 506, 287
Llama, J., Jardine, M., Mackay, D. H., & Fares, R. 2012, MNRAS, 422, L72
Maggio, A., Pillitteri, I., Scandariato, G., et al. 2015, ApJ, 811, L2
Massi, M., Neidhöfer, J., Carpentier, Y., & Ros, E. 2005, A&A, 435, L1
Matsakos, T., Uribe, A., Königl, A. 2015, A&A, 578, A6
Maxted, P. F. L., Serenelli, A. M., & Southworth, J. 2015, A&A, 577, A90
Meibom, S., Barnes, S. A., Platais, I., et al. 2015, Nature, 517, 589
Miller, B. P., Gallo, E., Wright, J. T., & Pearson, E. G. 2015, ApJ, 799, 163
Moutou, C., Deleuil, M., Guillot, T., et al. 2013, Icarus, 226, 1625
Nutzman, P. A., Fabrycky, D. C., & Fortney, J. J. 2011, ApJ, 740, L10
Ogilvie, G. I. 2014, ARA&A, 52, 171
Ogilvie, G. I., & Lin, D. N. C. 2007, ApJ, 661, 1180
Oliver, R., Ballester, J. L., & Baudin, F. 1998, Nature, 394, 552
Queloz, D., Bouchy, F., Moutou, C., et al. 2009, A&A, 506, 303
Pallavicini, R., Cutispoto, G., Randich, S., & Gratton, R. 1993, A&A, 267, 145
Pillitteri, I., Günther, H. M., Wolk, S. J., Kashyap, V. L., & Cohen, O. 2011, ApJ, 741, L18
Pillitteri, I., Wolk, S. J., Lopez-Santiago, J., et al. 2014a, ApJ, 785, 145
Pillitteri, I., Wolk, S. J., Sciortino, S., & Antoci, V. 2014b, A&A, 567, A128
Pillitteri, I., Maggio, A., Micela, G., et al. 2015, ApJ, 805, 52
Poppenhaeger, K., & Schmitt, J. H. M. M. 2011, ApJ, 735, 59
Poppenhaeger, K., Robrade, J., & Schmitt, J. H. M. M. 2010, A&A, 515, A98
Poppenhaeger, K., & Wolk, S. J. 2014, A&A, 565, L1
Rauer, H., Catala, C., Aerts, C., et al. 2014, ExA, 38, 249
Ricker, G. R., Winn, J. N., Vanderspek, R., et al. 2015, J. Astron. Tel. Inst. Sys. 1, 014003
Rieger, E., Kanbach, G., Reppin, C., et al. 1984, Nature, 312, 623
Sanchis-Ojeda, R., & Winn, J. N. 2011, ApJ, 743, 61
Sanchis-Ojeda, R., Fabrycky, D. C., Winn, J. N., et al. 2012, Nature, 487, 449
Santos, N. C., Udry, S., Mayor, M., et al. 2003, A&A, 406, 373
Schröter, S., Czesla, S., Wolter, U., et al. 2011, A&A, 532, A3
Shkolnik, E., Walker, G. A. H., & Bohlender, D. A. 2003, ApJ, 597, 1092
Shkolnik, E., Walker, G. A. H., Bohlender, D. A., Gu, P.-G., Kürster, M. 2005, ApJ, 622, 1075
Shkolnik, E., Bohlender, D. A., Walker, G. A. H., & Collier Cameron, A. 2008, ApJ, 676, 628
Silva-Valio, A., Lanza, A. F., Alonso, R., & Barge, P. 2010, A&A, 510, A25
Silva-Valio, A., & Lanza, A. F. 2011, A&A, 529, A36
Somers, G., & Pinsonneault, M. H. 2015, MNRAS, 449, 4131
Souchay, J., Mathis, S., & Tokieda, T. 2013, Tides in Astronomy and Astrophysics, Lecture Notes in Physics, 861
Winn, J. N., & Fabrycky, D. C. 2015, ARA&A, 53, 409
Zahn, J.-P. 2008, EAS Publications Series, 29, 67

Acknowledgements: The CoRoT space mission has been developed and operated by CNES, with the contribution of Austria, Belgium, Brazil, ESA, Germany, and Spain.

The CoRoT Legacy Book
© The authors, 2016
DOI: 10.1051/978-2-7598-1876-1.c239

III.9-2

Tidal evolution of CoRoT massive planets and brown dwarfs and of their host stars

S. Ferraz-Mello

Instituto de Astronomia, Geofísica e Ciências Atmosféricas (IAG), Universidade de São Paulo, Brasil
e-mail: sylvio@iag.usp.br

1. Introduction

The CoRoT exoplanets and brown dwarfs are, by far, the most suitable extrasolar planetary systems for the appraisal of the consequences of the exchanges and losses of mechanical energy and angular momentum associated with the tidal deformation of the bodies.

Given the almost impossibility of the direct observation of the very slow tidal changes in the orbital and rotational elements, the only way to assess the strength of these changes is by comparing the current values of those elements to their assumed primordial values. For that sake, the main tracers of the past tidal effects in the observed extrasolar planetary systems are the stellar rotational period and the orbital eccentricity. One element strongly affected by tides is the rotation of the exoplanet; however, besides not observed, the rotation capture into a steady supersynchronous state (a.k.a. pseudo-synchronous) predicted by classical tidal theories, is very fast and close-in exoplanets are expected to be in that state with no memory of its past evolution.

The privilege of the CoRoT exoplanets over others stem from several reasons:

- the better signal-to-noise ratio of space photometric measurements;
- the careful follow-up observations using last-generation spectrographs. They allowed for the determination of the true planetary masses and for the accurate modelling of the host stars, which resulted in the reasonable knowledge of their physical characteristics and ages;
- the better orbital eccentricities resulting from the joint analysis of transits and radial velocities observed in close epochs, instead of estimations based only on the asymmetry of the radial velocity curves when transits are not observed;
- the continuous photometry over long timespans, in many cases allowing for the determination of the stellar rotational periods without the inclination indetermination of the spectroscopically measured $V_{\rm rot} \sin I$.

When all these elements and parameters are available, the existing theories may be used to have an estimation of the past evolution of the system and the ruling out of scenarios in contradiction with our knowledge of planetary and stellar formation and of the planetary migration, may be used to constrain the tidal parameters entering in the theories. This is a fundamental contribution because the currently used tidal parameters of exoplanets and their host stars are just extrapolations from solar system analogs and the imprecision in their knowledge do not allow us to make reliable predictions of the future evolution of these systems. The actual knowledge of the real parameters is currently limited to the results issued from simulations of the distribution of the initial eccentricity values of close-in planets (Jackson et al. 2008), and from the analysis of the survival of some short-period planets around evolving stars and of the limits for circularization of planets with highly eccentric orbits (Hansen 2012).

One extra factor favoring the use of the CoRoT systems in the study of tidal phenomena is the great proportion of very massive planets and brown dwarfs among them. About 1/3 of the discovered CoRoT planets have masses larger than 2 $M_{\rm Jup}$. The large masses of the companions enhance tidal effects and thus allow for more robust analyses.

In this paper, we select among the 30 discovered CoRoT systems those that may be considered as paradigms, or, at least, as very significant examples of tidal evolution scenarios of extrasolar planetary systems.

In order to model the evolution of the selected systems, we need to use one of the available tidal theories. We adopt the creep tide theory (Ferraz-Mello 2013), for which we dispose of codes allowing us to obtain the variation of the stellar rotational period and of all orbital elements with high formal precision, even when the orbital eccentricities become very large. It is important to stress that all available theories are more or less equivalent when the considered bodies are predominantly fluid, with low Reynolds numbers (Stokes fluids) and should give comparable results to those presented in this paper. It is also necessary to use one theory to assess the stellar loss of rotational angular momentum through the magnetic phenomena associated with the stellar winds. We adopt the formulas proposed by Bouvier et al. (1997). These formulas account in a satisfactory way for the rotation of single stars observed in clusters of known ages (Bouvier 2013), once the very active initial phases are over, and allows one to reproduce the Skumanich's law (Skumanich 1972). More complete theories exist taking into account more complex patterns of the magnetic activity of the stars, but they involve physical parameters not known for the considered stars (see Matt et al. 2012).

The theories used here are the same that were used to study the interplay of tidal evolution and stellar wind braking in the rotation of stars hosting massive close-in planets by Ferraz-Mello et al. (2015).

2. CoRoT 33. The paradigm

All favorable circumstances are present in this system formed by an active G star and a massive brown dwarf in a close-in orbit. The modelling of the tidal evolution of this system unravelled a typical scenario which, in less marked circumstances, happens also in systems with massive planets as CoRoT-27 and KEPLER-75 (see Ferraz-Mello et al. 2015). In its young ages, once the star is decoupled from the disk and is no longer subject to significant changes, we should expect to find it as a fast rotator.

The evolution of the stellar rotation is controlled by two effects: the torques due to the tides raised by the companion on the star and the leakage of angular momentum due to the magnetic wind braking of the star. Since the magnetic braking $\dot{\Omega}$ is proportional to Ω^3, the braking dominates the initial evolution of the stellar rotation, when the angular rotational velocity Ω is large. However, as the age and the rotational period grow, the braking weakens and, after some time, the tidal effects dominate over the braking and the stellar rotation is accelerated. The energy spent accelerating the star rotation leads the planet to spiral towards the star and, if it lives long enough, it will fall on the star, transferring to it all of its angular momentum. In the case of CoRoT-33, the age of the star is large and it allowed the system to reach this latter stage. The brown dwarf is slowly falling towards the star, the rotation of which is being slowly accelerated.

Figure III.9-2.1 shows the expected evolution of CoRoT-33 during its lifetime. The estimated stellar tidal relaxation factor $\gamma_{\rm st}$ for this star, depending on the actual orbital and rotational parameters used, lies between 30 and 60 s^{-1}. The formulas relating the tidal relaxation factor and the quality factor Q (see Ferraz-Mello 2013) indicate that this result corresponds to Q in the interval $3{-}6 \times 10^6$, which is in the mid of the interval $7 \times 10^5{-}4.5 \times 10^7$ that we obtain from Hansen's (2012) results for a sample of planet hosting stars, if we adopt the stellar Love number $k_2 = 0.2$.

Several experiments were done letting the companion's rotation to vary freely. The results showed that in that case, the companion takes about 1−2 Gyr to reach a synchronous rotation. However the results for the evolution of the stellar rotation and of the orbital elements (a, e) of the companion are the same as those obtained when the capture in the steady supersynchronous stationary rotation is assumed ab initio.

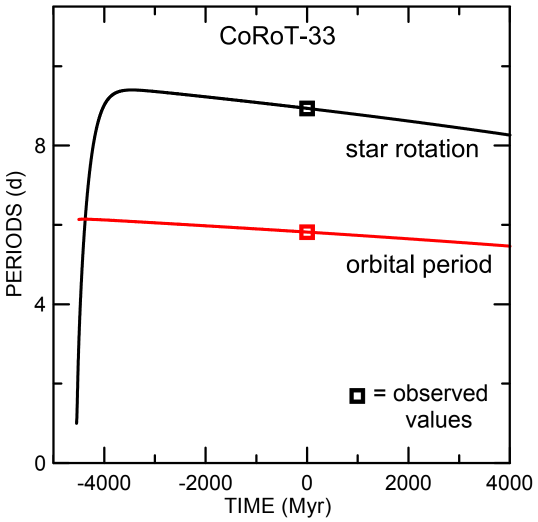

Fig. III.9-2.1. Simulations of the evolution of the rotational period of CoRoT-33 (black) and of the orbital period of the companion CoRoT-33b (red). Adopted stellar tidal relaxation factor: ~36 s^{-1}.

We may mention that the past evolution of the system is critically dependent on the current rotational period. If $\gamma_{\rm st}$ is different, we may have either a star whose rotation was recently too fast or too slow. However, the numerical accuracy required to determine $\gamma_{\rm st}$ is not real. The spectroscopically determined rotational period has large dispersion (~1 d) and the photometric period may be different from the actual rotational period. Some striking commensurabilities between the stellar rotational period and the orbital period in some extrasolar planetary systems (e.g. 3/2 in the present case), allow us to suspect that the magnetic fields controlling, on the surface of the stars, the features responsible for the measured periodic variations in the star's light are modulated by the orbital period of the massive close-in companions (see Béky et al. 2014).

To conclude, let us add that the comparison of the solutions with and without the consideration of the magnetic braking shows that the circularization of the orbit of the companion and its fall toward the star are both accelerated by the angular momentum leakage since, in this case, the stellar energy losses are also contributing to the planet fall.

CoRoT-27

CoRoT-27 is very similar to CoRoT-33. Aged and with a super-Jupiter as companion, the same evolutionary processes seen in CoRoT-33 are present in this case (see Ferraz-Mello et al. 2015). The best representation of the parameters of this system was obtained assuming $\gamma_{\rm st} = 90\ \mathrm{s}^{-1}$ (corresponding to $Q = 2.7 \times 10^6$ if $k_2 = 0.2$).

CoRoT-23

Another system showing a similar behavior is CoRoT-23. The study of the evolution of the stellar rotation with the data given in Table III.9-2.1 results in $\gamma_{\rm st} \sim 8\ \mathrm{s}^{-1}$; this value corresponds to the quality factor $Q = 4 \times 10^5$ (if $k_2 = 0.2$), which is below the lower limit of the interval determined by Hansen (2012). The discovery paper (Rouan et al. 2012)

Table III.9-2.1. Basic parameters of the CoRoT systems discussed in this paper.

Star	Spect. type	Star mass ($M_\odot$)	Compan. mass (M_{Jup})	Orbital period (d)	Rotation period (d)	Eccentricity	Age (Gyr)
CoRoT-2[1]	G7V	0.97 ± 0.06	3.31 ± 0.16	1.742996(2)	4.52 ± 0.02^a	<0.06	0.2−4.0
CoRoT-3[2,13]	F3	1.37 ± 0.09	21.8 ± 1.0	4.256799(4)	$\sim 3.65^a$ [15]	0.012(10)	1.6−2.8
CoRoT-5[3]	F9V	1.0 ± 0.02	$0.467\ ^{+0.047}_{-0.024}$	4.037896(2)	$>30^b$	$0.09^{+0.09}_{-0.04}$	6.9 ± 1.4
CoRoT-11[4]	F6V	1.27 ± 0.05	2.33 ± 0.27	2.994325(21)	1.73 ± 0.22^b	<0.2	2.0 ± 1.0
CoRoT-14[5,14]	F9V	1.13 ± 0.09	6.94 ± 0.5	1.51214	5.6 ± 0.5^a	0	0.4−8.0
CoRoT-15[6]	F7V	1.32 ± 0.12	63.3 ± 4.1	3.06036(3)	^{c}	0	1.14−3.35
CoRoT-16[7]	G5V	1.10 ± 0.08	0.535 ± 0.085	5.35227(2)	$<60\ ^b$	0.33 ± 0.1	6.7 ± 2.8
CoRoT-18[8,13]	G9V	0.95 ± 0.15	3.47 ± 0.38	1.900070(3)	$5.4 \pm 0.6\ ^a$	<0.08	0.05−1.0
CoRoT-20[9]	G2V	1.14 ± 0.08	4.24 ± 0.23	2.48553345(7)	$11.5 \pm 3.1\ ^b$	0.562(13)	<1
CoRoT-23[10]	G0V	1.14 ± 0.08	2.8 ± 0.25	3.6314(1)	$9.0 \pm 1.0\ ^{b,d}$	0.16 ± 0.02	$7.2^{+0.5}_{-1.0}$
CoRoT-27[11]	G2	1.05 ± 0.11	10.39 ± 0.55	3.57532(6)	12.7 ± 1.7^b	<0.065	4.2 ± 2.7
CoRoT-33[12]	G9V	0.86 ± 0.04	59.0 ± 1.8	5.819143(18)	8.936 ± 0.015^a	0.0700(16)	>4.6

Notes. (a) photometric; (b) $\times \sin I$; (c) photometric modulations at 2.9, 3.1 and 6.3 d; (d) id. at 10.5 d. (1) Alonso et al. (Alonso et al. 2008); (2) Deleuil et al. (2008); (3) Rauer et al. (2009); (4) Gandolfi et al. (2011); (5) Tingley et al. (2011); (6) Bouchy et al. (2011); (7) Ollivier et al. (2012); (8) Hébrard et al. (2011); (9) Deleuil et al. (2012); (10) Rouan et al. (2012); (11) Parviainen et al. (2014); (12) Csizmadia et al. (2015); (13) Moutou et al. (2013); (14) Ferraz-Mello et al. (2015); (15) Tadeu dos Santos (priv. comm.).

mentions a peak in the power spectrum of the photometric measurements at 10.5 d. If this value is adopted for the rotational period, the resulting γ_{st} and Q are doubled and are in agreement with Hansen's determinations.

3. CoRot 3. The dissipation in an F star

CoRoT-3b is a brown dwarf in orbit around an F3 star. In all other systems involving a nonactive F star with a massive companion (e.g. CoRoT-15, KELT-1, HAT-P-2), the stellar rotational period is very close to the orbital period of the companion, what means that the system has lost completely the memory of its past evolution and do not allow even for a rough estimate of the stellar tidal dissipation factor γ_{st}. In the case of CoRoT-3, however, the stellar rotation is faster than the orbital period, indicating that the synchronization has not yet been reached. The value 3.65 d obtained by Tadeu dos Santos (priv. comm.) from a reanalysis of the Rossiter-McLaughlin effect in the observations done by Triaud et al. (2009), is reinforced by the existence of a peak at about 3.6 days in the power spectrum of the photometric signal.

We present on Fig. III.9-2.2, the tracks corresponding to stellar relaxation factors between 40 and 120 s^{-1}. In all cases, the star has a fast initial rotation and the brown dwarf is in an orbit above the synchronous (or corotation) orbit. The strong tidal interaction between the companion and the star slows down the star's rotation, which tends to approximate the synchronization. The companion, on its turn, is being accelerated by the tidal torque due to the fast rotating star and earns energy, moving away from the star.

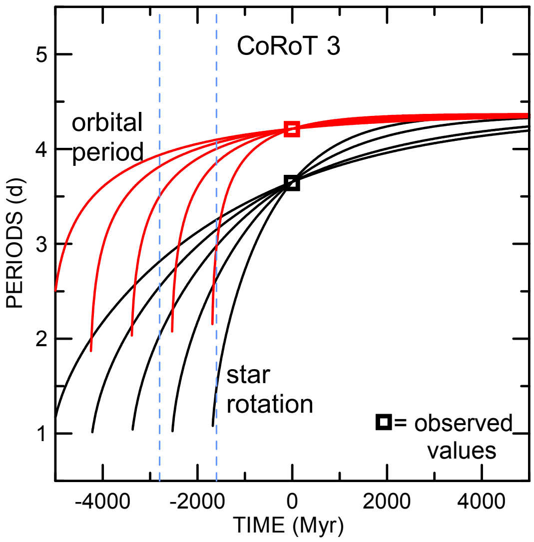

Fig. III.9-2.2. Simulations of the evolution of the rotational period of CoRoT-3 (black) and of the orbital period of the companion CoRoT-3b (red). Adopted stellar tidal relaxation factors (starting from the steepest curves): 40, 60, 80, 100, 120 s^{-1}. The dashed vertical lines show the stellar age range.

We may take advantage of the large mass of the brown dwarf and select the evolutionary tracks compatible with the age of the system and its rotational period. The curves leading to a fast stellar rotation in a time corresponding to the age of the system (1.6−2.8 Gyr) are those for which γ_{st} is between 40 and 70 s^{-1}, which corresponds to $Q \sim 6-9 \times 10^6$ (if $k_2 = 0.2$). Given that we have used a planar model and that the study of the Rossiter-McLaughlin effect indicates an obliquity larger than 30 degrees, it is prudent to bracket this value with a somewhat larger interval. The value is of the same order as the values found for G stars (as CoRoT-33 and CoRoT-27, for example), and their comparison serves to estimate the role played in the stellar tidal dissipation by the existence of a convective zone.

The system may be evolving towards a double synchronization as already indicated by previous studies of this star by Carone (2012). The dissipation in the planet is negligible; tests with several values of the planetary tidal relaxation factor were done and did not show any change in the results.

CoRoT-11

The rotational evolution of the F6V star CoRoT-11 has been studied by Lanza et al. (2011) with a model adopting a magnetic braking of about 1/4 of the value adopted by Bouvier et al. (1997) for less massive stars. That study allowed them to constrain the value of the stellar tidal quality factor averaged over the life of the system to the interval $5 \times 10^5 – 2.5 \times 10^6$ (for $k_2 = 0.2$). These values match the lower part of the interval determined by Hansen (2012) for general host stars. Lanza et al. (2011) also note that their results are 3–15 times smaller than the prediction from the theoretical results of Barker and Ogilvie (2009) for the quality factor of a similar star.

The study of this system is made particularly difficult by the uncertainty on the current eccentricity of the system. Lanza et al. (2011) adopted $e = 0$ on the grounds that a circular orbit is compatible with the available radial velocity measurements.

4. CoRoT 15. The double synchronization

Because of its mass and spectral type (F7V), CoRoT-15 is not expected to be active and the evolution may be fully controlled by the tidal interactions. In the past, this system may have shown a situation similar to that of CoRoT-3 (see Fig. III.9-2.2), but in the case of CoRoT-15, because of the larger mass of the companion and its closer proximity to the star, this process was faster and the full synchronization may have been reached a long time ago. It may be currently in a state in which the eccentricity is zero and all periods, rotational and orbital, are equal. Any attempt to model the recent evolution of the system by assuming that the stellar rotational period is different from the orbital period results into physically unacceptable solutions where the star is showing a too fast or a too slow rotation a short time ago. In addition, no residual eccentricity may have survived the fast damping due to those conditions.

The only alternative to this scenario is the presence of a residual activity (see Barker & Ogilvie 2009). If a small activity, say, around 10 percent of that of a G star is accepted, the situation is almost the same except that the system will no longer be stationary. The brown dwarf will be slowly falling on the star whose rotation will be accelerated preserving the synchronism. But, even in this case, the system would not be expected to show significant changes during the star's remaining lifetime.

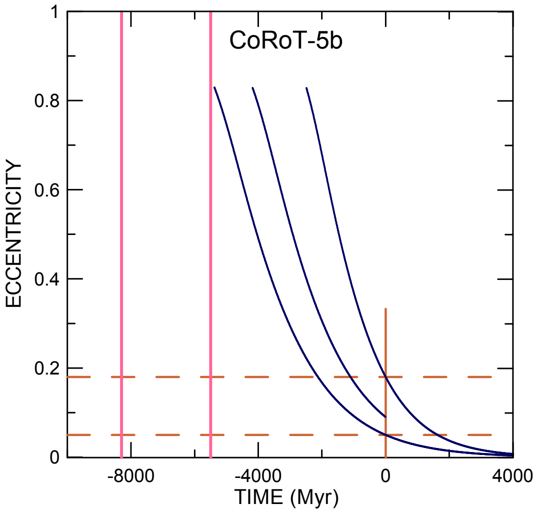

Fig. III.9-2.3. Simulations of the past tidal evolution of the eccentricity of CoRoT-5b for initial eccentricities 0.05, 0.09 and 0.18. Adopted planetary tidal relaxation factor: 200 s^{-1}. The vertical lines show $t = 0$ and the stellar age range. The horizontal lines show the error bar of the observed eccentricity. (Adapted from Ferraz-Mello 2013).

5. CoRoT-5. Planetary tide and dissipation

In this system, the memory of the past evolution is kept by the eccentricity and it was the first for which the analysis of the discussed models was used to estimate the tidal relaxation factor of one hot Jupiter (Ferraz-Mello 2013). The simulations of this system show a significant rate of circularization and the eccentricity must have been larger in the past. However, if the tidal dissipation is larger than a certain limit, we are forced to assume that the eccentricity has been too high in a recent past. All general mechanisms responsible for important eccentricity enhancement are related to events expected to happen only in the early life of the system (see Malmberg & Davies 2009). Therefore the rate of circularization of the system may not impose high eccentricities in a recent time. Fig. III.9-2.3 shows the solutions corresponding to the planetary tidal relaxation factor $\gamma_{\rm pl} = 200\ s^{-1}$ for initial eccentricities within the range resulting from the analysis of the observations (we used the more probable value and the minimum and maximum of the interval of confidence).

The limit 200 s^{-1} corresponds to the quality factor $Q = 5 \times 10^6$ (if $k_2 = 0.35$) and is inside the range $2 \times 10^6 – 2 \times 10^7$ determined by Hansen (2012) from his analysis of survival of close-in exoplanets. However, it is at least one order of magnitude larger than the values that we obtain by extrapolating to the bloated radius of CoRoT-5b, the values of Q determined for the giant planets of our Solar System (see Ferraz-Mello 2013). It is worth noting that if a relaxation factor 10 times smaller is adopted, the resulting larger circularization rate would impose eccentricities close to 1 in the past Gyr, what would be impossible to explain with the current knowledge of the exoplanets orbital evolution.

The present planetary rotation does not interfere with the results. As extensively studied by Carone (2012), the rotation of the close-in planets in the CoRoT systems is

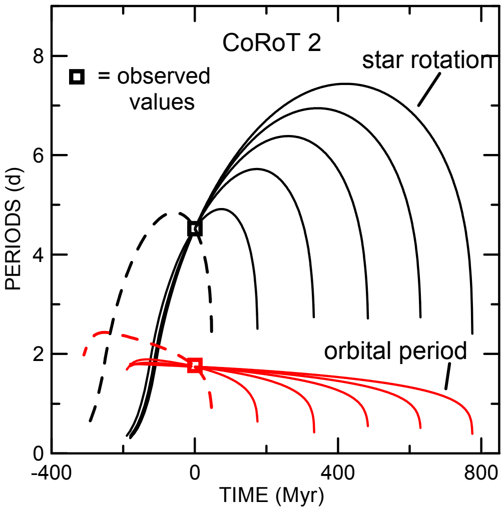

Fig. III.9-2.4. Simulations of the evolution of the rotational period of of CoRoT-2 (black) and of the orbital period of the planet CoRoT-2b (red). Adopted stellar tidal relaxation factors: 5 (dashed line), 20, 40, 60, 80, 100 (solid lines) s^{-1}. (Taken from Ferraz-Mello et al. 2015)

quickly (less than 1 Myr) driven to a stationary solution. In this case, because of the past high eccentricity, the rotation may have been soon captured in a supersynchronous stationary solution and must be evolving since then in the stationary solution often called pseudo-synchronous solution. The stellar rotation, on its turn, is very slow and does not affect the results.

6. CoRoT-2. A gyrochronology example

The host star of this system is likely a very young star. Its X-ray luminosity and strong chromospheric emission indicate a stellar age of about 200-300 Myr (Poppenhaeger & Wolk 2014). The low age is the source of the main difficulty. The stellar rotation did not yet reach the point where tidal torques and angular momentum leakage are close to equilibrate themselves, and it is not possible to make an estimation of the stellar tidal relaxation factor. For this reason, we present on Fig. III.9-2.4, for comparison, the tracks corresponding to stellar tidal relaxation factors between 20 and 100 s^{-1}. The first noteworthy feature in this fountain-like plot is that the evolution of the past stellar rotation is strongly controlled by the magnetic braking. The role of the tidal forces is secondary and we should assume very strong dissipation (i.e., a very small γ_{st}) to see a solution not coincident with the dominant ones. The convergence of the paths to the path corresponding to braking only (i.e. to the Skumanich's law) points to the origin of the system 200 Myr ago, exactly as it would result from the application of the gyrochronology rules without taking the tides into account (see Brown 2014). The low age of the star brings with it another difficulty. The star is bloated ($R = 1.465 \pm 0.029\ R_\odot$) and still contracting. This introduces a new factor in the problem: The rotation has an unmodelled component of acceleration not considered in the used models, and the actual age may be larger than that predicted by gyrochronology rules.

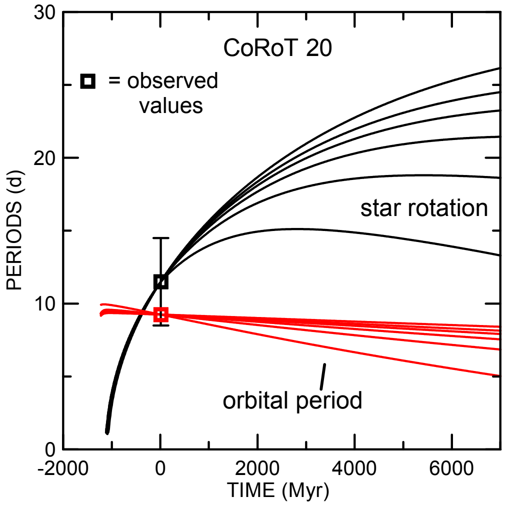

Fig. III.9-2.5. Simulations of the evolution of the rotational period of of CoRoT-20 (black) and of the orbital period of the planet CoRoT-20b (red). Adopted stellar tidal relaxation factors (starting from the lower curves): 10, 20, 30, 40, 50, 70 s^{-1}.

CoRoT-18

Several other stars in the CoRoT family show similar behavior. The most similar case is CoRoT-18 (see Ferraz-Mello et al. 2015) which also is a bloated young star just a bit older than CoRoT-2.

CoRoT-14

A second case showing some resemblance, but not as young as the previous ones, is CoRoT-14. In this case, in order to obtain an evolution leading to the current orbital and rotational elements, we would need to assume a much smaller tidal dissipation (much larger γ_{st}). Several hypotheses were discussed considering this F9V star (see Ferraz-Mello et al. 2015). Besides the possibility of having some actual parameter different of the published ones, we may also suspect that the measured surface rotation does not reflect the rotation of the inner radiative core, which would be rotating much faster.

7. CoRoT-20. A high eccentricity system

This is also a star of low age in which the angular momentum leakage is dominating. As for CoRoT-2 and CoRoT-18, the age of the star is not large enough to allow us to estimate the value of the stellar tidal relaxation factor γ_{st} but, in compensation, the past rotation of the star was dominated by the magnetic brake and the system is well suited for the estimation of its age via gyrochronology. As in the case of CoRoT-2, we use a grid of values and construct the fountain-plot shown on Fig. III.9-2.5 and see that the evolutionary tracks converge to a fast-rotating star in ~1.1 Gyr.

The lack of knowledge of the stellar tidal relaxation factor does not allow us any definite prediction of its future evolution. However, for the expected values of the relaxation factor, the system is stable. The orbit is spiralling

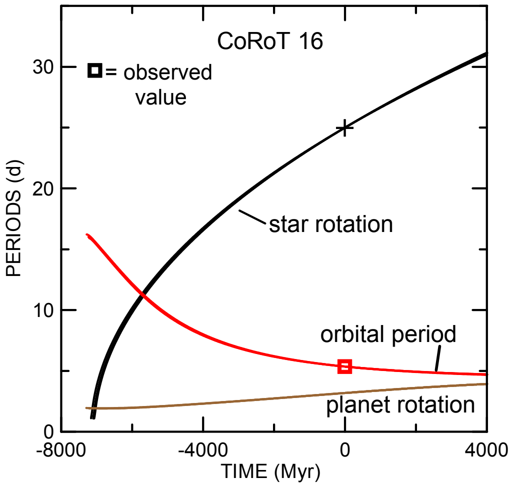

Fig. III.9-2.6. CoRoT-16: simulations of the evolution of the stellar (black) and planetary (brown) rotational periods and of the orbital period of the planet (red). Adopted stellar tidal relaxation factors between 30 and 80 s^{-1} (superposed).

towards the star, but at a slow pace. The great difference between this cases and the previous ones is that the current orbit of the companion is very eccentric; the rate of circularization may be significant, but in no case the eccentricity is expected to be close to zero in the star's lifetime.

The rotation of the star will evolve following the patterns described in previous sections. It is worth recalling that the previous studies of this system (Deleuil et al. 2011; Carone 2012) have already pointed out the stability of the system and that, in the absence of magnetic braking, the system would have been a candidate for future double synchronization.

8. CoRoT-16. A limit case

CoRoT-16b is a hot Saturn in an orbit beyond the limit where the tidal interactions with the star influence significantly the stellar rotation. The large indetermination in the given stellar rotational period does not allow us to use a gyrochronology model to determine the star's age, but if we consider the inverse problem, we see that the known isochronal age of the star may be used to better constrain the current stellar rotational period to the neighborhood of 25 d.

Figure III.9-2.6 shows the evolution of the three periods present in this system: the orbital period and the rotational periods of both the star and the planet. The thick lines are the superposition of solutions obtained using stellar relaxation factors $\gamma_{\rm st}$ between 30 and 80 s^{-1}. The rate of circularization of the orbit is not large and it will last yet some time before circularization, which may happen by the end of the star's lifetime.

The significant eccentricity of the orbit can be used to constrain the planetary tidal relaxation factor. As for CoRoT-5b, the past evolution of the eccentricity depends on the adopted eccentricity. Taking into account the error bar of the current eccentricity, we get, for the limit value, the estimate: $\gamma_{\rm pl} > 30$ s^{-1}, which corresponds in terms of the quality factor to $Q > 9 \times 10^5$. This limit is almost equal to the value 8×10^5 adopted in the discovery paper (Ollivier et al. 2012). It is lower than the limit found for CoRoT-5b. However, this estimate is strongly affected by the error bars in the stellar period and in the orbital eccentricity. If a more accurate redetermination would be possible, we should expect an improved larger limit.

9. Conclusion

This paper shows that several of the CoRoT planetary systems had their tidal evolution studied with some accuracy due to the high-quality of the determined physical parameters, rotational and orbital elements. For these systems, it has been possible to constrain the values of the tidal relaxation factor of the host star or of the planet and the results, with only a partial exception, agree with the estimates of the tidal dissipation quality factor in the extended sample of short-period planetary systems studied by Hansen (Hansen 2012).

These successful cases may be seen as paradigms or, at least, as significant examples of what can yet be done using other exoplanetary systems. The main perspective concerns systems discovered by KEPLER. Many of these systems are now being observed from ground with last-generation spectrographs and we may expect that these follow-up observations will produce more accurate masses, ages, rotational and orbital elements so that they may be included in the set of successful case studies, as it was already done for KEPLER-75 (see Ferraz-Mello et al. 2015). We may also have these paradigms in mind when planning new missions, as PLATO. With relatively brighter stars as targets, we may hope that the exoplanetary systems to be discovered by PLATO be observed from the ground in epochs not too distant from the epochs of the space photometric observations so that the determination of the eccentricities can actually benefit of the complementarity of the two observational techniques and be obtained with better accuracy.

Acknowledgements. This investigation was supported by grants CNPq 306146/2010-0, FAPESP 2014/13407-4 and by INCT Inespaço procs. FAPESP 2008/57866-1 and CNPq 574004/2008-4. The help of Mr. E.S. Pereira in the calculation of some complementary examples is acknowledged.

References

Alonso, R., Auvergne, M., Baglin, A., et al. 2008, A&A, 482, L21
Barker, A. J., & Ogilvie, G. I. 2009, MNRAS, 395, 2268
Béky, B., Holman, M. J., Kipping, D. M., & Noyes, R. W. 2014, ApJ, 788, 1
Bouchy, F., Deleuil, M., Guillot, T., et al. 2011, A&A, 525, A68
Bouvier, J., Forestini, M., & Allain, S. 1997, A&A, 326, 1023
Bouvier, J. 2013, EAS Publ. Series Vol. 62, 143
Brown, D. J. A. 2014, MNRAS 442, 1844
Carone, L. 2012, Doctoral dissertation, Universität zu Köln.
Csizmadia, S., Hatzes, A., Gandolfi, G., et al. 2015, A&A (in press). Preprint [`arXiv:1508.05763`]
Deleuil, M., Deeg, H. J., Alonso, R., et al. 2008, A&A, 491, 889
Deleuil, M., Bonomo, A. S., Ferraz-Mello, S., et al. 2012, A&A, 538 A145

Ferraz-Mello, S., Rodríguez, A., & Hussmann, H. 2008, Celest. Mech. Dyn. Astr. 101, 171 and Errata: Celest. Mech. Dyn. Astr.: 104, 319-320 (2009) [arXiv:0712.1156]
Ferraz-Mello, S. 2013, Celest. Mech. Dyn. Astr. 116, 109
Ferraz-Mello, S., Santos, M., Folonier, H., et al. 2015, ApJ, 807, 78
Gandolfi, D., Hébrard, G., Alonso, R., et al. 2011, A&A, 524, A55
Hansen, B. M. S. 2012, ApJ, 757: 6
Hébrard, G., Evans, T. M., Alonso, R., et al. 2011, A&A, 533, A130
Jackson, B., Greenberg, R., & Barnes, R. 2008, ApJ, 678, 1396
Lanza, A. F., Damiani, C., & Gandolfi, D. 2011, A&A, 529, A50
Malmberg, D., & Davies, M. B. 2009, MNRAS, 394, L26
Matt, S. P., MacGregor, K. B., Pinsonneault, M. H., & Greene, T. P. 2012, ApJ, 754, L26
Moutou, C., Deleuil, M., Guillot, T., et al. 2013, Icarus, 226, 1625
Ollivier, M., Gillon, M., Santerne, A., et al. 2012, A&A, 541, A149
Parviainen, H., Gandolfi, D., Deleuil, M., et al. 2014, A&A, 562 A140
Poppenhaeger, K., & Wolk, S. J. 2014, A&A, 565, L1
Rauer, H., Queloz, D., Csizmadia, S., et al. 2009, A&A, 506, 281
Rouan, D., Parviainen, H., Moutou, C., et al. 2012, A&A, 537, A54
Skumanich, A. 1972, ApJ, 171, 565
Tingley, B., Endl, M., Gazzano, J.-C., et al. 2011, A&A, 528, A97
Triaud, A. H., Queloz, D., Bouchy, F., et al. 2009, A&A 506, 377

Acknowledgements: The CoRoT space mission has been developed and operated by CNES, with the contribution of Austria, Belgium, Brazil, ESA, Germany, and Spain.

Part IV

Decisive breakthroughs for stellar physics

The CoRoT Legacy Book

DOI: 10.1051/978-2-7598-1876-1.c040

Part IV

Decisive breakthroughs for stellar physics

Stellar variability is a longstanding issue in stellar physics and covers a large number of underlying physical processes such as stellar oscillations, stellar rotation, binarity, and star-disk interaction. Photometric observations are therefore potentially able to kill several birds with one stone by giving us access to all those mechanisms through the investigation of one single observable: the stellar light-curve. However, this is only possible if the accuracy of the observations is high enough, the duration of the observations is long enough, and the duty cycle is good enough. In 2006 all those requirements were fulfilled by the CoRoT mission that provided highly-accurate quasi-uninterrupted and long-duration photometric observations for a large number of stars. In that respect, CoRoT allowed decisive breakthroughs for stellar physics.

In these chapters, we intend to provide an overview of the scientific results obtained by the exploitation of the CoRoT light-curves in stellar physics. The first chapter, *Insights on the internal structure of stars as provided by seismology*, focuses on the numerous constraints on the internal structure of stars inferred thanks to stellar seismology. It is twofold because it adresses both; the classical and solar-like pulsations. The former type of pulsations, which originates mainly from thermal instabilities, are encountered in a wide variety of stars while the latter type of pulsations concerns low-mass stars which develop an outer convective envelope as it drives and damps these oscillations. Prior to CoRoT, only a handful of seismic constraints were available for a few stars. However, since the launch of CoRoT, followed by *Kepler*, it is possible to infer the internal structure of thousands of stars from the main-sequence to the central helium-burning phase.

The second chapter, *Pulsating red giant stars: ensemble asteroseismology and galactic archeology*, addresses new fields which emerged thanks to CoRoT. Based on the numerous seismic contraints on red giants, it has been possible to develop a statistical approach using global seismic indicators (also named seismic indices) to infer physical constraints on stellar structure and evolution of evolved stars. An additional benefit of ensemble asteroseimology is the determination of stellar global parameters such as the stars masses, radii, or ages. This has been used to investigate the Galactic stellar populations since it shed new light on stellar populations in the Milky Way. Moreover, the synergies between asteroseismology and large spectroscopic surveys is leading to the emergence of a chemodynamical investigation of the Galaxy.

The last chapter, *The wealth of stellar variability: stellar activity, binary, and star-disk interaction*, is dedicated to stellar variability as induced by stellar activity, binarity and star-disk interactions. The first part addresses surface rotation, convection and magnetic activity as well as their interplay. CoRoT allowed us to have surface constraints on those essential ingredients of stellar dynamos. The second part of the chapter is dedicated to binarity, which is another source of stellar variability. Indeed, CoRoT's contributed to the detection of numerous multiple systems and to the characterisation of the evolution of several binary systems, allowing to unravel physical processes occuring on different time-scales. Several binary systems were also used as proof-of-concept to show the potential of the synergy between asteroseismology and binarity. The last part of this chapter concerns the rich harvest of observational constraints obtained for young stars and the interaction with their disk. Particular emphasis is also laid on the coordinated synoptic investigation of NGC 2264 that is a multiwavelenght observational campaign including ground-based and space-borne facilities among which CoRoT.

The aforementioned works demonstrate the leap forward that has been performed thanks to the ultra-precise and long duration photometry provided by CoRoT. Its datasets cover the whole Hertzsprung–Russell diagram in different part of the sky and thus offered (and still offers) a rich harvest of observational constraints on many physical processes up to now hardly understood. The pioneering detection of solar-like oscillations in hundreds of stars has paved the way for making decisive progress in the modelling of stellar structure and evolution. The seismic analysis of CoRoT targets has brought significant constraints on specific physical processes inside stars, but also yielded a wealth of methods and procedures to exploit seismic data on solar-like pulsators to their full potential. The harvest of CoRoT was luxuriant and permitted us to incredibly boost our current understanding of stars and particularly of red giants. This led to the emergence of ensemble asteroseismology as a strong driver for stellar and galactic science. Beyond asteroseismology, the results described in this review emphasize the large possibilities opened thanks to CoRoT. The investigation of the major ingredients of stellar dynamos was made possible. Star interactions with its environment was another issue addressed because CoRoT also allowed a detailed study of the binarity, accretion process, star-disk interaction, inner disk structure and rotation of a coeval sample of stellar objects. Therefore, all those results open the way to a complete description of the thousands of stellar systems observed around ours, including the relation between the star and the planets of these systems.

Obviously, the interpretation of CoRoT's data is a long term ongoing process and will not be completed before a long time. This review is thus a snapshot and the situation will certainly evolve in the forthcoming years along with the exploitation of the observations. Indeed, CoRoT's observations provided a large number of observational constraints that will certainly be breeding ground for future theoretical progress. We also emphasize that it is not intended to provide a comprehensive view but rather to show and highlight how CoRoT allowed us to make significant progress in a number of fields or in some cases permitted the emergence of new fields. In that respect, the *Kepler* mission and its wealth of scientific achievements will not be addressed in detail in this review, even if it will be mentioned when useful.

K. Belkacem
LESIA, Observatoire de Paris, PSL Research
University, CNRS, Université Pierre et Marie Curie,
Université Paris Diderot, 92195 Meudon, France

The CoRoT Legacy Book

DOI: 10.1051/978-2-7598-1876-1.c041

IV.1

Insights on the internal structure of stars as provided by seismology

Classical pulsators and Solar-like oscillations

A. Grotsch-Noels[1] and S. Deheuvels[2, 3]

[1] Institut d'Astrophysique et de Géophysique, Liège University, Allée du 6 Août, 17, 4000 Liège, Belgium
[2] Université de Toulouse, UPS-OMP, IRAP, Toulouse, France
[3] CNRS, IRAP, 14, avenue Edouard Belin, 31400 Toulouse, France

1. Introduction

One of the key objectives of the CoRoT mission relied on stellar seismology, as a tool to infer the physical mechanisms taking place in stellar interiors. Stellar pulsations can be split into two sub-classes; classical pulsations and solar-like pulsations. The first, thoroughly discussed in Sect. 2, are encountered in a wide variety of stars and mainly originate from thermal instabilities. Such oscillations have been observed for a long time from the ground and enabled us to unveil several fundamental physical questions such as stellar opacities (see for instance the reviews by Gautschy & Saio 1995, 1996; Samadi et al. 2015). However, by allowing us to measure micro-variability, CoRoT helped us to make a leap forward by providing access to the internal inner-most layers of a number of stars such as γ Doradus or β Cephei stars (Sects. 2.1 and 2.6). Moreover, it raised new questions about the nature of several type of pulsations as exemplified by the δ Scuti or Be stars (Sects. 2.2 and 2.7). As the nature of these oscillations is not always fully understood and is sometimes complexified by intricate combinations with rotation or magnetic fields, CoRoT's observations provided a large number of observational constraints that will certainly be breeding ground for future theoretical progress.

The second type of pulsations, called solar-like oscillations, concerns all stars that develop an outer convective envelope (so mainly low-mass stars) as the latter drives and damps these oscillations. This is addressed in Sect. 3. Indeed, prior to the CoRoT's launch, only a handful of targets were known to exhibit solar-like oscillations and their interpretation was quite thorny as ground-based observations do not allow for the necessary precision, duration, and duty-cycle. Only a few years after, the situation dramatically changed and several hundreds oscillating main-sequence stars and thousands of red-giant stars have been detected (Sect. 3.1). Thus, both the number and quality of the observations have been considerably improved and it is not much of a stretch to think that CoRoT enabled us to make a great leap forward. Analyzing light-curves of oscillating stars yields very precise oscillation frequencies intricately related to the internal structure of stars. The absolute values of oscillation frequencies bear a lot of information content on physical processes taking place in stars but previously out of reach (Sect. 3.2). For instance, specific frequency combinations enable us to isolate and probe localized regions of the star such as the interfaces between radiative and convective regions, allowing us to measure the extra-mixing related to penetration of convective elements (Sect. 3.3) or rotation (Sect. 3.5). Consequently, significant advances are now possible given this propitious context provided one brings together theoretical efforts and highly accurate observational constrains. CoRoT also opened new opportunities such as the precise and accurate characterization of planet-host stars (Sect. 3.5) and as such was the pathfinder for future missions such as PLATO (Rauer et al. 2014).

2. Classical pulsators (by A. Grotsch-Noels)

Classical pulsators cover nearly all the populated area of the Hertzsprung-Russell (HR) diagram. Figure IV.1.1 shows their location along the main sequence (MS) and in the classical instability strip (IS), defined by long-dashed cyan lines.

Although some pulsation properties were already known in the nineties, the amazing successes gathered by SOHO for the Sun (surface helium abundance, importance of diffusion, rotation profile…) were stimulating incentives to attempt at reaching similar goals in stars, despite enormous technical challenges. The aim was to detect extremely small light variations (down to one ppm) and to extract the frequencies responsible for these brightness fluctuations. To reach such performances, long observing times devoid of day/night alternations were required and space was thus the ideal asteroseismic laboratory. By revealing their microvariability, measuring their oscillations at the ppm level,

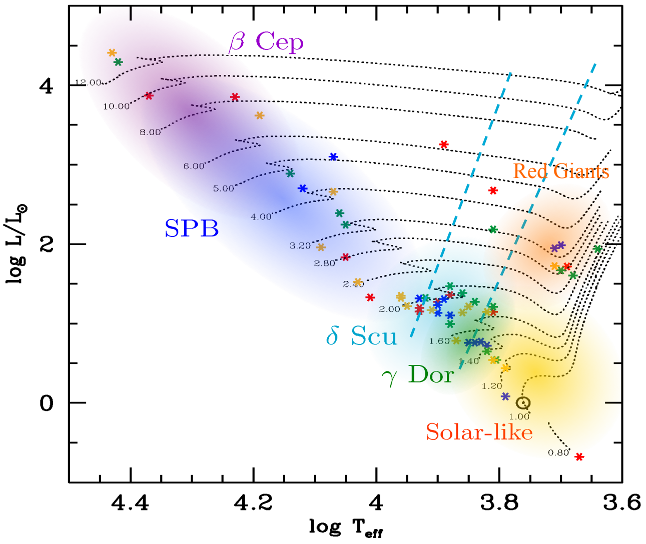

Fig. IV.1.1. Location of classical, solar-like and red giant pulsators in the HR diagram. Long dashed cyan lines show the Cepheids and RR Lyrae stars classical instability strip. Courtesy of A. Miglio.

CoRoT has provided a new vision of stars, never reached before by any ground-based observation.

Discoveries were indeed numerous. For classical pulsators let us cite just a few examples: the first detection of pre main sequence (PMS) γ Doradus variables (Zwintz et al. 2013, see Sect. 2.1), the discovery of hundreds of frequencies in δ Scuti stars (Poretti et al. 2009, see Sect. 2.2), the first detection of a deviation from a constant period spacing in gravity modes in a Slowly Pulsating B (SPB) star (Degroote et al. 2010a, see Sect. 2.5) and the spectacular time evolution of the frequency spectrum of a Be (emission lines B) star during an outburst (Huat et al. 2009, see Sect. 2.7), but also innovative probing in RR Lyrae stars (Poretti et al. 2010b, see Sect. 2.3), Cepheids (Poretti et al. 2014, see Sect. 2.4), OB stars (Degroote et al. 2010b, see Sects. 2.6 and 2.8), and sdB stars (Van Grootel et al. 2010, see Sect. 2.9). Interpreting those results opened new horizons in our vision of stars and galaxies. In the following sections we shall travel among the regions of the HR diagram populated by classical pulsators and we shall discuss these breakthrough contributions to stellar astrophysics, based on CoRoT's data.

2.1. A nursery for young γ Doradus stars

γ Doradus stars are pulsating in a high-order g-mode regime. They have periods similar to SPB stars (see Sect. 2.5), from 0.3 to 3 days. Their masses are however much smaller, about 1.4 to 2.1 $M_\odot$. These stars are cool enough to have a convective envelope. Most of the γ Doradus stars are indeed cooler than the red edge of the δ Scuti (or classical) Instability Strip. Their excitation mechanism is a modulation of the radiative flux at the base of the convective envelope, first proposed by Guzik et al. (2000) and later confirmed by Dupret et al. (2005) using a time-dependent convection (TDC) treatment involving the interaction of convection with pulsation. Because the depth of the convective envelope plays a major role in the driving mechanism, the theoretical predictions for the γ Dor instability strip are very sensitive to the mixing-length parameter used in the MLT treatment of convection and the observed location of its red edge is indeed a strong constraint on the mixing-length parameter.

These stars are of particular interest since their mass range covers the transition between a structure with a radiative core and a structure with a convective core, which can grow in mass during part of their main-sequence phase of evolution. The transition is due to the growing contribution of CNO cycle reactions to the total nuclear energy production. This constitutes a sharp transition in the chemical composition profile, which induces a very subtle signature in the gravity modes frequency spectrum. According to the asymptotic theory, periods of high-order (k) g-modes are regularly spaced with a spacing ($\Delta P = P_{k+1} - P_k$) decreasing as the degree of the modes increases. As the star evolves during MS, a higher and higher peak, starting at the limit of the fully mixed region, develops in the Brunt-Väisälä frequency distribution, as a result of the formation of the μ-gradient region. This sharp feature in the Brunt-Väisälä frequency shows up as a periodic component in the g-mode period spacing. The period spacing is no longer constant but it oscillates around a constant mean value. The non-rotating theory was extensively discussed in Miglio et al. (2008) for γ Doradus stars and SPB stars.

However, γ Doradus stars frequencies can be of the order or even higher than their rotation frequencies. Therefore, rotation has a non-negligible effect on their oscillation properties. Using the Traditional Approximation of Rotation (TAR), Bouabid et al. (2013) carried out a non-adiabatic analysis on a grid of models covering the γ Dor mass range. With this TAR approximation, the effect of the Coriolis force on the frequencies and the stability of high-order g-modes could be estimated. The effect of the Coriolis force depends on the type (prograde sectoral or not) of mode and increases with their periods. This analysis showed that the g-mode period spacing is no longer periodically oscillating around a constant value. The mean value between two consecutive period-spacing minima decreases with increasing period for non prograde sectoral modes and increases with the period for prograde sectoral modes. Moreover, the periodicity of the oscillation depends on the mode periods. For non prograde sectoral modes, the period interval between two consecutive period-spacing minima decreases with increasing period, while it is the contrary for prograde sectoral modes. However, the number of modes between two minima remains constant.

It was thus highly challenging to search for the presence of periodic components in the period spacing. The frequency resolution from a CoRoT long run was however too small to clearly reveal such components in period spacing for γ Dor stars. But CoRoT had opened up the way and in a recent paper (Van Reeth et al. 2015), 67 γ Dor stars observed by *Kepler* during 4 years were analyzed with unprecedented detail. Period spacing patterns could be found for 50 of them. Moreover, a strong correlation between the spectroscopic $v \sin i$ and the period spacings could be established, confirming the influence of rotation on γ Dor-type pulsations as proposed by Bouabid et al. (2013).

Although it is generally assumed that γ Dor stars are MS stars, some of them could also be PMS stars. Bouabid et al. (2011) derived the theoretical arguments, which could help distinguishing between these two possibilities. In particular, they computed the instability strip for PMS γ Dor stars and found that it covers the same effective temperature range as the MS γ Dor instability strip but the frequency domain of unstable modes in PMS models is greater than in MS models. Moreover, the differences between MS and PMS internal structures bear a signature in the average values of the period spacing, as well as in the dependence of the period spacing on the radial-order of the modes, opening the window to determination of the evolutionary phase of γ Dor stars from their pulsation properties.

During a 23-day observing run in March 2008, CoRoT observed 636 members of the young open cluster NGC 2264. The so-called Christmas tree cluster, is located in the constellation Monoceros relatively close to us at a distance of about 1800 light years. Its age is estimated to be between 3 and 8 million years. At such a young age, the cluster is an ideal target to investigate many different scientific questions connected to the formation of stars and early stellar evolution and in particular to search for γ Dor pulsators, which would definitely be PMS γ Dor stars. The CoRoT observations led to the discovery of two PMS γ Dor candidates, namely NGC 2264 VAS 20 and NGC 2264 VAS 87 (Zwintz et al. 2013). Moreover, the presence of hybrid δ Scuti/γ Doradus pulsations (showing at the same time gravity γ Dor and acoustic δ Scuti modes) was confirmed in members of NGC 2264.

High-precision light curves obtained from the CoRoT faint-field during LRa01 led to the detection of 418 γ Dor and 274 δ Sct/γ Dor hybrid candidates (Hareter 2012). The bona fide γ Dor are mostly concentrated at the cool border of the δ Sct strip. In contrast, the hybrids fill the whole δ Sct instability strip without a noticeable concentration.

Detection of transits in the faint-field allowed the discovery of γ Dor stars belonging to eclipsing binaries (see for instance Maceroni et al. 2013, see also Sect. 3, Part V, Chap. 3). In particular the eclipsing binary CID 100866999, observed during LRc01, showed large-amplitude hybrid γ Dor/δ Sct star with two clearly distinct frequency domains (Chapellier & Mathias 2013). The large number of detected frequencies led to a detailed analysis of the interaction between them. According to the model proposed by Kennedy et al. (1993) for the Sun, the low g-mode frequencies trapped in the stellar interior produce oscillatory perturbations of the p-mode cavities and are responsible for the formation of a pair of weak spectral sidelobes symmetrically located about the unperturbed p-mode frequency. A period spacing of 0.03493 d could also be derived for a family of $\ell = 1$ modes with a very small dispersion of about 0.002 d. Following the amplitudes of the periodic behavior of ΔP obtained in Miglio et al. (2008), such a constant period spacing would only be compatible with a quasi ZAMS (zero-age main-sequence) central hydrogen abundance.

2.2. A forest of pulsation modes in δ Scuti stars

δ Scuti stars are MS and close to MS stars in the mass range 1.5 to 2.5 $M_\odot$ for a solar chemical composition and 1 to 2 $M_\odot$ in low metallicity conditions. They are located in the lower part of the classical Instability Strip. They pulsate in radial and non-radial modes with periods between about 30 minutes to 8 hours. Their photometric amplitudes can be greater than 0.3 magnitude, in which case they belong to a subclass called HADS (High Amplitude Delta Scuti). However, the vast majority of all δ Scuti stars are small-amplitude variables, pulsating mainly with nonradial acoustic modes. The excitation mechanism of δ Scuti stars is the κ-mechanism acting mostly in the HeII ionization zone near 48000 K.

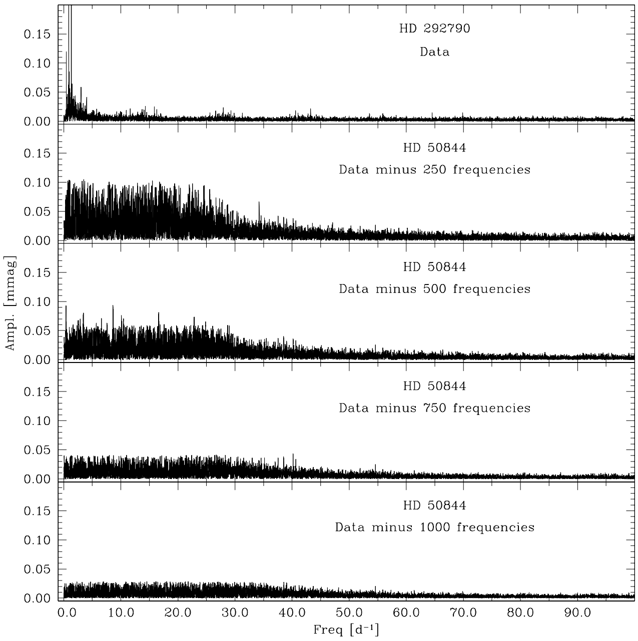

Fig. IV.1.2. The amplitude spectra of a comparison star, the rotational variable HD 292790, is shown in the top panel. The other 4 panels displays the richness of the spectra of the CoRoT δ Scuti star HD 50844. © Astronomische Nachrichten, 331, 1049.

Prior to the CoRoT launch, ground-based observations of δ Scuti stars enabled the detection of a multitude of low amplitude pulsation modes with, however, a big question mark as to their true nature as pulsation modes or their just belonging to the signal noise (Garrido & Poretti 2004). The first δ Scuti CoRoT target, observed during the Initial Run, brought an answer to that question. As can be seen in the spectra displayed on Fig. IV.1.2, hundreds of frequencies in the range 0−30 d^{-1} were indeed discovered in the analysis of the CoRoT time series on HD 50844, an evolved star located near the TAMS (terminal age main sequence) and slightly underabundant in heavy elements (Poretti et al. 2009, 2010a). The richness of δ Scuti spectra was thus confirmed. For the sake of mode identifications, the CoRoT data were complemented by ground-based high-resolution spectroscopy with FEROS, mounted on the ESO/MPI telescope at La Silla. It appeared that a large number of high degree (up to $\ell = 14$) modes were excited, which seems to imply that cancellation effects are not sufficient in removing the related flux variations at the CoRoT noise level. This analysis also revealed that the dominant frequency peak was associated with the fundamental radial mode.

Another interpretation for the presence of such a huge number of frequencies has been proposed, especially in order to refute the absence of cancellation effects in disk-integrated photometry. Instead of high-degree acoustic modes, most of the peaks in the Fourier spectra could result from non-white, frequency-dependent, granulation background noise. The less numerous remaining peaks would still be non-radial low degree p-modes (Kallinger & Matthews 2010). CoRoT targets HD 174936 and HD 50844 were tested for that purpose and granulation timescales where found to be consistent with those expected from stars with recognized surface granulation. However, another argument was put forward by Poretti et al. (2010a). They argued that the amplitude spectra of HD 171856, a non-variable star of the same spectral type as HD 50844, does not show any trace of granulation noise, which would plead for a high degree p-mode interpretation of the spectrum of HD 50844 if the surface conditions of both stars are really similar.

In the presence of such a high number of modes, a periodic pattern in the frequency spectra of the CoRoT target HD 174966 was searched for and a large frequency separation, $\Delta\nu$, could be extracted (García Hernández et al. 2013). The related mean density derived from a grid of model can thus reach a 6% level of accuracy. The CoRoT target CID 102749568 was also scrutinized for the possible presence of frequency patterns and distinct peaks in frequency spacings were obtained (Paparó et al. 2013). Combining CoRoT photometry with spectroscopy and stellar modeling, the physical stellar parameters were then derived while the observational mode identification could be confirmed, with the dominant mode being the first radial overtone.

2.3. A step forward in solving the Blazhko mystery in RR Lyrae stars

RR Lyrae stars were observed in the faint field of CoRoT with the aim of shedding some new light on the variability of these stars and especially of gathering new data to help solve the mystery of the Blazhko effect, which is a periodic modulation of the amplitudes and phases of the main pulsation mode. CoRoT data brought new evidence on a long term variation of the Blazhko period, which means that the Blazhko mechanism has now not only the requirement to explain the regular structures observed in the frequency spectra but it must also reproduce the long term variability observed by CoRoT.

Another important issue raised by CoRoT is the excitation of additional modes, preferentially the second overtone, leading to a regime of double-mode pulsation that may be part of the Blazhko phenomenon. Moreover significant peaks were present in V1127 Aql and CID 101128793 with the immediate inference of the presence of non-radial pulsations in horizontal branch stars (Poretti et al. 2010b).

A systematic analysis of CoRoT RR Lyrae stars was recently done aiming at detecting the presence of period doubling first observed in the *Kepler* RR Lyrae sample. This is a dynamical effect where a new limit cycle comes out from another limit cycle with a period twice as long as the preceding one. In the frequency domain a period doubling shows up as half-integer frequencies. As could be expected from the *Kepler* results, period doubling is an ephemeral phenomenon detectable only for short time intervals. It could result from complex interactions between radial and nonradial modes in RR Lyrae stars and be an important ingredient in the explanation of the Blazhko effect. The detailed asteroseismology of RR Lyrae stars is now within reach (Szabó et al. 2014).

2.4. A puzzling pulsation spectrum in a Cepheid

The faint CoRoT field led to another important discovery. CID 0223989566 was found to be a triple-mode Cepheid with the two largest amplitude modes being the first and second radial overtones while the faintest mode is either a radial mode or an isolated non-radial mode whose period is much longer that that of the first overtone mode. The period ratio between the first overtone and the longest period mode is quite unusual and makes CID 0223989566 a unique object in our Galaxy (Poretti et al. 2014).

2.5. An imprint of the hydrogen profile in slowly pulsating B stars

Slowly pulsating B (SPB) stars revealed to be important CoRoT targets (Degroote et al. 2010b). These are late to mid-type B stars showing a frequency spectrum dominated by high order gravity modes excited by the κ-mechanism at work in layers where partial ionization of iron group elements produces an opacity peak at a temperature of about 200 000 K. In addition the most evolved of these stars may present mixed modes i.e. modes with a g-character in deep layers and p-character in the envelope. The masses of SPB stars typically range from 2.5 to 8 $M_\odot$ and their periods cover a rather wide domain, from about a third of a day to several days (see for example Aerts et al. 2006b).

In this mass range, the main sequence phase is characterized by a convective core, in which all the H-burning CNO reactions take place, surrounded by a mostly radiative envelope except for tiny convective layers related to partial ionization of helium and/or iron group elements. Above the convective core where mixing of chemicals is instantaneous and efficient, some layers can be affected by partial or total mixing during the main sequence phase of evolution. The extent of this extra mixed zone as well as the mixing efficiency are, however, difficult to assess. This additional mixing has very important consequences since it involves longer time scales for nuclear burning phases and may in particular affect the value of the stellar mass at the transition between those stars which end up their life as white dwarfs and those which face a final supernova explosion. Physical reasons for this extra-mixing are various, either a mixing induced by internal rotation or a mixing resulting from convective bubbles crossing the convective core boundary to enter the radiative zone where they finally lose their identity (overshooting), or even some other poorly known processes.

As hydrogen is transformed into helium in the core, the opacity decreases and the convective core mass becomes smaller and smaller, leaving behind it a region of varying chemical composition, the so-called μ-gradient region. If the extra-mixing is assumed to produce an instantaneous mixing, the fully mixed region covers the convective core and the extra-mixing region. In that case, the μ-gradient region starts just on top of the fully mixed region and the μ-profile is sharp. On the other hand, if a diffusive approach is adopted to treat the extra-mixing, a non instantaneous mixing takes place and produces a smoother μ-profile.

Whatever the way the mixing is performed, the affected region is rather thin and constitutes a sharp transition region, which induces a periodic component in the g-mode

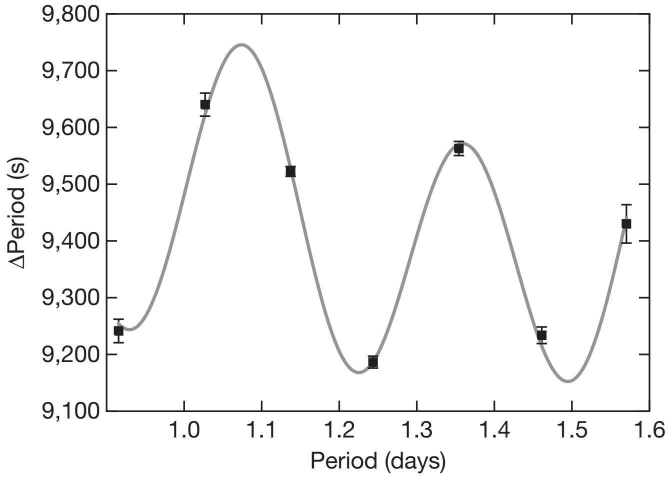

Fig. IV.1.3. Period spacing of g-modes in terms of the period of successive radial orders, observed in HD 50230. © Nature, 464, 259.

period spacing, as was shown by Miglio et al. (2008) (see also Sect. 2.1). A constant period spacing is indeed found in homogeneous ZAMS theoretical stellar models while periodic deviations from this constant value are seen in models affected by a sharp transition region. The period of the deviation, Δk, expressed in numbers of radial order k, can be written

$$\Delta k \simeq \Pi_\mu / \Pi_0 \qquad (1)$$

where Π_μ^{-1} and Π_0^{-1} are respectively the buoyancy radius of the sharp transition and the total buoyancy radius ($\Pi_x^{-1} = \int_{x_0}^{x} \frac{|N|}{x'} \mathrm{d}x'$). Observing a periodic deviation from a constant value of the period spacing is thus a powerful tool to directly locate the μ-gradient region and probe stellar cores.

When a diffusive extra-mixing is adopted, the μ-gradient is smoother and so is the Brunt-Väisälä frequency. The period of the deviation remains similar but the amplitude of the oscillation is modulated by a factor $1/\mathrm{P_k}$ leading to an almost constant period spacing if the smoothing is effective enough. This would be the case for instance with a rotational extra-mixing.

This phenomenon has been detected in two hybrid B stars observed by CoRoT (showing at the same time acoustic β Cephei and gravity SPB modes): (1) HD 50230, a slow rotator, identified as a spectroscopic binary, for which an extra-mixing with a somewhat smooth shape is clearly required in the modeling (see Fig. IV.1.3 from Degroote et al. 2010a) (see also Degroote et al. 2012); and (2) HD 43317, a rapid rotator in which an almost constant period spacing is found (Pápics et al. 2012).

In the *Kepler* era new results are booming and a number of SPB stars are now analyzed. Among them, the cool SPB star KIC 10526294 is a very slow rotator (rotation period of 188 days) for which 19 consecutive g-modes were detected, showing an almost constant period spacing (Pápics et al. 2014a,b). With the *Kepler* SPB star KIC 7760680, as many as 36 consecutive g-modes have been extracted. This star has the potential to become the Rosetta Stone of SPB stars. The period spacing clearly shows a modulation related to a smooth extra-mixing as well as a decrease with the radial order associated with rotational effects (Pápics et al. 2015, see also Sect. 2.1).

One can say that CoRoT really opened up the way to a direct scrutiny of the internal structure of such stars bringing new and important constraints not only on the amount of extra-mixing but also on the efficiency of the mixing.

2.6. Probing the extra-mixing and the iron enrichment in β Cephei stars

β Cephei stars are early B-type stars covering a mass range from about 8 to 20 $M_\odot$. They present radial and non-radial pulsations with typical periods of the order of 2 to 8 hours. Their non-radial pulsation modes are low order g- and p-modes excited by the κ-mechanism acting in the iron group elements opacity peak at ∼200 000 K. Most of them are slow to moderate rotators but still a significant fraction of them can reach rotation velocities of 50–100 km s^{-1} and even, for a few of them, 200–300 km s^{-1}. Evidences of the presence of a magnetic field have also been detected in some of them.

Their internal structure is rather similar to that of SPB stars (see Sect. 2.5), with a convective core surrounded by a mostly radiative region, in which can be embedded a convective shell due to the iron opacity peak at ∼200 000 K. The main difference from an SPB stellar structure comes from the fact that the radiative gradient in the layers adjacent to the convective core boundary is very close to the adiabatic gradient, which can induce a semi-convective region in the most massive β Cephei stars. Moreover those layers can be affected by overshooting from the convective core and/or by a rotational mixing. Indeed, the modeling of β Cephei stars does generally not take into account the structural changes due to rotation except in the form of this possible extra-mixing taking place in the layers surrounding the convective core. The μ-gradient profile outside the convective core is thus an open question since it depends on the presence and the efficiency of the extra-mixing.

It would be extremely interesting to establish a relation between the extent of this extra-mixed zone and the rotation velocity and/or the magnetic field for these stars and CoRoT was the perfect laboratory for such a purpose. Although not the most favorite targets in the early days of the preparation of the CoRoT mission, it soon appeared that a lot of scientific returns could be expected from β Cephei stars (see the review by Degroote et al. 2010b). Ground-based asteroseismology had indeed already proven its ability to probe the rotation profile and the extent of the extra-mixed region in some β Cephei stars (see for example Aerts et al. 2003). However, it proved not obvious at all to derive a one-to-one extent of this extra-mixed zone (Goupil & Talon 2009). A rather large extent seems to be required to model θ Ophiuchi (Briquet et al. 2007) while a much smaller one is favored for HD 129929 (Dupret et al. 2004; Thoul et al. 2004), for β Canis Majoris (Mazumdar et al. 2006), for δ Ceti (Aerts et al. 2006a) and for 12 Lacertae (Dziembowski & Pamyatnykh 2008; Desmet et al. 2009). This extra-mixed zone could even be absent in the structure of the CoRoT target V1449 Aquilae (HD 180642, Aerts et al. 2011) (see also, for ν Eridani, Pamyatnykh et al. 2004; Ausseloos et al. 2004). One must

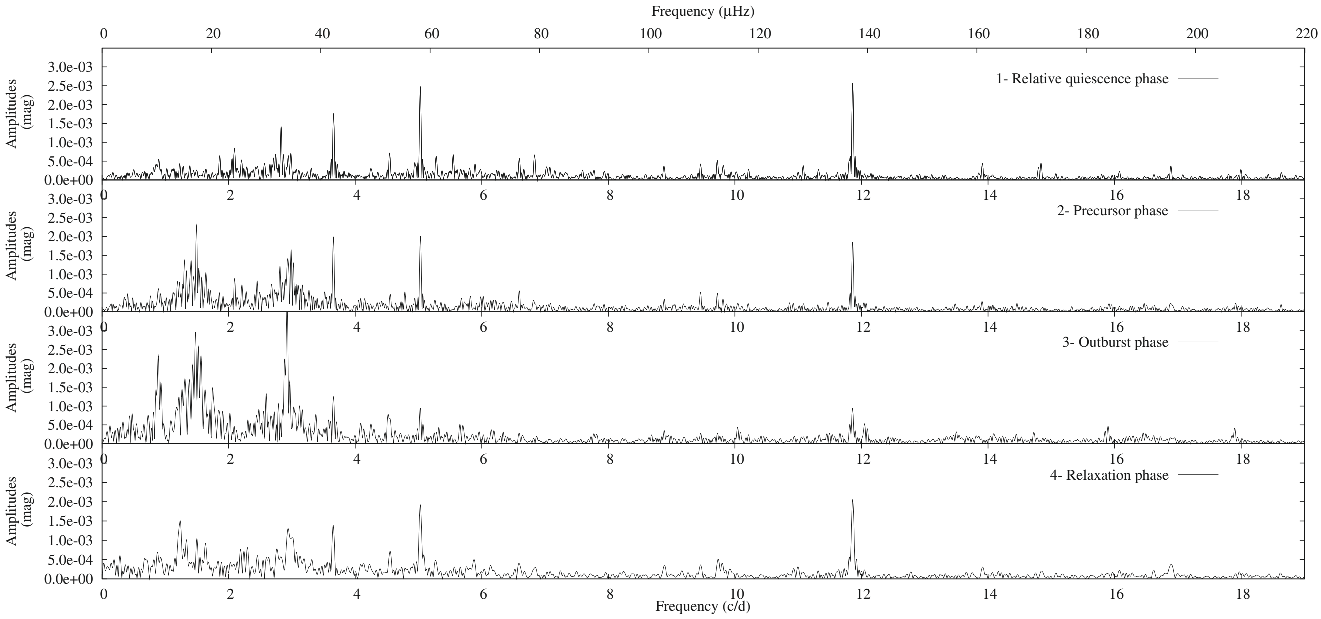

Fig. IV.1.4. Stochastically excited *g*-modes and acoustic *p*-modes in the spectrum of CoRoT Be star HD 49330 at quiescence, precursor, outburst, and relaxation phases (*from top to bottom panels*). From Huat et al. (2009) © A&A.

however proceed with caution in deriving asteroseismic constraints on extra-mixing since the results may depend on the number on well identified observed modes and on the assumptions made on the physics at work inside the star, such as the chemical mixture and the adopted extra-mixing processes for instance (Salmon 2014).

Magnetic fields could also play an important role in the asteroseismic inferences from β Cephei stars. Seismic analyses of V2052 Ophiuchi show that this star although rapidly rotating, which would favor extra-mixing, could be devoid of such a region. The magnetic field detected in this star could be the reason for this lack of extra-mixing (Briquet et al. 2012). Research is presently intensifying in order to detect and interpret magnetic stars in CoRoT (see for example Briquet et al. 2013) and *Kepler* (see the review by Neiner et al. 2015).

Moreover, some discrepancies with theoretical predictions appeared, especially in the analysis of hybrid β Cephei/SPB pulsators, since the excitation of low frequency modes was not accounted for by theory, and some iron enrichment in the excitation zone was proposed (see for example Miglio et al. 2007a; Dziembowski & Pamyatnykh 2008). The instability strips for SPB and β Cephei stars are indeed highly sensitive to the stellar metallicity since the operating κ-mechanism is related to the iron opacity peak (see for example Miglio et al. 2007b, and references therein). However it has been argued that, should an iron enrichment be the solution of the problem, chemically inhomogeneous HgMn stars would then present excited pulsation modes (Turcotte & Richard 2003). The seismic analysis of the CoRoT HgMn star HD 45975 seems to preclude any iron anomaly as the origin of the mode excitation since no pulsations were detected in this star (Morel et al. 2014).

Some SPB and β Cephei candidates have even been detected in the ultra low metallicity environment of the Magellanic Clouds, which is irreconcilable with theory. Instead of a chemical anomaly, an increased opacity could be the solution. A quest for a revision of opacity in conditions prevailing at the iron opacity bump, especially for the Ni opacity, has thus been advanced (Salmon et al. 2012) and new efforts are now being made in that direction (see for example Le Pennec & Turck-Chièze 2014).

An unexpected surprise came from V1449 Aql, which is a known large-amplitude β Cephei star. Solar-like oscillations (see Sect. 3) were indeed detected, which was a first in the asteroseismology of massive stars (Belkacem et al. 2009).

2.7. A live outburst in a Be star

In case of rapid rotation, especially when the rotation velocity is close to the break-up velocity, the structure and the evolution is deeply affected and hydro- and magnetohydrodynamical processes must enter the stellar modeling. The best laboratories for these processes are Be stars, which are rapidly rotating B stars surrounded by a gaseous disk formed of material ejected from the star, which is, in essence, the origin of the Be phenomenon. Asteroseismology of Be stars requires state-of-the-art modeling, including rotational effects, coupled with a pulsational analysis taking into account the Coriolis and the centrifugal accelerations.

Late Be type CoRoT targets HD 181231 and HD 175869 are very rapid rotators, about 20 times more rapid than the Sun. Their seismic analysis seems to require a centrally mixed zone about 20% larger than what is expected from convection only (Neiner et al. 2012). This already puts important constraints on the way hydro- and magnetohydrodynamical processes are implemented in the modeling.

But another CoRoT Be star, HD 49330, had a very exciting surprise in store. Observed by CoRoT during an outburst of matter towards its circumstellar disk, its frequency spectrum suffered drastic changes. Firstly dominated by acoustic modes the spectrum showed the appearance of gravity modes with amplitudes strictly in line with the outburst (Huat et al. 2009). Figure IV.1.4 shows the appearance and disappearance of stochastically excited g-modes in phase opposition with the acoustic p-modes present during the quiet phases. Such a link between the nature of the excited modes and a dynamical phenomenon is of course a gold mine in our quest for the understanding of the Be phenomenon. This was the first time that a clear evidence could link Be stars outbursts with their pulsations. An entirely new scenario was then proposed: the transport of angular momentum by waves or pulsation modes increases the stellar rotation and brings it to its critical value at the surface, leading to an ejection of matter into the circumstellar disk (see Neiner et al. 2013).

2.8. Unusual behaviours in O stars

A bunch of six O stars have been observed by CoRoT (Degroote et al. 2010b). Among them HD 46150 and HD 46223, members of the galactic cluster NGC 2264 (see Sect. 2.1) and HD 46966, member of the OB association Mon OB2, do not seem to pulsate, which is in agreement with stellar modeling of stars with similar global parameters. Their light curves seem to be dominated by red noise and clearly indicates a different origin than non-radial pulsations. The physical cause of this red noise is unclear, but it could be related to sub-surface convection, granulation, or stellar wind inhomogeneities (Blomme et al. 2011).

On the contrary, HD 46202 definitely shows β Cephei type modes. However, none of the observed modes are found theoretically excited, which is a recurrent problem in the upper part of the HR diagram (Briquet et al. 2011, see also Sect. 2.6).

The frequency spectrum of the Plaskett's star HD 47129 shows a peak with six harmonics with periods in the range 4h to 1d (Mahy et al. 2011). Plaskett's star is a non-eclipsing binary system composed of two massive O stars. The high rotation velocity of the secondary induces a large temperature gradient between the poles and the equator, making the determination of the spectral class ambiguous at least. Different physical origins for the observed frequencies have been looked at and the presence of non-radial pulsations seems to be the more plausible explanation. Although difficult to model given the uncertainties on the global parameters, it seems that the observed frequencies can be reproduced by radial and non-radial ($\ell = 1$) low-order modes.

CoRoT O star HD 46149 had another surprise in its basket. Solar-like oscillations (see Sect. 3) were indeed observed and their frequency range as well as their frequency spacings were found to be compatible with theoretical expectations (Degroote et al. 2010c).

2.9. Unraveling the helium burning core in sdB stars

Type-B subdwarfs (sdB) are located on the extreme horizontal branch in the HR diagram. With a very limited mass range, from 0.3 to 0.7 $M_\odot$, they are evolved stars, having undergone core hydrogen burning as well as the red giant phase. They are currently transforming helium into carbon and oxygen in a convective core surrounded by radiative quasi-pure helium layers and a very tiny hydrogen-rich envelope, whose mass is less than about 0.02 $M_\odot$. They have indeed been striped down through a process still under debate during an earlier phase of evolution, and as a result, they are hot and compact. With no hope of ascending the asymptotic giant branch they end up as cooling white dwarfs.

Among sdB stars, two classes of pulsators have been discovered. The short period pulsators, sdBV$_\mathrm{r}$, are the hottest ones with $\mathrm{T_e} \gtrsim 28\,000$ K, and periods covering a range of 100 to 600 s, typical of low-degree low-order p-modes. The long period sdB, sdBV$_\mathrm{s}$, are cooler, with $\mathrm{T_e} \lesssim 30\,000$ K, and periods of 1–2 h, attributed to low-degree mid-order gravity modes. The mode excitation results from the classical κ-mechanism acting in layers where partial ionization of iron group elements takes place. In order to enhance the efficiency of this exciting region, the competition between atomic diffusion and radiative levitation is assumed to increase the local content of iron group elements (Charpinet et al. 1997).

The hot long period sdB KPD 0629–0016 was selected as the CoRoT primary target in SRa03. The analysis revealed a large number of g-modes, with 17 clearly identified and 7 more candidates. The oscillations cover a range of 90–400 μHz with a dominant peak at 205.29 μHz (P = 1.353 h) (Charpinet et al. 2010). It was the very first time that the frequencies of such a large number of oscillation modes were reliably measured in an sdB pulsator, showing the power of CoRoT over ground-based observations in the asteroseismology of sdB stars.

A forward modeling approach has been carried out by Van Grootel et al. (2010). This means that a grid of theoretical sdB models, with known g-mode frequencies, was used with the aim of matching simultaneously the observed independent frequencies. This method has the advantage of delivering at the same time the structural stellar parameters and the identification of the modes. The derived global parameters are typical of a hot sdB star (see Table 2 in Van Grootel et al. 2010) but more importantly, the characteristics of the helium burning core were ascertained, thanks to the g-modes power to probe the very deep layers of the star. This core has a mass including 46 % of the total mass, probably indicating than an additional mixing must be invoked in the layers surrounding the purely convective core.

3. Solar-like oscillations
(by S. Deheuvels)

In the Sun, oscillation modes are stochastically excited by turbulent motions in the outer convective envelope. In principle, similar oscillations are expected in all stars that possess a convective envelope, which is the case of low-mass ($M \leqslant 1.5\ M_\odot$) main-sequence stars, but also of red giants. The detection and precise characterization of solar-like oscillations in stars other than the Sun had been longed for by the stellar physics community for decades, owing mainly to the impressive results provided by helioseismology. The modes excited by convection in solar-like pulsators are high-order[1] acoustic modes. They nearly follow asymptotic relations (Tassoul 1980) and are thus roughly equally spaced in frequency by the so-called large separation $\Delta\nu$. This makes

---

[1] Except for stars at the tip of the red giant branch.

it much easier to identify the observed modes, which is a prerequisite for exploiting them to probe the internal structure of stars.

Before the launch of CoRoT, solar-like oscillations had been detected in only a handful of main-sequence stars from the ground, and the interpretation of their oscillation spectra was hampered by the short duration of the observations and the strong aliasing due to the low duty-cycle. The long duration (observing runs ranging from 20 to 170 days) and the very high duty cycle (close to 90%) of CoRoT observations were particularly well suited for detecting and characterizing solar-like oscillations, and the first detections lived up to the expectations (Michel et al. 2008).

The detection of solar-like oscillations with CoRoT was expected mainly for low-mass main-sequence stars and subgiants. Less expected was the impressive richness of this class of pulsators, which was revealed by CoRoT observations. Solar-like oscillations were indeed clearly detected in hundreds of red giants, and very interestingly also in massive main-sequence stars. We here give a brief overview of these successes.

3.1. A profusion of pulsating solar-like stars across the HR diagram

3.1.1. Main-sequence solar-like pulsators

Over all, oscillations were unambiguously detected in 12 main-sequence solar-like pulsators with CoRoT observations, which produced oscillation spectra of unprecedented frequency resolution. The quality of CoRoT seismic data is well illustrated by the échelle diagram[2] of the CoRoT target HD 49385 shown in Fig. IV.1.5, in which the identification of $\ell = 0$, 1, and 2 modes is visually clear.

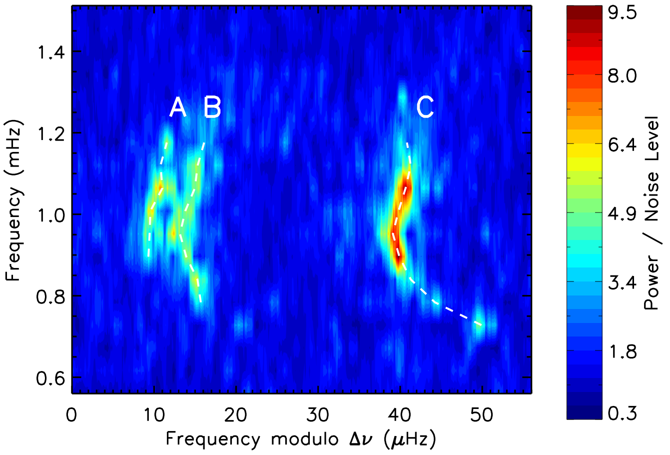

Fig. IV.1.5. Echelle diagram of the oscillation spectrum of CoRoT solar-like pulsator HD 49385. Three ridges appear, corresponding to $\ell = 0$, 1, and 2 (labelled as B, C, and A, respectively). Figure taken from Deheuvels et al. (2010) © A&A.

The extraction of the mode parameters (now commonly referred to as peak-bagging) for the first CoRoT targets has paved the way for all subsequent analyses of this type. Methods based on maximum-likelihood estimation (MLE) were adapted from helioseismology (e.g. Appourchaux et al. 2008). These methods are now commonly used, in particular for solar-like pulsators observed with the *Kepler* satellite, and they were progressively improved to the point of being nearly automated today. The first CoRoT targets (HD 49933, Appourchaux et al. 2008 and HD 181420, Barban et al. 2009), which were chosen as F-type stars owing to the expectedly high amplitudes of their oscillation modes, clearly showed that the analysis of solar-like oscillation spectra is not always as straightforward as in the solar case. The mode amplitudes revealed comparable to expectations, but their lifetimes were shorter by a factor three, which complicated the identification of the modes. Bayesian methods, consisting of adding well-chosen prior information to the MLE procedures, combined with Markov chain Monte Carlo techniques helped solve this identification problem (Benomar et al. 2009a,b; Gaulme et al. 2009). Dedicated techniques using the autocorrelation of the time series were also established to estimate global seismic parameters (such as the large separation and the frequency of maximum power of the oscillations $\nu_{\max}$, see Sect. 2, Part V, Chap. 2) in the case of lower signal-to-noise-ratio oscillations (Mosser et al. 2009; Mosser & Appourchaux 2009; García et al. 2009).

3.1.2. Subgiants

After the end of the main sequence, the frequencies of g modes increase owing to core contraction, and they become of the same order of magnitude as those of p modes. This gives rise to so-called mixed modes, which behave both as p-modes in the envelope and as g-modes in the core. Such modes have a unique potential for seismic diagnostics since the detection of pure g modes in solar-like stars remains out of reach (Appourchaux et al. 2010). The theoretical existence of mixed modes had been known for long (Dziembowski 1971; Scuflaire 1974; Aizenman et al. 1977), but they had not been unambiguously detected in solar-like pulsators, until CoRoT observations showed evidence of their presence in the oscillation spectrum of the target HD 49385 (Deheuvels & Michel 2010). The bending in the $\ell = 1$ ridge that can be seen in the low-frequency part of the échelle diagram (Fig. IV.1.5) is a typical signature of mixed modes in subgiants. These modes made it possible to establish the subgiant status of the star and opened the interesting opportunity to probe the structure of its core (see Sect. 3.3). Since then, mixed modes produced remarkable diagnostics about stellar interiors, especially with the detection of such modes in red giants. The potential of mixed modes has now been further exploited using the data from *Kepler*, and provided novel constraints on the internal rotation of subgiants (Deheuvels et al. 2012, 2014) and red giants (Beck et al. 2012; Mosser et al. 2012).

3.1.3. Red giants

As extensively discussed in Sect. 2, Part V, Chap. 2, before the launch of CoRoT, radial solar-like oscillations had been detected in red giants (Frandsen et al. 2002), but it

---

[2] An echelle diagrams is built by chopping the oscillation spectrum in sections Δν-wide, which are then piled up onto one another. This has the advantage of lining up modes of like degree in ridges.

remained uncertain whether non-radial modes could be detected in red giants. They were thought to be damped far more strongly than radial modes (Dziembowski et al. 2001), and first observations led to think that they might indeed have very short lifetimes, which would blur the oscillation spectra of giants (Stello et al. 2006). This was contradicted thanks to CoRoT observations with the detection of long-lived non-radial mixed modes in hundreds of red giants (De Ridder et al. 2009). These detections were understood with the theoretical computation of expected amplitudes and lifetimes of mixed modes in red giants by Dupret et al. (2009). This has opened a novel and very rich field in asteroseismology, and the seismology of red giants has produced major progress in stellar evolution (see Sect. 2, Part V, Chap. 2) and in galactic stellar population studies (see Sect. 3, Part V, Chap. 2).

3.1.4. Massive stars

As mentioned in Sects. 2.6 and 2.8, it had been suggested before that the thin convective region caused by the ionization of iron in massive stars could stochastically excite oscillations in a way similar to the solar convective envelope. The signature of such oscillations was found for the first time in a 10-$M_\odot$ β Cephei star observed with CoRoT (Belkacem et al. 2009). Similar modes were later detected in a CoRoT O-type star (Degroote et al. 2010c). These detections open interesting opportunities to better understand stars in this mass range and to learn more about the excitation mechanisms in solar-like pulsators.

3.2. Seismic modeling of CoRoT solar-like pulsator

The unprecedentedly long duration of CoRoT observations yielded estimates of the frequencies of solar-like oscillation modes with a typical precision of a few tenths of μHz. These new observables were used as precious additional constraints to model stellar interiors. The exploitation of CoRoT data has led to the development of new methods to model stars using asteroseismic constraints, and to improve existing methods.

The seismic data provided by CoRoT and now also by *Kepler* have been used to provide estimates of the most fundamental stellar parameters of the observed solar-like pulsators, such as their masses, radii, and ages. For this purpose, two different approaches were followed. The first one uses global parameters (the mean large separation of acoustic modes $\Delta\nu$ and the frequency $\nu_{\max}$ of maximum power of the oscillations) as seismic constraints, and yields estimates of stellar parameters by interpolating through large grids of stellar models (Chaplin et al. 2014). The advantages of this technique are its quickness, which makes it an interesting tool for ensemble asteroseismology (see Sect. 2, Part V, Chap. 2) and its applicability to low signal-to-noise targets, where individual modes cannot be detected, but powerful methods have been proposed to estimate global seismic parameters (Roxburgh 2009; Mosser & Appourchaux 2009). This approach was successfully applied to several CoRoT targets (Mosser et al. 2009; García et al. 2009; Gaulme et al. 2010). The second approach consists in performing a detailed modeling of specific targets using the properties of individual oscillations modes (either their frequencies of combinations of them), which is now referred to as “à la carte” or “boutique” modeling. This alternative approach is more time-consuming but obviously much more precise. Using the CoRoT target HD 52265 as a test-case, Lebreton et al. (2014) performed a very detailed study of these two approaches, and showed how asteroseismology improves the precision achieved on stellar parameter determination. For this specific target, they obtained age, mass, and radius estimates with uncertainties of ∼10%, 7%, and 3%, respectively, taking into account observational errors and current state-of-the-art model uncertainties. This work will undoubtedly serve as a reference for future asteroseismic modeling of solar-like pulsators.

For low signal-to-noise targets, an interesting approach has been suggested by Ozel et al. (2013), which consists in searching for a well-constrained stellar twin, i.e. a star whose stellar parameters are well-known and which shares similar surface and global seismic parameters with the studied target. A differential modeling can then be led to estimate differences in fundamental stellar parameters between the star and its well-characterized stellar twin. This approach was successfully applied to CoRoT target HD 175272, which was found to be a stellar twin of another CoRoT target HD 181420 (Ozel et al. 2013).

Another challenge was the seismic modeling of subgiants using the properties of mixed modes, whose large potential for seismic diagnostic of stellar interiors has already been mentioned. The timescale over which the frequencies of mixed modes are modified in these stars is small compared to the evolution timescale, which makes the usual approaches to seismic modeling (computation of grids of models or automatic optimization procedures) generally inefficient. Deheuvels & Michel (2011) proposed an alternate approach consisting in a two-step procedure, which was successfully applied to the CoRoT subgiant HD 49385, and was later adapted to red giants (Deheuvels et al. 2012).

The precise measurement of oscillation mode frequencies in stars of diverse masses and evolutionary stages combined with the improvement of seismic modeling techniques has given the opportunity to better understand certain physical processes which so far hindered our progresses in the modeling of stellar evolution. We now describe the main advances produced by CoRoT data.

3.3. Mixing beyond convective cores and envelopes

Several processes are expected to extend the size of convective regions beyond the Schwarzschild frontier (overshooting, rotational mixing,...), but since we lack a realistic description of these mechanisms, the actual size of convective zones remains uncertain. This generates in particular large uncertainties in our determination of stellar ages for stars that have a convective core because this core plays the role of a reservoir for nuclear reactions. Observational constraints on the size of convective regions are therefore crucial.

3.3.1. Core overshoot

The CoRoT satellite was well suited for obtaining such constraints. The boundary of the mixed region associated to the convective core generates variations in the sound speed profile on length scales shorter than the wavelength of acoustic modes. This introduces an additional oscillatory signal in the mode frequencies, which conveys information about the size of the mixed core. For the main-sequence solar-like pulsator HD 49933, Goupil et al. (2011) found that an extension of the mixed core produced by standard models (without overshooting nor rotational mixing) over a distance of 0.25 to 0.3 H_P is required to reproduce the observed frequency separation $\delta\nu_{01}$. By adding rotational mixing, they showed that it cannot account in itself for such a large extension, and that core overshooting should be responsible for an extension of the mixed core over about 0.2 H_P. On the other hand, Escobar et al. (2012) found that no extra-mixing beyond the convective core is required for the main-sequence star HD 52265.

Another powerful seismic diagnostic for the extent of convective cores is given by mixed modes in subgiants. Indeed, the coupling between p- and g-modes is linked to the Brunt-Väisälä profile in the core, which retains information about the size of the convective core at the end of the main sequence, provided the star is not too evolved (Deheuvels & Michel 2010). The detection of mixed modes in the subgiant HD 49385 offered a great opportunity to use such a diagnostic. Deheuvels & Michel (2011) found that models with a convective core that is extended over a distance of 0.18 and 0.2 H_P reproduce the frequencies of observed mixed modes at closest, but they could not exclude the case of a very small overshoot below 0.05 H_P.

The measurement of the size of the mixed core in stars with different masses, chemical composition, and evolutionary stages offers the opportunity to calibrate the extension of convective cores as a function of stellar parameters. By complementing results from CoRoT and using *Kepler* data, Deheuvels et al. (2016) recently proposed such a calibration with stellar mass for the evolution codes CESAM2K and MESA. This should decrease the uncertainties on stellar ages, especially for stars near the end of the main sequence (see Lebreton et al. 2014). On the longer term, we expect these measurements to provide constraints to theoretical models of the different processes that can extend convective cores.

3.3.2. Envelope overshoot

Overshooting below convective envelopes has a less direct impact on stellar evolution than core overshooting, but it can help us understand this theoretically challenging phenomenon. The abrupt transition between convective and radiative energy transport induces a glitch in the sound speed profile, which causes acoustic modes to oscillate as a function of frequency. The period of this oscillation yields an estimate of the depth of the boundary of the convective envelope (BCE). Such a measurement has been tried for HD 49933 by Mazumdar et al. (2012), who obtained rather loose constraints on the depth of the BCE. Using a similar diagnostic, Lebreton & Goupil (2012) were able to show that the convective envelope of the CoRoT solar-like pulsator HD 52265 is extended over a distance of 0.95 H_P compared to the classical Schwarzschild boundary. By comparison, Christensen-Dalsgaard et al. (2011) showed that an overshooting over a distance of 0.37 H_P is needed at the base of the convective envelope of the Sun. The difference between the overshooting distances of the two stars might be linked to the fact that HD 52265 has roughly twice the abundance of heavy elements of the Sun.

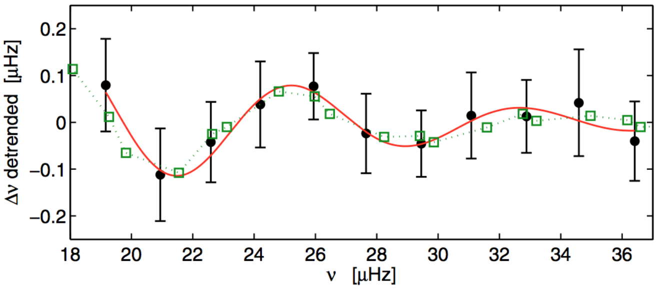

Fig. IV.1.6. Detection of an oscillatory trend in the large separations $\Delta\nu(\nu)$ of a CoRoT red giant, which is produced by the second helium ionization zone. Figure taken from Miglio et al. (2010) © A&A.

3.4. Structure of outer convective layers

The structure of the outer convective zones of Sun-like stars remains a source of uncertainty in our modeling and understanding of these stars. It constitutes a poorly determined transition zone between what is seen from the star at the surface and the internal part that we "interpolate" with theoretical models, structurally and chemically speaking. The seismic observations of CoRoT have provided additional constraints that will help us to better understand these regions.

3.4.1. Helium ionization zones

Similarly to the effect of the BCE, the second helium ionization zone (HIZ) produces an oscillatory behavior in the mode frequencies because of the bump that it creates in the first adiabatic exponent Γ_1. The signature of the HIZ has been detected in the second differences of the main-sequence pulsator HD 49933 (Mazumdar et al. 2012) and in the large separations of a bright red giant (Miglio et al. 2010), as can be seen on Fig. IV.1.6. The period of the oscillation provides a model-independent estimate on the depth of the HIZ, which can be confronted to stellar models. But also, the amplitude of the oscillation is directly related to the helium abundance in the envelope, which could thus be estimated in the future for CoRoT targets using methods that were applied to the Sun (Monteiro & Thompson 1998; Basu et al. 2004) and recently successfully adapted to a *Kepler* target (Verma et al. 2014). This opportunity is interesting because the current uncertainty on the initial helium abundance in stars[3] limits the precision to which stellar masses can be estimated, owing to the well-known correlation between helium abundance and stellar mass (e.g. Lebreton et al. 2014).

3.4.2. Mode amplitudes and widths

The amplitudes and lifetimes of solar-like pulsations depend on the driving and damping of these modes, i.e. on

---

[3] The helium abundance in the envelope is hard to estimate from spectroscopy because useful lines of helium are generally absent in the spectra of cool stars.

the properties of convection in the outer envelope (see Samadi et al. 2015 for a comprehensive review). The seismic data obtained with CoRoT enabled us for the first time to measure the amplitudes and line-widths of individual modes in stars other than the Sun. These measurements made it possible to test models of excitation and damping of acoustic modes by turbulent convection.

Theoretical models predict mode amplitudes to scale with $(L/M)^s$, where s ranges from 0.7 to 1.5. CoRoT observations were found to be in agreement with this scaling and favor values of s in the lower end of this interval (Baudin et al. 2011). By combining seismic estimates of the mode widths of HD 49933 from CoRoT data (Benomar et al. 2009b) with theoretical mode excitation rates for this star, Samadi et al. (2010b,a) derived expected mode amplitudes for this star[4]. They showed that the effects of metallicity must be taken into account, and in doing so they found an agreement with the observed mode amplitudes of HD 49933 within 1-σ errors, except at higher frequencies, which might reveal some deficiencies in the modeling of mode excitation.

The detection of oscillations in thousands of red giants with CoRoT and *Kepler* gave the opportunity to test whether or not the amplitude scaling relations can be extended to the red giant branch. Baudin et al. (2011) extracted mode amplitudes for several hundreds of CoRoT red giants. Samadi et al. (2012) showed that for red giants stars, non-adiabatic effects need to be taken into account when converting velocity amplitudes that are predicted from 3D simulations into intensity amplitudes. Even then, the predicted mode amplitudes for red giants were found to be underestimated by about 40%. Solving this discrepancy will require a better knowledge of the depth at which the mode inertia need to be computed and a more realistic treatment of the interaction between convection and pulsations and more precisely a non-adiabatic treatment of mode compressibility (Samadi et al. 2012).

Baudin et al. (2011) also extracted the mode linewidths for the solar-like pulsators observed by CoRoT. They found that the mode linewidths of main sequence pulsators vary very sharply with the star's temperature ($\Gamma \propto T_{\mathrm{eff}}^m$ with $m = 16.2 \pm 2$), which was later confirmed by Appourchaux et al. (2012) with *Kepler* data and is now understood as a consequence of the compensation between the work integral and mode inertia in the damping rates (Belkacem et al. 2012). This sheds new light on the unexpectedly large width of the modes of F stars such as HD 49933 (Appourchaux et al. 2008). According to Baudin et al. (2011), this scaling relation does not extend to red giants *Kepler* data, which would suggest a possible change in the regime responsible for mode damping between main-sequence and red-giant stars (Corsaro et al. 2015). Belkacem et al. (2012) however performed fully non-adiabatic calculations with the MAD code (Dupret 2001) including time-dependent convection, and they were able to reproduce the observed mode linewidths of both *Kepler* main sequence stars and CoRoT red giants (see Fig. IV.1.7) with the same physical background. This brings an interesting validation to the theoretical computation of mode damping rates, and suggests that a similar damping mechanism operates in main-sequence stars and in red giants. *Kepler* observations, which are longer than those of CoRoT, should yield mode linewidths for red giants higher on the RGB ($T_{\mathrm{eff}} < 4200$ K), which will make it possible to further test our damping rate models.

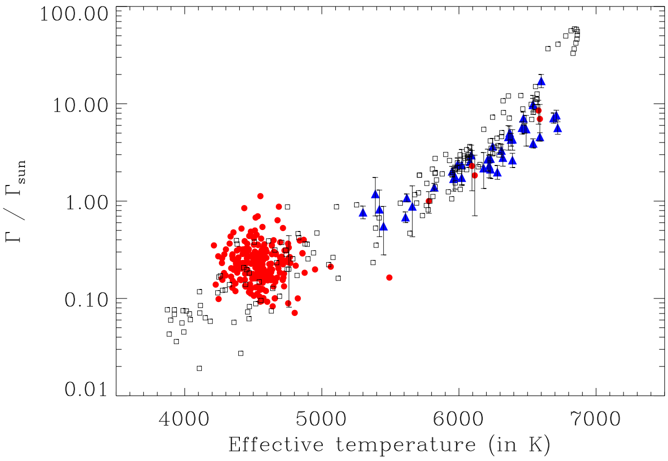

Fig. IV.1.7. Mode linewidths of stochastically-excited modes measured for CoRoT red giants (red circles) and *Kepler* main-sequence stars (blue triangles) plotted versus T_{eff}. The mode widths predicted from non-adiabatic calculations (black symbols) show a remarkable agreement with observations. Figure taken from Belkacem et al. 2012).

3.4.3. Near-surface effects

The structure of super-adiabatic outer layers in the convective envelope remains poorly understood because convective transport is inefficient in this region, which makes the mixing length theory inappropriate. This is currently a major problem for seismology because the frequencies of individual modes depend on the structure of the super-adiabatic layers. Empirical corrections of these so-called near-surface effects have been proposed (Kjeldsen et al. 2008; Ball & Gizon 2014) but a better understanding of the super-adiabatic layer is needed to solve this problem. The combination of the recent progress in the 3D hydrodynamical modeling of stellar atmospheres to the precise 1D modeling of stellar interiors thanks to CoRoT seismic data provides ways testing existing empirical corrections and to propose alternative more realistic corrections (Sonoi et al. 2015).

3.5. Stellar rotation from seismology

Reaching a better understanding of the effects of rotation on stellar structure and evolution was one of the main objectives of the CoRoT mission. Helioseismology has shown that the radiative interior of the Sun rotates as a solid-body down to about 30% of the solar radius (Schou et al. 1998; Chaplin et al. 1999), which brought evidence that an additional transport of angular momentum occurs inside the Sun. The origin of this transport, which could be wave-driven or have a magnetic origin, remains unknown.

Rotation is known to lift the degeneracy between modes of same radial order and angular degree but different

---

[4] These calculations provided predictions for the surface velocity amplitudes of the mode that needed to be converted into intensity amplitudes using the method of Michel et al. (2009) in order to be compared to the observed amplitudes.

azimuthal orders. The intensity of this rotational splitting provides an average of the rotation rate in the cavity in which the waves propagate. By observing stars almost continuously over periods of several months, the CoRoT satellite made it possible to reach the level of precision required to measure the splitting of modes caused by rotation. Note that in order to obtain localized information about the internal rotation profile, one needs to measure the splittings of modes that probe significantly different regions inside the star. This could be achieved for the Sun, because higher-degree modes could be detected. Since the surface of solar-like pulsators other than the Sun cannot be resolved, the contribution from higher-degree modes cancels out owing to disk-averaging. As a consequence, it was not expected that CoRoT observations of main sequence stars could produce inversions of the internal rotation like obtained for the Sun. However, important information could be derived about the rotation of solar-like stars.

For solar-like pulsators observed by CoRoT, the rotational splitting is comparable to the mode width, which complicated its extraction from oscillation spectra. Estimating the splittings of individual modes is still out of reach, but an average splitting for all detected modes was successfully measured for HD 49933 (Appourchaux et al. 2008; Benomar et al. 2009b; Benomar et al. 2015), HD 181420 (Barban et al. 2009), and HD 52265 (Gizon et al. 2013), and ambiguity still remains for HD 49385 (Deheuvels et al. 2010) and HD 43587 (Boumier et al. 2014). The measurement of an average splitting is relevant since all the p-modes that are detected in solar-like pulsators probe roughly the same regions and therefore are expected to be split approximately the same way by rotation. The observed modes are mainly sensitive to the rotation in the superficial layers, but also to a lesser extent to the rotation in the radiative interior.

It is well known that low-mass stars are braked during the main sequence because they lose angular momentum through a magnetized wind generated by the convective envelope. Having access to precise and reliable rotation periods for stars whose mass and age can also be constrained by seismology, as is the case for the aforementioned CoRoT targets, will give precious observational constraints to calibrate theoretical relations of angular momentum loss (e.g. Kawaler 1988), which will be helpful for gyrochronology.

Interesting information can also be drawn on differential rotation by confronting seismic data, which provide an estimate of the rotation rate in the cavity probed by the observed modes, to other measurements of the surface rotation rate. The case of the CoRoT target HD 52265, a K-type solar-like pulsator hosting a planetary companion, is illustrative in that sense. Beside the measurement of the average rotational splittings of acoustic modes, the surface rotation rate was estimated:

- by photometry: the signature of starspot modulation was found in the CoRoT lightcurve of the star (Ballot et al. 2011);
- by combining the spectroscopic $v \sin i$ to the radius of the star obtained from the seismic modeling (Escobar et al. 2012), and its inclination angle i from seismology (Gizon et al. 2013).

Interestingly, these three measurements agree remarkably well, as shown by Fig. IV.1.8. It is important to stress that the rotational splittings of p modes are also sensitive to the rotation in the interior of the star, and in particular in the radiative region, so the agreement between seismic rotation rate and surface rotation rate from photometry and spectroscopy gives an upper bound to the amount of radial differential rotation that exists inside the star.

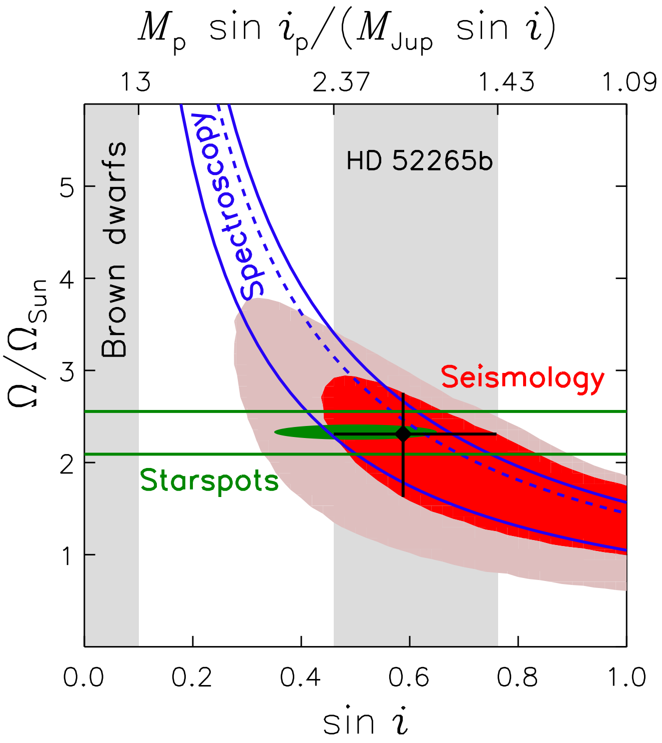

Fig. IV.1.8. Constraints on the surface rotation of HD 52265 from seismology (black diamond with 1σ error bars), from spectroscopy (blue lines) and from the modulation of the lightcurve caused by star spots (horizontal green lines). © Proceedings of the National Academy of Science, 110, 13267.

This point was recently quantified by Benomar et al. (2015) who confronted the average rotation seen by acoustic modes to the photometric and spectroscopic estimates of the surface rotation rates in CoRoT and *Kepler* targets. They found good agreements between these quantities and concluded that the difference in the rotation rates between the radiative interior and the surface is no more than a factor two in most of the main-sequence stars, regardless of their age. This strengthens the hypothesis conveyed by helioseismology that the rotation profiles of solar-like stars are made nearly rigid by an efficient angular momentum transport, the origin of which remains to establish.

It was also proposed to interpret the difference between the mean rotation obtained through seismology and the photometric estimate of the surface rotation as the result of a latitudinal gradient of rotation in the envelope (Ouazzani & Goupil 2012). Provided this effect can be separated from that of a potential radial gradient of rotation in the interior, this would yield interesting constraints on the latitudinal rotation profile near the surface. Note also that the latitudinal dependence of the modes differs for modes of different angular degree and if the rotational splittings of $\ell = 1$ and $\ell = 2$ modes could be estimated separately, one could also obtain constraints on the latitudinal rotation profile. This has however not been managed so far.

Since then, rotational splittings could be measured in the mixed modes of red giants using the longer datasets of the *Kepler* mission. This gave evidence for differential rotation in these stars, the core spinning faster than the envelope (Beck et al. 2012). The mean core rotation rate measured in subgiants (Deheuvels et al. 2012, 2014) and red giants (Mosser et al. 2012; Deheuvels et al. 2015) with *Kepler* data was found to be several orders of magnitude lower than predicted by rotationally-induced mechanisms of angular momentum transport, which showed that an additional efficient redistribution of angular momentum occurs in the radiative interiors of these stars.

3.6. Asteroseismology of planet hosts

The CoRoT mission has marked the beginning of the contribution of asteroseismology to the study of the evolution of exoplanetary systems. The determination of the properties of detected exoplanets is usually limited by the imprecise knowledge of the host star's properties. In particular, the mean density of detected planets, which is crucial to determine the planet's internal composition, is foremost dependent on the stellar mass and radius estimates. One key contribution from asteroseismology is that it can provide a better characterization of the host star. This was illustrated in the case of HD 52265 which hosts a hot Jupiter: the analysis of the acoustic modes provided an estimate of the stellar inclination angle (Gizon et al. 2013). In the case of the Saturn-like planet host HD 46375, the analysis of the faint solar-like oscillations of the star provided an estimate of the large separation of acoustic modes, which was sufficient to improve the mass estimate of the planet by a factor two (Gaulme et al. 2010). In the wake of these first successes, seismic estimates of the properties of 33 planet-candidate host stars were obtained using *Kepler* data (Silva Aguirre et al. 2015), and the PLATO mission, selected by ESA, will detect solar-like oscillations in tens of thousands main-sequence stars, including numerous planet hosts.

References

Aerts, C., Thoul, A., Daszyńska, J., et al. 2003, Science, 300, 1926

Aerts, C., De Cat, P., Kuschnig, R., et al. 2006a, ApJ, 642, L165

Aerts, C., Waelkens, C., De Cat, P., et al. 2006b, Journal of the American Association of Variable Star Observers (JAAVSO), 35, 58

Aerts, C., Briquet, M., Degroote, P., Thoul, A., & van Hoolst, T. 2011, A&A, 534, A98

Aizenman, M., Smeyers, P., & Weigert, A. 1977, A&A, 58, 41

Appourchaux, T., Michel, E., Auvergne, M., et al. 2008, A&A, 488, 705

Appourchaux, T., Belkacem, K., Broomhall, A.-M., et al. 2010, A&ARv, 18, 197

Appourchaux, T., Benomar, O., Gruberbauer, M., et al. 2012, A&A, 537, A134

Ausseloos, M., Scuflaire, R., Thoul, A., & Aerts, C. 2004, MNRAS, 355, 352

Ball, W. H., & Gizon, L. 2014, A&A, 568, A123

Ballot, J., Gizon, L., Samadi, R., et al. 2011, A&A, 530, A97

Barban, C., Deheuvels, S., Baudin, F., et al. 2009, A&A, 506, 51

Basu, S., Mazumdar, A., Antia, H. M., & Demarque, P. 2004, MNRAS, 350, 277

Baudin, F., Barban, C., Belkacem, K., et al. 2011, A&A, 529, A84

Beck, P. G., Montalban, J., Kallinger, T., et al. 2012, Nature, 481, 55

Belkacem, K., Samadi, R., Goupil, M.-J., et al. 2009, Science, 324, 1540

Belkacem, K., Dupret, M. A., Baudin, F., et al. 2012, A&A, 540, L7

Benomar, O., Appourchaux, T., & Baudin, F. 2009a, A&A, 506, 15

Benomar, O., Baudin, F., Campante, T. L., et al. 2009b, A&A, 507, L13

Benomar, O., Takata, M., Shibahashi, H., Ceillier, T., & García, R. A. 2015, MNRAS, 452, 2654

Blomme, R., Mahy, L., Catala, C., et al. 2011, A&A, 533, A4

Bouabid, M.-P., Dupret, M.-A., Salmon, S., et al. 2013, MNRAS, 429, 2500

Bouabid, M.-P., Montalbán, J., Miglio, A., et al. 2011, A&A, 531, A145

Boumier, P., Benomar, O., Baudin, F., et al. 2014, A&A, 564, A34

Briquet, M., Morel, T., Thoul, A., et al. 2007, MNRAS, 381, 1482

Briquet, M., Aerts, C., Baglin, A., et al. 2011, A&A, 527, A112

Briquet, M., Neiner, C., Aerts, C., et al. 2012, MNRAS, 427, 483

Briquet, M., Neiner, C., Leroy, B., Pápics, P. I., & MiMeS Collaboration. 2013, A&A, 557, L16

Chapellier, E., & Mathias, P. 2013, A&A, 556, A87

Chaplin, W. J., Christensen-Dalsgaard, J., Elsworth, Y., et al. 1999, MNRAS, 308, 405

Chaplin, W. J., Basu, S., Huber, D., et al. 2014, ApJS, 210, 1

Charpinet, S., Fontaine, G., Brassard, P., et al. 1997, ApJ, 483, L123

Charpinet, S., Green, E. M., Baglin, A., et al. 2010, A&A, 516, L6

Christensen-Dalsgaard, J., Monteiro, M. J. P. F. G., Rempel, M., & Thompson, M. J. 2011, MNRAS, 414, 1158

Corsaro, E., De Ridder, J., & García, R. A. 2015, A&A, 579, A83

De Ridder, J., Barban, C., Baudin, F., et al. 2009, Nature, 459, 398

Degroote, P., Aerts, C., Baglin, A., et al. 2010a, Nature, 464, 259

Degroote, P., Aerts, C., Samadi, R., et al. 2010b, Astron. Nachr., 331, 1065

Degroote, P., Briquet, M., Auvergne, M., et al. 2010c, A&A, 519, A38

Degroote, P., Aerts, C., Michel, E., et al. 2012, A&A, 542, A88

Deheuvels, S., & Michel, E. 2010, Ap&SS, 328, 259

Deheuvels, S., & Michel, E. 2011, A&A, 535, A91

Deheuvels, S., Bruntt, H., Michel, E., et al. 2010, A&A, 515, A87

Deheuvels, S., García, R. A., Chaplin, W. J., et al. 2012, ApJ, 756, 19

Deheuvels, S., Doğan, G., Goupil, M. J., et al. 2014, A&A, 564, A27

Deheuvels, S., Ballot, J., Beck, P. G., et al. 2015, A&A, 580, A96

Deheuvels, S., Brandaõ, I. M., Silva Aguirre, V., et al. 2016, A&A, 589, A93

Desmet, M., Briquet, M., Thoul, A., et al. 2009, MNRAS, 396, 1460

Dupret, M. A. 2001, A&A, 366, 166

Dupret, M.-A., Thoul, A., Scuflaire, R., et al. 2004, A&A, 415, 251

Dupret, M.-A., Grigahcène, A., Garrido, R., Gabriel, M., & Scuflaire, R. 2005, A&A, 435, 927

Dupret, M.-A., Belkacem, K., Samadi, R., et al. 2009, A&A, 506, 57

Dziembowski, W. A. 1971, Acta Astron., 21, 289

Dziembowski, W. A., & Pamyatnykh, A. A. 2008, MNRAS, 385, 2061

Dziembowski, W. A., Gough, D. O., Houdek, G., & Sienkiewicz, R. 2001, MNRAS, 328, 601

Escobar, M. E., Théado, S., Vauclair, S., et al. 2012, A&A, 543, A96

Frandsen, S., Carrier, F., Aerts, C., et al. 2002, A&A, 394, L5

García, R. A., Régulo, C., Samadi, R., et al. 2009, A&A, 506, 41

García Hernández, A., Moya, A., Michel, E., et al. 2013, A&A, 559, A63

Garrido, R., & Poretti, E. 2004, in IAU Colloq. 193: Variable Stars in the Local Group, eds. D. W. Kurtz, & K. R. Pollard, ASP Conf. Ser., 310, 560

Gaulme, P., Appourchaux, T., & Boumier, P. 2009, A&A, 506, 7

Gaulme, P., Deheuvels, S., Weiss, W. W., et al. 2010, A&A, 524, A47

Gautschy, A., & Saio, H. 1995, ARA&A, 33, 75

Gautschy, A., & Saio, H. 1996, ARA&A, 34, 551

Gizon, L., Ballot, J., Michel, E., et al. 2013, Proceedings of the National Academy of Science, 110, 13267

Goupil, M. J., Lebreton, Y., Marques, J. P., et al. 2011, J. Phys. Conf. Ser., 271, 012032

Goupil, M. J., & Talon, S. 2009, Communications in Asteroseismology, 158, 220

Guzik, J. A., Kaye, A. B., Bradley, P. A., Cox, A. N., & Neuforge, C. 2000, ApJ, 542, L57

Hareter, M. 2012, Astron. Nachr., 333, 1048

Huat, A.-L., Hubert, A.-M., Baudin, F., et al. 2009, A&A, 506, 95

Kallinger, T., & Matthews, J. M. 2010, ApJ, 711, L35

Kawaler, S. D. 1988, ApJ, 333, 236

Kennedy, J. R., Jefferies, S. M., & Hill, F. 1993, in GONG 1992. Seismic Investigation of the Sun and Stars, ed. T. M. Brown, ASP Conf. Ser., 42, 273

Kjeldsen, H., Bedding, T. R., & Christensen-Dalsgaard, J. 2008, ApJ, 683, L175

Le Pennec, M., & Turck-Chièze, S. 2014, in IAU Symp. 301, eds. J. A. Guzik, W. J. Chaplin, G. Handler, & A. Pigulski, 229

Lebreton, Y., & Goupil, M. J. 2012, A&A, 544, L13

Lebreton, Y., Goupil, M. J., & Montalbán, J. 2014, in EAS PS, 65, 99

Maceroni, C., Montalban, J., Gandolfi, D., Pavlovski, K., & Rainer, M. 2013, VizieR Online Data Catalog, 355, 20060

Mahy, L., Gosset, E., Baudin, F., et al. 2011, A&A, 525, A101

Mazumdar, A., Briquet, M., Desmet, M., & Aerts, C. 2006, A&A, 459, 589

Mazumdar, A., Michel, E., Antia, H. M., & Deheuvels, S. 2012, A&A, 540, A31

Michel, E., Baglin, A., Auvergne, M., et al. 2008, Science, 322, 558

Michel, E., Samadi, R., Baudin, F., et al. 2009, A&A, 495, 979

Miglio, A., Bourge, P.-O., Montalbán, J., & Dupret, M.-A. 2007a, Communications in Asteroseismology, 150, 209

Miglio, A., Montalbán, J., & Dupret, M.-A. 2007b, MNRAS, 375, L21

Miglio, A., Montalbán, J., Noels, A., & Eggenberger, P. 2008, MNRAS, 386, 1487

Miglio, A., Montalbán, J., Carrier, F., et al. 2010, A&A, 520, L6

Monteiro, M. J. P. F. G., & Thompson, M. J. 1998, in New Eyes to See Inside the Sun and Stars, eds. F.-L. Deubner, J. Christensen-Dalsgaard, & D. Kurtz, IAU Symp., 185, 317

Morel, T., Briquet, M., Auvergne, M., et al. 2014, A&A, 561, A35

Mosser, B., & Appourchaux, T. 2009, A&A, 508, 877

Mosser, B., Michel, E., Appourchaux, T., et al. 2009, A&A, 506, 33

Mosser, B., Goupil, M. J., Belkacem, K., et al. 2012, A&A, 548, A10

Neiner, C., Mathis, S., Saio, H., et al. 2012, A&A, 539, A90

Neiner, C., Mathis, S., Saio, H., & Lee, U. 2013, in Progress in Physics of the Sun and Stars: A New Era in Helio- and Asteroseismology, eds. H. Shibahashi, & A. E. Lynas-Gray, ASP Conf. Ser., 479, 319

Neiner, C., Briquet, M., Mathis, S., & Degroote, P. 2015, in IAU Symp., 307, 443

Ouazzani, R.-M., & Goupil, M.-J. 2012, A&A, 542, A99

Ozel, N., Mosser, B., Dupret, M. A., et al. 2013, A&A, 558, A79

Pamyatnykh, A. A., Handler, G., & Dziembowski, W. A. 2004, MNRAS, 350, 1022

Paparó, M., Bognár, Z., Benkő, J. M., et al. 2013, A&A, 557, A27

Pápics, P. I., Briquet, M., Baglin, A., et al. 2012, A&A, 542, A55

Pápics, P. I., Moravveji, E., Aerts, C., et al. 2014a, A&A, 570, A8

Pápics, P. I., Moravveji, E., Aerts, C., et al. 2014b, A&A, 570, C4

Pápics, P. I., Tkachenko, A., Aerts, C., et al. 2015, ApJ, 803, L25

Poretti, E., Michel, E., Garrido, R., et al. 2009, A&A, 506, 85

Poretti, E., Mantegazza, L., Niemczura, E., et al. 2010a, Astron. Nachr., 331, 1049

Poretti, E., Paparó, M., Deleuil, M., et al. 2010b, A&A, 520, A108

Poretti, E., Baglin, A., & Weiss, W. W. 2014, ApJ, 795, L36

Rauer, H., Catala, C., Aerts, C., et al. 2014, Experimental Astronomy, 38, 249

Roxburgh, I. W. 2009, A&A, 506, 435
Salmon, S. 2014, Ph.D. Thesis, University of Liège, Belgium
Salmon, S., Montalbán, J., Morel, T., et al. 2012, MNRAS, 422, 3460
Samadi, R., Ludwig, H.-G., Belkacem, K., et al. 2010a, A&A, 509, A16
Samadi, R., Ludwig, H.-G., Belkacem, K., Goupil, M. J., & Dupret, M.-A. 2010b, A&A, 509, A15
Samadi, R., Belkacem, K., Dupret, M.-A., et al. 2012, A&A, 543, A120
Samadi, R., Belkacem, K., & Sonoi, T. 2015, ArXiv e-prints
Schou, J., Antia, H. M., Basu, S., et al. 1998, ApJ, 505, 390
Scuflaire, R. 1974, A&A, 36, 107
Silva Aguirre, V., Davies, G. R., Basu, S., et al. 2015, MNRAS, 452, 2127
Sonoi, T., Samadi, R., Belkacem, K., et al. 2015, A&A, 583, A112
Stello, D., Kjeldsen, H., Bedding, T. R., & Buzasi, D. 2006, A&A, 448, 709
Szabó, R., Benkő, J. M., Paparó, M., et al. 2014, A&A, 570, A100
Tassoul, M. 1980, ApJS, 43, 469
Thoul, A., Scuflaire, R., Ausseloos, M., Aerts, C., & Noels, A. 2004, Communications in Asteroseismology, 144, 35
Turcotte, S., & Richard, O. 2003, Ap&SS, 284, 225
Van Grootel, V., Charpinet, S., Fontaine, G., Green, E. M., & Brassard, P. 2010, A&A, 524, A63
Van Reeth, T., Tkachenko, A., Aerts, C., et al. 2015, ArXiv e-prints
Verma, K., Antia, H. M., Basu, S., & Mazumdar, A. 2014, ApJ, 794, 114
Zwintz, K., Fossati, L., Ryabchikova, T., et al. 2013, A&A, 550, A121

Acknowledgements: The CoRoT space mission has been developed and operated by CNES, with the contribution of Austria, Belgium, Brazil, ESA, Germany, and Spain.

The CoRoT Legacy Book

DOI: 10.1051/978-2-7598-1876-1.c042

IV.2

Pulsating red giant stars

Ensemble asteroseismology and Asteroseismology of stellar populations in the Milky way

B. Mosser[1] and A. Miglio[2]

[1] LESIA, Observatoire de Paris, PSL Research University, CNRS, Université Pierre et Marie Curie, Université Paris Diderot, 92195 Meudon, France
[2] School of Physics and Astronomy, University of Birmingham, Edgbaston, Birmingham, B15 2TT, UK

1. Introduction

Asteroseismology of low-mass stars has provided us with a much more precise method for determining stellar global parameters than classical methods such as isochrone fitting (e.g. Lebreton & Goupil 2014). The determination of accurate stellar parameters is a fundamental and longstanding problem in astrophysics (e.g. Soderblom 2010). Nevertheless, such a determination is only possible by means of stellar models and therefore suffers from our deficient knowledge of the physical processes taking place in stars. It motivated the development of a new field called ensemble asteroseismology as described thoroughly in Sect. 2. The wealth of red giants observed by CoRoT as well as the knowledge of their oscillation spectra (Sect. 2.2) made it possible to adopt a statistical approach. The foundations of such an approach are the relations between global seismic quantities, such as the large separation or the frequency of the maximum height of the power spectrum, and stellar parameters. Initially, these scaling relations were used to predict the characteristics of the oscillations (e.g. Ulrich 1986; Brown et al. 1991). CoRoT permitted to go beyond by using the scaling relations for unravelling the structure and evolution of low-mass red giant stars (Sect. 2.3).

Such a wealth of seismic indices also allowed the development of a novel approach for investigating the Galactic stellar populations (Sect. 3). For instance, the global seismic constraints have been used for inferring accurate distances as well as an estimate of the red giant ages. All this information brings new lights for investigating stellar populations in the Milky Way. A step further is also permitted by the opportunity gathered by the synergies between asteroseismology and large spectroscopic surveys (Sect. 3.2), which is ending up with the emergence of a chemodynamical investigation of the Galaxy.

2. Ensemble asteroseismology (by B. Mosser)

Before the launch of CoRoT, asteroseismic observations were limited to a handful of targets. With high-precision radial velocity measurement, observations could be performed on one single object only at the same time. A six-week photometric campaign using nine telescopes allowed the simultaneous monitoring of about 20 red giants in the open cluster M67 (Stello et al. 2007). CoRoT, offering the possibility to observe simultaneously and continuously thousands of targets and to derive their seismic properties, has promoted a new concept: ensemble asteroseismology. This concept is developed in this chapter: the measurement of global seismic parameters allows us to examine the properties of large populations of stars at different evolutionary stages.

2.1. The situation before CoRoT: the case of red giants

The power of seismology, as illustrated by Earth seismology and helioseismology (e.g., Tong & Garcia 2015), has motivated attempts for detecting solar-like oscillations in red giants as well as in less-evolved stars having an external convective layer (e.g., Gilliland et al. 1993). Here, we show the difficulties observations had to face for detecting solar-like oscillations in red giants and the progress they permitted. We do not address large-amplitude oscillations in semi-regular variable or Mira stars, but restrict our attention to red giants.

2.1.1. Ambiguous and unambiguous identifications

The first unambiguous detection of solar-like oscillations of a red giant star was reported by Frandsen et al. (2002). They monitored the G7III red giant ξ Hya during one month with the CORALIE spectrometer at the 1.2-m Swiss Euler telescope. Oscillations were identified in the frequency range 50–130 μHz, with amplitudes slightly smaller than $2\,\mathrm{m.s^{-1}}$. The consensus resulted from the combination of different positive signatures, which are all related to global properties that prefigured the bases of ensemble asteroseismology. Other observations were inconclusive in terms of seismic analysis but participated to the movement toward positive detections (e.g., Kallinger et al. 2005; Kim et al. 2006; Stello et al. 2007). According to the current knowledge about solar-like oscillations, earlier results can be a posteriori confirmed or disconfirmed, using global properties from what is now called ensemble asteroseismology (Sect. 2.3).

2.1.2. The case of ε Ophiuchi

As Procyon for less-evolved stars (e.g., Arentoft et al. 2008; Bedding et al. 2010, and references therein), the G9.5III red giant ε Oph has played an important role as it was supposed to be a favorable target. Barban et al. (2004) reported the results of a two-month bi-site ground-based campaign, with unambiguous detection of solar-oscillation in the red giants ε Oph and η Ser. The frequency $\nu_{\max}$ of maximum oscillation signal was clearly identified, contrary to the large separation $\Delta\nu$. A deeper analysis of ε Oph was then performed by De Ridder et al. (2006), who could measure the frequency $\nu_{\max}$ of maximum oscillation, but still hesitated between two values of the large separation, which are each-other day aliases (4.8 or 6.7 μHz). These observations largely benefitted from the high stability and accuracy of high-resolution spectrometers designed for exoplanetary search. With the space-borne MOST data, oscillations around 60 μHz were confirmed (Barban et al. 2007), with maximum amplitudes around 130 ppm and a large separation of 5.3 ± 0.1 μHz. The authors derived a mass of about 2 $M_\odot$, assuming that the observed modes are radial. The identification of non-radial modes remained however debated. With a reanalysis of the MOST data, Kallinger et al. (2008a) found that the best model fit both radial and nonradial modes. The small scatter of the frequencies indicated then, against previous analysis, that the lifetimes of the modes could be as long as 10–20 days. Mazumdar et al. (2009) reanalyzed the data and tested if the star is burning hydrogen in a shell on the red giant branch (RGB) or is burning helium in the core. The radius they derived from the asteroseismic analysis matches the interferometric value quite closely. They found a mass of 1.85 ± 0.05 $M_\odot$ but could not fix the evolutionary status.[1]

2.1.3. Mode lifetimes? Non-radial modes?

The case study of ε Oph showed that many issues were debated, among which the mode lifetimes and the presence of non-radial modes. Stello et al. (2006) revisited lifetimes in the oscillation spectrum of ξ Hya and concluded that the data are consistent with mode lifetimes of 2 days. The reanalysis of the oscillation spectrum of ε Oph allowed two interpretations: only short-lived radial modes (Barban et al. 2007) or a mix of radial and nonradial modes with moderate lifetimes (Kallinger et al. 2008a).

In fact, observations of the K1.5 red giant Arcturus were more conclusive. Retter et al. (2003) showed that its amplitude spectrum observed with the star tracker on WIRE has a significant excess of power at low frequency. The variability of Arcturus was presumably explained by sound waves, the contribution of granulation only being likely ruled out by Doppler observations conducted earlier. A further analysis by Tarrant et al. (2007) based on a 2.5-yr long photometric time series by the SME imager on board the Coriolis satellite provided the measurement of the damping time, which was quite long (24 ± 1 days). Their results also hinted at the possible presence of non-radial modes.

Hekker et al. (2006) argued that the line profile variations in three stars (among which ε Oph) already analyzed with other tools suggest the presence of non-radial modes. Kallinger et al. (2008b) reported the detection of non-radial modes in MOST photometry of the red giant HD 20884, but this result was presented by the Editor as “an important and controversial topic”.[2]

2.1.4. Empirical and theoretical predictions

For all these observations, global seismic properties and scaling relations were used to guide the analysis: the large separation was scaled to the inverse of the dynamical time, proportional to the square root of the mean density (Eddington 1917); the frequency $\nu_{\max}$ was scaled to the atmospheric cutoff frequency (Brown et al. 1991). The empirical scaling relations of Kjeldsen & Bedding (1995) were successfully used for estimating the expected frequency range and amplitudes. Stello et al. (2008) presented the analysis of eleven giants observed with the WIRE satellite and reported the first confirmation that $\nu_{\max}$ can be predicted for K giants by scaling from the solar acoustic cutoff frequency. They used such an approach to provide an estimate of the stellar masses, and claimed a precision level of about 20%. Theoretical work could not decide if radial and non-radial modes were equally excited. Dziembowski et al. (2001) predicted that, for red giants, non-radial mode amplitudes should be lower than radial mode amplitudes. No reliable information was available for lifetimes.

2.1.5. Practical limitations before CoRoT

A necessary ingredient for successful seismic observations is long duration, especially for red giants that oscillate at low frequency due to their low mean density. Before CoRoT, ground-based Doppler observations reached excellent performance with high signal-to-noise ratio (Fig. IV.2.1) but

---

[1] From the statistical point of view gained with the CoRoT and Kepler observations, ε Oph is likely a secondary-clump star.

[2] Having demonstrated that combining different epoch observations of red giants is feasible, Kallinger et al. (2012) clearly showed that non-radial modes were present in ε Oph; this conclusion has been possible only after the CoRoT observations.

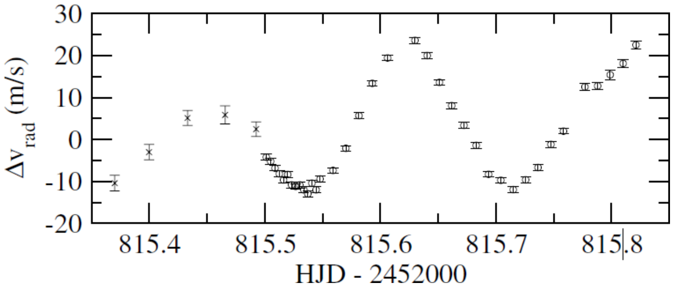

Fig. IV.2.1. Doppler time series showing the oscillations in the red giant ε Oph, observed with CORALIE (circles) and ELODIE (crosses), illustrating that the sensitivity is not an issue (from De Ridder et al. 2006) © A&A.

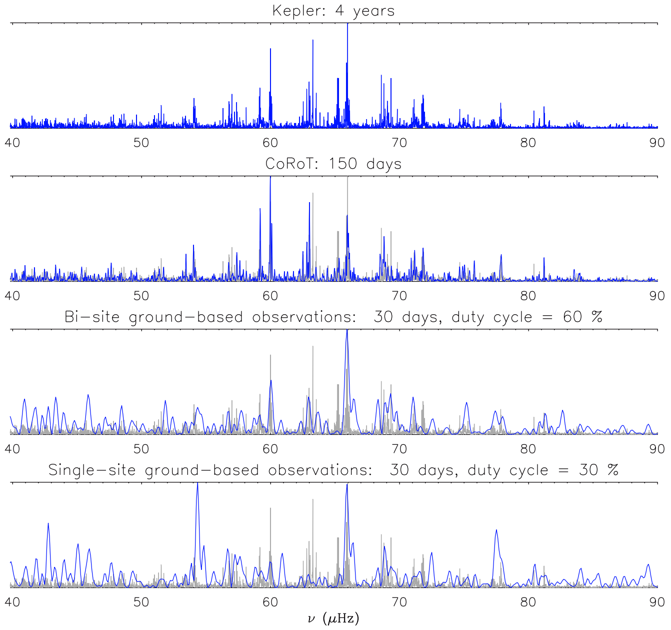

Fig. IV.2.2. Simulation of the oscillation spectrum of a 1.3-$M_\odot$ star on the RGB, as observed with Kepler, CoRoT, or ground-based observations. In all panels, the 4-year long spectrum is indicated in grey as a reference. The noise level is supposed to be similar in all graphs.

remained affected by the day aliases and provided controversial measurements.[3]

The large success of CoRoT comes from the ability to observe thousands of red giants continuously for months, and the surpassing quality of Kepler comes from even longer observation capability. This is illustrated on Fig. IV.2.2, which shows how a clear oscillation signal in a typical red-clump star observed by CoRoT or Kepler is unclear with short observation duration and single or bi-site observations. When the observation conditions are degraded, the equidistance between modes disappears, distinguishing radial and non-radial modes is impossible, and measuring the life time is illusory since the frequency resolution is too poor.

2.2. Toward ensemble asteroseismology

2.2.1. The CoRoT red giant revolution

Everyone agrees that red giant asteroseismology is one of the greatest success of CoRoT and Kepler. This success however started in unfavorable conditions, since red giants represent hostile harbors for exoplanets. If we consider a typical red clump star with a radius about 10 $R_\odot$, a planetary transit will be a hundred time dimmer than around a main-sequence star, whereas hot Jupiters do not provide any transit since their orbit is engulfed in the stellar envelope. As a consequence, red giants were first discarded from the preferred target list. They were however observed in the faint field LRc01, so that De Ridder et al. (2009) could report:

- the presence of radial and non-radial oscillations,
- for more than 300 red giant stars;
- mode lifetimes of the order of a month.

So, the main questions raised by previous observations were unambiguously answered by this pioneering work. One important feature of the red giant oscillation spectrum remained however hidden at that time: mixed modes were not identified, despite the fact they are present, as in the spectrum of the red giant CID 101600807; according to Fig. 4 of De Ridder et al. (2009), this is a star belonging to the secondary clump. Such an evidence is only a posteriori obvious, when the story is well known.

2.2.2. Structure of the oscillation spectrum

Following this firework, the harvest could start. Hekker et al. (2009) aimed at understanding the distribution of the frequencies $\nu_{\max}$ of maximum oscillation power and searched for a possible correlation between $\nu_{\max}$ and the large separation $\Delta\nu$. They determined the first properties of the background signal and the oscillation signal. Indeed, these properties are the different signatures of the convection that breaks just below the photosphere (e.g., Mathur et al. 2011; Mosser et al. 2012a; Samadi et al. 2013), with an incoherent signature that gives raise to the different scales and granulation, whereas the excited waves filtered by the star give raise to the oscillation modes.

An important leap forward was proposed by Kallinger et al. (2010), who depicted the properties of selected targets, performed grid modelling, and deduced reliable estimates for the stellar mass and radius from scaling relations (see Sect. 2.3). Mosser et al. (2010) extended the analysis toward a larger set of stars in the CoRoT fields LRc01 and LRa01, characterized according to their location in a color-magnitude diagram, with J−K in the range [0.6, 1.0] and K brighter than 12. They identified more than 1800 red giants showing solar-like oscillations among 4600 light curves and obtained accurate distributions of the stellar parameters for about 930 stars. Such global analysis on large sets of stars has opened the way to ensemble asteroseismology, with reliable estimates of mass and radius for several hundred red giants as well as precise information about the stellar population distribution and the red clump.

---

[3] Before the space mission MOST, ground-based seismic photometric observations remained limited to a specific case (M67) and could not be made with dedicated photometers. Star trackers onboard the HST and WIRE were not designed for satisfying the extremely demanding specifications for seismology.

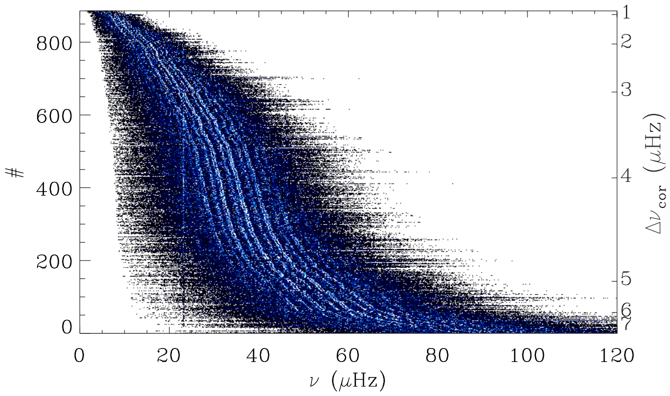

Fig. IV.2.3. CoRoT red giant power spectra stacked into an image after sorting on the large separation. Each line corresponds to one star. The sorting takes the red universal oscillation pattern into account and reveals the structure common to all red giants. The vertical line at 23.2 μHz is the signature of the low-Earth orbit (Auvergne et al. 2009). Figure from Mosser et al. (2011b) © A&A.

2.2.3. Structure homology and universal oscillation pattern

CoRoT observations have shown a simple and useful property of the red giant oscillation pattern: following the interior structure homology, the oscillation pattern has also homologous properties. Structure homology is induced by generic physics: the thermodynamical conditions of the hydrogen-burning shell are related on the one side with the helium core, and on the other side with the convective envelope, so that the core and envelope properties are closely linked together (e.g., Kippenhahn & Weigert 1990; Montalbán et al. 2013). The remarkably regular structure is illustrated on Fig. IV.2.3: oscillations with the same radial orders and angular degrees show clear ridges.

The concept of universal red giant oscillation pattern was introduced by Mosser et al. (2011b), as an alternative form to the usual asymptotic expansion (Tassoul 1980). The second-order asymptotic expansion expresses, for low angular degree ($\ell \ll n$) modes observed around $\nu_{\max}$, as

$$\begin{aligned} \nu_{n,\ell} \quad = \quad & \Big(n + \varepsilon_{\rm obs}(\Delta\nu_{\rm obs}) + d_{0\ell}(\Delta\nu_{\rm obs}) \\ & + \frac{\alpha}{2}\,(n - n_{\max})^2\Big)\ \Delta\nu_{\rm obs}, \qquad (1) \end{aligned}$$

where the dimensionless parameter $n_{\max}$ is defined by $\nu_{\max}/\Delta\nu_{\rm obs} - \varepsilon_{\rm obs}$. The observed large separation $\Delta\nu_{\rm obs}$ and the frequency of maximum oscillation signal $\nu_{\max}$ are the only free parameters. The radial offset $\varepsilon_{\rm obs}$ helps locating the radial ridge; the non-radial offsets $d_{0\ell}$ express the shifts of the different degrees ℓ compared to the radial modes; the second-order term α depends on $n_{\max}$ (Mosser et al. 2013b). The quadratic form of Eq. (1) differs from the usual asymptotic expansion since it is based on the large separation $\Delta\nu_{\rm obs}$ observed at $\nu_{\max}$. Hence, $\Delta\nu_{\rm obs}$ differs from the asymptotic value $\Delta\nu_{\rm as}$ which should, but cannot, be measured at very high frequency. The relationship between the observed and asymptotic values of the large separation is discussed in Mosser et al. (2013b).

The power of Eq. (1) is shown on Fig. IV.2.4. The clear identification of the ridges, each one corresponding to a given radial order n and angular degree ℓ, demonstrates the universality of the oscillation pattern. With Kepler, the scaling properties were extended at larger $\Delta\nu$ by Corsaro et al. (2012) and at lower $\Delta\nu$ by Mosser et al. (2013a).

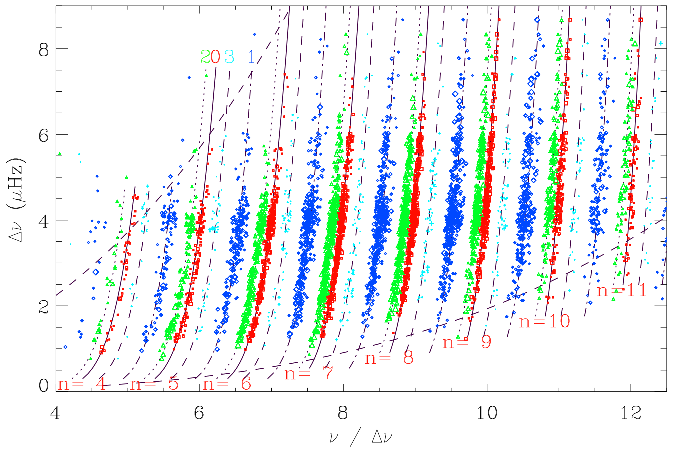

Fig. IV.2.4. Identification of the oscillation modes reported in Fig. IV.2.3, with radial modes in red, dipole modes in dark blue, $\ell = 2$ modes in green, $\ell = 3$ modes in light blue. The solid grey lines superimposed on the ridges indicate the fits of ε for each radial order n. The fits of d_{01}, d_{02} and d_{03} are superimposed on the respective ridges (respectively dash-dot, dot, and dash lines for ℓ =1, 2, and 3). The dark dashed lines, derived from the scaling relation dealing with the oscillation excess power, delineate the region where the modes have noticeable amplitudes. Figure from Mosser et al. (2011b) © A&A.

2.2.4. Global seismic parameters and evolutionary stages

The measurement of the global seismic parameters carries a rich information. For instance, histograms of the seismic parameters clearly emphasize the red clump and helps identifying the secondary clump stars, massive enough for having ignited helium in non-degenerate conditions (Girardi 1999). The comparison between observed and simulated populations, first performed by Miglio et al. (2009), based on the CoRoT data (Hekker et al. 2009), is discussed in Sect. 3.

A further global seismic parameter is derived from the period spacing of dipole modes. In subgiants and red giants with a radiative core, dipole modes are not pure pressure modes but show a mixed character; they result from the coupling of sound waves in the envelope and gravity waves in the radiative inner region. The period spacing varies with ν^{-2} and also depends on the nature of the mixed mode. It is close to the asymptotic period spacing ($\sqrt{2}\pi^2/\int N_{\rm BV}\,{\rm d}\ln r$ for dipole modes) for gravity-dominated mixed modes, but much below for pressure-dominated mixed modes. Mixed modes in CoRoT red giants were identified by Mosser et al. (2011a). Regardless modelling, period spacings help distinguishing the evolutionary stages of red giants, with significant population differences in the different fields observed by CoRoT. This work opened the way for identifying the asymptotic period spacings in Kepler data (Mosser et al. 2012c), measuring the core rotation (Mosser et al. 2012b), and tracing seismic evolutionary tracks (Mosser et al. 2014).

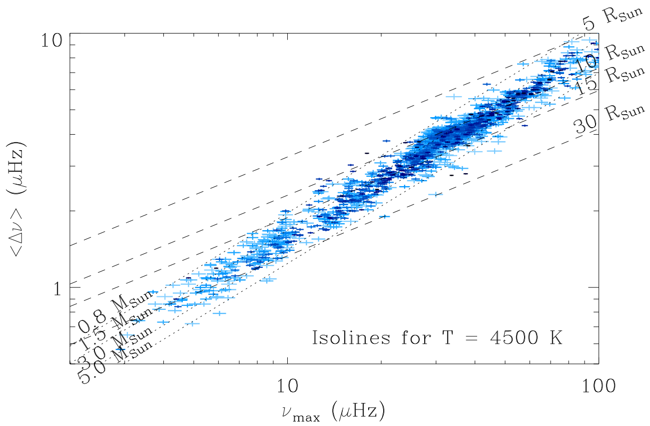

Fig. IV.2.5. $\nu_{\rm max}$ - $\langle\Delta\nu\rangle$ relation for red giants in LRa01 and LRc01. Isoradius and isomass lines, derived from the scalings given by Eqs. (2) and (3), are given for a mean effective temperature of 4500 K. Figure from Mosser et al. (2010) © A&A.

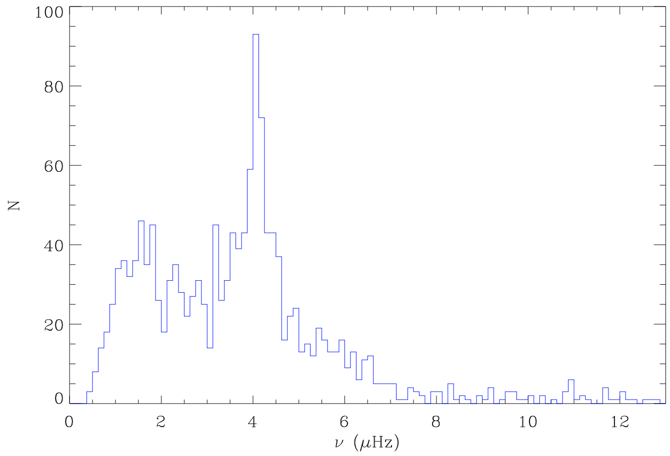

Fig. IV.2.6. Histogram of $\Delta\nu$ of red giants observed during the run LRc01. The peak around 4 μHz is the signature of the red clump. The deficit above 7 μHz is due to the magnitude bias in the detection (Table IV.2.1).

2.3. Scaling relations and ensemble asteroseismology

2.3.1. Light curves and detection

Light curves with a new treatment were recently delivered. The full comparison of the different pipelines providing the global seismic parameters is ongoing. Here, we derive information from the envelope autocorrelation function of the time series (Mosser & Appourchaux 2009) and compare the new data of the LRc01 to the treatment conducted by Mosser et al. (2010). All light curves of the first long run LRc01 were considered, not only those with color indices presumably corresponding to red giants. This allows us to treat all possible red giants, regardless any problems in any prior classification of targets.

The distribution of the large separation is shown on Fig. IV.2.6. The new treatment allows us to enlarge the frequency range where oscillations are detected, with large separations in the interval [0.5–12.5 μHz]. Previous studies were limited within the range [0.75–9.5 μHz]. This new interval approximately corresponds to stellar radii in the interval [5–35 $R_\odot$]. Table IV.2.1 shows how the detection depends on the stellar magnitude. Unsurprisingly, the dimmer the magnitude, the more rare the reliable detection of solar-like oscillations. It also emphasizes a bias inherent to the properties of the seismic signal: at dim magnitudes, the global seismic parameters can be detected only for evolved red giants, according to the scaling relation that governs the oscillation amplitude (Mosser et al. 2012a). Table IV.2.1 indicates the limit value $(\Delta\nu)_{\rm lim}$, corresponding to the typical maximum large separation than can be measured as a function of the visible magnitude. Determining the evolutionary status of these stars is also crucial for forthcoming Galactic archeology analysis (Sect. 3): we could do this for about 25% of the red giants showing solar-like oscillations. The complete study and comparison of all fields observed by CoRoT is in progress (de Assis Peralta et al., in prep.).

Table IV.2.1. Distribution of the detection as a function of magnitude. $\mathcal{N}_1$ is the number of available light curves and $\mathcal{N}_2$ is the number of red giants showing solar-like oscillations.

Magnitude interval		$\mathcal{N}_1$	$\mathcal{N}_2$	$\mathcal{N}_2/\mathcal{N}_1$ %	$(\Delta\nu)_{\rm lim}$ μHz
11	12	99	43	43.4	12.1
12	13	735	365	49.6	11.8
13	14	1890	586	31.0	10.8
14	15	3673	399	10.8	7.8
15	16	5010	94	1.9	5.4
total		11 407	1487		

2.3.2. Seismic masses and radii

Kallinger et al. (2010) have studied in detail a subsample of faint giant stars obtained in the faint field of CoRoT. Having modelled the convective background noise and the oscillation power excess, they deduced estimates for the stellar mass and radius. Indeed, the importance of the seismic parameters $\Delta\nu_{\rm obs}$ and $\nu_{\rm max}$ is emphasized by their ability to provide relevant estimates of the stellar mass and radius, since they are respectively related to the square root of the mean density and to the acoustic cutoff frequency, hence to surface gravity, of the stars (Brown et al. 1991):

$$\frac{R}{R_\odot} \simeq \left(\frac{\nu_{\rm max}}{\nu_{\rm max,\odot}}\right)\left(\frac{\Delta\nu}{\Delta\nu_\odot}\right)^{-2}\left(\frac{T_{\rm eff}}{T_\odot}\right)^{1/2}, \tag{2}$$

$$\frac{M}{M_\odot} \simeq \left(\frac{\nu_{\rm max}}{\nu_{\rm max,\odot}}\right)^{3}\left(\frac{\Delta\nu}{\Delta\nu_\odot}\right)^{-4}\left(\frac{T_{\rm eff}}{T_\odot}\right)^{3/2}. \tag{3}$$

Mainly empirical, these relations prove to be operant throughout many evolutionary stages (e.g., White et al. 2011a; Belkacem et al. 2013).

However, the calibration of the seismic scaling relations remains an issue. Different works have shown that the extrapolation from the Sun to evolved stars induces small biases and provides too high masses for red giants (e.g., Miglio et al. 2012a; Epstein et al. 2014). We may notice that the very first papers to use the scaling relations, Kallinger et al. (2010) and Mosser et al. (2010), provided an external calibration that reduced the seismic mass. However, this correction has been omitted by further work.

It is also clear that the calibration process of the scaling relations requires precise steps. One of this step is out of reach actually: the determination of $\nu_{\max}$ is purely phenomenological and lacks a precise theoretical definition. However, the theoretical approach based on 3D-atmospheric models carried out by Belkacem et al. (2013) indicates that $\nu_{\max}$ scales with the acoustic cut-off frequency and the Mach number as $\nu_c\ \mathcal{M}^3$ (see also Belkacem et al. 2011); this provides strong clues for the relevance of the relation $\nu_{\max} \propto \nu_c$ since $\mathcal{M}$ only shows small variation with stellar evolution. Observationally, the agreement between the spectroscopic measurement of $\log g$ and $\nu_{\max}$ (e.g., Pinsonneault et al. 2014) provides us with a good argument about the relevant use of $\nu_{\max}$.

The large separation is a better defined parameter. However, we have too many definitions for it: the large separation we measure at $\nu_{\max}$ (e.g., Mosser & Appourchaux 2009) neither corresponds to the asymptotic definition linked to twice the acoustic radius, nor to the dynamical frequency ν_0 that scales as $\sqrt{\mathcal{G}M/R^3}$. Even if $\Delta\nu_{\mathrm{obs}}$ provides an acceptable proxy of the dynamical frequency ν_0, the relationships between these parameters must be investigated in order to accurately calibrate Eqs. (2) and (3) and make the best of the high-quality seismic data (Belkacem et al. 2013).

2.3.3. Stellar evolution

As noted by Stello et al. (2009) on the basis of ground-based and CoRoT observations, the frequencies $\nu_{\max}$ and $\Delta\nu$ are closely linked together. They measured $\Delta\nu \propto \nu_{\max}^{0.772\pm0.005}$. This relation, derived from the empirical scaling relations defining $\Delta\nu$ and $\nu_{\max}$, was interpreted as the signature of solar-like oscillations. It is now expanded up to the upper red and asymptotic giant branches, where solar-like oscillations correspond to semi-regular variability (Mosser et al. 2013a). From Eqs. (2) and (3), the scaling between $\nu_{\max}$ and $\Delta\nu_{\mathrm{obs}}$ expresses

$$\Delta\nu_{\mathrm{obs}} \simeq \nu_0 \propto M^{-1/4}\ T_{\mathrm{eff}}^{3/8}\ \nu_{\max}^{3/4}. \tag{4}$$

On the main sequence, the frequency $\Delta\nu_{\mathrm{obs}}$ scales as $\nu_{\max}^{0.8}$ (Verner et al. 2011). The discrepancy between this exponent and the 3/4 value in Eq. (4) is due to the fact that low-mass and high-mass evolution tracks evolve in different regions of the main sequence. On the contrary, the observed scaling exponent on the RGB is closer to 3/4 (Fig. IV.2.5) since the RGB is drawn by the evolution of low-mass stars. Stars with a mass in the range 0.9–1.8 $M_\odot$ are present at all stages of the RGB, hence for all $\nu_{\max}$, so that the stellar mass plays no significant role in Eq. (4).

The validity of Eq. (4) is observed over six decades in frequency in the red giant regime (Fig. 2 of Mosser et al. 2013c). This indicates that we can use red giants to track stellar evolution, especially when the information of mixed modes is used (Fig. IV.2.7).

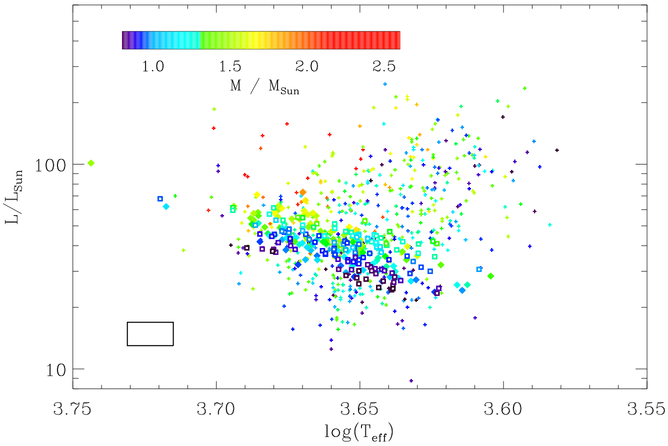

Fig. IV.2.7. HR diagram of the targets with best SNR ratios of LRa01 and LRc01, © A&A, 532, A86. Masses are estimated from the seismic scaling relations. For clarity, individual bars are not represented. Cross are replaced by open squares for red-clump stars and diamonds for secondary-clump stars. The mean 1σ error box is given in the lower-left corner of the diagram.

2.3.4. Mode lifetimes and amplitudes

Predicting oscillation amplitudes involves non-adiabatic physics and is much more complex than computing eigenfrequencies. Amplitudes depend on a balance between mode driving (also referred to as excitation rate) and mode damping (which is proportional to the mode linewidth). Simulations of the excitation are based on 3-D modelling of the upper stellar envelope (Samadi et al. 2015, for a review). Large efforts in this direction are currently made, since such simulations can also be used to address the surface-effect correction due to non-adiabatic effects (Sonoi et al. 2015). Excitation rates of solar-like oscillations across the HR diagram were predicted by Samadi et al. (2007). Assuming adiabatic pulsations, they computed the mode amplitude in terms of surface velocity, converted them into intensity fluctuations, and found that the energy supply rate scales as $(L/M)^{2.6}$ for both main-sequence and red giant stars. The scaling based on the adiabatic intensity-velocity scaling relation results in an under-estimation by a factor of about 2.5 with respect to the CoRoT seismic measurements; this factor is reduced to 1.4 when using non-adiabatic velocity-intensity conversion factors.

These theoretical expectations can be confronted to observations. The scaling of the mode amplitudes with mass and luminosity derived from ensemble asteroseismology shows a more complex dependence than L/M. As an important result, one should note that the ratio between the energy put into the granulation and into the oscillations does not vary with evolution: the ratio $H_{\max}/B_{\max}$ hardly depends on $\nu_{\max}$ ($H_{\max}$ and $B_{\max}$ are respectively the mean heights of the oscillations and of the background at $\nu_{\max}$ (Mosser et al. 2010; Mathur et al. 2011; Mosser et al. 2012a)).

Amplitudes of radial modes in red giants were also investigated by a detailed analysis of oscillation spectra (i.e. measurements of individual mode heights and mode linewidths) for several hundreds of CoRoT red giants (Baudin et al. 2011). Line widths are small, of about a few tenths of a μHz; their scaling with T_{eff} shows no important variation, contrary to main-sequence stars. In contrast, Belkacem et al. (2012) theoretically exhibited a scaling as a power law with a large exponent of 10.8. Alternatively, Corsaro et al. (2012) proposed a scaling varying exponentially with $T_{\rm eff}$, valid from the main sequence to the red giant domain. Their measurements, based on Kepler data, benefit from longer observations: measuring lifetimes requires in fact that modes are resolved, with a duration at least 10 times larger (Appourchaux & Grundahl 2015). So, even Kepler data are limited for measuring oscillation lifetimes of evolved red giants radial modes, so that this point remains an issue.

For long-lived dipole mixed modes, the situation is more complex than for radial modes, but Dupret et al. (2009) and Grosjean et al. (2014) could provide the lifetimes of radial and non-radial mixed modes with a time-dependent treatment of convection, for high-mass and low-mass red giants, respectively.

2.3.5. Helium ionization zones

Miglio et al. (2010) found evidence for a periodic component in the oscillation frequencies of in HD 181907 (HR 7349) analyzed by Carrier et al. (2010). As for less-evolved stars (Sect. 3, Part V, Chap 1), the modulation was interpreted as the seismic signature of a sharp structure variation caused by a local depression of the sound speed that occurs in the helium second-ionization region. Such a signature was also observed in a larger set of CoRoT data, but not studied in detail (Fig. 6 of Mosser et al. 2010). It appears at all evolutionary stages, since it is also clearly present in the luminous high-mass red giant studied and in detail by Baudin et al. (2012). Recently, with a large survey of Kepler red giants, Vrard et al. (2015) showed that RGB and red clump stars have distinct signatures that can be used to derive the location of the helium second-ionization region but are not precise enough to derive the helium mass fraction.

2.3.6. Rotation

Probing the stellar rotation with seismology requires long-duration observation, unfortunately out of reach with CoRoT. Experience gained with Kepler stars shows that more than one year of observation is necessary to detect the core rotation period, typically between 10 and 30 days, in a red giant starting to ascend the RGB, and more than two years for measuring it for red clump stars (e.g., Mosser et al. 2012b; Deheuvels et al. 2014). This limitation is not only a question of frequency resolution; it relies in fact on the detection of gravity dominated mixed modes, whose lifetimes is year long.

Even if undetectable, rotation plays a significant role in red giants, as shown by modelling (Lagarde et al. 2015). Seismic data are now so precise that making the best of them requires the introduction of rotation in the models. Furthermore, Belkacem et al. (2015b,a) showed the intricacy of oscillation and rotation. They developed a formalism that provides a modelling of the wave fluxes in both the mean angular momentum and the mean energy equation. This proves that mixed modes extract angular momentum from the innermost regions of subgiants and red giant, and are a promising candidate to explain the observed spin-down of the core of evolved red giants.

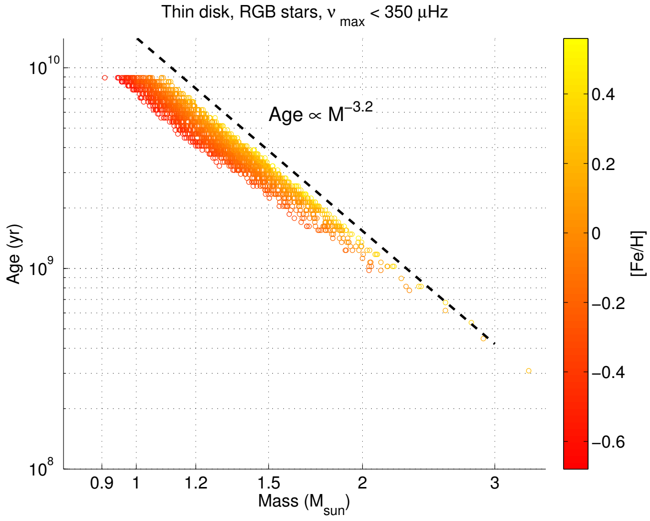

Fig. IV.2.8. Age-mass-metallicity relation for red giants in a TRILEGAL (Girardi et al. 2005) synthetic population representative of thin-disc stars. From Davies & Miglio (2016).

3. Asteroseismology of stellar populations in the Milky Way (by A. Miglio)

Once data from the first CoRoT observational run had been analysed, and solar-like oscillations had been detected in thousands of red giant stars (Hekker et al. 2009), it became clear that the newly available observational constraints $\Delta\nu$ and $\nu_{\rm max}$ would allow novel approaches to the study of Galactic stellar populations. Miglio et al. (2009) presented a first comparison between observed and predicted seismic properties of giants in the first CoRoT field, which highlighted the expected signatures of red-clump stars in both distributions.

As described in Sect. 2, average seismic parameters may be combined with estimates of surface temperature to infer radii and masses for all stars with detected oscillations. A step forward in studies of stellar populations with seismic constraints was then taken when empirical and/or theoretical support for the seismically inferred masses and radii became available (Belkacem et al. 2011; White et al. 2011b; Miglio et al. 2012a; Miglio 2012; Miglio et al. 2013a; Belkacem et al. 2013).

First, it was soon realised that solar-like oscillating red giants may be used as accurate distance indicators probing regions out to about 10 kpc: as in the case of eclipsing binaries the distance to each red giant may be estimated from the absolute luminosity, which is obtained from the asteroseismically determined radius and $T_{\rm eff}$. Giants observed by CoRoT may be used as distance indicators, crucially mapping regions at different Galactocentric radii (Miglio et al. 2012b, 2013b).

Second, and foremost, seismically determined masses of RGB stars make it possible to estimate the ages of thousands field stars. The age of low-mass red-giant stars is largely determined by the time spent on the main sequence, hence by the initial mass of the red giant's progenitor ($\tau_{\rm MS} \propto M/L(M) \propto M_{\rm ini}^{-(\nu-1)}$ with $\nu = 3{-}5$, e.g. see Kippenhahn et al. 2012 and Fig. IV.2.8). Solar-like oscillating giants cover a mass range from $\simeq$0.9 to $\simeq$3 $M_\odot$, which

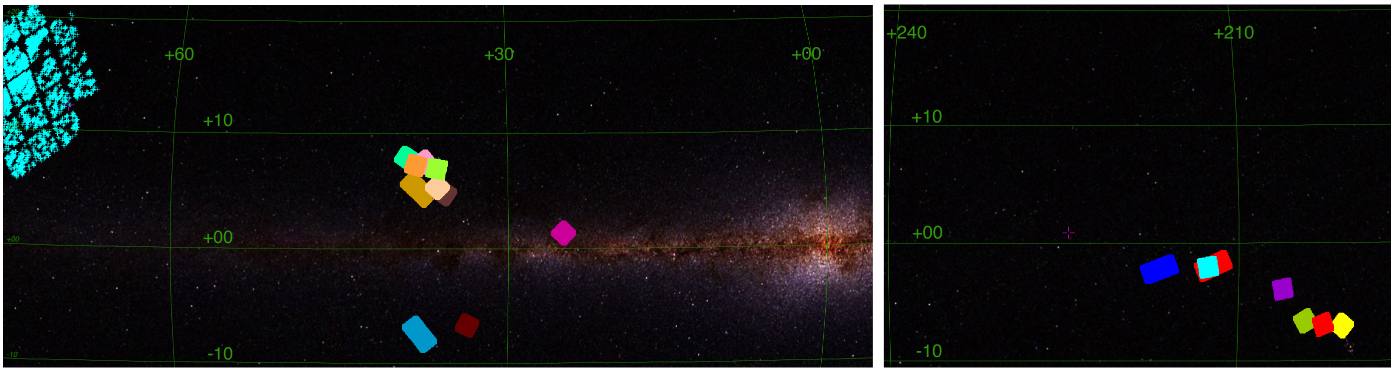

Fig. IV.2.9. Position in galactic coordinates of stars observed by CoRoT in the centre (*left panel*) and aniticentre (*right panel*) fields. The Kepler field of view is also shown in the top-left corner of the left panel. This figure was made using the Aladin Sky Atlas (Bonnarel et al. 2000), and the background image is based on the 2MASS catalogue (Skrutskie et al. 2006).

in turn maps to an age range spanning ≃0.3 to ≃12 Gyr, i.e., the entire Galactic history.

A first example of Galactic archeology utilising asteroseismic constraints is the differential population study presented in Miglio et al. (2013b). On the basis of comparisons with synthetic stellar populations, the authors interpreted the differences in the mass distributions as being due mainly to the different average heights of the observed fields below the galactic plane. Since it is believed that dynamical processes in the disc increase the velocity dispersion of stars with time, it follows that older stellar populations reach greater heights above and below the plane. Other data had already hinted at a similar dependence, as for instance an increase of the velocity dispersion of stars with increasing age (Holmberg et al. 2009), or the correlation between scale height and [O/Fe] (Bovy et al. 2012), but they were only available for stars in the immediate solar vicinity.

While these first results demonstrated the potential of solar-like oscillating K giants as probes of the Milky Way's structure and evolution, significant steps forward are now being taken and this approach is being significantly refined and extended. Spectroscopic constraints have now become available for and are adding crucial constraints on age-velocity and age-metallicity relations as well (see Sect. 3.2). Moreover, it is now possible to extend these studies to stars probing the Galaxy at different heights from the plane and at different Galactocentric radii by considering data collected by Kepler, K2 (Howell et al. 2014), and by harvesting data from the numerous fields that CoRoT has observed (see Fig. IV.2.9).

3.1. Data available

Only two CoRoT long-observational runs have been analysed so far (Hekker et al. 2009; Mosser et al. 2011a; Miglio et al. 2013b). Data collected in 15 additional runs, crucially exploring stellar populations at different galactocentric radii, are yet to be exploited. Figure IV.2.10 shows the number of stars targeted in CoRoT's observational campaigns in the colour-magnitude range expected to be populated by red giants with detectable oscillations. The analysis of these data is currently ongoing, and complement the observations by K2 (Howell et al. 2014), which will also map several regions of the Milky Way, although with data of shorter duration (∼80 d).

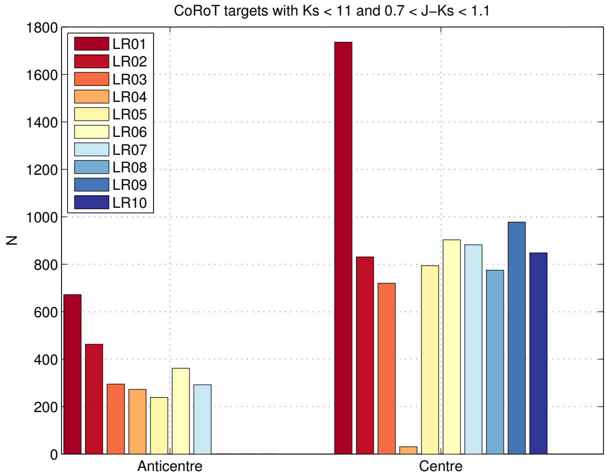

Fig. IV.2.10. Number of stars observed in CoRoT's exofields in the colour-magnitude range expected to be populated by red giants with detectable oscillations ($0.7 < J - K_s < 1.1, K_s < 11$). The analysis of the first two observational runs led to the detection of oscillations in about 1600 (LRc01) and 400 (LRa01) stars, as reported in Hekker et al. (2009) and Mosser et al. (2010). The varying number of stars per field reflects different target selection functions used, the failure of 2 CCD modules, as well as the different stellar density in each field.

Moreover, in the last few observing runs of CoRoT, thanks to the coordination between the asteroseismology and exoplanet thematic teams, it was possible to define a target selection function which can be easily taken into account when comparing with synthetic populations. As an example we report here the selection criteria adopted for LRc09. By comparison with expected populations (see Fig. IV.2.11) a colour cut $0.7 \leq J - K \leq 1.2$ was adopted to minimise contamination by red dwarfs. Such a target selection function will allow robust comparisons against synthetic populations, and is simpler to account for compared to that of the nominal Kepler mission (Farmer et al. 2013) and of the first CoRoT fields (Miglio et al. 2013a).

3.2. Synergies with spectroscopic surveys

Since the CoRoT asteroseismic data provide a very accurate ($\sigma_{\log g} \sim 0.05$ dex) way to determine surface gravities (e.g., see Bruntt et al. 2010; Morel & Miglio 2012; Creevey et al. 2013), they can also play an important rôle in helping to calibrate spectroscopic analyses. This prompted the establishment of formal collaborations between CoRoT and large spectroscopic surveys, such as APOGEE (Majewski et al. 2010), the Gaia ESO Public Spectroscopic Survey (Gilmore et al. 2012), and GALAH (De Silva et al. 2015).

On top of increasing the precision and accuracy of spectroscopic analyses (e.g. see Morel 2015), the combination of asteroseismic and spectroscopic observations opens the possibility to combine accurate ages of tens of thousands of stars with constraints on kinematics and on chemical abundances and build chemodynamical maps as a function of age in various regions of the Galaxy. This will be used to quantify, by comparison with predictions of chemodynamical models of the Galaxy, the relative importance of various processes which play a rôle in shaping the Milky Way, for example in-situ star formation, mergers, and dynamical processes such as diffusion and migration of stars (e.g. see Freeman & Bland-Hawthorn 2002; Chiappini et al. 2015).

Work has only recently started on combining spectroscopic and seismic constraints. A first surprising result from the CoRoT & APOGEE collaboration (CoRoGEE) was reported in Chiappini et al. (2015). The authors detected stars rich in alpha elements which appear to be massive, hence likely to be young stars. This finding has potentially ground-breaking implications on the widely accepted use of [α/Fe] as a proxy for age. Interestingly, the CoRoT data seem to suggest a higher fraction of these stars in the inner Galaxy, providing a clue to explain their origin. Stars with similar, unexpected, properties were also found among K giants observed by Kepler and APOGEE (Martig et al. 2015).

A first comprehensive work based on exploiting the combination of asteroseismic and spectroscopic constraints is presented in Anders (2016). This work made use of CoRoGEE stars in LRc01 and LRa01 and enabled, for the first time, studies of the [α/Fe]-[Fe/H]-age relation outside the Solar vicinity. Even with this first, small sample of stars, it was possible to place robust constraints on the chemical evolution of the Milky Way's stellar disc, finding, for instance, strong signatures of inside-out formation of the Galactic disc (Chiappini et al. 1997). Also, when comparing these findings to chemical-evolution models, some interesting discrepancies appeared, such as the existence of super-metal-rich stars, and the exact shape of the [α/Fe]-[Fe/H] distribution in the inner regions of the disc, suggesting that a significant fraction of stars now observed near the Solar neighbourhood might have migrated from inner regions.

3.3. The rôle of CoRoT

CoRoT has been the pioneer in providing data for studies of the Milky Way using asteroseismic constraints. It has also been instrumental in fostering direct collaborations and discussions between expert researchers in Galactic evolution, specialists in stellar structure, asteroseismology, stellar populations synthesis, and spectroscopists[4]. The discussions that stemmed from the interpretation of CoRoT data, were then expanded into strategies for the coordinated analyses of data from Kepler, and from future space missions. For instance, results from CoRoT provided compelling scientific motivation to include Galactic archeology as part of the programme of K2 (Howell et al. 2014), PLATO (Rauer et al. 2014), and TESS (Ricker et al. 2014) missions.

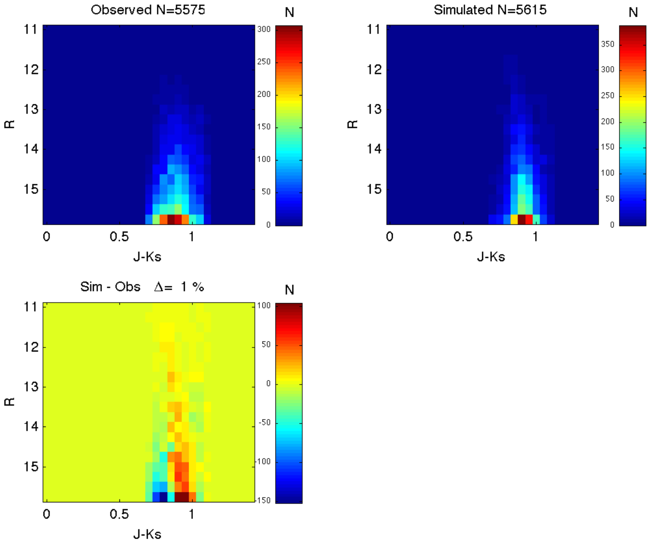

Fig. IV.2.11. Star counts in colour-magnitude bins for all stars in the FOV and in TRILEGAL (Girardi et al. 2005; Girardi et al. 2015) synthetic population, assuming reddening at infinity by Drimmel et al. (2003) only for stars selected by a colour–magnitude criterion, $0.7 \leq J-K \leq 1.2$, and here $R < 16$.

However, rather than relegating CoRoT to the role of pioneer, it is worth recalling that the exploitation of CoRoT data, in particular in combination with chemodynamical constraints, has only just started. The analysis of data in various observing fields (see Figs. IV.2.9 and IV.2.10) will generate ages and chemical abundance patterns of field stars over a large radial range of the Milky Way, adding strong observational evidence to address open questions concerning, e.g., the star formation history in the disc, star aggregates and streams, and quantify effects of radial migration and disc heating (Freeman 2012).

References

Anders, 2016, A&A, submitted

Appourchaux, T., & Grundahl, F. 2015, Asteroseismology observations and space missions, eds. V. C. H. Tong, & R. A. Garcia

Arentoft, T., Kjeldsen, H., Bedding, T. R., et al. 2008, ApJ, 687, 1180

Auvergne, M., Bodin, P., Boisnard, L., et al. 2009, A&A, 506, 411

Barban, C., De Ridder, J., Mazumdar, A., et al. 2004, in SOHO 14 Helio- and Asteroseismology: Towards a Golden Future, ed. D. Danesy, ESA SP, 559, 113

Barban, C., Matthews, J. M., De Ridder, J., et al. 2007, A&A, 468, 1033

Baudin, F., Barban, C., Belkacem, K., et al. 2011, A&A, 529, A84

Baudin, F., Barban, C., Goupil, M. J., et al. 2012, A&A, 538, A73

---

[4] see e.g. `http://www.asterostep.eu/`

Bedding, T. R., Kjeldsen, H., Campante, T. L., et al. 2010, ApJ, 713, 935

Belkacem, K., Goupil, M. J., Dupret, M. A., et al. 2011, A&A, 530, A142

Belkacem, K., Dupret, M. A., Baudin, F., et al. 2012, A&A, 540, L7

Belkacem, K., Samadi, R., Mosser, B., Goupil, M.-J., & Ludwig, H.-G. 2013, in ASP Conf. Ser. 479, eds. H. Shibahashi, & A. E. Lynas-Gray, 61

Belkacem, K., Marques, J. P., Goupil, M. J., et al. 2015a, A&A, 579, A31

Belkacem, K., Marques, J. P., Goupil, M. J., et al. 2015b, A&A, 579, A30

Bonnarel, F., Fernique, P., Bienaymé, O., et al. 2000, A&AS, 143, 33

Bovy, J., Rix, H.-W., Hogg, D. W., et al. 2012, ApJ, 755, 115

Brown, T. M., Gilliland, R. L., Noyes, R. W., & Ramsey, L. W. 1991, ApJ, 368, 599

Bruntt, H., Bedding, T. R., Quirion, P.-O., et al. 2010, MNRAS, 405, 1907

Carrier, F., De Ridder, J., Baudin, F., et al. 2010, A&A, 509, A73

Chiappini, C., Matteucci, F., & Gratton, R. 1997, ApJ, 477, 765

Chiappini, C., Anders, F., Rodrigues, T. S., et al. 2015, A&A, 576, L12

Corsaro, E., Stello, D., Huber, D., et al. 2012, ApJ, 757, 190

Creevey, O. L., Thévenin, F., Basu, S., et al. 2013, MNRAS, 431, 2419

Davies, G. R., & Miglio, A. 2016, Astron. Nachr., in press

De Ridder, J., Barban, C., Carrier, F., et al. 2006, A&A, 448, 689

De Ridder, J., Barban, C., Baudin, F., et al. 2009, Nature, 459, 398

De Silva, G. M., Freeman, K. C., Bland-Hawthorn, J., et al. 2015, MNRAS, 449, 2604

Deheuvels, S., Doğan, G., Goupil, M. J., et al. 2014, A&A, 564, A27

Drimmel, R., Cabrera-Lavers, A., & López-Corredoira, M. 2003, A&A, 409, 205

Dupret, M.-A., Belkacem, K., Samadi, R., et al. 2009, A&A, 506, 57

Dziembowski, W. A., Gough, D. O., Houdek, G., & Sienkiewicz, R. 2001, MNRAS, 328, 601

Eddington, A. S. 1917, The Observatory, 40, 290

Epstein, C. R., Elsworth, Y. P., Johnson, J. A., et al. 2014, ApJ, 785, L28

Farmer, R., Kolb, U., & Norton, A. J. 2013, MNRAS, 433, 1133

Frandsen, S., Carrier, F., Aerts, C., et al. 2002, A&A, 394, L5

Freeman, K. 2012, in Red Giants as Probes of the Structure and Evolution of the Milky Way, eds. A. Miglio, J. Montalbán, & A. Noels, ApSS Proceedings

Freeman, K., & Bland-Hawthorn, J. 2002, ARA&A, 40, 487

Gilliland, R. L., Brown, T. M., Kjeldsen, H., et al. 1993, AJ, 106, 2441

Gilmore, G., Randich, S., Asplund, M., et al. 2012, The Messenger, 147, 25

Girardi, L. 1999, MNRAS, 308, 818

Girardi, L., Groenewegen, M. A. T., Hatziminaoglou, E., & da Costa, L. 2005, A&A, 436, 895

Girardi, L., Barbieri, M., Miglio, A., et al. 2015, Astrophys. Space Sci. Proc., 39, 125

Grosjean, M., Dupret, M.-A., Belkacem, K., et al. 2014, A&A, 572, A11

Hekker, S., Aerts, C., De Ridder, J., & Carrier, F. 2006, A&A, 458, 931

Hekker, S., Kallinger, T., Baudin, F., et al. 2009, A&A, 506, 465

Holmberg, J., Nordström, B., & Andersen, J. 2009, A&A, 501, 941

Howell, S. B., Sobeck, C., Haas, M., et al. 2014, PASP, 126, 398

Kallinger, T., Zwintz, K., Pamyatnykh, A. A., Guenther, D. B., & Weiss, W. W. 2005, A&A, 433, 267

Kallinger, T., Guenther, D. B., Matthews, J. M., et al. 2008a, A&A, 478, 497

Kallinger, T., Guenther, D. B., Weiss, W. W., et al. 2008b, Communications in Asteroseismology, 153, 84

Kallinger, T., Weiss, W. W., Barban, C., et al. 2010, A&A, 509, A77

Kallinger, T., Matthews, J. M., Guenther, D. B., et al. 2012, in Progress in Solar/Stellar Physics with Helio- and Asteroseismology, eds. H. Shibahashi, M. Takata, & A. E. Lynas-Gray, ASP Conf. Ser., 462, 156

Kim, K. M., Mkrtichian, D. E., Lee, B.-C., Han, I., & Hatzes, A. P. 2006, A&A, 454, 839

Kippenhahn, R., & Weigert, A. 1990, Stellar Structure and Evolution

Kippenhahn, R., Weigert, A., & Weiss, A. 2012, Stellar Structure and Evolution

Kjeldsen, H., & Bedding, T. R. 1995, A&A, 293, 87

Lagarde, N., Miglio, A., Eggenberger, P., et al. 2015, ArXiv e-prints

Lebreton, Y., & Goupil, M. J. 2014, A&A, 569, A21

Majewski, S. R., Wilson, J. C., Hearty, F., Schiavon, R. R., & Skrutskie, M. F. 2010, in IAU Symp. 265, eds. K. Cunha, M. Spite, & B. Barbuy, 480

Martig, M., Rix, H.-W., Aguirre, V. S., et al. 2015, MNRAS, 451, 2230

Mathur, S., Hekker, S., Trampedach, R., et al. 2011, ApJ, 741, 119

Mazumdar, A., Mérand, A., Demarque, P., et al. 2009, A&A, 503, 521

Miglio, A. 2012, Asteroseismology of Red Giants as a Tool for Studying Stellar Populations: First Steps, eds. A. Miglio, J. Montalbán, & A. Noels, 11

Miglio, A., Montalbán, J., Baudin, F., et al. 2009, A&A, 503, L21

Miglio, A., Montalbán, J., Carrier, F., et al. 2010, A&A, 520, L6

Miglio, A., Brogaard, K., Stello, D., et al. 2012a, MNRAS, 419, 2077

Miglio, A., Morel, T., Barbieri, M., et al. 2012b, in Eur. Phys. J. Web Conf., 19, 5012

Miglio, A., Chiappini, C., Morel, T., et al. 2013a, in Eur. Phys. J. Web Conf., 43, 3004

Miglio, A., Chiappini, C., Morel, T., et al. 2013b, MNRAS, 429, 423

Montalbán, J., Miglio, A., Noels, A., et al. 2013, ApJ, 766, 118

Morel, T. 2015, Astrophys. Space Sci. Proc., 39, 73

Morel, T., & Miglio, A. 2012, MNRAS, 419, L34
Mosser, B., & Appourchaux, T. 2009, A&A, 508, 877
Mosser, B., Belkacem, K., Goupil, M., et al. 2010, A&A, 517, A22
Mosser, B., Barban, C., Montalbán, J., et al. 2011a, A&A, 532, A86
Mosser, B., Belkacem, K., Goupil, M., et al. 2011b, A&A, 525, L9
Mosser, B., Elsworth, Y., Hekker, S., et al. 2012a, A&A, 537, A30
Mosser, B., Goupil, M. J., Belkacem, K., et al. 2012b, A&A, 548, A10
Mosser, B., Goupil, M. J., Belkacem, K., et al. 2012c, A&A, 540, A143
Mosser, B., Dziembowski, W. A., Belkacem, K., et al. 2013a, A&A, 559, A137
Mosser, B., Michel, E., Belkacem, K., et al. 2013b, A&A, 550, A126
Mosser, B., Samadi, R., & Belkacem, K. 2013c, in SF2A-2013: Proceedings of the Annual meeting of the French Society of Astronomy and Astrophysics, eds. L. Cambresy, F. Martins, E. Nuss, & A. Palacios, 25
Mosser, B., Benomar, O., Belkacem, K., et al. 2014, A&A, 572, L5
Pinsonneault, M. H., Elsworth, Y., Epstein, C., et al. 2014, ApJS, 215, 19
Rauer, H., Catala, C., Aerts, C., et al. 2014, Exper. Astron., 38, 249
Retter, A., Bedding, T. R., Buzasi, D. L., Kjeldsen, H., & Kiss, L. L. 2003, ApJ, 591, L151
Ricker, G. R., Winn, J. N., Vanderspek, R., et al. 2014, in SPIE Conf. Ser., 9143, 20
Samadi, R., Georgobiani, D., Trampedach, R., et al. 2007, A&A, 463, 297
Samadi, R., Belkacem, K., Ludwig, H.-G., et al. 2013, A&A, 559, A40
Samadi, R., Belkacem, K., & Sonoi, T. 2015, ArXiv e-prints
Skrutskie, M. F., Cutri, R. M., Stiening, R., et al. 2006, AJ, 131, 1163
Soderblom, D. R. 2010, ARA&A, 48, 581
Sonoi, T., Samadi, R., Belkacem, K., et al. 2015, A&A, 583, A112
Stello, D., Kjeldsen, H., Bedding, T. R., & Buzasi, D. 2006, A&A, 448, 709
Stello, D., Bruntt, H., Kjeldsen, H., et al. 2007, MNRAS, 377, 584
Stello, D., Bruntt, H., Preston, H., & Buzasi, D. 2008, ApJ, 674, L53
Stello, D., Chaplin, W. J., Basu, S., Elsworth, Y., & Bedding, T. R. 2009, MNRAS, 400, L80
Tarrant, N. J., Chaplin, W. J., Elsworth, Y., Spreckley, S. A., & Stevens, I. R. 2007, MNRAS, 382, L48
Tassoul, M. 1980, ApJS, 43, 469
Tong, V., & Garcia, R. 2015, Extraterrestrial Seismology, eds. V. C. H. Tong, & R. A. Garcia
Ulrich, R. K. 1986, ApJ, 306, L37
Verner, G. A., Elsworth, Y., Chaplin, W. J., et al. 2011, MNRAS, 415, 3539
Vrard, M., Mosser, B., Barban, C., et al. 2015, A&A, 579, A84
White, T. R., Bedding, T. R., Stello, D., et al. 2011a, ApJ, 742, L3
White, T. R., Bedding, T. R., Stello, D., et al. 2011b, ApJ, 743, 161

Acknowledgements: The CoRoT space mission has been developed and operated by CNES, with the contribution of Austria, Belgium, Brazil, ESA, Germany, and Spain.

The CoRoT Legacy Book
© The authors, 2016
DOI: 10.1051/978-2-7598-1876-1.c043

IV.3

The wealth of stellar variability

Stellar rotation and activity, Binaries and Stars with disks

F. Baudin[1], C. Maceroni[2], and S. H. P. Alencar[3]

[1] Institut d'Astrophysique Spatiale, UMR8617, CNRS, Université Paris XI, Bâtiment 121, 91405 Orsay Cedex, France
[2] INAF-Osservatorio Astronomico di Roma, via di Frascati 33, 00040 Monteporzio Catone, Italy
[3] Departamento de Física – ICEx – Universidade Federal de Minas Gerais Av. Antônio Carlos, 6627 – 31270-901 Belo Horizonte, MG – Brasil

1. Introduction

CoRoT made a decisive step forward not only in stellar seismology and galactic populations studies but also in a number of other physical phenomena encompassed by stellar variability. Surface activity is one example and is the outward sign of surface rotation and magnetic activity as described in Sect. 2. In this domain, CoRoT observations motivated the investigation of the surface rotational behavior of stars along with their evolution (Sect. 2.1), the highlighting of spot evolution and magnetic cycles (Sect. 2.2), as well as the study of surface convection across the Hertzsprung–Russell diagram (Sect. 2.3). CoRoT's dataset then opened the way to a multivariate-like approach in which rotation, convection, and magnetic field are investigated together as key ingredients of stellar dynamos. Moreover, it is worth mentioning that such studies were previously restricted to the Sun but, with the advent of ultra-precise and long-duration photometry, we are beginning to address similar issues in other stars.

CoRoT also led to important advances in the field of binary stars as described in Sect. 3. Indeed, a few targets in the bright fields were dedicated to the observation of known binaries but it appears that a large number of binaries have been discovered in the faint fields. As for red giants, this led to a number of discoveries and surprises. For instance, it allowed for statistical investigations (Sect. 3.1) as well as the discovery of new type of binary stars (Sect. 3.2). In that respect, CoRoT's main contributions relied on the precision and the duration of the observations which made it possible to follow the evolution of several binary systems and to unravel physical processes occuring on different time-scales. Finally, CoRoT's observations demonstrated the fruitful synergy between binarity and asteroseismology as a tool for determining independently the stellar parameters of each component (Sect. 3.3).

Last but not least, a rich harvest of observational constraints has been obtained on young stars as described in Sect. 4. This allowed a further step in our knowledge of star-disk interactions which is crucial for the scenarios of star formation but also for our understanding of the initial steps of stellar evolution. A striking example is the coordinated synoptic investigation of NGC 2264 (Sect. 4.2), which consisted in a multiwavelenght observational campaign including space-borne and ground-based facilities. Due to its intrinsic abilities, CoRoT contributed significantly by providing 40 days of continuous observations. This campaign made it possible to investigate several young stars and their environement by providing a wealth of data which led to a harvest of scientific results.

2. Stellar rotation and activity (by F. Baudin)

The two main objectives of the CoRoT mission (namely search for exoplanets and stellar seismology) were based on a sole capacity: ultra precise photometry. This capacity allows many more scientific objectives to be aimed at, concerning the physics responsible for the micro-variability of stars, beyond that caused by oscillations. Manifestations of magnetic fields and signature of granulation are among the main sources of this micro-variability (binaries or stellar disks for example are others, see Sects. 3 and 4).

2.1. Thousands of star's rotation periods measured

Stars show very different behaviors concerning their rotation. Some rotate faster than others, some show differential rotation (in surface or in their interior - but here, we will focus on surface rotation). These behaviors are related to the structure and evolution of the stars and are also a fondamental ingredient of stellar magnetism (with a direct application to gyrochronology). Rotation is driven by several mechanisms, mainly star contraction and expansion during its evolution, but also its interaction with its disk in its early phases of evolution. CoRoT data, thanks to their ultra-high photometric precision for a very large sample of stars, are perfectly suited to tackle the questions related to these physical mechanisms.

Among works aiming at rotation measurements based on CoRoT data, Affer et al. (2012) used some of the first observation runs, LRc01 and LRa01, thus covering field stars in the center and anti-center directions. An initial sample of 8341 light curves was used to measure rotation periods by two methods: the Lomb-Scargle Normalized periodogram and an auto-correlation analysis. About 2000 light curves had to be rejected because of the discontinuities caused by particle impacts on the detector[1]. Finally, after checking for coherence between the two analysis methods and some other rejections (due for example to eclipsing binaries or pulsators), a total of 1727 periods of rotations were reliably measured, including F, G and K stars (however, only 4 F stars were identified in the center direction preventing any interpretation). Resulting distributions show bimodal shapes (Fig. IV.3.1). A first peak, with periods from 5 to 15 days is interpreted as representing a population of young stars, while a second peak, including periods from 15 to 35 days is interpreted as due to an older population. Using gyrochronology expressing the rotation period as a function of age and $B-V$, Affer et al. (2012) have found that more than 500 stars of their sample are younger than the Hyades (~650 Myr). The observed sample is consistent with results from X-ray surveys supporting the presence of an excess of young stars in the solar neighborhood. However, as pointed out by the authors, it should not be forgotten that the CoRoT sample is biased towards dwarfs because of the exoplanet search objective that drove the target selection.

An even larger analysis was performed by De Medeiros et al. (2013) who started from all light curves available at that time (a total of 124 471). The analysis was based on a semi-automated process and a severe selection of light curves in order to ensure the reliability of the results. Among other criteria, this selection process rejected low signal-to-noise ratios and tested against signals that could mimic that of rotation modulation, such as semi-regular pulsators'. Attention was also paid to the influence of discontinuities in the data[1]. This process resulted in the measurement of 4206 rotation periods, across the H-R diagram (Fig. IV.3.3). 216 targets were common with Affer et al. (2012) and the results show an excellent agreement with them. Results (Fig. IV.3.4) show an increase of rotation periods with the color difference $J-H$ (which increases with increasing effective temperature - for main sequence stars and unreddened measurements). This increase can be at least partially explained by evolution since higher values of $J-H$ correspond to a bias towards evolved –thus rotating slower– stars, as seen in Fig. IV.3.3 . An excess of long periods is noted in the galactic center, due to an excess of giants, whereas in the total sample, only one star is similar to the Sun in terms of rotation period and $J-H$ value.

As mentioned by several authors, rotation measurements are obviously biased towards young stars since they are more active and thus showing clearer photometric

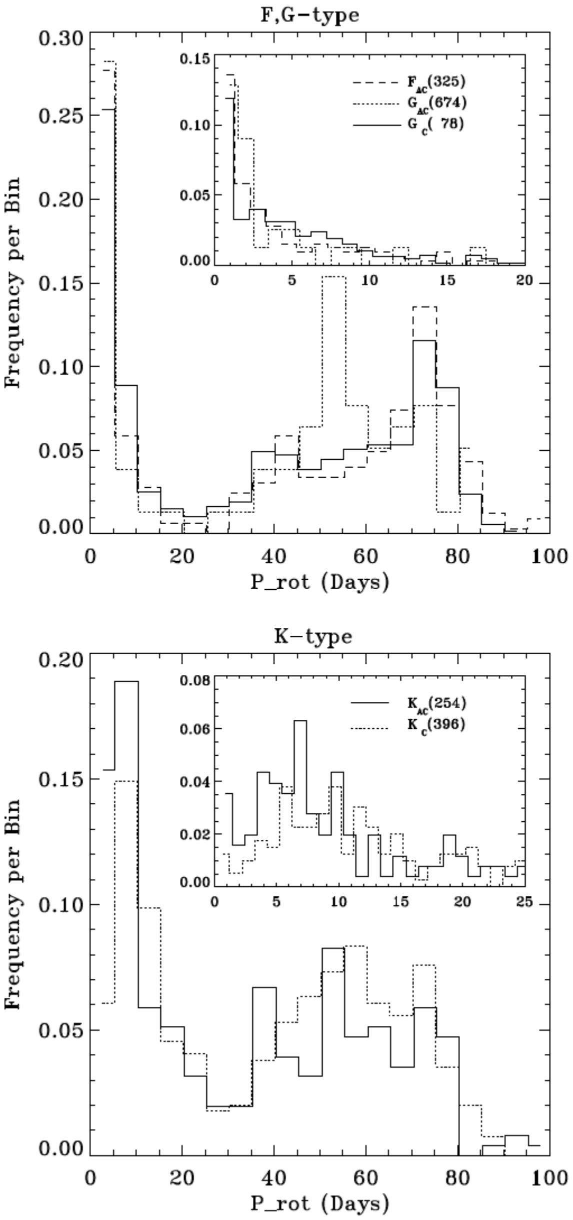

Fig. IV.3.1. Figure 10 of showing the bi-modal distribution of the rotation periods of the field stars they studied © MNRAS, 424, 11.

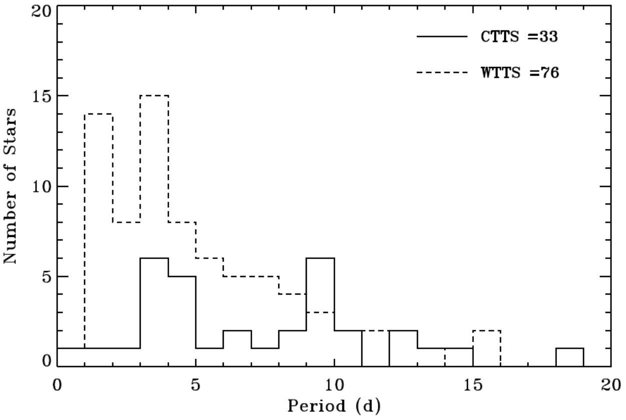

Fig. IV.3.2. Figure 5 of showing the distribution of the rotation periods of the CTTS and WTTS stars they studied © MNRAS, 430, 1433.

---

[1] Early versions of data were used for this work but most of these discontinuities are now corrected in the final version.

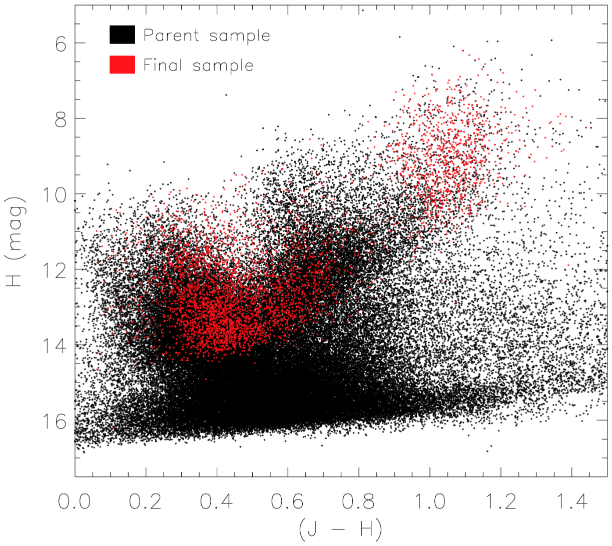

Fig. IV.3.3. Figure 9 of De Medeiros et al. (2013), showing the total number of targets considered at the start (in black) and the remaining ones at the end of the process (see text) © A&A.

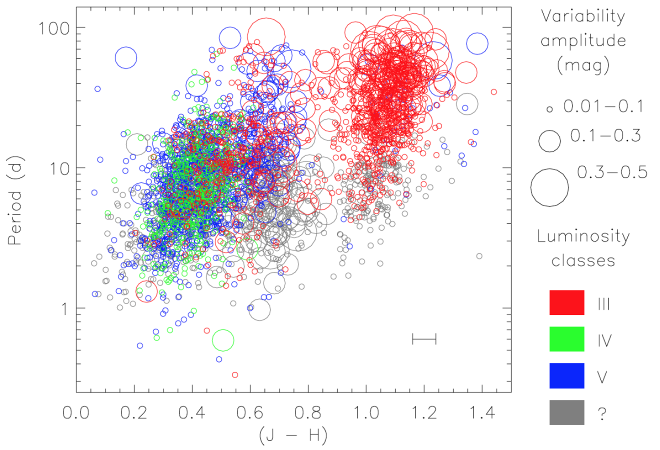

Fig. IV.3.4. Figure 13 of De Medeiros et al. (2013), showing the rotation periods measured versus the color index $J-H$. Symbol size relates to variability amplitude and color to luminosity class. The increase seen is compatible with stellar evolution © A&A.

modulation due to rotation. Stars similar to the Sun in terms of mass and age, with periods around solar values are thus rare. One case was found by do Nascimento et al. (2013) after a detailed analysis of CoRoT targets (using spectroscopic results from Sarro et al. 2013): CoRoT-102684698 which has a similar mass and also similar Lithium abundance, and a period $P_{\rm rot} = 29 \pm 5$ days.

However, any conclusion about stars sharing solar characteristics is made very difficult due to their very small number. In order to estimate if the Sun's rotation is anomalous or not, Leão et al. (2015) deepen the work of De Medeiros et al. (2013) by selecting a subsample from their catalog (plus other samples from *Kepler* catalogs), gathering solar type stars and comparing them to synthetic samples built in order to take into account the low number of solar rotators. Leão et al. (2015) propose that their subsample of 173 stars with $T_{\rm eff}$ and $\log(g)$ close to solar values is made of two populations, one of young stars, more numerous than the other group made of older stars. From global results based on CoRoT and *Kepler* data, they do not evidence an anomalous rotation period for the Sun.

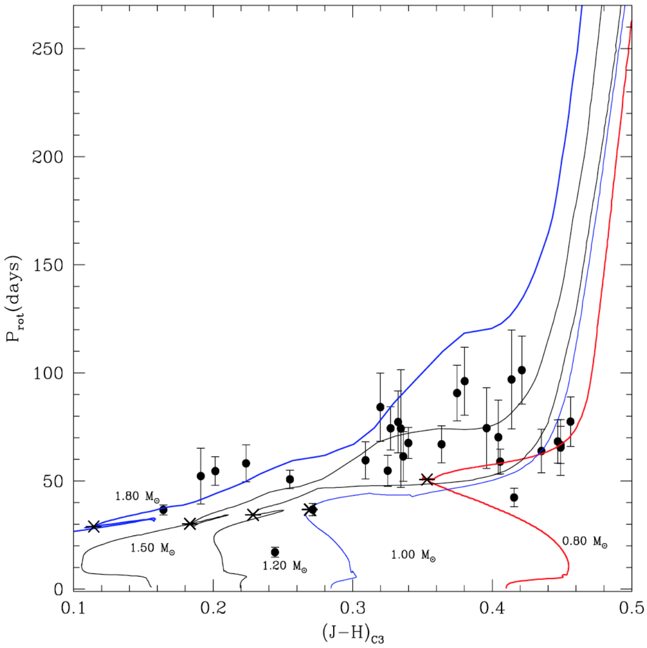

Fig. IV.3.5. Figure 3 of do Nascimento et al. (2012), showing the periods measured (black filled circles) and evolution tracks versus the color difference. $(J-H)_{C_3}$ relates to a combination of colors minimizing the effect of reddening. Asterisks locate the beginning of the sub giant branch © A&A.

More focused rotation period measurements were also performed. Affer et al. (2013) applied the same method than Affer et al. (2012) to T Tauri stars observed in NGC2264, a young cluster (3 Myr) in the solar vicinity (760 pc) observed for ~23 days during run SRc01. Two well separated sub-categories of stars were selected: the Weakly T Tauri Stars (WTTS, for which variaability is induced by spots) and Classical T Tauri Stars (CTTS, for which variability is due to the presence of a disk). Rotation was measured for 76 WTTS and 33 CTTS. Despite the small size of the samples, a clear difference is seen (Fig. IV.3.2): CTTS are slower rotators (with a mean rotation period $\langle P_{\rm rot}\rangle = 7.0$ days) than WTTS ($\langle P_{\rm rot}\rangle = 4.2$ days). This is interpreted as the result of the presence of an inner disk for CTTS, slowed down by disk locking due to strong magnetic fields. This in turn can help in constraining the interactions between the star and its disk that will drive the rotation history of a young star.

Another focused work is the one of do Nascimento et al. (2012) who measured the rotation periods of subgiants, analyzing only long duration light curves (150 days). This allowed the measurement of slow rotators, with $P_{\rm rot}$ between 30 and 100 days. These periods are in good agreement with the modeling of stellar evolution including rotation of the Fig. IV.3.5, validating the description of late rotation evolution for stars of the masses considered here.

2.2. Stellar magnetic activity measured down to the spot level

Since one of the main scientific objective of CoRoT is the detection of transiting planets in front of their parent star,

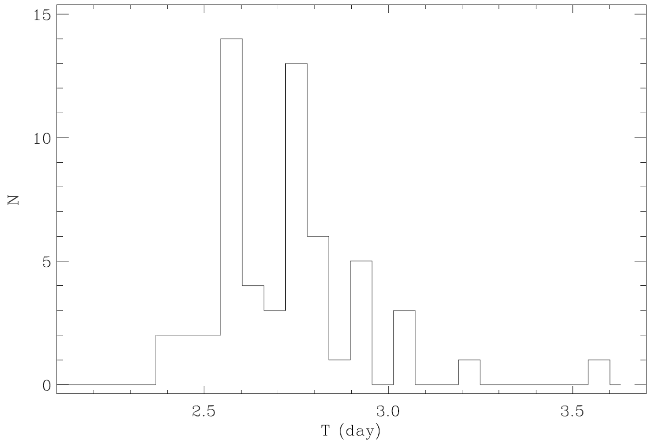

Fig. IV.3.6. Figure 6 of Mosser et al. (2009a), showing the distribution of rotation periods of individual spots. Their distribution is consistent with the wide rotation peak observed in the Fourier spectra of the light curve © A&A.

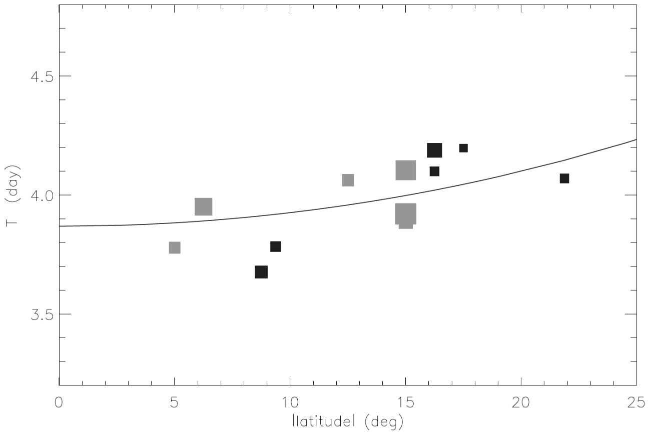

Fig. IV.3.7. Figure 8 of Mosser et al. (2009a), showing the rotation period of individual spots increasing with their latitude, as a signature of differential rotation © A&A.

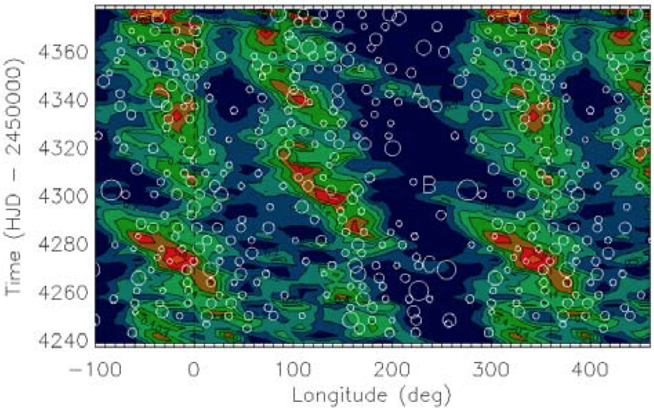

Fig. IV.3.8. Figure 4 of Lanza et al. (2009b), showing (in red and green) the fitted spotted area of CoRoT-2a. The inclined ridges are the signature of the differential rotation. Results of Silva-Valio & Lanza (2011) are superimposed as white circles that represent the spots derived from their independent analysis using the transits of the planet (see text) © A&A.

its ultra-high photometric precision allows also the detection of transiting inhomogeneities on stellar surfaces. The most visible are magnetic spots, like sunspots which signature is visible in disk-integrated solar light curves. The clear signature of starspots in some CoRoT light curves allows the modeling of the observed intensity variation by assuming simple models of starspots. An extreme example is HD175726, showing intensity peak-to-peak variations up to 1% (Mosser et al. 2009b).The difficulty lies in the degeneracy of the problem since many parameters are necessary to describe the signature of a transiting starspot: its size and intensity contrast (obviously correlated), its intrinsic temporal behavior (which is modulated by the rotation period) but also its position on the star (linked to the inclination angle of the star). Several methods were applied to achieve such a modeling. For example, Mosser et al. (2009a) modeled 4 light curves which, except for HD175726, shows intensity variations of the order of 2–3 mmag, comparable to an active Sun. All are relatively rapid rotators ($2.7\,\mathrm{d} \leq P_{\mathrm{rot}} \leq 3.9\,\mathrm{d}$). The high degeneracy of the problem was overcome by imposing a small number (2–3) of starspots per rotation. The methods was tested with simulated light curves that showed the reliability of the results in terms of rotation period and differential rotation for mid-inclined stars (with a risk of under-estimation). Pole-on and edge-on stars appear to be the most difficult cases. However, the method showed its reliability by applying it to sub-series of long time series of the same star and leading to similar results. For example, differential rotation is observed in 3 out of the 4 modeled stars (Figs. IV.3.6 and IV.3.7).

Other attempts to model the light curves of stars in order to extract an information on the presence of starspots were achieved by Lanza et al. (2009b,a, 2010, 2011). These works focus on stars hosting planets: respectively CoRoT-2a, -4a, and -6a. They rely on another method for the light curve modeling, based on the division the star's surface in small elements, each associated to a parameter accounting for the presence of spot or faculae (or no magnetic signature at all). The parameters for each element are fitted in order to reproduce the observed integrated light curve. The application of this method to stars hosting transiting planets allows the inclination angle of the star to be fixed. A striking results of these works is that, as in 3 stars out of 4 in Mosser et al. (2009a), differential rotation was detected in the 3 planet hosting stars. The measured amplitude of this differential rotation varies from one star to another, from very few percent up to more than 10%. A signature of this differential rotation is visible in the map of the fitted spotted area (Fig. IV.3.8) of CoRoT-2a's star, a young Sun ∼0.5 Gyr old that has been observed for 142 days while the measured rotation period of the star is 4.5 days. The flux modulation of this star is 20 times larger than that of the Sun at maximum of activity. The star hosting CoRoT-2a presents another striking result: the modulation of the measured spotted area with time, which shows an apparent short-term periodicity (Fig. IV.3.9) with a period of $\sim(28.9 \pm 4.8)$ days. This could be the signature of a star-planet interaction[2] as proposed by Lanza (2008) since its period approaches 10 times the synodic period of the planet. This cyclicity could also be compared to the so-called Rieger cycle observed in the Sun (Rieger et al. 1984) which corresponds to a short-term periodicity (154 days) in the occurrence of solar flares, and also in the spotted area (Oliver et al. 1998). A proposed interpretation for this

---

[2] For more findings about star-planet relations, see Sect. III.9.1

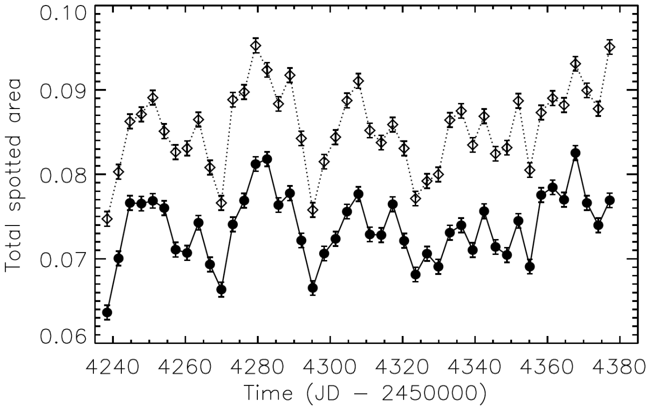

Fig. IV.3.9. Figure 6 of Lanza et al. (2009b), showing the fitted total spot area (for two models) along time. For both models, a clear periodicity is visible © A&A.

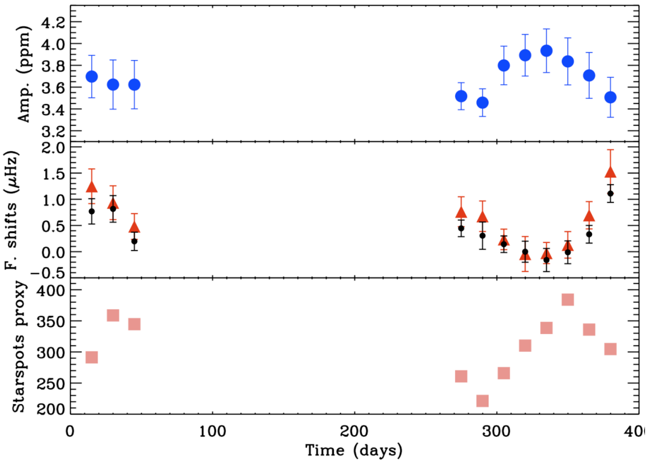

Fig. IV.3.10. Fig. 1 of showing how mode frequencies and amplitudes evolve in an anti-correlated manner for the two first observations of HD49933 by CoRoT. The activity also shows a correlated behavior with a ∼30-day lag © Science, 329, 1032.

oscillation is the propagation of Rossby-type waves in the sub-photospheric layers (Lou 2000).

This star presents also a common feature with the star hosting CoRoT-6a: the presence of active longitudes are observed in the fitted spot map. In CoRoT-2a, two active longitudes are found, 180° apart, with one of them affected by a retrograde migration. In the case of CoRoT-2a, an independent analysis of Huber et al. (2010) as well as another of Silva-Valio & Lanza (2011) (see below) confirmed the presence of these active longitudes. The active longitude detected in the case of CoRoT-6a (an F9 star with a rotation period of ∼6.3 days, observed for 145 days) is even more interesting since it appears to remain at a somewhat constant distance in longitude to the sub-planetary point (with however an important gap: ∼200°). A related observation is made in CoRoT-4a host star: the spotted area, if not showing an active longitude, shows nevertheless its maximum at a constant longitude with respect to the sub-planetary point. However, some caution is necessary since this star was observed for only 58 days.

As stated above, light curve modeling with the aim of mapping spots (or other heterogeneities) is a highly degenerated problem. There is however a case particularly favorable to this modeling: when a planet transits a spotted stellar photosphere, the details of the light curve during transits is rich in information about the occulted spots. This approach has been developed by Silva-Valio et al. (2010), Silva-Valio & Lanza (2011) in the case of CoRoT-2a. With the hypothesis of a planet orbiting in the equatorial plane, the latitude of the spots can be fixed. The little variations in the light curve during the transit (see Fig. IV.3.11) can be fitted with three parameters: the longitude of the spot, its size (its radius when it is supposed circular) and its intensity. The details of the light curve bring additional information for the determination of the radius, limiting the degeneracy with the intensity of the spot. A first analysis (Silva-Valio et al. 2010) was based on 7 to 9 spots per transit modeling. A second analysis (Silva-Valio & Lanza 2011) used a smaller number (5 spots in average), consequently increasing the average size of the spots from 0.46 R_p to 0.53 R_p (R_p being the radius of the planet). In both cases, it makes the average size of the spots of the order of 100 000 km, several times larger than the largest sunspots. In average, 16.5% of the star surface are covered by spots, confirming that CoRoT-2a star is much more active than the Sun. The re-analysis of Silva-Valio & Lanza (2011) is particularly interesting since the results of Lanza et al. (2009b) for the same star showed the existence of active longitudes. The results of Silva-Valio & Lanza (2011) are superimposed to those of Lanza et al. (2009b) in Fig. IV.3.8 and show an excellent agreement about the spot distribution as obtained by the two different methods, confirming the existence of the active longitudes.

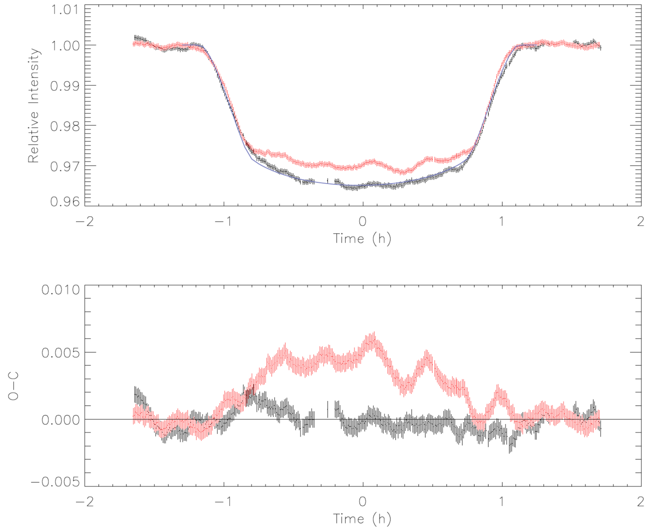

Fig. IV.3.11. Fig. 2 of Silva-Valio et al. (2010), showing the details of a planet transit (CoRoT-2a) during which the signature of occulted spots become visible (red curve) compared to a transit with almost no spot occulted (black curve) © A&A.

The link between the manifestation of magnetism in surface and the interior of the Sun, evidenced by the frequency shift of acoustic oscillations is well known. The Sun was the only star in which such a link had been observed. One more time, the CoRoT ultra-high precision photometry allowed similar observations in another star, HD49933, in which oscillation frequency shifts were related to surface activity (García et al. 2010). The oscillations of this star behave like those of the Sun: mode frequencies increase when their amplitudes decrease, in correlation with the observed magnetic activity (see Fig. IV.3.10). Frequency shifts and amplitude variations were measured globally for HD49933 from the two first CoRoT time series of this star (of 60 and 137 days, spanning more than 400 days in total), while the activity was measured through a proxy made from the variance of the intensity variations. This star, rotating much faster than the Sun ($P \sim 3.4$ days), seems to present a much shorter activity cycle, rising in approximately 60 days during the second time series used. As in the solar case, frequencies increase when the activity increases but a time lag of ∼30 days is observed in the case of HD49933. The same authors (Salabert et al. 2011) confirmed their findings by studying the frequency shifts versus frequency for two periods of 90 and 47 days corresponding to a quiet and an active regime respectively. They found a behavior quite similar to that of the Sun, with the frequency shifts reaching their maximum of 2 μHz at 2100 μHz (for HD49933, $\nu_{\max} \sim 1800$ μHz), followed by a downturn at 2300 μHz (and an upturn at higher frequency).

Mathur et al. (2013) looked for the same correlated behavior between modes properties and magnetic activity for three other stars observed by CoRoT (HD49385, HD52265 and HD181420) but did not reach significant results despite using complementary spectroscopic observations (Ca H profiles).

2.3. Another source of micro-variability seen by CoRoT: surface convection

Signatures of magnetic features are not the only ones originating from the photosphere or above and seen in light curves. An important physical process contributes too: the surface convection. The granules induced by this convection have a characteristic time close to the acoustic oscillation periods and thus exhibit power in the Fourier spectra in the form of a continuous background on the top of which the oscillation modes appear as narrow peaks. This background is often modeled as a more or less modified Lorentzian profile $P(\nu)$ centered on the zero frequency, following the initial idea of Harvey (1985) based on the description of a noise process with memory:

$$P(\nu) = \frac{4\sigma^2\tau}{1 + (2\pi\nu\tau)^\alpha}, \tag{1}$$

where σ and τ characterize the height and width of the profile. Harvey (1985) uses $\alpha = 2$ but other authors (*e.g.* Aigrain et al. 2004; Michel et al. 2009) use other values. Ludwig et al. (2009) compared spectra from 3D hydrodynamical simulations to spectra from F stars observed by CoRoT (mainly HD49933, but also HD181420 and HD181906). While the simulated spectra (derived from a solar model) are in agreement with observations of the Sun, some non negligible discrepancies appear between simulated spectra for HD49933 and the observed one. Even if these hydrodynamical models are sensitive to the global characteristics of the star (such as $\log(g)$ or $T_{\rm eff}$), the spectra of HD181420 and HD181906 (which have similar stellar characteristics) are very similar to that of HD49933, suggesting a lack in the hydrodynamical description. Samadi et al. (2013) compared characteristics of the granulation spectra (σ and τ) from grid of models to observed ones (from Kepler) and noted that the largest discrepancies occur for F stars. They suggest that the source of the discrepancies could be the photospheric magnetic field of these stars, following the results of Chaplin et al. (2011) who noted that acoustic oscillations in F stars were the most sensitive to damping by magnetic field. Since oscillation are excited by surface convection, it strongly suggests that a proper description of the effect of magnetic field on convection in the hydrodynamical models is necessary.

3. Binaries (by C. Maceroni)

CoRoT lead to a revolution also in the field of binary stars. The two main assets of the mission, high accuracy and long term monitoring, provided extraordinary data for binary star studies, allowing the detection of effects immeasurable before. Besides, CoRoT made possible a fruitful synergy between asteroseismology and binarity, two independent and complementary sources of information on stellar properties.

Among the bright field targets there were a few known bright eclipsing binaries (EBs), but others were added to this list when their unknown binary nature was revealed by the observations (e.g. HD 174884, see below). In the faint fields EBs resulted to be, as expected, the majority of regular variables.

3.1. Statistical properties of the eclipsing binaries in the faint fields

A complete list of CoRoT eclipsing binaries from the exoplanet fields is in preparation and will be available in Exodat (`http://cesam.oamp.fr/exodat/`) (M. Deleuil, private communication), but several partial lists have been compiled during the mission. So far the most complete and useful for eclipsing binary studies is the CoRoT unofficial online catalog[3] assembled by J. Devor. This catalog provides not only the parameters describing the light curve (orbital period, eclipse depth and duration), but as well the system parameters, as derived by a new algorithm based on JKTEBOP eclipsing binary model (Popper & Etzel 1981; Southworth et al. 2004) and Markov Chain Monte Carlo (MCMC). A full analysis of this data set will appear elsewhere (Devor et al., in prep.), we use here some of the online data for a first look at the orbital period distribution.

The catalog contains the eclipsing/ellipsoidal binaries detected in the initial run (IRa01), in eleven long runs (LRc01...LRc06, LRa01...LRa05) and five short runs (SRc01, SRc02, SRa01...SRa03) for a total number of 1437 systems. Some of the selected objects, however, had doubtful classification because of the difficulty in discriminating, with an automatic algorithm and on the basis of a single light curve, between light variation due to low-inclination ellipsoidal systems and that due to surface spots or pulsation. We performed, therefore, a manual vetting of the curves which yielded a “bona fide” sample of 1142 binaries.

The binary frequency in the observed fields has a mean value of 0.9 ± 0.2%, i.e. about twice the frequency obtained from large ground-based surveys (e.g. OGLE). That is due to the long term monitoring and high accuracy of CoRoTphotometry, which allows to detect systems difficult to discover from the ground.

---

[3] `www.astro.tau.ac.il/~jdevor/CoRoT_catalog/catalog.html`

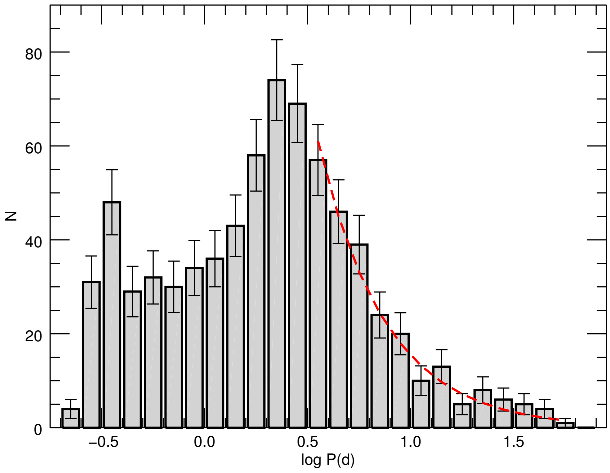

Fig. IV.3.12. Period distribution of the bona fide sample. The error bars are derived from the Poisson statistics uncertainties based on the number of systems. The red broken line is an estimate of the effects of discovery selection according to Maceroni & Rucinski (1999) © A&A.

The orbital period distribution of the "bona fide" sample is shown in Fig. IV.3.12. The secondary peak at short period is a well known feature and is generally attributed to the effect of secular evolution producing orbit shrinking in wider binaries. That can be due to angular momentum loss, due to magnetic braking of wind, in synchronized solar-type binaries (Vilhu 1982; van't Veer & Maceroni 1989), and/or to the Kozai mechanism in triple systems (Kozai 1962; Fabrycky & Tremaine 2007). The drop after maximum is essentially due to the decrease of the probability of eclipse with increasing period, because of the reduced range of inclinations producing eclipses. Moreover, the tail of the distribution is affected by the run duration (varying from ∼160 d to ∼80 days for long runs and from ∼60 to ∼30 days for the initial and the short runs). For illustrative purpose, the dashed line is the expected observed distribution of EBs from a population of binaries with a flat log P distribution. The curve corresponds to a selection effect proportional to $P^{-4/3}$, according to a simplified computation proposed by Maceroni & Rucinski (1999). Their simple estimate computes the probability that a distant observer notices eclipses by evaluating the solid angle subtended by the sum of the fractional radii (R/a, with a the system semi-axis) relative to visible hemisphere, i.e., by dividing it by 2π sr. This relative solid angle is given by the integral of the eclipse relative durations over the range of inclinations that can result in eclipses. The same proportionality is obtained by considering the fraction of the sky that one star 'sees' covered by the companion. If it is assumed that the range of variation of the sum of the component radii is much smaller than that of the orbital separation, this probability scales as a^{-2} and hence $P^{-4/3}$. The displayed curve is the best fit, with fixed exponent, to the distribution for $\log P > 0.5$.

Figure IV.3.13 shows the period distribution of subsamples, according to the galactic coordinates. Panel a) shows the distribution dividing the whole sample according to the direction (Center and Anticenter). The former has a more marked bimodal distribution, with a larger fraction of systems in the short period bins. A Kolmogorov-Smirnoff test of the hypothesis that the two samples are drawn from the same population yields a very low probability $KS = 0.0018$. The difference could be an indication of an older population in the direction of the galactic center fields, as that will imply a larger fraction of low-mass components (which can accomodate in a smaller orbit) and a longer time for efficient shrinking of the orbit.

This indication is in qualitative agreement with the results of differential population studies by means of oscillating giants (Miglio et al. 2013) in the first CoRoT long runs (LRa01 and LRc01). According to their analysis the sample of giants in LRc01 is characterised by a lower mean mass and higher age than that in the opposite direction. The fields considered in their study, however, have different galactic latitude, b, ($b \simeq -8$ for LRc01 and $b \simeq -2$ for LRa01) and a difference in b could also be a factor modifying the distributions.

To disentangle the effect of galactic latitude and longitude on the distribution, samples from fields of similar latitude or longitude are compared in the other panels. All the distribution pairs have a low value of KS. Evidently, an higher percentage of shorter period binaries appears in the higher latitude fields for both center and anticenter directions, and, as well, in the center direction with respect to the anticenter.

We also checked if the effect could also be related to the different amount of interstellar absorption, which is rather different and patchy in the various fields. To this purpose we used the population synthesis code TRILEGAL (Girardi et al. 2005) to compute the expected distribution of mass and age in the different CoRoT fields, using the reddening maps of Schlafly & Finkbeiner (2011). We also checked the effect on the results of varying A_V, the total absorption along the line of sight, of the same field. The details will be published elsewhere, but in general we can say that higher absorption provides slightly older and less massive "observed" samples and hence, indirectly, a larger number of shorter period binaries, because of the above mentioned mechanisms (angular momentum loss in spin-orbit synchronised solar-type binaries and Kozai mechanism in triple systems). Looking at panels b) and c) of Fig. IV.3.13 we see instead that the distribution is more bimodal, with a secondary peak in the period domain typical of contact binaries, in the high-b fields, where the average absorption is lower. We can conclude, therefore, that the effect is due to a difference in population.

The situation is less clear when comparing the distributions in the d) panel (LRc versus LRa high-b fields), where one probably sees the combination of two effects working in the same sense: the simulations suggest indeed older population for the LRc fields, which however have, as well, a higher average interstellar absorption. The difference in the population properties should be, however, the main reason of the different distribution shape, because the simulations show that the effect of absorption is a secondary one, even in presence of strong variations.

3.2. New binary types

The in-depth study of a number of CoRoT eclipsing systems lead to many discoveries. The accuracy played a fundamental role in the detection of new variable types, the monitoring with dense sampling over several months allowed to follow processes evolving on different timescales, from minutes to hundred days.

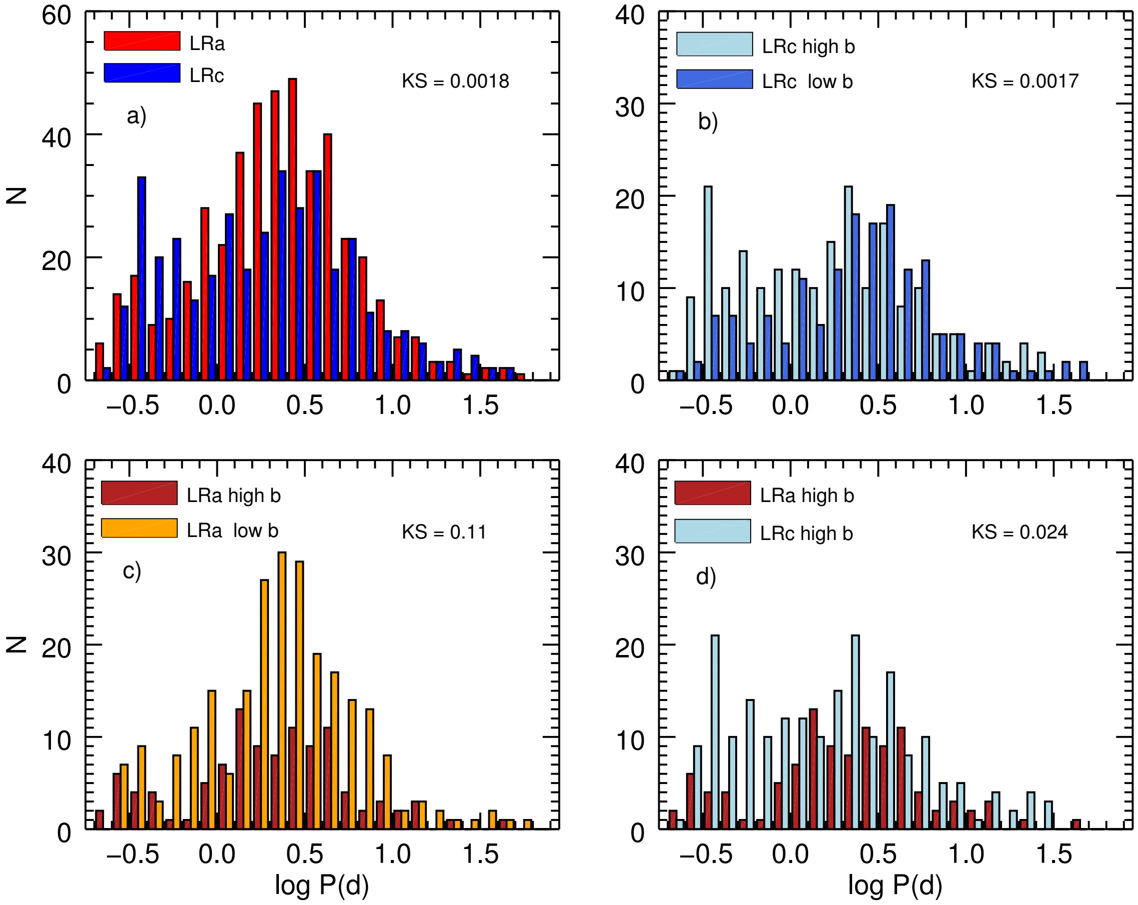

Fig. IV.3.13. The orbital period distribution of different EB subsamples. Panel **a)**: LRa and LRc indicate, respectively, the fields in the CoRoT Anticenter and Center directions. *Other panels*: the high and low galactic latitude refer to fields with galactic latitude absolute value $|b| > 5$ and ≤ 5.

CoRoT photometry discovered several beaming binaries, as predicted before the launch by Zucker et al. (2007) and first observed in the light curve of a *Kepler* target, KIC 7975824 (KPD 1946+4340) (Bloemen et al. 2011). These binaries show minute flux variations due to relativistic beaming (of the order of a few hundred ppm for systems with orbital period of 10–100 days and late-type components). Beaming (also called Doppler beaming or boosting) is due to the star radial velocity (RV): because of the motion the spectrum is shifted in wavelength, the photon emission rate is modulated, and the photons are slightly beamed in the direction of motion (light aberration). The resulting tiny light variation contains information on the radial velocity of the components. Beaming is, however, a subtractive effect, being the radial velocity of the components in anti-phase. Effects of opposite sign sum up weighted by the component fluxes, so that the effect strength is larger in binaries with components of very different flux (where, in practice, beaming from only one star is measured) and is null for identical components. In the most favourable case the analysis of the beaming effect in a light curve allows to extract the RV curve of the brighter component, but more frequently only its RV amplitude. Beaming provides the same information of a single-lined spectroscopic binary, with the advantage of a less demanding effort in terms of observing time. Moreover, beaming allows to discover non-eclipsing binaries from photometry alone. The example is the discovery of seventy-two non-eclipsing binaries from CoRoT light curves by Tal-Or et al. (2015). These are short period non-eclipsing binaries discovered thanks to the combined effect of beaming, ellipsoidal variations and reflection.

The beaming effect was invoked to interpret the unequal height of light-curve maxima (the so-called O'Connell effect) in CID 105906206 (da Silva et al. 2014). The system is a short period ($P \simeq 3\overset{\mathrm{d}}{.}69$) totally eclipsing detached binary, with a δ Sct primary component. The asymmetry of light-curve maxima appeared after pre-whitening the light curve with more than 200 frequencies found by using a harmonic analysis. The detached configuration, the stability of the feature over 160 days (and ~50 rotation cycles being the system components close to corotation), and the agreement of the beaming parameters with the radial velocity amplitude suggested the interpretation of the feature as due to beaming.

Another recently defined class of binaries is that of Heartbeat binaries (HBB). These are short period systems characterized by a strongly eccentric orbit and ellipsoidal light variation. The name derives from the unusual light-curve shape which, in non-eclipsing systems, recalls that of ECG tracings. In this case the light curve shows a single variation around periastron due to surface deformation and mutual irradiation of the components. The presence of tidally induced pulsation in the light curve is another distinctive property.

The shape of the HBB light curve was theoretically predicted by Kumar et al. (1995). The iconic heartbeat binary

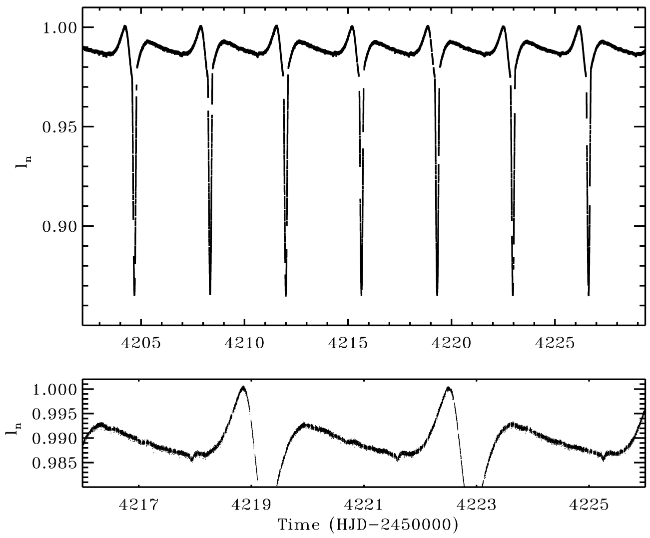

Fig. IV.3.14. *Upper panel*: the complete CoRoT light curve of HD 174884 as normalized flux vs HJD. *Lower panel*: a blow-up, spanning approximately three periods, showing the tiny secondary minimum (first occurrence at reduced HJD of around 4218). Reprinted from Astronomy and Astrophysics (Maceroni et al. 2009) © A&A.

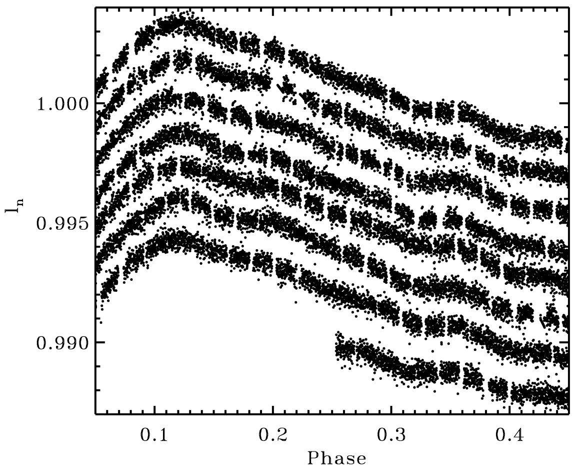

Fig. IV.3.15. Sections of the original light curve of HD 174884, phased according to the orbital period of 3.657 days and vertically shifted for better clarity. The seven observed orbital periods go bottom-up. An quasi regular pattern can clearly be seen in each curve. Reprinted from Astronomy and Astrophysics (Maceroni et al. 2009) © A&A.

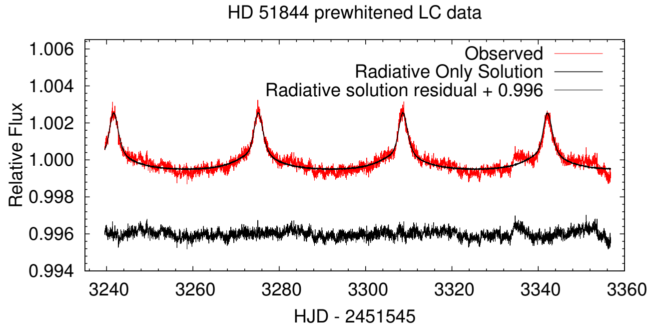

Fig. IV.3.16. The periastron brightenings in the light curve of HD 51844 and the corresponding best fit. Reprinted from Astronomy and Astrophysics (Hareter et al. 2014) © A&A.

is the *Kepler* target KOI-54 (Welsh et al. 2011) which was the first announced system of the class; more than hundred heartbeat binaries were discovered afterwards among the *Kepler* targets (Hambleton et al. 2013).

The original criteria for HBB definition excluded eclipsing systems, but this restriction was dropped afterwards (Hambleton et al. 2013), considering that eclipse is only an aspect-dependent event. With this broader definition the ante-litteram example of heartbeat systems is actually a CoRoT target: the eclipsing binary HD 174884, (Maceroni et al. 2009) whose light curve is shown in Fig. IV.3.14. The system is formed by two late B stars and the difference in depth between the two minima (the secondary depth is 1% of the primary) is entirely due to the high eccentricity ($e \simeq 0.3$) and the orientation of the orbit with respect to the observer. The pulsation analysis on the residual curve, after removal of the binary signal, revealed the presence of overtones of the orbital frequency, which can actually even be spotted by eye in the original curve (Fig. IV.3.15) and were interpreted as tidally induced pulsations.

A more classical HBB is HD 51844 (Hareter et al. 2014), a double-lined spectroscopic binary with a δ Sct component of spectral type Am. The system has an orbital period of 33.498 days, a high eccentricity ($e \simeq 0.48$) and is formed by almost twin components of mass $\simeq 2\ M_\odot$. In spite of that, only one star (the secondary) pulsates with measurable amplitude. The fact that similar stars exhibit completely different stability against pulsation is not new: only a fraction of field stars in the δ Sct instability strip of the HR diagram pulsates. When, however, the twin stars are components of close binaries, the conclusion is that the pulsational properties can significantly differ even for stars of the same age and chemical composition, which poses a challenging problem to theory.

The periastron brightening of the light curve of HD 51844 (Fig. IV.3.16) allowed to constrain the binary model even in absence of eclipses. Additional remarkable findings of this investigation are the high overtones of the orbital period in the frequency spectrum (interpreted as tidally induced pulsations) and the discovery of resonances, found for the first time in a δ Sct star.

3.3. Case studies

CoRoT offered for the first time the possibility of combining in an effective way the information coming from duplicity and from pulsation, thanks to the continuous monitoring of a large number of targets. When the pulsating stars belong to a binary there is an independent way of determining the component absolute parameters. This is of fundamental importance for asteroseismic studies as it allows to constrain the component modeling. A few cases have already been described in the previous section, but other are worth mentioning for the new insight offered by the synergy with asteroseismic studies.

Only one eclipsing system with a γ Dor component was known before CoRoT launch (VZ CVn, Ibanoğlu et al. 2007) but its sparse photometry from ground did not allow to really exploit the combination of eclipses and pulsations. CoRoT discovered a number of γ Dor pulsators

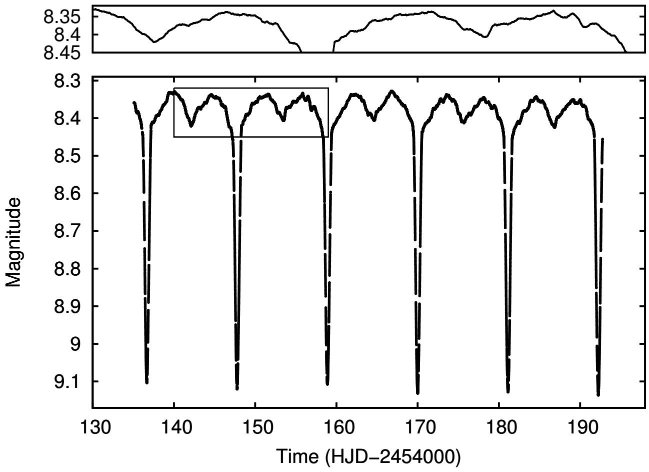

Fig. IV.3.17. The complete CoRoT light curve of AU Mon. The *upper panel* shows an enlarged segment of the curve with very clear rapid non-orbital variations. Reprinted from Monthly Notices of the Royal Astronomical Society (Desmet et al. 2010) © Monthly Notices of the Royal Astronomical Society.

in EBs (Sokolovsky et al. 2010; Maceroni et al. 2013) including hybrid γ Dor/δ Sct (Chapellier & Mathias 2013) and a possible detection in a triple system (Dolez et al. 2009). In addition, CoRoT made possible to investigate seismically unexplored regions of the HR diagram, such as that of very massive stars: the investigation of the young O-type binary HD 46149 (a double-lined spectroscopic binary Degroote et al. 2010) evidenced the presence of solar-like oscillations in a massive O-type star, while that of HD 50230 (Degroote et al. 2012) revealed a a prototypical hybrid pulsator in a B-type wide binary and allowed to put constraint on the component internal structure (Degroote et al. 2010).

The continuous monitoring over months and the dense sampling of the light curve offered as well the opportunity to study in depth binary systems with a complex configuration and presenting variability on different time scales. An example is the analysis of the eclipsing binary AU Mon (Desmet et al. 2010), a strongly interacting Be + G semi-detached system with an orbital period of ~11.11 days, whose light curve is shown in Fig. IV.3.17. In addition to eclipses, the study evidenced variability on a long time scale ($416^{\rm d}$), which was detected by combining of the CoRoT light curve (spanning $56^{\rm d}$) with pre-existing photometry of the system. The variability was interpreted in terms of matter surrounding the mass exchanging components and, thanks to eclipse mapping, modeled as an accretion disc by Mimica & Pavlovski (2012). Afterwards, a complementary investigation, based on optical and archival UV spectroscopy, evidenced the presence of a stream+disc+bright-spot around the Be primary (Atwood-Stone et al. 2012). The CoRoT photometry showed, as well, additional periodic variability (on a scale of a tenth of a day) which was interpreted as due to non-radial pulsations of the Be star. To be noticed that the corresponding frequencies are not predicted by theory but were observed in other CoRoT Be targets (as HD 49300, Huat et al. 2009). Finally, the Scargle periodogram of the CoRoT light curve is characterized by a power excess in agreement with solar-type pulsations of the G-type component.

Another complex and rare system is CID 223992193 (Gillen et al. 2014), a detached EB formed by two pre-main sequence dwarfs ($P_{orb} \simeq 3^{\rm d}\!.84$). The detailed modelling of the large amplitude out-of-eclipse variations (Fig. IV.3.18) combined to that of high-resolution spectroscopy and of the infrared SED revealed the presence of dust in the inner cavity of a circumbinary disc. The small amount of dust necessary to explain the out-of-eclipse variations could be present in the accretion streams from the disc itself.

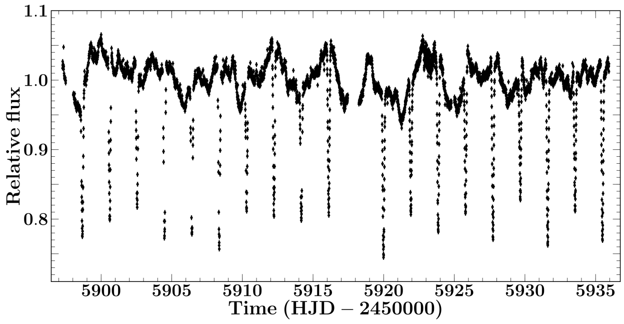

Fig. IV.3.18. The light curve of CID 223992193 as obtained by CoRoT in the run SRa05 (December 2011/January 2012), the system was observed also during the short run SRa01 (March 2008). Reprinted from Astronomy and Astrophysics (Gillen et al. 2014) © A&A.

Finally unusual binaries were detected as by-products of planet transit search, which ended sometimes in the serendipitous discovery of rarely observed binary systems, as for CID 110680825 (CoRoT LRa02_E2_0121, Tal-Or et al. 2011). In this case a Neptun-sized planet candidate target turned out to be a hierarchical triple system formed by a far giant primary and a grazing eclipsing binary of orbital period $\simeq 36^{\rm d}\!.3$. The inner system is formed by A- and F-type components. The reason for the false positive planet detection is dilution of the inner-binary light curve by the light of the giant companion, mimicking a less deep transit. A very sophisticated analysis allowed to detect also a tiny secondary minimum, only 0.07% deep, and to characterise the system, which is the second known of this type after HD 181068 (Derekas et al. 2011). The original light curve and the minima of the phase-folded one are shown in Fig. IV.3.19.

Similarly, the study of the transit candidate CID 101186644 (Tal-Or et al. 2013) revealed a strongly eccentric eclipsing binary with a period of ~20.7 days. The interesting system component is in this case a low-mass, dense late M-dwarf secondary, the smallest and densest detected so far ($R = 0.104\ R_\odot$, $M = 0.096\ M_\odot$). The detection is important because of the small number of stars in the region of very low mass stars ($M < 0.2\ M_\odot$). At variance with most other similar objects this M-dwarf has a radius in agreement (or perhaps even smaller) than that predicted by theoretical models. Its discovery weakens, therefore, the claim that low-mass star are larger than predicted by evolutionary models.

In conclusion CoRoT provided a rich harvest of scientific results in the field of binary stars and certainly much more will come from the exploitation of its legacy archive.

4. Stars with disks (by S.H.P. Alencar)

Disks are ubiquitous to the star formation process. They are the sites of planet formation and may interact with

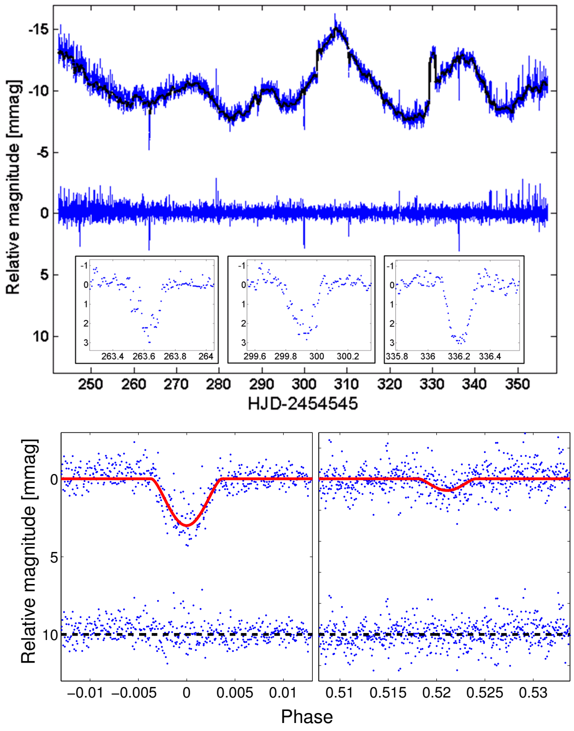

Fig. IV.3.19. *Upper figure*: The white light curve of CID 110680825. Top: the calibrated light curve (up-shifted by 10 mmag) after rebinning and removal of outliers; the long-term trend is overplotted in black. Middle: the detrended light curve. Insets: zoom on the three individual transit-like events. *Lower figure*: the primary and secondary eclipses in the phase-folded light curve with the best model overplotted with a solid red line. The residuals are downshifted by 10 mmag. Reprinted from Astronomy and Astrophysics (Tal-Or et al. 2011) © A&A.

the central star through the stellar magnetic field. T Tauri stars are low ($M \leq 2\ M_{\odot}$) mass stars of a few million years. Many of them, called classical T Tauri stars (CTTSs), still present accretion signatures from a circumstellar disk (Ménard & Bertout 1999). Understanding the accretion process acting in the star-disk system and disk evolution are some of the major challenges in the study of star formation nowadays. Accretion has a long and important impact in the initial evolution of low mass stars, regulating its fundamental properties (mass and angular momentum), and some of its most remarkable features (energy excess with respect to stars of the same age and mass that no longer accrete and mass loss through collimated jets). The discovery of thousands of extrasolar planets in the last decades has increased the importance of the evolution and dissipation of accretion disks around young stars, since they directly impact the study of planetary formation. The characterization of the accretion process in young stellar systems and their disks is therefore an important step to the establishment of credible scenarios of star and planet formation.

In young low-mass stars, magnetic fields can reach several kilogauss (Johns-Krull et al. 2001), causing the truncation of the inner disk region and directing the accreting material towards the star. The magnetospheric accretion process leads to the development of magnetic accretion columns that extend from the inner disk regions, at a few stellar radii from the star, to the stellar surface, originating accretion shocks at the surface of the star, where the accreting, nearly free-fall, material is rapidly decelerated (Bouvier et al. 2007b). The stellar magnetic field is also responsible for the transfer of angular momentum from the star to the disk, allowing the young accreting systems to rotate well below break-up velocity, despite the accretion and contraction processes at work (Affer et al. 2013; Gallet & Bouvier 2015). These various components (inner disk structure, accretion columns and shocks) are not directly observable due to our distance to star forming regions, but they generate spectral and photometric features that can be analysed to understand the accretion and outflow flux structure and its dynamics.

4.1. First CoRoT observations of NGC 2264

The CoRoT satellite allowed the observation of additional programs in short runs, not necessarily related to its main objectives of finding exoplanets and studying asteroseismology. The first additional program completed by CoRoT, in 2008, was the 23-day continuous observation of NGC 2264, a young (∼3 Myr) stellar cluster located at about 760 pc from the Sun (Dahm 2008). This was the only young cluster in the CoRoT “eyes” and a unique opportunity to study young stars with precise and high-cadence photometry. The CoRoT data on NGC 2264 yielded the most exquisite light curves ever obtained of young star-disk systems and originated very detailed analysis of variability in these systems. This initial campaign provided clues on the relation between accretion and X-ray variability (Flaccomio et al. 2010), it allowed the study of the circumstellar structure of accreting systems (Alencar et al. 2010), rotation in the Pre-Main Sequence (Affer et al. 2013), pulsations in young intermediate mass stars (Zwintz et al. 2013), and several young eclipsing binary systems were also discovered (Gillen et al. 2014).

Alencar et al. (2010) analysed the light curves of all the classical T Tauri stars of NGC 2264 observed by CoRoT and classified them in three simple categories: spot-like, which are periodic light curves dominated by variability due to starspots, AA Tau-like, periodic light curves whose variability is due to extinction by circumstellar dust, and irregular, which includes all the non-periodic light curves (Fig. IV.3.20). They showed that the highly dynamical star-disk interaction mediated by the stellar magnetic field observed in the classical T Tauri star AA Tau (Bouvier et al. 1999, 2003, 2007a) is apparently common among CTTSs (28% ± 6% of CTTSs in their sample presented AA Tau-like light curves). AA Tau-like light curves are observed in high inclination systems with respect to our line of sight and the light curves are dominated by extinction due to circumstellar material located at the inner disk edge. The interaction of the stellar magnetic field with the inner disk creates a warp that occults the star as the system rotates. The observed minima typically vary at each rotational cycle (Fig. IV.3.20), implying that the star-disk interaction and the inner disk structure is dynamic on a rotational timescale. Alencar et al. (2010) also showed that the inner disk warp is located close to the disk corotation radius, by comparing the period distribution of AA Tau-like systems and spot-like ones, the latter ones necessarily corresponding

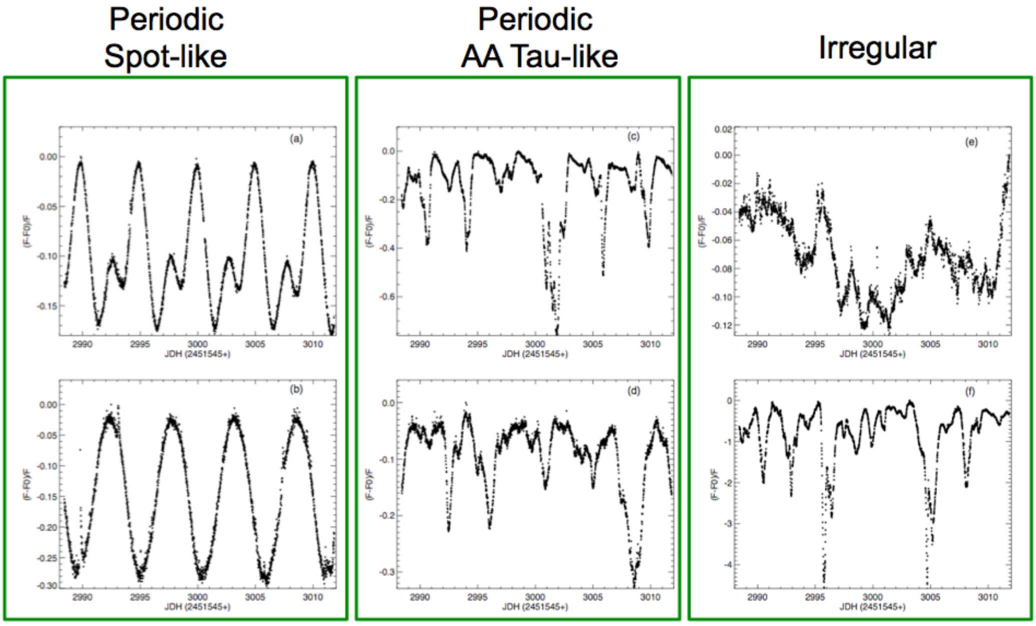

Fig. IV.3.20. CoRoT light curves of classical T Tauri stars, showing different morphological types. Spot-like light curves are periodic and due to spots at the stellar surface. AA Tau-like light curves are also periodic and due to obscuration of the central star by an inner disk warp. The irregular light curves include accretion-burst systems **(e)**, non-periodic circumstellar dust distribution **(f)** and light curves that are not clearly dominated by a unique physical process. Figure adapted from Alencar et al. (2010) © A&A.

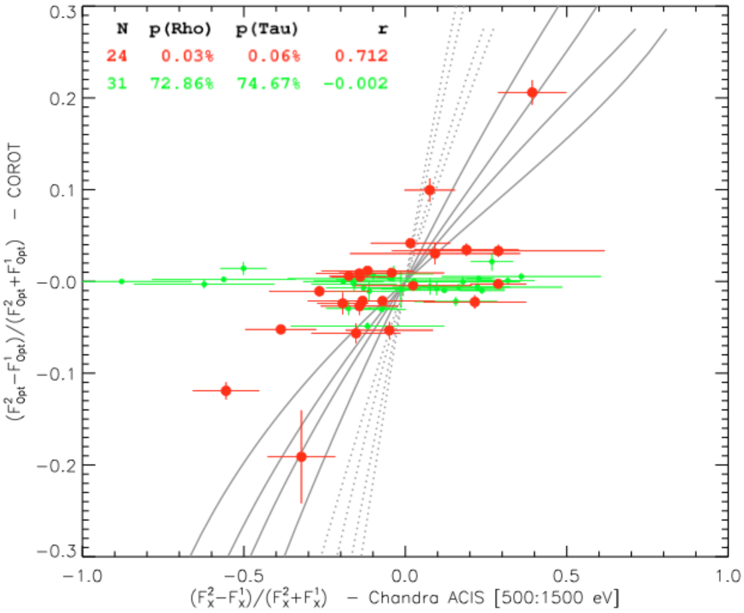

Fig. IV.3.21. Optical and soft X-ray variability for the WTTSs (green points) and CTTSs (red points) of NGC 2264 observed by CoRoT and Chandra. The lines indicate the effect of absorption on a constant source with average $A_V = 1.0$, assuming a standard interstellar gas/dust ratio (dotted lines), and a 5 times higher gas/dust ratio (solid lines). The four lines in each set refer to the combinations of two plasma temperatures, 0.6 and 5.0 keV, and two different assumptions for the spectrum-dependent extinction law in the wide CoRoT band: $A_{CoRoT}/A_V = 1.0$ and $A_{CoRoT}/A_V = A_I/A_V = 0.61$. Figure from Flaccomio et al. (2010) © A&A.

to the stellar rotation periods, since the spots are located at the stellar surface.

Flaccomio et al. (2010) showed that, for CTTSs, soft-X-ray (0.5–1.5 keV) and optical variabilities were correlated (Fig. IV.3.21), while no correlation was found between optical and hard X-rays (1.5–8.0 keV), or between optical and either soft or hard X-rays for the non-accreting weak line T Tauri stars (WTTSs). The observed correlation was explained in terms of variable absorption from circumstellar material, in a scenario similar to the one proposed for AA Tau-like systems. The slope of the observed correlation implies a significant dust depletion in the circumstellar

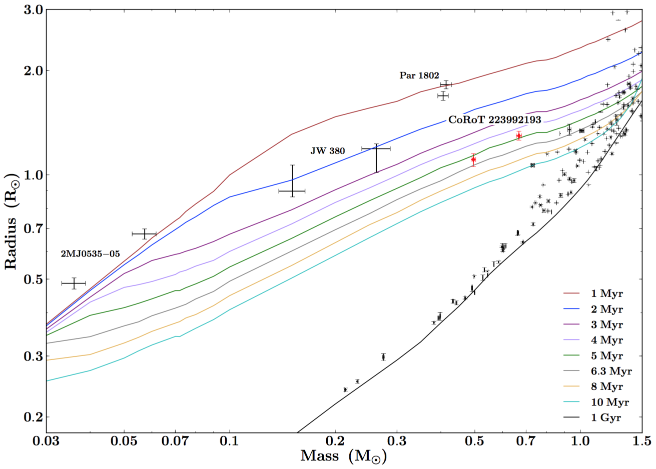

Fig. IV.3.22. Mass-radius relation for the three lowest-mass eclipsing binaries known in the Orion Nebula Cluster (black points) and CoRoT 223992193 (red points) compared with theoretical isochrones of Baraffe et al. (1998) with $Y = 0.282$, [M/H] $= 0$ and mixing length $\alpha = 1.9$. Figure from Gillen et al. (2014) © A&A.

material (gas/dust ratio ~5 times higher than the standard value for interstellar material).

Affer et al. (2013) presented a detailed analysis of the period distribution of all the CoRoT observed members of NGC 2264. They showed that CTTSs rotate slower than the WTTSs (Fig. IV.3.2), as also observed by other authors (Lamm et al. 2005; Cieza & Baliber 2007). This agrees with the proposed disk-locking scenario (Shu et al. 1994; Hartmann 2002), in which the interaction between the stellar magnetic field and the inner disk is able to transfer angular momentum from the star to the disk, despite the ongoing accretion and contraction.

Some eclipsing binary systems were discovered with the CoRoT observations of NGC 2264 and the most promising ones are being followed-up. CID 223992193 was the first binary system analysed from the sample and turned up to be a very interesting double-lined, detached eclipsing binary, composed of two young M dwarfs, possibly surrounded by a circumbinary disk from which the young stars may still be accreting (see Sect. 3.3 as well as Figs. IV.3.18 and IV.3.22 and Gillen et al. 2014). This binary system allows to test evolutionary models in a region where only a few stars are known and may also constitute a good laboratory to understand accretion from circumbinary disks.

4.2. The Coordinated Synoptic Investigation of NGC 2264

In December 2011, a new multiwavelength observational campaign of NGC 2264, called the *Coordinated Synoptic Investigation of NGC 2264* (CSI 2264), was organised. It included 40 days of continuous and simultaneous optical photometric observations with the CoRoT and MOST satellites, 30 days of infrared (IR) photometry with the *Spitzer* satellite and 3.5 days of X-ray observations with the Chandra satellite (Cody et al. 2014). Eleven ground-based telescopes were also involved in the campaign, providing, among other data, u-band observations with Megacam/CFHT and 20 epochs of VLT/FLAMES in two cluster fields. Very precise optical, 3.6 and 4.5 μm light curves were obtained for nearly 500 NGC 2264 members, about a third of which are accreting star-disk systems. The wealth of data from CSI 2264, combined with the 2008 campaign, permitted to probe young stellar systems variability in different timescales, from minutes to years, with optical and IR photometry of very high quality.

The CSI 2264 campaign demonstrated the diversity of the photometric behaviour of classical T Tauri stars and showed that 81% of the disk-bearing stars were variable in the optical and 91% in the mid-infrared. The CTTS light curves could be grouped in seven different variability classes, according to a light curve morphology analysis based on metrics of periodicity, stochasticity, and symmetry, that were associated with different physical processes and system geometries (Fig. IV.3.23 and Cody et al. 2014). The data are consistent with variability due to variable circumstellar obscuration, unsteady accretion, rotating starspots, and rapid structural changes in the disk, but sometimes more than one process could be acting simultaneously. Cody et al. (2014) showed that periodical and aperiodical optical dippers constitute the largest variability category (21% of the variable sample), and that the optical and IR variability were not correlated in over 50% of the observed systems (Fig. IV.3.24).

The spatial association between the inner disk warp caused by the stellar magnetosphere, the accretion columns along magnetic field lines and the accretion shock, that was previously only demonstrated for the classical T Tauri star AA Tau (Bouvier et al. 2007a), was confirmed for the stars with periodic and aperiodic extinction events ("dippers") in NGC 2264 (Fonseca et al. 2014; McGinnis et al. 2015). Average values of inner disk warp maximum height of 0.23 times its radial location were found, consistent with AA Tau, with variations on average of 11% between rotation cycles, indicating a very dynamical star-disk interaction.

Short duration, narrow flux dips associated with circumstellar material lifted up above the disk midplane were observed in the CoRoT and *Spitzer* light curves of a few systems (Stauffer et al. 2015). These narrow flux dips can be associated with dust in the inner disk region and the accretion funnel. Some of the narrow dips were periodical and occured superposed on sinusoidal variariations due to cold spot at the stellar photosphere, like in the light curve of Mon-21 (Fig. IV.3.25). Since both variabilities presented the same period, it confirms that, at least in this case, the stellar rotation rate is locked to the Keplerian rotation period at the inner disk, a long debated theoretical prediction (Koenigl 1991; Collier Cameron & Campbell 1993).

A well populated class of young stars with accretion-burst light curves was observed in detail for the first time (Fig. IV.3.26 and Stauffer et al. 2014). This type of systems were predicted by magneto-hydrodynamic simulations (Kulkarni & Romanova 2008), but difficult to find due to their rapid variability. Typically, optical and infrared bursts last from several hours to one day, with amplitudes of about 5%−50% the quiescent value. The high cadence of the CoRoT and *Spitzer* observations allowed the identification of several burst systems, whose variability arises from enhanced mass accretion rates, as confirmed by their high UV excess and very strong Hα emission lines.

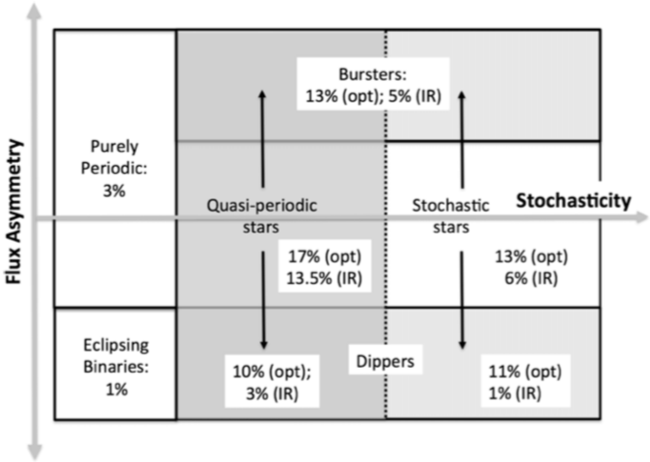

Fig. IV.3.23. Distribution of optical and IR light curves among the different light curve classes. © The Astronomical Journal, 147, 82.

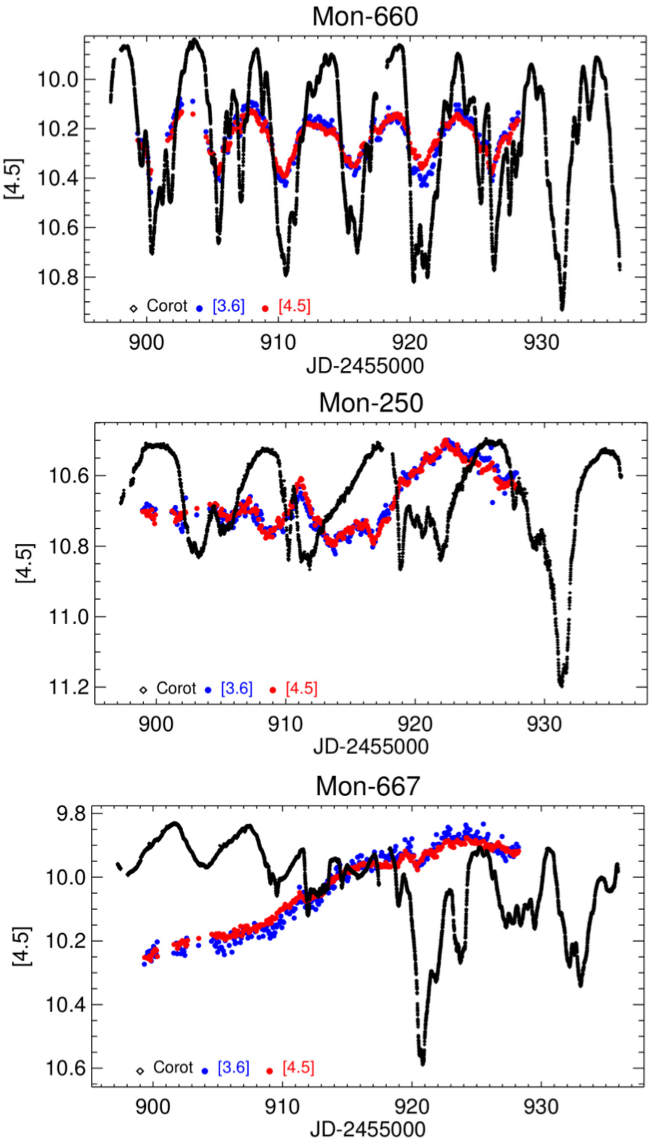

Fig. IV.3.24. Simultaneous CoRoT and *Spitzer* light curves of CTTSs in NGC 2264 that show different degrees of correlation. The top panel shows a system that presents very well correlated optical and IR light curves. The middle panel presents a system where the optical and IR variations are almost anti-correlated, while the bottom panel shows a CTTS that presents no correlation between the optical and IR light curves. Figures from McGinnis et al. (2015) © A&A.

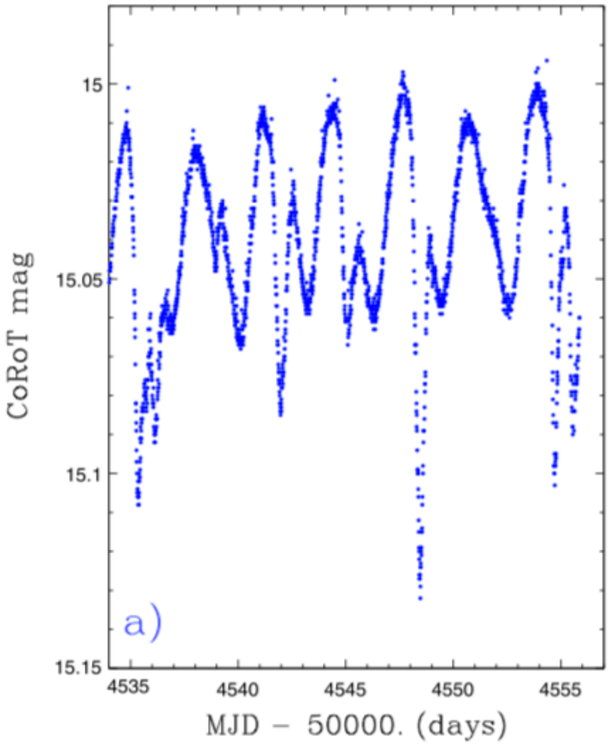

Fig. IV.3.25. CoRoT light curve of Mon-21 that shows spot-like sinusoidal variations with narrow dips due to circumstellar material superposed. © The Astronomical Journal, 149, 130.

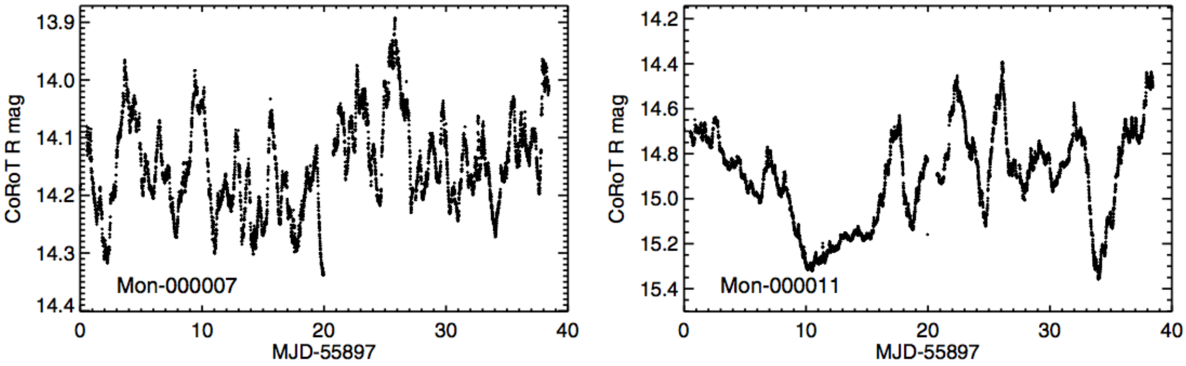

Fig. IV.3.26. CoRoT light curves of CTTSs that show accretion bursts. © The Astronomical Journal, 147, 83.

The association between accretion and inner disk evolution was demonstrated and is related to the morphology of the CoRoT light curves (Sousa et al. 2015). Accretion burst systems present high mass accretion rates and thick inner disks, the AA Tau-like systems show intermediate mass accretion rates and have disks in the transition region between thick to anemic, while most Classical T Tauri stars with spot-like light curves present low mass accretion rates and low mid-infrared excess. Accretion was observed to be highly dynamic and to occur in stable and unstable regimes, as predicted by MHD simulations (Kurosawa & Romanova 2013). It was also shown that the star-disk systems can alternate between stable and unstable accretion states in timescales of just a few years (Sousa et al. 2015).

Acknowledgements. C.M. acknowledges J. Devor and T. Mazeh for making available the unofficial Corot binary catalog. S.H.P.A acknowledges financial support from CNPq, CAPES and Fapemig.

References

Affer, L., Micela, G., Favata, F., & Flaccomio, E. 2012, MNRAS, 424, 11
Affer, L., Micela, G., Favata, F., Flaccomio, E., & Bouvier, J. 2013, MNRAS, 430, 1433
Aigrain, S., Favata, F., & Gilmore, G. 2004, A&A, 414, 1139
Alencar, S. H. P., Teixeira, P. S., Guimarães, M. M., et al. 2010, A&A, 519, A88
Atwood-Stone, C., Miller, B. P., Richards, M. T., Budaj, J., & Peters, G. J. 2012, ApJ, 760, 134
Baraffe, I., Chabrier, G., Allard, F., & Hauschildt, P. H. 1998, A&A, 337, 403
Bloemen, S., Marsh, T. R., Østensen, R. H., et al. 2011, MNRAS, 410, 1787

Bouvier, J., Chelli, A., Allain, S., et al. 1999, A&A, 349, 619

Bouvier, J., Grankin, K. N., Alencar, S. H. P., et al. 2003, A&A, 409, 169

Bouvier, J., Alencar, S. H. P., Boutelier, T., et al. 2007a, A&A, 463, 1017

Bouvier, J., Alencar, S. H. P., Harries, T. J., Johns-Krull, C. M., & Romanova, M. M. 2007b, Protostars and Planets V, 479

Chapellier, E., & Mathias, P. 2013, A&A, 556, A87

Chaplin, W. J., Bedding, T. R., Bonanno, A., et al. 2011, ApJ, 732, L5

Cieza, L., & Baliber, N. 2007, ApJ, 671, 605

Cody, A. M., Stauffer, J., Baglin, A., et al. 2014, AJ, 147, 82

Collier Cameron, A., & Campbell, C. G. 1993, A&A, 274, 309

da Silva, R., Maceroni, C., Gandolfi, D., Lehmann, H., & Hatzes, A. P. 2014, A&A, 565, 55

Dahm, S. E. 2008, The Young Cluster and Star Forming Region NGC 2264, ed. B. Reipurth, 966

De Medeiros, J. R., Ferreira Lopes, C. E., Leão, I. C., et al. 2013, A&A, 555, A63

Degroote, P., Aerts, C., Baglin, A., et al. 2010, Nature, 464, 259

Degroote, P., Aerts, C., Michel, E., et al. 2012, A&A, 542, A88

Derekas, A., Kiss, L. L., Borkovits, T., et al. 2011, Science, 332, 216

Desmet, M., Frémat, Y., Baudin, F., et al. 2010, MNRAS, 401, 418

do Nascimento, J.-D., da Costa, J. S., & Castro, M. 2012, A&A, 548, L1

do Nascimento, Jr., J.-D., Takeda, Y., Meléndez, J., et al. 2013, ApJ, 771, L31

Dolez, N., Vauclair, S., Michel, E., et al. 2009, A&A, 506, 159

Fabrycky, D., & Tremaine, S. 2007, ApJ, 669, 1298

Flaccomio, E., Micela, G., Favata, F., & Alencar, S. P. H. 2010, A&A, 516, L8

Fonseca, N. N. J., Alencar, S. H. P., Bouvier, J., Favata, F., & Flaccomio, E. 2014, A&A, 567, A39

Gallet, F., & Bouvier, J. 2015, A&A, 577, A98

García, R. A., Mathur, S., Salabert, D., et al. 2010, Science, 329, 1032

Gillen, E., Aigrain, S., McQuillan, A., et al. 2014, A&A, 562, A50

Girardi, L., Groenewegen, M. A. T., Hatziminaoglou, E., & da Costa, L. 2005, A&A, 436, 895

Hambleton, K., Degroote, P., Conroy, K., et al. 2013, in EAS PS, 64, eds. K. Pavlovski, A. Tkachenko, & G. Torres, 285

Hareter, M., Paparó, M., Weiss, W., et al. 2014, A&A, 567, A124

Hartmann, L. 2002, ApJ, 566, L29

Harvey, J. 1985, in Future Missions in Solar, Heliospheric & Space Plasma Physics, eds. E. Rolfe, & B. Battrick, ESA SP, 235, 199

Huat, A.-L., Hubert, A.-M., Baudin, F., et al. 2009, A&A, 506, 95

Huber, K. F., Czesla, S., Wolter, U., & Schmitt, J. H. M. M. 2010, A&A, 514, A39

Ibanoğlu, C., Taş, G., Sipahi, E., & Evren, S. 2007, MNRAS, 376, 573

Johns-Krull, C. M., Valenti, J. A., Piskunov, N. E., Saar, S. H., & Hatzes, A. P. 2001, in Magnetic Fields Across the Hertzsprung-Russell Diagram, eds. G. Mathys, S. K. Solanki, & D. T. Wickramasinghe, ASP Conf. Ser., 248, 527

Koenigl, A. 1991, ApJ, 370, L39

Kozai, Y. 1962, AJ, 67, 591

Kulkarni, A. K., & Romanova, M. M. 2008, MNRAS, 386, 673

Kumar, P., Ao, C. O., & Quataert, E. J. 1995, ApJ, 449, 294

Kurosawa, R., & Romanova, M. M. 2013, MNRAS, 431, 2673

Lamm, M. H., Mundt, R., Bailer-Jones, C. A. L., & Herbst, W. 2005, A&A, 430, 1005

Lanza, A. F. 2008, A&A, 487, 1163

Lanza, A. F., Aigrain, S., Messina, S., et al. 2009a, A&A, 506, 255

Lanza, A. F., Pagano, I., Leto, G., et al. 2009b, A&A, 493, 193

Lanza, A. F., Bonomo, A. S., Moutou, C., et al. 2010, A&A, 520, A53

Lanza, A. F., Bonomo, A. S., Pagano, I., et al. 2011, A&A, 525, A14

Leão, I. C., Pasquini, L., Ferreira Lopes, C. E., et al. 2015, A&A, 582, A85

Lou, Y.-Q. 2000, ApJ, 540, 1102

Ludwig, H.-G., Samadi, R., Steffen, M., et al. 2009, A&A, 506, 167

Maceroni, C., & Rucinski, S. M. 1999, AJ, 118, 1819

Maceroni, C., Montalbán, J., Michel, E., et al. 2009, A&A, 508, 1375

Maceroni, C., Montalbán, J., Gandolfi, D., Pavlovski, K., & Rainer, M. 2013, A&A, 552, A60

Mathur, S., García, R. A., Morgenthaler, A., et al. 2013, A&A, 550, A32

McGinnis, P. T., Alencar, S. H. P., Guimarães, M. M., et al. 2015, A&A, 577, A11

Ménard, F., & Bertout, C. 1999, in NATO Advanced Science Institutes (ASI) Series C, 540, eds. C. J. Lada, & N. D. Kylafis, 341

Michel, E., Samadi, R., Baudin, F., et al. 2009, A&A, 495, 979

Miglio, A., Chiappini, C., Morel, T., et al. 2013, in Eur. Phys. J. Web Conf., 43, 3004

Mimica, P., & Pavlovski, K. 2012, in IAU Symp. 282, eds. M. T. Richards, & I. Hubeny, 63

Mosser, B., Baudin, F., Lanza, A. F., et al. 2009a, A&A, 506, 245

Mosser, B., Michel, E., Appourchaux, T., et al. 2009b, A&A, 506, 33

Oliver, R., Ballester, J. L., & Baudin, F. 1998, Nature, 394, 552

Popper, D. M., & Etzel, P. B. 1981, AJ, 86, 102

Rieger, E., Kanbach, G., Reppin, C., et al. 1984, Nature, 312, 623

Salabert, D., Régulo, C., Ballot, J., García, R. A., & Mathur, S. 2011, A&A, 530, A127

Samadi, R., Belkacem, K., Ludwig, H.-G., et al. 2013, A&A, 559, A40

Sarro, L. M., Debosscher, J., Neiner, C., et al. 2013, A&A, 550, A120

Schlafly, E. F., & Finkbeiner, D. P. 2011, ApJ, 737, 103

Shu, F., Najita, J., Ostriker, E., et al. 1994, ApJ, 429, 781

Silva-Valio, A., & Lanza, A. F. 2011, A&A, 529, A36
Silva-Valio, A., Lanza, A. F., Alonso, R., & Barge, P. 2010, A&A, 510, A25
Sokolovsky, K., Maceroni, C., Hareter, M., et al. 2010, Communications in Asteroseismology, 161, 55
Sousa, A., Alencar, S., Bouvier, J., et al. 2015, ArXiv e-prints
Southworth, J., Maxted, P. F. L., & Smalley, B. 2004, MNRAS, 351, 1277
Stauffer, J., Cody, A. M., Baglin, A., et al. 2014, AJ, 147, 83
Stauffer, J., Cody, A. M., McGinnis, P., et al. 2015, AJ, 149, 130
Tal-Or, L., Santerne, A., Mazeh, T., et al. 2011, A&A, 534, A67
Tal-Or, L., Mazeh, T., Alonso, R., et al. 2013, A&A, 553, A30
Tal-Or, L., Faigler, S., & Mazeh, T. 2015, A&A, 580, A21
van't Veer, F., & Maceroni, C. 1989, A&A, 220, 128
Vilhu, O. 1982, A&A, 109, 17
Welsh, W. F., Orosz, J. A., Aerts, C., et al. 2011, The ApJS, 197, 4
Zucker, S., Mazeh, T., & Alexander, T. 2007, ApJ, 670, 1326
Zwintz, K., Fossati, L., Ryabchikova, T., et al. 2013, A&A, 550, A121

Acknowledgements: The CoRoT space mission has been developed and operated by CNES, with the contribution of Austria, Belgium, Brazil, ESA, Germany, and Spain.

Part V

CoRoT paved the road to the future

The CoRoT Legacy Book

DOI: 10.1051/978-2-7598-1876-1.c050

Part V

CoRoT paved the road to the future

The objective of this part is to show how the knowledge acquired by the CoRoT mission translates into the future projects.

Three years before CoRoT's launch, the Canadian microsatellite MOST had shown the superiority of space to monitor micro-variations in starlight. Following this opening, CoRoT was the first space mission to really demonstrate the pioneering science that would result from ultra-precise, long duration and continuous space-based photometric measurements.

Chapter V.1 deals with the managerial and technical aspects, and shows how CoRoT, as a pioneer mission, had to invent original approaches.

The very specific programmatic framework, the very low budget and the extremely short duration of the development phase have been mastered because the CoRoT Team had to explore new horizons in terms of organization and management methods.

The CoRoT team has also determined the major technical difficulties of this new domain. It has established the first requirements, defined the first principles and trades-off, addressed and validated several sub-system concepts, and finally demonstrated the potential of these techniques. One can now speak about a technical CoRoT "heritage", declined in its various scientific successors such as CHEOPS and PLATO, as presented in Chapter V.2.

Chapter V.3 is a short description of these upcoming space missions designed primarily for exoplanet science, but largely open to asteroseismology and stellar astrophysics studies. These future missions, some already launched and gathering data, include Kepler-K2, a reconfigured *Kepler* mission (see Chapter ajouter V.I.5) with a mission profile very similar to that of CoRoT, the BRITE-Constellation, a group of six nanosatellites devoted to precision photometry of the brightest stars of the sky, CHEOPS, dedicated to the detailed study of a few super-Earth and Neptune-sized objects orbiting bright stars, TESS, an all sky transit survey to detect exoplanets transiting nearby stars, and finally PLATO, a super-CoRoT with a combination of scientific goals, a core program aiming at detecting and characterizing exoplanets, and a guest program dedicated to stellar and galactic astrophysics.

The coming years promise an exciting adventure to exoplanet and stellar physics researchers, and CoRoT definitely marked the start of this wonderful journey.

The CoRoT Legacy Book

DOI: 10.1051/978-2-7598-1876-1.c051

V.1

Lessons learned from CoRoT

T. Lam-Trong

CNES, Centre spatial de Toulouse, 18 avenue Edouard Belin, 31401 Toulouse Cedex 9, France

1. General

The CoRoT mission had the ambition to perform high precision stellar photometry on stars for long and continuous periods, to detect both exoplanets and stellar oscillations. This leads to quite unusual and demanding specifications.

Because of very limited available resources, it was clearly a design-to-cost mission. But it was not a "faster, better, cheaper" approach in which there are plenty of management and technical dead-ends. We have taken risks but without any sacrifice in terms of final validation.

Another factor even more driving than the cost was the planning. Only 3 and a half years from the final mission adoption (mid-2003) to the launch decision (end-2006).

So both planning and cost have pushed the project towards unusual and original ways of management and technical approaches.

2. Technical approach

2.1. The basic low-cost choices

The basic low-cost choices are:

- the choice of the class of satellite: "small" satellite (600 kg, 500 W);
- the use of a standard bus (PROTEUS);
- the choice of the orbit: a low Earth orbit (LEO), imposed by the using of a small bus with limited quantity of propellant:
  - 900 km pure polar orbit ($i = 90°$, no rotation of the orbit plane),
  - because of the Sun, each observation duration (run) is limited to 150 days. Consequently, it is not possible to detect planets with a period >50 days.

2.2. The development logics

The technical approach that we have developed is, first of all, based on the compliance to the needs rather than the seeking for absolute performances in terms of solutions. So, we did a permanent hunting of what is nice to have beyond what is mandatory.

The development logic is characterized by a high level of risk taking which has been carefully analyzed, assumed and publicly displayed. It consists essentially in:

- planning activities in parallel;
- postponing some tests at the higher level (of integration);
- limiting the qualification of the ground segment. This position has been fully validated a posteriori. Indeed, the flight data turned out to be significantly different from simulated data and their use in qualification of the ground segment would have been misleading;
- reducing the duration of the operational qualification, relying on the gained experience with the previous missions, which used the same platform (PROTEUS).

2.3. The technical challenges

We have met some difficult technical challenges, for instance:

- *The pointing stability*
  Because of the non-uniformity of the pixel-to-pixel response, the pointing jitter produces noise in the frequency domain. In order to keep this noise much lower than the photon noise, a stability of 0.25 pixel is required. That means a stability of $0.5''$ (2.4 microrad), which is equivalent to continuously aiming at a football 100 km away. This level of accuracy, never reached before, is achieved by using the instrument in the control loop.
  In order to achieve such a performance, we have developed an innovative solution by using the instrument as a star sensor with much higher accuracy compared to standard star sensors.
  The principle (See Fig. V.1.1) is to measure the gap between the current line of sight and the required one by measuring the barycenter of the light spot of 2 preselected stars among those selected for the asteroseismology mission. The gap between this barycenter and the target is sent (in the form of 3 angles) to the closed-loop attitude controller of the satellite (combined Kalman filtering with data coming from the gyrometers).

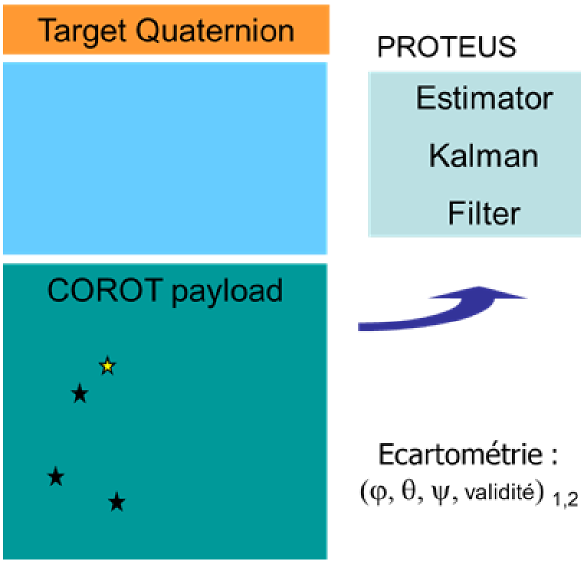

Fig. V.1.1. Block Diagram of the Corot attitude control. © CNES

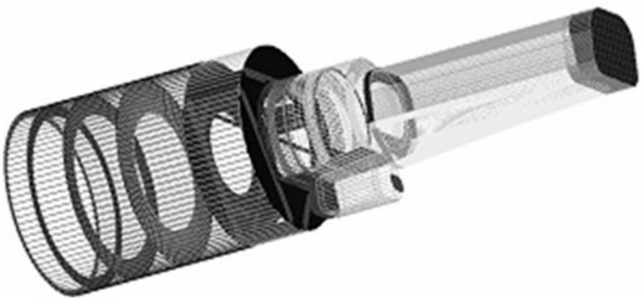

Fig. V.1.2. COROT Baffle. © CNES

We have never tested this function on ground in a representative way (only in open-loop). To mitigate the risk, we have developed and used extensively digital simulations. A posteriori, these simulations did fit perfectly the real behavior in orbit.

- *The protection against the stray light*
  One important source of stray light is the light reflected by the Earth. It varies during the orbit. The first estimates of this pollution led to pay attention to it.
  That led to design a telescope with an off-axis unfocused parabolic (2 mirrors) system completed with a baffle (see Fig. V.1.2), which has a rejection factor never achieved before (10^{-13} at 20 degrees).
  Once again, the baffle has never been tested on ground in a representative light environment.
  Then we did rely on simulations made by two independent teams (CSL and CNES).
  The following diagram (Fig. V.1.3) shows the rejection ratio vs. the angle of attack (with respect to the line of sight).
- *The thermal stability*
  The quantum efficiency and the dark current are function of temperature. In order to fight against the periodic noise (orbital period) induced by fluctuations of temperature, the CCD must be at –40 °C with a stability better than 0.05 °C over 1 hour.
  In order to reach this performance, a modular concept has been used, with separate and isolated "cells". The performance realized in flight is better than 15 mK.
  The thermal control has the following approach:
  - the instrument is split into independent cells which have each dedicated requirements (average temperature, stability, etc.) and dedicated control (mainly passive).
    The design drivers which have been applied are:
  - homogenization of each cell by using internal conductive and radiative coupling;
  - accommodation of external radiators in front of thermal sinks, as stable as possible;
  - drainage of heat towards radiative surfaces;
  - since the mass was not an issue for CoRoT, use of the thermal inertia to improve the temperature stability.

The following diagram (Fig. V.1.4) shows the different thermal cells of the instrument.

3. The management approach

3.1. Learn to work together

The CoRoT organization is complex and hybrid, mixing classical contractual relationship (customer vs. provider) and partnerships based on the principle of the "best effort".

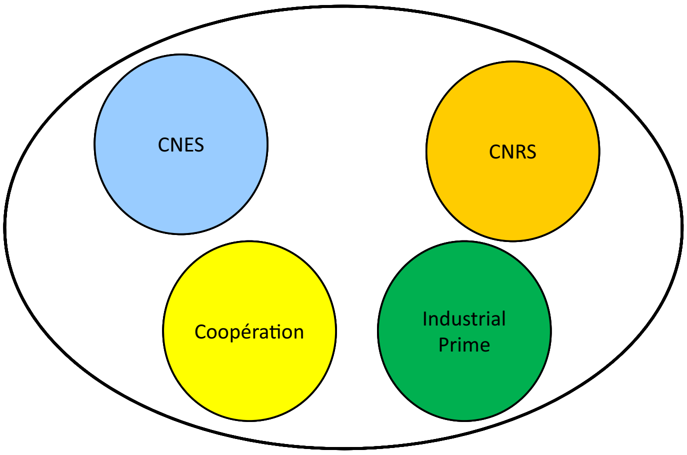

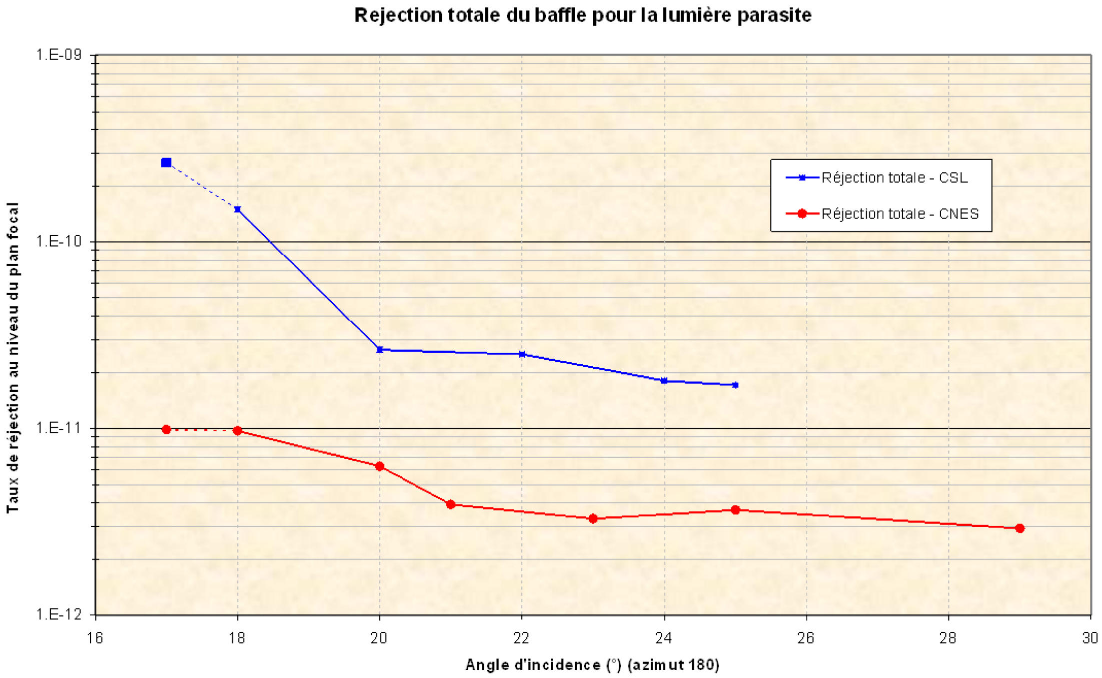

Fig. V.1.3. Straylight rejection simulation. © CNES

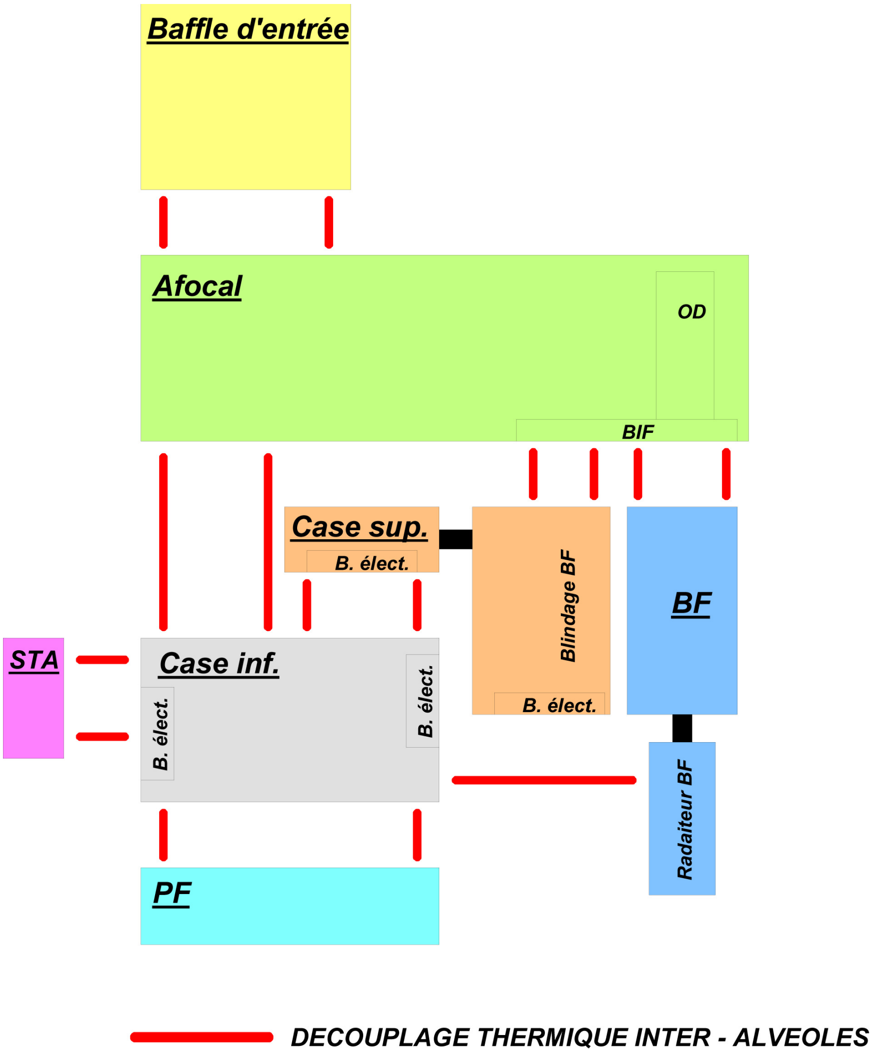

Fig. V.1.4. COROT Thermal Control Architecture. © CNES

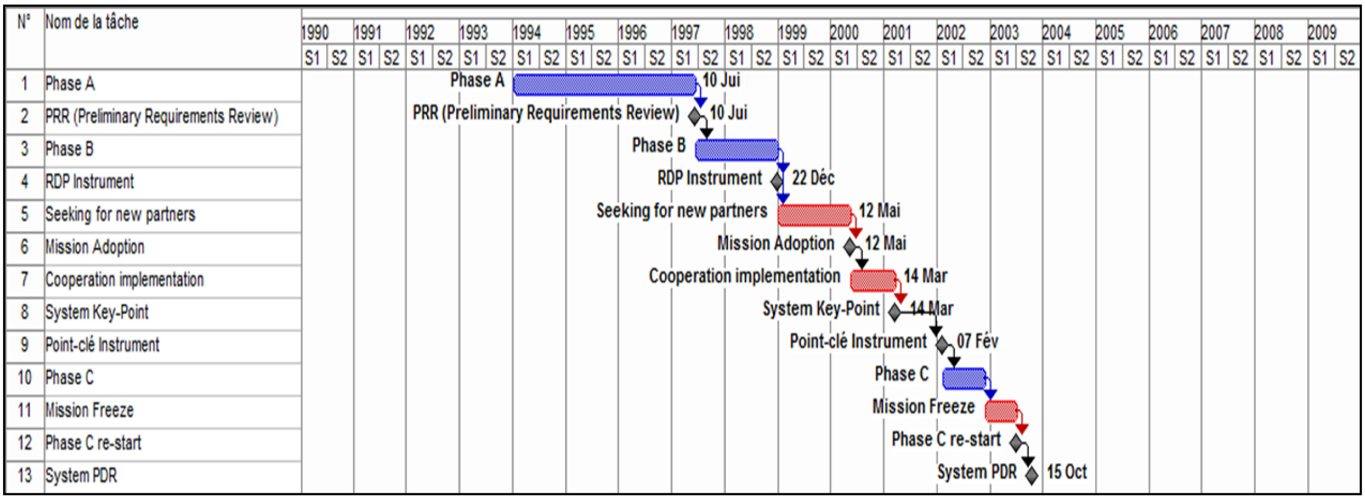

Fig. V.1.5. COROT Schedule Overview. © CNES

The lesson learned from the CoRoT project is that, in such an organization, relationships based on power do not work and the consensus should be privileged.

We have learned to work together with different cultures and vocabularies, between Europeans, with Brazilians, between scientists and engineers.

3.2. The challenges for the management

The counterpart of international cooperation is a complex management of the project with a high number of interfaces. There are plenty of complexity factors:

- the responsibility of CNES at all levels, from the procurement of parts up to the whole system integration and going through equipment, subsystems, the instrument and the ground and space segments;
- the different nature of relationship between actors: agreement with international partners, convention with the French laboratories (CNRS) and the contract with manufacturers. The project has to manage 6 international agreements, 3 conventions and more than 100 contracts;
- the difference of cultures and experience which leads to always privilege the content to the form.

3.3. The management of the planning

3.3.1. The CoRoT history

The maturation phase has been very long, roughly 10 yr!

That is a major paradox of this mission, 10 yr to decide and only 3 yr to make it a reality. The main lesson learned is that there is a big progression margin in the process of decision, all the risks being put unreasonably in the development phase. That is not rational (see Fig. V.1.5).

3.3.2. The CoRoT final development

The "out-of-norms" short duration

In order to be the first hunter in space of exoplanets and to keep at least a 2-year advance with respect to the large Kepler mission of NASA, it was mandatory for it to be launched by the end of 2006.

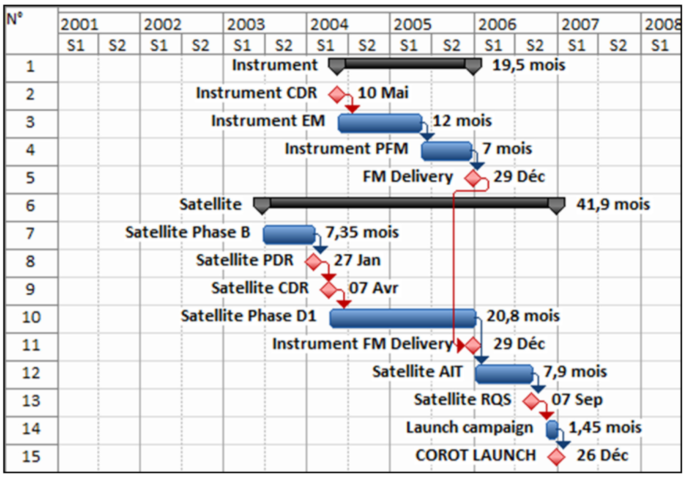

Fig. V.1.6. COROT master planning. © CNES

The final green light to make CoRoT has been given in mid-2003, that meant 3,5 years to finish the design and the manufacturing of the instrument, the satellite and the ground segment.

The only way to be able to do that was to build a reverse master planning from December 2006 back to 2003 and then to define deadlines for each activity.

The duration of the development of CoRoT (see Fig. V.1.6)is outside the norms in which it should have been, at least twice longer. the following show how fast the activities ran:

- the instrument flight model was integrated and qualified within 7 months;
- the satellite was integrated and qualified within 8 months.

The exceptional convergence of the planning

A good indication of the performance is given by the so-called "trend curve" (see Fig. V.1.7).

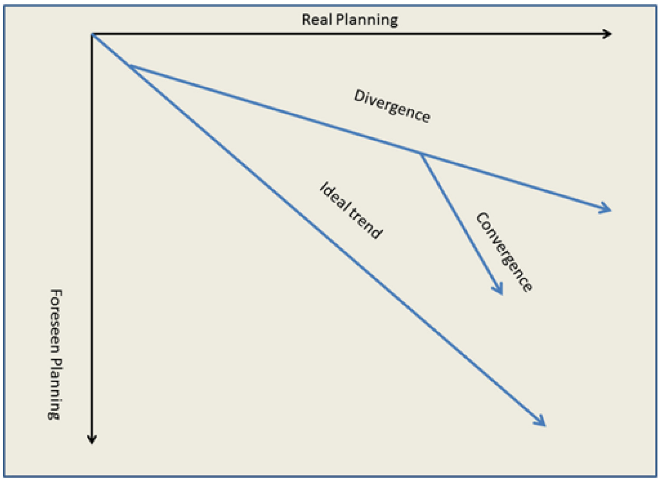

Fig. V.1.7. General Development Trend Curve. © CNES

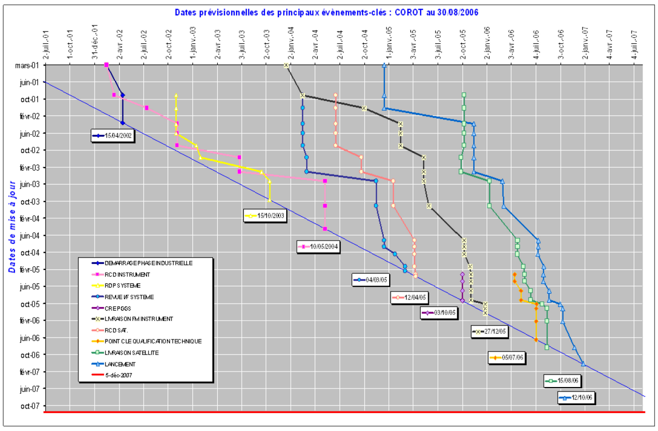

Fig. V.1.8. COROT Development Trend Curve. © CNES

The following diagram (Fig. V.1.8) is interesting as it shows the rapid convergence of the planning.

3.4. The management of resources

With the passing of time, it appears clearly today that the success of the CoRoT mission is the result of the exceptional quality of the available manpower. This quality has led to a permanent production by everyone of added value, driven by a spirit based on confidence, consensus and best efforts.

The totality of human resources spent in the project is around 500 men-year. The following diagram (Fig. V.1.9) shows the distribution of the manpower between the cooperation partners, the French laboratories and CNES.

The total cost of the development is around 170 M€ (110 M€ of external costs and 60 M€ of manpower).

3.5. The management of risks

In such a design-to-cost project with a very tight schedule, the risk taking is a permanent part of the daily management.

Some examples of risk taking are: the parallel implementation of a lot of tasks, the validation by analyses and simulation then by test, the late validation of major components at the instrument level only, after the final integration.

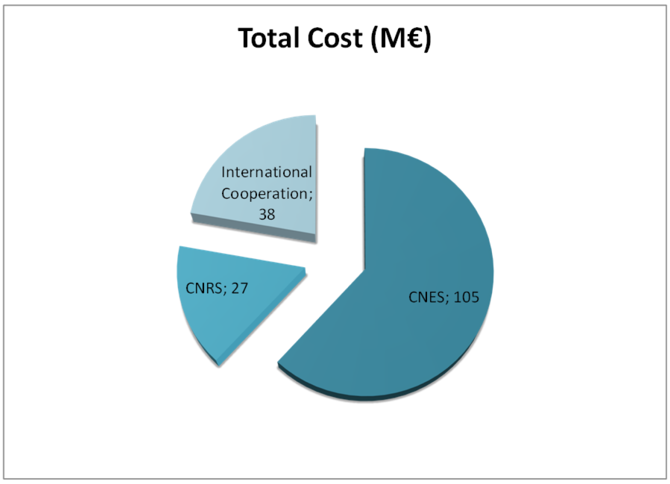

Fig. V.1.9. COROT Total Cost Distribution. © CNES

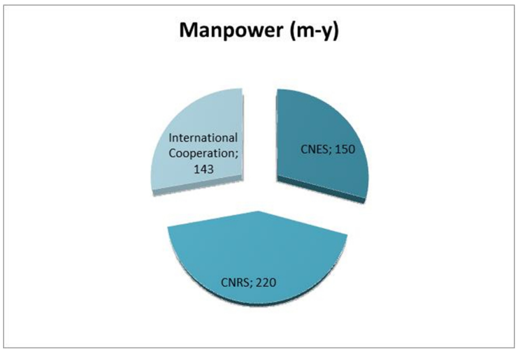

Fig. V.1.10. COROT Manpower Distribution. © CNES

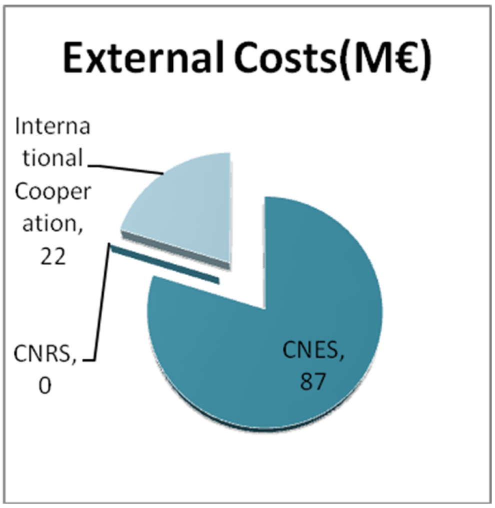

Fig. V.1.11. COROT External Cost Distribution. © CNES

Yes, we have taken a lot of risks but always with a full knowledge of them by using a rigorous process of risk analysis and mitigation. All the in-flight technical performances have been better than the requirements and the life duration has been twice the required one.

The success of this development is the demonstration that the risk-taking process applied in the CoRoT mission was pertinent.

4. Conclusion

The CoRoT project has been a very complex project, with difficulties which are out of the normal range of any space project. The root cause is the process of decision which has been too long (more than a decade) and having as a consequence a very tight schedule after the final decision in mid-2003 for a launch at the end of 2006.

So, we have been obliged to develop a new approach and logic for the development. We have refused to apply a “faster, cheaper” approach but we have found the good compromise between the three poles which are the technical performances, the schedule and the cost.

The price we have paid is quite expensive in terms of pressure and personal investment for all the CoRoT team but that was largely balanced by the success of this project and, what is most important, by the extraordinary and exciting human adventure lived by all the actors of CoRoT.

Acknowledgements: The CoRoT space mission has been developed and operated by CNES, with the contribution of Austria, Belgium, Brazil, ESA, Germany, and Spain.

The CoRoT Legacy Book
© The authors, 2016
DOI: 10.1051/978-2-7598-1876-1.c052

V.2

CoRoT heritage in future missions

M. Ollivier[1, 2], D. Tiphène[2], R. Samadi[2], and P. Levacher[3]

[1] Institut d'Astrophysique Spatiale, UMR8617, CNRS, Université Paris XI, Bâtiment 121, 91405, Orsay Cedex, France
[2] LESIA – Observatoire de PARIS
[3] Laboratoire d'Astrophysique de Marseille

1. CoRoT heritage: The CHEOPS mission (by M. Ollivier)

Among the space missions dedicated to accurate stellar photometry, CHEOPS (ESA-2013, Fig. V.2.1) is certainly the mission that benefits the most from the CoRoT developments.

CHEOPS is the first mission of the ESA S programme (small missions, with a fast development concept and an ESA contribution limited to 50 M€). It is dedicated to the accurate photometry of stars with known planets (from Jupiter size to super Earths) identified by radial velocimetry in order to determine, when planets transit, their radius with an accuracy of 10% and their global density with an accuracy of about 30%. CHEOPS aims also at providing first order characterisation of transiting planets with an atmosphere that will be studied by next generation of spectro-photometers.

In order to reduce the development time and associated costs, CHEOPS uses subsystems and developments made in the context of CoRoT:

- the orbit and the altitude at which CHEOPS will observe benefit from CoRoT ones (polar orbit). As a consequence, the space environment seen by the satellite will be known before the lauch, and particularly the amount of proton impacts due to South Atlantic anomaly crossing;
- the CCD is a 1k × 1k E2V component based on the same technology as the CCDs used by CoRoT. As a consequence, all the calibrations done on CoRoT CCDs can be reproduced identically. In the same time, the ageing of the detector can be anticipated, with, for example, an increase with time of the dark current, of the coefficient of transfer inefficiency, of bad pixels due to protons impacts, etc.;
- the thermal control of the CCD is based on the same principle. The focal plane is linked to a radiator at about −40 °C, and the working temperature of the focal array is stabilised at a slightly higher temperature thanks to a servo-control thermal heater;
- the attitude in orbit control system (AOCS), where the instrument is used to determine accurately the direction of the line of sight thanks to the measurement of the photocentre of stars in the field, is directly derived from the CoRoT AOCS principle. In the case of CoRoT, 2 bright stars in the bright stars channel, used also for the science programme, were monitored to provide an error signal to the control system of the satellite;
- the optical baffle, in front of the telescope, used to drastically reduce the amount of the scattered light (off axis-light) is developed by the same company as CoRoT. The requirements and the concept of the baffle are the same, using the same materials, the same shape for the vans, and probably the same black coating;
- the device used to open the telescope protective cover is the same as CoRoT. It is a one-shot device that allows a soft but complete opening of the cover without introducing parasitic moves;
- the surface of CHEOPS PSF is comparable to the size of the faint stars channel CoRoT PSF, i.e.: about 500 square arcsec. As a consequence, the level of contamination by faint background stars will be the

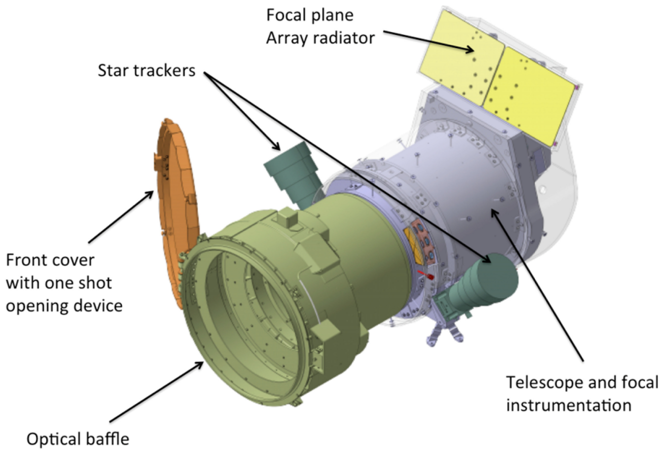

Fig. V.2.1. The CHEOPS photometer. Adopting the concept developed for CoRoT, the CHEOPS photometer is made of a telescope with a focal plane array which is passively cooled down by means of a radiator, the temperature being controlled by a servo-system slightly heating the detector at the reference temperature. The scattered light is strongly reduced by the use of an optical baffle in front of the telescope. The telescope is pointed by using star trackers, the fine-tuning being controlled by the instrument itself (© Bern University).

same (assuming a similar stellar density). The contamination study strategy can thus be adapted from the CoRoT strategy;

– last but not least, the ground segment and in particular, the reduction pipeline is strongly inspired by the CoRoT pipelines. Even if CHEOPS is downloading 200 × 200 pixels imagettes, the photometric light curves extracted from the images are obtained more or less in the same way as CoRoT light curves imagettes. Of course, the CHEOPS pipeline has to take into account the specificity of the observations (rotating field, defocused tri-foiled PSF, etc.)

For more information see CHEOPS: CHaracterising ExOPlanet Satellite, Definition study report, 2013, ESA/SRE, 7, available on ESA website

2. CoRoT heritage: The PLATO mission (by D. Tiphène, R. Samadi, P. Levacher)

The PLATO mission belongs to the M-class missions of the ESA Cosmic Vision 2015–2025 program.

PLATO re-uses the concept of high accuracy photometry used by CoRoT mission.

What characterises PLATO at first look is the high number of cameras instead of a single photometer in most general cases. It comes directly from the need of an instrument with a large entrance pupil to fulfil the needed signal-to-noise ratio, but with a pupil divided by several cameras to have both a high number of bright stars without saturation and reach a high signal-to-noise ratio. That comes, as for CoRoT, by the need to confirm by ground observations the events detected on-board, to check if they are effectively exoplanets or other detections, and these accurate observations (with large Earth telescopes) are only possible for bright stars (magnitudes up to about 11). Unlike COROT, PLATO will allow a seismic study of the host stars brighter than magnitude 11. This will enable the precise characterisation of the planet host star, including its age and mass.

Taking into account the constraints of CoRoT, in particular for stray light reduction, and therefore the very large optical baffle behind the instrument, PLATO has completely changed the approach by selecting an orbit far from the Earth: Lagrange point L2 of the Sun-Earth system. Such an orbit also authorises the use of the immense field of view we have mentioned, and long observation periods up to 3 years on the same part of the sky, with limited constraints on the satellite attitudes. The PLATO thermal concept also takes advantage of the selected orbit avoiding large thermal variable fluxes on the instrument; CoRoT's orbit was a 895 km polar orbit with large thermal variations on the outer of the instrument due to the proximity of the Earth. The thermal of a photometer should be optimised to guaranty a very stable environment to the temperature-sensitive equipments (detectors, optics…).

The main driver for choosing the PLATO instrument basic configuration is related to the need to optimise simultaneously the number and the brightness of observed cool dwarfs and subgiants. The concept of overlapping field-of-view, offering a very wide field of view covered by a variable number of cameras, was a natural consequence of this main idea. In addition to this basic motivation, the overlapping field-of-view allows to re-observe, during the PLATO step-and-stare phase, some stars for which particularly interesting planets were detected in the long monitoring phases of the mission (in particular telluric planets in the habitable zone), but only with a subset of telescopes, therefore without reaching the required photometric precision for seismic analysis during these phases. During the step-and-stare phase, these targets can be put in the part of the field observed with all the 32 telescopes, thus reaching the best photometric precision, giving us the potential to fulfil photometric requirements.

The detector saturation level is linked to the pupil size, optical transmission, exposure time, full well capacity (FWC), PSF size and shape, quantum efficiency of the charge-coupled device (CCD), and star brightness. The FWC of CoRoT CCDs was reduced by the choice of advanced inverted mode operation to limit the surface dark current at −40 °C. With the pupil size selected and the PSF size largely constrained by confusion issues, a special effort was made on the PLATO CCDs for a large increase of the FWC, in order to improve the access to bright stars, which are of major interest for science. Moreover, the preparation of CoRoT has shown the possibility to exploit photometrically slightly saturated spots, an option which Kepler is using extensively as well. For PLATO, this possibility will also be used to increase the useful magnitude range; the dimensioning of signal chains is such that saturation occurs for normal cameras between 8.3 and 9.5 depending on the position of the star in the field of view, further assuming that PLATO bright stars photometry could be studied by four magnitudes on saturated images. Moreover, the performances of cameras are strongly linked to its temperature stability. Cameras shall be strongly isolated from temperature variable (or not controlled) sources (sunshield inner surfaces, optical bench...). As for CoRoT, the power dissipated inside the FPA is fixed on timescales higher than the cycle time.

PLATO has the double particularity to be a very high accurate relative photometer and to have a science bandwidth at very low frequencies. The periodic perturbations in the seismic observation range (100 sec–4 days) shall be reduced as much as possible. The resulting need is a very low instrumental noise in the science frequency bandwidth, in terms of random noise or parasitic lines, fixed or slightly moving in the Fourier spectrum; this constraint was already a strong scientist CoRoT requirement. For this last need in particular, the resulting constraint is to limit the number of various oscillators, each with its own frequency to avoid or limit the risk of beating between these oscillators. All the activities of the cameras are synchronised by a unique reference clock distributed to all sensitive boxes. Indeed, the level of noise required at instrument level is very low, an EMC coupling between electronics boxes or between cables at such low levels is inevitable and could not be seen during EMC tests, due to a low detector sensitivity at room temperature. This could be a high risk of damage in the performances for the two scientific programs. Then, the general philosophy for the PLATO photometers is to synchronise all the activities especially on low level analog electronics (detectors, attached video electronics and their power supplies), and in their close environment (camera with active thermal control). With this precaution, an eventual EMC coupling between two or several subsystems will only result on a fixed pattern in the data, which can be managed like other stable perturbations.

Early in the CoRoT mission analysis, the perturbations and sources of noise having an important impact on the quality of the data have been identified:

- after each integration phase, CCD pixels are read out while they remain sensitive to the incident light (no shutter) and produce the "smearing" effect. Each star image has a uniformly bright "tail" along columns. The magnitude of this offset depends on the ratio of the readout time to the integration time. CoRoT has shown that this offset could be measured and subtracted;
- variations of the satellite pointing direction induce short-term displacements of the stars, called jitter. Hence, due to the fixed position of the photometric mask, small part of the star flux can be detected by pixels outside the mask, and then not sum in the photometrical signal. Additionally, part of the flux from a neighbouring parasite can enter the mask and pollute the photometry of the target. In either case, the flux of the target will be modulated by the coherent and incoherent variations of the pointing direction of the satellite;
- PLATO should be more sensitive to confusion than CoRoT: stars fainter than around magnitude 11 are expected to be perturbed by fainter stars (contaminants). Three different types of perturbations are identified: photon noise from the contaminants, combined effect of confusion and satellite jitter, and the flux of the contaminant introducing a bias on the measurement of the depth of transit and for seismic analysis;
- deriving for each star the associated sky background flux is of major importance, not only for the analysis of the transit depth or the seismic analysis, but also for the photometry measurements based on weighted mask and for the photometric jitter correction. Indeed, an incorrect value for the background level decreases the efficiency of the weighted mask with respect to the confusion problem as well as the efficiency of the photometric jitter correction;
- the kinematic differential aberration is due to the relativistic effect related to the satellite motion with respect to the stars; the angle between two stars varies with time. This effect is true for all missions and will be more important for PLATO due to the large field of view;
- for PLATO, the instrument response functions will be more complex than the CoRoT ones. The star light curves will be different for each camera due to the different gain of each electronic chain, the different quantum efficiency of each CDD, and the differing aperture and transparency of each telescope. Furthermore, crosstalk between different electronic chains are expected to occur and will introduce an absolute offset on the photometry measurements. Although this bias will be constant, it will nevertheless be different from one camera to another. Therefore, before comparing and averaging (temporally and spatially) the light curves associated with the same star but coming from different telescopes, it will be necessary to transform the digital signal into a signal that can be directly compared and averaged. This is why a correction of the global gain of the instrument (optical, CDD and electronic) as well the crosstalk patterns must be performed prior any comparison and averaging of the light curves. CoRoT has measured the varying of the global gain of electronics chains with the temperature;
- the occurrence of a cosmic ray or a glitch can perturb a light curve. Such outliers introduce important artefacts, in particular on the Fourier analysis. Hence, impacted measurements must be removed and replaced by a representative value of the star flux;
- long-term trend has been measured by CoRoT; a long-term decrease of the intensity at long-time scale (from weeks to several months) has appeared due to the aging of the optics and of the CCD, and has been corrected afterward on-ground; similar correction will be applied on the individual PLATO light curves;
- thermo-elastic differential variations of the PLATO telescope structures will induce a variation of the line of sight of a given telescope with respect to the pointing direction of the fast telescope used as reference for the pointing. These variations will in turn induce additional and undesirable displacements of the stars, which have the same impact on the photometry as the kinematic differential aberration mentioned above, whereas these effects did not exist in CoRoT photometer, which had only one telescope.

The data processing chain (board and ground) of the space mission PLATO is currently being defined. During the assessment study phase (2008–2009) as well as the phase A (2010–2011), a preliminary definition of the data processing chain has been proposed. This work benefited greatly from the experience gained on CoRoT. This is not surprising. Both missions have similar requirements and characteristics. Indeed, like CoRoT, PLATO requires a very high photometry precision (34 ppm per hour at $V = 11$ for PLATO, 8 ppm per hour at $V = 6$ for CoRoT) and a very long-term stability of the measurements (several months). Furthermore, like for CoRoT, in order to archive the scientific requirements of the PLATO mission is it necessary to correct the raw data from undesirable disturbances, such as the satellite jitter described above.

Several methods for correcting the noise induced by the jitter have been investigated by the CoRoT data processing algorithm team (called GT2S[1]). It turned out that the most efficient were the ones developed by De Oliveira Fialho et al.[2]. This method requires knowing the point-spread function (PSF) of the camera with a spatial resolution significantly smaller than the pixel size and at different positions of the field of view. It is also required to know the angular displacements of each target. Once these information are available, we can then predict and correct the relative variation of the flux induced by the satellite jitter. This "jitter correction" will be implemented in the PLATO on-ground data processing chain and operated on the raw PLATO light curves.

Building a super-resolved PSF from pixel-resolved ones is possible, in practice, through the exploitation of subpixel motion. Before starting an observation sequence, several

---

[1] GT2S: Groupe Traitement Segment Sol.

[2] Jitter Correction Algorithms for the COROT Satellite – De Oliveira et al. 2007, PASP, 119, 337).

different calibration processes need to be applied. A time-series of small imagettes are then acquired during the motion of the satellite. These imagettes are downloaded and then inverted (on-ground) to produce the PSFs at the target location. While CoRoT used times-series of small imagettes acquired during a few days at the beginning of each observation sequence[3], PLATO will rely on a microscanning technique that will be operated during the calibration phases of the missions. In this approach, the instrument's attitude control system is used to execute a slow, controlled perturbation of the line of sight of the telescope in such a way that the image of a star on the CCD will move over the area of about a square pixel.

Zodiacal stray light is expected to be the major contributor to the background for PLATO; in the case of CoRoT, the stray light was mostly due to Earth. This source is expected to vary on the long term (approximately one month). Since the momentum wheels will be unloaded approximately each week, we will use this as an opportunity to recalibrate the background map. In terms of spatial distribution, the Zodiacal stray light is also expected to vary at large scale-length. Accordingly, we can expect that such variation can be modelled using a functional form (e.g. a bivariate polynomial). The parameters of this functional form will be fitted during the configuration mode using several measurements of the background performed at different locations of a full image. Once the free parameters are adjusted, they will be used during the observation mode to derive the background associated with each target.

The overall architecture of the pipeline is directly inherited from the CoRoT mission, and allows anticipating known perturbations. Some of the specific corrections used for PLATO are identical to the ones used for CoRoT, such as the jitter correction, and some others are strongly inspired by the work done during the CoRoT mission.

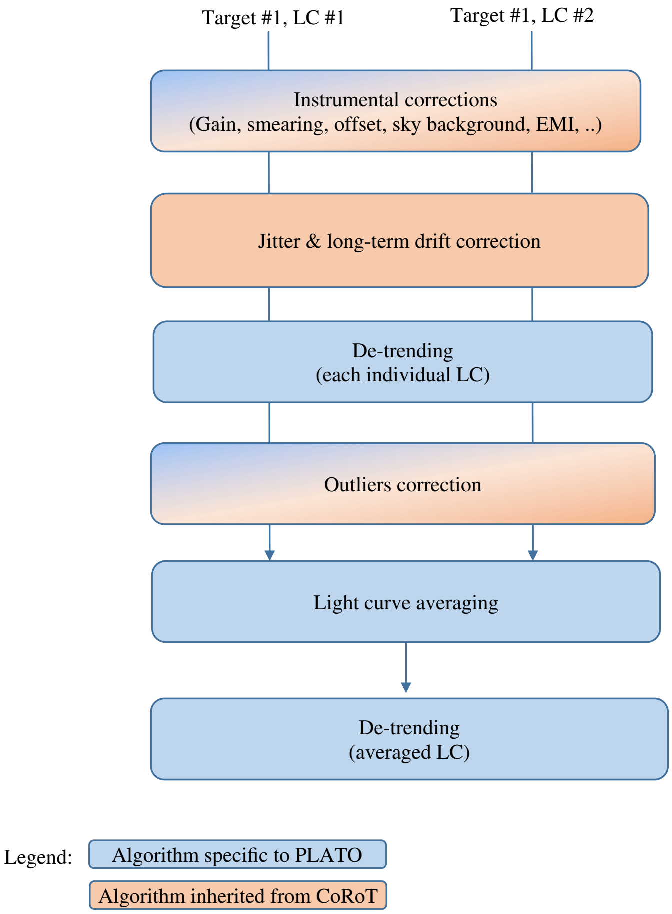

Fig. V.2.2. Preliminary design of the on-ground processing pipeline for the PLATO mission. © Emmanuel Grolleau, LESIA

Acknowledgements: The CoRoT space mission has been developed and operated by CNES, with the contribution of Austria, Belgium, Brazil, ESA, Germany, and Spain.

---

[3] Radiation effects on space-based stellar photometry: theoretical models and empirical results for CoRoT Space Telescope – Pinheiro da Silva et al. 2008, MNRAS, 384, 1337.

The CoRoT Legacy Book

DOI: 10.1051/978-2-7598-1876-1.c053

V.3

Present and future space missions for ultra-precision photometry

A. P. Hatzes[1], W. W. Weiss[2], H. Rauer[3,4], and A. Grotsch-Noels[5]

[1] Thüringer Landessternwarte Tautenburg, Sternwarte 5, 07778 Tautenburg, Germany
[2] Department of Astrophysics, University of Vienna, Türkgenschanzstr. 17, 1180 Vienna, Austria
[3] Zentrum für Astronomie und Astrophysik, TU Berlin, Hardenbergstr. 36, 10623 Berlin, Germany
[4] Institut für Planetenforschung, Deutsches Zentrum für Luft- und Raumfahrt, Rutherfordstrasse 2, 12489 Berlin, Germany
[5] Dept. of Astrophysics, Geophysics and Oceanography, University of Liège, Belgium

1. Introduction

We are in a golden era for the study of transiting exoplanets and stellar physics using space-based telescopes. One legacy of CoRoT is that it marked the start of this era. CoRoT was the first to demonstrate the pioneering science that would result from ultra-precise, long duration and continuous space-based photometric measurements. Its two main science programs worked in parallel. One searched for transiting planets among a total of ~100 000 stars. The other performed asteroseismology on 156 bright stars. Kepler shortly followed in CoRoT footsteps. Together they started the space photometry revolution.

CoRoT and Kepler highlighted the advantages of photometry with a space telescope in spite of the higher cost. A ground-based telescope can simply not compete with the exquisite photometric precision and superb sampling of a space based counterpart. The detection of small transiting planets and solar-like oscillations benefit immensely from all these improvements. One can strongly argue that ultra-precision space photometry launched a golden age in both transiting planets and asteroseismology.

Ground-based transit programs such as WASP and HAT-P have had spectacular success at finding almost 200 transiting planets, but these ground-based searches had two large disadvantages. First, they are severely biased towards finding giant planets. Of the exoplanets discovered by these transit searches the smallest planets have a radius of approximately 0.5 R_{Jup}. By comparison, CoRoT detected several hundreds of Neptune-size candidates while Kepler detected several thousands, most of these in multiple systems. Clearly, only space-based surveys can get the complete census of the planet population down to the smallest (Earth-sized planets). Gas giants represent only a small fraction of the full planet population.

Second, space photometry is also more efficient at detecting transiting exoplanets. CoRoT discovered a giant planet for roughly every 3000 stars monitored, comparable to that of Kepler. On the other hand the ~200 transiting giant planets discovered by ground-based surveys required the monitoring of many hundreds of thousands if not millions of stars. The detection efficiency of ground-based surveys is roughly a factor of 10–20 worse than those from space.

Although CoRoT and Kepler were spectacularly successful, they suffered from one serious drawback, they generally targeted quite faint ($V > 12$) stars. This made the follow-up observations for both complementary seismology data and the confirmation and characterization of planets through high resolution spectroscopy challenging. For example, CoRoT detected several hundreds of transits with depths consistent with Neptune- or super-Earth-sized planets. However, radial velocity confirmation of these were nearly impossible since most of the targets were in the magnitude range $V = 13$–16. Only upper limits to the planetary mass could be determined. The brightness of the host stars for the Kepler discovered planets are not much better.

The faintness of the CoRoT and Kepler transit candidates have stressed the telescope resources needed for follow-up observations. The study of the properties (temperature, composition, etc.) of the transiting exoplanet's atmosphere using either in-transit spectroscopy or secondary eclipses is an important next step in the characterization of exoplanets. However, the atmospheric signature of a planet is a million times fainter than the light of the star which means that these measurements can only be made on relatively bright stars. It is for this reason that atmospheric studies have only been performed on a handful of transiting planets. CoRoT and Kepler have discovered a large number of transiting planets, but these are ill-suited for atmospheric studies due to the faintness of the host star.

Space is also the place for stellar oscillation studies. From the ground, the photometric precision is ultimately limited by the atmospheric scintillation noise. Furthermore, the data gaps due to the diurnal cycle of the sun and bad weather makes it challenging and frustrating to acquire sufficient data to detect all oscillation modes. For example, from the ground using coordinated observations from a network of telescopes scattered across the globe, one can detect 10 pulsation modes in a delta-Scuti star using 170 hrs of data (Breger et al. 1995). With 550 hrs continuous observations, the mode count increases to 19 (Breger 1995). In its initial run of just 58 d, CoRoT detected hundreds of pulsation modes in a delta-Scuti star (Poretti et al. 2009). Thanks to space photometry, the largest work load for asteroseismology has shifted from data acquisition to data modeling.

It is beyond the scope of this paper to discuss all the exciting asteroseismic results from CoRoT and Kepler. However, it is worth mentioning the radial and non-radial pulsations in giant stars, first found by CoRoT (De Ridder et al. 2009) and which blossomed into a vibrant sub-field of asteroseismology under Kepler. Without space photometry, asteroseismology would still be in its infancy rather than the mature field it is today.

Asteroseismology is also of immense importance to exoplanet studies. The accurate parameters of planet hosting stars, such as mass and radius, translate into accurate parameters for the planet. The age of exoplanets, important for understanding the evolution of planetary systems, is one of the more poorly known stellar parameters. This is even more difficult for stars lying off the main sequence which can be either very young, or very old. For example, the mass and radius Kepler-423 can be fit by evolutionary tracks with either 25 million years (Myr) or 11 gigayears (Gyr) tracks (Gandolfi et al. 2015). Asteroseismology can deliver accurate values for these important parameters and again space photometry has enabled us to do so.

Also in this respect, CoRoT and Kepler had limitations. CoRoT could perform asteroseismolgy on very few bright planet hosting stars (Escobar et al. 2012), but these were using the bright star seismo-field. The faint star exo-field, which delivered all of CoRoT's planet discoveries, had much fainter stars and with poorer time sampling which made asteroseismic measurements impossible. Kepler was able to perform some asteroseismology on the host stars of its detected planets (e.g. Batalha et al. 2011), but these were only for a few of the stars that were sufficiently bright. Clearly what is needed is a wide-field transit search program for which the asteroseismic measurements are made with the same data used to detect transiting planets.

The upcoming space missions will remedy the limitations of CoRoT and Kepler. Two of these (TESS and PLATO) will perform a wide-angle search for transiting planets, but for stars with $V < 11$. PLATO will have a strong asteroseismic component so that accurate stellar parameters will be obtained. These missions will provide transiting planet candidates for which it will be much easier to perform spectroscopic follow-up measurements. The discovered exoplanets will also provide important targets for characterization studies with the James Webb Space Telescope.

In this paper we give a short description of upcoming space missions, many designed primarily for exoplanet science, but these can also be used to enable a broad range of studies in stellar astrophysics. These include Kepler-K2, BRITE-Constellation, Gaia, CHEOPS, TESS, and PLATO. The Micro-Oscillations of STars (MOST) satellite is still providing ultra-precise photometric data, but this was already presented in Chapter 1 and will not be discussed here.

2. K2: Kepler reborn

The period between November 2012 and May 2013 was a bad time for exoplanet and asteroseismic science. In the space of less than a year, both CoRoT and Kepler experienced hardware malfunctions. For CoRoT it was the loss of the second Data Processing Unit (DPU) in November 2012 that ended its ability to collect data. For Kepler it was the failure of its second reaction wheel in May 2013. The spacecraft could still continue to collect and transmit data, but with only two reaction wheels it was impossible to stabilize the pointing of the telescope in order to obtain ultra-precise light curves. A key science objective of Kepler, to detect Earth-sized planets in the habitable zone of sun-like stars, was thus severely compromised.

Fortunately for the astronomical community, Kepler was able to recover some capabilities and have a new life as the K2 mission. After a careful study NASA determined that by targeting fields along the ecliptic this would minimize the force of the solar wind on the spacecraft. The use of thrusters could compensate for the lost reaction wheel so that the pointing was good enough to continue exoplanet science.

The mission profile of K2 looks very reminiscent of the one for CoRoT. In each target field K2 observes about 10 000 stars for a maximum of about 75 days. This is about twice the number of stars, but for half the observing length of a typical CoRoT field. Figure V.3.1 shows the target fields for the proposed two year K2 mission. Currently, these are 10 fields well spread along the ecliptic. Also shown, for comparison, are the approximate location of the "eyes of CoRoT", regions of the sky that were accessed by CoRoT fields. Keep in mind, though, that one pointing of CoRoT covered approximately one-tenth of the sky of a K2 pointing.

Of particular interest is the fact that K2 fields cover some very important open clusters. Table V.3.1 lists some of the clusters that are in the K2 fields and their estimated ages. These range from a few Myr out to ~4 Gyr for M 67. CoRoT was only able to study one cluster, NGC 2264 (age ~1–4 Myr) in detail (Cody et al. 2014). The original Kepler field had four clusters (NGC 6866, NGC 6811, NGC 6819, and NGC 6791) that have ages >1 Gyr. K2 will thus greatly increase the number of open clusters observed by both CoRoT and Kepler. These clusters will provide important laboratories for a wide range of exoplanet and stellar science. These include:

- the evolution of planetary systems and star-planet interactions. Clusters of well known ages can probe the evolution of planets, hot Jupiters in this case. Young stars tend to be more active which enhances the chance of star-planet interactions.
- the evolution of stellar angular momentum. Angular momentum and its loss via the coupling between the star

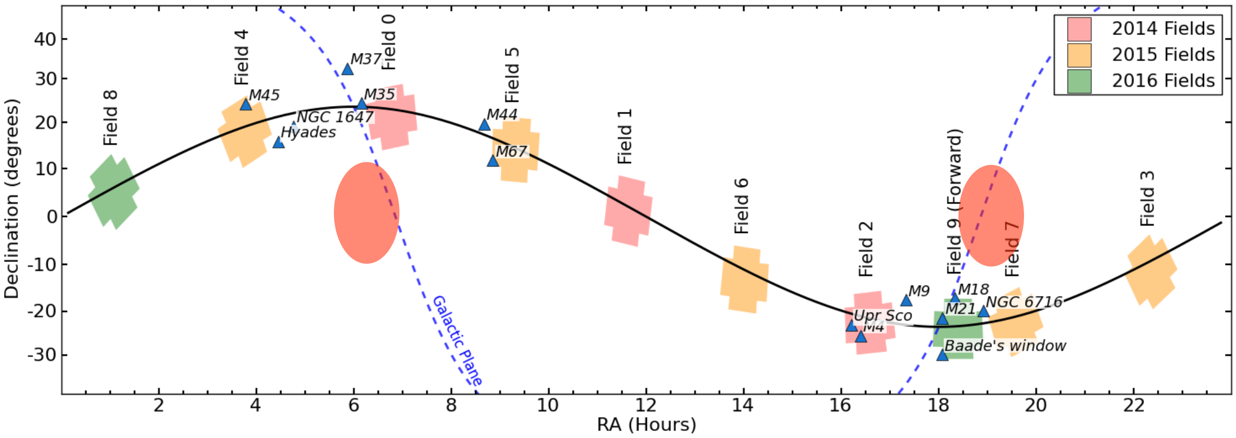

Fig. V.3.1. The designated fields for the 2-yr K2 mission as of October 2015. The red ovals mark approximately the eyes of CoRoT (from `www.keplerscience.arc.nasa.gov/K2/Fields.shtml`).

Table V.3.1. Open Clusters in the K2 Fields.

Cluster	Age
Messier 21	4–8 Myr
Messier 18	32 Myr
NGC 6716	100 Myr
Pleiades	125 Myr
Messier 35	110 Myr
Messier 37	520 Myr
Hyades	625 Myr
Praesepe	625 Myr
Messier 67	4 Gyr

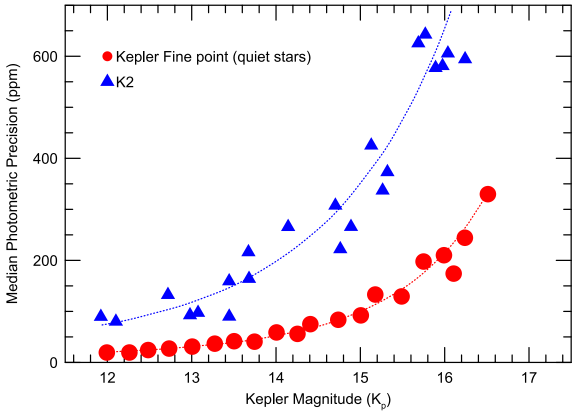

Fig. V.3.2. The photometric precision of K2 compared to Kepler with fine guiding. (Red dots) Kepler photometric precision for the quietest G-dwarfs. (Blue triangles) K2 photometric precision of targets covering a wide range of spectral types and intrinsic stellar variability. Source: NASA (`www.keplerscience.arc.nasa/K2`).

and the accretion disk is a driving force in the early evolution of young stars. This can be better understood by studying clusters with a wide range of ages.

- the evolution of stellar variability and magnetic activity. Ultra-precise stellar light curves enable us to study the magnetic structure of active stars as traced by cool starspots (e.g. Lanza et al. 2009; Fröhlich et al. 2009). K2 can study this as a function of stellar age.
- Asteroseismology of young stellar objects. Asteroseismolgy is the only means of checking the evolutionary status of young stars, probing the internal structure and comparing these to stellar evolutionary tracks (e.g. Zwintz et al. 2014).

Galactic populations will also be studied with K2 both in clusters and in the field. CoRoT and Kepler were able to map out parts of our Galaxy, but K2 will provide stellar masses, radii and ages of red giants over a wider coverage in the Milky Way. Combined with Gaia (see below) and large spectroscopic surveys (see also PLATO in Sect. 6 and references therein) these asteroseismic data will allow us to extend the range of the age-metallicity relations that was started with CoRoT and Kepler. K2 pointings also cover the star forming region Upper Scorpius stellar association with an age of ∼10 Myr. This may give us some early hints as to the early phases of the formation of planetary systems as well as to the occurrence of stellar pulsations in very unevolved stars.

To achieve these science objectives, K2 must demonstrate it can still acquire exquisite data. The dominant factor limiting the photometric precision of K2 is the low frequency motion of the space craft due to the solar wind and the firing of the thrusters which causes a drift of the targets across the detector pixels. In spite of these problems, the precision is quite good. Figure V.3.2 compares the photometric precision of K2 (triangles) to Kepler fine pointing (points) from quiet G-type stars, i.e. the best estimate of the true measurement error Kepler could achieve. We should note that the K2 targets have a wide range of spectral types and intrinsic variability which may be the source of much of the scatter.

The photometric precision of K2 is 50 parts per million (ppm) for 6.5 hours observation on a 12th magnitude G-type star. This is about a factor of four worse than the best Kepler could do with fine pointing. Overall over the full magnitude range $V = 12$–15, K2 has about four times the photometric error that Kepler could achieve on the quietest stars. As we learn more about the performance of the instrument, astronomers will have better tools for reducing K2 photometry. The photometric performance of K2 is bound to improve.

Despite the diminished pointing performance of K2 with respect to the original Kepler mission, it is capable

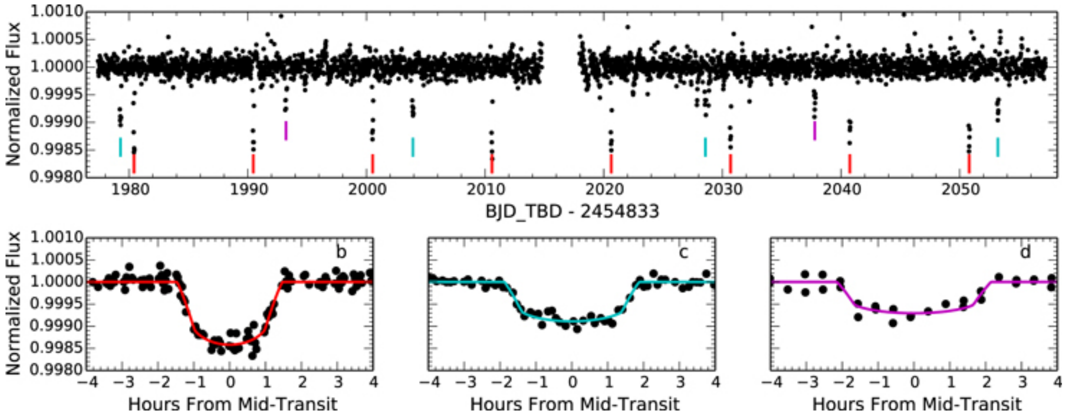

Fig. V.3.3. The K2 photometry of the M dwarf K2-3 (*top*) along with the phase folded light curves and transit fits (*bottom*) of the three transiting super-Earths (from Crossfield et al. 2015) © ApJ.

of ultra-precise photometry as demonstrated by its ability to still detect small transiting planets. Using K2 light curves, Crossfield et al. (2015) discovered three super-Earths around the M dwarf stars K2-3 (Fig. V.3.3). The transit depths were only 0.07–0.15% deep corresponding to planet radii of 1.5–2.1 $M_\oplus$. Orbital periods were 10–44 d. K2 clearly will continue to provide high quality exoplanet science, so long as the two remaining reaction wheels remain operational.

3. BRITE-Constellation

BRITE-Constellation is a group of 6 nanosatellites developed by the Space Flight Laboratory (SFL), Toronto, and devoted to precision photometry of the brightest stars in the sky in two colours (Weiss et al. 2014). The design requirement was an accuracy of at least 1 mmag per orbit for stars with $V \leq 3.5$ mag. However, depending on the individual satellite and observing conditions, also stars as faint as $V = 6$ mag have been observed with comparable accuracy. Frequency spectra with a noise level down to 0.1 mmag and up to 300 d^{-1} have been obtained for bright star data which cover nearly 6 months.

The Austrian BRITEs have been launched into a dusk-dawn orbit, the Polish BRITEs have a sun-synchronous orbit, and BRITE-Toronto a polar orbit with an annual drift of the ascending node of 40 min. These different orbits, a consequence of the required piggy-bag launches, put a severe work load on the mission scientist responsible for optimising the science output of BRITE-Constellation from the technical point of view. Each of the nanosatellites has a size of $20 \times 20 \times 20$ cm^3 and a weight close to 7 kg (Fig. V.3.4). Telecommunication is provided by ground stations in Graz, Toronto, Vancouver, and Warsaw.

The field-of-view is 24 deg × 20 deg and is monitored with a KAI-11002 CCD. An innovative aspect of the BRITE satellites is their 3-axes stabilisation to an accuracy of about 1.5 arcmin, which qualifies them as a pilot small-size space project in astrophysics. The filters were chosen with a central wavelength as different as possible, considering the spectral sensitivity of the CCD detector, and a band width resulting in comparable count rates for BRITE-Constellation main science targets. Figure V.3.5 shows a comparison of BRITE filters with standard photometric filters.

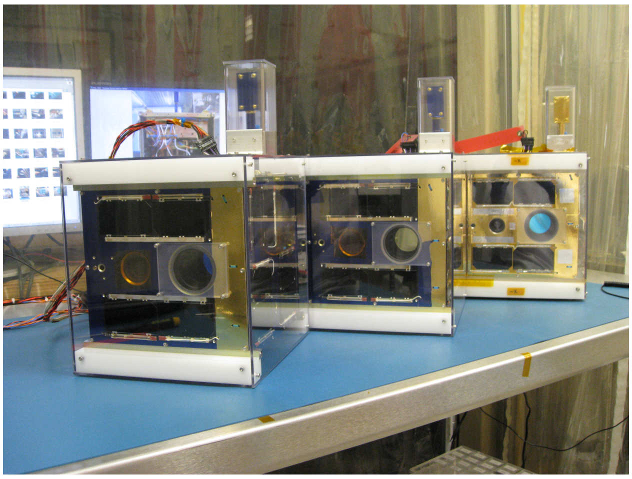

Fig. V.3.4. Three BRITE nanosatellites at SFL, ready for shipment © Space Flight Laboratory, University of Toronto.

Table V.3.2. BRITE-Constellation.

Name	F	Launcher	T0	Orbit km
Austria:				
TUGSAT-1	$\tilde{B}$	PSLV-C20	Feb. 2013	781 × 766
UniBRITE	$\tilde{R}$	PSLV-C20	Feb. 2013	781 × 766
Poland:				
B-Lem	$\tilde{B}$	DNEPR	Nov. 2013	600 × 900
B-Heweliusz	$\tilde{R}$	LM-4B	Aug. 2014	600 × 630
Canada:				
B-Toronto	$\tilde{R}$	DNEPR	Jun. 2014	620 × 770
B-Montréal	$\tilde{B}$	DNEPR	Jun. 2014	620 × 1450†

Notes. F – filter; Launcher (PSLV-C20 from India, DNEPR from Russia, and LM-4B from China); T0 – launch date; Orbit – km above ground; $^{(\dagger)}$ for reasons unknown, BRITE-Montréal did not release from the upper stage of DNEPR.

The “menu card” from which targets can be chosen for BRITE-Constellation is illustrated in Fig. V.3.6. Nearly the entire parameter space of the HRD is populated by stars brighter than $V = 4.5$ mag, and particularly all instability strips currently known, except of WDs and hot subdwarfs, are covered. The BRITE nanosatellites measure

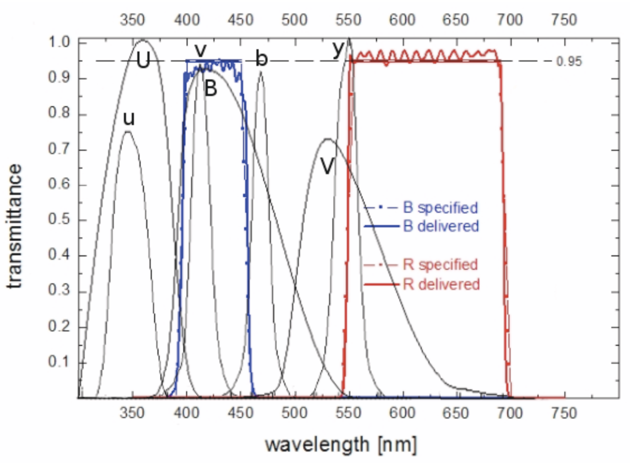

Fig. V.3.5. BRITE filters in comparison to those of the Johnson and Strömgren system.

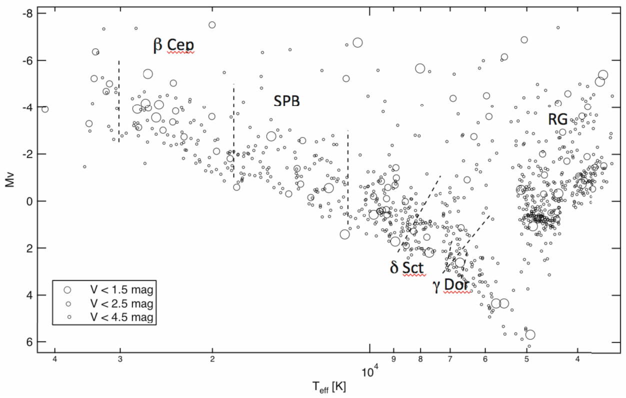

Fig. V.3.6. Hertzsprung-Russell diagram for stars brighter than $V = 4.5$ mag. This is the sample from which the primary BRITE-Constellation targets are drawn. See text for more details.

brightness and temperature variations of the brightest stars on timescales ranging from a few minutes to several months (and perhaps years) via dual-broadband photometry resulting in a continuous precise photometric timeseries.

Stellar groups with V down to 5.5 mag and that are of particular interest include OB (62 stars in Fig. V.3.6), β Cep (29), CP (22), Be (20), EB (12), δ Sct (7), HgMn (7), RR Lyr (3), roAp (1). However, the majority of stellar targets fall into two principal categories:

- *hot luminous H-burning stars.* These O- to F-type stars can contribute to solving outstanding problems such as the efficiencies of convection, mixing and overshooting in massive stars and the influence of rapid rotation on their structure and evolution.
- *cool luminous stars.* Asymptotic Giant Branch (AGB) stars, cool giants and cool supergiants can be used to measure the time scales involved in surface granulation and differential rotation which can constrain turbulent convection models. Though oscillations in solar-type dwarfs have amplitudes of only a few ppm in luminosity, p-mode pulsations in cool giants and g-modes in massive stars and cool giants can have larger amplitudes up to parts per thousand which can be detected by BRITE.

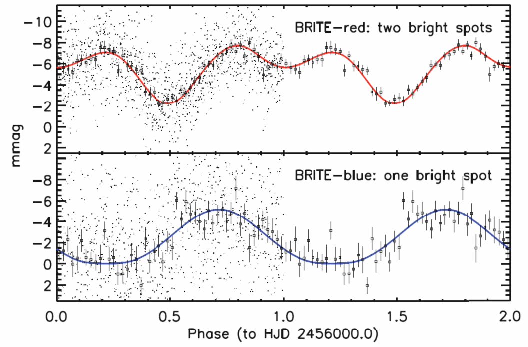

Fig. V.3.7. Rotation ($P_{\rm rot} = 4.4790^d$) of the roAp star α Cir, observed by the red-sensitive (*top*) and blue-sensitive (*bottom*) BRITEs. Phase-binned averages with 1σ errors are given together with the theoretical light curve obtained for a spot model. Phases 0 to 1 show also the phase-binned original BRITE data which latter are only 1-sec exposures, and three per minute.

Constant stars may also teach us much towards understanding stellar variability. BRITE will enlarge the base of stars measured to be constant (within low noise limits) which can serve as photometric standards for other studies.

Last, but not least, there is a chance that BRITE will detect transiting exoplanets (see Passegger 2013; Weiss et al. 2012). Because these transiting planets will occur among the brightest stars, these targets will be amenable to characterization studies of the exoplanet's atmosphere.

We highlight a few of the preliminary results of BRITE in order to illustrate the potential of nanosatellites in general and BRITE in particular. Figure V.3.7 shows the brightness variation of the rapidly oscillating Ap star α Cir ($V = 3.19$, spectral type = A7VpSiCrEu) due to inhomogeneities in its atmosphere (Weiss et al. 2016). This star was also observed at the beginning of the mission with a non-optimised set-up. The brightness varies with the rotational period of 4.48 d. The pulsational variations of 6.8 min have low amplitudes and are not evident in the figure.

HD 201433 is a peculiar B-type star (B9SiMg) that shows rotational modulated light variations with a period of 1.13 d (Catalano & Renson 1998). With a V-mag = 5.7 it is fainter than the typical BRITE targets. B-Toronto observed this star with the red filter (Fig. V.3.8) using a chopping technique implemented in 2015 in order to cope better with CCD radiation damage. We should note that this is a preliminary data reduction developed by R. Kuschnig as a quick operational check. A more refined data reduction should improve the quality of the light curve.

Mainly due to restrictions in telecommunication, BRITE-Constellation observes simultaneously up to 25 stars in its rather large field of view. Figure V.3.9 hows the target fields, as of Fall 2015, containing as many requested and scientifically relevant targets as possible. Targets that have already been observed are marked in red and these were typically observed continuously for up to 180 days.

Due to technical differences, such as star sensors, ageing effects of the CCDs, etc. the data quality depends on the satellite, the filter used and the colour index of a star. Optimisation of the science return of BRITE-Constellation has to take these limitations into account. Figure V.3.10 illustrates the median photometric standard deviation per orbit for stars with different brightnesses that were observed for 147 days during the Centaurus field run in 2014 before

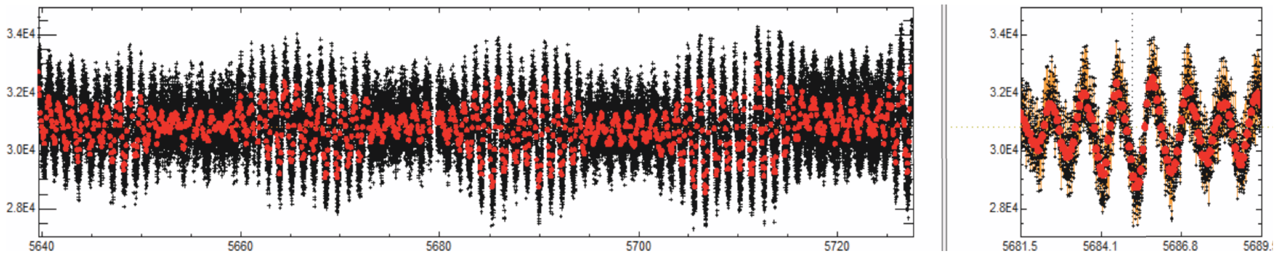

Fig. V.3.8. (*Left*) BRITE-red photometry of HD 201433 (B9V, $V = 5.7$) using a quick-look, preliminary data reduction developed by R. Kuschnig. (*Right*) Zoom into the center of the light curve.

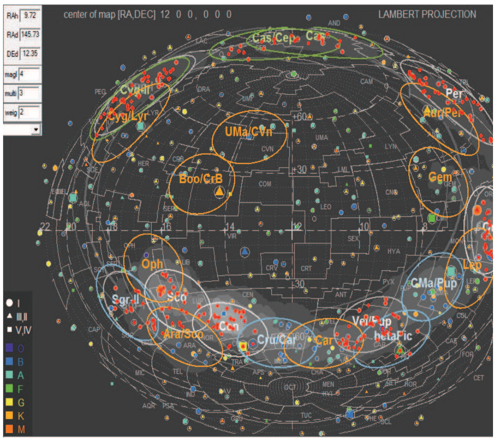

Fig. V.3.9. BRITE sky and target fields presently chosen.

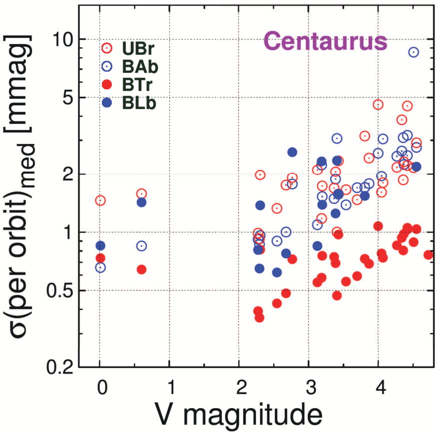

Fig. V.3.10. Median sigma-per-orbits are presented individually for the four BRITEs (TUGSAT-1 (BAb), UniBRITE (UBr), B-Lem (BLb) and B-Toronto (BTr), and for the stars observed in the Centaurus field before chopping has been introduced – Andrzej Pigulski and Adam Popowicz, private communication.

the introduction of chopping (i.e. changing the pointing of a BRITE between two fixed positions on the CCD for every second exposure).

After an observing run has been completed, the data are reduced with tools developed by PHOTT (BRITE Constellation's Photometry Tiger Team) and photometry of individual stars finally distributed to the respective proposers.

Additional information about technical details, programming policy and cooperating teams can be found at the Brite-Constellation website[1].

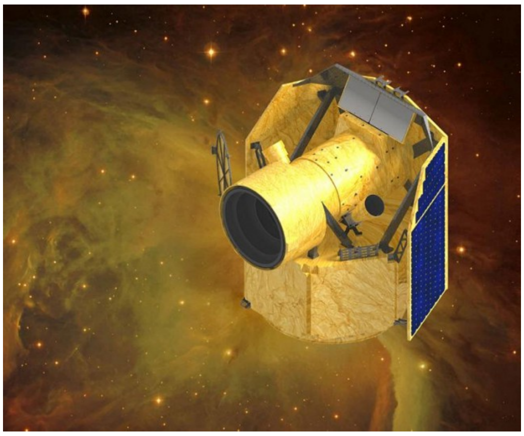

Fig. V.3.11. Artist's rendition of the CHEOPS spacecraft. © ESA.

4. CHEOPS

The first transiting planet, the gas giant HD 209458b (Charbonneau et al. 2000) was first discovered by radial velocity measurements and follow-up photometric measurements later detected the transit. Smaller planets are now relatively easy to detect with radial velocity measurements of bright stars. However, it is very difficult to get the requisite precision using ground-based observations in order to detect possible transits. For example, the RV-discovered transiting hot Neptune, 55 Cnc-e required the space based telescopes MOST (Winn et al. 2011) and *Spitzer* (Demory et al. 2011) to detect the transit. This demonstrated that it is sometimes worthwhile to invest space resources to search for a transit – you sometimes get lucky. However, such a strategy will not work for a large number of RV-detected planets. Space telescopes are general use facilities that are heavily over-subscribed. Time allocation committees may be reluctant to allocate precious telescope time on the ≈90% chance that a transit will not even occur due to an unfavorable orbital inclination. Clearly, a space telescope dedicated for these types of observations is needed and the CHaracterization ExOPlanet Satellite (CHEOPS, see Fig. V.3.11) will fill that role (Fortier et al. 2014).

CHEOPS is different from the CoRoT and Kepler space missions in that it is not an exoplanet discovery mission. Rather, it is dedicated to using ultra-precise photometric measurements to search for transits of bright stars known to host planets from radial velocity measurements. For short period planets there a 10% probability or greater that the planet has an orbital inclination to cause a transit. There will be a chance that CHEOPS will not observe a transit, but if it does, significant science will come out since these

---

[1] `http://www.brite-constellation.at`

events will be around relatively bright stars. Furthermore, the mass of the planet is already known from the radial velocity measurements.

CHEOPS is the first of the European Space Agency's (ESA) "small missions" and it is planned for launch in 2018. It will have a 32-cm on-axis Ritchey-Chretien telescope, i.e. roughly the size of the CoRoT telescope. However, because it is targeting single stars, CHEOPS will not have a wide field of view. A dedicated field stop and baffling system will minimize stray light since CHEOPS will be in a low-earth orbit. CHEOPS will build on the experience of CoRoT in terms of the baffling and field stop combination and the mission technology that was already used on CoRoT. Tests indicate that the stray light should be less than 10 ppm. CHEOPS will have a photometric precision of 150 ppm per minute for a $V = 9$ magnitude star

CHEOPS will exploit the fact that the predicted transit times of the planet should be known from the radial velocity orbit. Thus it must only look at the star for a short time, unlike a discovery mission which must collect data continuously over several months. Ground-based surveys are finding more and more low-mass planets in short period orbits, so there will be an ample list of targets for CHEOPS to look at.

The recent radial velocity discovery of the system of four low mass around the bright star ($V = 5.5$) HD 219134 from the HARPS-N Rocky Planet Search Program (Motalebi et al. 2015) demonstrates that CHEOPS will have a good chance of detecting transits around a modest number of RV-discovered exoplanets. The inner planet of HD 219134 orbits the star in 3.98 d. Spitzer observations detected a transit corresponding to a radius of 1.6 $R_\oplus$. A transiting super-Earth around such a bright star is an ideal target for atmospheric studies using in-transit spectroscopy or observations at the secondary eclipse of the planet. CHEOPS should increase the sample size of such interesting targets.

The key science goal of CHEOPS is to detect super-Earth and Neptune-sized objects around bright stars and determine the planetary radius. This, combined with the known planetary mass from radial velocity measurements means we can derive an accurate bulk density of the planet which can be compared to planetary structure models. Because CHEOPS is targeting relatively bright stars, the discovered transiting planets will be ideal for further spectroscopic studies from the ground and the James Webb Space Telescope (JWST) in order to characterize the exoplanetary atmosphere.

Another science aim of CHEOPS is to obtain ultra-precise transit light curves for discoveries made by TESS (see below). It can do so because CHEOPS will have a superior photometric accuracy due to its larger collecting area compared to TESS. CHEOPS will also provide more precise light curves for the Next-Generation Transit Survey (NGTS) that will also target smaller planets compared to previous ground-based transit surveys.

CHEOPS will also be able to do additional science with 20% open to the community through a competitive scientific review.

5. TESS

NASA's Transiting Exoplanet Survey Satellite (TESS) will search for exoplanets transiting bright, nearby stars and is scheduled for launch in 2017. TESS is unique to other space missions in terms of its orbit. It will have a highly elliptical orbit with a perigee of 17 R_{Earth} and an apogee of 59 R_{Earth}. The orbital period of 13.7 d period is in a 2:1 resonance with the lunar orbit. The orbit of TESS will be inclined with the respect to the ecliptic plane which will eliminate long eclipses by the Moon and the Earth. One advantage of this orbit compared to a low-earth polar orbit like that of CoRoT is that it will be above the radiation belts so the flux of high energy particles will be low. This should avoid the loss of data and discontinuities in the light curves caused by the high energy particles. This was often a problem for CoRoT light curves and these may have played a role in the loss of the DPUs.

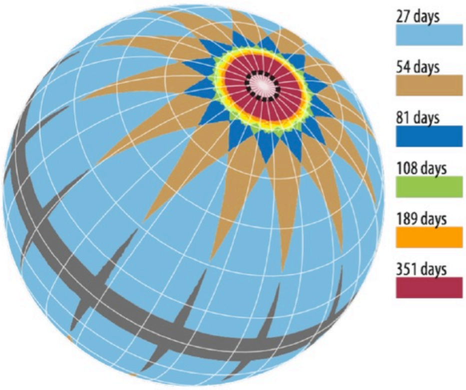

Fig. V.3.12. The duration of observations for TESS targets on the celestial sphere. The dashed black circle at the ecliptic pole represents the JWST continuous viewing zone. (From Ricker et al. 2014).

Since bright stars are distributed throughout the sky, TESS will be the first space-based all sky transit survey. TESS will employ four CCD cameras, each with an aperture of 10.5 cm that will cover an area of the sky 24 × 20 square degrees. Stars will be monitored for an interval of one month to one year depending on the star's ecliptic latitude. TESS will survey a total of about 200 000 main sequence stars. Figure V.3.12 shows the duration of TESS observations on the celestial sphere. The nominal life of the mission is two years.

The maximum orbital period for a planet that TESS can detect is about 10 d for most stars, but this can be more than 40 d for stars located at the ecliptic poles. Of course TESS will detect single transit events stemming from planets in longer orbits, but the period determination will not be possible. However, a rough estimate of the period will come from the transit duration and since TESS is targeting bright stars, such single transit candidates would be easily monitored by radial velocity measurements.

TESS should reach a precision of 200 ppm in one hour on a star with an I_C magnitude of 10. Saturation occurs for the central pixel at approximately $I_C = 7.5$. This is not necessarily the bright limit for TESS since the excess charge is spread over other CCD pixels and is thus conserved. High precision photometry for brighter targets can still be achieved so long as all the excess charge remains within the aperture. The expected brightness limit for TESS is therefore expected to be $I_C \approx 4$.

Ricker et al. (2014) estimated the expected planet yield of TESS using simulations that included: 1) a realistic

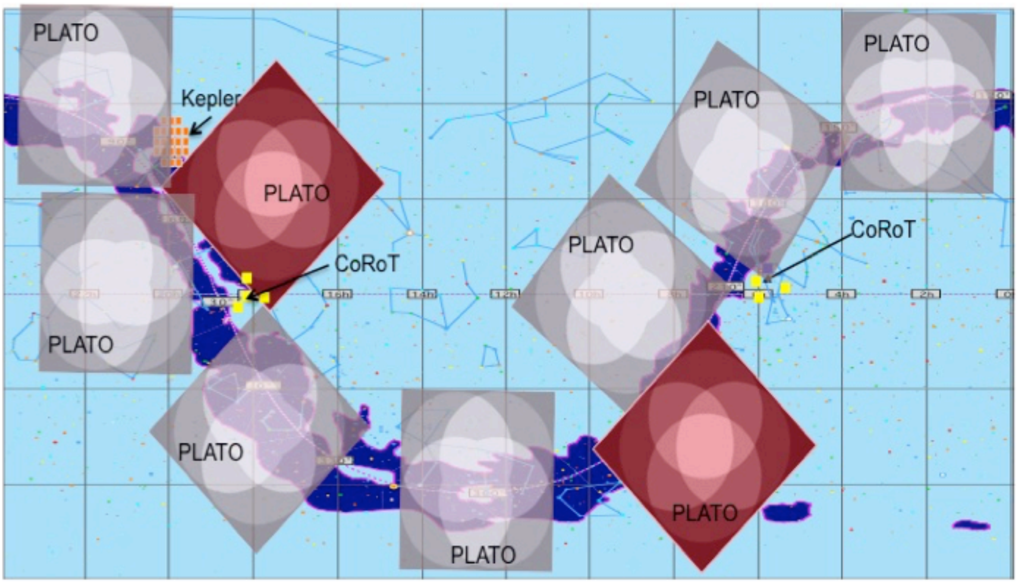

Fig. V.3.13. Schematic comparison of observing approaches. Large squares: approximate size of the PLATO 2.0 field. A combination of short (white squares) and long (red squares) duration pointings is able to cover a very large part of the sky (Rauer et al. 2014). Note that the final locations of long and step-and-stare fields will be defined after mission selection and are drawn here for illustration only. Yellow squares: CoRoT target fields in the galactic centre and anti-centre direction. *Upper left corner*: the Kepler target field.

distribution of stars and eclipsing binaries; 2) occurrence rates and orbital properties based on Kepler results; 3) variations in the background noise due to variations in the stellar surface density and zodiacal light; and 4) variations in the duration of TESS observations. TESS is expected to find thousands of Neptune-sized exoplanets, as well as hundreds of so-called super-Earths in the size range 1.25–2 $R_\oplus$. For Earth-sized planets, the yield is expected to be in the tens.

TESS will be able to perform asteroseismology on a fraction of the target stars, but not to the extent that the PLATO mission will (see below). Asteroseismic measurements are important as they provide accurate stellar parameters such as mass and radius which are important for deriving accurate planetary parameters. TESS is expected to be able to detect p-mode oscillations in about 6000 stars including

- Most stars brighter than $V = 7.5$;
- Approximately 75 stars with spectral types later than the Sun;
- About 2000 upper-main and subgiants;
- Virtually all giant stars.

A more detailed description of the TESS mission can be found in Ricker et al. (2014).

6. PLATO

6.1. Description of the mission

PLATO (PLAnetary Transits and Oscillations of stars) has been selected as ESA's M3 mission in the context of ESA's Cosmic Vision 2015–2025 program, with launch foreseen in 2024 (Rauer et al. 2014). PLATO's main goal is to detect extrasolar planets by photometric transits and to characterize their radius, mass and age. This will be done for a large number of planets in a variety of systems, including planets in the habitable zone of solar-like stars. The PLATO mission will characterize the bulk properties of planets with high accuracy. The goal is to achieve an accuracy of at least 3% for the planet radius and 10% in the planet mass and age for terrestrial planets orbiting a bright solar-like star.

In addition, PLATO core science will be complemented by a significant guest observer program investigating e.g. variable and pulsating stars, stars with mass loss, transient phenomena, and galactic science (see Sect. 6.5.2). With this combination of scientific goals, including exoplanet science in combination with asteroeismology, PLATO builds on the heritage of CoRoT in the European community.

The PLATO satellite will be launched by a Soyuz 2-1b rocket into an orbit around the L2 Lagrangian point. The nominal mission lifetime is 6.5 yr. A baseline observing scenario has been defined for the purpose of mission planning. It includes two "long pointings", staring at target fields for 3 and 2 yr, respectively (see Fig. V.3.13). This phase is followed by a "step-and-stare" phase of 2–5 months observation duration per target field. The long pointings enable PLATO to detect planets out to the habitable zone of solar-like stars. The short pointings widen the sky coverage and will obtain asteroseismic data on a variety of stars that are needed to improve stellar models. This is a pre-requisite to push further the accuracy of our knowledge of stellar parameters and thus planet parameters. The final observing sequence of PLATO will be fixed approximately two years before launch in order to optimize the strategy to the needs of the science community at that time.

The PLATO instrument consists of 34 telescopes with 12-cm aperture each. Of these, 32 telescopes are called "normal" telescopes and are arranged into 4 groups of 8 telescopes each. To widen the area on the sky surveyed for exoplanets, these "normal" telescopes are offset from each other by 9.2° thus providing a total field-of-view of about 2100 square degrees. All "normal" telescopes operate in white light. The telescopes consist of 6 lenses mounted in a tube and protected by a baffle from straylight. The focal plane of each camera consists of 4 CCD detectors with 4510 × 4510 pixels and a plate scale of 15 arcsec per pixel. For the "normal" cameras, these detectors provide a light curve sampling of 25 s for the bright target sample. "Imagettes" are masks around each target star in which the data are readout and sent to the ground for processing. For the larger statistical sample, these lightc urves are processed on board and they will be binned to 600 s time resolution. Two additional so-called "fast" cameras are identical telescopes except that their read-out speed is higher (2.5 s) to support the fine-guidance of the satellite. Furthermore, the "fast" telescopes will be equipped with a red and a blue filter, respectively, to aid in the asteroseismic investigation of variable stars.

Although both are transit search missions, we should note that PLATO differs from TESS in two key points. First, PLATO's pointings will be significantly longer than TESS. This will enable the characterization of transiting rocky planets out to the habitable zone of a solar-like star. It also will find much smaller close-in planets than TESS. Second, PLATO will perform accurate asteroseismic measurements for a significantly larger number of stars than TESS. To reach the required precision in planet radius and mass, it is essential to derive the properties of their host stars with sufficient accuracy. Furthermore, ages of exoplanetary systems can only be derived from the age of their host star. The PLATO core program will therefore combine the detection of photometric transits with asteroseismic analyses of the host stars in order to obtain their precise characterization (see below).

6.2. Exoplanet detection with PLATO

While planetary radii can be derived directly from the satellite photometric light curves, the determination of planet masses requires an extensive ground-based observational follow-up program to measure the radial-velocity (RV) component of the host stars. RV measurements are very time consuming and these stress the available ground-based telescope resources. This is particularly true for small planets which have a small RV amplitude. Realistically, RV measurements on a large scale can only be performed for planets orbiting bright stars. The main target sample of PLATO will therefore focus on stars <11 mag.

To reach the required precision for asteroseismology characterization, a high S/N ratio is needed. The main PLATO target sample will therefore reach 34 ppm in 1 hour for stars <11 mag. This goal can be reached for about 85 000 stars, with 20 000 of them in the two long-pointings. For planets orbiting these stars, the full characterization in terms of accurate radii, masses and ages can be obtained. In addition, PLATO will observe more than 245 000 stars (up to 1 million when we include the step-and-stare phase) with <13 mag. This large sample is still bright enough even to detect a large number of small planets, but it will not allow for RV and asteroseismic measurements. It will therefore be of comparable performance to most of the stellar samples surveyed by Kepler and CoRoT. It will add to the statistical information on planet candidates, increase our understanding of planet formation as a function of location in galaxy, provide inputs to TTV searches, and last but not least it will enable a wide range of additional science.

PLATO will be able to detect transits of thousands of planets in its stellar samples. For more than 100 of the planets detected in the bright stellar sample, highly accurate radii can be combined with accurate masses and ages, including terrestrial planets in the habitable zone of solar-like stars. This estimate assumes resources for ground-based follow-up comparable to those provided by a so-called "large program" at ESO. The resulting sample of terrestrial planets with highly accurate radii, masses and ages at orbital periods beyond 3 months will be a unique contribution of PLATO. Furthermore, many of the well-characterized PLATO planets orbiting bright stars and are key targets for investigations of their atmospheres, e.g. with JWST (see below), or by a dedicated future exoplanet spectroscopy satellite.

The PLATO legacy, that is the final data base of its light curves and derived stellar and planetary parameters, will provide a huge opportunity for science beyond the mission lifetime of PLATO. Together with data from the Gaia satellite, PLATO will provide a wealth of data for stellar science. Also the number of characterized planets from PLATO will increase with time, as teams continue to measure RV data of PLATO planets long after the satellite has stopped operating.

6.3. Asteroseismology with PLATO

The main goals of PLATO asteroseismology program will be to provide precise global parameters of stars hosting planets. This is an accuracy of at most 10% for the stellar mass, 2% for the stellar radius and 10% for the stellar age. Stellar radii will be directly obtained from the combination of effective temperatures (from ground-based high resolution spectroscopy follow-up program and Gaia) and absolute luminosities (from Gaia distance measurements). Asteroseismology then will provide the stellar mean density through the scaling relations, which leads to the precise determination of the stellar mass. The determination of mass and radius is thus essentially independent of stellar modeling.

Ages, on the contrary, require theoretical stellar models in order to fit the observed parameters. This process is thus highly dependent on the physical assumptions used in the model computation. This clearly shows that a better understanding of the physical processes involved in stellar evolution is a key factor to a better knowledge of the planet properties. In particular, the presence of an extra-mixed zone surrounding the convective core in low-mass stars is still a highly debatable question, which involves our poor knowledge (and/or poor numerical treatment) of rotation, convective penetration and convective overshooting. It is, however, of crucial importance since it drastically affects the duration of core hydrogen burning and thus ages of stars.

This important aspect of the interaction of planet finding and host star characterization will benefit from the asterosesimic analyses of a large number of stars of various masses, chemical composition, and ages. This will bring constraints on stellar interiors and more widely, to our understanding of stellar evolution. For that purpose, large

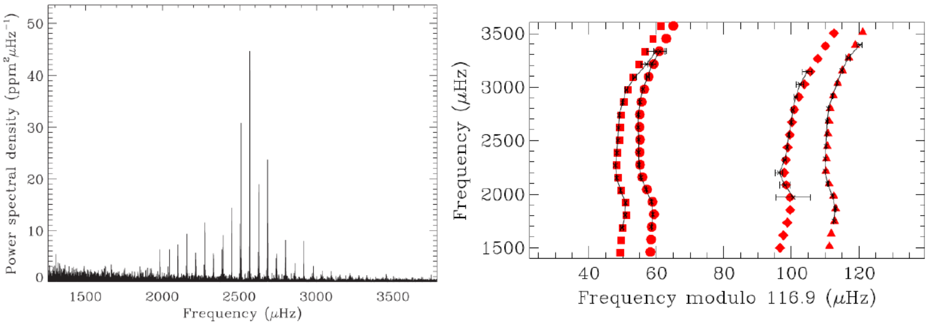

Fig. V.3.14. (*Left*) The p-mode oscillation spectrum of 16 Cyg B derived from three months of Kepler photometry (from Metcalfe et al. 2012). (*Right*)) The Echelle diagram of 16 Cyg B based on the full Kepler time series (from Metcalfe et al. 2015) © ApJ.

grids of stellar models including wide ranges of physical parameters will be used. From a combination of asteroseismic and classical observable constraints, a precision of the order of 10% on the age will be within reach.

6.4. Comparative planetology with PLATO

By combining the asteroseismic data along with the transit results (transit depth, RV orbital curve, etc.) PLATO will enable us to perform comparative exo-planetology to a higher accuracy than is currently available and for a large number of stars. As an example that demonstrates the potential of PLATO we consider the case of Kepler-78b. This is the only Earth-size planet whose mass has been determined via RV measurements. Kepler light curves reveal a planet with a radius of 1.16 ± 0.19 $R_\odot$ in an 8.5 hr orbit (Sanchis-Ojeda et al. 2013). Radial velocity measurements yield a planet mass of 1.69–1.76 $M_\odot$ (Howard et al. 2013; Pepe et al. 2013). This results in an Earth-like density of $\approx$5.5 gm cm^{-3}. However, the planet can have a density as high as 7.9 gm cm^{-3} (Grunblatt et al. 2015) or as low as 2.5 gm cm^{-3} (Hatzes 2014). The difficulty in determining the structure of Kepler-78 b can be traced to the challenge in obtaining precise RV measurements on such a faint target ($V = 11.72$) and the poor knowledge of the stellar parameters.

Figures V.3.14 and V.3.15 demonstrates how PLATO can improve things by providing asteroseismic stellar parameters, and target stars more amenable to precise RVs. The left panel of Fig. V.3.14 shows the p-mode power spectrum of the planet hosting star 16 Cyg B derived from the first 3 months of Kepler photometry (Metcalfe et al. 2012). The right panel shows the so-called Echelle diagram using the full Kepler data set (Metcalfe et al. 2015). These data give a taste of what PLATO could obtain on its brighter targets. Astrometric modeling of the Echelle diagram by Metcalfe et al. (2015) yields a stellar radius of $R = 1.229 \pm 0.008$ $R_\odot$ (0.65% error) and stellar mass of $M = 1.08 \pm 0.02$ $M_\odot$ (1.85% error).

Figure V.3.15 shows the location of an Earth-like planet (i.e. Kepler-78b-like) in the density versus radius diagram. The tracks show the structure for planets that are Earth-like: iron-core and silicate mantel, Mercury-like: large iron core and thin silicate mantel, and Moon-like: large silicate mantel with small iron core. The error box (large red dotted parallelogram) shows the nominal error based on the errors of the pertinent parameters to Kepler-78b (Sanchis-Ojeda et al. 2013; Grunblatt et al. 2015). Note that Kepler-78 is fainter compared to the core targets of PLATO. The error box is so large that we could not distinguish between the possible structure tracks for this hypothetical short-period planet.

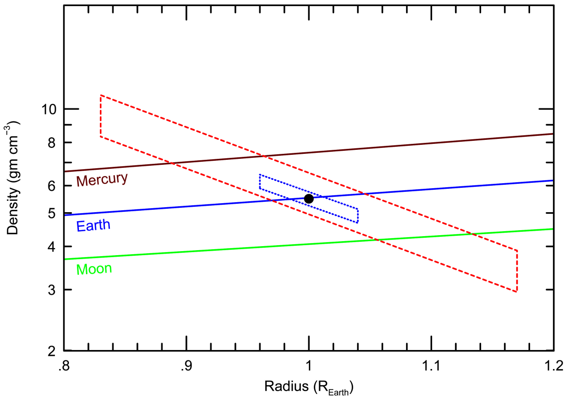

Fig. V.3.15. The density versus radius tracks for planets with a Mercury-like, Earth-like, and Moon-like internal structures. The large red-dashed square shows the error box we would currently have for a Kepler-78-like planet with the radius and density of the Earth (dot). The small blue-dotted box shows the error box we could obtain for a PLATO target,

The smaller blue dotted parallelogram shows the error box assuming that we can derive seismic values for the stellar radius and mass with an accuracy comparable to 16 Cyg B. Since PLATO is targeting stars brighter ($V < 11$ mag) than Kepler-78b, we should be able to achieve a better precision on the velocity amplitude of the host star about the barycenter (3% compared to 15 %). Largely because of the improved accuracy on the stellar parameters and better quality RV measurements we could be able to determine whether such a hypothetical short-period planet has an internal structure like the Earth, Mercury, or the Moon. With current measurements we only would know that an exoplanet like Kepler-78b was a terrestrial planet, but with PLATO we would know what *kind* of terrestrial planet it is. PLATO, because of its use asteroseismology, will enable us truly to perform comparative exo-planetology.

6.5. Complementary program of stellar physics

One major advantage of PLATO over CoRoT and Kepler is its large sky covering, including not only stars in different parts of the Galaxy, but also stellar ensembles, such as binaries and clusters. Stellar physics as well as galactic physics will greatly benefit from such unprecedented investigation. Some examples are given below (see also Rauer 2014).

6.5.1. Stellar structure and evolution

PLATO will be able to investigate several important aspects of stellar structure and evolution.

a) Extra-mixing and chemical profile in stars

Asteroseismology of red giants observed by CoRoT and Kepler have proven to be extraordinary rich in providing constraints on their global properties. Moreover the presence of gravity-dominated modes (from more than 300 days of Kepler data) and the analysis of their period spacings led to the possibility of discriminating between red giants ascending the red giant branch and those quietly burning helium in the so-called red-clump phase (Bedding et al. 2011; Mosser et al. 2012). This additionally brought some unexpected strong constraints on the extent of mixing zones during core helium burning as well as during core hydrogen burning (Montalbán et al. 2013).

Slowly pulsating B (SPB) stars show a frequency spectrum consisting mostly of high-order gravity modes. Their period spacing should therefore be constant, at least for Zero Age Main Sequence (ZAMS) chemically homogeneous models. Once a hydrogen profile develops as a result of the decrease with time of the convective core mass, a periodic component superposes on the constant period spacing. This has indeed been observed in one SPB star (Degroote 2010).

The extent of the mixed core in main sequence massive stars plays a key role in the presence of an intermediate convection zone (ICZ) in post-MS blue supergiants. If the mixed zone is too large, no ICZ can develop at all. Such an ICZ is however essential to allow the excitation of g-modes (detected by MOST in one blue supergiant) in these highly centrally condensed stars (Saio 2006; Godart et al. 2009; Moravveji et al. 2012).

Hot B subdwarfs (sdB) and white dwarfs present frequency spectra that are also very sensitive to their chemical profiles. These are not attainable through direct observations and still poorly constrained by theory. Asteroseismology is thus the only reliable tool to understand better the structure of these stars.

The detailed frequency spectrum of a huge number of such stars of very different types that will be observed by PLATO can thus bring invaluable constraints on the mixing processes affecting the chemical profile in stars and thus their lifetimes.

b) Angular momentum transport

An important question in stellar modeling is the internal rotation profile as a function of the evolutionary phase. From Kepler data, it has been possible to estimate the rotation frequency difference between the core and the envelope in red giants (Beck et al. 2012) and to show that an important angular momentum coupling between core and envelope was absent from stellar modeling (Eggenberger et al. 2012; Marques et al. 2013). A possible clue to this problem could be brought by internal gravity waves, which could transport angular momentum and affect the rotation profile (Shiode et al. 2013).

This very important aspect of stellar evolution, which requires a precise determination of rotational splittings in the frequency spectra, is well within the reach of PLATO.

c) Probing stellar evolution with clusters

The possibility offered by PLATO to observe young open clusters as well as globular clusters is an invaluable gift to stellar evolution. Young open clusters will provide pre-main sequence stars as well as pre-supernova massive objects while globular clusters will bring their amount of MS, red giants and white dwarf stars to this work. Asteroseismic analyses of all these targets will undoubtedly and drastically increase our knowledge of stellar evolution.

6.5.2. Structure and evolution of our Galaxy

The chemical enrichment of our Galaxy has left its imprint in the distribution of stars of different masses, ages, and chemical composition. The key point in drawing a reliable picture of these imprints is our ability to measure distances and ages for stars at different directions and locations in the Galaxy.

One of the greatest successes of the CoRoT mission came from the realization that asteroseismic analyses of red giants could indeed provide a powerful tool to study this enrichment. Masses and radii of red giants are direct outputs of the scaling relations while their period spacings allow us to specify their evolution state, either ascending the red giant branch, or burning helium in the red clump.

With the additional knowledge of the effective temperature and of the chemical composition, intrinsic luminosities, and hence distances, and ages can be readily determined, with a 15% uncertainty for the ages (Miglio 2012, 2013). Data from thousands of red giants taken by the limited pointings of CoRoT and Kepler have already been used to draw a partial 3D map of our Galaxy (see Fig. V.3.16). The first hints at a new age-metalicity relation are starting to appear which could help discriminating between different scenarios for the formation of our Galaxy (Chiappini 2006).

To reach these objectives, spectroscopic analyses of huge numbers of stars are required. In particular metalicity is crucial not only in the stellar modeling, but also for the asteroseismic determination of stellar masses and ages. This is at the origin of a large collaboration involving scientists working on the Milky Way, stellar evolution, and asteroseismology with those specialists involved in large spectroscopic surveys. These include the Gaia-ESO Survey (GES), the Apache Point Observatory Galactic Evolution Experiment (APOGEE) and the Galactic Archaeology with Hermes Survey (GALAH).

The large number of red giants that PLATO will observe will result in a nearly complete mapping of the chemical gradient of our galaxy. This may open a new view on its evolution.

7. Other missions

There are two other important space missions worth mentioning, Gaia and the James Webb Space Telescope (JWST). Although these missions do not strictly build on the legacy of CoRoT in terms of taking long time series of

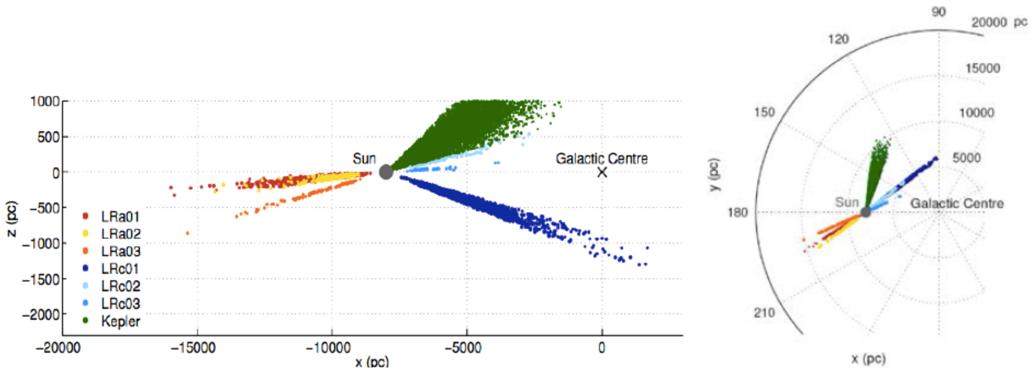

Fig. V.3.16. Spatial distribution of the red giants with asteroseismic characterization observed by CoRoT (six long runs color coded in the graph) and by Kepler (green points). The left panel shows a projection on the x-z plane and the right panel, a projection on the galactic plane. From Miglio et al. (2012).

ultra-precise photometric measurements, they are still important both for exoplanets and stellar physics. In particular, TESS and PLATO will provide important exoplanet targets for JWST.

7.1. Gaia

Gaia is an astrometric mission that is the successor to the Hipparcos mission. It uses the same measurement principles developed with the highly successful earlier mission. Gaia was launched in December 2013 and it began routine observations in August 2014. Gaia's scientific goal is to measure the distances, positions, and space motions of $\sim 10^9$ stars in our Galaxy.

Gaia has an astrometric accuracy that depends on the brightness stars. For bright stars with $V \approx$ 7–12 the astrometric accuracy is $\sim$10 μas and degrades to 20–25 μas for stars at $V \approx 15$. For the faintest stars at $V \approx 20$ the astrometric accuracy should still be 300 μas, significantly better than the $\approx$1000 μm precision Hipparcos achieved on much brighter targets.

Gaia's foremost contribution to stellar physics is that it will obtain a detailed three-dimensional distribution of stars in the Milky Way. This will help us understand its current dynamics, formation, and evolutionary history. Asteroseismic studies will add accurate ages for stars to this study. However, to fully understand the structure and evolution of our Galaxy, we must know the stars' location in the Milky Way and Gaia will provide these.

Besides stellar distances and proper motions Gaia will also provide stellar surface temperatures and RV measurements for a large number of stars. The RV precision varies from 1 $\mathrm{km\,s^{-1}}$ to 15 $\mathrm{km\,s^{-1}}$ depending on the brightness of the star. Stellar radii can be derived by combining the distances, absolute luminosities and stellar temperatures.

Gaia will also have an impact on exoplanet science. One significant contribution of Gaia to exoplanets is that it will be able to derive the true mass of the radial velocity discovered planets. For these only a minimum mass is derived since an orbital solution only yields the mass multiplied by the sine of the orbital inclination. Gaia's astrometric measurements will give of us the orbital inclination and thus true mass of most of the exoplanets discovered by the radial velocity method.

Gaia will also discover a large number of giant planets. Perryman et al. (2014) made an assessment of this number using the estimates of planet occurrence and the current performance of Gaia. They estimate that almost 17 000 planets will be detected around host stars with r-magnitude <17.5. The detected masses will be in the range of 0.12–15 M_{Jup} and the orbital semi-major axes, a, in the range 0.037–6.87 AU. Thus Gaia will fill an important region of the exoplanet mass versus semi-major axis parameter space that is not covered by transit search missions.

A significant fraction of these will be in multiple systems. Casertano et al. (2008) estimate that $\sim$1000 multiple-planet systems will be detected and measured by Gaia. Astrometric measurements of the giant planet υ And c made with the Fine Guidance Sensor of the Hubble Space Telescopes indicate a mutual inclination of the two planets of 30° (McArthur et al. 2010). It will be of interest to see how frequent such misaligned systems are. Gaia should be able to perform co-planarity tests of $\sim$150 systems (Casertano et al. 2008).

7.2. The James Webb Space Telescope

JWST is the successor to the Hubble Space Telescope (HST). With a mirror diameter of 6.5 m, it will be the largest astronomical reflecting telescope flown in space. It will orbit at the L2 Lagrange point where continuous observations are possible without significant blocking of the Earth. It is scheduled for launch in late 2018. The design is for a 5-yr mission life, but with a goal of 10 yr.

JWST will play a significant role in the characterization of exoplanetary atmospheres. Owing to its large aperture, it is supremely suited for studying the absorbed light of transiting exoplanets during the primary (in-transit spectroscopy), or the radiated light near secondary eclipse (Clampin et al. 2009). JWST will observe at wavelengths of 0.6–28.5 μ. This is in contrast to the 0.1–2.5 μ wavelength range of HST which had one-seventh of the collecting area of JWST.

There are several instruments that are particularly important for atmospheric studies of transiting planets. The Near InfraRed Camera (NIRCam) will provide photometric capabilities and low resolution spectroscopy. Pick-off optics separate the light into a short (0.6–2.3 μm) and a long (2.4–5.0 μm) wavelength path. NIRCam has a grism in the long wavelength channel that will provide spectroscopy at a resolving power, $R = \lambda/\delta\lambda \sim 2000$.

The Near InfraRed Spectrograph (NIRSpec) will operate in the wavelength range 0.6–5.0 μm and is ideally suited for measuring the transmission spectroscopy of an exoplanet during the transit. A prism will provide low resolution ($R = 100$) over 0.7–5.0 μm. Three gratings will cover the 1–5 μm at $R = 1000$, and another three the same wavelength band, but at higher resolution ($R = 2700$).

The Mid-Infrared Instrument (MIRI, Wright et al. 2004) will provide a wealth of information for exoplanet occultations (secondary eclipse). The instrument covers the wavelength range 5–28 μm where the occultation contrast is maximized. MIRI will provide direct imaging capabilities for producing a mid-IR secondary eclipse light curve as well as slitless low resolution spectroscopy at $R \sim 100$. Medium resolution spectroscopy ($R = 3000$) is possible in four spectral regions: 4.96–7.77 μm, 7.71–11.90 μm, 11.90–18.35 μm, and 18.35–28.30 μm.

Deming et al. (2009) investigated the capabilities of JWST for the characterization of exoplanet atmospheres using the predicted sensitivities of the respective instruments. JWST instrumentation can be used to detect the spectra of super-Earths and such features such as carbon dioxide as well as the secondary eclipse of of exo-Neptunes.

JWST will be able to perform follow-up studies of the TESS discoveries. If it achieves its goal of a 10-yr mission life, then it should be able to perform atmospheric studies of the first PLATO discoveries.

8. Summary

The next 10–20 yr promises to be exciting times for exoplanet science, astroseismology, and stellar astrophysics. At the end of the future missions described here we will have light curves for well over one million stars using ultra-high precision space-based photometry. We can anticipate tens of thousands of new planets and transiting systems. We will also have astroseismic data for tens of thousands of stars and measurements of the stellar rotation periods and activity cycles for countless others. And of course, we will find new phenomena. For the discovered exoplanets a significant fraction of these will be around relatively bright stars which means, we will have accurate planetary radii, masses, and bulk densities.

PLATO will build on the CoRoT experience and exploit synergy of stellar and exoplanetary science. Using accurate bulk parameters of planetary mass, radius, and bulk density which is only possible because of the use of asteroseismic tools, scientists will be able to perform accurate comparative exo-planetology. This will give us a better understanding of diversity of planet densities and thus internal structures of exoplanets as a function of stellar mass, orbital distances, and planetary age. Thanks to its complementary program, PLATO will increase our understanding of stellar structure and evolution, essentially in constraining still poorly understood transport processes. With thousands of red giants observed in a wide galactic covering, it will also be in the front row of a new vision of the evolution of our Galaxy.

Spectral features have been detected in the atmospheres of only a handful of exoplanets. This will change with the discoveries from TESS and PLATO and the launch of JWST. The rough chemical composition, atmospheric temperature profile, and possible cloud features, etc. will be known for many explanets down to the super-Earth range ($R = 2$–$4\ R_\oplus$, $M = 2$–$5\ M_\oplus$).

We have only discussed the approved space missions at the time of this writing. A mission dedicated to the study of the atmospheres of transiting planets, Ariel, has been proposed as an M-class mission to ESA. Although it will have a smaller aperture (1.1-m) compared to JWST, all the telescope time will be dedicated to transit studies. This is unlike JWST where the exoplanet scientists will have to compete with the rest of the astronomical community for the precious telescope time. Not so for a mission like Ariel. The number of exoplanets for which we have characterized their atmospheres may well go from the tens to hundreds.

The Gaia mission will provide us with a better understanding of the structure and evolution of our Galaxy, but this requires accurate measurements of stellar ages. This can only come from asteroseismic measurements that will be provided by PLATO.

In short the next 10–15 yr promises to be an exciting journey for exoplanet and stellar researchers. One can well argue that CoRoT marked the start of this wonderful journey.

References

Beck, P. G., Montalbán, J., Kallinger, Th., et al. 2012, Nature, 481, 55

Batalha, N. M., Borucki, W. J., Bryson, S. T., et al. 2011, 729, 27

Bedding, T. R., Mosser, B., Huber, D., et al. 2011, Nature, 471, 608

Breger, M. 1995, DSSN, 9, 14

Breger, M., Handler, G., Nather, R. E., et al. 1995, A&A, 297, 473

Casertano, S., Lattanzi, M. G., Sozzetti, A., et al. 2008, A&A, 482, 699

Catalano, F. A., & Renson, P. 1998, A&AS, 127, 421

Charbonneau, D., Brown, T. M., Latham. D., & Mayor, M. 2000, ApJ, 529, 45

Chiappini, C. 2006, in Abundances and Mixing in Stars in the Milky Way and its Satellites, ESO Astrophysics Symposia, Berlin, Springer, 358

Clampin, M. 2009, Astro2010: The Astronomy and Astrophysics Decadal Survey, Science White Papers, 46

Cody, A. M., Stauffer, J., Baglin, A., et al. 2014, AJ, 147, 82

Crossfield, I. J. M., Petigura, E., Schlieder, J. E., et al. 2015, ApJ, 804, 10

Degroote, P. 2010, Ph.D. Thesis, Katholieke Universiteit Leuven

Deming, D., Seager, S., Winn, J., et al. 2009, PASP, 121, 952

Demory, B.-O., Gillon, M., Deming, D., et al. 2011, A&A, 533, 114

De Ridder, J., Barban, C., Baudin, F., et al. 2009, Nature, 459, 398

Eggenberger, P., Montalbán, J., & Miglio, A. 2012, A&A, 544, 4

Escobar, M. E., Théado, S., Vauclair, S., et al. 2012, A&A, 543, 96

Fortier, A., Beck, T. Benx, W., et al. 2014, SPIE, 9143, 2J

Fröhlich, H.-E., Kükor, M., Hatzes, A. P., & Strassmeier, K. G. 2009, A&A, 506, 263

Gandolfi, D., Parviainen. J., Deeg. H. J., et al. 2015, A&A, 576, A11

Godart, M., Noels, A., Dupret, M.-A., & Lebreton. Y. 2009, MNRAS, 296, 1833

Grunblatt, S. K., Howard, A. W., & Haywood, R. D. 2015, 808, 127

Hatzes, A. P. 2014, A&A, 2014, 568, 84

Howard, A., Sanchis-Ojeda, R., Marcy, G. W., et al. 2013, Nature, 5-3, 381

Lanza, A. F., Pagano, I., Letto, G., et al. 2009, A&A, 493, 193

Marques, J. P., Goupil, M. J., & Lebreton, Y. 2013, A&A, 549, 74

McArthur, B. E., Benedicte, G. F., Barnes, R., et al. 2010, ApJ, 715, 1203

Metcalfe, T. S., Chaplin, W. J., Appourchaux, T., et al. 2012, ApJ, 748, 10

Metcalfe, T. S., Creevey, O. L., & Davies, G. R. 2015, ApJ, 811, 37

Miglio, A. 2012, Astrophysics and Space Science Proceedings, 26, 11

Miglio, A., Morel, T., Barbieri, M., et al. 2012, in European Physical Journal Web of Conferences, 19, 05012

Miglio, A., Chiappini, C., Morel, T., et al. 2013, MNRAS, 429, 423

Montalbán, J., Miglio, A., Noels, A., et al. 2013, ApJ, 766, 118

Moravveji, E., Moya, A., & Guinan, E. F. 2012, ApJ, 749, 74

Mosser, B., Elsworth, Y., Hekker, S., et al. 2012, A&A, 537, 30

Motalebi, F., Udry, S., Gillon, M., et al. 2015, A&A, In press

Passegger, V. M. 2013 The probability of finding planets with Brite-Constellation, Master Thesis, University of Vienna, Faculty of Earth Sciences, Geography and Astronomy

Pepe, F., Cameron, A. C., Latham, D., et al. 2013, Nature, 503, 377

Perryman, M., Hartman, J., Bakos, G. A., & Lindegren, L. 2014, ApJ, 797, 14

Poretti, E., Michel, E., Garrido, R., et al. 2009, A&A, 506, 85

Rauer, H., Catala, C., & Aerts, C. 2014, Exper. Astron., 38, 249

Ricker, G. R., Winn, J. N., Vanderspek, R., et al. 2014, Proc. SPIE, 9143, 20

Sanchis-Ojeda, R., Rappaport, S., Winn, J. N., et al. 2013, ApJ, 54, 9

Saio, H. 2006, MmSAI, 77, 393

Shiode, J. H., Quataert, E., Cantiello, M., & Bildsten, L. 2013, MNRAS, 430, 1736

Weiss, W. W., Passegger, V. M., & Rowe, J. 2012 IAU Symp. 293 Proceedings [arXiv:1211.5439]

Weiss, W.W., Fröhlich H.-E., Pigulski A., et al. 2016, A&A, 588, A54

Winn, J. N., Matthews, J. M., Dawson. R. I., et al. 2011, ApJ, 737, 18

Wright, G. S., Ricke, G., Colina, L., et al. 2004, Proc. SPIE, 5847, 653

Zwintz, K., Fossati, L., Ryabchikova, T., et al. 2014, Science, 345, 550

Acknowledgements: The CoRoT space mission has been developed and operated by CNES, with the contribution of Austria, Belgium, Brazil, ESA, Germany, and Spain.